Characterization of the Behaviors of Amphiphilic Bacterial Signaling Molecules in Solution and at Interfaces of Soft Materials

By

Curran G. Gahan

A dissertation submitted in partial fulfillment of

the requirements for the degree of

Doctor of Philosophy

(Chemical and Biological Engineering)

at the

UNIVERSITY OF WISCONSIN-MADISON

2021

Date of final oral examination: 06/10/2021

The dissertation is approved by the following members of the Final Oral Committee:

David M. Lynn, Professor, Chemical and Biological Engineering
Helen E. Blackwell, Professor, Chemistry
Reid C. Van Lehn, Assistant Professor, Chemical and Biological Engineering
Michael D. Graham, Professor, Chemical and Biological Engineering

Characterization of the Behaviors of Bacterial Amphiphilic Signaling Molecules in Solution and at Interfaces of Soft Materials

Under the Supervision of Professor David M. Lynn

At the University of Wisconsin - Madison

The work reported in this thesis focuses broadly on characterizing and exploiting the behaviors of bacterial quorum sensing (QS) signals, inhibitors, and QS-controlled products in solution and at interfaces with synthetic soft materials. Particular emphasis is placed on (i) characterizing the self-assembly of amphiphilic QS signals in aqueous solution, (ii) characterizing interactions of QS signals and products with lipid membranes and (iii) the discovery of new QS inhibitors (QSIs) and the incorporation of QSIs into polymeric materials for potential wound-healing applications. The second chapter of this thesis characterizes the self-assembly of N-acyl homoserine lactones (AHLs), a class of amphiphilic and non-ionic QS signal used by gram-negative bacteria, in aqueous solution and demonstrates that these molecules can self-assemble into spherical micelles and small vesicles in ways that are dictated by the length of their aliphatic tails, a behavior that is consistent with those of other families of amphiphilic molecules. In the subsequent three chapters, it is demonstrated that AHLs can interact with model self-assembled lipid membranes in ways that lead to substantial membrane remodeling and the growth of extended tubules and hemispherical caps from the membranes. These studies further show that the remodeling observed is modulated by both AHL structure and membrane composition in a way that is at least partially related to the ability of an AHL to translocate across the lipid membrane. The fundamental understanding gained

in these previous four chapters is then applied to provide a basis for the design of lipid vesicles that can detect and respond to communities of bacteria that are actively engaging in QS. We demonstrate that these responsive vesicles can also be used to perform high-throughput screens and identify new small-molecule inhibitors of QS in *Staphylococcus aureus*. Finally, hydrolytically degradable polymer microparticles loaded with potent synthetic inhibitors of *S. aureus* QS are investigated as a modular basis for potential anti-virulence approaches to control bacterial infection and wound healing in a murine dermonecrosis abscess model. The last two chapters of this thesis focus on using optical and electron microscopy to characterize two other soft materials platforms: multilayer assemblies of polymer capsules and lipid-protein aggregates.

This thesis is dedicated to my wife Laura

Acknowledgements

During Spring 2021 commencement, keynote speaker John Gottman reminded me of the fact that success in any endeavor is amplified by the people around you, and that anything you undertake in your life does not need to be done alone. I am blessed to have had a tremendous group of educators, collaborators, friends, and family around me these past five years and sincerely thankful to everyone that supported me throughout my life. To that end, I want to acknowledge them by name here. First, I would like to thank my PhD advisor Prof. David Lynn for all his support, and for always pushed me to improve in my critical thinking, presentation, writing, and research skills. Dave gave me the freedom to explore new areas and techniques while always reminding me to approach my projects in a scientifically backed, and hypothesis driven manner. I feel fortunate to have learned from a talented scientist and mentor who always treated his students with respect, compassion, and an attitude of encouragement. Before I got to UW-Madison, there were many educators that pushed me to expand my horizons, believed in my ability to succeed, and cultivated my curiosity in the world around me. Of note I would like to thank Ms. Greeno, Ms. Kohler, Mr. Fowler, and especially Mr. O'Connel who fostered my love of the chemical sciences. From my time as an undergraduate I want to recognize and thank my advisors Prof. Skip Rochefort and Prof. Travis Walker for guiding and supporting me in my early research endeavors.

There are a number of other faculty and staff members at UW-Madison that have supported me through this process. To begin, I would like to thank Prof. Reid Van Lehn and Prof. Helen Blackwell for their support of me in our research collaborations over the years. Both have acted like additional advisors to me, and I am thankful for all the knowledge they bestowed upon me. I would also like to thank Prof. Reid Van Lehn, Prof. Hellen Blackwell, and Prof. Michael Graham

for their service on my thesis committee. Additionally, I would like to acknowledge and thank the incredible equipment supervisors at UW-Madison that make all the experimental work possible: Mike Efremov and Anna Kiyanova from the SMLC, Alex Kvit at the NIAC, and Lance Rodenkirch from the Optical Imaging Core. These talented individuals are often underappreciated for the work they do. I want to be sure they know how thankful I am for the hard work they put in every day facilitating the research that gets done at this university. Finally, I would like to thank Desiree Benefield for her training and support in learning how to use the TEM. Using the TEM has been my favorite part of graduate school and would not have been possible without her.

Many of the projects described in this thesis would not have been possible without the talented graduate student collaborators I have had the pleasure of working with. From the Van Lehn group, I would like to thank Samartha Patel, whose work has provided a sound fundamental basis to the phenomenon described in this thesis. My research has also benefited from collaboration with many members of the Blackwell group, namely Korbin West, Tom Polaske, Kayleigh Nyffeler, Michelle Boursier, Daniel Manson, and Matthew Styles. Additionally, I would like to thank Brandon Hoover for his work on the α-synulcean project and Tim Smith, Isabel Foreman-Ortiz, and Travis Nelson all of whom took the time to teach me how to use various pieces of experimental equipment on campus.

I would next like to acknowledge past and present members of Prof. David Lynn's research group, all of whom have supported me over these past five years. It was a true honor working with an outstanding group of scientists and engineers including Gavin Guo, Visham Appadoo, Benjamin Ortiz Cardona, Harshit Agarwal, Christopher Eom, Uttam Manna, Lawrence Chen,

Fengrui Wang, Bill Breining, Douglas Chang, Claire Lundberg, and La'Darious Quinn. I thank each of them for the support and friendship that they have provided over this journey. I would also like to acknowledge Ritvind Suketana and Zach Ehmer for their contributions as undergraduate researchers and for teaching me many lessons about being an effective mentor. Special recognition is owed to Gavin Guo, Visham Appadoo, and Benjamin Ortiz Cardona all three of whom welcomed me into the lab and supported me through many of my early failures in a way that accelerated my growth into the independent researcher I am today, and for that I will forever be grateful. Finally, I would like to acknowledge Harshit Agarwal with whom I have spent the majority of my time in graduate school. He has been a constant source of inspiration and support over the last five years and my graduate school experience would not have been as positive, fun, or successful without his help.

I would also like to thank my friends in Madison for the support, laughter and encouragement throughout graduate school. These people have always acted as the "life" that balances the overwhelming amount of "work" that graduate school can be. Specifically, I would like to thank my fellow graduate students Hector Fuster, Taylor Cook, Jake Gold, Jon Dwyer, James Papadopoulos, Chandler Est, Jonathan Sheavley, Alec Linot, Michael Rebarchik, Harshit Agarwal, and Andrea and Gehrig Keane. Additionally, I would like to thank my friends Dan Schumacker and Stephanie Nelson for showing me and Laura what it means to be a true Wisconsinite.

Finally, I would like to acknowledge the greatest support group in my life, my family. I would like to give all my thanks and appreciation to my parents Kim and Greg who from a young

age fostered my love of science, and have supported me in all of my endeavors, pushing me to be the best that I could be in everything I have ever done. Without them I would not be the man, the scientist, or the researcher I am today. Additionally, I would like to thank all my family that have supported me throughout my life including my brother Kevan, my sister Cailin, my Nana and Papa, and Grandma Ellie who were never more than a phone call away for encouragement during this entire process. Additionally, I would like to give thanks to my in-laws Deb, Larry, Amanda, Andy, and Mike for all of their support throughout graduate school. Last, but certainly not least, I want to thank my wife Laura, for who this thesis is dedicated, for the constant love and support she shows me. Through it all Laura has been steadfast by my side during both the ups and downs of this journey, and I would not have been able to do this without her. I love you Laura and can not wait to see where the rest of our lives lead.

Table of Contents

Abstract i

Acknowledgments iv

List of Figures, Schemes, and Tables xi

Chapter 1: Introduction and Overview 1

Background 2
Scope and Organization 10
References 15

Chapter 2: Bacterial Quorum Sensing Signals Self-Assemble in Aqueous Media to Form Micelles and Vesicles: An Integrated Experimental and Molecular Dynamics Study 23

Abstract 24
Introduction 25
Materials and Methods 29
Results and Discussion 37
Summary and Conclusions 54
References 57
Supporting Information 62

Chapter 3: Bacterial Quorum Sensing Signals Promote Large-Scale Remodeling of Lipid Membranes 84

Abstract 85
Introduction 86
Materials and Methods 89
Results and Discussion 99
Summary and Conclusions 128
References 130
Supporting Information 138

Chapter 4: Interactions of Bacterial Quorum Sensing Signals with Model Lipid Membranes: Influence of Acyl Tail Structure on Multi-Scale Response 150

Abstract 151
Introduction 152
Materials and Methods 155
Results and Discussion 161

Summary and Conclusions 174
References 176
Supporting Information 181

Chapter 5: Interactions of Bacterial Quorum Sensing Signals with Model Lipid Membranes: Influence of Membrane Composition on Membrane Remodeling 186

Abstract 187
Introduction 188
Materials and Methods 191
Results and Discussion 196
Summary and Conclusions 215
References 217
Supporting Information 224

Chapter 6: Identification of Small Molecules That Strongly Inhibit Bacterial Quorum Sensing Using a High-Throughput Lipid Vesicle Lysis Assay 246

Abstract 247
Introduction 248
Materials and Methods 250
Results and Discussion 255
Summary and Conclusions 269
References 270
Supporting Information 275

Chapter 7: Sustained Release of a Synthetic Autoinducing Peptide Mimetic Strongly Attenuates MRSA Infections *In Vivo* 290

Abstract 291
Introduction 292
Materials and Methods 294
Results and Discussion 298
Summary and Conclusions 309
References 311
Supporting Information 317

Chapter 8: Membrane Remodeling and Stimulation of Aggregation Following α-Synuclein Adsorption to Phosphotidylserine Vesicles 329

Abstract 330
Introduction 331
Materials and Methods 334

Results....338
Discussion....356
Conclusions....361
References....362
Supporting Information....369

Chapter 9: Polymer Coatings Comprised Entirely of Soft and Semi-Permeable Microcapsules....402

Abstract....403
Introduction....404
Materials and Methods....406
Results and Discussion....410
Summary and Conclusions....424
References....425
Supporting Information....431

Chapter 10: Summary and Recommendations for Future Work....433

Summary of Findings....434
Recommendations for Future Work....436
References....443

List of Figures, Schemes, and Tables

Chapter 2:
Figure 1 26
Figure 2 37
Figure 3 39
Table 1 40
Figure 4 43
Figure 5 47
Figure 6 48
Figure 7 50
Figure S1 62
Figure S2 64
Figure S3 66
Figure S4 67
Figure S5 70
Figure S6 74
Figure S7 76
Figure S8 77
Table S1 78
Table S2 79
Figure S9 80
Figure S10 81
Figure S11 82
Figure S12 82

Chapter 3:
Figure 1 87
Figure 2 100
Figure 3 101
Figure 4 106
Figure 5 110
Figure 6 114
Figure 7 116
Figure 8 118
Figure 9 121
Figure 10 127
Figure S1 138
Figure S2 139
Figure S3 141
Figure S4 142
Figure S5 143
Figure S6 144
Figure S7 145
Figure S8 146
Figure S9 147

Chapter 4: Figure 1 153
Table 1 162
Figure 2 165
Figure 3 168
Figure 4 172
Figure S1 182
Figure S2 183
Figure S3 185

Chapter 5: Figure 1 189
Figure 2 200
Figure 3 201
Figure 4 204
Figure 5 205
Figure 6 207
Figure 7 210
Figure 8 212
Figure S1 224
Figure S2 226
Figure S3 227
Figure S4 228
Figure S5 230
Figure S6 231
Figure S7 235
Figure S8 236
Figure S9 240
Figure S10 241
Figure S11 243

Chapter 6: Figure 1 256
Figure 2 257
Figure 3 259
Figure 4 261
Figure 5 263
Figure 6 266
Figure 7 268
Table S1 275
Figure S1 276
Figure S2 277
Figure S3 278
Figure S4 279
Figure S5 280
Figure S6 281
Figure S7 283

Table S2 284
Table S3 285
Figure S8 286

Chapter 7: Figure 1 299
Figure 2 300
Figure 3 304
Figure 4 305
Figure 5 308
Figure S1 317
Figure S2 318
Figure S3 319
Figure S4 320
Figure S5 321
Figure S6 322
Figure S7 322
Figure S8 324
Figure S9 325
Images of mouse lesions from day 7 of abscess experiments 326

Chapter 8: Figure 1 339
Figure 2 340
Figure 3 342
Figure 4 346
Figure 5 347
Figure 6 351
Figure 7 354
Figure 8 356
Table S1 381
Table S2 381
Table S3 382
Table S4 382
Figure S1 383
Figure S2 384
Figure S3 385
Figure S4 386
Figure S5 387
Figure S6 387
Figure S7 388
Figure S8 388
Figure S9 389
Figure S10 390
Figure S11 390
Figure S12 391
Figure S13 392

Figure S14 393
Figure S15 394
Figure S16 395
Figure S17 396
Figure S18 397
Figure S19 398

Chapter 9: Figure 1 412
Figure 2 414
Figure 3 416
Figure 4 418
Figure 5 421
Figure 6 423
Figure S1 431
Figure S2 432

Chapter 1

Introduction and Overview

Background – Part I – Characterizing the Behaviors of Bacterial QS Signals in Solution and their Interactions with Lipid Membranes

Bacterial quorum sensing (QS) is a cell-cell communication system used by bacteria to assess population density and coordinate gene expression to adapt to changing environments.[1, 2] These cellular communication mechanisms generally depend upon the dissemination and reception of chemical signals that are passed between bacteria, and vary widely between bacterial species. Traditionally, these signals have been assumed to freely diffuse between adjacent cells with minimal interaction with other materials and organisms present in the environment.[3, 4] Recently, it has been suggested that the transport of these signals may occur by more complex mechanisms than previously expected, with QS signals having been reported to: i) interact with naturally-occurring soft materials such as host-cell lipid membranes,[5, 6] ii) be packaged into bacterial outer membrane vesicles,[7, 8] or iii) self-assemble in solution.[9, 10] N-acyl-homoserine lactones (AHLs), a class of amphiphilic signaling molecules used by Gram-negative bacteria, are particularly well suited to interact with soft materials due to their amphiphilic structure, which consists of a relatively polar homoserine lactone head group and an aliphatic tail of varying length. It has been suggested that long-tailed AHLs can behave like other natural and synthetic surfactants, having been reported to aggregate in solution[9, 10] and at air-water interfaces,[11] and to interact with lipid bilayers.[5, 6, 12, 13]

The work reported in Chapters 2-5 builds upon previous reports by addressing fundamental questions about the behaviors of AHLs and the amphiphilic QS-controlled products they regulate in solution and with self-assembled lipid membranes. The results of these fundamental studies suggest potential roles that AHLs could play beyond bacterial QS including interkingdom signaling and bacterial control over host-cell behaviors, and sheds light on potential reasons

bacterial signals evolved to mimic design principles common in synthetic surfactant and colloid chemistry. Additionally, the results presented in this thesis also provide guidance that could, with further development, prove useful for the design of synthetic self-assembled materials that selectively respond to bacterial signals or their QS-regulated products in ways that are useful in the context of sensing, drug delivery, and other fundamental and applied areas. In the following sections, background and context is provided for several themes and concepts relevant to the research described in the chapters that follow.

Bacterial Quorum Sensing

Many species of bacteria engage in cell-cell communication to assess population density and coordinate gene expression to adapt to changing environments.[1, 2] This process, colloquially known as bacterial quorum sensing (QS), is facilitated by the intercellular exchange of signaling molecules that are produced by individual bacteria and then released into the environment. The concentration of these signaling molecules in the extracellular environment therefore increases in a manner that is proportional to the population density of the bacterial community. When a cellular population density known as "quorum," with a corresponding concentration of QS signals, is reached, the signaling molecules bind to their cognate protein receptors,[14-17] initiating gene expression of group behaviors[1, 2, 18] including swarming motility and the production of toxins,[19] biofilms,[20, 21] and biosurfactants.[22] While the outcomes of QS (e.g., biofilm and toxin production) are beneficial to the bacteria, they have proven to be burdensome in many environmental and clinical settings.[23-26] Additionally, these group behaviors, especially the formation of bacterial biofilms, make the bacteria more efficient at resisting environmental stresses, antimicrobial agents, and host immune responses due to the bacterial cells being imbedded in a thick film of polymers

and proteins.[27-30] As more bacterial species become antibiotic-resistant, bacterial QS has gained increased academic and industrial attention as an alternative means of attenuating bacterial infection and shifting the behaviors of growing communities of bacteria in a non-virulent direction.[15, 31, 32]

The chemical signals that facilitate bacteria QS are a diverse and interesting collection of compounds that differ between bacterial species. Gram-positive bacteria use peptide-based signaling molecules[33] and Gram-negative bacteria typically use a variety of small-molecule signals,[1] with some species of bacteria using more than one signal.[34] In this thesis, we will primarily be discussing two classes of QS signals: autoinducing peptides (AIPs) used by the model Gram-positive pathogen *Staphylococcus aureus*[33] and N-acyl homoserine lactones (AHLs) used by a host of Gram-negative organisms, but notably here the opportunistic pathogen *Pseudomonas aeruginosa*.[1] Both AIPs and AHLs vary structurally even between strains of the same bacterial species.[1] For example, the aliphatic tail of an AHL has been found naturally to range from four to eighteen carbons in length and can have hydroxy or ketone substitutions on the third carbon of the aliphatic tail.[6, 8, 35] It is of note that long-chained AHLs have an amphiphilic structure similar to common surfactants with a relatively polar, homoserine lactone, 'head' group and a non-polar, aliphatic 'tail'. This apparent amphiphilicity leads to AHLs exhibiting behaviors like other common natural and synthetic surfactants, including the ability to undergo molecular self-assembly[9, 10] and interact with other self-assembled materials[5, 6, 12, 13] as described below.

Molecular Self-Assembly I. Single Species Aggregation

Molecular self-assembly is the process by which molecules spontaneously adopt defined arrangements without guidance from external driving forces.[36] In this thesis, self-assembly will

refer specifically to the arrangement of amphiphilic species (molecules with a combination of polar and non-polar chemical functionalities) into supramolecular structures such as spherical micelles and vesicles.[37, 38] In aqueous solution, these molecular arrangements are driven by the hydrophobic effect,[39, 40] which causes the tails of an amphiphile to arrange into a variety of nanostructures. This behavior only occurs over a threshold concentration known as the critical aggregation concentration (CAC), a thermodynamic transition point below which amphiphiles exist exclusively in their monomeric state, but above which they begin to form supramolecular assemblies.[37, 41, 42] The structure and geometry of the resulting assemblies is generally controlled by the structure and geometry of their constituent amphiphilic monomers, as defined by a theoretical packing parameter.[37, 38] As a rule of thumb, single-tailed, ionic amphiphiles aggregate into spherical micelles in aqueous solution, while multi-tailed amphiphiles, such as phospholipids, form lamellar or inverted structures, but these molecular arrangements can be affected by environmental factors such as light, temperature, ionic strength, and pH.[37, 38, 43-46] It is especially difficult to predict the aggregate nanostructures formed by non-ionic, single-tailed amphiphiles *a priori* and this often requires experimental characterization to determine. In Chapters 2-4 of this thesis, we use biophysical characterization tools to measure the critical aggregation concentrations and nanostructures formed by AHLs and their amphiphilic, QS-controlled products in solution as a step toward understanding the complex behaviors of AHLs in solution, potential mechanisms of molecular transport, and potential handles that change their interactions with other self-assembled structures as described in the next section.

Molecular Self-Assembly II. Interactions of Amphiphiles with Other Self-Assembled Structures

It is well established that amphiphilic species can interact with one another in solution.[47-50] At the correct compositions and concentrations, two or more amphiphiles can form mixed aggregates that are either similar or different from aggregates formed by the constituent amphiphiles alone.[47-50] Additionally, amphiphilic species that are added to an environment containing self-assembled structures (e.g., lipid bilayers, spherical micelles, inverted hexagonal structures) can associate themselves with these aggregates, potentially in ways that change the phase or physical properties of those structures.[51] For example, much of the work reported in this thesis aims to understand the interactions of AHLs with lipid bilayers, a soft materials platform that is ubiquitous in living systems and commonly used in a number of other types of synthetic soft materials.[45, 52-54] The interactions between a surfactant species and lipid membrane depend heavily on the physical properties (e.g., structure, geometry, and charge) of both the amphiphile and the lipid.[51] These interactions have been observed to facilitate changes in the rigidity, fluidity, and curvature of the bilayer along with bilayer phase changes, permeabilization, pore formation, and dissolution, all of which have been well-described in previous articles.[51, 55-57] When studying these interactions, a number of model lipid membrane platforms have been used, with some of the most common being large and giant unilamellar vesicles (LUVs and GUVs) and supported lipid bilayers (SLBs), each of which allow researchers to probe different responses of lipid membranes to interactions with amphiphilic species.[58-60]

Of particular relevance to the work reported in this thesis are previous studies that use fluorescence microscopy and quartz crystal microbalance with dissipation (QCM-D) to probe large-scale membrane reformations that occur in SLBs as a response to single-tailed amphiphiles intercalating into lipid membranes.[50, 61-66] In a series of previous reports, Cho and coworkers

introduced a number of antimicrobial surfactants to lipid bilayers of varying compositions and observed the formation of extended microtubules and hemispherical caps on the surface of the bilayer.[50, 62, 64-66] These structural reformations were subsequently demonstrated to be modulated by the structure (e.g., tail length, head group structure, and charge) and aggregated states of the surfactants studied, giving insights into rules that govern surfactant-bilayer interactions.[62, 66] Additional studies also demonstrated that multicomponent lipid membranes, including both charged phospholipids and cholesterol, also modulated the interactions of these surfactants with bilayers.[51, 64]

In this thesis, we build upon an existing body of research related to bacterial QS by addressing fundamental questions about the behavior of amphiphilic QS signals and the amphiphilic products they control in their environment. As previously discussed, QS signals have traditionally been assumed to simply diffuse through their environment between adjacent bacterial cells.[3, 4] Therefore, substantial research effort has been directed toward understanding how these signals interact with their cognate receptors and the downstream behaviors they control, as opposed to mechanisms underlying their transport in solution.[67-69] However, there is a growing body of evidence to suggest that the interactions of amphiphilic QS signals (e.g., AHLs) with their environment may be more complex than previously assumed. For example, these signals have been reported to associate within bacterial outer membrane vesicles,[7, 8] interact with host-cell membranes,[5, 6] and aggregate in aqueous solution.[9, 10]

In Chapters 3-6 of this thesis, we describe the use of characterization techniques traditionally used in the study of surfactant, colloid, and interface science to understand the interactions of AHLs and other QS-controlled products with model lipid membranes, with specific emphasis on large-scale reformations that occur upon contact of AHLs with lipid membranes.

These behaviors raise many fundamental questions related to whether the structural amphiphilicity of AHLs impacts their behavior in solution or how they interact with other self-assembled materials. Additionally, it is of interest to understand how the structure of an individual AHL changes these interactions. More broadly, the studies reported in this thesis give rise to additional questions about the role these potential complex behaviors play beyond mediating bacterial communication, including processes such as interkingdom signaling and bacterial control of host-cell response. Our results also provide guidance that could, with further development, prove useful for the design of synthetic self-assembled materials that selectively respond in ways that are useful in the context of sensing, drug delivery, and in other fundamental and applied areas.

Background – Part II – Discovery and Use of Chemical Tools to Control Bacterial QS

With a rising number of antibiotic-resistant bacterial strains appearing each year, there has been increased interest in research aimed at exploring new approaches to combat infections.[70-72] Anti-virulence strategies have become particularly appealing as they are able to attenuate the severity of an infection by inhibiting the production of host-harming virulence factors without killing the infecting organism, which subsequently allows the host's immune system to clear the infection.[73-76] Because these anti-virulence strategies do not put selective pressure on the organism, it is suggested that organisms are less likely to develop resistance to these strategies.[73-76] In many human pathogens, QS plays a key role in regulating the production of bacterial virulence factors and, therefore, targeted inhibition of these communication pathways is a route by which bacterial infection can be controlled and virulence can be attenuated.[77, 78] Toward this goal, a large body of research has focused on finding chemical tools that inhibit these communication pathways. Despite the demand for new and more potent inhibitors of bacterial QS, the chemistries that have been

explored are limited, with many of the compounds being derived from the rational design of native QS signals and screening assays, but many suffer from limitations on potency, selectivity, solubility, and chemical stability.

There are several factors that currently limit the discovery and implementation of new and more potent QS inhibitors,[79] including i) the general low-throughput nature of common phenotypic assays,[80] and ii) differences in the QS systems of wild isolates as compared to the laboratory strains used in screening campaigns and modified to produce reporter strains.[81, 82] Therefore, there is a need to develop new high-throughput phenotypic assays of bacterial QS that expedite the discovery of new anti-virulence agents. Additionally, once QS inhibitors are identified, there are open questions around the ability of these compounds to transition from *in vitro* discovery to *in vivo* applications due to potentially accelerated degradation or sequestration from contact with host tissues and enzymes.[83-85]

In this thesis, Chapters 6 and 7 focus on developing an assay for the discovery of new chemical tools that inhibit QS in bacterial pathogens and delivering potent QS inhibitors *in vivo* to control bacterial infection, respectively. These studies are specifically focused on inhibiting the QS systems of the opportunistic pathogen S. *aureus,* as it is responsible for nearly 20,000 fatal infections in the United States per year and has a rising number of antibiotic resistant strains, including methicillin-resistant *S. aureus* (MRSA), which necessitates the development of new methods for controlling bacterial infection.[86] Chapter 6 of this thesis presents a new assay that detects the presence of amphiphilic virulence factors produced under the control of QS. This assay is then used in a high-throughput screen for the discovery of new small molecule inhibitors of QS in *S. aureus*. The work presented in Chapter 7 then demonstrates the efficacy of potent peptic inhibitors of the *S. aureus agr* system at controlling bacterial virulence *in vivo* and provides a

blueprint for using a controlled release strategy to amplify the efficacy of anti-virulence strategies to combating bacterial infections.

Scope and Organization of This Thesis

The chapters of this thesis are focused broadly on developing a fundamental understanding of the behaviors of bacterial signaling molecules and inhibitors both in solution and as they interact with other soft materials. The work described in Chapter 2 of this thesis characterizes the self-assembly of AHLs in solution, including the aggregated nanostructures that they form. Chapters 3-5 focus on understanding the interactions of AHLs and other amphiphilic, QS-controlled bacterial products with model lipid membrane systems of varying complexity. Chapter 6 uses the fundamental understanding of the amphiphilic molecules produced by cooperative phenotypes of bacteria to develop sensors of bacterial communities that have active QS systems and then screen for QS inhibitors. In Chapter 7, we exploit the loading and release characteristics of potent QS inhibitors of *S. aureus* from polymer matrices to develop anti-virulence approaches to controlling bacterial infections. Finally, Chapters 8 and 9 use the characterization tools used in the previous chapters to analyze new soft materials systems, covalent assemblies of polymer capsules, and lipid-protein aggregates.

While each of these chapters is organized in a manner that follows a logical, academic flow, every chapter is written as a stand-alone unit that permits independent reading out of the sequence in which they appear. Below, a brief overview of the content of each of the following chapters of this thesis is provided.

The studies described in Chapter 2 demonstrate that long-chained AHLs are able to self-assemble in defined buffer and relevant bacterial growth media. Two independent biophysical

characterization methods, static light scattering and surface tension measurements, are used to measure the critical aggregation concentrations (CACs) of some common, naturally-occurring AHLs, finding that AHL self-assembly follows patterns similar to other families of surfactants, with molecules of increasing tail length having lower CACs. The aggregate morphologies formed by AHLs in solution are investigated both by molecular dynamics simulations and observations by transmission electron microscopy, demonstrating that AHLs of differing head group structure and tail length form different nanostructures in solution.

Chapter 3 reports on the ability of the long-chained AHL 3-oxo-C12-AHL and its hydrolysis product, 3-oxo-C12-HS, to promote large-scale remodeling in model lipid membranes. These experiments were motivated by the observation that supernatants of *P. aeruginosa* cultures could lead to the formation of long, thin microtubules that can retract and collapse into hemispherical caps on the surface of supported lipid bilayers (SLBs). Further characterization of SLBs by fluorescence microscopy and quartz crystal microbalance with dissipation (QCM-D) reveals both 3-oxo-C12-AHL and 3-oxo-C12-HS to promote similar restructuring events and to be transported across bilayers. Molecular dynamics (MD) simulations complement these experimental results by predicting differences in the thermodynamic barriers to translocation of 3-oxo-C12-AHL and 3-oxo-C12-HS across a bilayer. The relative magnitude of the thermodynamic barriers to translocation are reflected in both the type and extent of reformation and associated dynamics that are observed experimentally. Our experimental observations can thus be interpreted in terms of accumulation and relief of asymmetric stresses in the inner and outer leaflets of a bilayer upon the intercalation and translocation of these bacterial amphiphiles. These results provide insight into roles that 3-oxo-C12-AHL and its hydrolysis product may play beyond mediating bacterial communication and provide guidance that could prove useful for the design of

synthetic self-assembled materials that selectively respond to bacterial communities in ways that are useful in the context of sensing and drug delivery.

Chapter 4 builds upon the outcomes of Chapters 2 and 3 by exploring the membrane remodeling that is observed from the interaction of naturally occurring, structurally-diverse AHLs with model lipid membrane systems. AHLs with tails from ten to sixteen carbons in length and the presence or absence of a 3-oxo-substitution in the head group were investigated. In an initial set of experiments, the CACs of these AHLs were measured by light-scattering to understand their aggregated states in subsequent experiments. Characterization by fluorescence microscopy and QCM-D revealed that AHLs containing 3-oxo groups led to the formation of extended tubules on the surface of the bilayer that could collapse into hemispherical caps over time; in contrast, AHLs that did not have a 3-oxo group led exclusively to the formation of hemispherical caps on the surface of the bilayer. In view of the theoretical framework developed in Chapter 3 and previously published MD simulations, we attribute this dichotomy in behavior to the ability of unsubstituted AHLs to translocate more quickly across the bilayer and relieve asymmetric bilayer stresses. Additional dye leakage experiments demonstrate that AHLs with a 3-oxo group facilitated more small-molecule transport across the membrane than their unsubstituted counterparts. Taken together, these results suggest that the structure of an AHL changes its interactions with lipid membranes and, therefore, vastly different bilayer reformation events may occur. These results give further insight into the design of materials that selectively respond to AHLs for potential sensing and drug delivery applications.

Chapter 5 continues to build upon the two previous chapters by exploring the interaction of 3-oxo-C12-AHL and its head-group hydrolysis product with lipid membranes that contain more than one lipid species. These bilayers were composed of mixtures of DOPC and three other

naturally occurring lipids; cholesterol, DOPS and DOPC. We demonstrate the ability to form these compositionally complex SLBs on SiO_2 surfaces and then introduce solutions of 3-oxo-C12-AHL and 3-oxo-C12-HS to them. The bilayer reformations observed as a result of these interactions are different in type and extent than those observed in single component DOPC bilayers. Potential mechanisms for these differences in interaction are discussed in detail. Taken together, the results of chapter 5 give further insight into the physical interactions that may control the interactions of AHLs and their hydrolysis products with host cell membranes that are composed of many different lipid species.

The work reported in Chapter 6 uses knowledge of the interactions between surfactants and model lipid membrane systems to develop lipid vesicles that sense and report upon quorate populations of bacteria. The reported sensors consist of lipid vesicles loaded with the self-quenching dye calcein that releases calcein and produces an increased fluorescence signal upon contact with amphiphilic virulence factors. We first demonstrate that vesicle lysis and subsequent calcein leakage is correlated to the onset of quorum and the production of bacterial virulence factors in a corresponding bacterial reporter assay. We then demonstrate that this sensing platform is sensitive to the presence of chemical tools that are known to inhibit or promote bacterial virulence factor production in both *S. aureus* and *P. aeruginosa*. These vesicles were then used as a platform to screen a 25,000-compound small-molecule library to identify previously unidentified inhibitors of *S. aureus* QS that were shown to be the most potent small-molecule inhibitors of the *S. aureus agr* system to date.

In Chapter 7, the ability of hydrolytically degradable PLGA materials containing *agr*-type QS peptide inhibitors to attenuate *S. aureus* infection *in vivo* is evaluated using a murine dermonecrosis abscess model. We first screened for inhibitors that are resistant to interference by

host tissue sequestration and degradation, and then designed and characterized PLGA microparticle formulations loaded with peptide inhibitors. We next demonstrated that the peptide inhibitors were effective at attenuating infection in murine abscess models, both through direct administration to the infection site and through controlled release from PLGA materials. When compared directly, we show that the controlled-release strategy outperformed direct administration. Together, these results provide a versatile platform that is compatible with a wide variety of polymers, QS inhibitors, and fabrication techniques that can be tailored to a range of different bacterial pathogens and infection types to pave the way for future fundamental studies of *S. aureus* QS *in vivo*, as well as the development of new wound healing strategies.

In Chapter 8, the relationship between lipid bilayer stability and the structural reformation observed due to contact with alpha-synuclein is investigated. The interaction of alpha-synuclein with acidic lipid bilayers is important not only for its normal function but also in its pathological aggregation and deposition as Lewy bodies in Parkinson's disease. Using a combination of experimental techniques and MD simulations it was demonstrated that alpha-synuclein induces extensive vesicle disruption and membrane remodeling into discoids, tubules, and ribbons when placed in contact with vesicles composed of the short-chained lipid DLPS, but not the long-chained DOPS. These results together provide new insight into the contribution of bilayer stability in membrane remodeling observed as a response to alpha-synuclein adsorption and aggregation on lipid vesicles.

Chapters 9 describes the design and characterization of new synthetic soft material surface coatings consisting of networks of hollow and semi-permeable polymeric microcapsules. These capsule assemblies were assembled by iterative immersion of substrates into suspensions of microparticles coated with polymer films presenting either (i) amine or (ii) amine-reactive

azlactone functionality, resulting in coatings of coated colloidal cores. These cores could be subsequently removed to yield multicomponent and compartmentalized coatings consisting of polymer capsules. Characterization by confocal microcopy and SEM revealed these assemblies to have disordered structures with hints of stratification resulting from the iterative assembly process. After fabrication, the residual azlactone groups in the capsule walls provided a means by which the properties of these assemblies (e.g. surface wetting and controlled release behaviors) could be tailored through reactions with amine-based nucleophiles. This new class of materials has potential applications in several applied contexts ranging from catalysis to controlled release to the development of polymeric surface coatings with tunable functionality.

Chapter 10, the final chapter of this thesis, provides a summary of the work described in Chapters 2-9, as well as insights on potential directions for future study building off the work reported in this thesis.

References

1. Miller, M. B.; Bassler, B. L., Quorum sensing in bacteria. *Annu. Rev. Microbiol.* **2001,** *55*, 165-199.

2. Waters, C. M.; Bassler, B. L., Quorum sensing: Cell-to-cell communication in bacteria. *Annu. Rev. Cell Dev. Biol.* **2005,** *21*, 319-346.

3. Kaplan, H. B.; Greenberg, E. P., Diffusion of autoinducer in involved in regulation of the Vibrio-fischeri luminescence system. *J. Bacteriol.* **1985,** *163* (3), 1210-1214.

4. Pearson, J. P.; Van Delden, C.; Iglewski, B. H., Active efflux and diffusion are involved in transport of Pseudomonas aeruginosa cell-to-cell signals. *J. Bacteriol.* **1999,** *181* (4), 1203-1210.

5. Davis, B. M.; Jensen, R.; Williams, P.; O'Shea, P., The Interaction of N-Acylhomoserine Lactone Quorum Sensing Signaling Molecules with Biological Membranes: Implications for Inter-Kingdom Signaling. *PLoS One* **2010,** *5* (10).

6. Song, D. K.; Meng, J. C.; Cheng, J.; Fan, Z.; Chen, P. Y.; Ruan, H. F.; Tu, Z. Y.; Kang, N.; Li, N.; Xu, Y.; Wang, X. B.; Shi, F.; Mu, L. B.; Li, T. F.; Ren, W. R.; Lin, X.; Zhu, J.;

Fang, X. H.; Amrein, M. W.; Wu, W. H.; Yan, L. T.; Lu, J. H.; Xia, T.; Shi, Y., Pseudomonas aeruginosa quorum-sensing metabolite induces host immune cell death through cell surface lipid domain dissolution. *Nat. Microbiol.* **2019,** *4* (1), 97-111.

7. Mashburn-Warren, L. M.; Whiteley, M., Special delivery: vesicle trafficking in prokaryotes. *Mol. Microbiol.* **2006,** *61* (4), 839-846.

8. Toyofuku, M.; Morinaga, K.; Hashimoto, Y.; Uhl, J.; Shimamura, H.; Inaba, H.; Schmitt-Kopplin, P.; Eberl, L.; Nomura, N., Membrane vesicle-mediated bacterial communication. *ISME J.* **2017,** *11* (6), 1504-1509.

9. Davis, B. M.; Richens, J. L.; O'Shea, P., Label-Free Critical Micelle Concentration Determination of Bacterial Quorum Sensing Molecules. *Biophys. J.* **2011,** *101* (1), 245-254.

10. Gahan, C. G.; Patel, S. J.; Boursier, M. E.; Nyffeler, K. E.; Jennings, J.; Abbott, N. L.; Blackwell, H. E.; Van Lehn, R. C.; Lynn, D. M., Bacterial Quorum Sensing Signals Self-Assemble in Aqueous Media to Form Micelles and Vesicles: An Integrated Experimental and Molecular Dynamics Study. *J. Phys. Chem. B* **2020,** *124* (18), 3616-3628.

11. Daniels, R.; Reynaert, S.; Hoekstra, H.; Verreth, C.; Janssens, J.; Braeken, K.; Fauvart, M.; Beullens, S.; Heusdens, C.; Lambrichts, I.; De Vos, D. E.; Vanderleyden, J.; Vermant, J.; Michiels, J., Quorum signal molecules as biosurfactants affecting swarming in Rhizobium etli. *Proc. Natl. Acad. Sci. U. S. A.* **2006,** *103* (40), 14965-14970.

12. Jakubczyk, D.; Barth, C.; Kubas, A.; Anastassacos, F.; Koelsch, P.; Fink, K.; Schepers, U.; Brenner-Weiss, G.; Brase, S., Deuterium-labelled N-acyl-l-homoserine lactones (AHLs)-inter-kingdom signalling molecules-synthesis, structural studies, and interactions with model lipid membranes. *Anal. Bioanal. Chem.* **2012,** *403* (2), 473-482.

13. Barth, C.; Jakubczyk, D.; Kubas, A.; Anastassacos, F.; Brenner-Weiss, G.; Fink, K.; Schepers, U.; Brase, S.; Koelsch, P., Interkingdom Signaling: Integration, Conformation, and Orientation of N-Acyl-L-homoserine Lactones in Supported Lipid Bilayers. *Langmuir* **2012,** *28* (22), 8456-8462.

14. Fuqua, C.; Greenberg, E. P., Listening in on bacteria: Acyl-homoserine lactone signalling. *Nat. Rev. Mol. Cell Biol.* **2002,** *3* (9), 685-695.

15. Camilli, A.; Bassler, B. L., Bacterial small-molecule signaling pathways. *Science* **2006,** *311* (5764), 1113-1116.

16. Amara, N.; Krom, B. P.; Kaufmann, G. F.; Meijler, M. M., Macromolecular Inhibition of Quorum Sensing: Enzymes, Antibodies, and Beyond. *Chem. Rev.* **2011,** *111* (1), 195-208.

17. Galloway, W.; Hodgkinson, J. T.; Bovvden, S.; Welch, M.; Spring, D. R., Applications of small molecule activators and inhibitors of quorum sensing in Gram-negative bacteria. *Trends Microbiol.* **2012,** *20* (9), 449-458.

18. Welch, M.; Mikkelsen, H.; Swatton, J. E.; Smith, D.; Thomas, G. L.; Glansdorp, F. G.; Spring, D. R., Cell-cell communication in gram-negative bacteria. *Mol. BioSyst.* **2005,** *1* (3), 196-202.

19. Chugani, S. A.; Whiteley, M.; Lee, K. M.; D'Argenio, D.; Manoil, C.; Greenberg, E. P., QscR, a modulator of quorum-sensing signal synthesis and virulence in Pseudomonas aeruginosa. *Proc. Natl. Acad. Sci. U. S. A.* **2001,** *98* (5), 2752-2757.

20. Davies, D. G.; Parsek, M. R.; Pearson, J. P.; Iglewski, B. H.; Costerton, J. W.; Greenberg, E. P., The involvement of cell-to-cell signals in the development of a bacterial biofilm. *Science* **1998,** *280* (5361), 295-298.

21. de Kievit, T. R., Quorum sensing in Pseudomonas aeruginosa biofilms. *Environ. Microbiol.* **2009,** *11* (2), 279-288.

22. Reis, R. S.; Pereira, A. G.; Neves, B. C.; Freire, D. M. G., Gene regulation of rhamnolipid production in Pseudomonas aeruginosa - A review. *Bioresour. Technol.* **2011,** *102* (11), 6377-6384.

23. Rumbaugh, K. P.; Griswold, J. A.; Hamood, A. N., The role of quorum sensing in the in vivo virulence of Pseudomonas aeruginosa. *Microbes Infect.* **2000,** *2* (14), 1721-1731.

24. Gooderham, W. J.; Hancock, R. E. W., Regulation of virulence and antibiotic resistance by two-component regulatory systems in Pseudomonas aeruginosa. *FEMS Microbiol. Rev.* **2009,** *33* (2), 279-294.

25. Coggan, K. A.; Wolfgang, M. C., Global Regulatory Pathways and Cross-talk Control Pseudomonas aeruginosa Environmental Lifestyle and Virulence Phenotype. *Curr. Issues Mol. Biol.* **2012,** *14* (2), 47-69.

26. Crone, S.; Vives-Florez, M.; Kvich, L.; Saunders, A. M.; Malone, M.; Nicolaisen, M. H.; Martinez-Garcia, E.; Rojas-Acosta, C.; Gomez-Puerto, M. C.; Calum, H.; Whiteley, M.; Kolter, R.; Bjarnsholt, T., The environmental occurrence of Pseudomonas aeruginosa. *APMIS* **2020,** *128* (3), 220-231.

27. Davies, D., Understanding biofilm resistance to antibacterial agents. *Nat. Rev. Drug Discovery* **2003,** *2* (2), 114-122.

28. Jensen, P. O.; Givskov, M.; Bjarnsholt, T.; Moser, C., The immune system vs. Pseudomonas aeruginosa biofilms. *FEMS Immunol. Med. Microbiol.* **2010,** *59* (3), 292-305.

29. Bridier, A.; Briandet, R.; Thomas, V.; Dubois-Brissonnet, F., Resistance of bacterial biofilms to disinfectants: a review. *Biofouling* **2011,** *27* (9), 1017-1032.

30. Epstein, A. K.; Wong, T. S.; Belisle, R. A.; Boggs, E. M.; Aizenberg, J., Liquid-infused structured surfaces with exceptional anti-biofouling performance. *Proc. Natl. Acad. Sci. U. S. A.* **2012,** *109* (33), 13182-13187.

31. Whiteley, M.; Diggle, S. P.; Greenberg, E. P., Progress in and promise of bacterial quorum sensing research. *Nature* **2017,** *551* (7680), 313-320.

32. Aframian, N.; Eldar, A., A Bacterial Tower of Babel: Quorum-Sensing Signaling Diversity and Its Evolution. *Annu. Rev. Microbiol.* **2020**.

33. Ng, W. L.; Bassler, B. L., Bacterial quorum-sensing network architectures. *Annu. Rev. Genet.* **2009,** *43*, 197-222.

34. Smith, R. S.; Iglewski, B. H., P-aeruginosa quorum-sensing systems and virulence. *Curr. Opin. Microbiol.* **2003,** *6* (1), 56-60.

35. Churchill, M. E. A.; Chen, L. L., Structural Basis of Acyl-homoserine Lactone-Dependent Signaling. *Chem. Rev.* **2011,** *111* (1), 68-85.

36. Whitesides, G. M.; Grzybowski, B., Self-assembly at all scales. *Science* **2002,** *295* (5564), 2418-2421.

37. Hiemenz, P. C.; Rajagopalan, R., Colloid Structures in Surfactant Solutions. In *Principles of Colloid and Surface Chemistry*, CCR Press: 1997; pp 355-404.

38. Israelachvili, J. N., *Intermolecular and Surface Forces, 3rd Edition*. Academic Press: 2011; pp 1-674.

39. Southall, N. T.; Dill, K. A.; Haymet, A. D. J., A view of the hydrophobic effect. *J. Phys. Chem. B* **2002,** *106* (3), 521-533.

40. Meyer, E. E.; Rosenberg, K. J.; Israelachvili, J., Recent progress in understanding hydrophobic interactions. *Proc. Natl. Acad. Sci. U. S. A.* **2006,** *103* (43), 15739-15746.

41. Aguiar, J.; Carpena, P.; Molina-Bolivar, J. A.; Ruiz, C. C., On the determination of the critical micelle concentration by the pyrene 1 : 3 ratio method. *J. Colloid Interface Sci.* **2003,** *258* (1), 116-122.

42. Scholz, N.; Behnke, T.; Resch-Genger, U., Determination of the Critical Micelle Concentration of Neutral and Ionic Surfactants with Fluorometry, Conductometry, and Surface Tension-A Method Comparison. *J. Fluoresc.* **2018,** *28* (1), 465-476.

43. Williams, R. J.; Phillips, J. N.; Mysels, K. J., The critical micelle concentration of sodium lauryl sulphate at 25-degrees-C. *Trans. Faraday Soc.* **1955,** *51* (5), 728-737.

44. Brown, P.; Butts, C. P.; Eastoe, J., Stimuli-responsive surfactants. *Soft Matter* **2013,** *9* (8), 2365-2374.

45. Mura, S.; Nicolas, J.; Couvreur, P., Stimuli-responsive nanocarriers for drug delivery. *Nat. Mater.* **2013,** *12* (11), 991-1003.

46. Fameau, A. L.; Arnould, A.; Saint-Jalmes, A., Responsive self-assemblies based on fatty acids. *Curr. Opin. Colloid Interface Sci.* **2014,** *19* (5), 471-479.

47. Lucassenreynders, E. H.; Lucassen, J.; Giles, D., Surface and bulk properties of mixed anionic-cationic surfactant systems .1. equilibrium surface tensions. *J. Colloid Interface Sci.* **1981,** *81* (1), 150-157.

48. Khan, A.; Marques, E. F., Synergism and polymorphism in mixed surfactant systems. *Curr. Opin. Colloid Interface Sci.* **1999,** *4* (6), 402-410.

49. Smith, T. J.; Wang, C. X.; Abbott, N. L., Redox-triggered mixing and demixing of surfactants within assemblies formed in solution and at surfaces. *J. Colloid Interface Sci.* **2017,** *502*, 122-133.

50. Yoon, B. K.; Park, S.; Jackman, J. A.; Cho, N. J., Supported lipid bilayer platform for characterizing the optimization of mixed nano-micelles. *Appl. Mater. Today* **2020,** *19*.

51. Heerklotz, H., Interactions of surfactants with lipid membranes. *Q. Rev. Biophys.* **2008,** *41* (3-4), 205-264.

52. Torchilin, V. P., Recent advances with liposomes as pharmaceutical carriers. *Nat. Rev. Drug Discovery* **2005,** *4* (2), 145-160.

53. Peer, D.; Karp, J. M.; Hong, S.; FaroKhzad, O. C.; Margalit, R.; Langer, R., Nanocarriers as an emerging platform for cancer therapy. *Nat. Nanotechnol.* **2007,** *2* (12), 751-760.

54. Liu, Q. T.; Boyd, B. J., Liposomes in biosensors. *Analyst* **2013,** *138* (2), 391-409.

55. Jones, M. N., Surfactant interactions with biomembranes and proteins. *Chem. Soc. Rev.* **1992,** *21* (2), 127-136.

56. Jones, M. N., Surfactants in membrane solubilisation. *Int. J. Pharm.* **1999,** *177* (2), 137-159.

57. Lichtenberg, D.; Ahyayauch, H.; Alonso, A.; Goni, F. M., Detergent solubilization of lipid bilayers: a balance of driving forces. *Trends Biochem. Sci.* **2013,** *38* (2), 85-93.

58. Chan, Y. H. M.; Boxer, S. G., Model membrane systems and their applications. *Curr. Opin. Chem. Biol.* **2007,** *11* (6), 581-587.

59. Peetla, C.; Stine, A.; Labhasetwar, V., Biophysical Interactions with Model Lipid Membranes: Applications in Drug Discovery and Drug Delivery. *Mol. Pharmaceutics* **2009,** *6* (5), 1264-1276.

60. Dimova, R.; Marques, C. M., The Giant Vesicle Book. 1 ed.; CRC Press: Boca Raton, 2019; pp 1-676.

61. Thid, D.; Benkoski, J. J.; Svedhem, S.; Kasemo, B.; Gold, J., DHA-Induced changes of supported lipid membrane morphology. *Langmuir* **2007,** *23* (11), 5878-5881.

62. Yoon, B. K.; Jackman, J. A.; Kim, M. C.; Cho, N. J., Spectrum of Membrane Morphological Responses to Antibacterial Fatty Acids and Related Surfactants. *Langmuir* **2015,** *31* (37), 10223-10232.

63. Flynn, K. R.; Martin, L. L.; Ackland, M. L.; Torriero, A. A. J., Real-Time Quartz Crystal Microbalance Monitoring of Free Docosahexaenoic Acid Interactions with Supported Lipid Bilayers. *Langmuir* **2016,** *32* (45), 11717-11727.

64. Kawakami, L. M.; Yoon, B. K.; Jackman, J. A.; Knoll, W.; Weiss, P. S.; Cho, N. J., Understanding How Sterols Regulate Membrane Remodeling in Supported Lipid Bilayers. *Langmuir* **2017,** *33* (51), 14756-14765.

65. Yoon, B. K.; Jackman, J. A.; Kim, M. C.; Sut, T. N.; Cho, N. J., Correlating Membrane Morphological Responses with Micellar Aggregation Behavior of Capric Acid and Monocaprin. *Langmuir* **2017,** *33* (11), 2750-2759.

66. Yoon, B. K.; Jackman, J. A.; Park, S.; Mokrzecka, N.; Cho, N. J., Characterizing the Membrane-Disruptive Behavior of Dodecylglycerol Using Supported Lipid Bilayers. *Langmuir* **2019,** *35* (9), 3568-3575.

67. Moore, J. D.; Rossi, F. M.; Welsh, M. A.; Nyffeler, K. E.; Blackwell, H. E., A Comparative Analysis of Synthetic Quorum Sensing Modulators in Pseudomonas aeruginosa: New Insights into Mechanism, Active Efflux Susceptibility, Phenotypic Response, and Next-Generation Ligand Design. *J. Am. Chem. Soc.* **2015,** *137* (46), 14626-14639.

68. O'Reilly, M. C.; Dong, S. H.; Rossi, F. M.; Karlen, K. M.; Kumar, R. S.; Nair, S. K.; Blackwell, H. E., Structural and Biochemical Studies of Non-native Agonists of the LasR Quorum-Sensing Receptor Reveal an L3 Loop "Out" Conformation for LasR. *Cell Chem. Biol.* **2018,** *25* (9), 1128-1139.

69. Boursier, M. E.; Moore, J. D.; Heitman, K. M.; Shepardson-Fungairino, S. P.; Combs, J. B.; Koenig, L. C.; Shin, D.; Brown, E. C.; Nagarajan, R.; Blackwell, H. E., Structure-Function Analyses of the N-Butanoyl L-Homoserine Lactone Quorum-Sensing Signal Define Features Critical to Activity in RhlR. *ACS Chem. Biol.* **2018,** *13* (9), 2655-2662.

70. Klein, E.; Smith, D. L.; Laxminarayan, R., Hospitalizations and deaths caused by methicillin-resistant Staphylococcus aureus, United States, 1999-2005. *Emerg. Infect. Dis.* **2007,** *13* (12), 1840-6.

71. David, M. Z.; Daum, R. S., Community-associated methicillin-resistant Staphylococcus aureus: epidemiology and clinical consequences of an emerging epidemic. *Clin. Microbiol. Rev.* **2010,** *23* (3), 616-687.

72. Tong, S. Y.; Davis, J. S.; Eichenberger, E.; Holland, T. L.; Fowler, V. G., Jr., Staphylococcus aureus infections: epidemiology, pathophysiology, clinical manifestations, and management. *Clin. Microbiol. Rev.* **2015,** *28* (3), 603-661.

73. Rasko, D. A.; Sperandio, V., Anti-virulence strategies to combat bacteria-mediated disease. *Nat. Rev. Drug. Discov.* **2010,** *9* (2), 117-128.

74. Allen, R. C.; Popat, R.; Diggle, S. P.; Brown, S. P., Targeting virulence: can we make evolution-proof drugs? *Nat. Rev. Microbiol.* **2014,** *12* (4), 300-308.

75. Dickey, S. W.; Cheung, G. Y. C.; Otto, M., Different drugs for bad bugs: antivirulence strategies in the age of antibiotic resistance. *Nat. Rev. Drug. Discov.* **2017,** *16* (7), 457-471.

76. Ford, C. A.; Hurford, I. M.; Cassat, J. E., Antivirulence Strategies for the Treatment of Staphylococcus aureus Infections: A Mini Review. *Front. Microbiol.* **2020,** *11*, 632706.

77. LaSarre, B.; Federle, M. J., Exploiting quorum sensing to confuse bacterial pathogens. *Microbiol. Mol. Biol. Rev.* **2013,** *77* (1), 73-111.

78. Azimi, S.; Klementiev, A. D.; Whiteley, M.; Diggle, S. P., Bacterial Quorum Sensing During Infection. *Annu. Rev. Microbiol.* **2020**.

79. Horswill, A. R.; Gordon, C. P., Structure-Activity-Relationship Studies of Small Molecule Modulators of the Staphylococcal Accessory Gene Regulator. *J. Med. Chem.* **2019,** *63* (6), 2705-2730.

80. Quave, C. L.; Horswill, A. R., Flipping the switch: tools for detecting small molecule inhibitors of staphylococcal virulence. *Front. Microbiol.* **2014,** *5* (706).

81. Traber, K. E.; Lee, E.; Benson, S.; Corrigan, R.; Cantera, M.; Shopsin, B.; Novick, R. P., agr function in clinical Staphylococcus aureus isolates. *Microbiology (Reading)* **2008,** *154* (Pt 8), 2265-2274.

82. Feltner, J. B.; Wolter, D. J.; Pope, C. E.; Groleau, M.-C.; Smalley, N. E.; Greenberg, E. P.; Mayer-Hamblett, N.; Burns, J.; Déziel, E.; Hoffman, L. R.; Dandekar, A. A., LasR Variant Cystic Fibrosis Isolates Reveal an Adaptable Quorum-Sensing Hierarchy in Pseudomonas aeruginosa. *mBio* **2016,** *7* (5), e01513-16.

83. Yarwood, J. M.; McCormick, J. K.; Paustian, M. L.; Kapur, V.; Schlievert, P. M., Repression of the Staphylococcus aureus accessory gene regulator in serum and in vivo. *J. Bacteriol.* **2002,** *184* (4), 1095-1101.

84. Peterson, M. M.; Mack, J. L.; Hall, P. R.; Alsup, A. A.; Alexander, S. M.; Sully, E. K.; Sawires, Y. S.; Cheung, A. L.; Otto, M.; Gresham, H. D., Apolipoprotein B Is an innate barrier against invasive Staphylococcus aureus infection. *Cell Host Microbe* **2008,** *4* (6), 555-566.

85. Elmore, B. O.; Triplett, K. D.; Hall, P. R., Apolipoprotein B48, the Structural Component of Chylomicrons, Is Sufficient to Antagonize Staphylococcus aureus Quorum-Sensing. *PLoS One* **2015,** *10* (5), e0125027.

86. Kourtis, A. P.; Hatfield, K.; Baggs, J.; Mu, Y.; See, I.; Epson, E.; Nadle, J.; Kainer, M. A.; Dumyati, G.; Petit, S.; Ray, S. M.; Emerging Infections Program, M. a. g.; Ham, D.; Capers, C.; Ewing, H.; Coffin, N.; McDonald, L. C.; Jernigan, J.; Cardo, D., Vital Signs: Epidemiology and Recent Trends in Methicillin-Resistant and in Methicillin-Susceptible Staphylococcus aureus Bloodstream Infections - United States. *Morb. Mortal. Wkly. Rep.* **2019,** *68* (9), 214-219.

Chapter 2

Bacterial Quorum Sensing Signals Self-Assemble in Aqueous Media to Form Micelles and Vesicles: An Integrated Experimental and Molecular Dynamics Study‡

‡ Portions of this chapter have previously been published as: Gahan, C. G.; Patel, S. J.; Boursier, M. E.; Nyffeler, K. E.; Jennings, J.; Abbott, N. L.; Blackwell, H. E.; Van Lehn, R. C.; Lynn D. M. "Bacterial Quorum Sensing Signals Self-Assemble in Aqueous Media to Form Micelles and Vesicles: An Integrated Experimental and Molecular Dynamics Study" *J. Phys. Chem. B* **2020**, *124*, 3616-3628. I designed and performed all experiments. S. J. Patel designed and performed all molecular dynamics simulations. M. E. Boursier and K. E. Nyffeler helped to design experiments. J. Jennings performed preliminary experiments. N. L. Abbott, R. C. Van Lehn, H. E. Blackwell and D. M. Lynn directed the project.

ABSTRACT: Many species of common bacteria communicate and coordinate group behaviors, including toxin production and surface fouling, through a process known as quorum sensing (QS). In Gram-negative bacteria, QS is regulated by *N*-acyl L-homoserine lactones (AHLs) that possess a polar homoserine lactone head group and a nonpolar aliphatic tail. Past studies demonstrate that AHLs can aggregate in water or adsorb at interfaces, suggesting that molecular self-assembly could play a role in processes that govern bacterial communication. We used a combination of biophysical characterization and atomistic molecular dynamics (MD) simulations to characterize the self-assembly behaviors of 12 structurally related AHLs. We used static light scattering and measurements of surface tension to characterize the assembly of four naturally occurring AHLs (3-oxo-C8-AHL, 3-oxo-C12-AHL, C12-AHL, and C16-AHL) in aqueous media and determine their critical aggregation concentrations (CACs). MD simulations and alchemical free energy calculations were used to predict thermodynamically preferred aggregate structures for each AHL. Those calculations predicted that AHLs with 10 or 12 tail carbon atoms should form spherical micelles, and that AHLs with 14 or 16 tail carbon atoms should form vesicles in solution. Characterization of solutions of AHLs using negative stain transmission electron microscopy (TEM) and dynamic light scattering (DLS) revealed aggregates with sizes consistent with spherical micelles or small unilamellar vesicles for 3-oxo-C12-AHL and C12-AHL, and the formation of large vesicles (~250 nm) in solutions of C16-AHL. These experimental findings are in general agreement with our simulation predictions. Overall, our results provide insight into processes of self-assembly that can occur in this class of bacterial amphiphiles and, more broadly, provide a potential basis for understanding how AHL structure could influence processes that bacteria use to drive important group behaviors.

Introduction

Quorum sensing (QS) is an intercellular signaling process by which bacteria assess their population densities and coordinate gene expression to regulate group behaviors and adapt to changing environments.[1-2] Outcomes of QS include the production of virulence factors[3] and the formation of bacterial biofilms,[1] both of which can be harmful to humans or costly in commercial and industrial contexts. In many common bacterial pathogens, QS is controlled by the production and dissemination of small-molecule or peptidic signals.[1-2, 4-5] The structures of these signals can vary widely amongst bacterial species and are known to influence the specificity of their interactions with their biomolecular targets through receptor-ligand interactions.[6-11] However, the structures and solution behaviors of QS signals also have the potential to mediate other interactions important to the transport of these molecules in solution, into cells, or through biofilms. In this study, we report fundamental physicochemical characterization and the results of integrated molecular dynamics (MD) simulation studies that provide new insights into the solution behaviors and self-assembly of *N*-acyl-L-homoserine lactones (AHLs; Figure 1), the most widely characterized signals that regulate QS in Gram-negative bacteria.[5, 7]

AHLs are amphiphilic and possess relatively polar, non-ionic L-homoserine 'head groups' and nonpolar alkyl 'tails'. Many past studies have identified roles that AHLs play in regulating QS in bacteria and have determined the influence of AHL structure on binding to cognate intracellular protein receptors.[12-14] Much of this work has focused on the opportunistic pathogen *Pseudomonas aeruginosa*, which uses both the short-tailed C4-AHL and the long-tailed 3-oxo-C12-AHL (Figure 1) for QS.[1, 5, 7] Although an understanding of the roles that AHLs play in modulating QS is

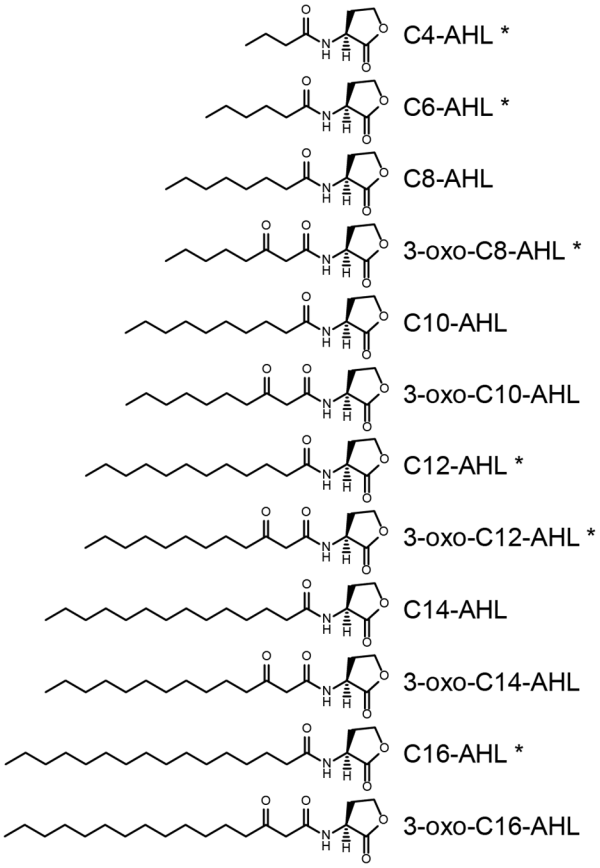


Figure 1: Structures of the naturally occurring AHLs examined in this study. AHLs indicated with asterisks were studied experimentally.

emerging, less is known about how these molecules are transported between cells in solution or within biofilms and the manners by which AHL structure can influence these processes. Kaplan *et al*. reported that AHLs with short tails containing four or six carbon atoms (*e.g.,* C4-AHL) can diffuse freely across bacterial membranes,[15] and Pearson *et al.* have demonstrated that AHLs with longer tails (*e.g.*, 3-oxo-C12-AHL) require active transport to be pumped out of cells (at least in *P. aeruginosa*).[16-17] Classical models of QS also assume that AHLs diffuse freely through the extracellular environment and into neighboring cells. However, AHLs also have the potential to exhibit behaviors such as cooperative self-assembly and surface activity that are common to other conventional amphiphiles, such as surfactants and lipids, which could enable alternate modes of

molecular transport. In support of this view, 3-oxo-C12-AHL and C16-AHL have both been found to be associated with the outer membrane vesicles of various bacterial species,[18] and inhibition of the production of outer membrane vesicles has been reported to inhibit QS.[19] Likewise, Song *et al.* recently reported that bacterial AHLs can insert selectively into lipid rafts found in mammalian cell membranes and trigger processes that lead to apoptosis.[20] These and other related results discussed below suggest that the amphiphilicity of AHLs can facilitate molecular self-assembly and allow them to adsorb or aggregate into nanostructures that could facilitate transport in bacterial communities.

To complement biological assays, model systems have been used to determine if AHLs demonstrate signatures of amphiphilic behavior. Daniels *et al.* reported that C6-AHL, 3-OH-C8-AHL, C10-AHL, C12-AHL and C14-AHL can form monolayers at air/water interfaces that have pressure-area isotherms characteristic of conventional amphiphile films.[21] Davis *et al.* demonstrated using static light scattering that long-tailed AHLs show characteristic signs of aggregation in aqueous buffers above certain critical concentrations that depend, at least in part, upon AHL structure (*e.g.*, tail length).[22] That work also demonstrated using dynamic light scattering (DLS) that 3-oxo-C14-AHL can form aggregates with hydrodynamic diameters of ~20 nm. When combined, those results are consistent with processes of self-assembly, but the hydrodynamic diameters of the aggregates reported by Davis *et al.* were substantially larger than those typically associated with spherical micelles formed by many other single-tailed surfactants,[22] and little is understood about the nanostructures of AHL aggregates or how changes in head and tail group structure could promote changes in aggregate morphology.

These past studies raise many intriguing questions about the roles that supramolecular processes could play in mediating bacterial communication. For example, would the aggregation

of AHLs tend to mute or amplify a signal? Could environmental factors alter such aggregation behavior and thereby serve as a tool with which to tune QS signaling? Could the structures of AHLs be tailored (permanently or transiently)[23] to alter aggregation, and thereby change QS outcomes? As a first step toward providing insight into the potential of AHL aggregation to affect or mediate these biological processes, this current study sought to systematically characterize the impacts of head and tail group structure on the self-assembly of a series of naturally occurring AHLs in defined buffer and in biologically relevant bacterial growth medium. We used two independent biophysical characterization techniques, light scattering and measurements of surface tension, to measure the critical aggregation concentrations (CACs) of some of the most common natural AHLs and characterize the sizes of the nanoscale and microscale aggregates that form in solution. We also characterized the sizes and morphologies of AHL aggregates using transmission electron microscopy (TEM). In combination with these experimental studies, we performed MD simulations to predict the impacts of head group structure and tail length on the thermodynamically preferred aggregate structures formed by these AHLs. The results of alchemical free energy calculations predicted that AHLs containing 10 or more tail carbon atoms should form nanoscale aggregates, with C12-AHL and 3-oxo-C12-AHL preferring to form spherical aggregates around 5 to 6 nm in diameter and C14-AHL, C16-AHL, 3-oxo-C14-AHL, and 3-oxo-C16-AHL preferring to form bilayer vesicles. These MD results and related structure predictions are consistent with the experimental characterization of aggregate size and morphology obtained using DLS and TEM. Overall, our results provide new insights into processes of self-assembly that occur in this important class of non-ionic amphiphiles and provide a potential basis for understanding how the chemical structures of AHLs could influence processes that bacteria use to drive group behaviors such as biofouling and toxin production.

Materials and Methods

Materials. Dimethyl sulphoxide (DMSO) and ethanol were obtained from Fisher Scientific (Pittsburgh, PA). Uranyl acetate (UA), Whatman grade 4 filter paper, and stock 5.0 M sodium hydroxide solution were purchased from Sigma Aldrich (Milwaukee, WI). AHLs were either purchased from Sigma Aldrich or synthesized as previously reported.[12, 24] Syringes (5 mL, 10 mL, and 30 mL) were obtained from Becton Dickinson (Franklin Lakes, NJ). Minisort X plus 0.2 μm syringe filters were acquired from Sartorius Stedim Biotech (Goettingen, Germany). Centrifuge tubes (1.7 mL), were purchased from Axygen products (Tewksbury, MA). DTS1070 folded capillary cuvettes were purchased from Malvern Panalytical (Westborough, MA). Luria-Bertani (LB) medium was obtained from Research Products Industrial (Mt. Prospect, IL). TEM grids (300 Mesh) were purchased from Electron Microscopy Sciences (Haltfield, PA). Deionization of distilled water was performed using a Milli-Q system (Millipore, Bedford, MA) yielding water with a resistivity of 18.2 MΩ. All materials were used as received without further purification unless otherwise specified.

General Considerations. Static and dynamic light scattering measurements were made using a Malvern Zetasizer and 1 cm x 1 cm plastic cuvettes. Zeta potential measurements were made using a Malvern Zetasizer and a DTS1070 folded capillary cell. During light scattering and zeta potential measurements, the detector was placed at an angle of 173° from the 632.8 nm incident laser. Surface tension measurements were acquired using a Nima Type 611 trough with a PS4 pressure sensor (Coventry, England) with Bolin Scientific paper Wilhelmy plates (Bolin Scientific, Gothenburg Sweden) or a Kruss K10T Tensiometer (Matthews, NC) with a platinum Du Noüy

ring or Wilhelmy plate. TEM images were acquired using a Techni T12 Microscope and Gatan 4k Ultrascan CCD camera.

Determination of Critical Aggregation Concentrations (CACs). For all experiments, the AHLs were stored in stock solutions at concentrations of 300 mM in DMSO for C4-AHL, C6-AHL and 3-oxo-C8-AHL and 20 mM, 25 mM, and 2 mM in DMSO for, C12-AHL, 3-oxo-C12-AHL, and C16-AHL, respectively. To prepare dilutions of these DMSO stocks to a desired concentration in aqueous solution, the stocks were first diluted in DMSO to 100 times the final aqueous concentration, and then diluted 1:100 into the desired buffer or medium. The solutions were allowed to sit for 30 minutes at the temperature stated for that experiment before characterization of the CAC. All AHL solutions were used within 3 hours of initial dilutions of the DMSO stocks to minimize the potential impact of AHL head group hydrolysis on the CAC.

Static Light Scattering. The CACs of the AHLs were determined by static light scattering by adapting methods described previously.[22] The desired solvent (water or LB medium) was filtered twice and then centrifuged at 2000 RPM for 3 minutes to remove particulates and air bubbles from the buffer. AHL solutions (1.2 mL) were prepared in a 1.7 mL Eppendorf tube. The samples were then centrifuged again at 1500 RPM for 2 minutes to sediment particulates and remove air bubbles, and allowed to sit thereafter in a constant temperature water bath for 30 minutes. Samples dispersed in water were maintained at 30 °C while those in LB medium were maintained at 37 °C. Aliquots (1 mL) of these samples were transferred to a cuvette and the scattered light intensity was measured three times per sample. Each measurement averaged the intensity of the light scattered by the sample over 5 seconds. Linear regression of increasing scattered light intensity at increasing AHL

concentrations was performed and used to determine the CAC of the AHL being tested as described in the Supporting Information.

Measurement of the Surface Tensions of AHL Solutions. Measurements of the surface tensions of AHL solutions were made using a paper Wilhelmy plate or Du Noüy ring by adapting a procedure described previously.[25] Linear regression of decreasing surface tension at increasing concentration of AHLs was used to determine the CACs of the AHLs as described in the Supporting Information. For measurements using a Nima Type 611 trough, the tensiometer was calibrated using an internal calibration program and checked by ensuring the surface tension of distilled, deionized water was near 72 mN/m. A dry paper Wilhelmy plate was immersed in PBS for 10 minutes at room temperature to hydrate before surface tension measurements were made. AHL solutions were prepared as described above and allowed to sit at room temperature, and then the hydrated Wilhelmy plate was dipped into the AHL solution and allowed to sit at the solution interface for 5 minutes. The surface tension (γ) was determined by measuring the change in force applied to the Wilhelmy plate by the solution while in contact with the solution interface and directly after removing the plate from solution. This change in force (F) was then used in the Wilhelmy equation,[25]

$$\gamma = \frac{F}{l \cos(\theta)} \quad (1)$$

where l is the wetted perimeter of the paper Wilhelmy plate (21 mm) and θ is the contact angle of water on the Wilhelmy plate, which is assumed to be 0º for a paper plate. For measurements made using a Kruss K10T Tensiometer, a platinum Du Noüy ring or Wilhelmy plate was cleaned using a butane torch and immediately hung from the tensiometer balance. The internal gauge was then zeroed to the weight of the ring or plate. The tensiometer was calibrated by adjusting the balance

until a surface tension of ~72 mN/m was recorded for a solution of deionized, distilled water. The ring or plate was then immersed into the AHL solution until the internal motor was enabled and allowed to raise the ring or plate from the solution until the tensiometer balanced. For multiple measurements, the plate or ring was removed from solution, the balance was re-zeroed, and the process was repeated.

Characterization of Aggregate Sizes using Dynamic Light Scattering. DLS measurements of AHL solutions were made using a Malvern Zetasizer ZS Nano. Samples of AHLs were prepared at concentrations above their measured CACs in filtered Milli-Q water or LB medium and allowed to stand at 30 °C or 37 °C, respectively, for 30 minutes. Aliquots (1 mL) of the samples were then transferred to a 1 cm x 1 cm plastic cuvette, the cuvette was then placed in the Zetasizer for 2 minutes at the prescribed temperature, and the scattered light intensity was measured. The correlator measured the intensity correlation function for delay times ranging from 2 μs to 200 ms. The hydrodynamic diameters reported assume that the aggregates measured are spherical and diffuse purely by Brownian motion.

Characterization of Zeta Potential. Zeta potential measurements of AHL solutions were made using a Malvern Zetasizer ZS Nano. Samples of AHLs were prepared at concentrations above their measured CACs in filtered Milli-Q water and allowed to stand at 30 °C for 30 minutes. Aliquots (1 mL) of the samples were then transferred to a DTS1070 folded capillary cuvette, the cuvette was placed in the Zetasizer for two minutes at the prescribed temperature, and zeta potential measurements were performed. The zeta potential of the solution was measured 7 to 10 times per

sample and three independent samples were measured. The zeta potentials of the aggregates were calculated using the Smoluchowski model.

Characterization of AHL Aggregates using Transmission Electron Microscopy. Negative staining of AHL solutions for observation by TEM was performed using uranyl acetate (UA) and a procedure used in past studies to characterize self-assembled surfactant aggregates.[26-29] UA stain (2%) was prepared by mixing 100 mg of UA with 5 mL of boiling Milli-Q water for 5 minutes. Sodium hydroxide (20 μL, 5.0 M) was then added to the stain solution and the resulting solution was stirred for another 5 minutes. The solution was filtered through a 0.22 μm filter and stored in the dark prior to use. Immediately before sample staining, two drops (100 μL each) of the UA stain were pipetted on top of a sheet of parafilm. Solutions of AHLs at desired concentrations above their CACs were prepared in water as described previously and allowed to stand at room temperature for 30 minutes. An aliquot (3 μL) of the AHL solution was then pipetted onto a charged 300 mesh Cu TEM grid and allowed to sit for 1 minute. Excess solution was blotted off of the grid using filter paper, and the grid was immediately passed through a drop of stain. Excess stain was then blotted off, and the grid was submerged in another drop of stain for an additional 60 seconds. Excess stain was again blotted off and further removed using suction. The grid was allowed to air dry before being placed in a TEM grid holder. Stained samples were imaged using a Techni T12 TEM at 120 V accelerating voltage at one second exposure time on a Gatan 4k Ultrascan CCD camera.

Simulation Systems and Parameters. Atomistic MD simulations were performed to model the solution behavior and self-assembly thermodynamics of AHLs. Atomistic models were chosen to

capture the detailed chemistry of the AHL structures shown in Figure 1, including the difference between AHLs with and without a 3-oxo group. AHL structures were generated using the CHARMM-GUI Ligand Reader & Modeler.[30-31] The CHARMM36 force field was used to model the AHLs with the TIP3P model for water. Two types of simulations were performed: unbiased MD simulations to observe AHL self-assembly, and alchemical free energy calculations to compute the free energy change for aggregation (detailed below). In all simulations, Verlet lists were generated using a 1.2 nm neighbor list cutoff. Van der Waals interactions were modeled with a Lennard-Jones potential using a 1.2 nm cutoff that was smoothly shifted to zero between 1.0 nm and 1.2 nm. Electrostatic interactions were calculated using the smooth Particle Mesh Ewald method with a short-range cutoff of 1.2 nm, grid spacing of 0.12 nm, and 4^{th} order interpolation. Bonds were constrained using the LINCS algorithm. Unbiased simulations were performed using a leapfrog integrator with a 2-fs timestep, whereas alchemical free energy calculations were performed using a leapfrog stochastic dynamics integrator with a 2-fs timestep. All simulations were performed using Gromacs 2016.[32]

Initial configurations for the unbiased simulations consisted of AHL molecules placed on a grid spaced by 1.5 nm in each Cartesian direction. Unbiased simulations were performed for 64 C4-AHL molecules and for 64, 216, and 512 3-oxo-C12-AHL molecules. Initial simulation configurations for the alchemical free energy calculations consisted of either a single AHL in water or an AHL aggregate generated using PACKMOL.[33] Five different aggregate structures were generated: three spherical aggregates with 20, 50, and 100 AHL molecules, respectively; cylindrical aggregates with 150 AHL molecules; and bilayers with 128 AHL molecules (oriented with the normal parallel to the *z*-axis of the simulation box). Each system was solvated in water

after preparation. Snapshots of example systems as prepared are shown in the Supporting Information.

All simulation systems were energy minimized using the steepest descent method. The unbiased simulations were performed for 50 ns with the temperature maintained at 37 °C using a Berendsen thermostat with a time constant of 1.0 ps and the pressure maintained at 1 bar using an isotropic Berendsen barostat with a time constant of 5 ps and a compressibility of 4.5×10^{-5} bar^{-1}. For the alchemical free energy calculations, the energy minimized systems were first equilibrated with the temperature maintained at 37 °C using a Berendsen thermostat with a time constant of 1.0 ps and the pressure maintained at 1 bar using a Berendsen barostat with a time constant of 5 ps and a compressibility of 4.5×10^{-5} bar^{-1}. An isotropic barostat was used for the equilibration of spherical aggregates, whereas a semi-isotropic barostat was used for the equilibration of bilayers. A more elaborate pressure coupling protocol, involving both a semi-isotropic and an isotropic Berendsen barostat, was used for the equilibration of the cylindrical aggregates as detailed in the Supporting Information. Aggregate structures were equilibrated for 50 ns, and the single AHL in water was equilibrated for 5 ns. To confirm that the systems had reached equilibrium, the last 10 ns of each equilibration trajectory were divided into two blocks, then AHL center-of-mass density distributions were computed for each block and compared to ensure no further change in aggregate structure. Further details on this procedure are provided in the Supporting Information.

Alchemical Free Energy Calculation Theory and Implementation. The CAC is related to the free energy change for aggregation, $\Delta\mu_{aggr}$, by Equation 2:[34]

$$\Delta\mu_{aggr} = -(\mu_1^o - \mu_N^o) = RT \ln (CAC) \quad (2)$$

μ_N^o is the chemical potential of an amphiphile in an aggregate with aggregation number N (indicating the number of molecules in the aggregate), μ_1^o is the chemical potential of a single amphiphile in dilute solution, T is the temperature of the system, and R is the universal gas constant. $\Delta\mu_{aggr}$ depends on both the aggregate shape and N.[34]

$\Delta\mu_{aggr}$ was calculated using the thermodynamic cycle shown in Figure 2. μ_N^o is equal to the free energy change for inserting an AHL into an aggregate, $\Delta G_{0\rightarrow agg}$, and μ_1^o is equal to the hydration free energy of an AHL, $\Delta G_{0\rightarrow w}$. These free energies were obtained from alchemical free energy calculations and $\Delta\mu_{aggr}$ was then computed from their difference according to Equation 3:

$$\Delta\mu_{aggr} = -(\mu_1^o - \mu_N^o) = -(\Delta G_{0\rightarrow w} - \Delta G_{0\rightarrow agg}) \quad (3)$$

$\Delta G_{0\rightarrow w}$ was calculated by modifying the potential energy function of the system using two coupling parameters, λ_{elec} and λ_{vdw}, which scale the electrostatic and van der Waals interactions of the AHL with the rest of the system. Coupling parameters were varied from zero, corresponding to an AHL in solution, to one, corresponding to an AHL in the gas phase that does not interact with the rest of the system, in 21 independent simulations. The corresponding free energy change for this transformation was computed using the Multistate Bennett Acceptance Ratio (MBAR) method.[35] $\Delta G_{0\rightarrow agg}$ was similarly calculated in 27 independent simulations using three coupling parameters, λ_{elec}, λ_{vdw} and λ_{rest}, with λ_{rest} scaling the value of a harmonic restraint that was applied to ensure the AHL molecule remained in the aggregate as interactions with the system were modified. Complete details on all alchemical free energy calculations are provided in the Supporting Information.

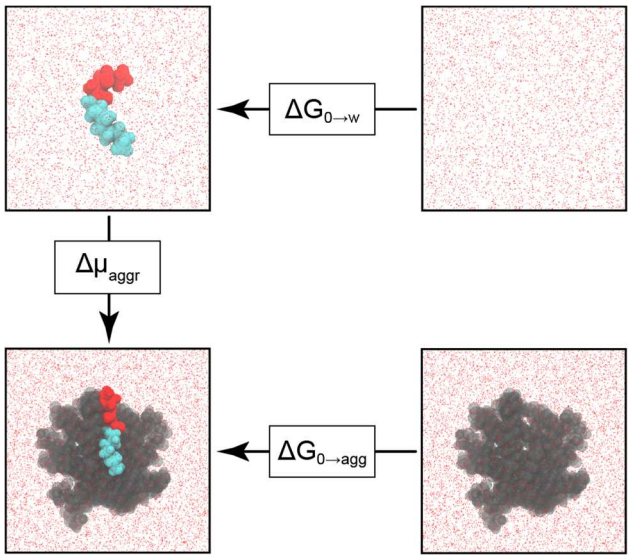


Figure 2: Thermodynamic cycle for calculating the free energy change for aggregation, $\Delta\mu_{aggr}$, for a representative AHL (3-oxo-C12-AHL). The head and tail groups of the AHL are drawn in red and cyan, respectively. The free energy change upon removing the AHL from the system was calculated by setting the coupling parameters to zero. The remaining AHLs in the aggregate are drawn in gray. Water is shown as red points.

Results and Discussion

Experimental Characterization of the Critical Aggregation Concentrations of AHLs

Davis *et al.* previously used static light scattering to characterize the aggregation behavior of AHLs in a sucrose buffer containing 0.5% DMSO (v/v) to aid in AHL solubility (whereas short-tailed AHLs are readily soluble in aqueous solution, longer-tailed AHLs can be difficult to dissolve in water).[22] Those past studies suggested that AHLs with more than 12 carbons in the alkyl tail form aggregates in solution, with reported CACs of 4 μM, 17 μM, and 247 μM for C12-AHL, 3-oxo-C14-AHL, and 3-oxo-C12-AHL, respectively. In contrast, AHLs with alkyl tails shorter than 12 carbons were not reported to aggregate at concentrations below 400 μM under these conditions. We performed a series of initial experiments using solutions of 3-oxo-C12-AHL prepared using the sucrose buffer reported by Davis *et al.* and 0.5% DMSO (v/v). Under these conditions, we

observed the rapid formation of large, visible white precipitates at high concentrations that frustrated meaningful characterization of the CAC by light scattering and necessitated the selection of an alternate medium for analysis. In all studies described below, we used solutions of AHLs prepared using either deionized water or LB medium (a common bacterial growth medium) containing 1% DMSO (v/v), unless otherwise noted. These conditions eliminated the formation of large visible precipitates and led to consistent and reproducible results in all of the experiments described below. Aqueous buffer and LB medium containing 1% DMSO (v/v) have been used in past studies to investigate natural and synthetic AHLs in bacterial cultures.[8-9, 12, 14] These conditions were thus also adopted here to permit potential future connections between the results of this physicochemical study and those past microbiological studies.

We used both static light scattering and surface tension measurements to characterize the aggregation behaviors of AHLs as a function of AHL concentration. These measurements are complementary and, thus, allowed us to characterize and confirm the formation of aggregated structures in solution using two different methods. Representative results arising from these two methods to characterize the CAC of 3-oxo-C12-AHL are shown in Figure 3 and are discussed in greater detail below.

We first characterized the CACs of C4-AHL and 3-oxo-C12-AHL, which again are the two native AHLs used to regulate QS in *P. aeruginosa.* Solutions of 3-oxo-C12-AHL in deionized water at 30 °C exhibited characteristic signs of aggregation corresponding to a CAC of 88 μM (Table 1; data sets from which CACs were extracted are included in the Supporting Information). These results are, in general, consistent with those reported by Davis *et al.*, although the CAC we report here (88 μM) is three-fold lower than the value reported in that past study (247 μM). This disparity is likely a result, at least in part, of differences in the solution conditions used here (we

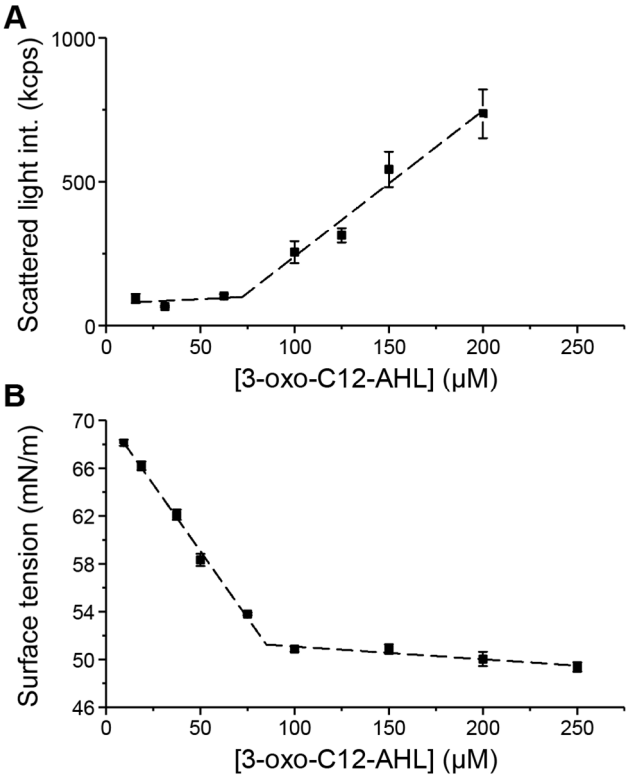


Figure 3: Representative plots illustrating the calculation of the CAC for 3-oxo-C12-AHL using (A) light scattering at 30 °C, and (B) surface tension measurements. Error bars represent the standard deviation of three measurements for a single sample. The dashed lines represent the linear regression in (A) and (B). The CAC is calculated as the AHL concentration at which the two regression lines intersect. CACs reported in the main text (Table 1) are the average of three independent samples. Data for all samples are presented in the Supporting Information.

note further that, in our hands, 3-oxo-C12-AHL begins to visibly precipitate in both sucrose buffer and water at a concentration of ~250 μM). The CAC measured here for 3-oxo-C12-AHL using light scattering (88 μM) was also similar to the CAC determined using surface tensiometry (97 μM, see Table 1). In contrast, while solutions of C4-AHL did show increased scattered light intensity at increasing concentrations of C4-AHL, they did not exhibit decreasing surface tension at increasing concentrations. The lack of surface activity associated with this short-tailed AHL is not consistent with processes of cooperative self-assembly typical of other amphiphilic molecules; the observation of scattered light intensity at increasing concentration in the absence of surface activity suggests that C4-AHL may behave more like a hydrotrope in aqueous solution.[36]

Table 1: Experimentally measured CACs of naturally occurring AHLs.

AHL	CACs (μM)		
	Light scattering		Surface tension
	Water[a]	*LB medium*[b]	*Water*[c]
C4-AHL	No aggregation		
3-oxo-C8-AHL	1920 ± 150	2020 ± 20	2170 ± 250
3-oxo-C12-AHL	88 ± 20	78 ± 17	97 ± 11
C12-AHL	3.7 ± 0.3	3.8 ± 0.4	4.0 ± 0.2
C16 AHL	0.12 ± 0.14	0.09 ± 0.02	0.16 ± 0.04[**]

Experiments performed at [a]30 °C in deionized water, [b]37 °C in LB medium, and [c]room temperature (RT) in deionized water. All experiments contained 1% DMSO in the aqueous phase. The CAC values reported are the averages and standard deviations of three replicates. [**]See SI (Figure S1B) for further discussion.

We next characterized the CACs of four additional native AHLs (C6-AHL, 3-oxo-C8-AHL, C12-AHL, and C16-AHL; Figure 1) using light scattering and surface tension measurements. The three longer-chained AHLs (*i.e.,* 3-oxo-C8-AHL, C12-AHL and C16-AHL) exhibited characteristic signs of aggregation in both measurements, with CACs of 1920 μM, 3.7 μM, and 120 nM, respectively, in the light scattering measurements (Table 1; data from which these results were extracted are included in the Supporting Information). Similar to the results for 3-oxo-C12-AHL, CACs determined by the surface tension measurements were in reasonable agreement with the CACs determined by static light scattering. We note that the concentrations of AHLs in solution and their corresponding changes in surface tension were small when compared to changes in surface tension observed for other common surfactants characterized using this surface tension measurements (see the Supporting Information for further discussion of light scattering and surface tension results).[37-39] We therefore used linear regressions of surface tension

against concentration, rather than logarithmic plots, to fit these data and obtain secondary measurements of the CAC.

In contrast to the longer-chained AHLs, for solutions of C6-AHL, linear regression of the scattered light intensity at increasing AHL concentrations resulted in negative values of CAC in several samples, and none were comparable to the concentrations at which surface tension was observed to become constant. As a result, we were unable to conclude whether assemblies formed in solutions of C6-AHL were likely to result from cooperative self-assembly. Further discussion of the behavior exhibited by C4-AHL and C6-AHL in these two measurements is provided in the Supporting Information.

Overall, we observed CACs to decrease as AHL tail length increased (Table 1). This behavior is similar to that of other families of cationic, anionic, and nonionic surfactants in aqueous solution.[21-22] The molecular structure of the AHL head group also had a significant impact on CAC; the addition of a single 3-oxo group to C12-AHL (to form 3-oxo-C12-AHL), resulted in an order of magnitude increase in the CAC from 3.7 μM to 88 μM (Table 1). This observation is generally consistent with results reported by Davis *et al.*, using these two AHLs.[22] In contrast with Davis *et al.* however, we observed that the shorter chained 3-oxo-C8-AHL did aggregate in solution.

We performed a second set of light scattering measurements to characterize AHL CACs in LB medium at 37 °C, a set of environmental conditions used in past microbiological studies of these compounds.[8-9, 12, 14] Table 1 shows that the changes in ionic strength and temperature did not impact the CACs of these AHLs compared to those in water at room temperature. In addition, to determine if the presence of additional DMSO in solution impacted the CACs of the AHLs studied, static light scattering measurements were performed on a solution of C12-AHL in water containing

1.5% DMSO. The CAC of C12-AHL measured under these conditions was 6.6 μM (data not shown), suggesting that the additional DMSO does not have a significant impact on the formation of aggregates. Finally, we characterized the zeta potentials of aggregates of these AHLs using solutions of 3-oxo-C12-AHL, C12-AHL, and C16-AHL at concentrations above their measured CACs in water at 30 °C. The aggregates in these solutions exhibited negative zeta potentials with magnitudes ranging from -20 mV to -44 mV (see Figure S3). When combined, these results support the view that non-ionic AHLs can engage in cooperative self-assembly and provide insight into structural features that can govern this behavior. We return to a discussion of additional physical characterization of these aggregates by transmission electron microscopy (TEM) and dynamic light scattering (DLS) in the sections below.

Unbiased Molecular Dynamics Simulations of AHL Aggregation

The experimental characterization methods used above do not provide information about the sizes, shapes, or morphologies of the AHL aggregates that form at or above CAC. To obtain molecular-scale insight into factors that could influence AHL self-assembly and resulting self-assembled structures, we performed 50-ns unbiased atomistic MD simulations of C4-AHL molecules and 3-oxo-C12-AHL molecules in water. Figure 4A-B shows the atomistic representation of these molecules. We first performed simulations of either 64 C4-AHL or 3-oxo-C12-AHL molecules initialized in well-separated positions in water. This number of molecules is similar to the typical aggregation number (*i.e.*, number of molecules per aggregate) for many nonionic surfactants.[40-42] Figure 4A shows that C4-AHL molecules remain dispersed at the end of the simulation. Conversely, Figure 4B shows that 3-oxo-C12-AHL molecules rapidly self-assemble within the same simulation timescale to form a spherical micelle. These results are

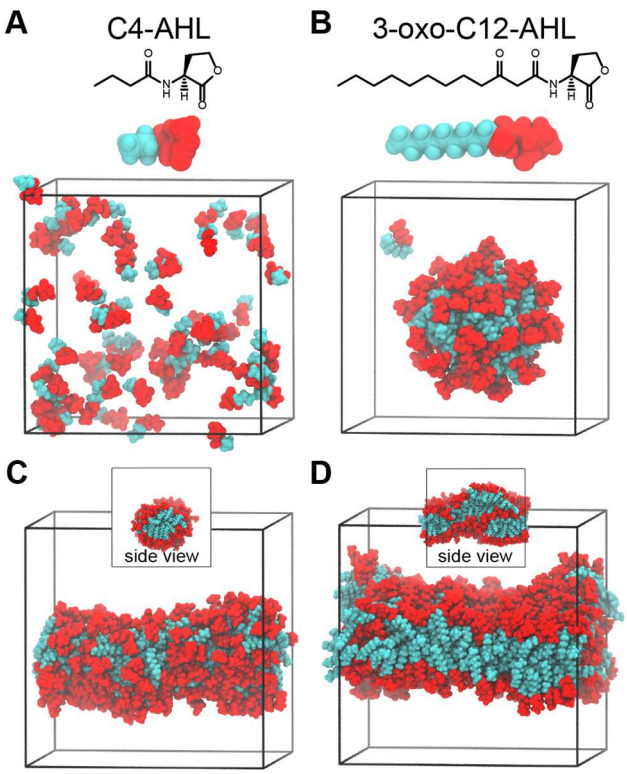


Figure 4: Simulation snapshots from 50-ns unbiased MD simulations. All snapshots are of final simulation configurations. Water molecules are not shown for clarity. AHL head groups are red and tail groups are cyan. (A) Simulation of 64 C4-AHL molecules in water, which remain dispersed within the simulation timescale. The structure of C4-AHL and corresponding atomistic MD representation are shown at top. (B) Self-assembly of 64 3-oxo-C12-AHL molecules in water to form a spherical micelle. The structure of 3-oxo-C12-AHL and corresponding atomistic MD representation are shown at top. (C-D) Self-assembly of 216 and 512 3-oxo-C12-AHL molecules to form (C) a cylindrical aggregate and (D) a bilayer-like structure. The insets show side views of the aggregates.

generally consistent with our experimental measurements, in which 3-oxo-C12-AHL exhibited characteristic signs of aggregation, but we were unable to clearly interpret the behavior of C4-AHL. We next performed additional unbiased MD simulations of 3-oxo-C12-AHL self-assembly with a larger number of molecules to determine whether non-spherical structures with larger aggregation numbers could also form. Rather than form multiple smaller micelles, Figure 4C shows that simulations of 216 3-oxo-C12-AHL molecules self-assemble into a cylindrical aggregate. Furthermore, Figure 4D shows that collections of 512 3-oxo-C12-AHL molecules self-

assemble into a bilayer-like structure. These results suggest that AHLs can form extended aggregates that would have much larger sizes than conventional micelles. However, the actual concentration of AHLs in these simulations is much higher than values used in the experiments above; thus, these simulations can only qualitatively confirm and predict self-assembly trends in agreement with related experimental observations (see further discussion below).

Free Energy Calculations for the Determination of Self-Assembled Structures

The CACs of AHLs cannot be directly determined using the unbiased simulations because experimentally relevant aggregation numbers and AHL concentrations cannot be modeled at atomistic resolution. To complement the unbiased simulations and provide additional insight into trends observed in our experimental CAC results, we calculated $\Delta\mu_{aggr}$ using alchemical free energy calculations to compare self-assembly thermodynamics between simulations and experiments. In general, the aggregation free energy depends on both aggregate structure and the aggregation number.[34] We thus hypothesized that the structure that minimizes $\Delta\mu_{aggr}$ for a given AHL corresponds to the equilibrium structure formed by that AHL in solution. We computed $\Delta\mu_{aggr}$ for AHLs assembled into spheres, cylinders, and bilayers to correspond to the three limiting structures identified in the unbiased simulations. These calculations allowed us to test the hypothesis that cylindrical or bilayer structures could be lower free energy structures than spherical micelles for some AHLs, corresponding to the possible formation of extended aggregates in solution. For each AHL, we also modeled three spherical aggregates with different aggregation numbers (N = 20, 50, and 100). Known aggregation numbers for single-tailed surfactants are generally in this range.[40-43] Moreover these aggregation numbers produce roughly spherical micelles based on the calculation of the asphericity of the resulting aggregates (as described in the

Supporting Information), a parameter that has been used previously to validate the aggregation number for spherical micelles.[43] The aggregation numbers for the cylindrical aggregates and bilayers was effectively infinite because both structures spanned the periodic boundaries of the simulation boxes. We thus ignored potential end effects associated with these structures, although in an experimental system any self-assembled bilayer structure that formed in solution would likely lead to the formation of vesicles to eliminate end effects. Similarly, we also neglected the effect of vesicle curvature, which would introduce an additional elastic free energy term not considered in the alchemical free energy calculation. Simulations of 1-palmitoyl-2-oleoyl-glycero-3-phosphocholine (POPC) were performed as a control to validate our methodology; as expected, $\Delta\mu_{aggr}$ was lowest for a bilayer structure (see Supporting Information, section S8), which agrees with the experimental observation that lipids self-assemble into vesicles.

$\Delta\mu_{aggr}$ was only calculated for starting structures that remained stable during initial equilibration. All C4-AHL, C6-AHL, and 3-oxo-C8-AHL systems dispersed during equilibration, indicating that none of these AHLs formed stable aggregates in the simulations. These AHLs were excluded from the $\Delta\mu_{aggr}$ calculations. We note, however, that 3-oxo-C8-AHL was observed to form aggregates in the experiments described above, which contradicts the simulation results; this discrepancy could result from small systematic error in the simulation force field parameterization, as discussed further below. Starting structures generated for C8-AHL and 3-oxo-C10-AHL bilayers formed a slab of AHLs with no defined structure at the end of the equilibration, instead of a defined bilayer structure with the head groups arranged at the periphery of the aggregate and tail groups forming the core of the bilayer. We interpret this result to indicate that C8-AHL and 3-oxo-C10-AHL do not form stable bilayers and thus excluded these systems from the $\Delta\mu_{aggr}$ calculations.

Figure 5 reports values of $\Delta\mu_{aggr}$ for spherical micelles formed from 3-oxo-C12-AHL, C12-AHL, and C16-AHL calculated from simulations. Figure 5 also shows values of $\Delta\mu_{aggr}$ determined from our experimentally measured CACs using light scattering at 37 °C in LB medium using Equation 2, which can be compared to the simulation values to validate the modeling approach. We expected agreement for spherical micelles because they have smaller aggregation numbers than larger aggregates (*e.g.*, vesicles), which often require the input of external energy (*e.g.*, by sonication) to overcome kinetic barriers for spontaneous formation.[44-45] Simulation calculations of $\Delta\mu_{aggr}$ are reported for all three aggregation numbers because the preferred aggregation number of spherical micelles formed experimentally is unknown; thus, we anticipate that the aggregation number corresponding to the simulation value of $\Delta\mu_{aggr}$ that most closely matches the experimentally determined value would correspond to the experimentally observed micelle size. Both the simulation and experimental values of $\Delta\mu_{aggr}$ exhibit similar trends: increasing the aliphatic tail length decreases $\Delta\mu_{aggr}$ (indicating more favorable aggregation) while adding a 3-oxo group to C12-AHL increased $\Delta\mu_{aggr}$. The closest agreement between the simulated and experimentally determined values of $\Delta\mu_{aggr}$ was found for the largest spherical micelles studied (N = 100), suggesting that these micelles are thermodynamically preferred. This observation is consistent with prior studies of nonionic amphiphiles which exhibit aggregation numbers between 80-150.[46] The MD simulations do systematically underestimate the magnitude of $\Delta\mu_{aggr}$ compared to the experimental measurements, which may result from errors associated with force fields or underestimated aggregation numbers.[47] Nonetheless, these results demonstrate that our simulation methodology can predict qualitative trends for AHL self-assembly that agree with experimental observations, permitting further interrogation of self-assembly thermodynamics, and suggest that AHL micelles form with ~100 molecules per aggregate.

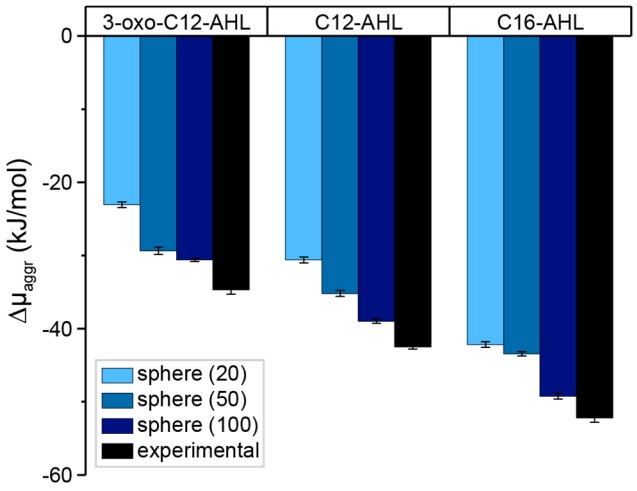


Figure 5: Comparison of $\Delta\mu_{aggr}$ using experimentally calculated CACs obtained by light scattering at 37 °C in LB medium to $\Delta\mu_{aggr}$ calculated using alchemical free energy calculations. The experimental error bars represent standard error and simulation error bars represent standard deviation.

We next sought to determine if extended aggregates could be more thermodynamically favorable than spherical micelles for some AHLs. Figure 6 and Table S2 of the Supporting Information show plots of $\Delta\mu_{aggr}$ for AHLs shown in Figure 1 (including AHL structures that were not characterized experimentally in the studies described above) as a function of tail length and the absence (Figure 6A) or presence (Figure 6B) of a 3-oxo group in the head group. $\Delta\mu_{aggr}$ is reported for all three spherical structures (N = 20, 50, and 100) as well as extended cylindrical and bilayer aggregates. In these plots, the lowest value of $\Delta\mu_{aggr}$ for any given AHL indicates the most thermodynamically preferred structure predicted for that compound. As the AHL tail length increases, extended aggregates (cylindrical aggregates and bilayers) are increasingly preferred compared to spherical micelles. In particular, the simulations predict that C14-AHL, C16-AHL, and 3-oxo-C16-AHL strongly prefer bilayer formation and that 3-oxo-C14-AHL should exhibit a similar thermodynamic preference for both extended cylinders and bilayers. These results are

generally consistent with trends based on the molecular packing parameter, as increasing the AHL tail length would increase the packing parameter to prefer increasingly planar structures consistent with extended aggregates.[34] These findings predict that, irrespective of the relatively small difference in the structures of their head groups, long-tailed C14- and C16-AHLs should self-assemble into vesicle-like structures at equilibrium. Our simulation results suggest that all other AHLs studied here (C8-, C10- and C12- AHLs) should prefer to form medium- to large-sized spherical aggregates containing 50 to 100 molecules, although we note that there is only a small difference between values of $\Delta\mu_{aggr}$ for spherical and extended aggregate structures for these AHLs.

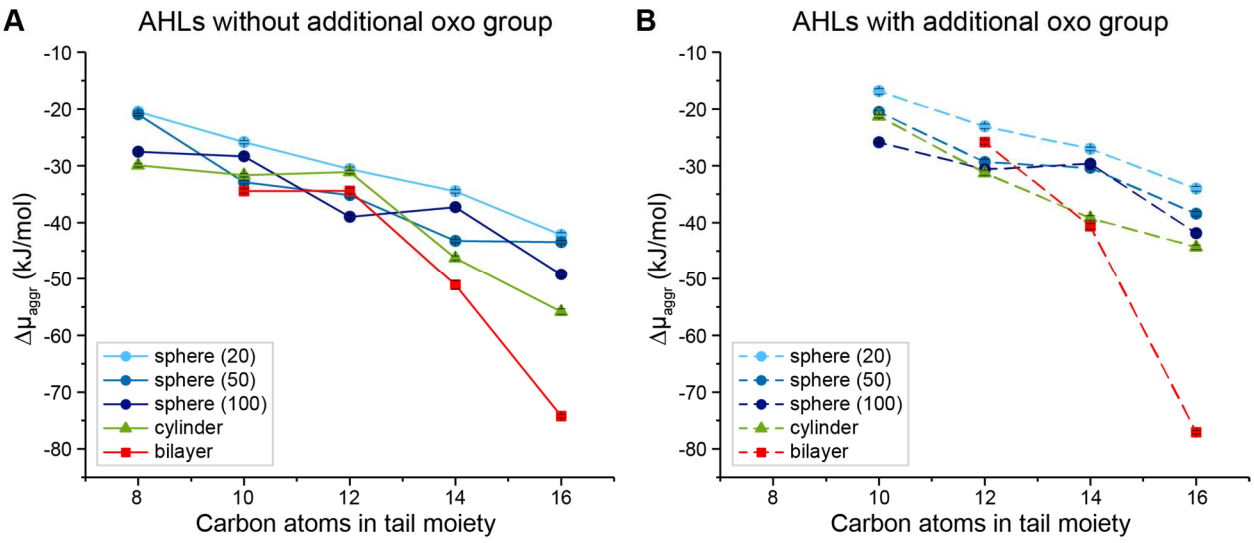


Figure 6: $\Delta\mu_{aggr}$ for each AHL structure in kJ/mol. The solid and dashed lines represent AHLs without and with the oxo additional group in the head moiety, respectively. Error bars represent the standard deviation and are generally smaller than the symbols.

Experimental Characterization of Aggregate Size and Morphology

We used TEM to characterize the sizes and structures of aggregates formed in solutions of AHLs and determine whether key outcomes predicted by our MD simulations could be observed

experimentally. In a first series of studies, we characterized aggregates formed in solutions of 3-oxo-C12-AHL and C12-AHL because our simulations predicted no strong thermodynamic bias for the formation of micelles or bilayer structures for these compounds. All imaging experiments were performed using solutions of AHLs at concentrations above their experimentally determined CACs (Table 1) in water at ambient room temperature, and samples were stained with a 2% uranyl acetate solution prior to imaging using a procedure reported in past studies to characterize surfactant self-assembly.[26-29] Panels A-D of Figure 7 show representative TEM images of aggregates formed by 3-oxo-C12-AHL (A-B) and C12-AHL (C-D) and reveal evidence of nanoscale structures in both samples. In general, these nanostructures and all others described below were spherical or quasi-spherical in shape, and they appeared to be singular particulate structures. We did not observe particle clustering, evidence of flocculation, or 'aggregates of aggregates', consistent with the observation of large and negative zeta potentials measured for solutions of these AHLs and the colloidal stability that that would impart (as described above; see Figure S3).

Further inspection of these images reveals these samples to be comprised of distributions of aggregates with substantially different sizes. Analysis of aggregate sizes using Image J revealed samples of 3-oxo-C12-AHL to contain both smaller aggregates with average diameters of 6.8 ± 1.7 nm and larger aggregates with average diameters of 36.4 ± 7.2 nm (histograms showing the results of these analyses are provided in Figure S9 of the Supporting Information). Analysis of samples of C12-AHL also revealed populations of both smaller and larger aggregates, with average diameters of 7.1 ± 1.8 nm and 22.1 ± 9.7 nm, respectively. In some samples of C12-AHL, we also occasionally observed the existence of a small number of substantially larger aggregates around

~50-200 nm in diameter (Figure S12); however, the vast majority of particles observed in these samples had average sizes on the order of 30 nm or below.

The average sizes of the smaller aggregates in samples of 3-oxo-C12-AHL and C12-AHL are similar to the sizes of the 100-molecule spherical aggregates predicted by our MD simulations

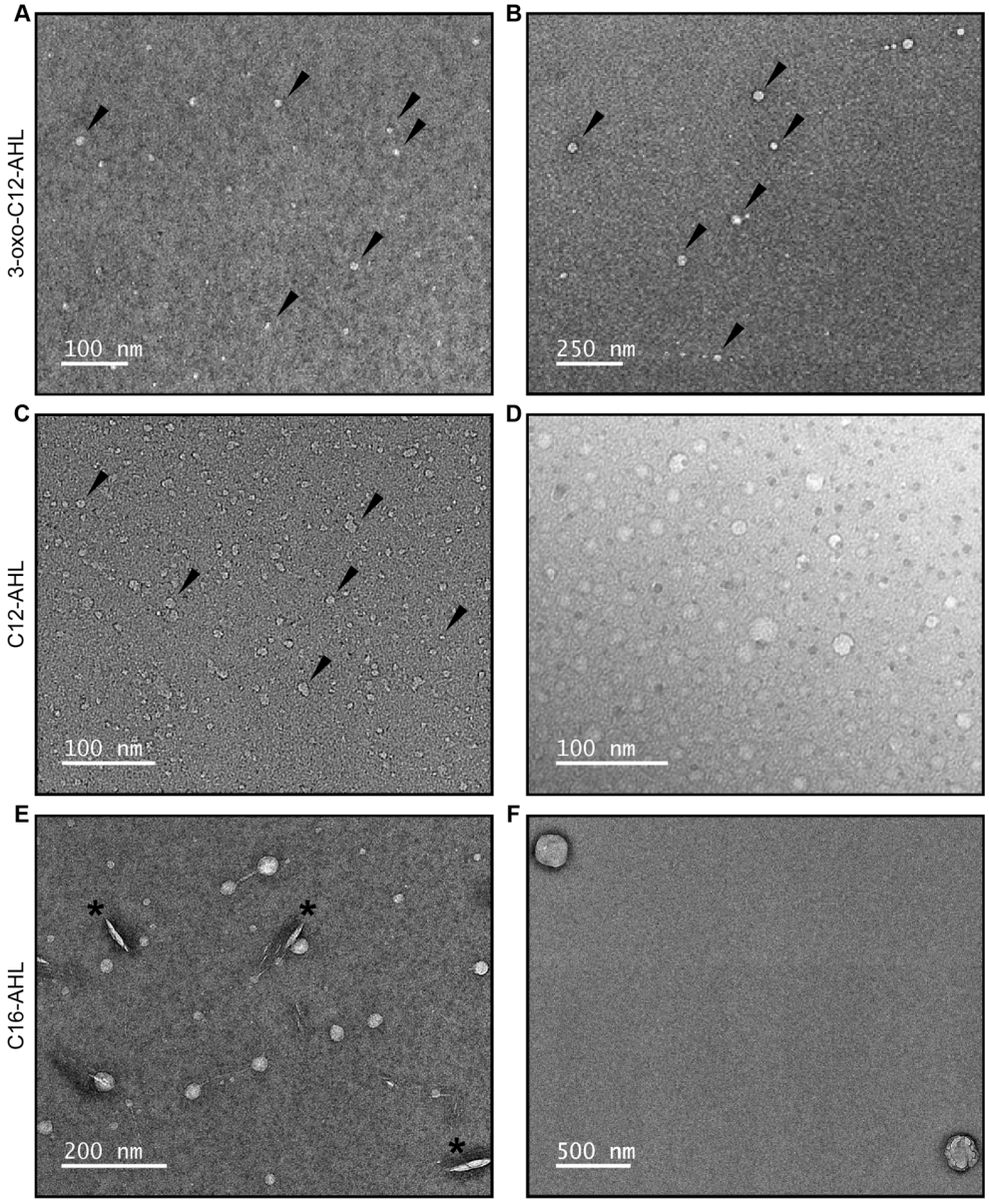


Figure 7: TEM images of samples of (A,B) 3-oxo-C12-AHL, (C,D) C12-AHL, and (E,F) C16-AHL in water. The black arrows in (A-C) identify representative examples of aggregates in these samples and the black asterisks in (E) identify defects arising from the staining of that sample.

(diameters were calculated to be ~6.1 nm and ~6.4 nm for 3-oxo-C12-AHL and C12-AHL, respectively; see Supporting Information for additional details of these calculations). These values are also consistent with sizes typically associated with micelles formed by conventional small-molecule amphiphiles. The sizes of the larger aggregates in these samples are larger than those reported for conventional micelles and are consistent with the presence of extended bilayer structures (for example, small unilamellar vesicles of phospholipids often form in a size range of 20-100 nm).[48] In general, these results are consistent with predictions arising from Figure 6, which predicts the aggregation free energies for spherical aggregates and extended cylindrical/bilayer structures to be similar for both C12-AHL and 3-oxo-C12-AHL, indicating that both types of aggregate structures may form in solution. We note, however, that our simulations did not consider the formation of alternative structures that could also fall within a similar size range, such as discoidal aggregates or multilayer structures. Our simulations also neglect the elastic free energy associated with forming small vesicles that could modify the size distribution.[48]

We also imaged samples prepared from solutions of C16-AHL, as the simulations above predicted that this compound should strongly prefer the formation of bilayer structures (Figure 6). The images shown in Figure 7E-F are generally consistent with that prediction. These images show aggregates with average sizes that are substantially larger than those shown in Figure 7A-D, with average diameters of 28.6 ± 7.2 nm (Figure 7E) and some structures as large as 250 nm (Figure 7F). We note that closer inspection of the image in Figure 7E also reveals some aggregates to be connected by long, thin tubular structures. The origin of these tubular structures is not clear, and we caution that they could be artifacts arising from shear experienced by these aggregates during the staining and preparation of these samples for analysis.[49-51] These observations are interesting, however, because they also hint at the possibility that these vesicular AHL aggregates could be

capable of undergoing further transformations or exhibiting other dynamic behaviors similar to those observed in other phospholipid vesicles or other self-assembled vesicle systems.[49-51]

Overall, the results of these TEM experiments are consistent with the results of our MD simulations, which predicted a transition from the formation of spherical micelles to the formation of more extended bilayer structures upon progression from C12-AHL to C16-AHL. In a subsequent series of imaging experiments, we used TEM to characterize solutions of 3-oxo-C8-AHL as a representative shorter-tailed AHL that was observed experimentally to form aggregates (Table 1) but was not predicted to form stable aggregates in our simulations. The results of those experiments are shown in Figure S11. In general, these samples consisted of larger aggregates with average diameters of ~60 nm, consistent with the formation of vesicular structures. We did not observe smaller aggregated structures similar to those shown in Figure 7A-D formed in solutions of C12-AHL and 3-oxo-C12-AHL. The factors influencing the apparent anomalous behavior of this shorter-tailed AHL are not currently understood.

The results of our TEM experiments reveal solutions of AHLs to contain aggregates with sizes that are generally consistent with those predicted by our MD simulations. We note, however, that negative stain TEM is inherently limited to characterization of relatively small numbers of particles. This method can also potentially introduce artifacts resulting from the dynamic reorganization of self-assembled structures during the staining/dehydration process. We therefore performed a final series of characterization experiments using DLS to provide additional information about the sizes of larger populations of hydrated aggregates suspended in aqueous solution. All DLS measurements reported here were prepared at 30 °C using solutions of AHLs in water at concentrations above their previously determined CACs; no particles of discernable size were observed at sub-CAC concentrations of AHL under these conditions. Autocorrelation

functions and corresponding calculated particle size distributions for all measurements discussed below are provided in Figure S10 of the Supporting Information.

Characterization of solutions of C16-AHL by DLS yielded number and intensity average size distributions with a single peak corresponding to particles with an average hydrodynamic diameter of ~100 nm. This value is consistent with the presence of larger vesicular structures and on the order of the sizes of aggregates observed for this AHL by TEM (Figure 7E-F), suggesting that the larger structures identified in Figure 7E-F were not the result of artifacts introduced during the staining of those samples. Characterization of solutions of C12-AHL also yielded unimodal number and intensity average size distributions corresponding to particles with average hydrodynamic diameters of ~350 nm. This average size is substantially larger than the sizes of particles observed by TEM for C12-AHL (Figure 7C-D), and our DLS results did not reveal evidence of a population of smaller aggregates (as observed by TEM; Figure 7C-D and Figures S12). As noted above, we did observe a small number of larger (~50-200 nm) aggregates in solutions of C12-AHL by TEM (Figure S12). It is possible that the presence of those larger particles, which would scatter substantially more light than a smaller particle, could obscure the presence of any micellar-sized aggregates that may be present in those samples. Such behavior has been observed previously for the DLS characterization of mixtures of nanoparticles having substantially different sizes, where often only the larger population of particles may be observed.[52-55] We note, in this context, that we did obtain autocorrelation functions that were consistent with a more complex distribution of particle sizes in solutions of 3-oxo-C12-AHL (Figure S10). However, solutions of this AHL proved difficult to characterize with run-to-run consistency. Multiple non-linear least squares algorithms including CONTIN analyses of those samples returned bimodal size distributions (Figure S10), which is consistent with the observation of both

small and large populations of aggregates in samples of this AHL by TEM. However, we were not able to obtain fits to the scattering functions that were sufficient to report meaningful size distributions for solutions of this AHL.

Finally, we note that Davis *et al.* previously reported the use of DLS to characterize solutions of 3-oxo-C14-AHL in aqueous buffer. That study reported the average hydrodynamic diameter of aggregates of that AHL to be ~22 nm and interpreted that result to suggest that 3-oxo-C14-AHL can self-organize into micelles. We did not characterize solutions of 3-oxo-C14-AHL experimentally as part of this current study. We comment, however, that 22 nm is substantially larger than the size expected for a conventional spherical micelle, and that aggregates of that approximate size are consistent with those of the larger vesicular aggregates observed in our TEM images of solutions of 3-oxo-C12-AHL and C12-AHL. We thus consider it possible that solutions of 3-oxo-C14-AHL, as characterized in that prior study, could also form larger vesicular structures. This possibility is further supported by the results of our MD simulations, which predict that the formation of cylinders or bilayer structures should be more thermodynamically favorable for 3-oxo-C14-AHL than the formation of spherical micelles (Figure 6).

Summary and Conclusions

In this work, we combined biophysical characterization techniques, electron microscopy, and MD simulations to investigate the self-assembly of 12 AHLs representative of the lipophilic signal class used by Gram-negative bacteria for quorum sensing (QS). We used static light scattering and surface tension measurements to determine that 3-oxo-C8-AHL, 3-oxo-C12-AHL, C12-AHL, and C16-AHL self-assemble in aqueous solution and to characterize their corresponding CACs. In general, CACs decreased with increasing tail length. The CAC for 3-oxo-C12-AHL was an order of magnitude higher than that of C12-AHL, revealing the impact of AHL

head group chemistry on self-assembly. Atomistic MD simulations predicted that 3-oxo-C12-AHL molecules self-assemble in unbiased simulations into spherical, cylindrical, or bilayer-like aggregates. We then utilized alchemical free energy calculations to determine thermodynamically preferred aggregate structures. These calculations determined that AHLs with 10 or 12 tail carbon atoms likely form spherical micelles containing approximately 100 molecules, while AHLs with 14 or 16 tail carbon atoms are likely to form vesicles in solution. DLS measurements and TEM images both confirmed the existence of aggregates in solution with sizes consistent with spherical micelles or small unilamellar vesicles for 3-oxo-C12-AHL and C12-AHL. In addition, the TEM images revealed the formation of large vesicles (~250 nm) in aqueous solutions of C16-AHL. These experimental findings are in general agreement with our simulation predictions. When combined, our results provide new physical insight into the aggregation behavior of AHLs in aqueous solution and further demonstrate the ability of atomistic MD simulations to quantify the thermodynamic preference of various aggregate morphologies.

In closing, we note that our results also raise several interesting questions regarding the potential biological relevance of AHL aggregation. Notably, the experimentally determined CAC of C16-AHL observed here (0.12 μM) is lower than the concentration reported to be present in some bacterial supernatants (5 μM),[18] suggesting that the vesicle-like aggregates observed here for C16-AHL could also potentially form in the presence of bacterial communities. We also recently reported the concentration of 3-oxo-C12-AHL in cultures of *P. aeruginosa* at low micromolar levels,[56] suggesting the possibility that this AHL (with a CAC of 88 μM) could also rise to concentrations needed form aggregates in cultures of this organism. We also note that AHLs can be present at substantially higher concentrations within bacterial biofilms (*e.g.*, as high as ~630 μM),[57] and there is a concentration gradient of AHLs in the vicinity of cells where local

concentrations may be sufficiently high to promote aggregation.[58-59] It is therefore possible that AHLs could form aggregates in biologically relevant environments, and that those aggregates could play roles in mediating the transport of AHLs between cells or within biofilms. It is, of course, also likely that aggregate structures containing AHLs could be formed by co-assembly of AHLs with other natural amphiphiles, such as phospholipids or other biosurfactants produced under the control of QS (*e.g.*, the rhamnolipids produced by *P. aeruginosa*).[60] Elucidating the potential biological impacts of AHL self-assembly and the potential for co-assembly with other biological or synthetic amphiphiles will require additional study. The results of this current work, however, provide the first necessary steps toward building a more rigorous understanding of QS signaling molecular transport mechanisms.

Acknowledgments. Financial support for this work was provided by the National Science Foundation through a grant provided to the UW-Madison Materials Research Science and Engineering Center (MRSEC; DMR-1720415). The authors acknowledge the use of instrumentation supported by the NSF through the UW MRSEC (DMR-1720415). C.G.G. was supported in part by a NSF Graduate Research Fellowship. K.E.N. was supported in part by the UW-Madison NIH Chemistry–Biology Interface Training Program (T32 GM008505), and the UW-Madison Office of the Vice Chancellor for Research and Graduate Education (with funding from the Wisconsin Alumni Research Foundation). The authors gratefully acknowledge Desirée Benefield for many helpful discussions and assistance with training and the acquisition and analysis of TEM images.

References

1. Miller, M. B.; Bassler, B. L. Quorum Sensing in Bacteria. *Annu. Rev. Microbiol.* **2001,** *55*, 165-199.

2. Waters, C. M.; Bassler, B. L. Quorum Sensing: Cell-to-Cell Communication in Bacteria. *Annu. Rev. Cell Dev. Biol.* **2005,** *21*, 319-346.

3. Chugani, S. A.; Whiteley, M.; Lee, K. M.; D'Argenio, D.; Manoil, C.; Greenberg, E. P. Qscr, a Modulator of Quorum-Sensing Signal Synthesis and Virulence in Pseudomonas Aeruginosa. *Proc. Natl. Acad. Sci. U. S. A.* **2001,** *98* (5), 2752-2757.

4. Papenfort, K.; Bassler, B. L. Quorum Sensing Signal-Response Systems in Gram-Negative Bacteria. *Nat. Rev. Microbiol.* **2016,** *14* (9), 576-588.

5. Whiteley, M.; Diggle, S. P.; Greenberg, E. P. Progress in and Promise of Bacterial Quorum Sensing Research. *Nature* **2017,** *551* (7680), 313-320.

6. Camilli, A.; Bassler, B. L. Bacterial Small-Molecule Signaling Pathways. *Science* **2006,** *311* (5764), 1113-1116.

7. Fuqua, C.; Greenberg, E. P. Listening in on Bacteria: Acyl-Homoserine Lactone Signalling. *Nat. Rev. Mol. Cell Biol.* **2002,** *3* (9), 685-695.

8. Gerdt, J. P.; McInnis, C. E.; Schell, T. L.; Rossi, F. M.; Blackwell, H. E. Mutational Analysis of the Quorum-Sensing Receptor Lasr Reveals Interactions That Govern Activation and Inhibition by Nonlactone Ligands. *Chem. Biol.* **2014,** *21* (10), 1361-1369.

9. Welsh, M. A.; Blackwell, H. E. Chemical Probes of Quorum Sensing: From Compound Development to Biological Discovery. *FEMS Microbiol. Rev.* **2016,** *40* (5), 774-794.

10. Galloway, W. R. J. D.; Hodgkinson, J. T.; Bovvden, S.; Welch, M.; Spring, D. R. Applications of Small Molecule Activators and Inhibitors of Quorum Sensing in Gram-Negative Bacteria. *Trends Microbiol.* **2012,** *20* (9), 449-458.

11. Amara, N.; Mashiach, R.; Amar, D.; Krief, P.; Spieser, S. A. H.; Bottomley, M. J.; Aharoni, A.; Meijler, M. M. Covalent Inhibition of Bacterial Quorum Sensing. *J. Am. Chem. Soc.* **2009,** *131* (30), 10610-10619.

12. Moore, J. D.; Rossi, F. M.; Welsh, M. A.; Nyffeler, K. E.; Blackwell, H. E. A Comparative Analysis of Synthetic Quorum Sensing Modulators in Pseudomonas Aeruginosa: New Insights into Mechanism, Active Efflux Susceptibility, Phenotypic Response, and Next-Generation Ligand Design. *J. Am. Chem. Soc.* **2015,** *137* (46), 14626-14639.

13. O'Reilly, M. C.; Dong, S. H.; Rossi, F. M.; Karlen, K. M.; Kumar, R. S.; Nair, S. K.; Blackwell, H. E. Structural and Biochemical Studies of Non-Native Agonists of the Lasr

Quorum-Sensing Receptor Reveal an L3 Loop "out" Conformation for Lasr. *Cell Chem. Biol.* **2018,** *25* (9), 1128-1139.

14. Boursier, M. E.; Moore, J. D.; Heitman, K. M.; Shepardson-Fungairino, S. P.; Combs, J. B.; Koenig, L. C.; Shin, D.; Brown, E. C.; Nagarajan, R.; Blackwell, H. E. Structure-Function Analyses of the N-Butanoyl L-Homoserine Lactone Quorum-Sensing Signal Define Features Critical to Activity in Rhir. *Acs Chem. Biol.* **2018,** *13* (9), 2655-2662.

15. Kaplan, H. B.; Greenberg, E. P. Diffusion of Autoinducer Is Involved in Regulation of the Vibrio-Fischeri Luminescence System. *J. Bacteriol.* **1985,** *163* (3), 1210-1214.

16. Pearson, J. P.; Van Delden, C.; Iglewski, B. H. Active Efflux and Diffusion Are Involved in Transport of Pseudomonas Aeruginosa Cell-to-Cell Signals. *J. Bacteriol.* **1999,** *181* (4), 1203-1210.

17. Moore, J. D.; Gerdt, J. P.; Eibergen, N. R.; Blackwell, H. E. Active Efflux Influences the Potency of Quorum Sensing Inhibitors in Pseudomonas Aeruginosa. *Chembiochem* **2014,** *15* (3), 435-442.

18. Toyofuku, M.; Morinaga, K.; Hashimoto, Y.; Uhl, J.; Shimamura, H.; Inaba, H.; Schmitt-Kopplin, P.; Eberl, L.; Nomura, N. Membrane Vesicle-Mediated Bacterial Communication. *Isme J.* **2017,** *11* (6), 1504-1509.

19. Mashburn-Warren, L. M.; Whiteley, M. Special Delivery: Vesicle Trafficking in Prokaryotes. *Mol. Microbiol.* **2006,** *61* (4), 839-846.

20. Song, D. K.; Meng, J. C.; Cheng, J.; Fan, Z.; Chen, P. Y.; Ruan, H. F.; Tu, Z. Y.; Kang, N.; Li, N.; Xu, Y.*, et al.* Pseudomonas Aeruginosa Quorum-Sensing Metabolite Induces Host Immune Cell Death through Cell Surface Lipid Domain Dissolution. *Nat. Microbiol.* **2019,** *4* (1), 97-111.

21. Daniels, R.; Reynaert, S.; Hoekstra, H.; Verreth, C.; Janssens, J.; Braeken, K.; Fauvart, M.; Beullens, S.; Heusdens, C.; Lambrichts, I.*, et al.* Quorum Signal Molecules as Biosurfactants Affecting Swarming in Rhizobium Etli. *Proc. Natl. Acad. Sci. U. S. A.* **2006,** *103* (40), 14965-14970.

22. Davis, B. M.; Richens, J. L.; O'Shea, P. Label-Free Critical Micelle Concentration Determination of Bacterial Quorum Sensing Molecules. *Biophys. J.* **2011,** *101* (1), 245-254.

23. Schweighauser, L.; Wegner, H. A. Chemical Talking with Living Systems: Molecular Switches Steer Quorum Sensing in Bacteria. *Chembiochem* **2015,** *16* (12), 1709-1711.

24. Hodgkinson, J. T.; Galloway, W.; Casoli, M.; Keane, H.; Su, X. B.; Salmond, G. P. C.; Welch, M.; Spring, D. R. Robust Routes for the Synthesis of N-Acylated-L-Homoserine Lactone (Ahl) Quorum Sensing Molecules with High Levels of Enantiomeric Purity. *Tetrahedron Lett.* **2011,** *52* (26), 3291-3294.

25. Shinoda, K.; Yamaguchi, T.; Hori, R. The Surface Tension and the Critical Micelle Concentration in Aqueous Solution of Beta-D-Alkyl Glucosides and Their Mixtures. *Bull. Chem. Soc. Jpn.* **1961,** *34* (2), 237-241.

26. Gewering, T.; Januliene, D.; Ries, A. B.; Moeller, A. Know Your Detergents: A Case Study on Detergent Background in Negative Stain Electron Microscopy. *J. Struct. Biol.* **2018,** *203* (3), 242-246.

27. Liu, C. Y.; Wang, Y. Z.; Chai, C. X.; Ullah, S.; Zhang, G. J.; Xu, B. C.; Liu, H. Q.; Zhao, L. Interfacial Activities and Aggregation Behaviors of N-Acyl Amino Acid Surfactants Derived from Vegetable Oils. *Colloids Surf., A* **2018,** *559*, 54-59.

28. Bajani, D.; Gharai, D.; Dey, J. A Comparison of the Self-Assembly Behaviour of Sodium N-Lauroyl Sarcosinate and Sodium N-Lauroyl Glycinate Surfactants in Aqueous and Aqueo-Organic Media. *J. Colloid Interface Sci.* **2018,** *529*, 314-324.

29. Patra, T.; Ghosh, S.; Dey, J. Cationic Vesicles of a Carnitine-Derived Single-Tailed Surfactant: Physicochemical Characterization and Evaluation of in Vitro Gene Transfection Efficiency. *J. Colloid Interface Sci.* **2014,** *436*, 138-145.

30. Jo, S.; Kim, T.; Iyer, V. G.; Im, W. Charmm-Gui: A Web-Based Graphical User Interface for Charmm. *J. Comput. Chem.* **2008,** *29* (11), 1859-65.

31. Kim, S.; Lee, J.; Jo, S.; Brooks, C. L.; Lee, H. S.; Im, W. Charmm-Gui Ligand Reader and Modeler for Charmm Force Field Generation of Small Molecules. *J. Comput. Chem.* **2017,** *38* (21), 1879-1886.

32. Pronk, S.; Pall, S.; Schulz, R.; Larsson, P.; Bjelkmar, P.; Apostolov, R.; Shirts, M. R.; Smith, J. C.; Kasson, P. M.; van der Spoel, D.*, et al.* Gromacs 4.5: A High-Throughput and Highly Parallel Open Source Molecular Simulation Toolkit. *Bioinformatics* **2013,** *29* (7), 845-854.

33. Martinez, L.; Andrade, R.; Birgin, E. G.; Martinez, J. M. Packmol: A Package for Building Initial Configurations for Molecular Dynamics Simulations. *J. Comput. Chem.* **2009,** *30* (13), 2157-64.

34. Israelachvili, J. N. *Intermolecular and Surface Forces*. 3rd ed.; Academic Press: 2011.

35. Shirts, M. R.; Chodera, J. D. Statistically Optimal Analysis of Samples from Multiple Equilibrium States. *J. Chem. Phys.* **2008,** *129* (12).

36. Eastoe, J.; Hatzopoulos, M. H.; Dowding, P. J. Action of Hydrotropes and Alkyl-Hydrotropes. *Soft Matter* **2011,** *7* (13), 5917-5925.

37. Lin, S. Y.; Lin, Y. Y.; Chen, E. M.; Hsu, C. T.; Kwan, C. C. A Study of the Equilibrium Surface Tension and the Critical Micelle Concentration of Mixed Surfactant Solutions. *Langmuir* **1999,** *15* (13), 4370-4376.

38. Chen, L. J.; Lin, S. Y.; Huang, C. C.; Chen, E. M. Temperature Dependence of Critical Micelle Concentration of Polyoxyethylenated Non-Ionic Surfactants. *Colloids Surf., A* **1998,** *135* (1-3), 175-181.

39. Patist, A.; Bhagwat, S. S.; Penfield, K. W.; Aikens, P.; Shah, D. O. On the Measurement of Critical Micelle Concentrations of Pure and Technical-Grade Nonionic Surfactants. *J. Surfactants Deterg.* **2000,** *3* (1), 53-58.

40. Ghosh, S. K.; Khatua, P. K.; Bhattacharya, S. C. Aggregation of Non Ionic Surfactant Igepal in Aqueous Solution: Fluorescence and Light Scattering Studies. *Int. J. Mol. Sci.* **2003,** *4* (11), 562-571.

41. Vishnyakov, A.; Lee, M. T.; Neimark, A. V. Prediction of the Critical Micelle Concentration of Nonionic Surfactants by Dissipative Particle Dynamics Simulations. *J. Phys. Chem. Lett.* **2013,** *4* (5), 797-802.

42. Zana, R.; Weill, C. Effect of Temperature on the Aggregation Behavior of Nonionic Surfactants in Aqueous-Solutions. *J. Phys. Lett.* **1985,** *46* (20), 953-960.

43. Lebecque, S.; Crowet, J. M.; Nasir, M. N.; Deleu, M.; Lins, L. Molecular Dynamics Study of Micelles Properties According to Their Size. *J. Mol. Graphics Modell.* **2017,** *72*, 6-15.

44. Segota, S.; Tezak, D. Spontaneous Formation of Vesicles. *Adv. in Colloid and Interface Sci.* **2006,** *121* (1-3), 51-75.

45. Gradzielski, M. Investigations of the Dynamics of Morphological Transitions in Amphiphilic Systems. *Curr. Opin. Colloid Interface Sci.* **2004,** *9* (3-4), 256-263.

46. Tummino, P. J.; Gafni, A. Determination of the Aggregation Number of Detergent Micelles Using Steady-State Fluorescence Quenching. *Biophys. J.* **1993,** *64* (5), 1580-1587.

47. Jusufi, A.; Panagiotopoulos, A. Z. Explicit- and Implicit-Solvent Simulations of Micellization in Surfactant Solutions. *Langmuir* **2015,** *31* (11), 3283-3292.

48. Huang, C. J.; Quinn, D.; Sadovsky, Y.; Suresh, S.; Hsia, K. J. Formation and Size Distribution of Self-Assembled Vesicles. *Proc. Natl. Acad. Sci. U. S. A.* **2017,** *114* (11), 2910-2915.

49. Karlsson, M.; Sott, K.; Davidson, M.; Cans, A. S.; Linderholm, P.; Chiu, D.; Orwar, O. Formation of Geometrically Complex Lipid Nanotube-Vesicle Networks of Higher-Order Topologies. *Proc. Natl. Acad. Sci. U. S. A.* **2002,** *99* (18), 11573-11578.

50. Karlsson, R.; Karlsson, A.; Orwar, O. Formation and Transport of Nanotube-Integrated Vesicles in a Lipid Bilayer Network. *J. Phys. Chem. B* **2003,** *107* (40), 11201-11207.

51. Sekine, Y.; Abe, K.; Shimizu, A.; Sasaki, Y.; Sawada, S.; Akiyoshi, K. Shear Flow-Induced Nanotubulation of Surface-Immobilized Liposomes. *Rsc Adv.* **2012,** *2* (7), 2682-2684.

52. Hagendorfer, H.; Kaegi, R.; Parlinska, M.; Sinnet, B.; Ludwig, C.; Ulrich, A. Characterization of Silver Nanoparticle Products Using Asymmetric Flow Field Flow Fractionation with a Multidetector Approach - a Comparison to Transmission Electron Microscopy and Batch Dynamic Light Scattering. *Anal. Chem.* **2012,** *84* (6), 2678-2685.

53. Panchal, J.; Kotarek, J.; Marszal, E.; Topp, E. M. Analyzing Subvisible Particles in Protein Drug Products: A Comparison of Dynamic Light Scattering (Dls) and Resonant Mass Measurement (Rmm). *AAPS J.* **2014,** *16* (3), 440-451.

54. Calzolai, L.; Gilliland, D.; Garcia, C. P.; Rossi, F. Separation and Characterization of Gold Nanoparticle Mixtures by Flow-Field-Flow Fractionation. *J. Chromatogr. A* **2011,** *1218* (27), 4234-4239.

55. Karow, A. R.; Gotzl, J.; Garidel, P. Resolving Power of Dynamic Light Scattering for Protein and Polystyrene Nanoparticles. *Pharm. Dev. Technol.* **2015,** *20* (1), 84-89.

56. Patel, N. M.; Moore, J. D.; Blackwell, H. E.; Amador-Noguez, D. Identification of unanticipated and novel N-acyl L-homoserine lactones (AHLs) using a sensitive non-targeted LC-MS/MS method. *PloS one* **2016,** *11* (10), e0163469.

57. Charlton, T. S.; de Nys, R.; Netting, A.; Kumar, N.; Hentzer, M.; Givskov, M.; Kjelleberg, S. A Novel and Sensitive Method for the Quantification of N-3-Oxoacyl Homoserine Lactones Using Gas Chromatography-Mass Spectrometry: Application to a Model Bacterial Biofilm. *Environ. Microbiol.* **2000,** *2* (5), 530-541.

58. Chopp, D. L.; Kirisits, M. J.; Moran, B.; Parsek, M. R. A Mathematical Model of Quorum Sensing in a Growing Bacterial Biofilm. *J. Ind. Microbiol. Biotechnol.* **2002,** *29* (6), 339-346.

59. Basu, S.; Gerchman, Y.; Collins, C. H.; Arnold, F. H.; Weiss, R. A Synthetic Multicellular System for Programmed Pattern Formation. *Nature* **2005,** *434* (7037), 1130-1134.

60. Soberon-Chavez, G.; Lepine, F.; Deziel, E. Production of Rhamnolipids by Pseudomonas Aeruginosa. *Appl. Microbiol. Biotechnol.* **2005,** *68* (6), 718-725.

Supporting Information for Chapter 2

Section S1. Additional details related to the measurement and calculation of experimental critical aggregation concentration (CAC)

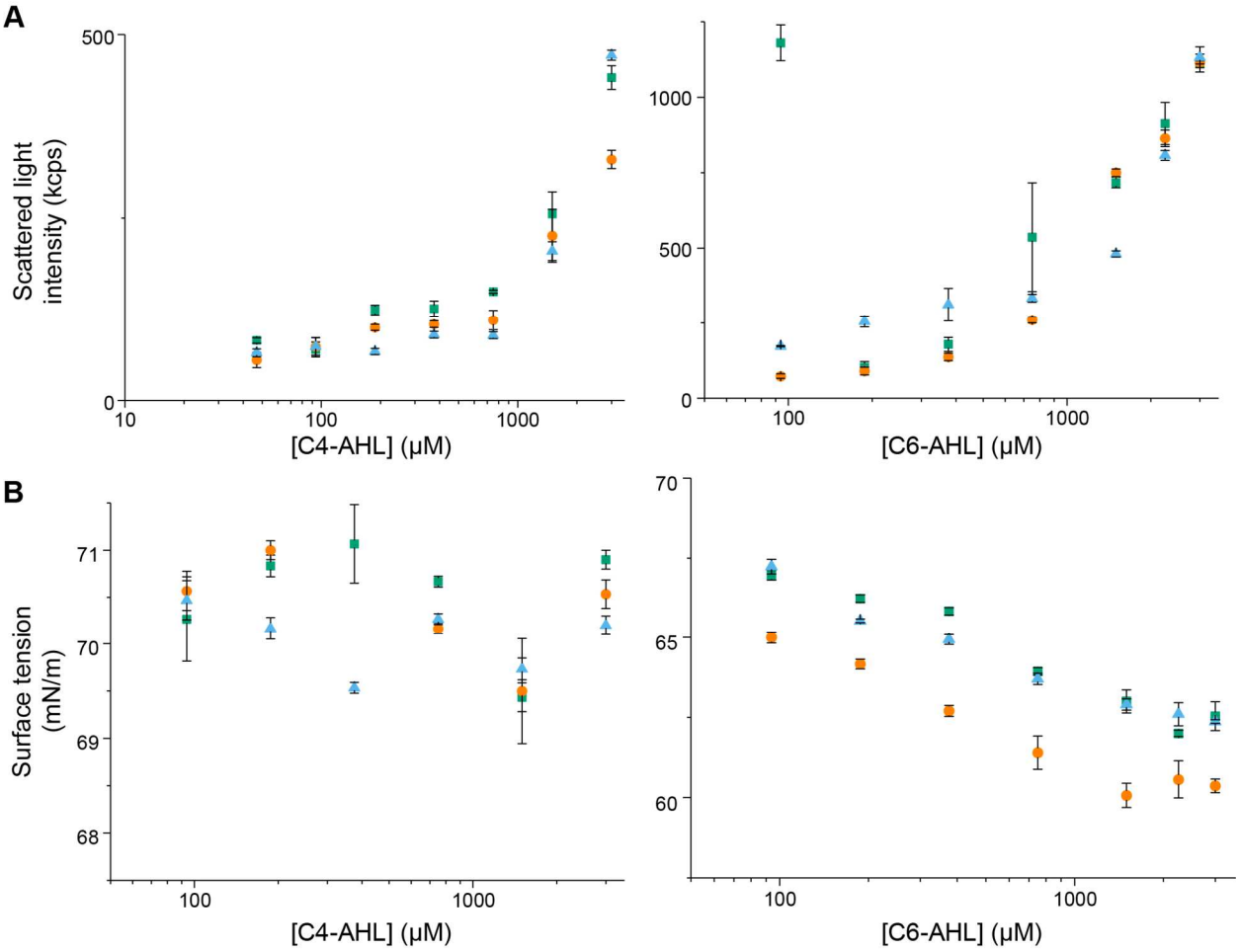


Figure S1. Static light scattering and surface tension data for C4-AHL and C6-AHL. A) Plots of scattered light intensity of a 532 nm incident laser, detected at 173°, at various concentrations of these two AHLs in distilled water containing 1% DMSO at 30 °C. B) Plots showing the surface tensions of solutions at various concentrations of these two AHLs in distilled water containing 1% DMSO at ambient room temperature. All points represent the average and standard deviation of three independent measurements of a single sample. Green, orange, and blue data points show results obtained for three sets of independently prepared samples.

Figure S1 shows the scattered light intensity (Figure S1A) and surface tension (Figure S1B) measured for solutions of C4-AHL and C6-AHL at various concentrations. While the intensity of scattered light increased with increasing concentration of both C4-AHL and C6-AHL, regressions

of the scattered light intensity against concentration yielded very low CAC values (near zero or negative concentrations). These measured values of CACs are either unphysical or do not follow trends commonly observed for self-assembled amphiphiles, for which the CAC typically decreases with increasing tail length. Additionally, C4-AHL exhibited little surface activity, with any change in the surface tension of solutions of this AHL appearing to be random at increasing concentrations. This result suggests a lack of amphiphilicity. While C6-AHL does exhibit surface activity, the surface tension and light scattering assays do not agree with one another, as regression of two of the three light scattering trials returned negative CAC values and the third (~200 μM) did not correspond to the concentrations at which surface tension was observed to become constant in the three surface tension trials (~1500 μM). General agreement between these two assays was observed for the other AHLs investigated (see main text), consistent with cooperative self-assembly. While the data discussed here leave open the possibility that some form of assembly or aggregation is occurring in solutions of C4-AHL and C6-AHL, the behaviors of these compounds deviates from those of longer-tailed AHLs, and we cannot confidently determine whether this behavior is driven by cooperative self-assembly.

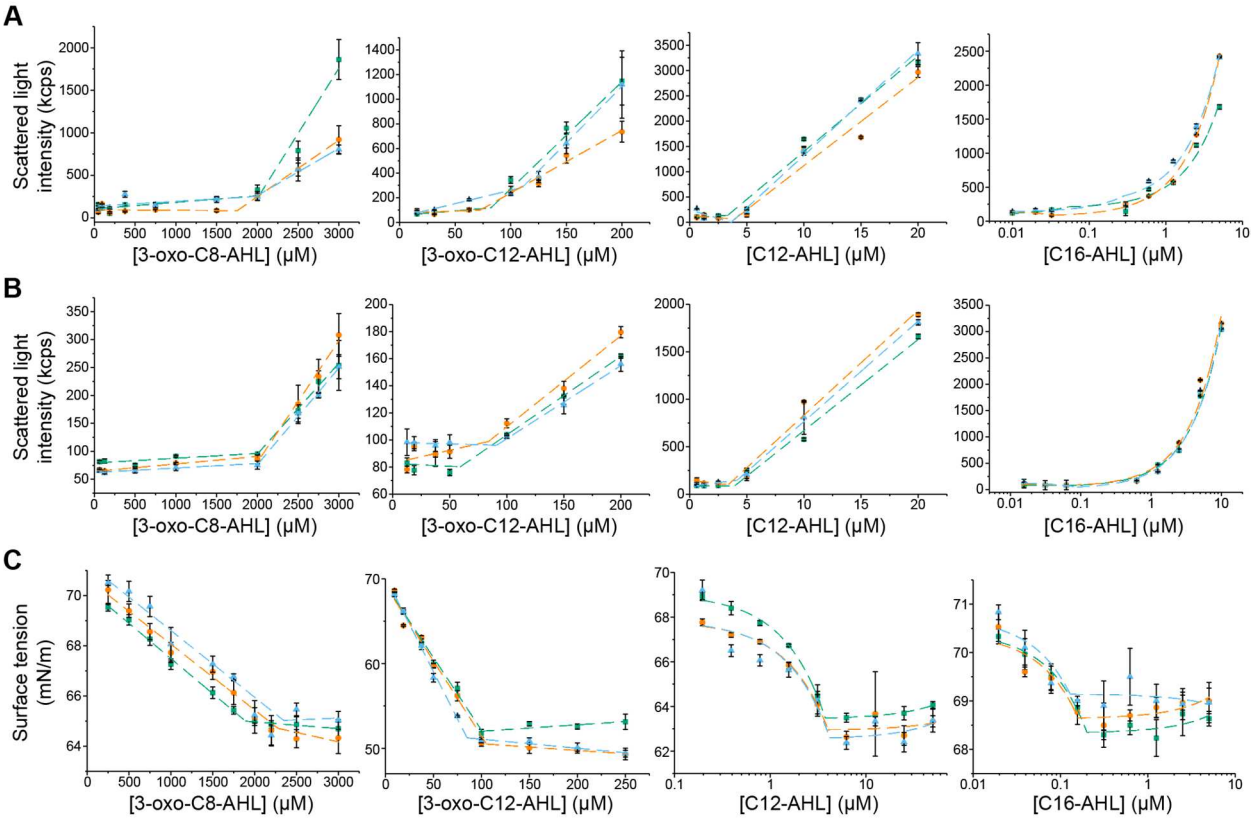


Figure S2. Determination of the CAC of 3-oxo-C8-AHL, 3-oxo-C12-AHL, C12-AHL, and C16-AHL using static light scattering and measurements of surface tension in aqueous media containing 1% DMSO. All points represent the average and standard deviation of three independent measurements of individual solutions of AHLs. Green, orange, and blue data points show results obtained for three sets of independently prepared samples. Note that AHL concentrations in some panels are plotted on a log scale. A) Plots of scattered light intensity of a 532 nm incident laser, detected at 173°, at various concentrations of AHLs in distilled water at 30 °C. B) Plots of scattered light intensity of a 532 nm incident laser, detected at 173° at various concentrations of AHLs in LB medium at 37 °C. C) Plots of the surface tensions of solutions of various concentrations of AHLs in distilled water at ambient room temperature.

Figure S2 shows the complete set of static light scattering and surface tension data used to determine the CACs listed in Table 1 of the main text. Linear regressions of scattered light intensity and surface tension against concentration were performed separately for the points above and below the concentration at which either (*i*) the scattered light intensity of AHL solutions began to increase at increasing AHL concentrations, or (*ii*) further increasing the concentration of AHLs in solution did not further decrease the surface tension of the solution. The CAC for each AHL was

defined as the concentration corresponding to the intersection of the regression lines. Measurement error (standard deviations of three measurements of an individual sample) was generally small compared to inter-sample deviation (differences in the average values of three individual samples at the same concentration). Measurement error was therefore not included in the error associated with the CACs. The CACs reported in Table 1 are the averages and standard deviations of the three samples.

As stated in the main text and reiterated here, we note that the concentrations of AHLs in solution and their corresponding changes in surface tension are small when compared to other common surfactants characterized using this assay.[1-3] This suggests that there is a low surface coverage of AHLs at the interface, likely due to the low concentrations at which the CACs occur. These low surface coverages could explain why a very small linear region was observed when surface tension is plotted against the logarithm of concentration (which for some trials, when regressed, measured a value of the CAC that was larger than the highest concentration of AHL measured). A linear regression of surface tension against concentration gave a better fit to the data and yielded CAC values that were consistent with those measured by static light scattering. This approach was therefore was used to analyze these surface tension data for the determination of a CAC.

We note that the changes in surface tension observed for solutions of C16-AHL are small even in comparison with the other AHLs tested here, likely due to the low CAC of the molecule. However, the concentration at which the surface tension becomes constant for C16-AHL does agree generally with the CACs determined using light scattering in both water and LB medium.

Section S2. Zeta potential measurements

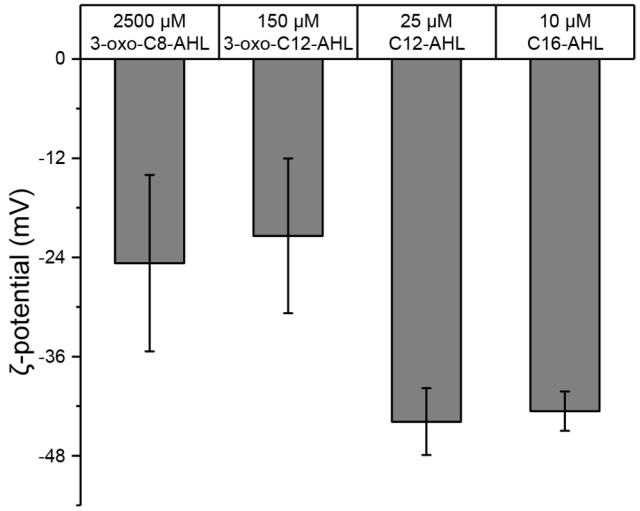


Figure S3. Zeta potentials measured for 2500 μM 3-oxo-C8-AHL, 150 μM 3-oxo-C12-AHL, 25 μM C12-AHL, and 10 μM C16-AHL solutions in distilled water containing 1% DMSO at room temperature. Values shown are the averages and standard deviations of seven to 10 measurements made of three independent samples.

Section S3. Details related to preparation of simulation systems

Initial configurations of spherical, cylindrical, and bilayer aggregates used for alchemical free energy calculations were generated using PACKMOL.[4] All aggregates were prepared by packing the AHLs into the desired geometry with head groups oriented away from the aggregate center. The cylindrical aggregates were formed with the principal axis aligned with the *z*-axis. The bilayers were formed with the surface normal aligned with the *z*-axis. The PACKMOL-generated spherical aggregate and bilayer systems were solvated with water, energy minimized, and equilibrated as stated in the main text, whereas a more elaborate approach was used to equilibrate the cylindrical aggregates as further described in Section S4 below. Figure S4 shows snapshots of example systems prepared using PACKMOL.

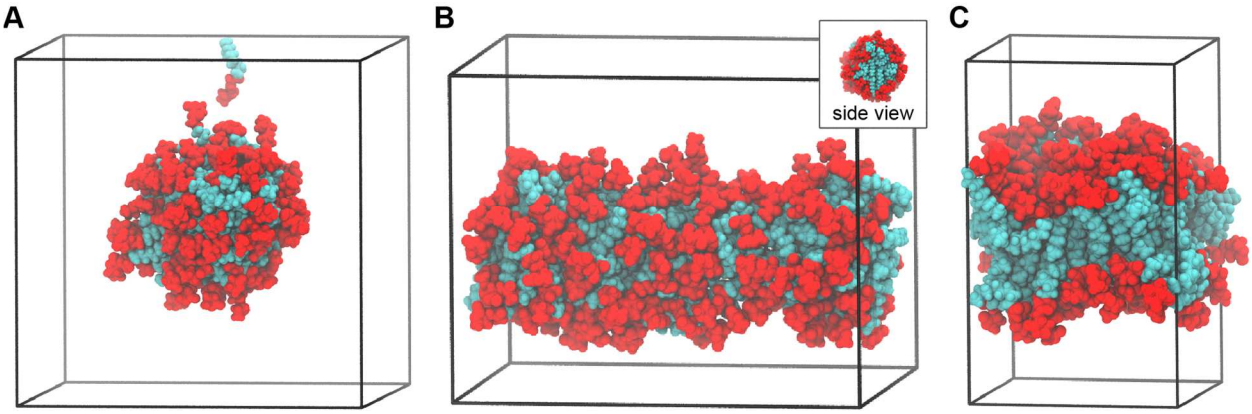


Figure S4. Simulation snapshots of PACKMOL-generated configurations at the end of equilibration for 3-oxo-C12-AHL aggregates. The color scheme is the same as Figure 4 of the main text and water is omitted for clarity. A) Spherical aggregate containing 100 AHLs. B) Cylindrical aggregate containing 150 AHLs. The inset shows the side view of the aggregate. C) Bilayer containing 128 AHLs.

Section S4. Preparation of simulated cylindrical aggregates

Preliminary simulations found that cylindrical aggregates simulated with semi-isotropic pressure coupling were not stable and deformed by compression along the long axis of the cylindrical aggregate. This behavior has been observed in previous literature.[5] An example of the resulting highly compressed structure is shown in Figure S5A. This aggregate displays AHL packing similar to that of a bilayer, which might indicate that the cylindrical aggregate is not the thermodynamically favorable structure. However, we sought to confirm this finding for all AHLs by developing a workflow to prepare stable cylindrical aggregates to facilitate the calculation of aggregation free energies.

In the modified workflow, we equilibrated the solvated PACKMOL-generated cylindrical aggregates for 30 ns using a semi-isotropic Berendsen barostat with a time constant of 5 ps and a compressibility of 4.5×10^{-5} bar^{-1}. All other parameters were the same as those stated in the main text. We then selected a single configuration from the resulting trajectory and performed an additional 50 ns of equilibration, initialized from the selected configuration, using an isotropic

Berendsen barostat (again with a time constant of 5 ps and a compressibility of 4.5×10^{-5} bar^{-1}) to prevent compression along a single axis. The configuration from the initial equilibration trajectory was selected based on two criteria: (1) the head group area in the cylindrical aggregate should be approximately the average of the head group area for the spherical aggregates and the head group area for the bilayer, and (2) the structure should be cylindrical, with head groups localized to the outer surface of the cylinder and tail carbon atoms located on the cylinder interior. We rationalized criterion (1) based on packing – the packing parameter for a cylinder lies between that of a spherical micelle and a bilayer and is inversely proportional to the head group area.[6]

To satisfy criterion (1), we estimated the head group area per AHL for the spherical and the bilayer aggregates from the last 5 ns of their equilibration trajectories. For the spherical aggregates, we first computed the density of nitrogen atoms in the AHL head groups as a function of the radial distance from the center of the aggregate and defined the radius of the aggregate as the radial distance corresponding to the peak of this distribution (as shown in Figure S5B). The head group area was then defined as the surface area of a sphere with this radius divided by the total number of AHLs in the aggregate. This head group area was averaged across the values obtained for spherical aggregates containing 20, 50, and 100 AHLs. The head group area per AHL for the bilayer was calculated by dividing the area of the of the simulation box in the *x*-*y* plane (the plane spanned by the bilayer) by one-half of the total number of AHLs in the bilayer. The expected head group area per AHL in the cylindrical aggregate was then obtained by averaging the head group area per AHL for the spherical aggregates and the bilayer. We next estimated the head group area for the cylindrical aggregate for each configuration in the semi-isotropic pressure coupling equilibration trajectory (as shown in Figure S5C). As with the spherical aggregates, we computed the density of nitrogen atoms as a function of the radial distance from the center of the aggregate

(projected into the *x*-*y* plane since the cylinder was aligned with the *z*-axis) and defined the cylinder's radius as the radial distance corresponding to the peak of this distribution. The head group area per AHL was then defined by calculating the surface area of a cylinder with this radius and dividing by the total number of AHLs. Using this approach, we selected the first configuration for which the head group area per AHL matched the expected value.

To satisfy criterion (2), we calculated the two-dimensional radius of gyration in the *x*-*y* plane using either the head group nitrogen atoms or the last tail carbon atoms using the GROMACS function *gmx gyrate*. The radius of gyration was calculated for 10 separate slices of the box along the *z*-axis to account for any curvature along the length of the aggregate. If the aggregate is cylindrical, then the radius of gyration calculated using the head group atoms should be larger than the radius of gyration computed using the tail carbon atoms; hence, we subtracted the radius of gyration calculated using the tail carbon atoms from the radius of gyration computed using the nitrogen atoms to determine if the configuration that was selected to satisfy criterion (1) also satisfies criterion (2). If the difference was greater than zero for all ten slices, then we accepted the selected configuration (as indicated by the dashed red line in Figure S5D; an example snapshot of such configuration is shown in Figure S4B) and performed the isotropic pressure coupling equilibration. If the difference was zero or negative, we selected the first configuration from an earlier time point in the trajectory for which the difference was greater than zero for all slices.

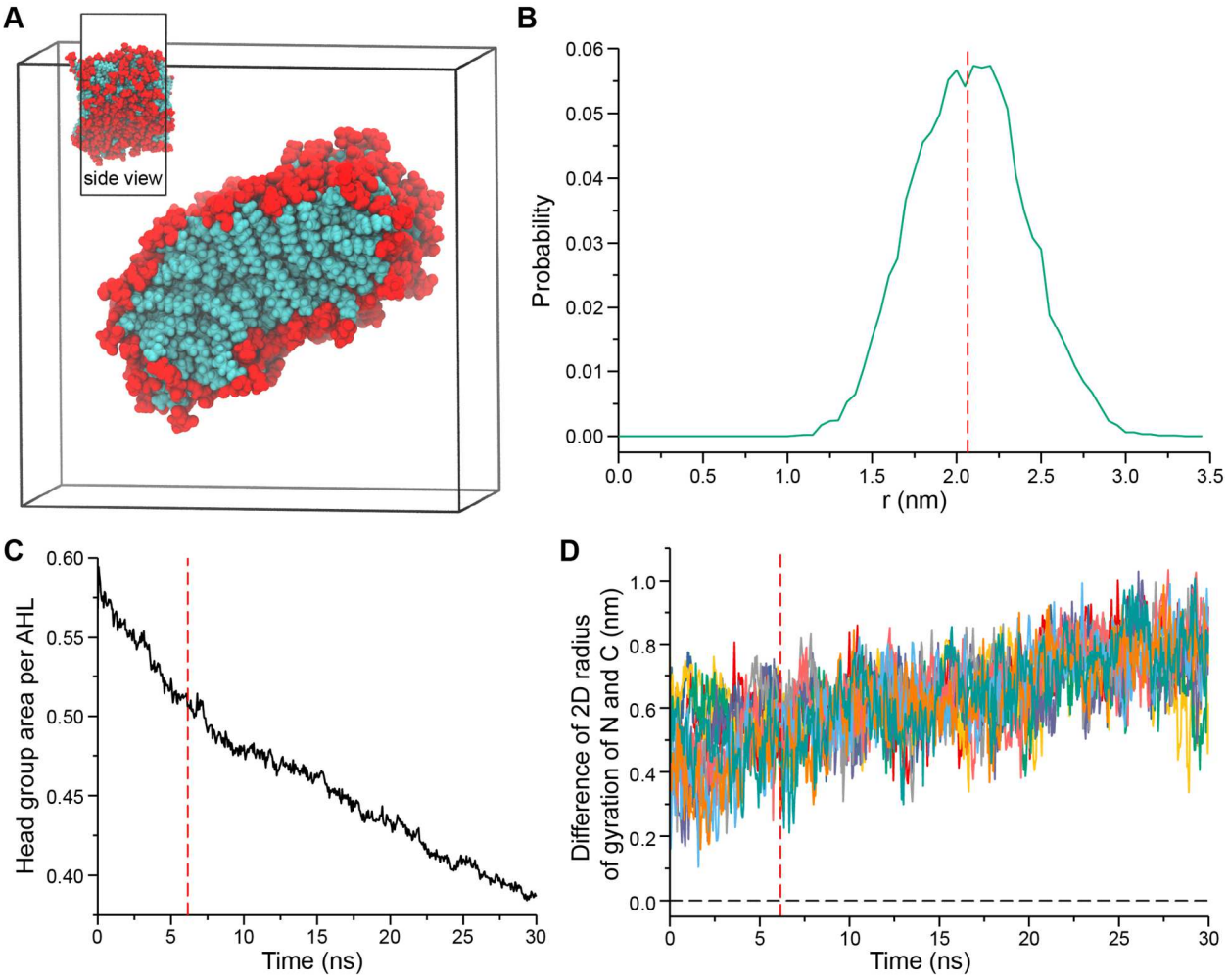


Figure S5. A) Snapshot of a C12-AHL aggregate that was initially prepared as a cylinder with 200 molecules at the end of a 40 ns equilibration trajectory using semi-isotropic pressure coupling. The color scheme is the same as Figure 4 of the main text and water is not shown for clarity. The aggregate is notably compressed along the long-axis and loses its initial cylindrical structure. B) Distribution of head group nitrogen atom distances from the aggregate center for a C12-AHL spherical aggregate with 100 molecules. The distribution was computed using the last 5 ns of the equilibration trajectory. The dashed red line indicates the radius of the aggregate used to calculate the surface area of the aggregate. C) Head group area per AHL calculated during the semi-isotropic pressure coupling equilibration trajectory for the C12-AHL cylindrical aggregate shown in part A. The dashed red line indicates the configuration selected for the isotropic pressure coupling equilibration trajectory. D) Difference between the two-dimensional radii of gyration computed using the nitrogen atoms and the tail carbon atom for the C12-AHL equilibration trajectory from part A. Each solid line indicates the calculation for one of ten different slices along the *z*-axis. The dashed red vertical line indicates the configuration selected for the isotropic pressure coupling equilibration trajectory.

Section S5. Details related to alchemical free energy calculations

The free energy change for aggregation, $\Delta\mu_{aggr}$, was calculated according to Equation (3) of the main text using the thermodynamic cycle indicated in Figure 2 of the main text. The free energy for removing a single AHL molecule from water, $-\Delta G_{0\rightarrow w}$, was calculated using an alchemical free energy approach in which the electrostatic and van der Waals interactions between the AHL and water were separately decoupled in 21 simulation windows. Electrostatic interactions were decoupled in 5 windows using a linear alchemical pathway with λ_{elec} = 0.0, 0.25, 0.5, 0.75, and 1.0, with $\lambda_{vdw} = 0.0$ in each window. Van der Waals interactions were decoupled in 16 windows in which λ_{vdw}= 0.0, 0.1, 0.2, 0.3, 0.4, 0.45, 0.5, 0.55, 0.6, 0.65, 0.7, 0.75, 0.8, 0.85, 0.9, 0.95, and 1.0, with λ_{elec}= 1.0 in each window.

The free energy for removing an AHL from an aggregate, $-\Delta G_{0\rightarrow agg}$, was similarly calculated using an alchemical free energy calculation by decoupling the interactions of a single AHL in an aggregate with solvent molecules and other AHLs. During these simulations, the elimination of interactions between the selected AHL and other AHLs in some simulation windows permitted the diffusion of the AHL out of the aggregate and into solution, which leads to poor convergence of the free energy. To prevent this issue, restraints were used to ensure that the AHL being decoupled remained within the aggregate. The free energy change associated with adding and removing these restraints must then be included in the total free energy calculations. Thus, $-\Delta G_{0\rightarrow agg}$ is calculated by adding the free energies for decoupling the electrostatic ($\Delta G^{elec}_{agg\rightarrow 0}$) and the van der Waals ($\Delta G^{vdw}_{agg\rightarrow 0}$) interactions of an AHL in an aggregate, along with free energies for applying restraints before decoupling the AHL ($\Delta G^{add\ rest}_{agg\rightarrow 0}$) and removing the restraints after decoupling the AHL ($\Delta G^{rem\ rest}_{agg\rightarrow 0}$), according to Equation S1:

$$-\Delta G_{0\rightarrow agg} = \Delta G_{agg\rightarrow 0}^{add\ rest} + \Delta G_{agg\rightarrow 0}^{elec} + \Delta G_{agg\rightarrow 0}^{vdw} + \Delta G_{agg\rightarrow 0}^{rem\ rest} \quad \text{(S1)}$$

Restraints were applied using a harmonic potential with details on the parameters for the restraints detailed in Section S6. $\Delta G_{agg\rightarrow 0}^{add\ rest}$ was calculated using 3 windows with λ_{rest} = 0.0, 0.75, and 1.0 and $\lambda_{elec} = \lambda_{vdw} = 0.0$ in each window. With $\lambda_{rest} = 1.0$ (*i.e.*, with restraints applied), the electrostatic interactions were then decoupled using a linear alchemical pathway with λ_{elec} = 0.0, 0.25, 0.5, 0.75, and 1.0 and $\lambda_{vdw} = 0.0$ in each window. Van der Waals interactions were then decoupled with λ_{vdw}= 0.0, 0.05, 0.1, 0.15, 0.2, 0.25, 0.3, 0.35, 0.4, 0.45, 0.5, 0.55, 0.6, 0.65, 0.7, 0.75, 0.8, 0.85, 0.9, 0.95, and 1.0, with λ_{elec}= 1.0 in each window. A total of 27 windows were utilized for each calculation. The free energy change for removing the restraints, $\Delta G_{agg\rightarrow 0}^{rem\ res.}$, was calculated analytically using Equation S2[7]:

$$\Delta G_{agg\rightarrow 0}^{rem\ rest} = -RT \ln \left[\frac{V^o}{V^{\text{eff}}}\right] \quad \text{(S2)}$$

Since the restraints are removed from a molecule that has no interactions with other molecules in the system, this expression is the free energy change associated with increasing the volume accessible to an ideal gas molecule. V^o = 1.661 nm^3 is the standard state volume and V^{eff} is the effective volume of the restrained molecule, which is calculated for each aggregate shape based on the volume accessible to an ideal gas molecule subject to a harmonic restraint with spring constant *k*. For spherical aggregates, V^{eff} was calculated using Equation S3:

$$V^{\text{eff}} = 4\pi \left\{ \int_0^\infty r^2 \exp\left(-\frac{k}{2RT}(r - r^o)^2\right) dr \right\} \quad \text{(S3)}$$

r^o is the equilibrium distance from the center of the sphere enforced by the restraint. For bilayers, the harmonic potential was applied in the *z*-direction and V^{eff} was calculated using Equation S4:

$$V^{\text{eff}} = A\left\{\int_{-\infty}^{\infty} \exp\left(-\frac{k}{2RT}(z - z^o)^2\right) dz\right\} \quad \text{(S4)}$$

A is the area of the *x*-*y* plane and z^o is the equilibrium distance from the center of the bilayer enforced by the restraint. For cylindrical aggregates, the harmonic potential was applied in the *x*-*y* plane and V^{eff} as calculated using Equation S5:

$$V^{\text{eff}} = 2\pi L\left\{\int_{0}^{\infty} r \exp\left(-\frac{k}{2RT}(r - r^o)^2\right) dr\right\} \quad \text{(S5)}$$

L is the average length of the cylinder and r^o is the equilibrium distance from the center of the sphere enforced by the restraint (calculated in the *x*-*y* plane). Additional details on the values of k, r^o, and z^o for each system are provided in Section S6.

For each simulation window of either an AHL in an aggregate or in solution, the initial configuration was energy minimized, then equilibrated in the NVT ensemble for 500 ps, then equilibrated in *NPT* ensemble for 500 ps. Simulation parameters for the alchemical free energy simulations were the same as for the unbiased equilibration simulations, expect a stochastic dynamics algorithm was used to integrate the equations of motion. The temperature was maintained at 310.15 K with a time constant of 1.0 ps, and the pressure was maintained at 1 bar using a Parrinello-Rahman barostat with a time constant of 5 ps and a compressibility of 4.5×10^{-5} bar^{-1}. After equilibration, each window was simulated for 8 ns, except for POPC for which it was for 24 ns because it is a larger molecule compared to the AHLs. Free energies were computed from the simulation windows using the Multistate Bennett Acceptance Ratio (MBAR) method.[8] The convergence of the alchemical free energy calculations was assessed using a protocol described in the literature.[9] The free energy was calculated using simulation configurations extracted

consecutively starting from the beginning of the simulation trajectory (labeled as the "forward" time series) and separately from the same number of consecutive configurations consecutively extracted starting from the end of the simulation trajectory (labeled as the "reverse" time series). Figure S6 plots forward and reverse free energy calculations for a single C12-AHL molecule in water and all five C12-AHL aggregates. Convergence is observed by a simulation time fraction of ~0.9 for all examples in Figure S6.

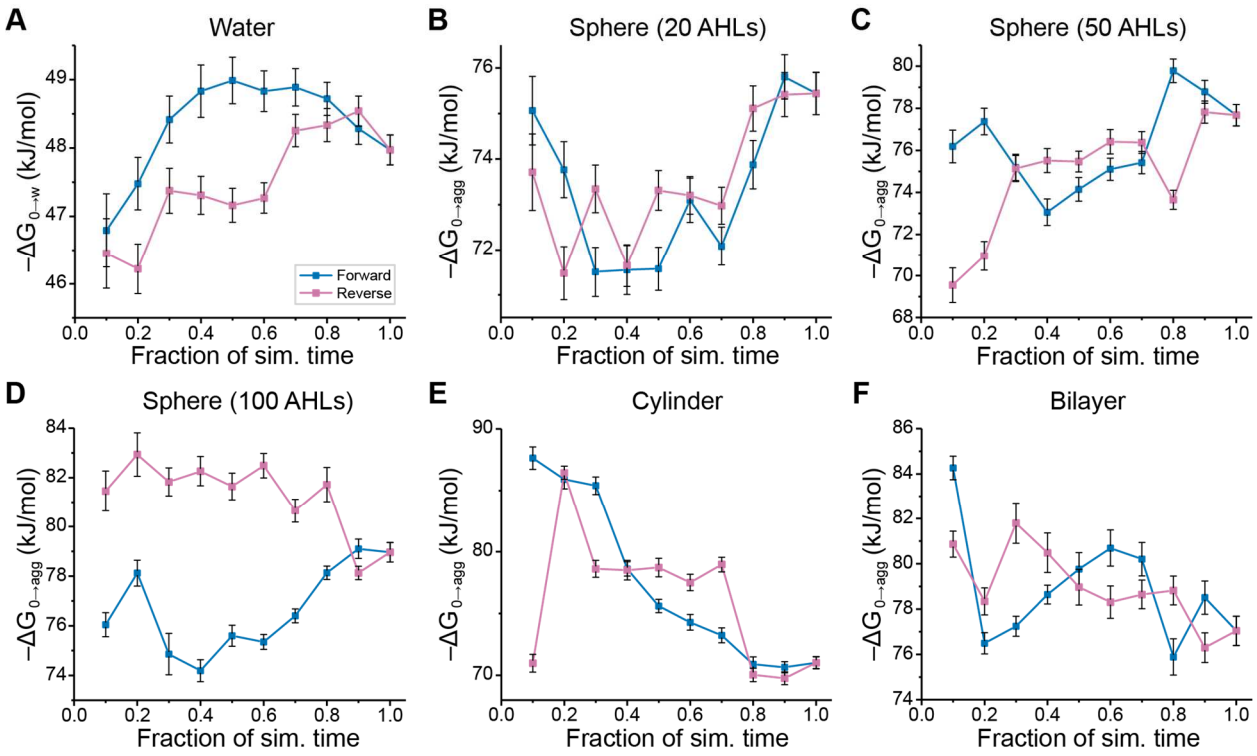


Figure S6. Representative plots illustrating the convergence of alchemical free energy calculations using the forward and the reverse time series of the C12-AHL in water (A), for the spherical aggregates with 20 (B), 50 (C), and 100 (D) AHLs, for the cylindrical aggregate (E), and for the bilayer (F).

Section S6. Aggregate structures and harmonic restraint parameters for free energy calculations

Distributions of the AHL center-of-mass (COM) distance from the aggregate COM were computed for each aggregate structure to assess equilibration and determine parameters for the harmonic restraints applied during the free energy calculations. For cylindrical aggregates, the COM distance was projected onto the *x*-*y* plane, or the plane perpendicular to the axis of the aggregate. For bilayers, the distance was projected onto the *z*-axis, or the axis normal to the bilayer. Distributions were computed separately using either the last 10 ns of the equilibration trajectory or two separate 5-ns blocks taken from the last 10 ns to assess convergence. If the three distributions nearly overlap, the system is equilibrated and the aggregate shape is well-defined. Distributions of C12-AHL COMs are shown in Figure S7 as an example of well-equilibrated structures. Similar calculations were performed to confirm convergence for all AHLs studied.

The spring constant, k, and the distance at which the AHL was restrained during the alchemical free energy calculations were defined separately for each aggregate based on the distributions of AHL COM distances computed during the equilibration trajectories. We defined r^o (Equations S3 and S5) as the distances in the radial direction (for spherical and cylindrical aggregates) and z^o (Equation S4) as the distance along the *z*-axis (for bilayers) corresponding to the peak in the distribution computed for each system from the last 5 ns of the equilibration run. The same distributions were then fitted with Gaussian curves to obtain an estimate of the spring constant value required for the harmonic restraints applied during the alchemical free energy calculation. This approach ensures that the restrained AHL molecule with all interactions decoupled still samples the same conformational space as unrestrained, fully interacting AHLs. Figure S7F shows an example Gaussian fit is plotted for the 20-molecule sphere of C12-AHL and

the corresponding distribution of the AHL COM distance from the last 5 ns of a 50 ns restrained simulation using the spring constant, *k*, obtained from the Gaussian fitting procedure. This comparison confirms that the calculated spring constant used for the alchemical free energy calculation reproduces the expected distribution of AHL COM distances even when intermolecular interactions are decoupled.

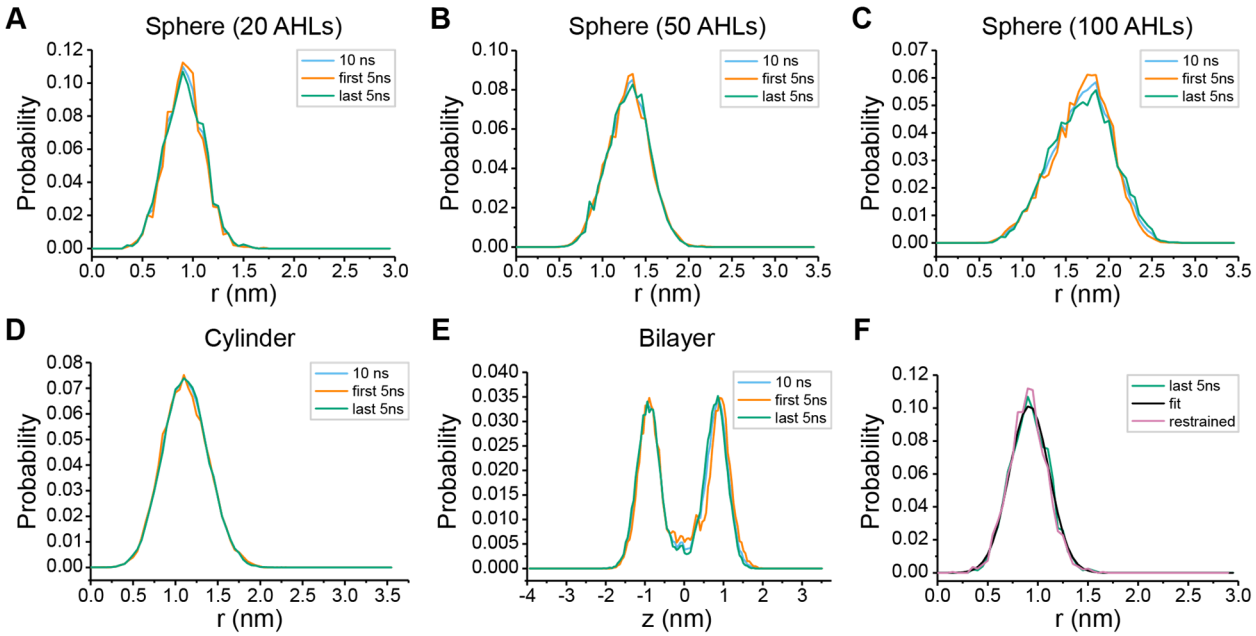


Figure S7. Distributions of the C12-AHL center-of-mass (COM) distance from the aggregate center for spherical aggregates with 20 (A), 50 (B), and 100 (C) AHLs and for the cylindrical aggregate (D) and bilayer (E). Blue, orange, and green curves represent distributions computed from the last 10 ns of the equilibration trajectory, or the 10-ns split into two 5-ns blocks. F) A Gaussian fit of the distribution of C12-AHL COM distances for the 20 molecule spherical aggregate (black line), computed using the last 5 ns of the equilibration trajectory (green line in A) and distribution of C12-AHL COM distance for the 20 molecule spherical aggregate from the last 5 ns of a restrained simulation run using the distance at which the AHL was restrained and the spring constant, *k*, obtained from the Gaussian fitting (purple line).

Section S7. Determination of shape and size of spherical aggregate from simulations

To quantify the shape of each spherical aggregate we calculated the asphericity, α_s, following previous work.[10] The asphericity is defined in Equation S6 as:

$$\alpha_s = \frac{(I_1 - I_2)^2 + (I_1 - I_3)^2 + (I_2 - I_3)^2}{\frac{1}{2}(I_1 + I_2 + I_3)^2} \quad \text{(S6)}$$

I_1, I_2, and I_3 are moments of inertia for the structure, defined such that $I_1 \leq I_2 \leq I_3$. The moments of inertia of the aggregates were calculated using *gmx principal* using the last 10 ns of the equilibration of the spherical aggregates. Figure S8A reports values of α_s obtained by averaging over configurations from the last 10 ns of the equilibration trajectory. α_s values close to zero indicate that the corresponding aggregates are more spherical. This plot indicates that for nearly all AHLs the asphericity increases once the aggregate contains 100 molecules, suggesting that the aggregates containing 20, 50, and 100 AHLs samples a reasonable range of asphericities.

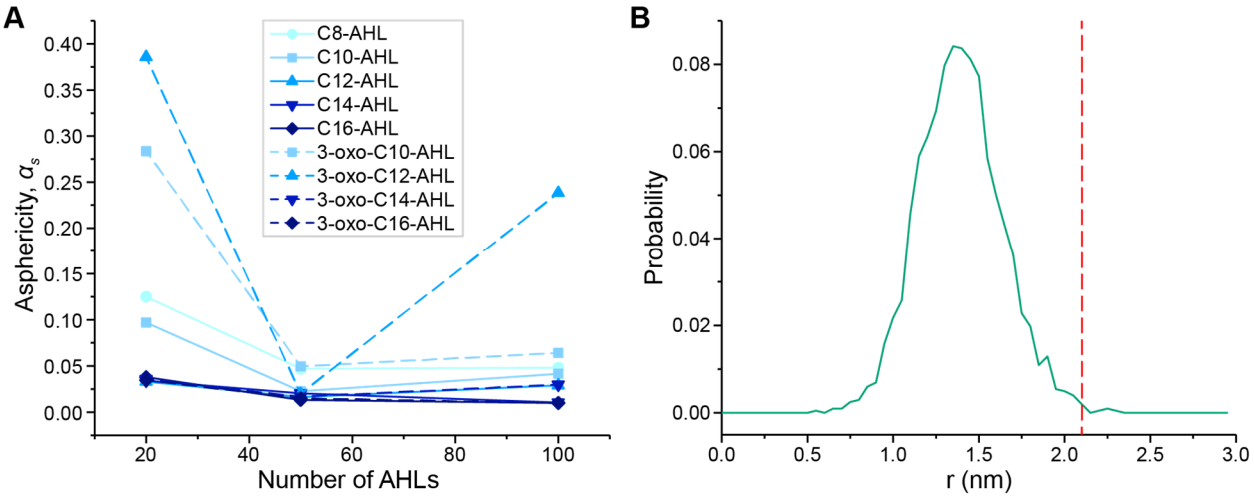


Figure S8. A) Asphericity as a function of number of AHLs in spherical aggregates. B) Distribution of head group lactone ring oxygen atom distances from the aggregate center for a C12-AHL spherical aggregate with 20 AHLs. The distribution was computed using the last 5 ns of the equilibration trajectory. The dashed red line indicates the aggregate radius, defined using this plot, that was compared to experimental TEM measurements.

The diameters of the spherical aggregates were estimated from the last 5 ns of the equilibration run. The diameter was defined using the distribution of head group lactone ring oxygen atom as function of the radial distance from the aggregate COM (Figure S8B). The diameter was defined as twice the radial distance for which (*i*) the radial distance was greater than the distance corresponding to the peak of the distribution and (*ii*) the value of the distribution fell below 0.003. Distributions of oxygen atoms were calculated in a similar way to distributions of AHL center of masses discussed in section S6.

Table S1. Spherical aggregate sizes estimated from simulations.

	Diameter of spherical aggregate (nm)		
AHL	20 molecules	50 molecules	100 molecules
C8-AHL	*4.1*	*4.8*	*6.0*
C10-AHL	*4.1*	*4.9*	*6.1*
C12-AHL	*4.2*	*5.1*	*6.2*
C14-AHL	*4.2*	*5.1*	*6.2*
C16-AHL	*4.3*	*5.2*	*6.3*
3-oxo-C10-AHL	*4.5*	*5.3*	*6.9*
3-oxo-C12-AHL	*4.0*	*4.5*	*5.9*
3-oxo-C14-AHL	*4.5*	*5.5*	*6.6*
3-oxo-C16-AHL	*4.6*	*6.0*	*6.5*

Section S8. Determination of free energy change for aggregation from alchemical free energy calculations

The values of $\Delta\mu_{aggr}$ from the alchemical free energy calculations plotted in Figure 6 of the main text are listed in Table S2. The errors in the free energies are the standard deviation as estimated by the alchemical free energy calculation tool.[9] Table S2 also lists $\Delta\mu_{aggr}$ computed from alchemical free energy calculations for spherical and bilayer aggregates of the zwitterionic lipid POPC. POPC is included as a control it prefers a bilayer structure and thus the bilayer should have

a lower value of $\Delta\mu_{aggr}$ than spherical aggregates. Because of the larger system size required for the POPC systems (due to the molecular size of the lipids), simulations of cylindrical aggregates were not performed.

Table S2. $\Delta\mu_{aggr}$ calculated for each AHL for spherical aggregates with 20, 50 and 100 AHLs, cylinders, and bilayers. All values are reported in kJ/mol. ** indicates that the simulation was not performed because the system was unable to maintain the indicated structure during equilibration (or due to computational expense in the case of the POPC cylinder).

	$\Delta\mu_{aggr}$ *(kJ/mol)*				
AHL	***Sphere (20 molecules)***	***Sphere (50 molecules)***	***Sphere (100 molecules)***	***Cylinder***	***Bilayer***
POPC	*-60.9 ± 0.8*	*-72.3 ± 1.1*	**	**	*-88.3 ± 1.5*
C8-AHL	*-20.5 ± 0.3*	*-21.0 ± 0.2*	*-27.5 ± 0.3*	*-29.9 ± 0.3*	**
C10-AHL	*-25.8 ± 0.3*	*-32.9 ± 0.3*	*-28.3 ± 0.4*	*-31.7 ± 0.3*	*-34.4 ± 0.4*
C12-AHL	*-30.6 ± 0.4*	*-35.2 ± 0.4*	*-39.0 ± 0.3*	*-31.1 ± 0.3*	*-34.4 ± 0.5*
C14-AHL	*-34.5 ± 0.3*	*-43.3 ± 0.3*	*-37.3 ± 0.3*	*-46.3 ± 0.4*	*-51.1 ± 0.7*
C16-AHL	*-42.2 ± 0.4*	*-43.4 ± 0.3*	*-49.2 ± 0.4*	*-55.8 ± 0.5*	*-74.2 ± 0.3*
3-oxo-C10-AHL	*-16.9 ± 0.5*	*-20.5 ± 0.3*	*-25.9 ± 0.1*	*-21.3 ± 0.3*	**
3-oxo-C12-AHL	*-23.1 ± 0.4*	*-29.4 ± 0.5*	*-30.6 ± 0.2*	*-31.2 ± 0.5*	*-25.8 ± 0.4*
3-oxo-C14-AHL	*-27.0 ± 0.3*	*-30.4 ± 0.3*	*-29.6 ± 0.5*	*-39.2 ± 0.4*	*-40.6 ± 0.5*
3-oxo-C16-AHL	*-34.0 ± 0.4*	*-38.5 ± 0.4*	*-41.9 ± 0.5*	*-44.4 ± 0.4*	*-77.1 ± 0.3*

Section S9. Analysis of aggregate sizes from TEM images

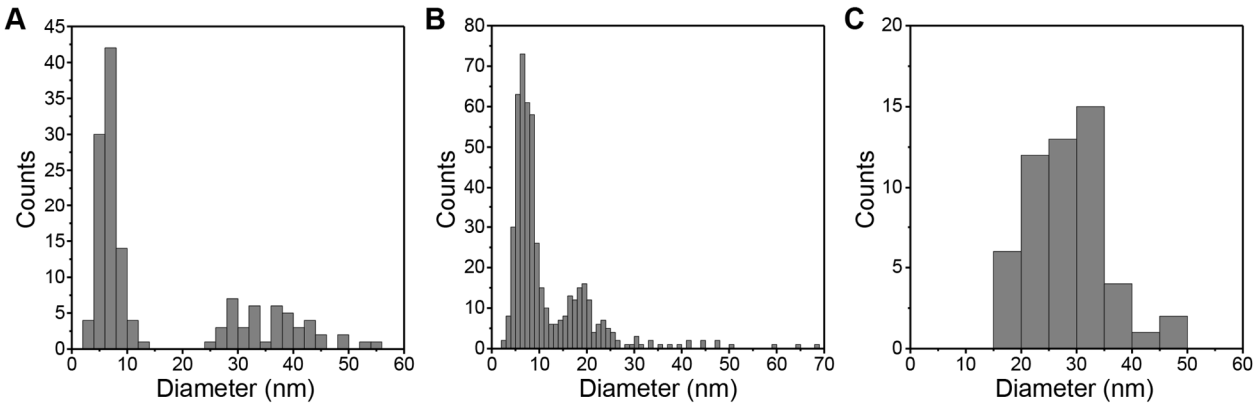


Figure S9. Histograms showing the distribution of diameters measured for aggregates observed in TEM images of samples prepared from solutions of AHLs. (A) Aggregates observed in 100 μM solutions of 3-oxo-C12-AHL (140 aggregates measured from the images shown in Figures 8A and 8B, and 3 additional images). (B) Aggregates observed in 6.25 μM and 12.5 μM solutions of C12-AHL (490 aggregates measured from the images shown in Figures 8C, 8D, and S12D; small and large aggregates were observed in solutions at both concentrations). (C) Aggregates observed in 1 μM solutions of C12-AHL (53 aggregates measured from the image displayed in Figure 8E).

The diameters of the aggregates imaged by TEM were measured using NIH ImageJ and reported in the histograms in Figure S9. The scale of the image was set by measuring the width of the scale bar generated by the TEM software in pixels and converting that to the appropriate physical length. The diameters of the aggregates imaged were then measured by drawing a straight line across the equator of the aggregates and measuring the length of that line. For particles that were oblong, the long axis of the particles was measured, which could lead to an overestimate in particle size. To determine the sizes of "small" and "large" aggregates found in solutions of 3-oxo-C12-AHL and C12-AHL (see main text), particles smaller than 13 nm and 12 nm respectively were considered "small" aggregates and aggregates larger than those values were designated as "large" aggregates. These values were chosen because they represent natural break points between the two modes of the distributions observed in the histogram.

Section S10. Characterization of aggregate sizes in solution of AHLs using DLS

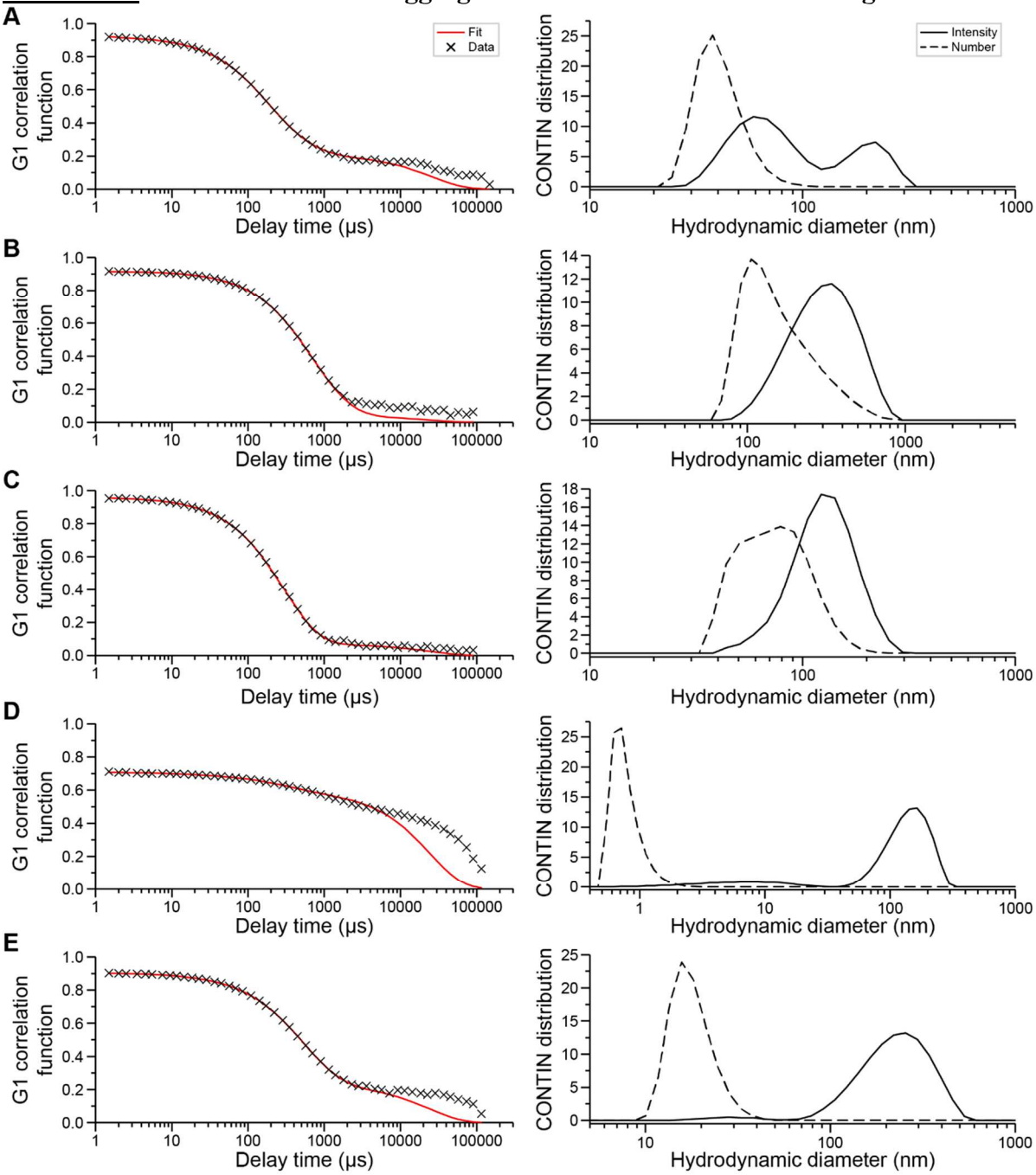


Figure S10. Results of DLS analyses of aggregates present in solutions of AHLs. (Left) Autocorrelation functions (ACFs) and corresponding CONTIN fits to the ACFs and (Right) Corresponding intensity and number averages size distributions for aggregated structures found in: (A) 3000 μM 3-oxo-C8-AHL, (B) 10 μM C12-AHL, (C) 5 μM C16-AHL and (D and E) 125 μM 3-oxo-C12-AHL. As also stated in the main text, and observed in this figure, CONTIN analysis poorly fits the raw autocorrelation function for 3-oxo-C12-AHL. While the CONTIN intensity and number average distributions for this molecule are displayed in the figure, they are only included to show the bimodal nature of the data, not for the determination of an aggregate size.

Section S11. Additional TEM images

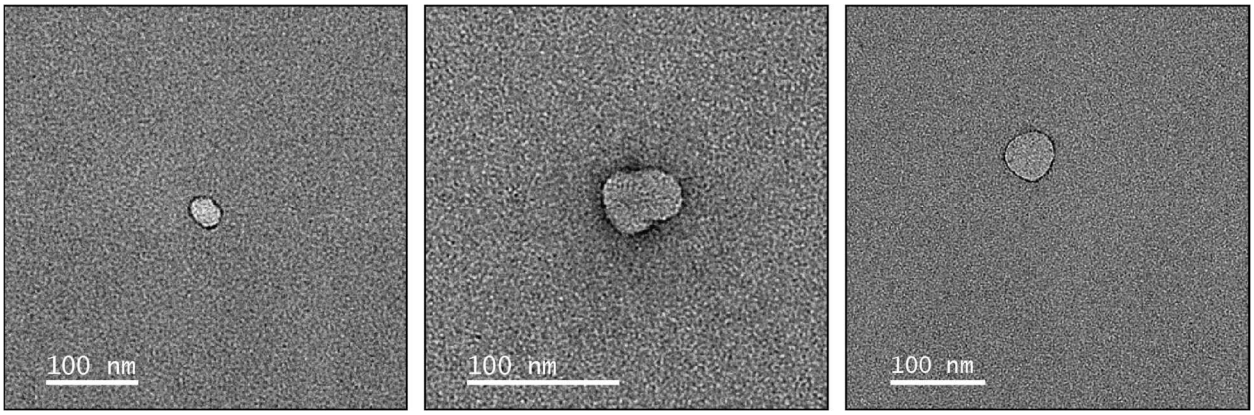


Figure S11. TEM images showing representative aggregates found in 3000 μM solutions of 3-oxo-C8-AHL.

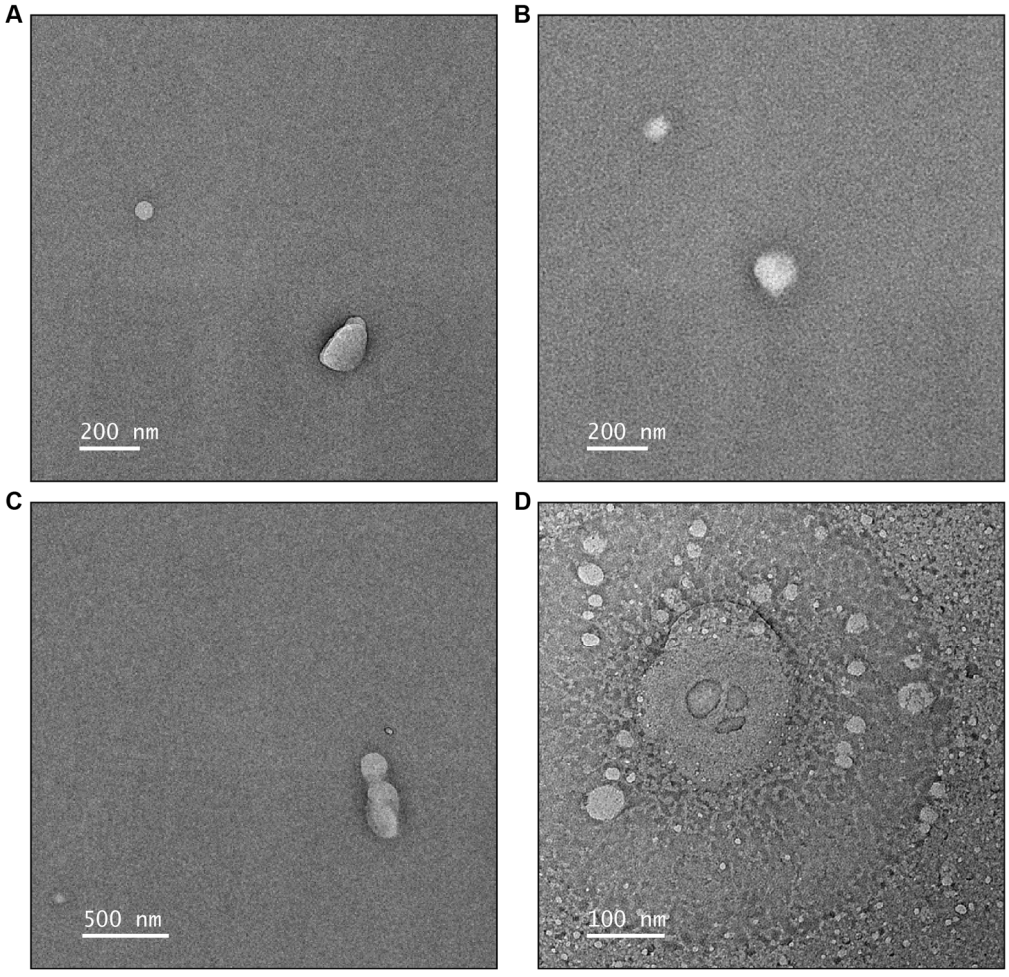


Figure S12. TEM images showing representative views of the largest aggregates found in (A-C) 50 μM C12-AHL solutions and (D) 6.25 μM C12-AHL solution. The aggregates shown in (A-C) roughly correspond to the sizes of aggregates observed by DLS in solutions of C12-AHL.

Supporting Information References

1. Lin, S. Y.; Lin, Y. Y.; Chen, E. M.; Hsu, C. T.; Kwan, C. C., A Study of the Equilibrium Surface Tension and the Critical Micelle Concentration of Mixed Surfactant Solutions. *Langmuir* **1999,** *15* (13), 4370-4376.

2. Chen, L. J.; Lin, S. Y.; Huang, C. C.; Chen, E. M., Temperature Dependence of Critical Micelle Concentration of Polyoxyethylenated Non-Ionic Surfactants. *Colloids Surf., A* **1998,** *135* (1-3), 175-181.

3. Patist, A.; Bhagwat, S. S.; Penfield, K. W.; Aikens, P.; Shah, D. O., On the Measurement of Critical Micelle Concentrations of Pure and Technical-Grade Nonionic Surfactants. *J. Surfactants Deterg.* **2000,** *3* (1), 53-58.

4. Martinez, L.; Andrade, R.; Birgin, E. G.; Martinez, J. M., Packmol: A Package for Building Initial Configurations for Molecular Dynamics Simulations. *J. Comput. Chem.* **2009,** *30* (13), 2157-64.

5. Haverkort, F.; Stradomska, A.; de Vries, A. H.; Knoester, J., Investigating the Structure of Aggregates of an Amphiphilic Cyanine Dye with Molecular Dynamics Simulations. *J. Phys. Chem. B* **2013,** *117* (19), 5857-5867.

6. Israelachvili, J. N., *Intermolecular and Surface Forces*. 3rd ed.; Academic Press: 2011.

7. Jakobtorweihen, S.; Yordanova, D.; Smirnova, I., Predicting Critical Micelle Concentrations with Molecular Dynamics Simulations and Cosmomic. *Chem. Ing. Tech.* **2017,** *89* (10), 1288-1296.

8. Shirts, M. R.; Chodera, J. D., Statistically Optimal Analysis of Samples from Multiple Equilibrium States. *J. Chem. Phys.* **2008,** *129* (12).

9. Klimovich, P. V.; Shirts, M. R.; Mobley, D. L., Guidelines for the Analysis of Free Energy Calculations. *J. Comput.-Aided Mol. Des.* **2015,** *29* (5), 397-411.

10. Wijmans, C. M.; Eiser, E.; Frenkel, D., Simulation Study of Intra- and Intermicellar Ordering in Triblock-Copolymer Systems. *J. Chem. Phys.* **2004,** *120* (12), 5839-5848.

Chapter 3

Bacterial Quorum Sensing Signals Promote Large-Scale Remodeling of Lipid Membranes‡

‡ Portions of this chapter have been published as: Gahan, C. G.; Patel, S. J.; Chen, L. M.; Manson, D. E.; Ehmer, Z. J.; Blackwell, H. E.; Van Lehn, R. C.; Lynn, D. M. "Bacterial Quorum Sensing Signals Promote Large-Scale Remodeling of Lipid Membranes" *Langmuir* **2021**. I designed and performed all experiments related to surface tension measurements, fluorescence microscopy of SLBs, QCM-D measurements of SLBs and calcein leakage experiments. S. J. Patel designed and performed all molecular dynamics simulations. L. M. Chen performed experiments related to GUVs. D. E. Manson synthesized 3-oxo-C12-HS. Z. J. Ehmer assisted in experimental design. H. E. Blackwell, R. C. Van Lehn and D. M. Lynn directed the project.

ABSTRACT: We report that *N*-acyl-L-homoserine lactones (AHLs), a class of nonionic amphiphiles that common bacteria use as signals to coordinate group behaviors, can promote large-scale remodeling in model lipid membranes. Characterization of supported lipid bilayers (SLBs) of the phospholipid DOPC by fluorescence microscopy and quartz crystal microbalance with dissipation (QCM-D) reveals the well-studied AHL signal 3-oxo-C12-AHL and its anionic head group hydrolysis product (3-oxo-C12-HS) to promote the formation of long microtubules that can retract into hemispherical caps on the surface of the bilayer. These transformations are dynamic, reversible, and dependent upon head group structure. Additional experiments demonstrate that 3-oxo-C12-AHL can promote remodeling to form microtubules in lipid vesicles and promote molecular transport across bilayers. Molecular dynamics (MD) simulations predict differences in thermodynamic barriers to translocation of these amphiphiles across a bilayer that are reflected in both the type and extent of reformation and associated dynamics. Our experimental observations can thus be interpreted in terms of accumulation and relief of asymmetric stresses in the inner and outer leaflets of a bilayer upon intercalation and translocation of these amphiphiles. Finally, experiments on *Pseudomonas aeruginosa*, a pathogen that uses 3-oxo-C12-AHL for cell-to-cell signaling, demonstrate that 3-oxo-C12-AHL and 3-oxo-C12-HS can promote membrane remodeling at biologically relevant concentrations and in the absence of other biosurfactants, such as rhamnolipid, that are produced at high population densities. Overall, these results have implications for the roles that 3-oxo-C12-AHL and its hydrolysis product may play in not only mediating intra-species bacterial communication, but also processes such as inter-species signaling and bacterial control of host-cell response. Our findings also provide guidance that could prove useful for the design of synthetic self-assembled materials that respond to bacteria in ways that are useful in the context of sensing, drug delivery, and in other fundamental and applied areas.

Introduction

Self-assembled lipid membranes are dynamic systems that respond to a variety of environmental stimuli, including changes in pH,[1,2] ionic strength,[3,4] and temperature,[1,5] through molecular reorganization,[6,7] phase changes,[5,8] and pore formation.[9,10] This dynamic behavior is central to life processes and has been exploited for the design of synthetic materials platforms for drug delivery, environmental sensing, separations, and in many other fundamental and applied contexts.[1,11-14] Both natural and synthetic lipid membranes can undergo structural transformations in the presence of molecules in their environment, including amphiphilic species that can adsorb to, intercalate into, or translocate across their inner and outer leaflets.[15,16] In this study, we report on large-scale remodeling of model synthetic lipid membranes promoted by contact with *N*-acyl-L-homoserine lactones (AHLs), a class of nonionic, small-molecule amphiphiles that species of Gram-negative bacteria use as intercellular signals to coordinate group behaviors,[17-19] including motility,[20] the production of sessile drug-resilient biofilms,[21,22] and the synthesis of virulence factors such as the biosurfactant rhamnolipid.[23] This signaling process is called quorum sensing (QS) and is widespread in common bacterial pathogens.

Of particular interest to the work described here are past reports demonstrating that AHLs, which possess a relatively polar L-homoserine lactone "head group" and an aliphatic "tail" of four to 20 carbons (Figure 1), can self-assemble in aqueous solution and at interfaces.[24-26] For example, past work by our group[26] and others[25] has demonstrated that long-chained AHLs (e.g., those possessing eight or more carbons in their tails) can self-assemble in solution to form spherical micelles or small (~20 nm) vesicles in a tail-length dependent manner. Daniels *et al.* have also demonstrated that AHLs can self-assemble and undergo phase changes when compressed at air-water interfaces.[24] Other groups have reported that AHLs are able to intercalate via their tails into

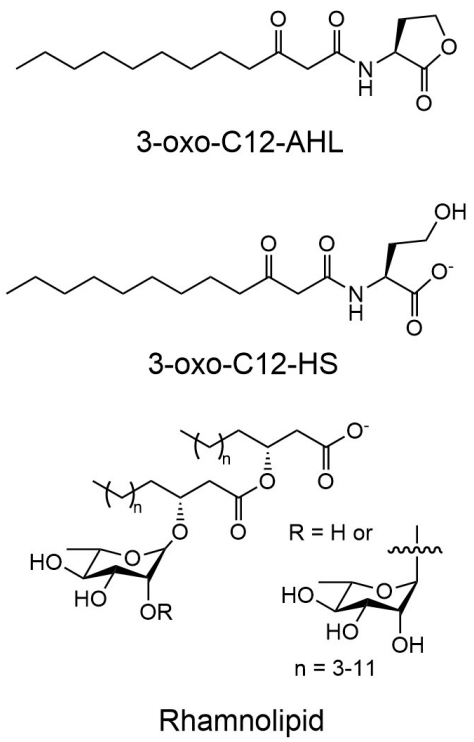


Figure 1: Structures of the amphiphilic compounds examined experimentally and by molecular dynamics simulations in this study.

the hydrophobic core of a lipid membrane,[27-29] leading to changes in a variety of membrane properties, including membrane depolarization[30] and the dissolution of lipid rafts.[31] Finally, studies by Lentini et al. have also, in the cases of 3-oxo-C8-AHL and the short-chained AHLs C4-AHL and 3-oxo-C6-AHL, demonstrated their translocation across model lipid bilayer systems.[32] These results are significant because, when combined, they hint at roles that these amphiphilic signaling molecules may play beyond their widely studied roles as mediators of bacterial cell-cell communication. For example, the ability of these molecules to self-assemble at or within lipid membranes may help facilitate the transport of these signaling molecules between bacterial cells,[29] attenuate their activity profiles, and could potentially underlie mechanisms by which communities of bacteria influence interspecies signaling, host-cell behavior, or even engage in interkingdom

signaling.[33,34] More broadly, the ability of AHLs to interact with lipid membranes suggests the potential to design synthetic materials that interact dynamically with bacterial communities.[32,35]

In this study, we demonstrate that 3-oxo-C12-AHL (Figure 1), an AHL with a 12-carbon tail produced by the opportunistic pathogen *Pseudomonas aeruginosa* and related bacteria, can interact with model supported lipid membranes (SLBs) in ways that promote large-scale remodeling. Characterization by fluorescence microscopy and quartz crystal microbalance with dissipation (QCM-D) reveal the formation of extended tubule structures up to hundreds of microns in length, as well as hemispherical caps that form on the surface of 1,2-dioleoyl-sn-glycero-3-phosphocholine (DOPC) lipid membranes upon exposure to solutions of 3-oxo-C12-AHL and its anionic head group hydrolysis product 3-oxo-C12-HS.[36] The nature and extent of remodeling is dependent upon the chemical structures of these amphiphiles and is at least partially reversible. These experimental observations can be interpreted in view of molecular dynamics (MD) simulations of thermodynamic barriers to translocation for 3-oxo-C12-AHL and 3-oxo-C12-HS. These simulations provide a theoretical framework for interpreting lipid remodeling in terms of differences in the intercalation and translocation of these compounds in the inner and outer leaflets of a lipid membrane. This framework also permits comparisons to the results of other past studies on the interaction of natural and synthetic amphiphiles with SLBs.[37] Finally, experiments using culture supernatants of wild-type *P. aeruginosa* and a related mutant strain demonstrate that 3-oxo-C12-AHL and 3-oxo-C12-HS can promote membrane remodeling at biologically relevant concentrations and in the absence of other biosurfactants (e.g., rhamnolipid) produced at high cell densities. These results provide insight into the potential roles that 3-oxo-C12-AHL and 3-oxo-C12-HS may play in bacterial communities, including QS mechanisms and potential mechanisms for interactions with non-self bacteria and their host organisms. Additionally, the results of these

studies with model lipid membranes provide guidance that could advance an important long-term goal—understanding the range of interactions that can occur between bacterial communities and synthetic self-assembled materials—thereby providing new principles for the development of responsive materials for drug delivery and sensing applications.

Materials and Methods

Materials. Dimethylsulfoxide (DMSO), sodium chloride (NaCl), calcein, sodium hydroxide (NaOH), lithium hydroxide (LiOH), magnesium sulphate, acetone, triethylphosphine oxide, Sephadex G-50, white, light mineral oil, and deuterium oxide (D_2O) were obtained from Sigma (St. Louis, MO). 1,2-Dioleoyl-sn-glycero-3-phosphocholine (DOPC) and 1,2-dihexanoyl-sn-glycero-3-phosphocholine (DHPC), L-α-phosphatidylglycerol (Egg PG), filter supports, and a Mini-prep extruder were purchased from Avanti Polar Lipids (Alabaster, AL). Lissamine rhodamine B 1,2-dipalmitoyl-sn-glycero-3-phosphoethanolamine, triethylammonium salt (Rho-DPPE) was acquired from Invitrogen (Carlsbad, CA). Rhamnolipids, 90% pure (commercial mixture of glycolipids isolated from *P. aeruginosa*) were purchased from AGAE Technologies (Corvallis, OR). Lennox formulation Luria-Bertani (LB) medium powder from Research Products International (Mt. Prospect, IL) was used for bacterial culture. Electrophoresis-grade sodium dodecyl sulfate (SDS) was purchased from Fisher Scientific (Pittsburgh, PA). Triton-X100 was obtained from Promega (Madison, WI). MOPS was purchased from MP Biomedical (Irvine, CA). Minisort X plus 0.2 μm syringe filters were acquired from Sartorius Stedim Biotech (Goettingen, Germany). Isopropanol (iPrOH) was purchased from Fisher Scientific (Waltham, MA). 100 nm polycarbonate extruder filters were purchased from Millipore (Billerica, MA). Water was purified

using a Milli-Q system (Millipore, Bedford, MA), yielding water with a resistivity of 18.2 MΩ. All materials were used as received without further purification unless otherwise specified.

Synthesis of 3-oxo-C12-AHL and 3-oxo-C12-HS. 3-oxo-C12-AHL was synthesized using a procedure previously described in the literature and matched the reported NMR spectra.[38] To synthesize 3-oxo-C12-HS, 3-oxo-C12-AHL (73 mg, 0.25 mmol) was added to a glass vial equipped with a stir bar and dissolved in acetone (1 mL). Aqueous lithium hydroxide (10 drops of 1M solution) was added to the vial, and the reaction was stirred at room temperature. Reaction progress was monitored by thin layer chromatography. Upon consumption of starting material, the reaction mixture was dried with magnesium sulfate, filtered, and concentrated under reduced pressure to yield 3-oxo-C12-HS as a white solid. NMR spectra are provided for 3-oxo-C12-HS in the Supporting Information.

Cell Culture and Supernatant Collection. The *P. aeruginosa* strains used in this study were: PAO1 (wild-type)[39] and PW6886 (*ΔrhlA*) (PAO1 *rhlA-E08::ISphoA/hah*; tetracycline resistant).[40] All strains were cultured in LB medium. Freezer stocks of each strain were streaked on an LB agar plate and allowed to grow overnight at 37 °C. Single colonies were then placed into 2 mL of fresh LB medium and allowed to grow overnight. Aliquots (30 µL) of these overnight cultures were diluted into 3 mL of fresh LB medium in 16 x 100 mm culture tubes and grown at 37 °C with shaking at 200 rpm. At designated timepoints, the cultures were aliquoted into 1.7 mL centrifuge tubes and centrifuged at 16,000 g for 5 minutes to pelletize the cells. The culture supernatants were isolated and passed through a sterile 0.22 µm filter. Supernatants were immediately frozen and then thawed directly before use.

Preparation of Biosurfactant Solutions. Stock solutions of rhamnolipid in buffer (1 mg/mL) were made fresh before each experiment. A buffer solution of 150 mM NaCl, 10 mM MOPS in Milli-Q H_2O (pH 7.4) was used unless otherwise noted. All aqueous solutions used in this study contained 1 vol% DMSO, except for bacterial supernatants and LB medium. The rhamnolipid stock solution was sonicated briefly to assist in dissolution. To make rhamnolipid solutions of the desired concentration, the stock solution was diluted with additional buffer. Stock solutions of 3-oxo-C12-AHL and 3-oxo-C12-HS (20 mM) were made in DMSO and stored at -4 °C between uses. Aliquots of the stock solution were thawed immediately prior to experiments. To prepare aqueous AHL solutions, the stock solutions were first diluted in DMSO to 100 times the final aqueous concentration, and then diluted 1:100 into buffer or a solution containing rhamnolipid. All AHL solutions were used within 1 hour of their preparation to minimize changes in the ratios of hydrolyzed and unhydrolyzed AHL head groups in solution.

Vesicle Fabrication. All large unilamellar vesicles (LUVs) were prepared using a freeze-thaw and vesicle extrusion procedure.[41] In brief, desired amounts of DOPC dissolved in chloroform were aliquoted into vials, and the chloroform was removed under a stream of N_2. For fluorescence microscopy experiments, 0.1 wt% of fluorescently labeled lipid (Rho-DPPE) was added to the chloroform stock solutions prior to drying under N_2. The lipids were further dried under vacuum for at least an hour. Either fresh LB medium (for supernatant experiments) or a low salt buffer solution (10 mM NaCl and 10 mM MOPS in water; for controlled biosurfactant experiments) was added to the dried lipids and vortexed vigorously to form a turbid 5 mg/mL DOPC suspension. These vesicle solutions were then subsequently frozen and thawed five times by alternatively

immersing them into an iPrOH/dry ice bath and a warm water bath (~50 °C). The resulting vesicle suspension was passed at least 11 times through a 100 nm PC filter using an Avanti Polar Lipids Mini-prep extruder. The resulting vesicles were characterized by dynamic light scattering (DLS) (Malvern Zetasizer, Westborough MA) and found to have a hydrodynamic diameter of ~140 nm, which agrees with previously reported literature.[42]

To prepare calcein-loaded vesicles for dye leakage experiments, the dried lipid solution was hydrated with a solution of calcein (70 mM) in buffer. The pH of the solution was adjusted to 7.4 with 10 M NaOH. After five freeze-thaw cycles and extrusion, the vesicles were separated from external, unloaded calcein using a hand-packed Sephadex G-50 size exclusion chromatography column. The concentration of the resulting purified vesicle solution was then quantified using ^{31}P NMR as described in the Supporting Information.[43]

Giant Unilamellar Vesicle (GUV) Fabrication and Imaging. GUVs were fabricated using a previously described inverted-emulsion protocol.[44] Briefly, a 99:1 ratio of DOPC:Egg PG (5 mg total) was mixed in chloroform with 0.1 wt% of the fluorescently labeled lipid Rho-DPPE and dried under a stream of N_2. The lipid was further dried under vacuum for at least an hour to remove residual solvent. This dried lipid mixture was then dissolved in mineral oil (1 mL). Buffer (40.5 μL) was added to 450 μL of the lipid-oil mixture and vortexed for 30 seconds to form a water-in-oil emulsion. A 450 μL aliquot of this emulsion was gently placed on top of buffer solution (450 μL) in a microcentrifuge tube and centrifuged for 30 minutes at 14,000*g*. After centrifugation, the lower aqueous phase (which contained the fabricated GUVs) was isolated and diluted into either an equal volume of buffer or a concentrated solution of 3-oxo-C12-AHL or rhamnolipid. This dilution resulted in a suspension of GUVs in either buffer, 100 μM of 3-oxo-C12-AHL, or 25

μg/mL of rhamnolipid for observation via optical microscopy. Only GUVs with a diameter greater than 15 μm were considered for investigation. We sorted each of the vesicles observed into two categories, those with external tubulation and those without. The proportions of vesicles in each group were calculated for three independent samples.

Optical Microscopy Experiments Using SLBs Formed by Vesicle Fusion Technique. Fluorescence microscopy experiments were performed on fluorescently labeled SLBs that were formed using the vesicle fusion (VF) technique in Ibidi microfluidic chambers (μ-Slide VI 0.5 Glass Bottom) unless otherwise noted.[45] The microfluidic chambers first were cleaned with a 1 M NaOH aqueous solution for ~30 minutes prior to SLB formation, and then washed with ample Milli-Q H_2O followed by either LB medium (for supernatant experiments) or buffer (for biosurfactant experiments). Previously prepared LUV stock solutions (5 mg/mL) were diluted with buffer to 0.1 mg/mL and introduced to the cleaned microfluidic chambers at a flow rate of 100 μL/min using a NE-300 "Just Infusion" syringe pump (Coral Springs, FL). The formation of the bilayer was monitored by microscopy to ensure the adsorption and subsequent fusion of LUVs into a SLB. When fusion was verified, the remaining vesicles in the flow cell were washed away by introducing LB medium or buffer to the flow cell at a flow rate of 100 μL/min. The resulting bilayer was tested for fluidity by performing a qualitative fluorescence recovery after photobleaching (FRAP) experiment. In initial control experiments, these SLBs responded to the presence of the amphiphile glycerol monolaurate (GML) in ways similar to those reported in past studies on the remodeling of DOPC membranes (see previous reports by Cho and coworkers[37]). Cell-free culture supernatants or solutions of test compounds were introduced into flow cells at a flow rate of 100 μL/min, and micrographs were acquired using an Olympus IX70 inverted

microscope (Center Valley, PA) and a Q-imaging EXi Aqua camera (Tucson, AZ) every 5 seconds for ~8 minutes (acquiring at least 100 images). Fluorescently-labeled lipids were excited with a Lumen Dynamics X-Cite Series 120PC-Q fiber coupled mercury lamp using the RFP channel (Monroe, LA). The bilayers were then washed with buffer solution at a flow rate of 100 μL/min to visualize changes in the bilayer structure as the test compounds were removed from solution.

Formation of DOPC SLBs Using the Bicelle Fusion Method. As a second means of preparing SLBs, we used a previously described bicelle formation technique.[46] In brief, DOPC and DHPC ([DOPC]/[DHPC]=0.25) were dissolved in chloroform, the solution was well mixed, and solvent was removed under a stream of N_2 and then under vacuum for at least one hour. The resulting lipid film was then hydrated by buffer to produce a 1 mM bicelle suspension by DOPC concentration. This solution was frozen and thawed five times by iteratively immersing the solution into an iPrOH and dry ice bath followed by a warm water bath (~50 °C). The bicelle stock solution was then diluted 1:16 for a final DOPC concentration of 0.063 mM and introduced to an NaOH treated Ibidi flow cell at a flow rate of 100 μL/min. The formation of a continuous bilayer was monitored by optical microscopy. Buffer was then introduced to the bilayer to wash away any remaining bicelle above the bilayer. The resulting bilayer was tested for fluidity by performing a qualitative FRAP experiment. Test compounds were then introduced into the flow cell at a constant concentration at a flow rate of 100 μL/min. Time-lapse micrographs were acquired every 5 seconds over ~8 minutes. The bilayers were then washed with buffer solution at a flow rate of 100 μL/min to visualize changes in bilayer structure as the test compounds were removed from solution.

Measurement of the Surface Tensions of Biosurfactant Solutions. Measurements of the surface tensions of 3-oxo-C12-AHL, 3-oxo-C12-HS, and rhamnolipid solutions were made by adapting a previously described procedure.[47] The surface tensions of the biosurfactant solutions was measured using a Nima Type 611 trough. The tensiometer was calibrated using an internal calibration program and checked by ensuring the surface tension of Milli-Q water was near 72 mN/m. A dry paper Wilhelmy plate was immersed in Milli-Q water for 10 minutes at room temperature to hydrate before surface tension measurements were made. Biosurfactant solutions were prepared in buffer as described above and allowed to sit at room temperature, and then the hydrated Wilhelmy plate was dipped into the biosurfactant solution and allowed to sit at the solution interface for 30 seconds. The surface tension (γ) was determined by measuring the change in force applied to the Wilhelmy plate by the solution while in contact with the solution interface and directly after removing the plate from solution. This change in force (F) was then used in the Wilhelmy equation,[47]

$$\gamma = \frac{F}{l \cos(\theta)} \quad \text{(Eq. 1)}$$

where l is the wetted perimeter of the paper Wilhelmy plate (21 mm) and θ is the contact angle of water on the Wilhelmy plate, which is assumed to be 0º for a paper plate.

Quartz Crystal Microbalance with Dissipation (QCM-D) Measurements. QCM-D measurements were performed using a Q-Sense E4 instrument (Bolin Scientific, Stockholm Sweden) with QSensor QSX 303 quartz crystal sensors coated with 50 nm of SiO_2 and with a fundamental frequency of 5 MHz (Bolin Scientific, Stockholm Sweden). Changes in the frequency (Δf) and dissipation (ΔD) were monitored at the third, fifth, seventh, ninth, and eleventh overtones, and data analysis was performed using the data from the seventh overtone. Each data set consisting

of individual test molecules at different concentrations was acquired on a single set of sensors to ensure consistency between measurements. In all tests, fluid was flowed over the crystals at 100 µL/min using an Ismatic IPC High Precision Multichannel Dispenser peristaltic pump (Wertheim, Germany). When received, the QCM-D sensors were treated with oxygen plasma for 10 minutes and then immediately immersed in a 2% SDS solution and allowed to sit for at least 30 minutes. The sensors were rinsed in Milli-Q water and dried under a stream of dry N_2. Immediately before conducting an experiment, the sensors were again treated with oxygen plasma for 10 minutes, placed into the measurement apparatus, and allowed to equilibrate their resonance under 100 µL/min flow of buffer solution.

For QCM-D measurements, SLBs were formed using the VF method.[45] Vesicle stock solutions (5 mg/mL) were diluted to 0.1 mg/mL in buffer and introduced to the sensor chamber. Adsorption of the vesicles to the surface and subsequent fusion were ensured by following the QCM-D traces over time. The formed bilayer was then washed with buffer for ~45 minutes. Biosurfactant solutions were added to the flow chamber and allowed to interact with the bilayer for 45 minutes. The bilayer was then washed with buffer to observe the desorption of biosurfactants from the bilayer over time. Representative QCM-D traces are shown for a single sensor in the results reported below, but further data analysis described and included in Figure S4 is from three or four (n=3-4) independent experiments run simultaneously on different crystals. During experiments, the measurement chamber was held at 25 ± 0.5 °C. Immediately following each experiment, the sensors were placed in a 2% SDS solution for 30 minutes, washed in Milli-Q water, and then dried under N_2 gas before storage.

Calcein Leakage Assay. Calcein leakage assays were performed in 96-well microtiter plates. In each well, a 10 μL aliquot of calcein vesicles (at a concentration of 1 mM DOPC by monomer) was combined with 90 μL of a biosurfactant solution. The plate was allowed to sit for 5 minutes and then the fluorescence intensity of the solution was read with an excitation of 480 nm and emission of 525 nm using a Tecan Infinite 200 Pro plate reader. All tests were repeated three times (n=3) for each batch of vesicles and were performed with three (n=3) independently produced batches of vesicles for a total of nine (n=9) fluorescence measurements. Statistical significance against the buffer control was determined using a one-way ANOVA with all nine normalized replicates for each condition used that was corrected for multiple comparisons using Dunnett's method. The fluorescence intensity for each reading was normalized using a procedure adapted from other publications and summarized in Equation 2 where: FI is the fluorescence intensity of the test solution, FI_{Buffer} is the fluorescence intensity of the calcein vesicles in buffer as the negative control, and $FI_{TX\text{-}100}$ was the fluorescence intensity of a vesicle solution containing 1% Triton X-100 (which is known to lyse vesicles) as a positive control.[48]

$$Normalized\ Flourescense = \frac{FI - FI_{Buffer}}{FI_{TX-100} - FI_{Buffer}} \quad \text{(Eq. 2)}$$

Free Energy Calculations. Molecular dynamics simulations with umbrella sampling[49] were performed to obtain potentials of mean force (PMFs) for the translocation of 3-oxo-C12-AHL, 3-oxo-C12-HS, two rhamnolipids with 10 carbons in the tail with one (rha-C10-C10) or two (rha-rha-C10-C10) rings in the head group, glycerol monolaurate (GML), and lauric acid across a DOPC bilayer containing 128 lipid molecules. All systems were modeled using the CHARMM36 force field with the TIP3P water model.[50] Molecular structures and force field parameters were generated using the CHARMM-GUI Input Generator.[51,52] Verlet lists were generated using a 1.2

nm neighbor list cutoff. Van der Waals interactions were modeled with a Lennard-Jones potential using a 1.2 nm cutoff that was smoothly shifted to zero between 1.0 nm and 1.2 nm. Electrostatic interactions were calculated using the smooth Particle Mesh Ewald method with a short-range cutoff of 1.2 nm, grid spacing of 0.12 nm, and 4^{th} order interpolation. Bonds were constrained using the LINCS algorithm. All systems were energy minimized using the steepest descent method. Simulations were performed in the *NPT* ensemble using a leapfrog integrator with a 2-fs timestep. For equilibration, the temperature was maintained at 310.15 K using a Berendsen thermostat with a time constant of 1.0 ps and the pressure was maintained at 1 bar using a semi-isotropic Berendsen barostat with a time constant of 5.0 ps and a compressibility of 4.5×10^{-5} bar^{-1}. For umbrella sampling, the temperature was maintained at 310.15 K using a velocity-rescale thermostat with a time constant of 1.0 ps and the pressure was maintained at 1 bar using a semi-isotropic Parrinello-Rahman barostat with a time constant of 5.0 ps and a compressibility of 4.5×10^{-5} bar^{-1}. All simulations were performed using Gromacs 2016.[53]

Umbrella sampling was performed using the z-component of the distance between the molecule center of mass and bilayer center of mass (denoted as z) as a collective variable. Each umbrella sampling calculation was performed using independent windows separated by 0.1 nm from z = 0 nm to z = 4 nm with z = 0 nm corresponding to the bilayer midplane. At least 41 windows were used for each molecule; 2 additional windows were added for 3-oxo-C12-AHL and rha-C10-C10 and 1 additional window was added for GML. In each case, the number of windows was selected to obtain convergence and ensure that the PMF was symmetric around z = 0. Harmonic restraints with force constants ranging from 200 kJ mol^{-1} nm^{-2} to 1500 kJ mol^{-1} nm^{-2} were applied to restrain sampling to a given value of z. Each window was equilibrated for 5 ns in the NPT ensemble and then sampled for 32 ns. The last 24 ns of this trajectory were split into two

independent 12-ns blocks and used to compute two PMFs as a function of z using the Weighted Histogram Analysis Method.[54] Plots demonstrating PMF convergence are shown in the Supporting Information.

Results and Discussion

To launch our investigations, we performed a series of initial studies to gauge the ability of and extent to which bacterial cultures (or supernatants obtained from bacterial cultures) can alter model lipid membrane systems. *P. aeruginosa* was chosen as a model organism for this study because it is a well-studied opportunistic pathogen, whose lipophilic QS signals and related bio-toxins have been linked to negative outcomes in both environmental and clinical settings.[55-58] We briefly describe the results of these experiments to provide a framework for the discussion of more detailed and systematic studies described below. For these initial experiments, we contacted supported lipid bilayers (SLBs) formed from DOPC with the supernatants of 24-hour cultures of *P. aeruginosa*. We selected SLBs as a model system for these initial studies rather than other lipid membrane systems (such as giant unilamellar vesicles, or GUVs), because they are compatible with a wide range of surface characterization techniques, including acoustic sensors (QCM-D)[59] and fluorescence microscopy,[37,60] and can be prepared using a variety of methods.[45,46,61] DOPC was chosen as a model lipid because it is widely used as a simple laboratory model for mammalian membranes, it is fluid at room temperature,[62] and it has been previously used by other groups to characterize the interactions of analytes with lipid membranes, thereby facilitating comparisons between the results of those past studies and the new experiments with the amphiphiles reported here.[37,63-65] To facilitate visualization by optical microscopy, the lipid membranes were doped with 0.1 wt% of the fluorescently labeled lipid Rho-DPPE. In all of the fluorescence microscopy

experiments described here, SLBs were formed on NaOH-treated glass in an Ibidi flow cell using the vesicle fusion (VF) technique, unless otherwise noted (see Methods for additional detail).[45] The adsorption and rupture of lipid vesicles into a SLB was monitored by optical microscopy and the fluidity of the SLBs was confirmed by a qualitative FRAP experiment before the introduction of bacterial supernatants or biosurfactants to the bilayers.

The introduction of cell-free *P. aeruginosa* culture supernatants to SLBs composed of DOPC resulted in large-scale and visually apparent reformations of the bilayers that are shown in the sequence of time lapse fluorescence micrographs included in Figure 2. We observed the growth

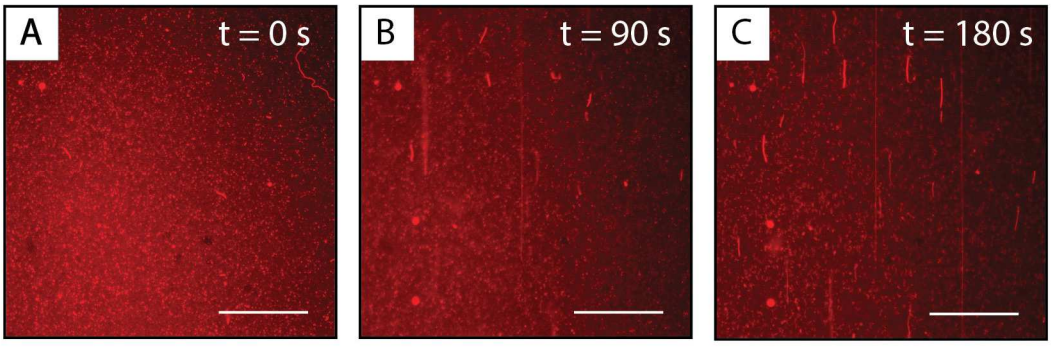


Figure 2: Representative top-down fluorescence micrographs of structural reformations observed in fluorescently labeled DOPC SLBs after the introduction of cell-free supernatants of *P. aeruginosa* cultures grown for 24 hours. The micrographs were acquired (A) 0 seconds, (B) 90 seconds, and (C) 180 seconds after the first membrane reformations were observed on the surface of the bilayer. The direction of flow in all the images is from the bottom to the top of the image. Scale bars are 30 µm.

of long, thin, bright red structures on the surfaces of the bilayers within the first minute of initiating the flow of supernatant into the flow cell. These structures ranged from 1-10 microns to hundreds of microns long (in many cases, longer than the observable field of view; Figure 2B). Some of these structures completely retracted into the underlying bilayer over the course of several minutes to form large pseudo-circular patches of increased fluorescence intensity (Figure 2C). In all of the

fluorescence micrographs shown here and in the studies described below, the direction of flow was from the bottom to the top of the field of view, and thus the long, thin structures observed in Figure 2 were aligned in the direction of flow.

The changes in bilayer structure and associated dynamics described above and shown in Figure 2 are similar to the restructuring of SLBs reported in past studies when SLBs were placed in contact with certain natural and synthetic surfactants.[37,60,63-65] In those studies, the presence of long, thin structures and pseudo-circular structures were interpreted to result from the formation of hollow microtubules and thin, water-filled, hemispherical caps. Cartoon representations (both

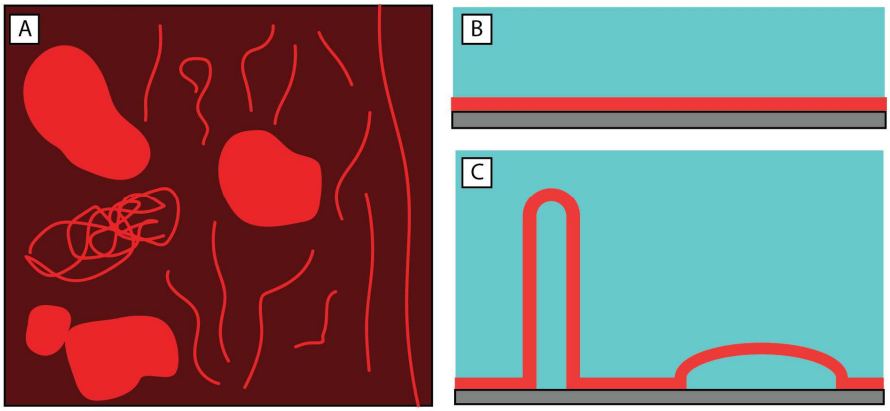


Figure 3: Illustrations depicting membrane reformations (microtubules and hemispherical caps) observed in our experiments and in past studies of interactions of natural and synthetic amphiphiles in contact with SLBs.[37] (A) Top-down depiction of a remodeled bilayer showing both long and short tubule structures and hemispherical caps. (B,C) Side view of (B) a SLB without any structural reformations and (C) a SLB with both (left) extended microtubules and (right) hemispherical caps after membrane reformation.

top-down and side view) of these structures are shown in Figure 3. Those past reports provide a framework for probing and interpreting the membrane restructuring observed in our experiments in the presence of bacterial supernatants. While there are many components present in bacterial supernatants that could interact with SLBs, the similarities in the membrane reformations observed in Figure 2 to those previously reported for SLBs in contact with natural and synthetic surfactants

suggested the possibility that the membrane restructuring observed in our experiments could be promoted by amphiphilic species present in the supernatant.[37,60,63-65]

In the experiments above, we used culture supernatant collected after 24 hours of *P. aeruginosa* growth, which has been previously shown to contain at least two amphiphilic species: the QS signal 3-oxo-C12-AHL and the QS-regulated biosurfactant rhamnolipid (Figure 1).[66] Rhamnolipid is a well-characterized bio-surfactant and is known to interact with and disrupt mammalian cell membranes.[67,68] The interactions of 3-oxo-C12-AHL with lipid membranes is less well understood, with several recent reports suggesting that it can intercalate into membranes[27,28] and lead to a depolarization of vesicle membranes[30] and the disruption of lipid rafts.[31] However, to the best of our knowledge, the large-scale reformation and remodeling of lipid membranes to form structures such as those shown in Figure 2 has not yet been reported. As noted above, the potential ability of these amphiphiles, either alone or in combination, to promote large-scale membrane remodeling bears on many interesting biological questions (e.g., underlying potential QS mechanisms, signal potency, interspecies signaling, and impacts on host cells) and has the potential to inform the design of new classes of soft materials that can interact with bacterial communities in new ways (e.g., for the development of novel sensors or smart drug delivery vehicles, etc.). These questions and the observations in Figure 2 motivated additional studies of the interactions of 3-oxo-C12-AHL and rhamnolipid with lipid membranes described in the sections below.

Characterization of Interactions of 3-oxo-C12-AHL and 3-oxo-C12-HS with DOPC Membranes Using Fluorescence Microscopy

We began our studies to systematically characterize the interaction of SLBs with components of bacterial supernatants by focusing on the signaling molecule 3-oxo-C12-AHL. Here we note that 3-oxo-C12-AHL has a homoserine lactone head group that can hydrolyze in aqueous media to form 3-oxo-C12-HS (Figure 1).[36] AHL head group hydrolysis occurs relatively rapidly (especially in *P. aeruginosa* cultures that become alkaline over time; $t_{1/2}$= ~10 hr at pH 8)[69,70] and yields an anionic compound that also has an amphiphilic structure and, as a result, has the potential to interact with membranes. It is, thus, important to note that any bacterial supernatant or solution containing 3-oxo-C12-AHL at pH ≥ 7 will likely consist of a mixture of these two components. To set the stage for understanding the interactions of 3-oxo-C12-AHL and 3-oxo-C12-HS, or combinations of these two amphiphiles, with lipid membranes, we measured the surface activity of each compound at the air-water interface using a Wilhelmy plate (Figure S1A; see Methods for details).[47]

Those studies revealed that 3-oxo-C12-AHL is more surface active than 3-oxo-C12-HS, which exhibited lower surface tensions at all concentrations tested (e.g., 46.7 mN/m as compared to 57.3 mN/m at 200 μM, respectively; see Figure S1A for all concentrations tested). Additionally, 3-oxo-C12-AHL exhibited a break in a plot of surface tension vs. concentration (denoted by an arrow in Figure S1), suggesting that it aggregates at a concentration between 100 μM and 125 μM under the conditions used here. The location of this break occurs in a range that is generally consistent with the value reported for the critical aggregation concentration (CAC) for this AHL in our past study, using a combination of light scattering and measurements of surface tension in water (88 ± 20 μM and 97 ± 11 μM, respectively; see that past study for a more detailed discussion

on the solution-phase self-assembly of 3-oxo-C12-AHL in aqueous media).[26] In contrast, 3-oxo-C12-HS did not exhibit a break in plots of surface tension vs. concentration in the range of concentrations examined in this study; as a result, we conclude that this hydrolyzed compound does not aggregate in this range of concentrations. These results, taken together, suggest that the chemical hydrolysis of the homoserine lactone head group of 3-oxo-C12-AHL alters its physical behavior in solution and at interfaces, leading to 3-oxo-C12-AHL being more surface active than 3-oxo-C12-HS. We will return to these observations again in the discussion below.

Additional fluorescence microscopy experiments similar to those described above with culture supernatants revealed that 3-oxo-C12-AHL and 3-oxo-C12-HS promote large differences in the structural reformations of DOPC SLBs. Figure 4 shows fluorescence microscopy images of SLBs after exposure to continuous flows of solutions containing different concentrations of 3-oxo-C12-AHL or 3-oxo-C12-HS for periods of 360 sec (additional images of bilayer reformation at intermediate timepoints can be found in Figures S2A and 2B). Images of SLBs that were subjected to the flow of buffer alone for at least 360 sec are shown in Figure 4A,B and reveal that flow alone and exposure to buffer do not cause observable large-scale reformation.

Figure 4C,D shows images of SLBs after the introduction of 3-oxo-C12-AHL (Figure 4C) or 3-oxo-C12-HS (Figure 4D) at 30 μM, which was the lowest concentration tested. This concentration is representative of AHL concentrations measured to be in planktonic cultures of *P. aeruginosa* after 24 hours of growth.[66] Within one minute of introduction of 30 μM 3-oxo-C12-AHL to the flow cell, we observed the formation of tubules ~5-40 μm long on the surface of the bilayer. These tubules were often observed to retract and collapse into hemispherical caps within 5-180 sec of forming. This behavior contrasted to that of SLBs treated with 30 μM 3-oxo-C12-HS solutions, which we observed to form extended tubules (~50 μm in length) that persisted on the

surface of the bilayer and did not appear to retract or collapse on the timescale of the experiment. The results shown in Figure 4C,D fall within the range of observations made using bacterial supernatants (in Figure 2), as well as those in past studies using synthetic surfactants,[37,60,64] and suggest that AHLs (and their hydrolyzed derivatives) alone can promote large-scale reformation at biologically relevant concentrations.

To explore this phenomenon further, we conducted additional experiments at concentrations of 3-oxo-C12-HS and 3-oxo-C12-AHL of up to 200 μM, a concentration that is above what is observed in planktonic bacterial cultures, but that is relevant in the context of elevated concentrations of AHL reported to be present in bacterial biofilms.[71] This is also, in our hands, the highest concentration at which 3-oxo-C12-AHL is soluble in the buffers used here. As shown in Figure 4, when 50 μM (Panel F), 100 μM (Panel H), 150 μM (Panel J), or 200 μM (Panel L) solutions of the hydrolyzed, 3-oxo-C12-HS compound were introduced to SLBs, we observed the formation of tubules ranging from 5-100 μm in length. These results are consistent with the behaviors observed after the introduction of 30 μM of 3-oxo-C12-HS to SLBs (Figure 4C), but with an increased number of tubules at elevated concentrations. In some cases, we observed a small number of the tubules to retract and form hemispherical caps at these higher concentrations (for example, see Figure 4I). However, the vast majority of tubules did not retract or form hemispherical caps, and tubules were the predominant restructuring phenomenon observed when SLBs were exposed to solutions containing 3-oxo-C12-HS.

The introduction of 3-oxo-C12-AHL to SLBs resulted in bilayer reformation that was more complex than that observed for 3-oxo-C12-HS. At 50 μM (Figure 4E), 3-oxo-C12-AHL promoted membrane restructuring similar to that observed at 30 μM (Figure 4C), where smaller tubules formed within the first minute of the experiment, many of which quickly collapsed into

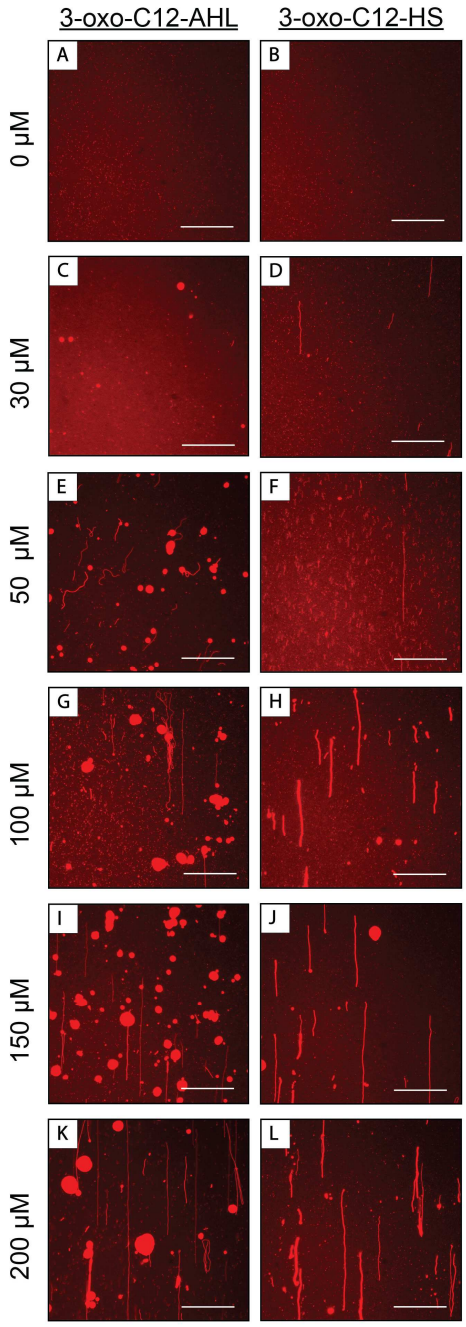


Figure 4: Representative top-down fluorescence micrographs of fluorescently labeled DOPC SLBs that are either (A, B) stable under a continuous flow of buffer or (C-L) have undergone structural reformations after interacting with a continuous flow of (*left images*: C, E, G, I, K) 3-oxo-C12-AHL or (*right images*: D, F, H, J, L) 3-oxo-C12-HS solutions. Images were acquired 360 seconds after the onset of membrane restructuring. The concentration of amphiphiles used in each experiment were (C,D) 30 µM, (E,F) 50 µM, (G,H) 100 µM, (I,J) 150 µM, or (K,L) 200 µM. The direction of flow in all images was from the bottom to the top of the image. Scale bars are 30 µm.

hemispherical caps, and some of which persisted throughout the time of the experiment. At higher concentrations of 100 μM (Figure 4G), 150 μM (Figure 4I), and 200 μM 3-oxo-C12-AHL (Figure 4K), combinations of hemispherical caps and extended tubules were also observed. However, in contrast to experiments at lower concentrations of 3-oxo-C12-AHL, we observed many more long, extended tubules that were several hundred microns in length, reminiscent of what we observed in Figure 2 and as described above for experiments using bacterial supernatants, as well as tubule bundles. We note that the critical aggregation concentration (CAC) of 3-oxo-C12-AHL is ~100 μM.[26] The differences in tubule formation observed at these higher concentrations relative to lower concentrations could therefore correlate to the extent of 3-oxo-C12-AHL aggregation, a factor that is known to impact the interaction of amphiphilic species with lipid membranes.[63,64] In addition to the tubules and hemispherical caps described above, at 150 μM (Figure 4I) and 200 μM (Figure 4K) we observed the flow of fluorescent material across the field of view in the direction of flow, suggesting that 3-oxo-C12-AHL at these high concentrations can undergo processes that result in the removal or dissolution of lipid material from the bilayer. We note here that our as-prepared SLBs contain punctate spots of red fluorescence (Figure 4A,B) prior to the introduction of any compounds. These punctate spots are often observed in SLBs formed by the vesicle fusion method and are typically interpreted as surface-bound vesicles that did not rupture during bilayer formation.[72] We also observed the formation of tubules and hemispherical caps in experiments where 200 μM 3-oxo-C12-AHL was introduced SLBs formed using an alternative bicelle fusion method that does not involve the use of vesicles (see Methods),[46] suggesting that the changes in morphology observed above do not arise from artifacts associated with the presence of unruptured vesicles.

Additional experiments revealed that the formation of these surface features was, in many cases, at least partially reversible upon the removal of compound and washing with buffer. Figure S3 shows images of a bilayer analogous to the one shown in Figure 4 after rinsing with buffer for at least eight minutes. These images show that tubules can retract and collapse into hemispherical caps, and that caps can subsequently shrink in size and, in some cases, disappear from the surface of the bilayer for all concentrations of 3-oxo-C12-HS and 3-oxo-C12-AHL tested. At higher concentrations of 3-oxo-C12-AHL (150 μM and 200 μM (Figure S3; insets in panels (H,J)), we also observed circular areas of decreased fluorescence, suggesting that some local removal of bilayer material could occur under these conditions. The observation of these darker patches is consistent with our observations, as discussed above, of fluorescent material floating across the field of view when high concentrations of 3-oxo-C12-AHL were introduced to the bilayers.

Taken together, these results are consistent with the results of our initial experiments performed with bacterial supernatant and show unambiguously that AHLs can cause large-scale membrane reformations. Additionally, our results show that 3-oxo-C12-AHL head group hydrolysis can change the physical properties of AHL and lead to differences in membrane reformation. The results described thus far provide additional evidence for conclusions emerging from a growing body of work suggesting that 3-oxo-C12-AHL can interact with lipid bilayers in ways that lead to changes in physical properties and structure.[27,28,30,31] To our knowledge, the results reported here are the first to demonstrate that the QS signal 3-oxo-C12-AHL and its hydrolysis product 3-oxo-C12-HS can interact with SLBs in ways that lead to large-scale structural reformation in the bilayer. Additional experiments to explore differences in the interactions of 3-oxo-C12-AHL and 3-oxo-C12-HS with lipid membranes, and the implications of these differences in behavior, are described in the sections below.

Characterization of the Interactions of 3-oxo-C12-AHL and 3-oxo-C12-HS with DOPC Membranes Using QCM-D

The results described above demonstrate that large-scale membrane remodeling occurs when a QS signal of an important bacterial pathogen, 3-oxo-C12-AHL, interacts with a model lipid membrane. Those results also reveal qualitative differences between the behaviors mediated by 3-oxo-C12-AHL and its naturally occurring hydrolysis product 3-oxo-C12-HS. To provide additional quantitative insight into these processes, we used quartz crystal microbalance with dissipation (QCM-D) to measure differences in the response of DOPC SLBs when introduced to solutions of 3-oxo-C12-AHL or 3-oxo-C12-HS (see Methods for additional details). After the SLBs were formed on SiO_2-functionalized quartz crystals using the vesicle fusion method[45] and washed with buffer, they were exposed to a flow of 3-oxo-C12-AHL or 3-oxo-C12-HS solutions (100 μL/min) at various concentrations. Figure 5 shows the changes in frequency (Δf, blue lines) and dissipation (ΔD, orange lines) in SLBs upon exposure to 3-oxo-C12-AHL (solid lines) or 3-oxo-C12-HS (dashed lines) at various concentrations and after a subsequent buffer wash (Δf and ΔD values at t=0 min correspond to values for a stable SLB assembled on the quartz crystal prior to the experiment). The solid arrows in Figure 5 indicate the time at which solutions containing compound were added to SLBs, while the dashed arrows indicate the time at which buffer washes were initiated. All data shown are representative QCM-D data sets of either three or four replicates. Full data analysis of all trials (mean and standard deviation of each concentration for each compound) can be found in Figure S4 and provide the Δf and ΔD values referred in the text below.

In general, we observed the introduction of 3-oxo-C12-AHL to (i) lead to more dramatic restructuring in DOPC SLBs, as indicated by the larger positive change in ΔD, and (ii) adsorb in greater amounts to the bilayer, as suggested by larger negative changes in Δf, when compared to

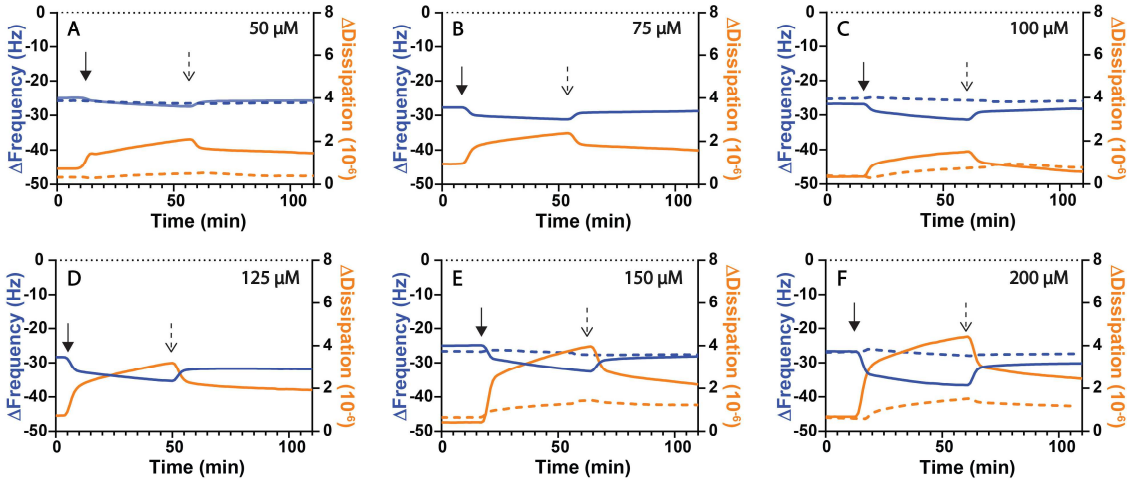


Figure 5: Representative QCM-D measurements of large-scale bilayer reformations in DOPC SLBs initiated by the introduction of (solid lines) 3-oxo-C12-AHL or (dashed lines) 3-oxo-C12-HS solutions at (A) 50 µM, (B) 75 µM, (C) 100 µM, (D) 125 µM, (E) 150 µM, (F) 200 µM. The changes in frequency (ΔFrequency, blue lines; referred to as Δf in the main text for brevity), and dissipation (ΔDissipation, orange lines; referred to as ΔD in the main text for brevity) shown are representative of three or four independent experiments. The initial measurement values (t=0 min) of these experiments correspond to a DOPC SLB on an SiO_2 surface. Either 3-oxo-C12-AHL or 3-oxo-C12-HS solutions were introduced to the bilayer at the time indicated by the solid arrow and a buffer wash was introduced at the time indicated by the dashed arrow.

3-oxo-C12-HS at a given concentration (Figure 5 and summarized in Figure S4). When 3-oxo-C12-AHL was introduced to the bilayer at 50 µM (Figure 5A), 75 µM (Figure 5B), and 100 µM (Figure 5C), we observed similar changes in frequency (-2.5 ± 0.1 Hz, -2.9 ± 0.3 Hz, and -4.0 ± 0.3 Hz) and dissipation (1.2 ± 0.2 $x10^{-6}$, 1.5 ± 0.2 $x10^{-6}$, and 1.1 ± 0.1 $x10^{-6}$). At the higher concentrations of 125 µM (Figure 5D), 150 µM (Figure 5E), and 200 µM (Figure 5F), which are above the CAC measured for 3-oxo-C12-AHL, we generally measured larger changes in Δf and ΔD at increasing concentrations, recording shifts of (-6.5 ± 0.5 Hz and 2.8 ± 0.4 $x10^{-6}$), (-6.3 ± 2.2 Hz and 3.1 ± 0.7 $x10^{-6}$), and (-8.8 ± 1.5 Hz and 4.0 ± 0.5 $x10^{-6}$), respectively. This apparent change in the general response in the bilayer below and above the CAC of 3-oxo-C12-AHL is similar to

that observed qualitatively in our fluorescence microscopy results (Figure 4). Additionally, the larger changes in frequency suggest that there is a greater mass of 3-oxo-C12-AHL adsorbing to the bilayer at higher concentrations. Upon washing the bilayers with buffer, all SLBs treated with 3-oxo-C12-AHL exhibited positive changes in Δf and negative changes in ΔD, suggesting that bilayer reformation is semi-reversible, in agreement with behaviors observed by fluorescence microscopy above. Together, these results further suggest that 3-oxo-C12-AHL is interacting with lipid bilayers in ways that lead to membrane restructuring in a semi-reversible fashion under all conditions examined here.

In contrast to 3-oxo-C12-AHL, the introduction of 3-oxo-C12-HS led to smaller shifts in Δf and ΔD in the SLBs. As shown in Figure 5 and summarized in Figure S4 the introduction of this hydrolyzed compound at 50 μM (Figure 5A) led to shifts of -0.9 ± 0.3 Hz and 0.3 ± 0.1 $x10^{-6}$ for Δf and ΔD, respectively. These smaller changes in both Δf and ΔD were also observed for 3-oxo-C12-HS at the higher concentrations of 100 μM (Figure 5C), 150 μM (Figure 5E), and 200 μM (Figure 5F) with shifts of (-1.0 ± 0.6 Hz and 0.6 ± 0.2 $x10^{-6}$), (0.0 ± 0.4 Hz and 0.7 ± 0.1 $x10^{-6}$), and (-0.4 ± 0.8 Hz and 0.8 ± 0.1 $x10^{-6}$) for Δf and ΔD, respectively. Similar to 3-oxo-C12-AHL, washing these treated bilayers with buffer also led to partial recovery of Δf and ΔD values, suggesting a semi-reversible desorption of 3-oxo-C12-HS from the membranes.

Taken together, the results above suggest that 3-oxo-C12-HS interacts with SLBs in a manner that leads to lower mass adsorption and membrane remodeling that is less extensive (or at least very different) than those observed for 3-oxo-C12-AHL at similar concentrations. The observation of lower mass adsorption for 3-oxo-C12-HS is consistent with our surface tension measurements, which, as discussed above, reveal that the hydrolyzed compound has lower surface activity than 3-oxo-C12-AHL at air-water interfaces. These QCM-D results are also consistent

with the observation and dynamics associated with the formation of microtubules and hemispherical caps observed in our fluorescence microscopy studies, which again are in line with previous reports documenting the interaction of 3-oxo-C12-AHL with lipid membranes and associated changes in bilayer properties.[27,28,30,31] These results do not provide mechanistic insight into what may be occurring, at a molecular level, to lead to these large changes in morphology. We return in sections below to the results of molecular dynamics (MD) simulations that provide additional perspective on physicochemical differences between 3-oxo-C12-AHL and 3-oxo-C12-HS that are likely to underlie the large changes in behavior observed experimentally here.

Characterization of Interactions of Rhamnolipid with DOPC Membranes

As introduced above, *P. aeruginosa* and several related species use 3-oxo-C12-AHL for QS to regulate many group behaviors, including the production of virulence factors such as rhamnolipid,[23] a biosurfactant known to interact with and disrupt lipid membranes.[67,68] Depending on the conditions, 3-oxo-C12-AHL and 3-oxo-C12-HS may therefore exist either alone (e.g., at low population densities; prior to quorum) or in combination with rhamnolipid (e.g., at high population densities; at or above quorum, as was the case in the experiments presented in Figure 2).[66] In view of the latter condition, we also sought to characterize the interaction of rhamnolipid with DOPC SLBs and determine the extent to which it may contribute to membrane remodeling, including the formation of tubules or hemispherical caps, under conditions similar to those examined above for 3-oxo-C12-AHL and 3-oxo-C12-HS. For these experiments, we selected a concentration of 40 μg/mL, which is the concentration of rhamnolipid measured to be present in 24-hour (high population density, or "quorate") cultures of *P. aeruginosa.*[66]

Figure 6 shows a representative QCM-D trace (Figure 6A) and selected fluorescence microscopy images of DOPC SLBs exposed to a constant flow of rhamnolipid solution (Figure

6B-D) and a subsequent buffer wash (Figure 6E). Within the first minute of introducing rhamnolipid solution to the bilayer, we observed the formation of extended tubule structures, a small proportion of which collapsed into hemispherical caps over the subsequent six minutes of the experiment (Figure 6B-D). As the rhamnolipid solution was flowed across the surface of the bilayer, we observed some fluorescently labeled material and detached tubules moving across the field of view in the direction of flow, suggesting that rhamnolipid was also removing material from the bilayers, as was observed in analogous studies above for high concentration solutions of 3-oxo-C12-AHL. Characterization by QCM-D revealed positive changes in frequency (Δf) upon exposure of the SLB to rhamnolipid (3.3 ± 0 Hz) and after a subsequent wash of the bilayer with buffer (2.5 ± 0.2 Hz), with smaller changes in dissipation (ΔD) than those observed for 3-oxo-C12-AHL. The positive changes in frequency, consistent with a removal of mass from the bilayer, are consistent with the observation of the loss or removal of fluorescent material from the bilayer by fluorescence microscopy. Experiments using higher concentrations of rhamnolipid (e.g., 100 μg/mL and 200 μg/mL) led to the formation of tubules, but also to more extensive removal of material from the bilayer during exposure and the formation of patches that appeared darker by fluorescence microscopy (Figure S5 Panels D-E and I-J). This observation is consistent with the well-known surfactant properties of rhamnolipid and its ability to disrupt membranes, which is an important part of its biological function as a bacterial virulence factor.[67,68] However, as a result of this behavior, we were unable to draw meaningful quantitative conclusions from the results of our QCM-D experiments at these higher concentrations. We can conclude, however, that rhamnolipid is able to interact with lipid bilayers in ways that lead to similar morphological changes as those observed for AHLs (e.g., both promote reformation into tubules and a small number of caps). It is likely that AHL-induced reformations would occur simultaneously with those promoted by

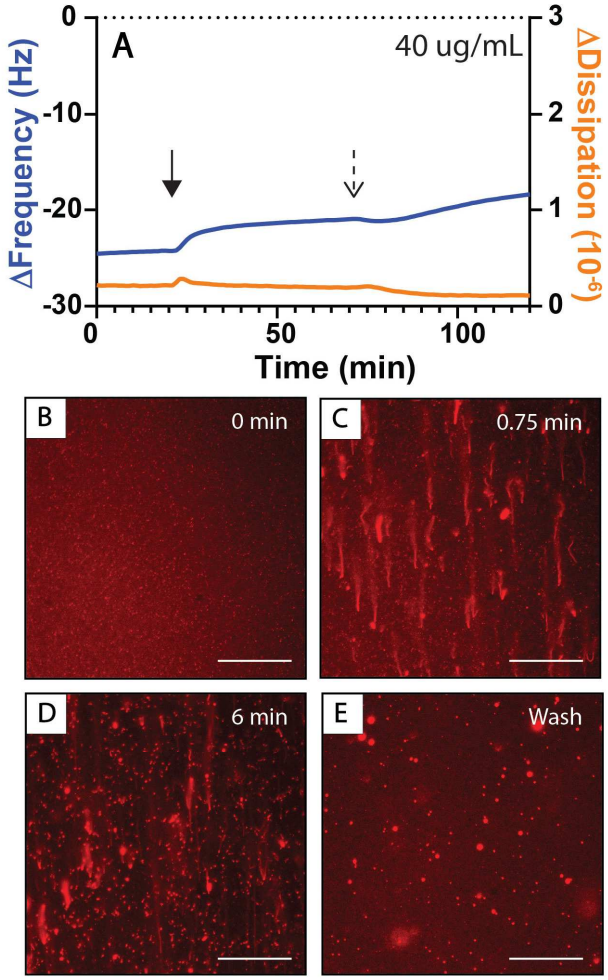
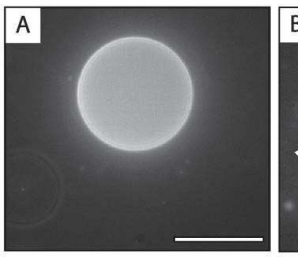


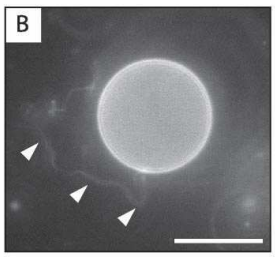
Figure 6: Measurements of membrane restructuring occurring in DOPC SLBs introduced to 40 µg/mL solutions of rhamnolipid. (A) QCM-D measurements of bilayer reformations initiated by the introduction of rhamnolipid solutions with changes in frequency (ΔFrequency, blue lines; referred to as Δf in the main text for brevity), and dissipation (ΔDissipation, orange lines; referred to as ΔD in the main text for brevity) shown are representative of three or four independent experiments. The initial measurement values (t=0 min) of these experiments correspond to a DOPC SLB on an SiO_2 surface. Rhamnolipid solutions were introduced to the bilayer at the time indicated by the solid arrow and the buffer was introduced at the time indicated by the dashed arrow. (B-E) fluorescence micrographs of bilayer restructuring occurring at (B) 0 sec, (C) 45 sec, and (D) 6 min after the first bilayer restructuring events had been observed or (E) after at least 8 minutes of washing the bilayer with buffer. The direction of flow in all images is from the bottom to the top of the image. Scale bars are 30 µm.

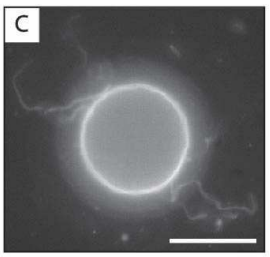
rhamnolipid, with more substantial disruption resulting from the strong surfactant behavior of rhamnolipid. (It is also possible that AHLs and rhamnolipid could act in concert or synergistically when both are present, but that possibility was not investigated or considered further here).

Bilayer Reformation in Unilamellar Vesicles: GUVs and Calcein Leakage

The SLBs used in the experiments above are a useful model and facilitate the characterization of interactions of surfactants with lipid bilayers using QCM-D and fluorescence microscopy on planar surfaces. We note, however, that SLBs are confined systems that are in close proximity to an underlying solid support. The membranes of biological systems and many other types of synthetic materials are, by contrast, free standing and can, therefore, exhibit behaviors that differ from those of SLBs. To confirm general observations made above using SLBs and provide additional insight into the interactions of 3-oxo-C12-AHL, 3-oxo-C12-HS, and rhamnolipid with unsupported lipid membranes, we also conducted experiments with giant unilamellar vesicles (GUVs) composed of DOPC (see Methods for additional details related to fabrication and characterization).[44] Figure 7 shows representative images of a GUV suspended in buffer alone (7A) and in contact with 100 μM 3-oxo-C12-AHL (7B) or 25 μg/mL rhamnolipid (7C). We observed that when either 3-oxo-C12-AHL or rhamnolipid was introduced to the GUVs, the vesicles formed long tubular structures protruding from the outer leaflet of the bilayer (as denoted by the arrowheads in panel 7B). It was more difficult to characterize these tubules because of the dynamic nature of this vesicle system, but these tubules were, in general, similar to those observed in our SLB experiments. Additionally, we note that we did not observe the formation of hemispherical caps in these GUV experiments, likely because free-standing (unsupported) vesicular systems such as GUVs have different mechanisms, relative to SLBs, by which they can







D

Condition	Percent Outer Tubulation
Buffer	4 ± 4%
3-oxo-C12-AHL (100 µM)	82 ± 7%
Rhamnolipid (25 µg/mL)	100 ± 0%

Figure 7: (A-C) Fluorescence microscopy images of DOPC GUVs (A) in buffer or (B,C) after being introduced to (B) 100 µM 3-oxo-C12-AHL or (C) 25 µg/mL rhamnolipid. The white arrowheads in (B) point to external tubules formed after incubation with 3-oxo-C12-AHL. (D) Percentage of vesicles observed to show signs of outer tubulation (see text) upon the addition of 3-oxo-C12-AHL, rhamnolipid, or buffer as a control. The value shown is the average and standard deviation of three (n=3) independent samples.

relieve asymmetrical bilayer stresses and the formation of hemispherical caps should not occur (and would, otherwise, be difficult to characterize) in these systems.[73] Overall, approximately 80% of the vesicles in contact with 3-oxo-C12-AHL formed tubules, as opposed to 100% in the rhamnolipid solution and approximately 5% in the buffer control (Figure 7D). These results provide insight into the interaction of these amphiphiles with unsupported lipid membranes that are a better approximation of a cell membrane (or a drug delivery vehicle, etc.) and suggest that the results observed in our SLB experiments are not artifacts arising from the surface supported nature of those bilayers or from defects that could be present in those systems.

We performed additional experiments with lipid vesicles to determine if the interactions with 3-oxo-C12-AHL and 3-oxo-C12-HS, and subsequent restructuring to form microtubules, could compromise membrane integrity in ways that could allow for leakage of vesicle contents or promote molecular transport across these membranes. To investigate this further, we used large unilamellar vesicles (LUVs) made of DOPC and loaded with the self-quenching fluorophore calcein, and a previously established calcein leakage assay (see Methods).[43,67] As a control

experiment, we first characterized the interaction of rhamnolipid, which is well known to disrupt and dissolve lipid vesicles, with calcein-loaded LUVs.[67] Upon addition of rhamnolipid-containing solution to LUVs, we observed an increase in the fluorescence of the solution at increasing rhamnolipid concentrations (Figure 8A), which is consistent with vesicle disruption and the release of encapsulated calcein. This is consistent with past studies and the well-known biosurfactant properties of rhamnolipid.[67]

As shown in Figure 8B, both 3-oxo-C12-AHL and 3-oxo-C12-HS also led to low but statistically significant levels of calcein leakage from DOPC vesicles at concentrations above 68 μM. 3-oxo-C12-AHL exhibited an approximately linear increase in the fluorescence signal with increasing concentration up to ~180 μM, the highest concentration tested here. In contrast, 3-oxo-C12-HS resulted in low levels (approximately 1.5% leakage) of calcein fluorescence at all concentrations above ~25 μM, a level that is statistically significant from the buffer controls. The difference in the extent of leakage shown in Figure 8 is consistent with the differences in bilayer reformation promoted in 3-oxo-C12-AHL and 3-oxo-C12-HS observed by fluorescence microscopy and QCM-D in SLBs. These compounds have different head groups, one of which is charged and one of which is neutral, which could lead to differences in their propensity to adsorb to, intercalate into or translocate across lipid membranes, and thus lead to differential changes in membrane structure or integrity.[16] This result is, to our knowledge, the first observation of the leakage of contents across a lipid membrane promoted by an AHL-type bacterial QS signal and could, with further study, provide insight into the previously unexplored biological roles of these compounds (e.g., as an independent virulence factor that is potentially capable of compromising host-cell membranes), or the ways in which they might interact with or trigger responses in synthetic lipid membranes (e.g., in the context of drug delivery or sensing, etc.). In the section

below, we describe the results of MD simulations that provide additional mechanistic insight into factors that govern the behaviors of these molecules at the surfaces of lipid membranes.

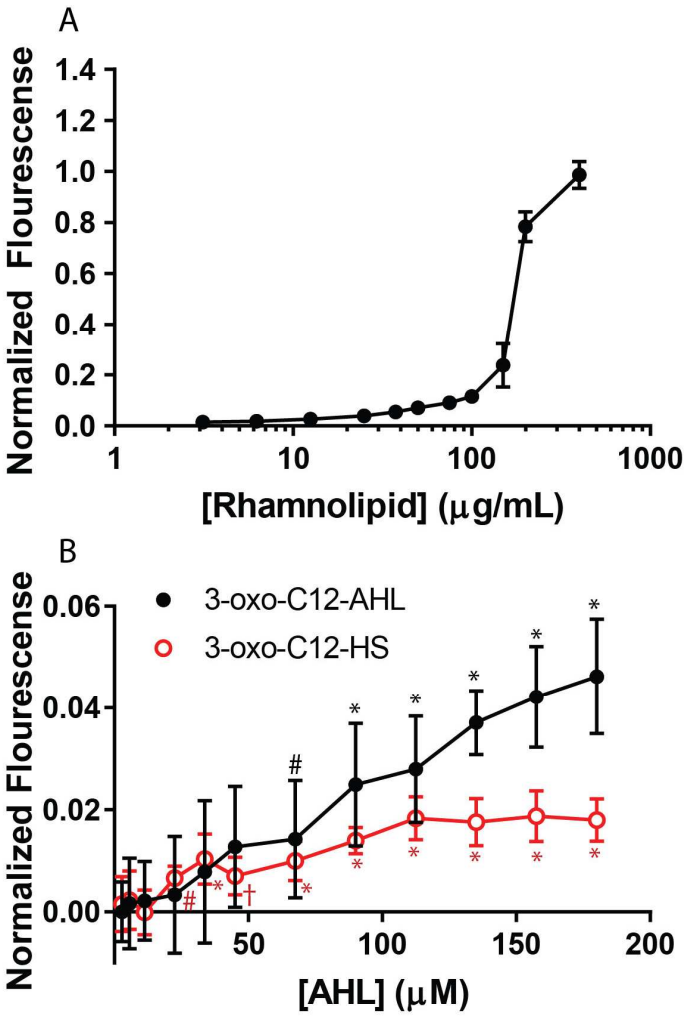


Figure 8: Normalized calcein fluorescence intensity values of (A) rhamnolipid and (B) 3-oxo-C12-AHL (black circles) and 3-oxo-C12-HS (red squares) at various concentrations interacting with 100 µM of calcein-loaded DOPC vesicles. Statistical significance compared to a buffer control is indicated for concentrations of 3-oxo-C12-AHL (black asterisks) and 3-oxo-C12-HS (red asterisks), with the following p values: $^{\#}p<0.05$, $^{\dagger}p<0.01$, $^{*}p<0.0001$. All points shown are the average and standard deviation of nine independent fluorescence measurements (see Materials and Methods). For the rhamnolipid measurements, some error bars are obscured by the size of the data point.

Molecular Dynamics Simulations of Amphiphile-Membrane Interactions

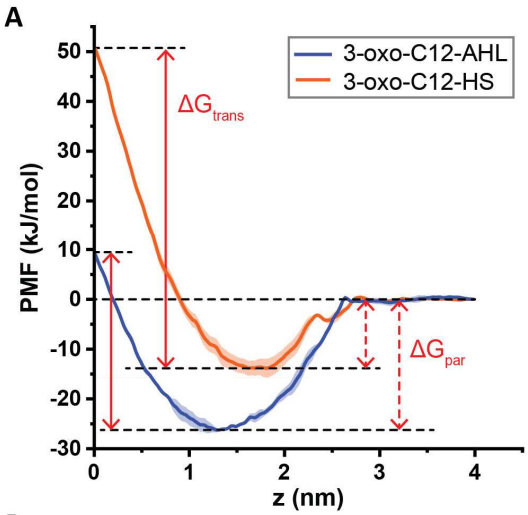
The studies above demonstrate that 3-oxo-C12-AHL and 3-oxo-C12-HS behave differently when in contact with lipid membranes. These differences are similar to those observed in past studies on the interactions of neutral and anionic surfactants in contact with SLBs.[37,60] For example, Cho and coworkers reported that the non-ionic surfactant glycerol monolaurate (GML) led to the formation of tubules that quickly collapsed into hemispherical caps when placed in contact with DOPC SLBs, and that the structurally similar anionic surfactant lauric acid (LA) led largely to the formation of tubules (that did not retract into hemispherical caps; structures of GML and LA shown in Figure S6).[37] In that study, the authors proposed that observed differences in bilayer reformation could arise from differences in the ability of GML and LA to translocate from the outer leaflet of a bilayer to the inner leaflet (e.g. by "flip-flop", or some similar mechanism) after adsorption, thus leading to asymmetric stresses that result in the formation of tubules or caps on the surface of the bilayer. To explore this proposal in further detail and provide insight into the thermodynamic barriers associated with the translocation of 3-oxo-C12-AHL and 3-oxo-C12-HS (and also GML and LA) across DOPC membranes, we performed a series of atomistic molecular dynamics (MD) simulations.

We first calculated the free energy profile for translocating 3-oxo-C12-AHL along the bilayer normal (z-direction) of a planar DOPC membrane using umbrella sampling, as shown in Figure 9A, and compared it to the free energy profile of 3-oxo-C12-HS. Snapshots from representative distances along the DOPC bilayer normal (z) are shown in Figure 9B. From these free energy profiles, we defined two free energy differences, the partition free energy (ΔG_{par}) and the translocation free energy (ΔG_{trans}), to compare the likelihood of each compound to intercalate into and translocate across the bilayer, respectively (Figure 9C).[74] ΔG_{par} is defined as the difference

in free energy between the PMF minimum and the reference state in solution (e.g., $z \geq -4$ nm). ΔG_{trans} is defined as the difference in free energy between the PMF maximum at the bilayer center and the PMF minimum.[74] In these contexts, a more negative value of ΔG_{par} indicates that it is favorable for a compound to partition into the lipid monolayer, and a more positive value of ΔG_{trans} indicates that it is less favorable for a surfactant to translocate across the lipid bilayer. ΔG_{par} (dashed arrows) and ΔG_{trans} (solid arrows) are visually defined in Figure 9A for 3-oxo-C12-AHL and 3-oxo-C12-HS.

As shown in Figure 9A and summarized in Figure 9C, our simulations predict that 3-oxo-C12-HS has a higher ΔG_{trans} than 3-oxo-C12-AHL (ΔG_{trans} = 67.59 kJ/mol and 35.57 kJ/mol, respectively) indicating that it is more difficult for the hydrolyzed 3-oxo-C12-HS to translocate across the lipid bilayer than it is for 3-oxo-C12-AHL. Our simulations also reveal that 3-oxo-C12-AHL has a more negative ΔG_{par} than 3-oxo-C12-HS, which indicates that 3-oxo-C12-AHL can partition itself into the bilayer more readily than the hydrolyzed compound, as expected in view of its non-ionic head group. This result is consistent with our surface tension and QCM-D measurements above, from which we found 3-oxo-C12-AHL to be more surface active and to a have more mass association with the bilayer than 3-oxo-C12-HS at a given concentration.

In addition to simulations of 3-oxo-C12-AHL and 3-oxo-C12-HS, we performed MD simulations of two representative 10-carbon tail rhamnolipids with one or two rhamnose sugars in the head group (Figures 9C and S7; rhamnolipid is relatively heterogeneous in nature, with the head group number (one or two) and lipid tail length varying with different bacterial growth conditions).[75] These simulations revealed that having two rhamnose units in the head group leads to a much more negative ΔG_{par} (-31.99 kJ/mol vs. -16.55 kJ/mol) and, therefore, is predicted to promote more favorable partitioning into the bilayer than rhamnolipid with a single sugar head



C

Molecule	ΔG_{par} (kJ/mol)	ΔG_{trans} (kJ/mol)
3-oxo-C12-AHL	-26.29 ± 0.32	35.57 ± 0.45
3-oxo-C12-HS	-13.87 ± 1.43	67.59 ± 4.15
rha-C10-C10	-16.55 ± 3.80	56.90 ± 4.53
rha-rha-C10-C10	-31.99 ± 0.15	62.68 ± 4.18
GML	-34.34 ± 0.96	22.70 ± 0.96
Lauric Acid	-21.71 ± 3.61	43.97 ± 4.77

Figure 9: Results of molecular dynamics simulations. (A) Potentials of mean force (PMFs) of 3-oxo-C12-AHL (blue) and 3-oxo-C12-HS (orange) as a function of the distance along the DOPC bilayer normal (z). The midplane of the membrane is at z = 0 nm and the PMF is set to zero at $z = 4$ nm. Each curve shows the average of two independent PMFs and error bars show the standard deviation. The plots also illustrate the definition of ΔG_{par} as the free energy difference between the PMF minimum and the value in solution and ΔG_{trans} as the free energy difference between the PMF minimum and maximum. (B) Snapshots showing configurations of AHLs and bilayers for different characteristic values of z in the PMF of 3-oxo-C12-AHL. A snapshot for z = 0 nm for 3-oxo-C12-HS is shown to highlight the local bilayer disruption that contributes to the larger value of ΔG_{trans}. Lipid head groups are yellow/orange, AHL heads are red, AHL tail groups are cyan, and water is drawn as red and white. Lipid tail groups are not shown for clarity. (C) Table showing ΔG_{par} and ΔG_{trans} values for all molecules simulated here.

group. However, the number of head group rhamnose units did not impact ΔG_{trans} significantly (62.68 kJ/mol vs. 56.90 kJ/mol). Finally, to permit comparisons and provide further insight into the interactions of LA and GML with DOPC SLBs, we calculated their PMFs along the bilayer normal, which revealed that nonionic GML has values of ΔG_{par} and ΔG_{trans} that are both lower than anionic LA (Figure 9C; Figure S7). These results suggest that GML should be more likely to interact with and translocate across the membrane, as previously predicted by Cho and coworkers.[37]

The relative magnitudes of ΔG_{par} and ΔG_{trans} calculated for the four single-tailed amphiphiles described above reveal the nonionic compounds 3-oxo-C12-AHL and GML to be more likely to intercalate into and translocate across DOPC membranes than the anionic compounds 3-oxo-C12-HS and LA. These differences in the propensity of a given amphiphile to partition itself into the bilayer correlate to the magnitude of response measured in the QCM-D experiments with 3-oxo-C12-AHL and 3-oxo-C12-HS in this study and with GML and LA in past studies.[37] Although it is not possible to explicitly compare the experimental QCM-D responses from these two different studies, we note that the relative magnitudes of the QCM-D response for these four compounds (GML > 3-oxo-C12-AHL > LA > 3-oxo-C12-HS) are generally in line with the predictions of our MD simulations (Figure 9C, Figure 5 and past work by Cho and coworkers[37]). Because ΔG_{par} describes an equilibrium between membrane-bound and solution-phase species, a more negative ΔG_{par} would suggest that a higher proportion of the molecules would associate with a bilayer at a given concentration. This higher degree of association would be subsequently reflected as a larger Δf, as more mass is associated to the surface of the bilayer, and lead to increased membrane restructuring, as measured by ΔD, due to increased lateral stresses in the bilayer, as discussed below.

Discussion of Potential Mechanisms for Bilayer Reformation

The combined results of our experimental and MD simulation studies provide support for the view that the differences in the restructuring of lipid bilayers observed here and in past studies[37] are driven by the differences in the ability of 3-oxo-C12-AHL and 3-oxo-C12-HS (or GML and LA) to translocate across the bilayer. The non-ionic amphiphiles 3-oxo-C12-AHL and GML, which predominantly lead to the formation of hemispherical caps in fluorescence microscopy experiments, have lower predicted barriers to translocation than the anionic compounds 3-oxo-C12-HS and LA, which lead to the formation of predominantly extended tubule structures. Overall, these results are consistent with a physical picture in which bilayer remodeling is driven by changes or differences in asymmetric stresses that develop between the outer and inner leaflets of a bilayer upon intercalation and/or translocation of an amphiphile.[7,16]

When an amphiphile inserts into the outer leaflet of a bilayer, it imparts an asymmetric, lateral stress on that leaflet that is not immediately matched by the inner leaflet. If the area of a bilayer is fixed, as would be the case in our SLB experiments or in a vesicle of fixed volume, a molecule that has a high barrier to translocation (or "flip-flop"), would continue to accumulate in the outer leaflet and continue to increase asymmetrical stress, driving the formation of regions of high curvature (such as tubules).[7] For amphiphiles with low translocation barriers, asymmetrical stress would be expected to be relieved rapidly by flip-flop, leading to the formation of lower curvature structures (such as hemispherical caps) as a means of relieving symmetric bilayer stresses.[7] For amphiphiles with intermediate barriers to translocation, this framework would predict the initial formation of high-curvature tubules that would, over time, transition to lower curvature structures such as hemispherical caps as translocation across the bilayer occurs and initial asymmetric stresses are relieved.[7,16] In line with these predictions, amphiphiles with high

predicted barriers to translation (3-oxo-C12-HS, rhamnolipid, and LA) generally lead to the formation of tubules that persist over the time course of fluorescence microscopy experiments, and amphiphiles with lower barriers to translocation (3-oxo-C12-AHL and GML) are observed to initially form tubules that transition to become hemispherical caps, suggesting that these two nonionic amphiphiles are able to translocate to inner leaflets on the timescales of these experiments.

The results above do not rule out other contributions to the reformation of these bilayers, including potential impacts that head group structure could have on spontaneous curvature and the formation of surfactant rich domains that could also lead to the formation of tubules and hemispherical caps.[76] However, the experiments in which we observed reversibility of amphiphile-induced reformation upon washing with buffer (see Figure S4 and discussion above) provide further support to the proposal that asymmetrical stresses between bilayer leaflets lead to the observed differences in bilayer reformation (Figure S3; past work by Cho and coworkers[37]). Here we assume that washing the bilayer with buffer and removing amphiphiles from solution can lead to an environment in which desorption of amphiphile from the outer leaflet of a bilayer can occur readily. In the case where an amphiphile is slow to translocate to the inner leaflet (e.g., 3-oxo-C12-HS, rhamnolipid, and LA), as the bilayer is washed and the amphiphile desorbs from the bilayer into solution, it subsequently relieves the asymmetrical stress present in the outer leaflet, promoting a transition from high curvature structures (e.g., tubules) to low curvature structures (e.g., hemispherical caps) and ultimately, in the limit of complete amphiphile desorption, to a flat bilayer. The shrinking and disappearance of tubules and caps was observed experimentally when SLBs that had been introduced to 3-oxo-C12-HS, rhamnolipid, and LA, were subsequently washed with buffer (Figure S3; see also past work by Cho and coworkers[37]). Alternatively, for amphiphiles

with low thermodynamic barriers to translocation (e.g., 3-oxo-C12-AHL and GML) that can flip-flop readily, amphiphiles in the inner leaflet can translocate back to the outer leaflet (e.g., as desorption from the outer leaflet occurs) to equilibrate stresses in the bilayer and eventually themselves desorb from the bilayer leading, ultimately, to a flat bilayer. In our experiments, we frequently observed the shrinking and, in some cases, the disappearance of hemispherical caps in bilayers that had been treated with 3-oxo-C12-AHL (and similar behavior was previously reported for GML[37]) upon washing with buffer.

Overall, the trends in amphiphile induced reformation observed experimentally here are strongly correlated to the thermodynamic barrier of the interacting amphiphile to translocation across the membrane and, thus, can be described by differences in asymmetric stresses that are likely to be present in the bilayers. In addition to providing insight into fundamental interactions of these natural nonionic and anionic amphiphiles with lipid membranes, our results also hint at experimental frameworks that could be used to characterize the timescales on which amphiphiles may translocate (e.g., by characterizing processes associated with the dynamics involved in the formation and deformation of tubules and hemispherical caps). Finally, the differences in membrane response characterized here could potentially be tuned or exploited to design self-assembled systems that respond selectively, and with a desired mode of membrane restructuring, to these or other specific classes of bacterial amphiphiles, providing new avenues for the design of sensing platforms with more selective responses or drug delivery vehicles that respond specifically to communities of bacteria that produce that amphiphile.

Characterization of Bilayer Remodeling Mediated by Mixtures of Amphiphiles Produced by Communities of Bacteria

We return now to a discussion of the results shown in Figure 2, which demonstrate that supernatants obtained from 24-hour cultures of *P. aeruginosa* can promote large-scale reformations in SLBs. The results above show that 3-oxo-C12-AHL, 3-oxo-C12-HS and rhamnolipid can each, individually, interact with lipid membranes and promote large-scale reformation. At 24 hours, cultures of *P. aeruginosa* should contain all three of these amphiphiles. We conducted additional experiments using SLBs and cell-free supernatants obtained from 6-hour cultures of *P. aeruginosa* that have been measured to contain approximately 10 μM 3-oxo-C12-AHL (and thus likely some low concentration of 3-oxo-C12-HS) and either no or low (< 5 μg/mL) concentrations of rhamnolipid.[66] As shown in Figure 10(A-C), these supernatants did not result in large-scale reformations similar to those observed the studies above by fluorescence microscopy. We did occasionally observe the formation of hemispherical caps (e.g., Figure 10C), but these features were relatively rare under the conditions and with the methods used here.

We note that the ~10 μM concentration of 3-oxo-C12-AHL in these supernatants is substantially lower than the concentrations of 3-oxo-C12-AHL used in the systematic studies above (Figure 4; 30 μM). We therefore conducted additional experiments using 24-hour supernatants of a mutant strain of *P. aeruginosa* (ΔrhlA) that is unable to produce rhamnolipid or its amphiphilic precursors under any conditions, even at high population densities, yet still produces 3-oxo-C12-AHL at native levels.[40,77] The results of that experiment are shown in Figure 10(D-F) and reveal the formation of tubules on the surface of the bilayer, a small proportion of which collapsed into hemispherical caps. This result likely arises from higher concentrations of 3-oxo-C12-AHL and its hydrolysis product 3-oxo-C12-HS in solution after 24 hours of bacterial

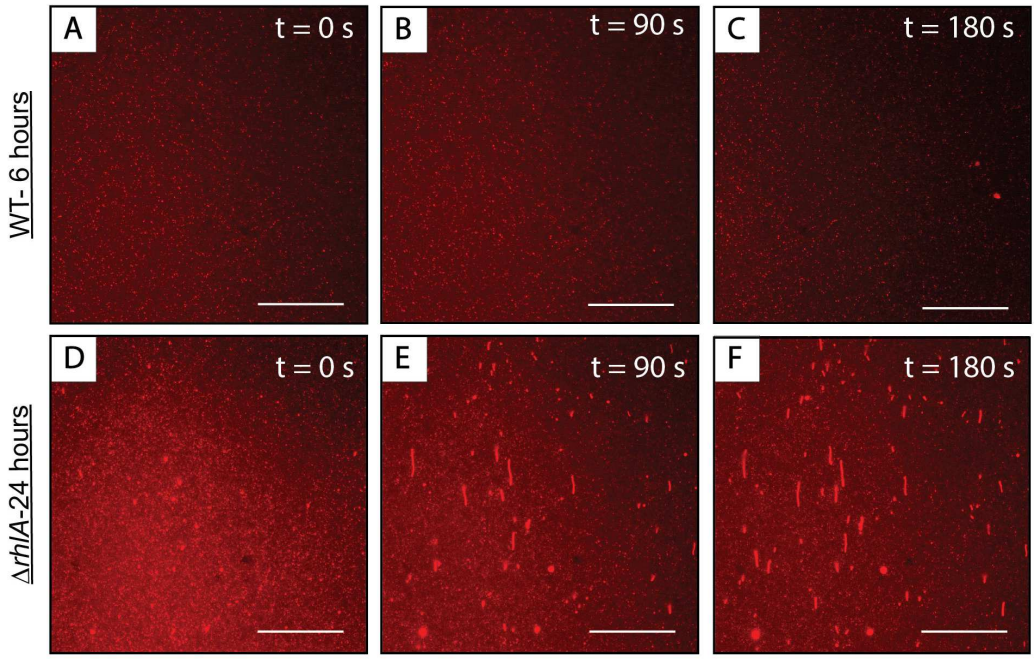


Figure 10: Representative top-down fluorescence micrographs of structural reformations occurring in fluorescently labeled DOPC SLBs after the introduction of cell-free supernatants of (A-C) wild type *P. aeruginosa* cultures grown for 6 hours or (D-F) mutant strain Δ*rhlA P. aeruginosa* cultures grown for 24 hours. The micrographs were acquired at (A, D) 0 seconds, (B, E) 90 seconds, and (C, F) 180 seconds after the first membrane reformations were observed on the surface of the bilayer. The direction of flow in all the images is from the bottom to the top of the screen. Scale bars are 30 μm.

growth. We consider it likely that 3-oxo-C12-AHL and 3-oxo-C12-HS could act in concert to promote bilayer remodeling. Further support for this is provided by experiments demonstrating that defined mixtures of these two amphiphiles can lead to membrane reformations in SLBs (see Figure S9; these results at least suggest that combinations of 3-oxo-C12-AHL and 3-oxo-C12-HS do not prevent bilayer reformation). In any case, the results of experiments with this mutant bacterial strain demonstrate that the production of 3-oxo-C12-AHL by bacteria can promote membrane remodeling in the absence of rhamnolipid. In a broader context, we note that 3-oxo-C12-HS is generally considered to be biologically inactive as a mediator of QS.[78] Our results

reported above (Figures 4, 5, 8) suggest that this hydrolyzed product, which can accumulate in bacterial cultures over time, could play other important roles in communities of bacteria.

The prospect that 3-oxo-C12-AHL and/or 3-oxo-C12-HS alone could promote membrane remodeling leads to intriguing questions and hypotheses about ways in which communities of bacteria may interact with each other, or with other species of bacteria at either low or high population densities. These results could also shed light on ways in which bacteria and communities of bacteria interact with host cells and provide potential guidance for the design and understanding of interactions of bacterial communities with synthetic materials (e.g., lipid-based materials for sensing and responsive drug delivery). Finally, we note that not all bacteria that produce 3-oxo-C12-AHL as their QS signal also produce biosurfactants such as rhamnolipid.[67,77] Our results therefore may also provide insight on how these bacterial species interact with their environment in the absence of biosurfactants or virulence factors that can otherwise interact with and disrupt lipid membranes.

Summary and Conclusions

The work reported here demonstrates that the bacterial QS signaling molecule 3-oxo-C12-AHL and its hydrolysis product 3-oxo-C12-HS can interact with model lipid membranes and promote large-scale membrane remodeling, including the formation of tubules and/or hemispherical caps. Our results obtained using fluorescence microscopy and QCM-D demonstrate that these processes are dynamic and reversible, and that they occur both in SLBs and unsupported lipid membranes (e.g., vesicles). Rhamnolipid, a virulence factor produced by *P. aeruginosa* under the control of QS, also promotes similar bilayer reformation but also leads to more substantial disruption and dissolution of bilayers, consistent with the well characterized biosurfactancy of this

amphiphile. Additional experiments using a vesicle-based dye leakage assay demonstrated that 3-oxo-C12-AHL and 3-oxo-C12-HS can also facilitate molecular transport across bilayers. MD simulations predict differences in the thermodynamic barriers to translocation of these amphiphiles across the bilayer in ways that are reflected in differences in type and extent of reformation and associated dynamics that are observed experimentally. These differences can be interpreted in terms of an accumulation and relief of asymmetric stresses in the inner and outer leaflets of a bilayer upon the intercalation and translocation of an amphiphile in ways that are similar to past experiments using other natural and synthetic amphiphiles. Finally, our results demonstrate that cultures of bacteria that produce 3-oxo-C12-AHL can promote membrane remodeling in SLBs in the absence of other biosurfactants such as rhamnolipid. Overall, our results suggest potential roles for 3-oxo-C12-AHL and its hydrolysis product that move beyond the context of assessing "self" population density to potential mechanisms for interspecies interactions and control of host cell response. More broadly, the results of these studies with model lipid membranes provide guidance that could be helpful for understanding the range of interactions between bacterial communities and synthetic self-assembled materials (e.g., SLBs and lipid vesicles) commonly used to design environmental sensors and drug delivery vehicles, and in other fundamental and applied contexts. Studies investigating the interactions of structurally diverse, naturally occurring AHLs with model SLBs of increasing complexity are currently underway and will be reported in due course.

Acknowledgements. Financial support for this work was provided by the NSF through a grant provided to the UW-Madison Materials Research Science and Engineering Center (MRSEC; DMR-1720415). S. J. P. and R. C. V. acknowledge support from the NSF (MCB-1817292). H. E. B. and D. E. M. acknowledge support from the NIH (R35 GM131817). C. G. G. was supported in

part by a NSF Graduate Research Fellowship. L. M. C. was supported in part by the UW-Madison NIH Chemistry-Biology Interface Training Program (T32 GM008505). The authors acknowledge the use of instrumentation supported by the NSF through the UW MRSEC (DMR-1720415) and the Extreme Science and Engineering Discovery Environment (XSEDE; ACI-1548562). NMR characterization was performed in facilities in the Department of Chemistry at UW-Madison that are supported by the NSF (CHE-0342998). The authors gratefully acknowledge Prof. Nicholas Abbott (Cornell) and Prof. Joel Pedersen (UW-Madison) for many helpful discussions. We thank Dr. Timothy Smith and Dr. Isabel Foreman-Ortiz for assistance with QCM-D training and for valuable discussions, Christopher Eom and Dr. M. R. Lee for assistance with NMR quantification experiments, and Thomas Polaske for assistance with bacterial cell culture.

References

1. Mura, S.; Nicolas, J.; Couvreur, P. Stimuli-Responsive Nanocarriers for Drug Delivery. *Nat. Mater.* **2013,** *12*, 991-1003.

2. Paliwal, S. R.; Paliwal, R.; Vyas, S. P. A Review of Mechanistic Insight and Application of pH-Sensitive Liposomes in Drug Delivery. *Drug Delivery* **2015,** *22*, 231-242.

3. Carrion, F. J.; Delamaza, A.; Parra, J. L. The Influence of Ionic-Strength and Lipid Bilayer Charge on the Stability of Liposomes. *J. Colloid Interface Sci.* **1994,** *164*, 78-87.

4. Garcia-Manyes, S.; Oncins, G.; Sanz, F. Effect of pH and Ionic Strength on Phospholipid Nanomechanics and on Deposition Process onto Hydrophilic Surfaces Measured by AFM. *Electrochim. Acta* **2006,** *51*, 5029-5036.

5. Cullis, P. R.; de Kruijff, B. Lipid Polymorphism and the Functional Roles of Lipids in Biological Membranes. *Biochim. Biophys. Acta* **1979,** *559*, 399-420.

6. Frolov, V. A.; Shnyrova, A. V.; Zimmerberg, J. Lipid Polymorphisms and Membrane Shape. *Cold Spring Harbor Perspect. Biol.* **2011,** *3*, a004747.

7. Staykova, M.; Arroyo, M.; Rahimi, M.; Stone, H. A. Confined Bilayers Passively Regulate Shape and Stress. *Phys. Rev. Lett.* **2013,** *110*, 028101.

8. Koynova, R.; Caffrey, M. Phases and Phase Transitions of the Phosphatidylcholines. *Biochim. Biophys. Acta, Rev. Biomembr.* **1998,** *1376*, 91-145.

9. Gozen, I.; Dommersnes, P. Pore Dynamics in Lipid Membranes. *Eur. Phys. J.: Spec. Top.* **2014,** *223*, 1813-1829.

10. Shinoda, W. Permeability Across Lipid Membranes. *Biochim. Biophys. Acta* **2016,** *1858*, 2254-2265.

11. Torchilin, V. P. Recent Advances with Liposomes as Pharmaceutical Carriers. *Nat. Rev. Drug Discovery* **2005,** *4*, 145-160.

12. Peer, D.; Karp, J. M.; Hong, S.; FaroKhzad, O. C.; Margalit, R.; Langer, R. Nanocarriers as an Emerging Platform for Cancer Therapy. *Nat. Nanotechnol.* **2007,** *2*, 751-760.

13. Liu, Q. T.; Boyd, B. J. Liposomes in Biosensors. *Analyst* **2013,** *138*, 391-409.

14. Tang, C. Y.; Zhao, Y.; Wang, R.; Helix-Nielsen, C.; Fane, A. G. Desalination by Biomimetic Aquaporin Membranes: Review of Status and Prospects. *Desalination* **2013,** *308*, 34-40.

15. Jones, M. N. Surfactant Interactions with Biomembranes and Proteins. *Chem. Soc. Rev.* **1992,** *21*, 127-136.

16. Heerklotz, H. Interactions of Surfactants with Lipid Membranes. *Q. Rev. Biophys.* **2008,** *41*, 205-264.

17. Miller, M. B.; Bassler, B. L. Quorum Sensing in Bacteria. *Annu. Rev. Microbiol.* **2001,** *55*, 165-199.

18. Waters, C. M.; Bassler, B. L. Quorum Sensing: Cell-to-Cell Communication in Bacteria. *Annu. Rev. Cell Dev. Biol.* **2005,** *21*, 319-346.

19. Welch, M.; Mikkelsen, H.; Swatton, J. E.; Smith, D.; Thomas, G. L.; Glansdorp, F. G.; Spring, D. R. Cell-Cell Communication in Gram-Negative Bacteria. *Mol. Biosyst.* **2005,** *1*, 196-202.

20. Daniels, R.; Vanderleyden, J.; Michiels, J. Quorum Sensing and Swarming Migration in Bacteria. *FEMS Microbiol. Rev.* **2004,** *28*, 261-289.

21. Davies, D. G.; Parsek, M. R.; Pearson, J. P.; Iglewski, B. H.; Costerton, J. W.; Greenberg, E. P. The Involvement of Cell-to-Cell Signals in the Development of a Bacterial Biofilm. *Science* **1998,** *280*, 295-298.

22. de Kievit, T. R. Quorum Sensing in *Pseudomonas aeruginosa* Biofilms. *Environ. Microbiol.* **2009,** *11*, 279-288.

23. Reis, R. S.; Pereira, A. G.; Neves, B. C.; Freire, D. M. G. Gene Regulation of Rhamnolipid Production in *Pseudomonas aeruginosa* - A Review. *Bioresour. Technol.* **2011,** *102*, 6377-6384.

24. Daniels, R.; Reynaert, S.; Hoekstra, H.; Verreth, C.; Janssens, J.; Braeken, K.; Fauvart, M.; Beullens, S.; Heusdens, C.; Lambrichts, I.; De Vos, D. E.; Vanderleyden, J.; Vermant, J.; Michiels, J. Quorum Signal Molecules as Biosurfactants Affecting Swarming in *Rhizobium etli*. *Proc. Natl. Acad. Sci. U. S. A.* **2006,** *103*, 14965-14970.

25. Davis, B. M.; Richens, J. L.; O'Shea, P. Label-Free Critical Micelle Concentration Determination of Bacterial Quorum Sensing Molecules. *Biophys. J.* **2011,** *101*, 245-254.

26. Gahan, C. G.; Patel, S. J.; Boursier, M. E.; Nyffeler, K. E.; Jennings, J.; Abbott, N. L.; Blackwell, H. E.; Van Lehn, R. C.; Lynn, D. M. Bacterial Quorum Sensing Signals Self-Assemble in Aqueous Media to Form Micelles and Vesicles: An Integrated Experimental and Molecular Dynamics Study. *J. Phys. Chem. B* **2020,** *124*, 3616-3628.

27. Jakubczyk, D.; Barth, C.; Kubas, A.; Anastassacos, F.; Koelsch, P.; Fink, K.; Schepers, U.; Brenner-Weiss, G.; Brase, S. Deuterium-Labelled N-Acyl-L-Homoserine Lactones (AHLs)-Inter-Kingdom Signalling Molecules-Synthesis, Structural Studies, and Interactions with Model Lipid Membranes. *Anal. Bioanal. Chem.* **2012,** *403*, 473-482.

28. Barth, C.; Jakubczyk, D.; Kubas, A.; Anastassacos, F.; Brenner-Weiss, G.; Fink, K.; Schepers, U.; Brase, S.; Koelsch, P. Interkingdom Signaling: Integration, Conformation, and Orientation of N-Acyl-L-Homoserine Lactones in Supported Lipid Bilayers. *Langmuir* **2012,** *28*, 8456-8462.

29. Toyofuku, M.; Morinaga, K.; Hashimoto, Y.; Uhl, J.; Shimamura, H.; Inaba, H.; Schmitt-Kopplin, P.; Eberl, L.; Nomura, N. Membrane Vesicle-Mediated Bacterial Communication. *ISME J.* **2017,** *11*, 1504-1509.

30. Davis, B. M.; Jensen, R.; Williams, P.; O'Shea, P. The Interaction of N-Acylhomoserine Lactone Quorum Sensing Signaling Molecules with Biological Membranes: Implications for Inter-Kingdom Signaling. *PLoS One* **2010,** *5*, e13522.

31. Song, D. K.; Meng, J. C.; Cheng, J.; Fan, Z.; Chen, P. Y.; Ruan, H. F.; Tu, Z. Y.; Kang, N.; Li, N.; Xu, Y.; Wang, X. B.; Shi, F.; Mu, L. B.; Li, T. F.; Ren, W. R.; Lin, X.; Zhu, J.; Fang, X. H.; Amrein, M. W.; Wu, W. H.; Yan, L. T.; Lu, J. H.; Xia, T.; Shi, Y. *Pseudomonas aeruginosa* Quorum-Sensing Metabolite Induces Host Immune Cell Death through Cell Surface Lipid Domain Dissolution. *Nat. Microbiol* **2019,** *4*, 97-111.

32. Lentini, R.; Martin, N. Y.; Forlin, M.; Belmonte, L.; Fontana, J.; Cornella, M.; Martini, L.; Tamburini, S.; Bentley, W. E.; Jousson, O.; Mansy, S. S. Two-Way Chemical Communication between Artificial and Natural Cells. *ACS Cent. Sci.* **2017,** *3*, 117-123.

33. Hughes, D. T.; Sperandio, V. Inter-Kingdom Signalling: Communication Between Bacteria and Their Hosts. *Nat. Rev. Microbiol.* **2008,** *6*, 111-120.

34. Kravchenko, V. V.; Kaufmann, G. F.; Mathison, J. C.; Scott, D. A.; Katz, A. Z.; Grauer, D. C.; Lehmann, M.; Meijler, M. M.; Janda, K. D.; Ulevitch, R. J. Modulation of Gene Expression via Disruption of NF-Kappa B Signaling by a Bacterial Small Molecule. *Science* **2008,** *321*, 259-263.

35. Zhou, J.; Loftus, A. L.; Mulley, G.; Jenkins, A. T. A. A Thin Film Detection/Response System for Pathogenic Bacteria. *J. Am. Chem. Soc.* **2010,** *132*, 6566-6570.

36. Yates, E. A.; Philipp, B.; Buckley, C.; Atkinson, S.; Chhabra, S. R.; Sockett, R. E.; Goldner, M.; Dessaux, Y.; Camara, M.; Smith, H.; Williams, P. N-Acylhomoserine Lactones Undergo Lactonolysis in a pH-, Temperature-, and Acyl Chain Length-Dependent Manner During Growth of *Yersinia pseudotuberculosis* and *Pseudomonas aeruginosa*. *Infect. Immun.* **2002,** *70*, 5635-5646.

37. Yoon, B. K.; Jackman, J. A.; Kim, M. C.; Cho, N. J. Spectrum of Membrane Morphological Responses to Antibacterial Fatty Acids and Related Surfactants. *Langmuir* **2015,** *31*, 10223-10232.

38. Hodgkinson, J. T.; Galloway, W.; Casoli, M.; Keane, H.; Su, X. B.; Salmond, G. P. C.; Welch, M.; Spring, D. R. Robust Routes for the Synthesis of N-Acylated-L-Homoserine Lactone (AHL) Quorum Sensing Molecules with High Levels of Enantiomeric Purity. *Tetrahedron Lett.* **2011,** *52*, 3291-3294.

39. Holloway, B. W. Genetic Recombination in *Pseudomonas aeruginosa*. *J. Gen. Microbiol.* **1955,** *13*, 572-581.

40. Jacobs, M. A.; Alwood, A.; Thaipisuttikul, I.; Spencer, D.; Haugen, E.; Ernst, S.; Will, O.; Kaul, R.; Raymond, C.; Levy, R.; Liu, C. R.; Guenthner, D.; Bovee, D.; Olson, M. V.; Manoil, C. Comprehensive Transposon Mutant Library of *Pseudomonas aeruginosa*. *Proc. Natl. Acad. Sci. U. S. A.* **2003,** *100*, 14339-14344.

41. Mayer, L. D.; Hope, M. J.; Cullis, P. R. Vesicles of Variable Sizes Produced by a Rapid Extrusion Procedure. *Biochim. Biophys. Acta* **1986,** *858*, 161-168.

42. Lapinski, M. M.; Castro-Forero, A.; Greiner, A. J.; Ofoli, R. Y.; Blanchard, G. J. Comparison of Liposomes Formed by Sonication and Extrusion: Rotational and Translational Diffusion of an Embedded Chromophore. *Langmuir* **2007,** *23*, 11677-11683.

43. Lee, M. R.; Raman, N.; Ortiz-Bermudez, P.; Lynn, D. M.; Palecek, S. P. 14-Helical Beta-Peptides Elicit Toxicity against *C. albicans* by Forming Pores in the Cell Membrane and Subsequently Disrupting Intracellular Organelles. *Cell Chem. Biol.* **2019,** *26*, 289-299.

44. Moga, A.; Yandrapalli, N.; Dimova, R.; Robinson, T. Optimization of the Inverted Emulsion Method for High-Yield Production of Biomimetic Giant Unilamellar Vesicles. *ChemBioChem* **2019,** *20*, 2674-2682.

45. Cremer, P. S.; Boxer, S. G. Formation and Spreading of Lipid Bilayers on Planar Glass Supports. *J. Phys. Chem. B* **1999,** *103*, 2554-2559.

46. Kolahdouzan, K.; Jackman, J. A.; Yoon, B. K.; Kim, M. C.; Johal, M. S.; Cho, N. J. Optimizing the Formation of Supported Lipid Bilayers from Bicellar Mixtures. *Langmuir* **2017,** *33*, 5052-5064.

47. Smith, T. J.; Wang, C. X.; Abbott, N. L. Redox-Triggered Mixing and Demixing of Surfactants within Assemblies Formed in Solution and at Surfaces. *J. Colloid Interface Sci.* **2017,** *502*, 122-133.

48. Lichtenberg, D.; Ahyayauch, H.; Alonso, A.; Goni, F. M. Detergent Solubilization of Lipid Bilayers: A Balance of Driving Forces. *Trends Biochem. Sci.* **2013,** *38*, 85-93.

49. Roux, B. The Calculation of the Potential of Mean Force Using Computer-Simulations. *Comput Phys Commun* **1995,** *91*, 275-282.

50. Best, R. B.; Zhu, X.; Shim, J.; Lopes, P. E. M.; Mittal, J.; Feig, M.; MacKerell, A. D. Optimization of the Additive Charmm All-Atom Protein Force Field Targeting Improved Sampling of the Backbone Phi, Psi and Side-Chain Chi(1) and Chi(2) Dihedral Angles. *J Chem Theory Comput* **2012,** *8*, 3257-3273.

51. Jo, S.; Kim, T.; Iyer, V. G.; Im, W. Charmm-Gui: A Web-Based Graphical User Interface for CHARMM. *J. Comput. Chem.* **2008,** *29*, 1859-1865.

52. Kim, S.; Lee, J.; Jo, S.; Brooks, C. L.; Lee, H. S.; Im, W. Charmm-Gui Ligand Reader and Modeler for CHARMM Force Field Generation of Small Molecules. *J. Comput. Chem.* **2017,** *38*, 1879-1886.

53. Pronk, S.; Pall, S.; Schulz, R.; Larsson, P.; Bjelkmar, P.; Apostolov, R.; Shirts, M. R.; Smith, J. C.; Kasson, P. M.; van der Spoel, D.; Hess, B.; Lindahl, E. Gromacs 4.5: A High-Throughput and Highly Parallel Open Source Molecular Simulation Toolkit. *Bioinformatics* **2013,** *29*, 845-854.

54. Hub, J. S.; de Groot, B. L.; van der Spoel, D. G. Wham- A Free Weighted Histogram Analysis Implementation Including Robust Error and Autocorrelation Estimates. *J Chem Theory Comput* **2010,** *6*, 3713-3720.

55. Rumbaugh, K. P.; Griswold, J. A.; Hamood, A. N. The Role of Quorum Sensing in the *in vivo* Virulence of *Pseudomonas aeruginosa*. *Microbes Infect.* **2000,** *2*, 1721-1731.

56. Gooderham, W. J.; Hancock, R. E. W. Regulation of Virulence and Antibiotic Resistance by Two-Component Regulatory Systems in *Pseudomonas aeruginosa*. *FEMS Microbiol. Rev.* **2009,** *33*, 279-294.

57. Coggan, K. A.; Wolfgang, M. C. Global Regulatory Pathways and Cross-Talk Control *Pseudomonas aeruginosa* Environmental Lifestyle and Virulence Phenotype. *Curr. Issues Mol. Biol.* **2012,** *14*, 47-69.

58. Crone, S.; Vives-Florez, M.; Kvich, L.; Saunders, A. M.; Malone, M.; Nicolaisen, M. H.; Martinez-Garcia, E.; Rojas-Acosta, C.; Gomez-Puerto, M. C.; Calum, H.; Whiteley, M.; Kolter, R.; Bjarnsholt, T. The Environmental Occurrence of *Pseudomonas aeruginosa*. *APMIS* **2020,** *128*, 220-231.

59. Reviakine, I.; Johannsmann, D.; Richter, R. P. Hearing What You Cannot See and Visualizing What You Hear: Interpreting Quartz Crystal Microbalance Data from Solvated Interfaces. *Anal. Chem.* **2011,** *83*, 8838-8848.

60. Thid, D.; Benkoski, J. J.; Svedhem, S.; Kasemo, B.; Gold, J. Dha-Induced Changes of Supported Lipid Membrane Morphology. *Langmuir* **2007,** *23*, 5878-5881.

61. Tabaei, S. R.; Choi, J. H.; Zan, G. H.; Zhdanov, V. P.; Cho, N. J. Solvent-Assisted Lipid Bilayer Formation on Silicon Dioxide and Gold. *Langmuir* **2014,** *30*, 10363-10373.

62. Ulrich, A. S.; Sami, M.; Watts, A. Hydration of DOPC Bilayers by Differential Scanning Calorimetry. *Biochim. Biophys. Acta-Biomembr.* **1994,** *1191*, 225-230.

63. Yoon, B. K.; Jackman, J. A.; Kim, M. C.; Sut, T. N.; Cho, N. J. Correlating Membrane Morphological Responses with Micellar Aggregation Behavior of Capric Acid and Monocaprin. *Langmuir* **2017,** *33*, 2750-2759.

64. Yoon, B. K.; Jackman, J. A.; Park, S.; Mokrzecka, N.; Cho, N. J. Characterizing the Membrane-Disruptive Behavior of Dodecylglycerol Using Supported Lipid Bilayers. *Langmuir* **2019,** *35*, 3568-3575.

65. Yoon, B. K.; Park, S.; Jackman, J. A.; Cho, N. J. Supported Lipid Bilayer Platform for Characterizing the Optimization of Mixed Nano-Micelles. *Appl. Mater. Today* **2020,** *19*, 100598.

66. Ortiz, B. J.; Boursier, M. E.; Barrett, K. L.; Manson, D. E.; Amador-Noguez, D.; Abbott, N. L.; Blackwell, H. E.; Lynn, D. M. Liquid Crystal Emulsions That Intercept and Report on Bacterial Quorum Sensing. *ACS Appl. Mater. Interfaces* **2020,** *12*, 29056-29065.

67. Laabei, M.; Jamieson, W. D.; Lewis, S. E.; Diggle, S. P.; Jenkins, A. T. A. A New Assay for Rhamnolipid Detection-Important Virulence Factors of *Pseudomonas aeruginosa*. *Appl. Microbiol. Biotechnol.* **2014,** *98*, 7199-7209.

68. Come, B.; Donato, M.; Potenza, L. F.; Mariani, P.; Itri, R.; Spinozzi, F. The Intriguing Role of Rhamnolipids on Plasma Membrane Remodelling: From Lipid Rafts to Membrane Budding. *J. Colloid Interface Sci.* **2021,** *582*, 669-677.

69. Glansdorp, F. G.; Thomas, G. L.; Lee, J. J. K.; Dutton, J. M.; Salmond, G. P. C.; Welch, M.; Spring, D. R. Synthesis and Stability of Small Molecule Probes for *Pseudomonas aeruginosa* Quorum Sensing Modulation. *Org. Biomol. Chem.* **2004,** *2*, 3329-3336.

70. Boursier, M. E.; Combs, J. B.; Blackwell, H. E. N-Acyl L-Homocysteine Thiolactones Are Potent and Stable Synthetic Modulators of the Rhlr Quorum Sensing Receptor in *Pseudomonas aeruginosa*. *ACS Chemical Biology* **2019,** *14*, 186-191.

71. Charlton, T. S.; de Nys, R.; Netting, A.; Kumar, N.; Hentzer, M.; Givskov, M.; Kjelleberg, S. A Novel and Sensitive Method for the Quantification of N-3-Oxoacyl Homoserine Lactones Using Gas Chromatography-Mass Spectrometry: Application Ito a Model Bacterial Biofilm. *Environ. Microbiol.* **2000,** *2*, 530-541.

72. Kim, M. C.; Gunnarsson, A.; Tabaei, S. R.; Hook, F.; Cho, N. J. Supported Lipid Bilayer Repair Mediated by Ah Peptide. *Phys. Chem. Chem. Phys.* **2016,** *18*, 3040-3047.

73. Dimova, R.; Marques, C. M., The Giant Vesicle Book. 1 ed.; CRC Press: Boca Raton, 2019; pp 1-676.

74. Jin, T.; Patel, S. J.; Van Lehn, R. C. Molecular Simulations of Lipid Membrane Partitioning and Translocation by Bacterial Quorum Sensing Modulators. *PLoS One* **2021,** *16*, e0246187.

75. Abdel-Mawgoud, A. M.; Lepine, F.; Deziel, E. Rhamnolipids: Diversity of Structures, Microbial Origins and Roles. *Appl. Microbiol. Biotechnol.* **2010,** *86*, 1323-1336.

76. Yoon, B. K.; Park, S.; Ma, G. J.; Kolahdouzan, K.; Zhdanov, V. P.; Jackman, J. A.; Cho, N. J. Competing Interactions of Fatty Acids and Monoglycerides Trigger Synergistic Phospholipid Membrane Remodeling. *J. Phys. Chem. Lett.* **2020,** *11*, 4951-4957.

77. Deziel, E.; Lepine, F.; Milot, S.; Villemur, R. Rhla Is Required for the Production of a Novel Biosurfactant Promoting Swarming Motility in *Pseudomonas aeruginosa*: 3-(3-Hydroxyalkanoyloxy)Alkanoic Acids (HAAs), the Precursors of Rhamnolipids. *Microbiology* **2003,** *149*, 2005-2013.

78. Wang, L. H.; Weng, L. X.; Dong, Y. H.; Zhang, L. H. Specificity and Enzyme Kinetics of the Quorum-Quenching N-Acyl Homoserine Lactone Lactonase (AHL-Lactonase). *J. Biol. Chem.* **2004,** *279*, 13645-13651.

Supporting Information for Chapter 3

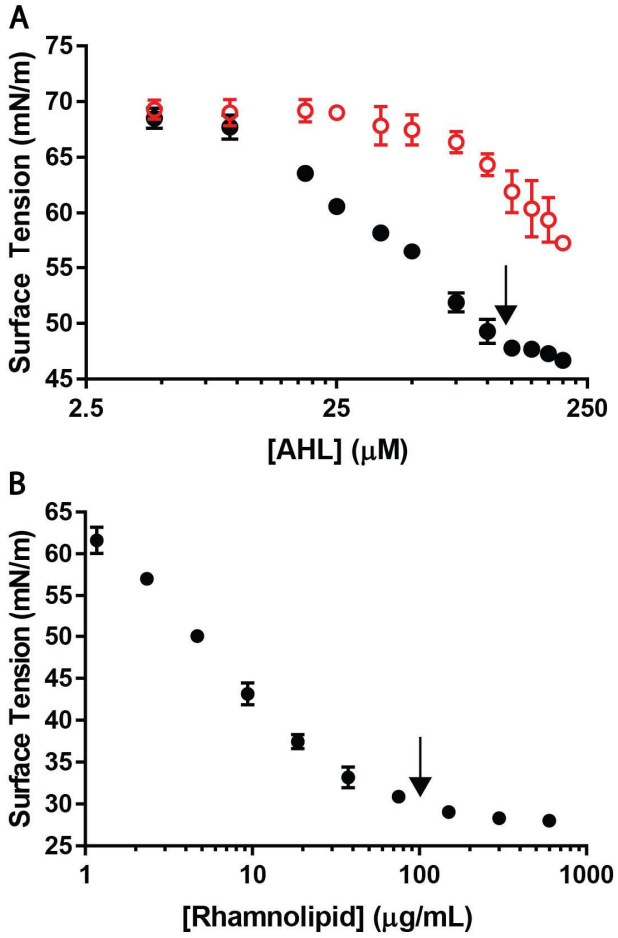


Figure S1: Surface tension measurements of (A) 3-oxo-C12-AHL (black, closed circles) and 3-oxo-C12-HS (red, open circles) or (B) rhamnolipid solutions at various concentrations. The data shown are the mean and a single standard deviation of three independent experiments. The breaks in the surface tension vs. concentration curves, which indicate the aggregation of 3-oxo-C12-AHL or rhamnolipid in solution, are indicated by arrows.

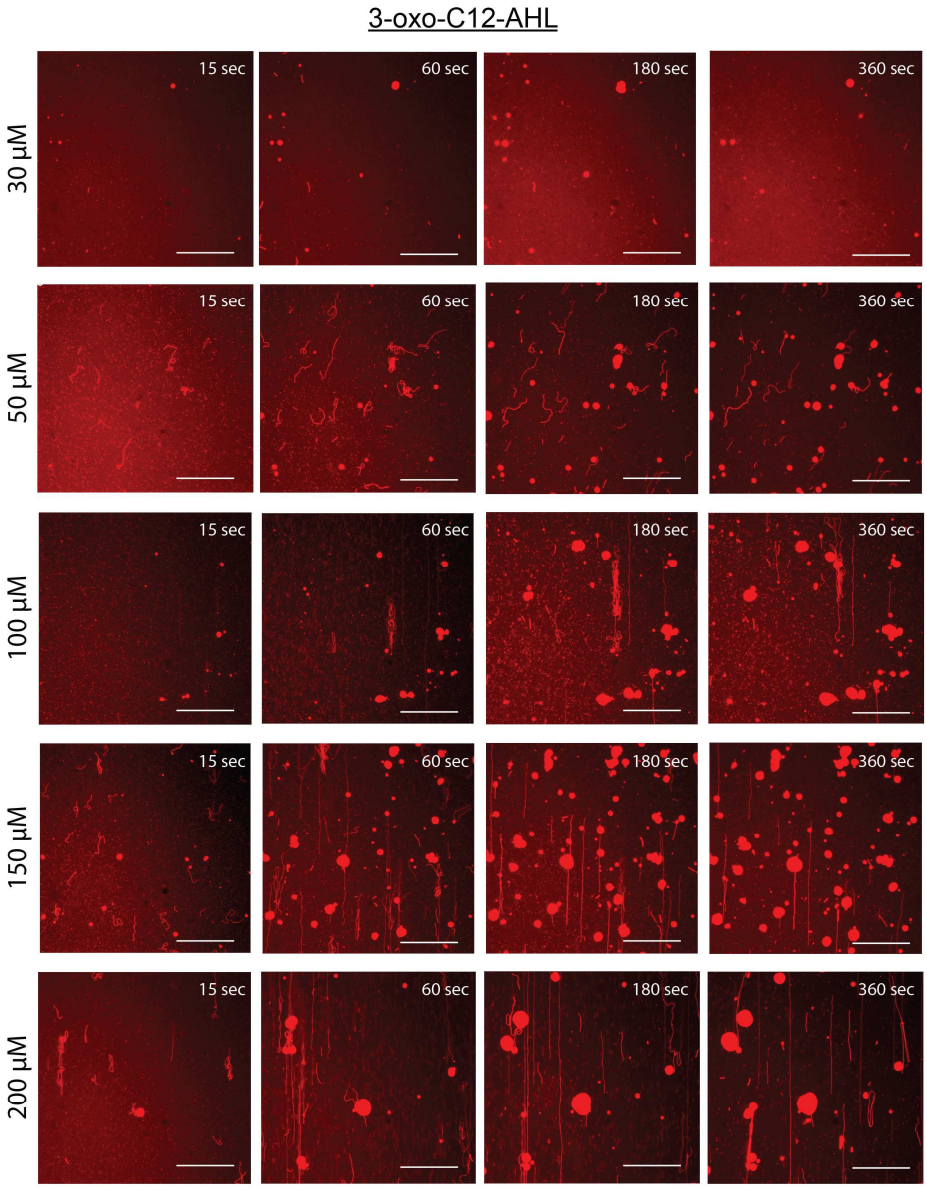


Figure S2a: Fluorescence micrographs showing the restructuring in DOPC SLBs after the introduction of 3-oxo-C12-AHL solutions at various concentrations over time. The images shown were taken at various time points indicated in the top-right corner of the images after the first membrane restructuring event was observed. The 360-second images shown here are the same as those shown in Figure 4 of the main text. The concentration of 3-oxo-C12-AHL used in each experiment is shown in the column to the left of the images. The direction of flow in all the images was from the bottom to the top of the screen. The scale bars represent 30 µM.

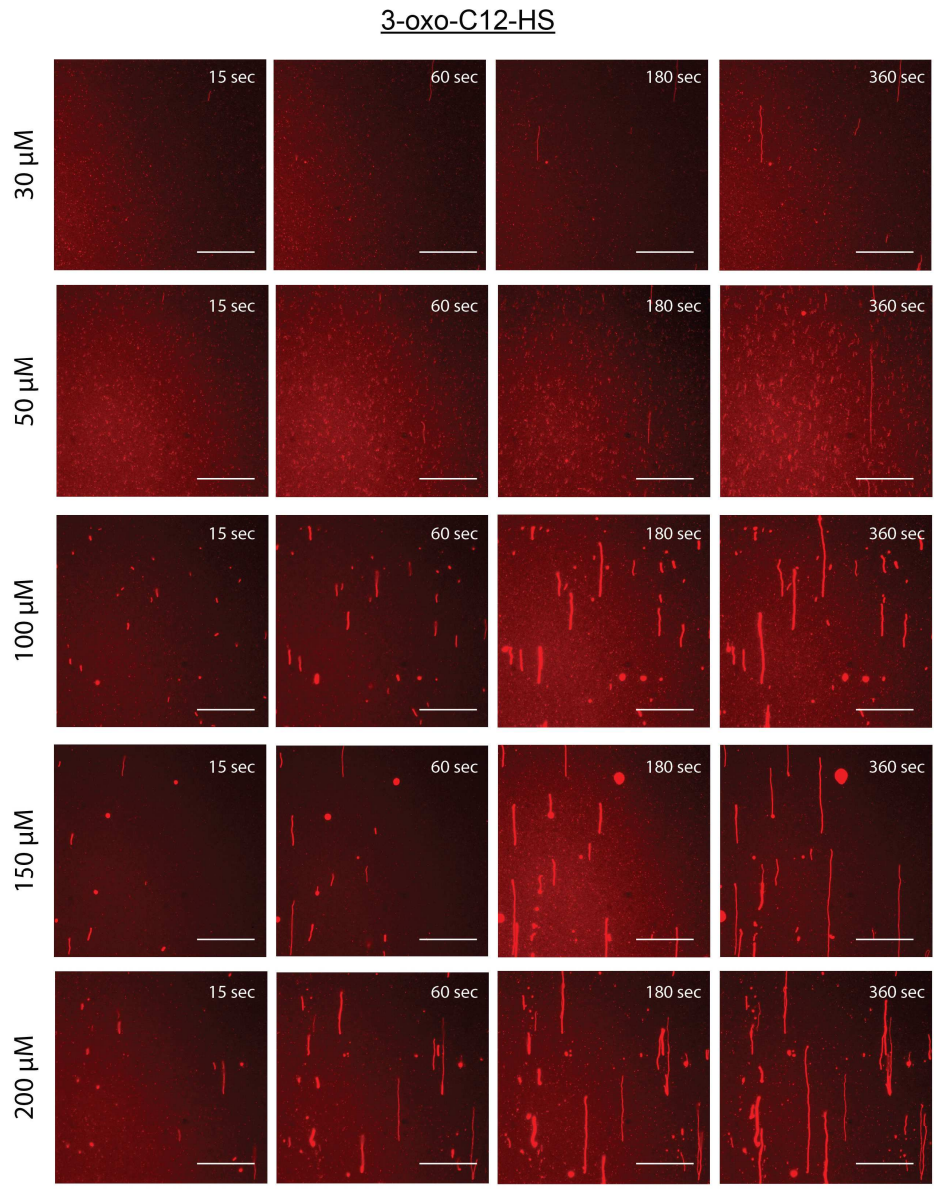


Figure S2b: Fluorescence micrographs showing the restructuring in DOPC SLBs after the introduction of 3-oxo-C12-HS solutions at various concentrations over time. The images shown were taken at various time points indicated in the top-right corner of the images after the first membrane restructuring event was observed. The 360-second images shown here are the same as those shown in Figure 4 of the main text. The concentration of 3-oxo-C12-HS used in each experiment is shown in the column to the left of the images. The direction of flow in all the images was from the bottom to the top of the screen. The scale bars represent 30 µM.

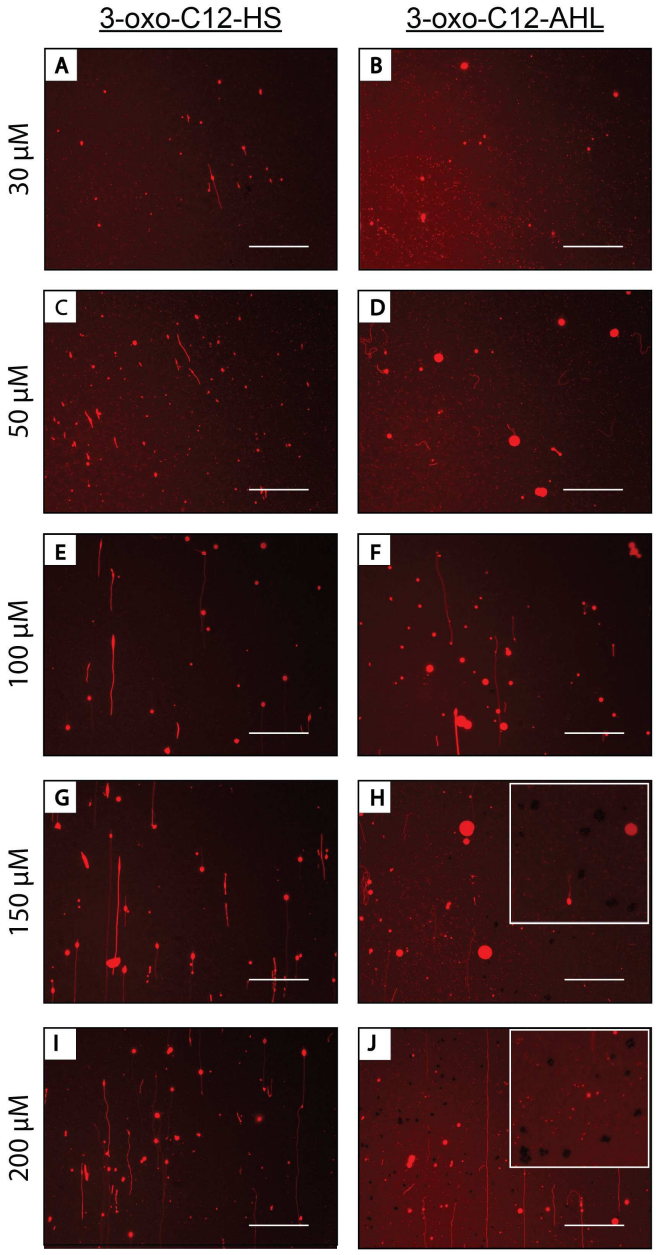


Figure S3: Representative top-down fluorescence micrographs showing DOPC SLBs that had previously been introduced to (A,C,E,G,I) 3-oxo-C12-HS or (B,D,F,H,J) 3-oxo-C12-AHL solutions at (A,B) 30 µM, (C,D) 50 µM, (E,F) 100 µM, (G,H) 150 µM, or (I,J) 200 µM after at least 8 minutes of washing under a continuous flow of buffer. The direction of flow in all images was from the bottom to the top of the image. Scale bars are 30 µm. The insets in H and J show circular areas of decreased fluorescence observed in the bilayer after washing it with buffer.

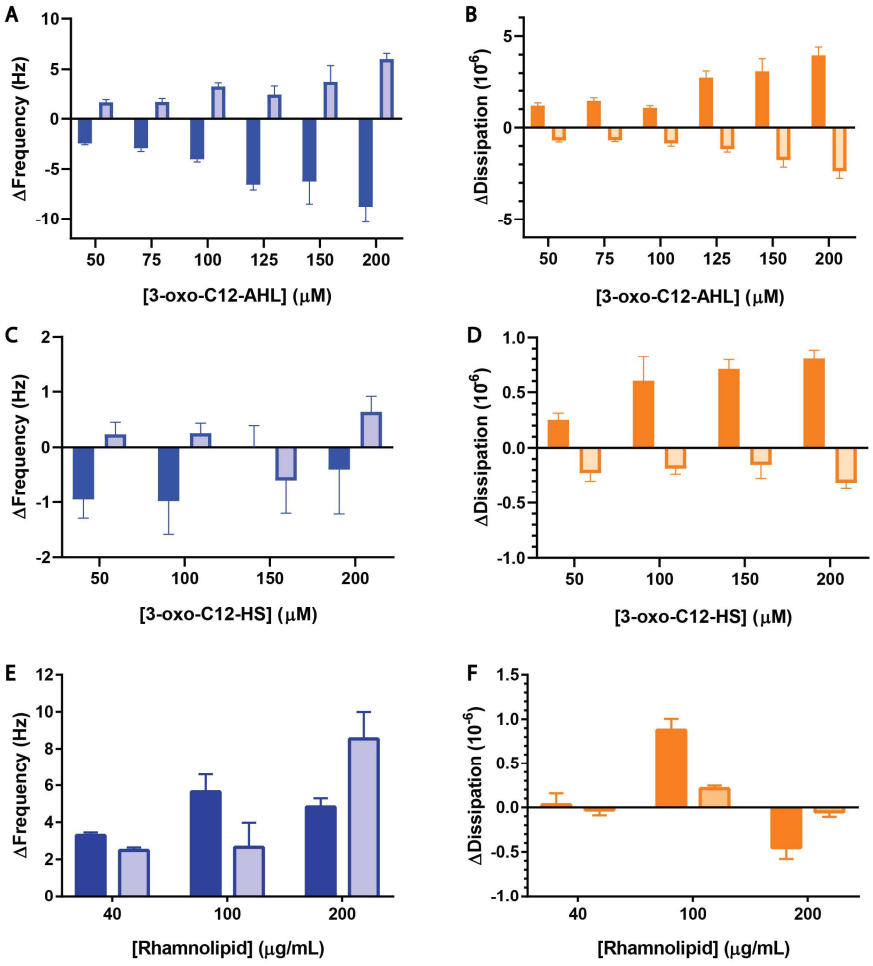


Figure S4: Changes in (A,C,E) frequency (ΔFrequency; referred to as Δf in the main text for brevity) and (B,D,F) dissipation (ΔDissipation; referred to as ΔD in the main text for brevity) for DOPC SLBs introduced to solutions of (A,B) 3-oxo-C12-AHL, (C,D) 3-oxo-C12-HS, and (E,F) rhamnolipid for 45 minutes (filled bars) or after 45 minutes of buffer wash (open bars) at various concentrations. The values shown are the means and a single standard deviation of three or four experiments (n= 3-4).

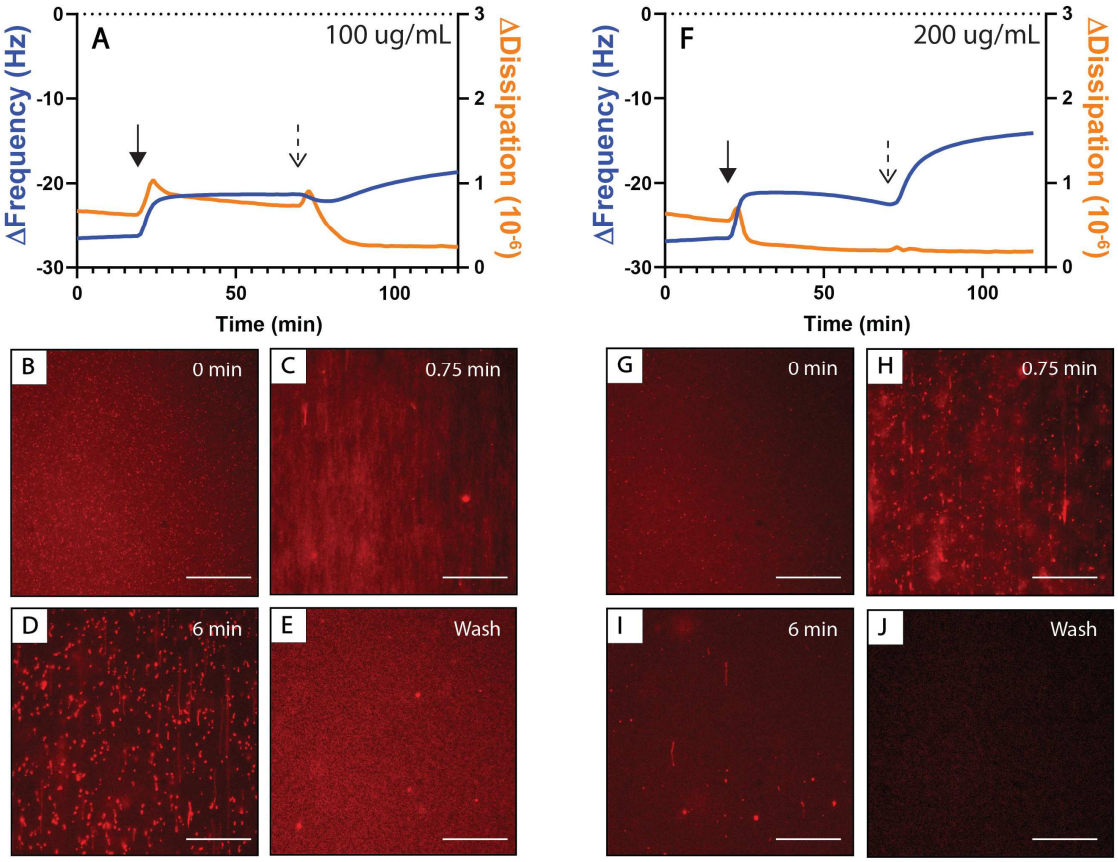
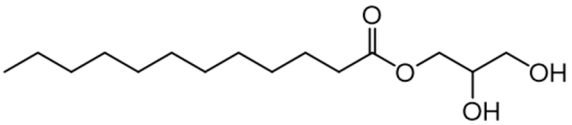
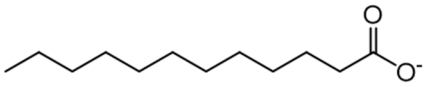


Figure S5: Measurements of membrane restructuring occurring in DOPC SLBs after introduction to (A-E) 100 µg/mL or (F-J) 200 µg/mL solutions of rhamnolipid. (A,F) QCM-D measurements of bilayer reformations initiated by the introduction of rhamnolipid solutions with changes in frequency (ΔFrequency, blue lines; referred to as Δf in the main text for brevity), and dissipation (ΔDissipation, orange lines; referred to as ΔD in the main text for brevity) shown are representative of three or four independent experiments. The initial measurement values (t=0 min) of these experiments correspond to DOPC SLBs on an SiO_2 surface. Rhamnolipid solutions were introduced to the bilayer at the time indicated by the solid arrow and the buffer was introduced at the time indicated by the dashed arrow. (B-E,G-J) fluorescence micrographs of bilayer restructuring occurring at (B,G) 0 sec, (C,H) 45 sec, and (D,I) 6 min after the first bilayer restructuring events had been observed or (E,J) after at least 8 minutes of washing the bilayer with buffer. The direction of flow in all images was from the bottom to the top of the image. Scale bars are 30 µm.



Glycerol monolaurate (GML)



Lauric acid

Figure S6: Chemical structures of glycerol monolaurate (GML) and lauric acid (LA).

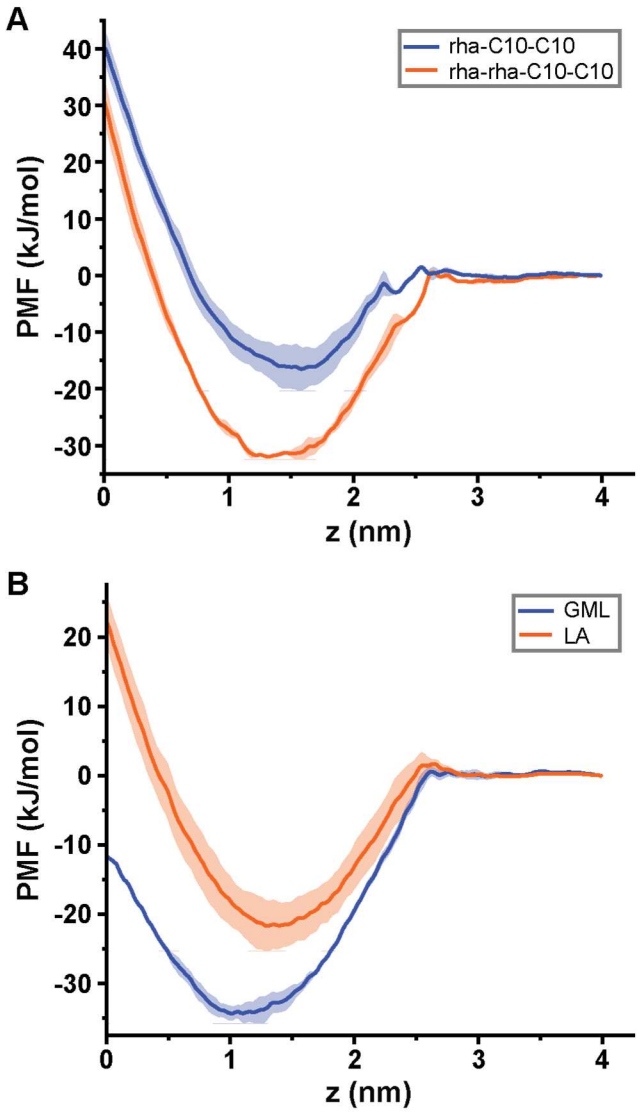


Figure S7: Potentials of mean force (PMFs) of (A) rha-C10-C10 (blue) and rha-rha-C10-C10 (orange), and (B) GML (blue) and LA (orange) as a function of the distance along the DOPC bilayer normal (z).

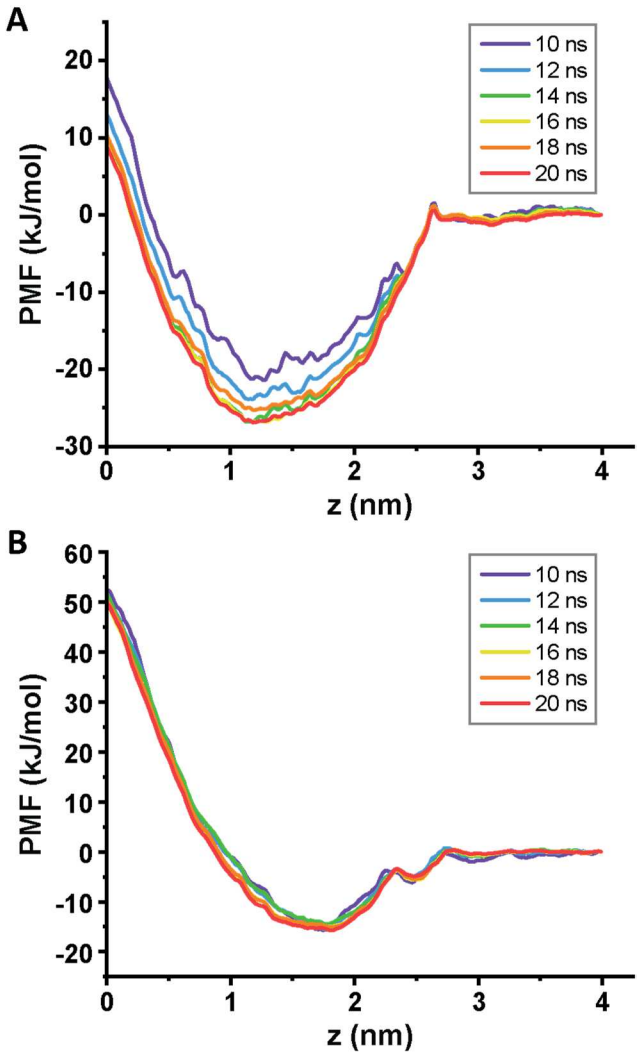


Figure S8: Representative convergence of the potentials of mean force (PMFs) computed using umbrella sampling as a function of the distance along the DOPC bilayer normal (z) for (A) 3-oxo-C12-AHL and (B) 3-oxo-C12-HS.

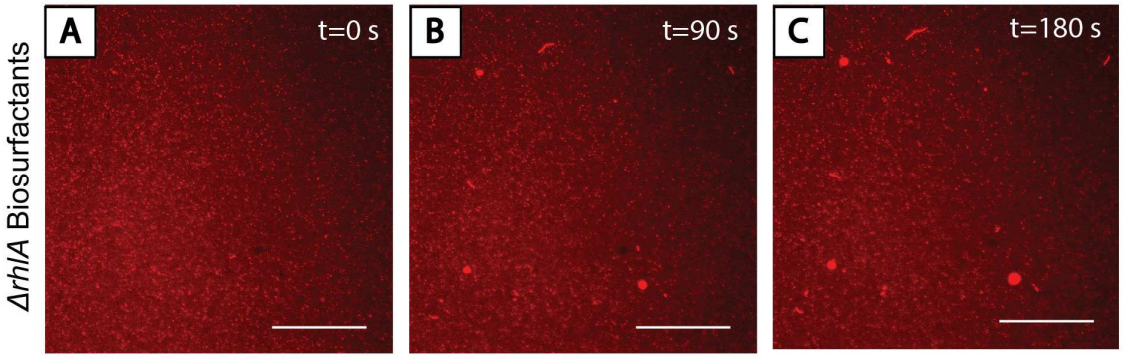
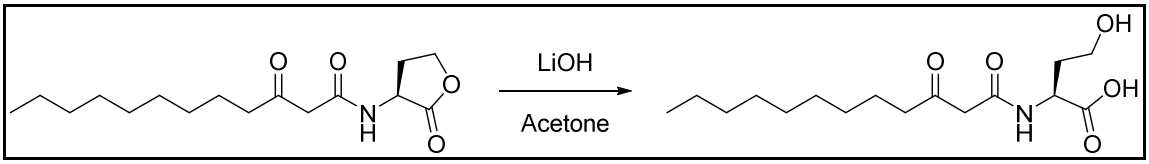
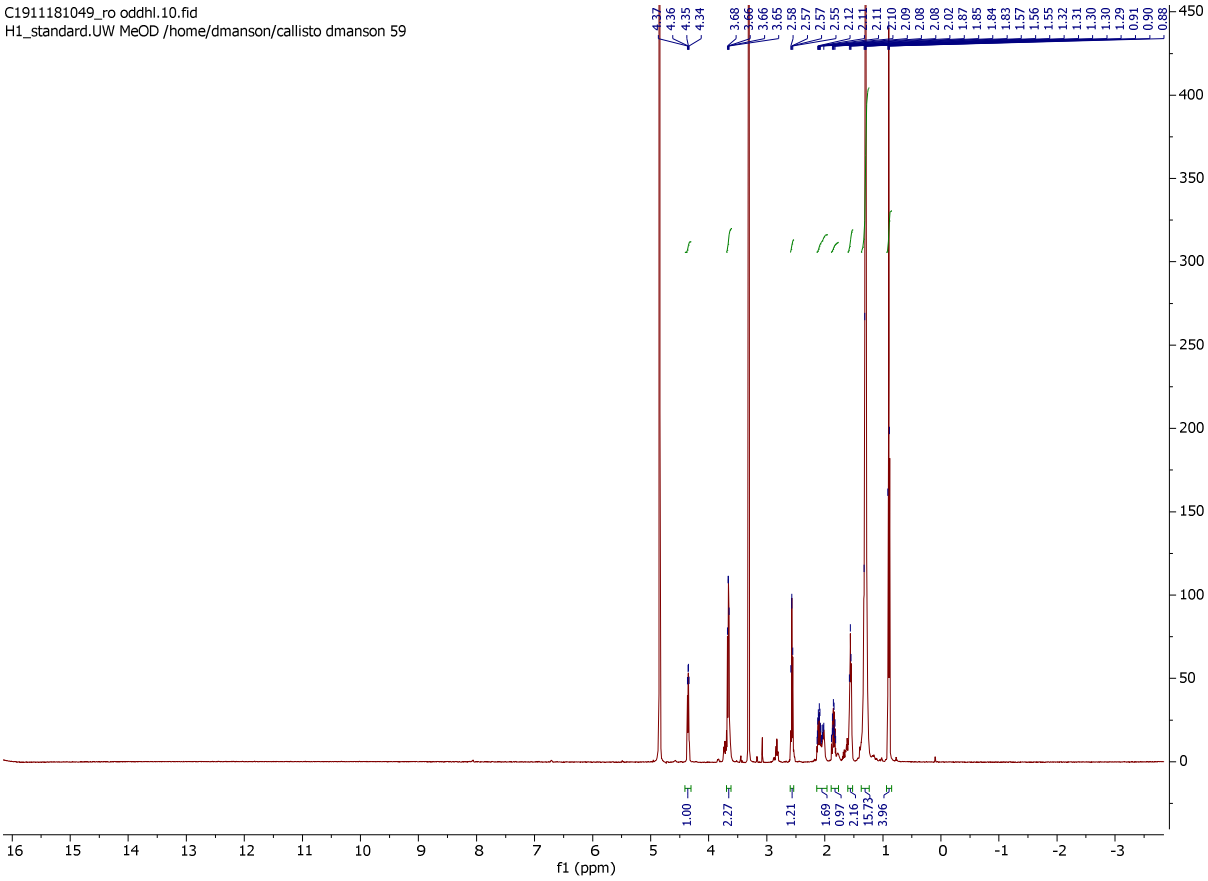
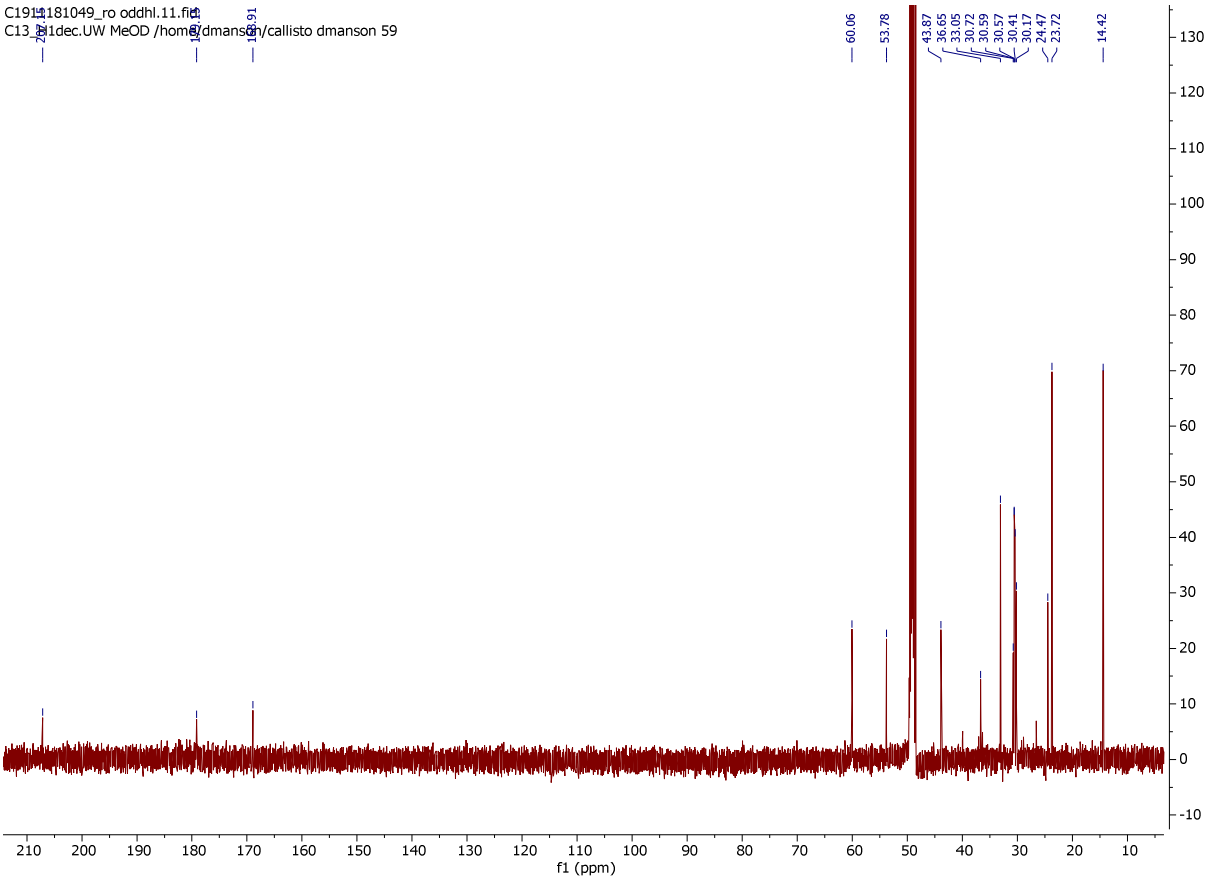


Figure S9: Representative top-down fluorescence micrographs of structural reformations occurring in fluorescently labeled DOPC SLBs after introduction to combinations of 3-oxo-C12-AHL (10 μM) and 3-oxo-C12-HS (20 μM) that are representative of the concentrations of these molecules in *ΔrhlA P. aeruginosa* cultures grown for 24-hours. The micrographs were acquired at (A) 0 seconds, (B) 90 seconds, and (C) 180 seconds after the first membrane reformations were observed on the surface of the bilayer. The direction of flow in all images was from the bottom to the top of the panel. Scale bars are 30 μm.

Synthesis Scheme of 3-oxo-C12-H Synthesis and Associated NMR Spectra. ^{1}H NMR (500 MHz, Methanol-d_4) δ 4.35 (dd, J = 8.4, 5.1 Hz, 1H), 3.66 (dd, J = 7.3, 5.8 Hz, 2H), 2.67 – 2.45 (m, 1H), 2.08 (dddd, J = 25.7, 14.9, 7.6, 5.2 Hz, 2H), 1.85 (ddt, J = 14.0, 8.4, 5.8 Hz, 1H), 1.66 – 1.47 (m, 2H), 1.42 – 1.17 (m, 12H), 0.90 (t, J = 6.9 Hz, 3H). ^{13}C NMR (126 MHz, MeOD) δ 205.75, 177.74, 167.51, 58.66, 52.37, 42.47, 35.25, 31.65, 29.32, 29.19, 29.17, 29.06, 29.01, 28.77, 23.07, 22.32, 13.02. ESI-EMM: $[M+Na]^+$ calculated 338.1938; measured 338.1933.







NMR Quantification of Phospholipids. To determine the concentration of phospholipids in stock solutions, quantitative $^{31}P[^{1}H]$ NMR spectroscopy was performed in 90% H_2O and 10% D_2O using a Bruker Avance-400 spectrometer with a BBFO probe. A relaxation delay (D1) of 11s was determined by inversion-recovery pulse sequence experiments. 890 µL of a phospholipid vesicle sample in water was mixed with 10 µL of Triton-X or rhamnolipid solution and 100 µL of a 100 mM triethylphosphine oxide internal standard solution in D_2O. All spectra were referenced relative to the phosphorus peak of the internal standard (~δ65ppm). Acquisition parameters were as follows: PULPROG=zgig30, D1=11s, SW=405ppm, O2P=3.75ppm, NS=64, DS=4, LB=1.

Chapter 4

Interactions of Bacterial Quorum Sensing Signals with Model Lipid Membranes: Influence of Acyl Tail Structure on Multi-Scale Response‡

‡ Portions of this chapter have been submitted for publication as: Gahan, C. G.; Van Lehn, R. C.; Blackwell, H. E.; Lynn, D. M. "Interactions of Bacterial Quorum Sensing Signals with Model Lipid Membranes: Influence of Acyl Tail Structure on Multi-Scale Response". I designed and performed all experiments. R. C. Van Lehn, H. E. Blackwell, and D. M. Lynn directed the project.

ABSTRACT: Many common bacteria use amphiphilic *N*-acyl-L-homoserine lactones (AHLs) as signaling molecules to coordinate group behaviors at high cell densities. Past studies demonstrate that AHLs can adsorb to and promote the remodeling of lipid membranes in ways that could underpin cell-cell or host-cell interactions. Here, we report that changes in AHL acyl tail group length and oxidation state (e.g., the presence or absence of a 3-oxo group) can lead to differences in the interactions of eight naturally occurring AHLs in solution and in contact with model lipid membranes. Our results reveal the presence of a 3-oxo group to impact remodeling when AHLs are placed in contact with supported lipid bilayers (SLBs) of the phospholipid DOPC. Whereas AHLs that have 3-oxo groups generally promote the formation of microtubules, AHLs that lack 3-oxo groups generally form hemispherical caps on the surfaces of SLBs. These results are interpreted in terms of the time-scales on which AHLs translocate across bilayers to relieve asymmetrical bilayer stress. Quartz crystal microbalance with dissipation (QCM-D) measurements also reveal 3-oxo AHLs to associate with DOPC bilayers to a greater extent than their non-3-oxo analogs. Finally, we observed 3-oxo AHLs to facilitate greater transport or leakage of molecular cargo across the membranes of DOPC vesicles relative to AHLs without 3-oxo groups, also suggesting increased bilayer disruption and destabilization. Our results reveal tail group structure to have substantial impacts on the interactions of AHLs with lipid membranes. These fundamental studies hint at interactions and associated multi-scale phenomena that may inform current interpretations of the behaviors of AHLs in biological contexts. These results could also provide guidance useful for the design of new classes of synthetic materials (e.g., sensor elements or drug delivery vehicles) that interact with or respond selectively to communities of bacteria that use 3-oxo AHLs for cell-cell communication.

Introduction

Quorum sensing (QS) is a cell-cell signaling process used by many common bacteria to assess population density and coordinate group behaviors at high cell numbers, including the production of virulence factors and the formation of bacterial biofilms that are detrimental and costly in clinical, commercial, and industrial settings.[1-7] QS is controlled by the production and dissemination of chemical signals that are often assumed to diffuse freely amongst individual cells in a bacterial community.[2, 5, 8] The structures of these signals can vary widely among species,[2, 9] and some species can produce more than one signal,[10] or even several classes of signals,[8] to regulate group behavior. While Gram-positive bacteria generally use peptide-based signals to modulate QS,[9, 11] certain Gram-negative bacteria, including common pathogens such as *Pseudomonas aeruginosa*, use small-molecule signals known as *N*-acyl-L-homoserine lactones (AHLs).[2, 8, 12] AHLs, as a class of signal, are shared across many different species of bacteria, and while they all have a conserved homoserine lactone (HL) head group, the structures of their acyl tails vary significantly. The impact of AHL structure on binding to their cognate intracellular receptors (i.e., LuxR-type proteins) is, in many cases, well characterized, and is believed to underpin the specificity of both intra-species and inter-species communication in bacteria.[8, 12-15] In this paper, we report that key changes in the tail group structures of many naturally occurring AHLs can also have substantial impacts on other important physicochemical behaviors, including self-association in aqueous solution and the nature of their interactions with model lipid membranes.

The work reported here was motivated by a growing body of work demonstrating that the amphiphilic nature of AHLs can lead to self-assembly in solution and at interfaces.[16-25] The HL ‘head’ group and the acyl ‘tail’ group of varying length and structure (e.g., ranging from 4-20

carbons, oxidation state in the 3-position, etc.) provide polar and hydrophobic motifs, respectively (Figure 1).[2, 12] This general structure resembles those of many other non-ionic amphiphiles and, provided that the tail groups are sufficiently long, can confer surface activity and resulting behaviors that are similar to those of other natural and synthetic surfactants. For example, we[23] and others[18] have reported that medium to long-chained AHLs (e.g., with aliphatic tails ranging in length from 8–16 carbons; Figure 1) can self-assemble into micelles or small vesicles in aqueous solution. Daniels et al. also demonstrated that some long-chained AHLs can self-assemble and undergo phase changes when compressed at air-water interfaces.[16] Finally, recent reports have demonstrated that AHLs can intercalate into lipid membranes,[19, 20] allowing them to translocate

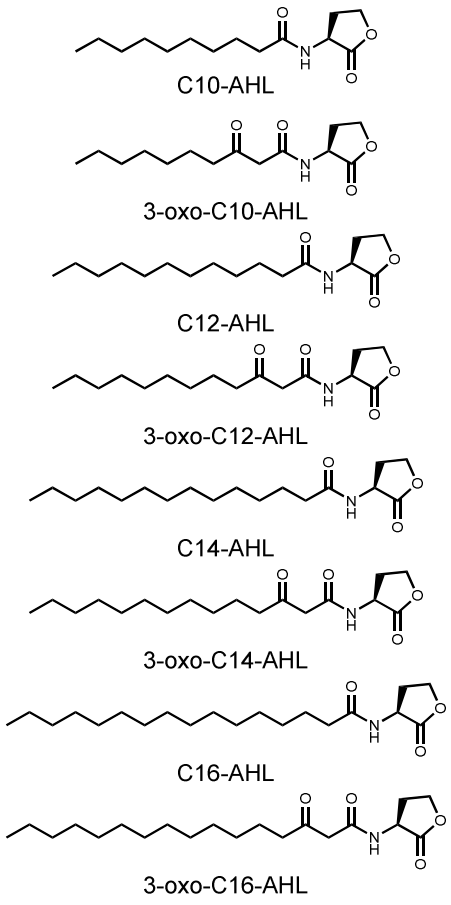


Figure 1: Chemical structures of the AHLs examined in this study.

across lipid bilayers,[21] promote membrane depolarization,[17] dissolve lipid phases[22] and, of particular interest to the work reported here, promote large-scale membrane remodeling.[25] These past studies reveal that both head group and aliphatic tail structure can have substantial impacts on the behaviors of AHLs, including self-association in solution[18, 23] and adsorption to[19, 20] and subsequent multi-scale phenomena[17, 22, 25] that occur when they come in contact with lipid bilayers. Overall, this growing understanding of the physicochemical properties of AHLs and the richness of behaviors in which they can engage provides insight into potential additional roles, beyond simple ligand-receptor interactions, that these signaling molecules could play in facilitating bacterial communication. These past studies also suggest roles that AHLs could play in mediating interactions with eukaryotic host cells or with other self-assembled synthetic materials, such as lipid membranes commonly used as vehicles for drug delivery.

We recently reported that 3-oxo-C12-AHL (Figure 1), a naturally occurring long-tailed AHL produced by *P. aeruginosa* and other related bacteria, can promote the formation of extended microtubules and large hemispherical caps on the surfaces of model lipid bilayers formed using the phospholipid DOPC.[25] That study also showed that 3-oxo-C12-HS—the anionic head-group hydrolysis product of 3-oxo-C12-AHL that arises naturally in *P. aeruginosa* cultures,[26, 27] but is biologically inactive as a modulator of QS—can also promote large scale remodeling, but in ways that differ substantially from those promoted by the non-ionic parent molecule 3-oxo-C12-AHL.[25] The work reported here sought to systematically investigate and characterize the impacts of AHL tail group structure on self-assembly and interactions with model lipid membranes using a family of natural AHLs produced by several different species of Gram-negative bacteria (Figure 1).[12]

In the sections below, we report qualitative and quantitative characterization of model supported lipid bilayers (SLBs) of DOPC in contact with eight different, but structurally related

AHLs with tail lengths of 10–16 carbons. Characterization by fluorescence microscopy and quartz crystal microbalance with dissipation (QCM-D) reveal each of these long-tailed AHLs to promote some form of significant large-scale membrane remodeling, with the type and extent of remodeling observed to vary substantially with changes in both tail length and chemical structure (e.g., with the presence or absence of a 3-oxo substituent in the tail). The results of additional dye-leakage assays using large unilamellar vesicles (LUVs) composed of DOPC also reveal AHL structure to play a role in facilitating the transport of molecular cargo across unsupported lipid membranes similar to those used in drug delivery and many sensing applications. The results of this study thus bear on fundamental questions related to processes that bacteria may use to communicate or control host-cell response, and provide guidance that could prove useful for the design of synthetic materials and self-assembling systems that respond to or communicate with bacterial communities.

Materials and Methods

Materials. Sodium chloride (NaCl), calcein, sodium hydroxide (NaOH), dimethylsulfoxide (DMSO), triethylphosphine oxide, chloroform, Sephadex G-50, and deuterium oxide (D_2O) and 3-oxo-C14-AHL were purchased from Sigma (St. Louis, MO). C16-AHL was purchased from Santa Cruz Biotechnology (Dallas, TX). Isopropanol (iPrOH) was purchased from Fisher Scientific (Waltham, MA). 1,2-Dioleoyl-sn-glycero-3-phosphocholine (DOPC), 1,2-dihexanoyl-sn-glycero-3-phosphocholine (DHPC), filter supports, and a Mini-prep extruder were obtained from Avanti Polar Lipids (Alabaster, AL). Lissamine rhodamine B 1,2-dipalmitoyl-sn-glycero-3-phosphoethanolamine, triethylammonium salt (Rho-DPPE) was purchased from Invitrogen (Carlsbad, CA). Sodium dodecyl sulfate (SDS) was obtained from Fisher Scientific (Pittsburgh, PA). Triton-X100 was purchased from Promega (Madison, WI). (*N*-Morpholino)propanesulfonic

acid (MOPS) was obtained from MP Biomedical (Irvine, CA). Disposable culture tubes (16 × 100 mm) were acquired from VWR (West Chester, PA). Plastic centrifuge tubes (1.7 mL) were purchased from Axygen products (Tewksbury, MA). Minisort X plus 0.2 μm syringe filters were obtained from Sartorius Stedim Biotech (Goettingen, Germany). Polycarbonate extruder filters (100 nm) were obtained from Millipore (Billerica, MA). A Milli-Q system (Millipore, Bedford, MA) was used to perform deionization of distilled water yielding water with a resistivity of 18.2 MΩ. All other AHLs in this study were synthesized according to previously reported methods.[13, 28] All materials were used as received without further purification unless otherwise specified.

Preparation of AHL Solutions. AHL stock solutions were prepared in DMSO at a concentration of 40 mM (3-oxo-C10-AHL), 20 mM (C10-AHL, 3-oxo-C12-AHL, C12-AHL, 3-oxo-C14-AHL) or 5 mM (C14-AHL, 3-oxo-C16-AHL, C16-AHL) and stored at -4 °C between uses. Immediately before experiments, aliquots of the stock solution were thawed and subsequently diluted in DMSO to 100 times the final aqueous concentration, and then further diluted 1:100 into buffer. All experiments that are described as being performed in a buffer solution were performed in 150 mM NaCl, 10 mM MOPS, pH 7.4 solution unless otherwise noted. All AHL solutions were used within one hour of initial dilution of the DMSO stocks into buffer. All aqueous solutions used in this study contained 1 vol% DMSO.

Static Light Scattering Measurements. The critical aggregation concentrations (CACs) of the AHLs used in this study were determined by static light scattering using a method described in our previous study.[23] The buffer used was filtered through a 0.22 μm filter and then centrifuged at 2000 rpm for 3 min to remove particulates and air bubbles from the buffer. AHL solutions (1.5

mL) were prepared in a 13 x 100 mm glass culture tube and allowed to sit thereafter at room temperature for 10 min. Aliquots (1.2 mL) of these samples were then transferred to a plastic cuvette and three independent measurements of the scattered light intensity were made per sample. Each measurement averaged the scattered light intensity of the sample over 5 sec time periods multiple times. Linear regression of increasing scattered light intensity with increasing AHL concentrations was used to determine the CAC of the AHL being tested. For some AHLs with longer tails, linear regressions of acquired data could not be performed with certainty. In these cases, we report estimated upper bounds of CAC values corresponding to the lowest concentration that was co-linear with values obtained at higher concentrations. Those reported values also corresponded to the lowest concentrations tested that exhibited clear deviations from background levels of scattered light intensity. For these longer-tailed AHLs, the values reported below thus represent an estimated upper bound of the CACs, and the actual CACs are likely lower than those values.

Optical Microscopy Experiments Using SLBs Formed by the Bicelle Fusion Method. Fluorescence microscopy experiments were performed using fluorescently labeled (0.1 wt% Rho-DPPE) SLBs formed using the bicelle fusion method in Ibidi microfluidic chambers (μ-Slide VI 0.5 Glass Bottom).[29] The microfluidic chambers were incubated with a 1 M NaOH solution for ~30 min prior to SLB formation, followed by washing with Milli-Q H_2O and buffer to neutralize the flow cell. DOPC and DHPC stocks in chloroform were mixed to a desired composition ([DOPC]/[DHPC] = 0.25), dried under a stream of N_2, and further dried under vacuum for at least one hour. The resulting lipid film was then hydrated using buffer to produce a 1 mM bicelle suspension as determined by DOPC concentration. This suspension was iteratively immersed into

an iPrOH/dry ice bath and then a warm water bath (~50 °C) followed by vigorous vortexing (5 times). The resulting bicelle stock solution was diluted 1:32 to yield a solution with a DOPC concentration of 0.031 mM and then introduced to the NaOH-treated Ibidi flow cell at a flow rate of 100 μL/min. Supported lipid bilayer (SLB) formation was monitored by optical microscopy. Buffer was then introduced to the flow cell to wash away any remaining bicelles. The fluidity of SLBs formed using this method was characterized by performing a qualitative fluorescence recovery after photobleaching (FRAP) experiment. AHL-containing solutions were then introduced to flow cells at a flow rate of 100 μL/min, and micrographs were acquired using an Olympus IX70 inverted microscope (Center Valley, PA) and a Q-imaging EXi Aqua camera (Tucson, AZ) every 5 sec for ~8 min (at least 100 images). A Lumen Dynamics X-Cite Series 120PC-Q fiber-coupled mercury lamp (Monroe, LA) was used to excite fluorescently-labeled lipids using the RFP channel. To visualize changes in bilayer structure when the test AHLs were removed from solution, bilayers were subsequently washed with buffer solution at a flow rate of 100 μL/min.

Quartz Crystal Microbalance with Dissipation (QCM-D) Measurements. QCM-D measurements were performed with QSensor QSX 303 quartz crystal (QC) sensors with a fundamental frequency of 5 MHz that were coated with 50 nm of SiO_2 using a Q-Sense E4 QCM instrument (Bolin Scientific, Stockholm Sweden). Changes in the frequency (ΔFrequency) and dissipation (ΔDissipation) of the QC sensors were monitored at the third, fifth, seventh, ninth, and eleventh overtones, and data analysis was performed using the data from the seventh overtone. An Ismatic IPC High Precision Multichannel Dispenser (Wertheim, Germany) peristaltic pump was used in all experiments to flow solutions over the crystals at 100 μL/min. QCM-D sensors were

treated with oxygen plasma for 10 min when received and then immediately immersed in a 2% SDS solution and allowed to sit in the solution for at least 30 min. The sensors were then rinsed in Milli-Q water and dried using dry nitrogen (N_2). Immediately before conducting an experiment, the sensors were again treated with oxygen plasma for 10 min and placed into the measurement apparatus, which was held at 25 ± 0.5 °C. The sensors were then allowed to equilibrate their resonance under a continuous 100 μL/min flow of buffer solution.

For QCM-D measurements, SLBs were formed using the bicelle fusion method as described above.[29] Bicelle stock solutions (1 mM; as determined by DOPC concentration) were diluted to 0.031 mM in buffer and introduced to the sensor chamber. Adsorption of the bicelles to the surface and subsequent fusion were monitored by following the QCM-D traces over time. The formed bilayer was washed with buffer for ~20 min to remove any remaining bicelles. AHL solutions were then added to the flow chamber and allowed to interact with the bilayer for 45 min, after which the bilayer was washed with buffer for at least 45 min to observe the desorption of amphiphiles from the bilayer over time. Representative QCM-D traces are shown for a single sensor in Figure S3, and the data analysis included in sections below is the average and standard deviation of 3 or 4 (n = 3–4) independent experiments run simultaneously on different crystals. Immediately following each experiment, the QC sensors were immersed in a 2% SDS solution for at least 30 min, washed in Milli-Q water, and dried under N_2 gas before storage.

Fabrication of Calcein-Loaded Vesicles. Calcein-loaded large unilamellar vesicles (LUVs) were prepared using a previously described freeze-thaw and vesicle extrusion procedure.[25, 30] In brief, DOPC dissolved in chloroform was aliquoted into vials, and the chloroform was subsequently removed under a stream of N_2 and further dried under vacuum for at least one hour. A 70 mM

calcein solution in buffer was then added to the dried lipids and vortexed vigorously to form a turbid 5 mg/mL DOPC solution. The calcein-containing solution was prepared by massing an appropriate amount of calcein, to which buffer was added and the pH of the solution was adjusted to 7.4 with 10 M NaOH. The vesicle solutions were then iteratively frozen and thawed (five times) by alternatively immersing them into an iPrOH/dry ice bath and a warm water bath (~50 °C). The resulting vesicle suspension was then passed at least 11 times through a 100 nm PC filter using an Avanti Polar Lipids Mini-prep extruder producing vesicles with a hydrodynamic radius of ~130 nm, which is consistent with previously reported literature.[31] The resulting vesicles were separated from external, unloaded calcein using a hand-packed Sephadex G-50 size exclusion chromatography column. ^{31}P NMR was used to quantify the concentration of the resulting purified vesicle solution, as described previously and in the Supporting Information.[32]

Calcein Leakage Assays. Calcein leakage assays were performed by combining and mixing 10 μL of a solution of calcein vesicles (at a concentration of 1 mM DOPC by monomer) with 90 μL of an AHL-containing solution in a well of a 96-well microtiter plate. The plate was allowed to sit for 5 min, after which the fluorescence intensity of the solution was measured at an excitation wavelength of 480 nm and an emission wavelength of 525 nm using a Tecan Infinite 200 Pro plate reader. All assays were repeated in triplicate (n = 3) for each batch of vesicles and were performed with three (n = 3) different, independently produced batches of vesicles for a total of nine (n = 9) fluorescence measurements. Statistical significance against the buffer control or other AHL-containing solutions was determined using a one-way ANOVA with all nine normalized replicates for each condition used that was corrected for multiple comparisons using the Tukey method. The fluorescence intensity for each reading was normalized using a procedure adapted from our past

study[25] and summarized in Equation 1, where: FI is the fluorescence intensity of the test solution, FI_{Buffer} is the fluorescence intensity of the calcein vesicles in buffer as the negative control, and $FI_{TX\text{-}100}$ is the fluorescence intensity of a vesicle solution containing 1% Triton X-100 (previously demonstrated to completely lyse vesicles at high concentrations)[33] as the positive control.

$$Normalized\ Flourescense = \frac{FI - FI_{Buffer}}{FI_{TX-100} - FI_{Buffer}} \quad \text{(Eq. 1)}$$

Results and Discussion

We recently reported that 3-oxo-C12-AHL can interact with model lipid membranes to form long microtubules and hemispherical caps on the surfaces of supported lipid bilayers (SLBs) and giant unilamellar vesicles (GUVs) composed of the phospholipid DOPC.[25] That study also demonstrated that changes in the AHL head group structure (e.g., the presence of an anionic, ring-opened homoserine moiety) can impact the nature of interactions and lead to large differences in membrane remodeling. To investigate the influence of AHL tail group structure on membrane reformation, we characterized interactions of DOPC SLBs with the set of AHLs shown in Figure 1. This family of AHLs contains differences in both the overall length (from 10 to 16 carbon atoms) and the oxidation state (the presence or absence of a 3-oxo group) of the hydrophobic tail that have been previously predicted by molecular dynamics (MD) simulations to influence thermodynamic preferences for partitioning into or translocating across a lipid bilayer and that could, thus, influence subsequent membrane remodeling and dynamics.[24]

To provide a basis for understanding and interpreting the behaviors of these AHLs with lipid membranes in studies described below, we first characterized the self-association of these amphiphilic compounds in aqueous solution. We previously reported the critical aggregation concentrations (CACs) of 3-oxo-C12-AHL, C12-AHL, and C16-AHL in water and bacterial

growth media, as determined using measurements of static light scattering.[23] We began our studies by measuring the CACs of all eight AHLs shown in Figure 1 in the buffer (150 mM NaCl, 10 mM MOPS, 1% DMSO; pH 7.4) and general environmental conditions used in all subsequent studies of lipid membrane interactions described below (see Methods). The CACs for these AHLs are summarized in Table 1 (see Figure S1 for corresponding light scattering results). We observed characteristic signs of aggregation for all AHLs tested with the exception of 3-oxo-C10-AHL, which did not aggregate within the concentration range tested here (up to 200 μM).

Table 1: Critical aggregation concentrations (CACs) of the AHLs shown in Figure 1.

Molecule	CAC (μM)[a,b]
3-oxo-C10-AHL	> 200
C10-AHL	62.4 ± 1.3
3-oxo-C12-AHL	59.5 ± 9.2
C12-AHL	1.4 ± 0.6
3-oxo-C14-AHL	3.1 ± 1.4
C14-AHL	≤ 0.31[c]
3-oxo-C16-AHL	≤ 0.63[c]
C16-AHL	≤ 0.08[c]

[a]The corresponding light scattering data from which these results are derived are shown in Figure S1. [b]Unless otherwise noted, CACs were determined by linear regression of light scattering data as described in the Supporting Information. [c]Estimated value corresponding to the lowest concentration of this molecule tested that was co-linear with values obtained at higher concentrations; this value also corresponds to the lowest concentration tested that exhibited a clear deviation from background levels of scattered light intensity, however in these cases linear regressions of acquired data could not be performed with certainty; the value shown thus represents an estimated upper bound of the CAC and the actual CAC is likely lower than this value (see Materials and Methods and Supporting Information for further discussion).

The CACs measured for 3-oxo-C12-AHL, C12-AHL, and C16-AHL in this medium were similar to those reported previously (in water and bacterial culture medium; see past studies[23] for additional discussion of the self-assembly of these AHLs in solution), and the CACs for 3-oxo-C10-AHL, C10-AHL, 3-oxo-C14-AHL, C14-AHL, and 3-oxo-C16-AHL all exhibited, in general, trends in behavior similar to other classes of surfactants with respect to changes in tail length.[34] At

each tail length, we observed the presence of a 3-oxo group to increase the CAC substantially, in some cases by as much as an order of magnitude; this general observation is similar to differences we reported for the CACs of C12-AHL and 3-oxo-C12-AHL reported previously in water and bacterial growth media.[23] Overall, these results support the view that these AHLs are amphiphilic in nature and provide a framework for interpreting their interactions with model lipid membranes, as aggregation has been previously reported to impact the interaction of amphiphiles with lipid membranes.[35] We return to these results again in the discussion below.

AHL Tail Group Structure Impacts Membrane Remodeling in Supported Lipid Bilayers

We characterized the impacts of AHL tail group structure on multi-scale remodeling in DOPC SLBs formed using a recently reported bicelle fusion technique.[29] We used this method, rather than the vesicle fusion method used in our past studies of membrane remodeling by 3-oxo-C12-AHL,[25] because it leads to SLBs that are more optically uniform than SLBs formed using vesicles.[29, 36] To facilitate observation of bilayer reformation using fluorescence microscopy, the SLBs used here contained 0.1 wt% of the fluorescently-labeled lipid Rho-DPPE. In all experiments, SLBs were formed on the surfaces of NaOH-treated glass flow cells, and bilayer reformation was characterized by fluorescence microscopy with the direction of fluid flow oriented from the bottom to the top of each microscopy image. All initial studies were conducted using 50 μM solutions of AHL because this concentration is just under the limit of solubility of C16-AHL, the longest-tailed AHL investigated here, in our hands.

The addition of 50 μM 3-oxo-C12-AHL to DOPC SLBs resulted in the immediate formation of thin microtubules, some of which ultimately retracted and collapsed into hemispherical caps over a period of approximately 90 sec (Figure 2; Figure S2). This behavior is

consistent with that observed upon the introduction of 3-oxo-C12-AHL to SLBs formed using the vesicle fusion method,[25] suggesting that the bicelle method used to form our SLBs does not have a significant impact on the nature or extent of membrane remodeling.

Figure 2 also shows images of SLBs six min after exposure to 50 μM solutions the other remaining AHLs (additional images at selected time points showing the results of these experiments are provided in Figure S2). Inspection of these images reveals large differences in membrane reformation as a function of tail group structure. Whereas AHLs containing a 3-oxo group in their aliphatic tails (i.e., 3-oxo-C10-AHL, 3-oxo-C12-AHL, 3-oxo-C14-AHL, and 3-oxo-C16-AHL) generally led to the growth of microtubules of varying lengths on the surface of the bilayer (many of which, again, collapsed over time into hemispherical caps), exposure to AHLs that lack a 3-oxo group in their tails (C10-AHL, C12-AHL, C14-AHL, and C16-AHL) generally led to the immediate and direct formation of structures that were similar to, but in many cases smaller and more irregularly shaped than, the hemispherical caps formed when 3-oxo compounds were introduced to the bilayer. We note that a very small number of the caps observed under these conditions appeared to result from the formation of short tubules (~5–40 μm in length) that collapsed into hemispherical caps shortly (between 5 sec and 4 min) after formation and did not otherwise persist over the timescales of the experiments described here (6 min). In addition, for AHLs containing a 3-oxo group, the extent of reformation varied qualitatively with tail length, with 3-oxo-C14-AHL leading to the most visually striking reformation and the highest areal density of tubules and hemispherical caps. We did not observe any clear qualitative correlations between tail length and the extent of bilayer reformation observed for AHLs that lack a 3-oxo group. Finally, and in general, hemispherical caps promoted by exposure to AHLs without 3-oxo

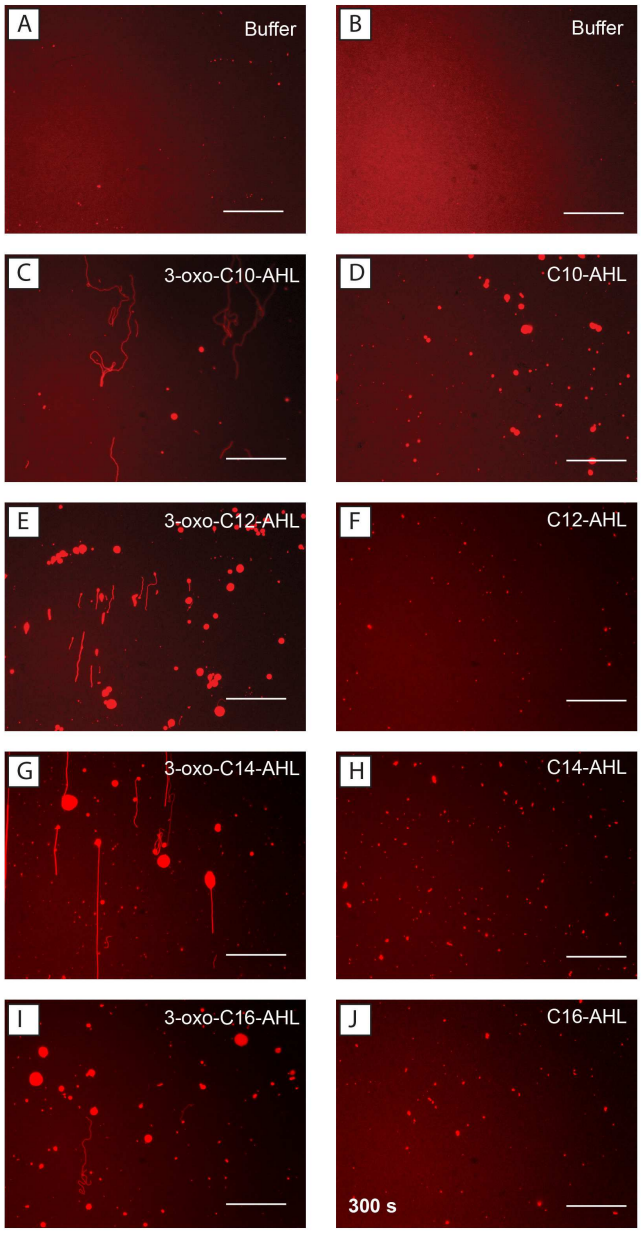


Figure 2: Representative top-down fluorescence micrographs of fluorescently-labeled DOPC SLBs that are either (A,B) stable under a continuous flow of buffer or (C-J) undergo structural reformations after exposure to a continuous flow of 50 µM solutions of (C) 3-oxo-C10-AHL, (D) C10-AHL, (E) 3-oxo-C12-AHL, (F) C12-AHL, (G) 3-oxo-C14-AHL, (H) C14-AHL, (I) 3-oxo-C16-AHL, and (J) C16-AHL. Images were acquired 360 sec after the onset of membrane restructuring, except for (J), which was acquired after 300 sec. The direction of flow in all images was from the bottom to the top of the image. Scale bars are 30 µm.

groups were smaller, but far more numerous, than those promoted by AHLs containing 3-oxo groups.

Our past work on the characterization of interactions of 3-oxo-C12-AHL with DOPC SLBs[25] provided a framework for understanding the formation and/or retraction of microtubules and hemispherical caps in terms of (i) the accumulation and relief of asymmetrical stresses that develop within a bilayer upon the intercalation of an amphiphile and (ii) thermodynamic barriers associated with the translocation of an amphiphile from the outer to the inner leaflet of a bilayer that alleviate these stresses. In this framework, molecules that have lower thermodynamic barriers to translocation (and that thus traverse the bilayer more rapidly) would generally be expected to promote the formation of lower-curvature hemispherical caps; molecules with higher barriers to translocation would be expected to form higher-curvature tubules as a means of relieving asymmetrical stresses between bilayer leaflets.[25] Molecules with intermediate barriers to translocation were proposed to form tubules that subsequently retract or collapse into hemispherical caps on the timescale during which flip-flop occurs.

Recently reported molecular dynamics (MD) simulations predict that AHLs containing 3-oxo groups in their tails generally have barriers to bilayer translocation that are approximately 5 kJ/mol higher than AHLs that lack 3-oxo groups.[24] These simulation predictions and the framework described above are generally consistent with the fluorescence microscopy observations reported here: AHLs containing 3-oxo groups, which have larger predicted thermodynamic barriers to translocation, generally form tubules that collapse into hemispherical caps (Figure 2; Figure S2), and the remaining AHLs, which do not contain 3-oxo groups and have lower predicted barriers to translocation, are observed to form hemispherical caps without first forming tubules. We note that differences in spontaneous curvature resulting from the presence of

a 3-oxo group in the tail could also play a role in promoting the different bilayer remodeling morphologies observed here, as suggested in other studies on amphiphile-induced reformation in SLBs.[37] We return to consideration of AHL translocation and impacts of tail group structure on bilayer reformation again below.

Characterization of the Interactions of AHLs with DOPC Membranes Using QCM-D

The microscopy results above reveal large, qualitative differences in the remodeling of supported DOPC membranes that result from differences in both AHL tail group oxidation state and length. To provide additional quantitative insight into these differences in behavior, we used quartz crystal microbalance with dissipation (QCM-D) measurements to examine changes in structural reformation in the presence of AHLs. Figure S3 shows changes in frequency (ΔFrequency, blue line) and dissipation (ΔDissipation, orange line) upon exposure of DOPC SLBs to AHL solutions (solid arrows) and subsequent buffer washes (dashed arrows). Each of those data sets is representative of either three or four independent replicates, the average and standard deviation of which are shown in Figure 3.

These experiments reveal that introduction of 50 μM 3-oxo-C12-AHL to SLBs yields changes in frequency and dissipation of -2.5 ± 0.6 Hz and 1.0 ± 0.2 x10^6 (Figure 3), respectively, which is consistent with the results of our prior studies using SLBs formed by vesicle fusion.[25] Exposure to solutions of C12-AHL resulted in changes in frequency and dissipation of -1.3 ± 0.8 Hz and 2.5 ± 1.0 x10^6, respectively. Interestingly, we observed larger changes in frequency for 3-oxo-C12-AHL than C12-AHL, but smaller dissipation changes, a result that was unexpected because, in all previous experiments by our laboratories[25] and others,[38] if an amphiphile promotes a larger change in frequency than another, it is generally accompanied by a larger change in

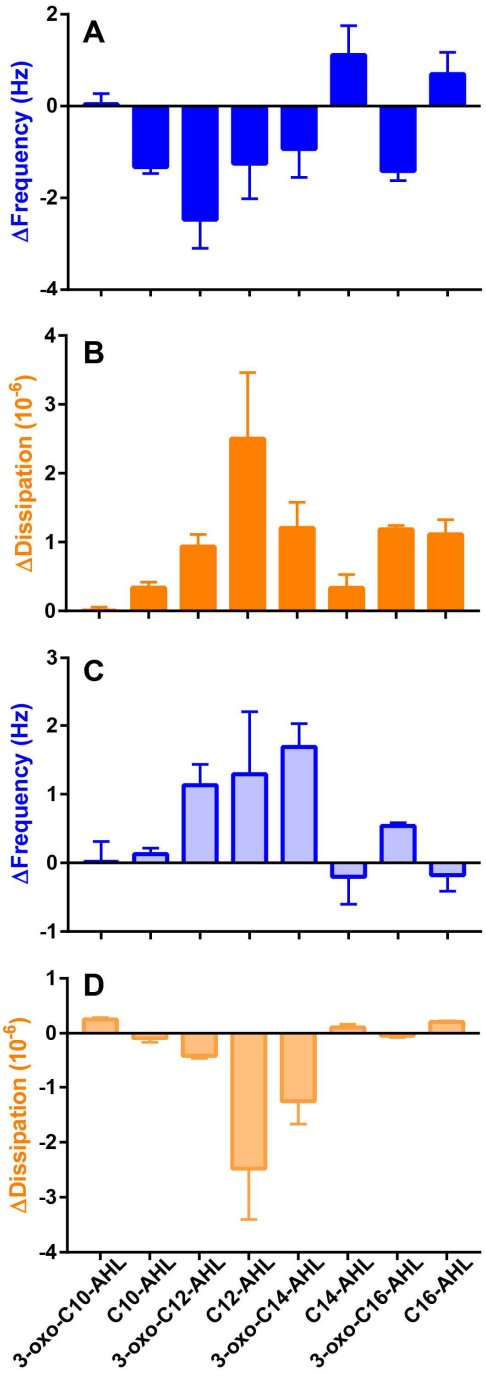


Figure 3: Changes in (A,B) frequency (ΔFrequency) and (C,D) dissipation (ΔDissipation) for DOPC SLBs introduced to solutions of the AHLs shown in Figure 1 for 45 min (A,C) or after 45 min of buffer wash at various concentrations (B,D). The values shown are the means and a single standard deviation of three or four experiments (n= 3–4).

dissipation. This deviation from expected behavior when comparing the interactions of 3-oxo-C12-AHL and C12-AHL with SLBs could potentially arise from differences in the aggregated states of the two molecules, as C12-AHL is aggregated at 50 μM while 3-oxo-C12-AHL is not (Table 1), a factor reported previously to alter the interactions of other amphiphiles with bilayers.[25, 35, 39] If this is the case, the larger changes in dissipation associated with interactions of C12-AHL could result from the adsorption of aggregates of C12-AHL to the surface of the bilayer.

We next measured changes in frequency and dissipation in DOPC SLBs exposed to the remaining AHLs using QCM-D. As shown in Figure 3 and Figure S3, all of these AHLs promoted some change in both frequency and dissipation when introduced to bilayers at a concentration of 50 μM. Introduction of 3-oxo-C10-AHL and C10-AHL, which are not aggregated at this concentration (Table 1), resulted in changes in frequency and dissipation of essentially zero for 3-oxo-C10-AHL and changes of -1.3 ± 0.1 Hz and 0.3 ± 0.1 x10^6 for C10-AHL, supporting a physical picture in which C10-AHL interacts with the bilayer to a greater extent and leads to more extensive bilayer reformation. This result is again consistent with the results of MD simulations, which predict that related AHL-type compounds that do not contain 3-oxo groups can interact preferentially with lipid bilayers relative to their counterparts that do contain 3-oxo groups.[24]

The opposite was observed when solutions of C14-AHL and 3-oxo-C14-AHL or C16-AHL and 3-oxo-C16-AHL, all of which exhibit aggregation at concentrations of 50 μM, were introduced to the bilayers. Changes in frequency and dissipation were measured to be (i) 1.1± 0.6 Hz and 0.3 ± 0.2 x10^6 and (ii) -0.9 ± 0.6 Hz and 1.2 ± 0.4 x10^6 for C14-AHL and 3-oxo-C14-AHL, respectively, and (iii) 0.7 ± 0.5 Hz and 1.2 ± 0.1 x10^6 and (iv) -1.4 ± 0.2 Hz and 1.2 ± 0.1 x10^6 for C16-AHL and 3-oxo-C16-AHL, respectively (Figure 3A,C and Figure S3(E-H)). These results suggest that, for AHLs with tails longer than 12 carbons, AHLs containing 3-oxo groups associate

with DOPC bilayers more than their non-3-oxo counterparts. We note that this result contrasts with the predictions of past MD simulations discussed above; however, those simulations explicitly considered interactions with AHLs in their monomeric states, and did not account for behaviors that could arise from the presence of AHL aggregates or their potential impacts on interactions of AHLs with bilayers.[24] There does not appear to be any discernable monotonic relationship between AHL structure and changes in dissipation, but we did observe that AHLs with tail lengths around 12 carbons led to increased changes in dissipation relative to their longer- or shorter-chained counterparts. Subsequent washing of AHL-treated membranes with buffer (at times denoted by the locations of the dashed arrows in Figure S3 and Figure 3B,D) resulted, in most cases, in the apparent semi-reversible desorption of AHLs, indicated by changes in frequency and dissipation opposite to those observed upon initial exposure of the bilayers to AHL.

Taken together, these results are generally consistent with the results of our fluorescence microscopy experiments and provide support for the conclusion that the oxidation state at carbon-3 of the acyl tail can impact the interactions of AHLs with lipid bilayers significantly. Our results suggest that AHLs containing 3-oxo groups can associate with bilayers to a greater degree than their non-3-oxo counterparts, as denoted by larger frequency changes upon interaction with the bilayers. We note that our results are generally consistent with a previous report by Song et al. on the adsorption of AHLs to the membrane fraction of mammalian cells.[22] In that study, the authors introduced exogenous AHLs to cultures of mammalian cells and reported the relative abundance of the AHLs in the supernatant, cytosolic, and membrane fractions, finding increased proportions of 3-oxo-C10-AHL, 3-oxo-C12-AHL, and 3-oxo-C14-AHL to be associated with the membrane fraction, as compared to otherwise identical, non-3-oxo AHLs. Additionally, the authors observed the interaction of 3-oxo-containing AHLs with cell membranes to lead to the disruption of ordered

lipid phases and, subsequently, to cell death (apoptosis). That past report suggests that changes in AHL tail group structure could play roles that extend beyond bacterial signaling, including bilayer-mediated mechanisms associated with potential inter-kingdom signaling and/or bacterial control over host-cell behaviors.[22] Our results outlined here provide further support for the view that differences in AHL tail group structure—and, in particular, differences in oxidation state at the third carbon of the acyl tail—can affect large changes in the structures and dynamics of model lipid membranes.

Influence of Tail Group on Transport of Cargo Across Membranes in Lipid Vesicles

We recently reported that 3-oxo-C12-AHL can facilitate the transport of encapsulated small-molecule cargo across the unsupported lipid membranes of large unilamellar vesicles (LUVs) composed of DOPC using a well-established calcein dye leakage assay.[25] In that study, we observed small but significant amounts of dye leakage across membranes treated with concentrations of AHLs that also promote the formation of tubules on the surface of SLBs. That work constituted the first demonstration, to our knowledge, that this bacterial signaling molecule can promote the transport of other molecules across lipid bilayers, and suggests that dynamics associated with large-scale membrane remodeling promoted by contact with AHLs can compromise membrane barrier properties and integrity. To further interrogate this hypothesis, we conducted a final series of experiments to characterize the influence of AHL acyl tail structure, and associated changes in bilayer reformation observed above, on membrane leakage. These experiments were performed using DOPC LUVs (vesicle diameter ~130 nm; see Materials and Methods) loaded with the self-quenching dye calcein, similar to those used in our previous study,[25]

and measurements of fluorescence in the surrounding solution were used to characterize membrane leakage (Figure 4).

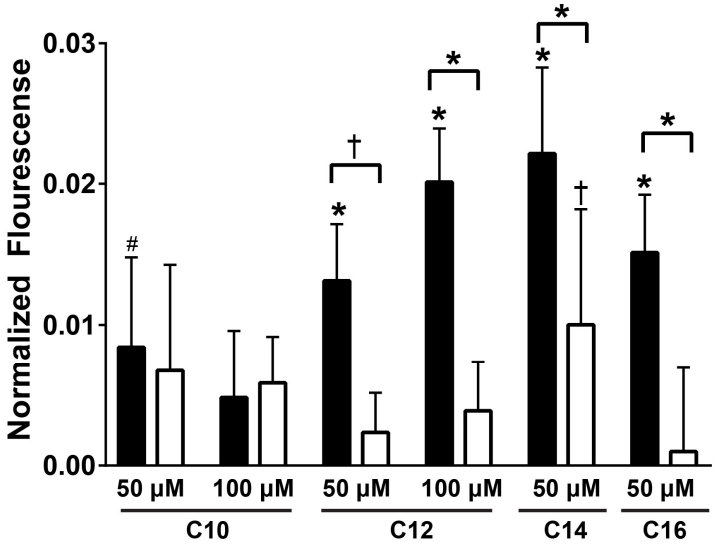


Figure 4: Normalized calcein fluorescence intensity values of solutions containing the AHLs shown in Figure 1 introduced at various concentrations to 100 µM of calcein-loaded DOPC vesicles. Black bars represent 3-oxo-containing AHLs and white bars represent non-3-oxo-containing AHLs. All values shown are the average and standard deviation of three independent experiments. ($^{\#}p < 0.05$, $^{\dagger}p < 0.005$, $^{*}p < 0.0005$). Significance indicators above individual bars indicate significance between that condition and the buffer control; bracketed significance indicators represent significance between two AHLs that vary by the presence or absence of a 3-oxo group.

Figure 4 shows changes in normalized fluorescence over time for solutions containing calcein-loaded LUVs in contact with AHLs that either contain a 3-oxo group (filled bars) or lack a 3-oxo group (open bars). Inspection of Figure 4 reveals low but statistically significant amounts of calcein leakage when 3-oxo-C10-AHL, 3-oxo-C12-AHL, 3-oxo-C14-AHL, C14-AHL and 3-oxo-C16-AHL were introduced to LUVs. In contrast, none of the remaining AHLs (C10-AHL, C12-AHL, C16-AHL) promoted dye leakage at levels that were significantly different from buffer controls. With the exception of 3-oxo-C10-AHL, all of the other 3-oxo AHLs promoted more leakage than their non-3-oxo counterparts. In general, these observations correlate to the nature of

bilayer reformations observed and described above, with the subset of AHLs that promote the formation of tubules (which may, or may not, subsequently collapse into hemispherical caps) leading to more dye leakage.

Previous reports have demonstrated that differences in the ability of amphiphiles to translocate across a bilayer can impact the ways through which they change the permeability of or solubilize a membrane.[40-42] At lower surfactant concentrations, below the concentration at which a surfactant fully solubilizes the membrane, amphiphiles that accumulate in the outer leaflet of the membrane, and therefore lead to accumulated asymmetric bilayer strain, have been suggested to temporarily permeabilize vesicles as they translocate across the bilayer to relieve that monolayer curvature strain.[40, 41, 43-45] Although the physical mechanism of molecular transport and leakage in our present work is not fully clear, it is likely to be related to the accumulation of monolayer curvature strain upon intercalation of AHLs that we propose, as described above, to lead to larger-scale membrane remodeling. This overall physical picture is consistent with the observation that AHLs that contain a 3-oxo group lead to dye leakage, and AHLs that lack a 3-oxo group do not. Finally, these results are interesting in the context of past reports suggesting that AHLs that contain a 3-oxo group can lead to programed cell death[22] or inhibit mammalian cell proliferation[46] at lower concentrations than their otherwise identical non-3-oxo counterparts, as highlighted above. We note that there could be several possible mechanisms through which AHLs could have an influence on cell proliferation,[47] including the membrane-facilitated apoptotic pathway described by Song et al.;[22] however, our results suggest a possibility that AHL-mediated membrane destabilization and/or reformation of host-cell membranes could also influence cell proliferation.

Summary and Conclusions

The work reported here demonstrates that differences in acyl tail group length and oxidation state can lead to large differences in the behaviors of eight structurally related bacterial AHLs in solution and in contact with model lipid membranes. Measurements of AHL aggregation in solution revealed trends with respect to tail length that are similar to those observed for other classes of amphiphiles, and that the presence of a 3-oxo group on the acyl tail substantially increased the CAC. The presence (or absence) of a 3-oxo group also has a substantial impact on the extent of large-scale membrane remodeling observed when AHLs are placed in contact with SLBs composed of the phospholipid DOPC. AHLs containing a 3-oxo group promoted the formation of tubules, some of which collapsed into hemispherical caps over time; AHLs that lack 3-oxo groups predominantly form hemispherical caps. These experimental results are in agreement with a theoretical framework proposed in past studies[25] suggesting that differences in the formation of tubules and caps in SLBs result from differences in the timescales on which AHLs are able to translocate across lipid bilayers to which they adsorb and, thereby, relieve asymmetrical bilayer stresses. QCM-D measurements revealed larger changes in frequency upon exposure of SLBs to solutions containing 3-oxo-AHLs relative to non-3-oxo AHLs, suggesting that AHLs containing 3-oxo groups associate with bilayers to a greater extent than their non-3-oxo counterparts. This result in the model lipid membranes used here is consistent with past observations in more complex systems that found AHLs containing 3-oxo groups to associate with the membrane fractions of mammalian cells to a greater degree than otherwise identical AHLs lacking a 3-oxo group.[22] Finally, AHLs containing 3-oxo groups facilitated greater transport of the self-quenching dye calcein across the unsupported membranes of DOPC vesicles, suggesting that the 3-oxo group may also play a role in bilayer disruption and destabilization. When combined, our results demonstrate

that tail-group oxidation state can have substantial impacts on the interactions of long-chained AHLs with lipid membranes.

The results of this study on model lipid membranes hint at interactions between AHLs and lipid bilayers, and several multi-scale phenomena that result from them, that could help provide insight into past observations on the influence of AHLs in biological contexts (e.g., to mediate bacterial cell-cell communication or inter-species host-cell interactions). In view of the dramatic changes caused by the presence of the 3-oxo group in these AHLs, it would also be interesting to examine AHLs with alternate oxidation states, such as naturally occurring 3-OH AHLs, or other non-native motifs at this position to potentially direct lipid membrane interactions toward specific desired outcomes. In this broad context, the results of this fundamental study could provide guidance for the design of new classes of synthetic materials that interact with or respond selectively to bacteria (for example, to design sensor elements or drug delivery vehicles that identify or respond differentially to communities of bacteria that use AHLs containing 3-oxo groups for communication). It is also possible that differences in bilayer reformation observed here, including the time scales over which tubules form and then collapse into caps, could, with further study, provide a basis for characterizing the relative time scales on which amphiphiles translocate across lipid bilayers. Studies to this end are currently underway and will be reported in due course.

Acknowledgements. Financial support for this work was provided by the National Science Foundation through a grant provided to the UW–Madison Materials Research Science and Engineering Center (MRSEC; DMR-1720415). The authors acknowledge the use of instrumentation supported by the NSF through the UW MRSEC (DMR-1720415). H. E. B.

acknowledges support from the NIH (R35 GM131817) for this work. NMR characterization was performed in facilities in the Department of Chemistry at UW–Madison that are supported by the NSF (CHE-0342998). C. G. G. was supported in part by a NSF Graduate Research Fellowship. The authors gratefully acknowledge Samarthaben Patel and Lawrence Chen for many helpful discussions and Thomas Polaske, Dr. Kayleigh Nyffeler, Dr. Daniel Manson, and Dr. Michelle Boursier for providing many of the AHLs used in this study.

References

1. Daniels, R.; Vanderleyden, J.; Michiels, J., Quorum sensing and swarming migration in bacteria. *FEMS Microbiol. Rev.* **2004,** *28* (3), 261-289.

2. Waters, C. M.; Bassler, B. L., Quorum sensing: Cell-to-cell communication in bacteria. *Annu. Rev. Cell Dev. Biol.* **2005,** *21*, 319-346.

3. de Kievit, T. R., Quorum sensing in *Pseudomonas aeruginosa* biofilms. *Environ. Microbiol.* **2009,** *11* (2), 279-288.

4. Coggan, K. A.; Wolfgang, M. C., Global Regulatory Pathways and Cross-Talk Control *Pseudomonas aeruginosa* Environmental Lifestyle and Virulence Phenotype. *Curr. Issues Mol. Biol.* **2012,** *14* (2), 47-69.

5. Rutherford, S. T.; Bassler, B. L., Bacterial quorum sensing: Its role in virulence and possibilities for its control. *Cold Spring Harb. Perspect. Med.* **2012,** *2* (11), a012427.

6. Whiteley, M.; Diggle, S. P.; Greenberg, E. P., Progress in and promise of bacterial quorum sensing research. *Nature* **2017,** *551* (7680), 313-320.

7. Crone, S.; Vives-Florez, M.; Kvich, L.; Saunders, A. M.; Malone, M.; Nicolaisen, M. H.; Martinez-Garcia, E.; Rojas-Acosta, C.; Gomez-Puerto, M. C.; Calum, H.; Whiteley, M.; Kolter, R.; Bjarnsholt, T., The environmental occurrence of *Pseudomonas aeruginosa*. *APMIS* **2020,** *128* (3), 220-231.

8. Papenfort, K.; Bassler, B. L., Quorum sensing signal-response systems in Gram-negative bacteria. *Nat. Rev. Microbiol.* **2016,** *14* (9), 576-588.

9. Ng, W. L.; Bassler, B. L., Bacterial quorum-sensing network architectures. *Annu. Rev. Genet.* **2009,** *43*, 197-222.

10. Welch, M.; Mikkelsen, H.; Swatton, J. E.; Smith, D.; Thomas, G. L.; Glansdorp, F. G.; Spring, D. R., Cell-cell communication in gram-negative bacteria. *Mol. BioSyst.* **2005,** *1* (3), 196-202.

11. Thoendel, M.; Kavanaugh, J. S.; Flack, C. E.; Horswill, A. R., Peptide Signaling in the Staphylococci. *Chem. Rev.* **2011,** *111* (1), 117-151.

12. Fuqua, C.; Greenberg, E. P., Listening in on bacteria: Acyl-homoserine lactone signalling. *Nat. Rev. Mol. Cell Biol.* **2002,** *3* (9), 685-695.

13. Moore, J. D.; Rossi, F. M.; Welsh, M. A.; Nyffeler, K. E.; Blackwell, H. E., A Comparative Analysis of Synthetic Quorum Sensing Modulators in *Pseudomonas aeruginosa*: New Insights into Mechanism, Active Efflux Susceptibility, Phenotypic Response, and Next-Generation Ligand Design. *J. Am. Chem. Soc.* **2015,** *137* (46), 14626-14639.

14. Boursier, M. E.; Moore, J. D.; Heitman, K. M.; Shepardson-Fungairino, S. P.; Combs, J. B.; Koenig, L. C.; Shin, D.; Brown, E. C.; Nagarajan, R.; Blackwell, H. E., Structure-Function Analyses of the N-Butanoyl-L-Homoserine Lactone Quorum-Sensing Signal Define Features Critical to Activity in RhlR. *ACS Chem. Biol.* **2018,** *13* (9), 2655-2662.

15. Welsh, M. A.; Blackwell, H. E., Chemical probes of quorum sensing: From compound development to biological discovery. *FEMS Microbiol. Rev.* **2016,** *40* (5), 774-794.

16. Daniels, R.; Reynaert, S.; Hoekstra, H.; Verreth, C.; Janssens, J.; Braeken, K.; Fauvart, M.; Beullens, S.; Heusdens, C.; Lambrichts, I.; De Vos, D. E.; Vanderleyden, J.; Vermant, J.; Michiels, J., Quorum signal molecules as biosurfactants affecting swarming in *Rhizobium etli*. *Proc. Natl. Acad. Sci. U. S. A.* **2006,** *103* (40), 14965-14970.

17. Davis, B. M.; Jensen, R.; Williams, P.; O'Shea, P., The Interaction of N-Acylhomoserine Lactone Quorum Sensing Signaling Molecules with Biological Membranes: Implications for Inter-Kingdom Signaling. *PLoS One* **2010,** *5* (10), e13522.

18. Davis, B. M.; Richens, J. L.; O'Shea, P., Label-Free Critical Micelle Concentration Determination of Bacterial Quorum Sensing Molecules. *Biophys. J.* **2011,** *101* (1), 245-254.

19. Jakubczyk, D.; Barth, C.; Kubas, A.; Anastassacos, F.; Koelsch, P.; Fink, K.; Schepers, U.; Brenner-Weiss, G.; Brase, S., Deuterium-labelled N-acyl-L-homoserine lactones (AHLs)-inter-kingdom signalling molecules-synthesis, structural studies, and interactions with model lipid membranes. *Anal. Bioanal. Chem.* **2012,** *403* (2), 473-482.

20. Barth, C.; Jakubczyk, D.; Kubas, A.; Anastassacos, F.; Brenner-Weiss, G.; Fink, K.; Schepers, U.; Brase, S.; Koelsch, P., Interkingdom Signaling: Integration, Conformation, and Orientation of N-Acyl-L-homoserine Lactones in Supported Lipid Bilayers. *Langmuir* **2012,** *28* (22), 8456-8462.

21. Lentini, R.; Martin, N. Y.; Forlin, M.; Belmonte, L.; Fontana, J.; Cornella, M.; Martini, L.; Tamburini, S.; Bentley, W. E.; Jousson, O.; Mansy, S. S., Two-Way Chemical Communication between Artificial and Natural Cells. *ACS Cent. Sci.* **2017,** *3* (2), 117-123.

22. Song, D. K.; Meng, J. C.; Cheng, J.; Fan, Z.; Chen, P. Y.; Ruan, H. F.; Tu, Z. Y.; Kang, N.; Li, N.; Xu, Y.; Wang, X. B.; Shi, F.; Mu, L. B.; Li, T. F.; Ren, W. R.; Lin, X.; Zhu, J.; Fang, X. H.; Amrein, M. W.; Wu, W. H.; Yan, L. T.; Lu, J. H.; Xia, T.; Shi, Y.,

Pseudomonas aeruginosa quorum-sensing metabolite induces host immune cell death through cell surface lipid domain dissolution. *Nat. Microbiol.* **2019,** *4* (1), 97-111.

23. Gahan, C. G.; Patel, S. J.; Boursier, M. E.; Nyffeler, K. E.; Jennings, J.; Abbott, N. L.; Blackwell, H. E.; Van Lehn, R. C.; Lynn, D. M., Bacterial Quorum Sensing Signals Self-Assemble in Aqueous Media to Form Micelles and Vesicles: An Integrated Experimental and Molecular Dynamics Study. *J. Phys. Chem. B* **2020,** *124* (18), 3616-3628.

24. Jin, T.; Patel, S. J.; Van Lehn, R. C., Molecular simulations of lipid membrane partitioning and translocation by bacterial quorum sensing modulators. *PLoS One* **2021,** *16* (2), e0246187.

25. Gahan, C. G.; Patel, S. J.; Chen, L. M.; Manson, D. E.; Ehmer, Z. J.; Blackwell, H. E.; Van Lehn, R. C.; Lynn, D. M., Bacterial Quorum Sensing Signals Promote Large-Scale Remodeling of Lipid Membranes. *Langmuir* **2021**, DOI: 10.1021/acs/langmuir.1c01204.

26. Yates, E. A.; Philipp, B.; Buckley, C.; Atkinson, S.; Chhabra, S. R.; Sockett, R. E.; Goldner, M.; Dessaux, Y.; Camara, M.; Smith, H.; Williams, P., N-acylhomoserine Lactones undergo lactonolysis in a pH-, temperature-, and acyl chain length-dependent manner during growth of *Yersinia pseudotuberculosis* and *Pseudomonas aeruginosa*. *Infect. Immun.* **2002,** *70* (10), 5635-5646.

27. Wang, L. H.; Weng, L. X.; Dong, Y. H.; Zhang, L. H., Specificity and enzyme kinetics of the quorum-quenching N-acyl homoserine lactone lactonase (AHL-lactonase). *J. Biol. Chem.* **2004,** *279* (14), 13645-13651.

28. Hodgkinson, J. T.; Galloway, W.; Casoli, M.; Keane, H.; Su, X. B.; Salmond, G. P. C.; Welch, M.; Spring, D. R., Robust routes for the synthesis of N-acylated-L-homoserine lactone (AHL) quorum sensing molecules with high levels of enantiomeric purity. *Tetrahedron Lett.* **2011,** *52* (26), 3291-3294.

29. Kolahdouzan, K.; Jackman, J. A.; Yoon, B. K.; Kim, M. C.; Johal, M. S.; Cho, N. J., Optimizing the Formation of Supported Lipid Bilayers from Bicellar Mixtures. *Langmuir* **2017,** *33* (20), 5052-5064.

30. Mayer, L. D.; Hope, M. J.; Cullis, P. R., Vesicles of variable sizes produced by a rapid extrusion procedure. *Biochim. Biophys. Acta* **1986,** *858* (1), 161-168.

31. Lapinski, M. M.; Castro-Forero, A.; Greiner, A. J.; Ofoli, R. Y.; Blanchard, G. J., Comparison of liposomes formed by sonication and extrusion: Rotational and translational diffusion of an embedded chromophore. *Langmuir* **2007,** *23* (23), 11677-11683.

32. Lee, M. R.; Raman, N.; Ortiz-Bermudez, P.; Lynn, D. M.; Palecek, S. P., 14-Helical Beta-Peptides Elicit Toxicity against *C. albicans* by Forming Pores in the Cell Membrane and Subsequently Disrupting Intracellular Organelles. *Cell Chem. Biol.* **2019,** *26* (2), 289-299.

33. Lichtenberg, D.; Ahyayauch, H.; Alonso, A.; Goni, F. M., Detergent solubilization of lipid bilayers: A balance of driving forces. *Trends Biochem. Sci.* **2013,** *38* (2), 85-93.

34. Powney, J.; Addison, C. C., The properties of detergent solutions. *Trans. Faraday Soc.* **1937,** *33* (2), 1243-1259.

35. Yoon, B. K.; Jackman, J. A.; Kim, M. C.; Sut, T. N.; Cho, N. J., Correlating Membrane Morphological Responses with Micellar Aggregation Behavior of Capric Acid and Monocaprin. *Langmuir* **2017,** *33* (11), 2750-2759.

36. Kim, M. C.; Gunnarsson, A.; Tabaei, S. R.; Hook, F.; Cho, N. J., Supported lipid bilayer repair mediated by AH peptide. *Phys. Chem. Chem. Phys.* **2016,** *18* (4), 3040-3047.

37. Yoon, B. K.; Park, S.; Ma, G. J.; Kolahdouzan, K.; Zhdanov, V. P.; Jackman, J. A.; Cho, N. J., Competing Interactions of Fatty Acids and Monoglycerides Trigger Synergistic Phospholipid Membrane Remodeling. *J. Phys. Chem. Lett.* **2020,** *11* (13), 4951-4957.

38. Yoon, B. K.; Jackman, J. A.; Kim, M. C.; Cho, N. J., Spectrum of Membrane Morphological Responses to Antibacterial Fatty Acids and Related Surfactants. *Langmuir* **2015,** *31* (37), 10223-10232.

39. Yoon, B. K.; Jackman, J. A.; Park, S.; Mokrzecka, N.; Cho, N. J., Characterizing the Membrane-Disruptive Behavior of Dodecylglycerol Using Supported Lipid Bilayers. *Langmuir* **2019,** *35* (9), 3568-3575.

40. Heerklotz, H., Membrane stress and permeabilization induced by asymmetric incorporation of compounds. *Biophys. J.* **2001,** *81* (1), 184-195.

41. Heerklotz, H., Interactions of surfactants with lipid membranes. *Q. Rev. Biophys.* **2008,** *41* (3-4), 205-264.

42. Lichtenberg, D.; Ahyayauch, H.; Goni, F. M., The Mechanism of Detergent Solubilization of Lipid Bilayers. *Biophys. J.* **2013,** *105* (2), 289-299.

43. Binder, H.; Lindblom, G., Charge-dependent translocation of the Trojan peptide penetratin across lipid membranes. *Biophys. J.* **2003,** *85* (2), 982-995.

44. Heerklotz, H.; Seelig, J., Leakage and lysis of lipid membranes induced by the lipopeptide surfactin. *Eur. Biophys. J.* **2007,** *36* (4-5), 305-314.

45. Zaragoza, A.; Aranda, F. J.; Espuny, M. J.; Teruel, J. A.; Marques, A.; Manresa, A.; Ortiz, A., Mechanism of Membrane Permeabilization by a Bacterial Trehalose Lipid Biosurfactant Produced by *Rhodococcus sp*. *Langmuir* **2009,** *25* (14), 7892-7898.

46. Chhabra, S. R.; Harty, C.; Hooi, D. S. W.; Daykin, M.; Williams, P.; Telford, G.; Pritchard, D. I.; Bycroft, B. W., Synthetic analogues of the bacterial signal (quorum sensing) molecule N-(3-oxododecanoyl)-L-homoserine lactone as immune modulators. *J. Med. Chem.* **2003,** *46* (1), 97-104.

47. Liu, Y. C.; Chan, K. G.; Chang, C. Y., Modulation of Host Biology by *Pseudomonas aeruginosa* Quorum Sensing Signal Molecules: Messengers or Traitors. *Front. Microbiol.* **2015,** *6*, 1226.

Supporting Information for Chapter 4

NMR Quantification of Phospholipids. To determine the concentration of phospholipids in stock solutions, quantitative $^{31}P[^{1}H]$ NMR spectroscopy was performed in 90% H_2O and 10% D_2O using a Bruker Avance-400 spectrometer with a BBFO probe. A relaxation delay (D1) of 11 sec was determined by inversion-recovery pulse sequence experiments. A phospholipid vesicle sample (890 µL in water) was mixed with 10 µL of Triton X-100 or rhamnolipid solution (to fully lyse the vesicles), and 100 µL of a triethylphosphine oxide (TPO) solution (100 mM in D_2O) was added as an internal standard. Integrations for phospholipid peaks were performed relative to the phosphorus peak of TPO (δ ~65 ppm). NMR acquisition parameters were as follows: PULPROG (pulse program) = zgig30, D1 (relaxation delay) = 11 s, SW (sweep width) = 405 ppm, O2P (transmitter frequency of f2 channel) = 3.75 ppm, NS (number of scans) = 64, DS (number of dummy scans) = 4, LB (line broadening factor) = 1.

Determination of CAC by Light Scattering. Figure S1 shows the static light scattering data used to determine the critical aggregation concentrations (CACs) listed in Table 1 of the main text. Linear regressions of scattered light intensity were performed separately for the points above and below the concentration at which the scattered light intensity of AHL solutions began to increase at increasing AHL concentrations. The CAC for each AHL was defined as the concentration corresponding to the intersection of these two regression lines. The CACs reported in Table 1 are the averages and standard deviations of the three samples shown as three separate colors in Figure S1. For some AHLs with longer tails, linear regressions of acquired data could not be performed with certainty. In these cases, we report estimated upper bounds of CAC values corresponding to the lowest concentration that was co-linear with values obtained at higher concentrations. Those reported values also corresponded to the lowest concentrations tested that exhibited clear deviations from background levels of scattered light intensity. For these longer-tailed AHLs, the values reported below thus represent an estimated upper bound of the CACs, and the actual CACs are likely lower than those values.

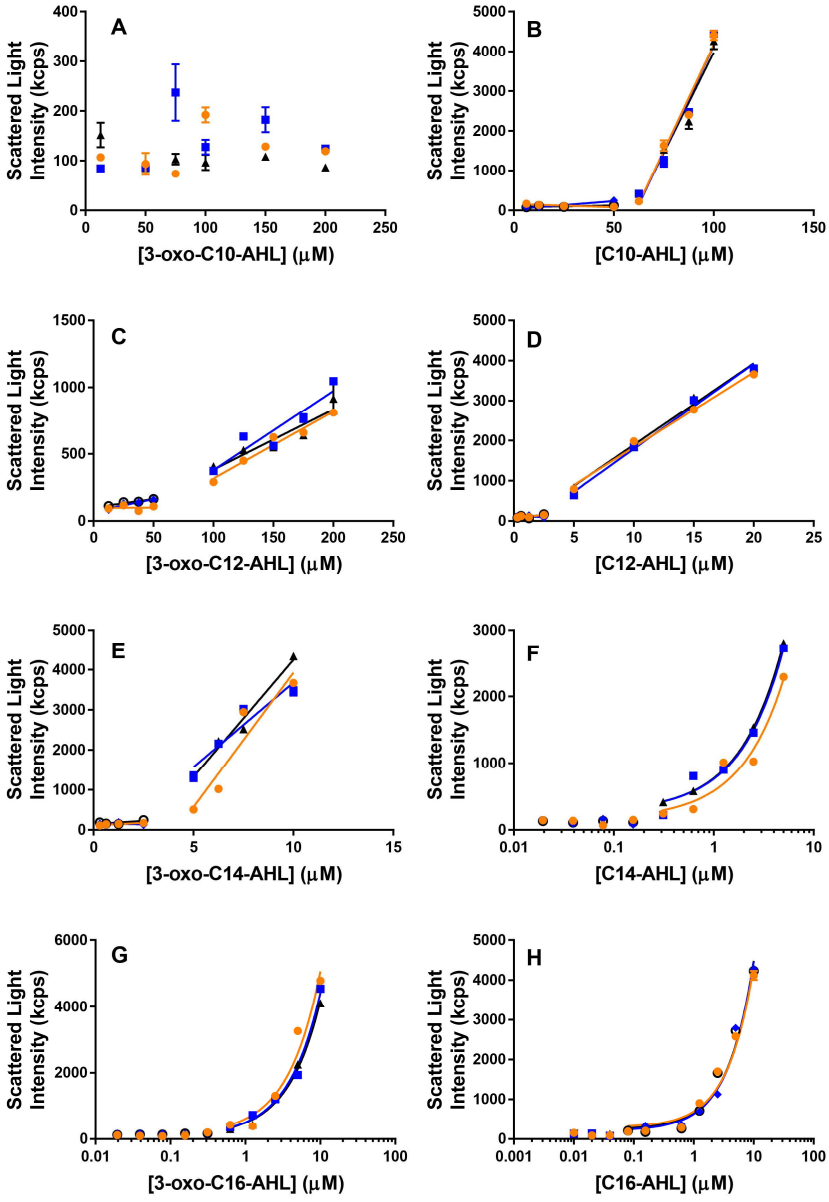


Figure S1: Determination of the critical aggregation concentrations (CACs) of the AHLs shown in Table 1 using static light scattering in buffer containing 1% DMSO. All points represent the average and standard deviation of three independent measurements of individual solutions of AHLs. Black, orange, and blue data points show results obtained for three sets of independently prepared samples. Note that AHL concentration in some panels is plotted on a log scale. The plots show the scattered light intensity of a 532 nm incident laser, detected at 173°, and at various concentrations of (A) 3-oxo-C10-AHL, (B) C10-AHL, (C) 3-oxo-C12-AHL, (D) C12-AHL, (E) 3-oxo-C14-AHL, (F) C14-AHL, (G) 3-oxo-C16-AHL, and (H) C16-AHL.

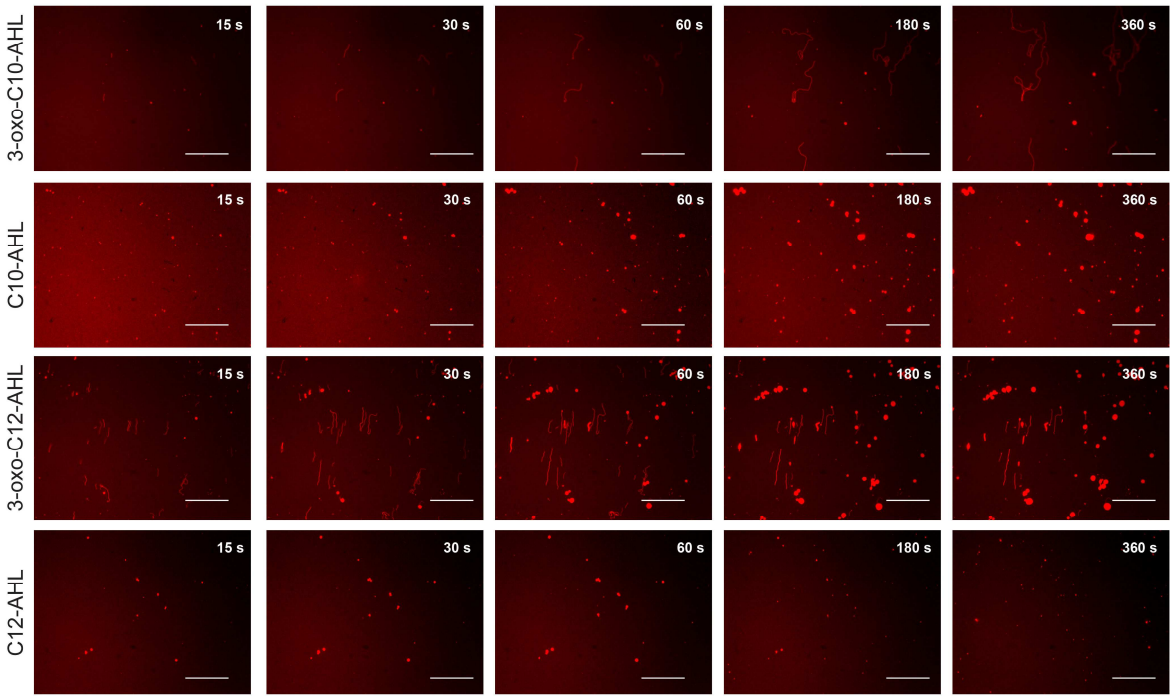


Figure S2A: Fluorescence micrographs showing the restructuring in DOPC SLBs after the introduction of 50 µM solutions of (*top to bottom*) 3-oxo-C10-AHL, C10-AHL, 3-oxo-C12-AHL, or C12-AHL over time. The images shown were acquired at various time points indicated in the top-right corner of the images after the first membrane restructuring event was observed. The 360-second images shown here are the same as those shown in Figure 2 of the main text. The AHL examined in each experiment is shown at the left of each row of images. The direction of flow in all the images was from the bottom to the top of the panel. Scale bars represent 30 µm.

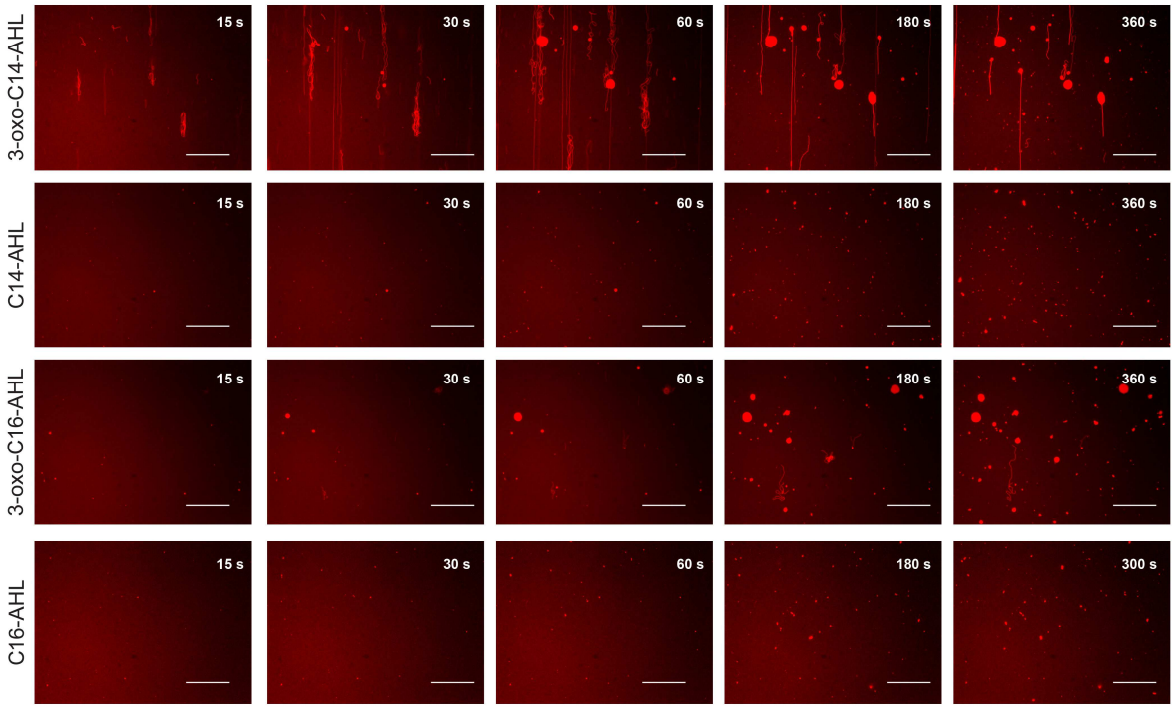


Figure S2B: Fluorescence micrographs showing the restructuring in DOPC SLBs after the introduction of 50 µM solutions of (*top to bottom*) 3-oxo-C14-AHL, C14-AHL, 3-oxo-C16-AHL, or C16-AHL over time. The images shown were acquired at various time points indicated in the top-right corner of the images after the first membrane restructuring event was observed. The 300-second or 360-second images shown here are the same as those shown in Figure 2 of the main text. The AHL examined in each experiment is shown at the left of each row of images. The direction of flow in all the images was from the bottom to the top of the panel. Scale bars represent 30 µm.

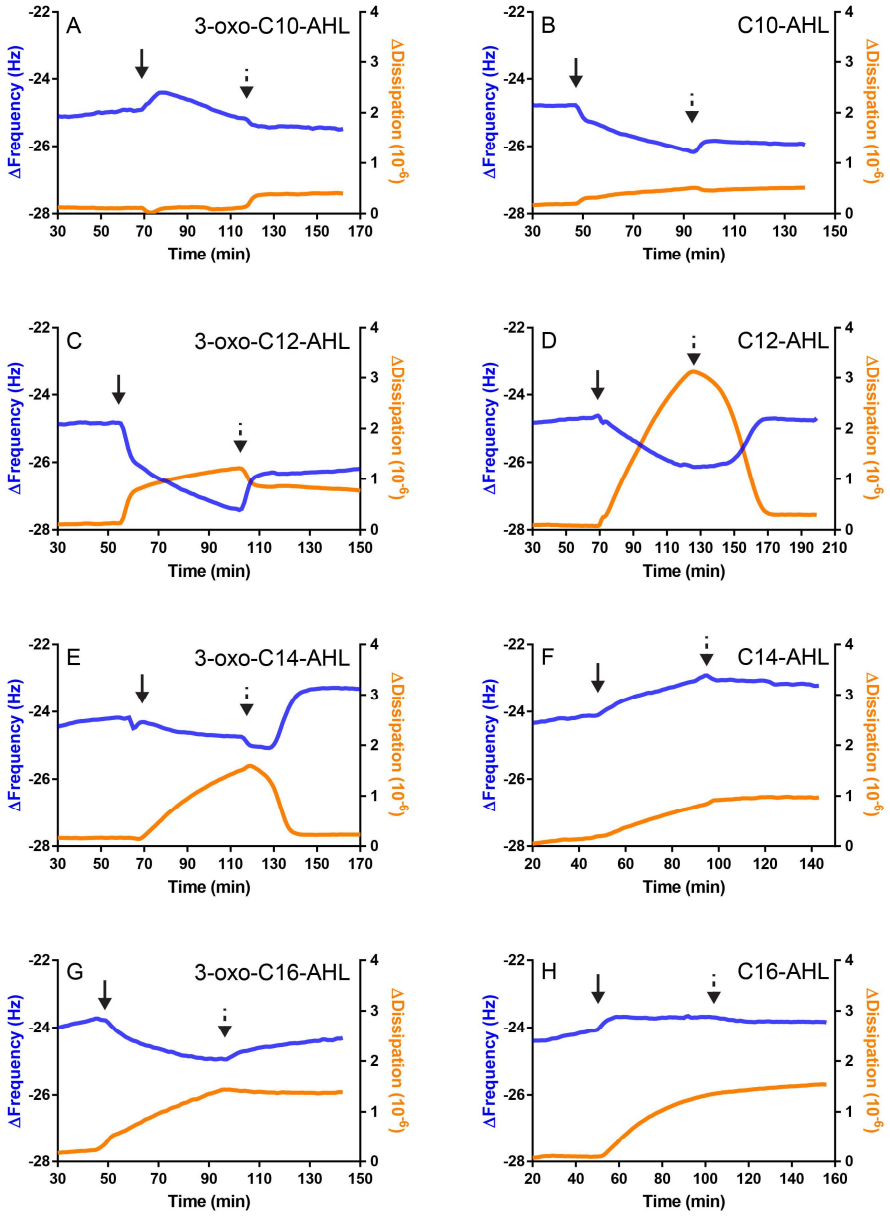


Figure S3: Representative QCM-D measurements of large-scale bilayer reformations in DOPC SLBs initiated by the introduction of 50 µM solutions of (A) 3-oxo-C10-AHL, (B) C10-AHL, (C) 3-oxo-C12-AHL, (D) C12-AHL, (E) 3-oxo-C14-AHL, (F) C14-AHL, (G) 3-oxo-C16-AHL, and (H) C16-AHL. The changes in frequency (ΔFrequency, blue lines) and dissipation (ΔDissipation, orange lines) shown are representative of three or four independent experiments. The initial measurement values (t = 0 min) of these experiments correspond to a DOPC SLB on an SiO_2 surface. AHL solutions were introduced to the bilayer at the time indicated by the solid arrow and a buffer wash was introduced at the time indicated by the dashed arrow.

Chapter 5

Interactions of Bacterial Quorum Sensing Signals with Model Lipid Membranes: Influence of Membrane Composition on Membrane Remodeling

ABSTRACT: We report on the influence of membrane composition on multi-scale remodeling in multicomponent lipid bilayers initiated by contact with the amphiphilic bacterial quorum sensing modulator 3-oxo-C12-AHL and its anionic head group hydrolysis product 3-oxo-C12-HS. We used fluorescence microscopy and quartz crystal microbalance with dissipation (QCM-D) to characterize membrane reformation that occurs when these amphiphiles are placed in contact with supported lipid bilayers (SLBs) composed of (i) 1,2-dioleoyl-sn-glycero-3-phosphocholine (DOPC) containing varying amounts of cholesterol, or (ii) mixtures of DOPC and either 1,2-dioleoyl-sn-glycero-3-phosphoethanolamine (DOPE; a conical zwitterionic lipid) or 1,2-dioleoyl-sn-glycero-3-phospho-L-serine (DOPS; a model anionic lipid). In general, we observe these mixed-lipid membranes to undergo remodeling events—including the formation and subsequent collapse of long tubules and the formation of hemispherical caps—upon introduction to biologically relevant concentrations of 3-oxo-C12-AHL and 3-oxo-C12-HS in ways that differ substantially from those observed in single-component DOPC membranes. These differences and associated dynamics can be understood in terms of the influence of membrane composition on timescales of molecular flip-flop, lipid packing defects, and lipid phase segregation in these materials. The lipid components investigated here are representative of classes of lipids that comprise cell membranes and many useful synthetic soft materials. These studies thus represent a first step toward an understanding of the ways in which membrane composition can impact interactions with this important class of bacterial signaling molecule. Overall, our results provide useful insight into interactions of AHLs with lipid membranes of increasing complexity and provide guidance that could be useful for the design of more sophisticated and compositionally complex self-assembled soft materials, including sensing elements or drug delivery vehicles, that can respond to molecules that mediate communication in communities of bacteria.

Introduction

The lipids that constitute the membranes of cells and many soft materials are structurally diverse and play important roles in facilitating cell function and imparting other useful behaviors.[1-5] The membranes of mammalian cells comprise at least seven structurally unique lipids, including cholesterol, phosphatidylcholine (PC), phosphatidylethanolamine (PE), and phosphatidylserine (PS).[1, 2] The relative compositions of these lipids influence many physical and mechanical properties of natural and synthetic membranes, including surface charge, bending rigidity, and curvature.[6-9] Membrane composition also play key roles in biological functions[1] such as protein binding specificity,[6] membrane fusion,[10] and cell division.[11] Most lipid-based assemblies are dynamic, and can undergo changes in physical properties, structural reformations and molecular reorganization as a response to environmental stimuli, including changes in pH[3, 12] and the presence of metal ions,[13-15] the adsorption of proteins,[16, 17] or interactions with small molecules,[18-21] in ways that can depend critically on the relative abundance of each constituent lipid.

The work reported here was motivated broadly by Chapters 3 and 4 of this thesis in which we demonstrated that N-acyl homoserine lactones (AHLs), a class of nonionic, small-molecule amphiphiles used by many Gram-negative bacteria to coordinate virulent behavior,[22-24] can interact with and promote large-scale reformations in model, single-component lipid membranes composed of the phospholipid 1,2-dioleoyl-sn-glycero-3-phosphocholine (DOPC).[25, 26] In this study, we sought to characterize interactions of AHLs with more complex, multi-component lipid membranes and better understand how differences in membrane composition and properties (e.g., fluidity, etc.) can impact subsequent multi-scale remodeling in response to these bacterial signals.

AHLs possess a relatively polar homoserine lactone head group and an aliphatic tail of varying length (e.g., 3-oxo-C12-AHL, Figure 1),[22, 23] and have previously been demonstrated to

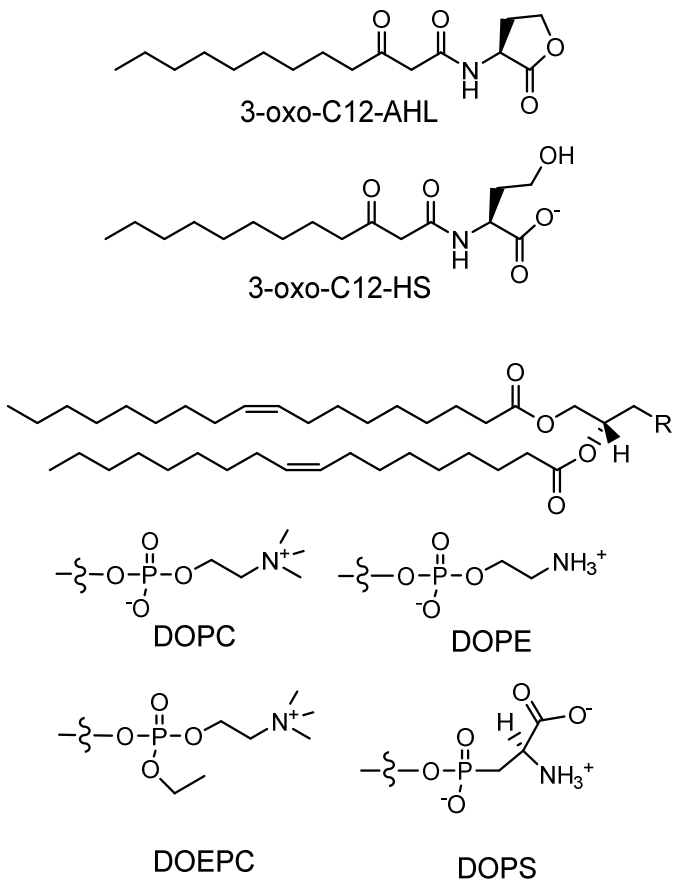


Figure 1: Structures of the AHLs and lipids used in this study.

undergo molecular self-assembly in solution[27, 28] and interact with other self-assembled structures, including lipid bilayers,[25, 26, 29-32] in ways that are similar to other classes of non-ionic surfactants.[18-20, 33] The homoserine lactone head group of AHLs is readily hydrolyzed in aqueous media, leading to anionic, ring-opened homoserine (HS) head group products[34, 35] (e.g., 3-oxo-C12-HS, Figure 1) that have also been demonstrated to interact with lipid membranes.[25] In Chapters 3 and 4 of this thesis, it was reported that 3-oxo-C12-AHL, 3-oxo-C12-HS, and other structurally diverse long-chained AHLs can interact with supported lipid bilayers (SLBs) composed of DOPC and promote the formation of extended micrometer-scale tubules and hemispherical 'caps' on the surfaces of the bilayers.[25, 26] That past work also demonstrated that changes in the head and tail group structures of AHLs can impact the nature of these remodeling

events substantially (e.g., leading to changes in the dynamics or relative proportions of these structures).[25, 26] The results of those studies provide useful insight into fundamental factors, such as the timescales on which amphiphilic molecules translocate across lipid bilayers, that influence multi-scale remodeling and provide guidance for the design of synthetic materials that can respond to chemical signatures produced by bacterial communities. The single-component membrane models used in those studies do not, however, reflect the compositional complexities that are typical of many biological membranes (or many synthetic soft materials systems)[1-5] and that likely underlie many unexplored or currently unappreciated roles that AHLs could play in mediating interactions of bacteria with these systems. Of particular interest, in this context, are recent past studies demonstrating that lipid bilayers containing cholesterol or lipid rafts can interact preferentially with AHLs, and that these interactions can lead to subsequent membrane depolarization[29] to a greater extent than observed in membranes of reduced complexity or the mixing of segregated lipid phases.[32]

Here, we report on the influence of lipid membrane composition on multi-scale phenomena arising from interactions of model SLBs with 3-oxo-C12-AHL and its head group hydrolysis product 3-oxo-C12-HS. We used fluorescence microscopy and quartz crystal microbalance with dissipation (QCM-D) to characterize multi-scale restructuring that occurs when these amphiphiles are placed in contact with SLBs comprising (i) DOPC containing varying amounts of cholesterol, or (ii) defined mixtures of DOPC and either 1,2-dioleoyl-sn-glycero-3-phosphoethanolamine (DOPE; a conical zwitterionic lipid) or 1,2-dioleoyl-sn-glycero-3-phospho-L-serine (DOPS; an anionic lipid) (see Figure 1). Each of these lipid components is representative of a class of lipids that are constituents of cell membranes;[2] these models thus represent a first, defined step toward understanding the ways in which membrane composition and structure can impact interactions

with AHLs. In general, we observe these multicomponent membranes to undergo remodeling events upon introduction to biologically relevant concentrations of 3-oxo-C12-AHL and 3-oxo-C12-HS that differ from those observed in single-component DOPC membranes.[25] These observations likely reflect large differences in constituent lipid translocation timescales,[21, 36] lipid packing,[6, 37, 38] lipid clustering,[15, 39-41] and spontaneous curvature generation[15, 42-44] in these mixed-lipid systems.

Overall, our results provide insight into ways that AHLs can interact with model lipid membranes of increasing complexity and provide additional support for the view that AHLs could potentially interact with more complex membranes of mammalian cells in ways that extend beyond their currently understood roles in bacterial communication. As suggested above, the results of these studies also provide guidance that could be useful for the design of more sophisticated and compositionally complex soft materials (e.g., sensor elements or drug delivery vehicles) that respond selectively to molecules that mediate communication in communities of bacteria.

Materials and Methods

Materials. 1,2-Dioleoyl-sn-glycero-3-phosphoethanolamine (DOPE), chloroform, sodium chloride (NaCl), calcium chloride ($CaCl_2$) dimethylsulfoxide (DMSO), calcein, sodium hydroxide (NaOH), Sephadex G-50, triethylphosphine oxide, and deuterium oxide (D_2O) were obtained from Sigma (St. Louis, MO). 1,2-Dioleoyl-sn-glycero-3-phosphocholine (DOPC), 1,2-dioleoyl-sn-glycero-3-phospho-L-serine sodium salt (DOPS), 1,2-dioleoyl-sn-glycero-3-ethylphosphocholine chloride salt (DOEPC), 1,2-dihexanoyl-sn-glycero-3-phosphocholine (DHPC), filter supports, and a Mini-prep extruder were purchased from Avanti Polar Lipids (Alabaster, AL). Lissamine rhodamine B 1,2-dipalmitoyl-sn-glycero-3-phosphoethanolamine, triethylammonium salt (Rho-

DPPE) was acquired from Invitrogen (Carlsbad, CA). Disposable culture tubes (16 × 100 mm) were purchased from VWR (West Chester, PA). Electrophoresis-grade sodium dodecyl sulfate (SDS) was obtained from Fisher Scientific (Pittsburgh, PA). Isopropanol (iPOH) was acquired from Fisher Scientific (Waltham, MA). Triton-X100 was obtained from Promega (Madison, WI). 3-(N-Morpholino)propanesulfonic acid (MOPS) was purchased from MP Biomedical (Irvine, CA). Minisort X plus 0.2 μm syringe filters were acquired from Sartorius Stedim Biotech (Goettingen, Germany). Polycarbonate extruder filters (100 nm) were purchased from Millipore (Billerica, MA). Deionization of distilled water was performed using a Milli-Q system (Millipore, Bedford, MA), with the resulting water with a resistivity of 18.2 MΩ. The AHLs in this study were synthesized according to previously reported methods.[25] All materials were used as received without further purification unless otherwise specified.

Preparation of AHL Solutions. 3-oxo-C12-AHL and 3-oxo-C12-HS stock solutions were prepared at a concentration of 20 mM in DMSO and stored at -4 °C. These stock solutions were thawed immediately before experiments were performed and first diluted into neat DMSO to 100 times the final aqueous concentration. These solutions in DMSO were then diluted 1:100 into buffer. To minimize changes in the ratios of hydrolyzed and unhydrolyzed AHL head groups in solution, all AHL solutions were used within 1 hour of initial dilutions of the DMSO stocks into buffer. All experiments described to take place in buffer were in 150 mM NaCl, 10 mM MOPS, pH 7.4 solution. In some experiments, where noted, the buffer also contained 2 mM $CaCl_2$.

Optical Microscopy Experiments Using SLBs Formed by the Bicelle Fusion Method. Fluorescence microscopy experiments were performed in Ibidi microfluidic chambers (μ-Slide VI

0.5 Glass Bottom) using fluorescently labeled SLBs (0.1 mol% Rho-DPPE) formed using a bicelle fusion method, as described in previous reports.[28, 45-47] The microfluidic chambers were cleaned by incubating a 1 M NaOH solution in the cell for ~30 minutes prior to SLB formation and then washing with ample Milli-Q H_2O and then buffer. Briefly, solutions of the long-chained lipids (DOPC, cholesterol, DOEPC, DOPS, or DOPE) and the short-chained lipid DHPC in chloroform were mixed ([long chained lipid]/[DHPC]=0.25), dried under a stream of dry N_2, and then placed under vacuum for at least an hour to remove any residual solvent. The lipid film was then hydrated by buffer or buffer containing 2 mM $CaCl_2$ to produce a 0.5 mM bicelle suspension, as determined by the total concentration of the long-chained lipid. This solution was then frozen and thawed five times by immersing the solution into an iPOH and dry ice bath and a warm water bath (~50 °C). After the samples were thawed in each cycle they were vigorously vortexed. The bicelle stock solution was then diluted 1:16 or 1:32 for a final long-chained lipid concentration of 0.031 mM or 0.016 mM (depending on the lipids being used) and introduced to an Ibidi flow cell at a flow rate of 100 µL/min. The formation of a continuous bilayer was monitored by optical microscopy, and then buffer was introduced to the bilayer to wash away any remaining bicelles. Solutions of 3-oxo-C12-AHL or 3-oxo-C12-HS at various concentrations were introduced to the SLBs at a flow rate of 100 µL/min, and micrographs were acquired using an Olympus IX70 inverted microscope (Center Valley, PA) and a Q-imaging EXi Aqua camera (Tucson, AZ) every 5 seconds for ~8 minutes (at least 100 images). Fluorescently labeled lipids were excited with a Lumen Dynamics X-Cite Series 120PC-Q fiber coupled mercury lamp using the RFP channel (Monroe, LA). After the introduction of 3-oxo-C12-AHL or 3-oxo-C12-HS solutions to the bilayer, they were subsequently washed with the appropriate buffer at a flow rate of 100 µL/min to visualize changes in the bilayer structure when the test compounds were removed from solution.

Characterization Using Quartz Crystal Microbalance with Dissipation (QCM-D). QCM-D measurements were performed using a Q-Sense E4 (Bolin Scientific, Stockholm Sweden) with QSensor QSX 303 quartz crystal sensors with a fundamental frequency of 5 MHz coated with 50 nm of SiO_2 (Bolin Scientific, Stockholm Sweden). Changes in frequency (ΔFrequency) and dissipation (ΔDissipation) as SLBs were formed or introduced to 3-oxo-C12-AHL or 3-oxo-C12-HS solutions were monitored at the third, fifth, seventh, ninth, and eleventh overtones and data analysis of multiple independent experiments was performed using the data from the seventh overtone. All graphs showing QCM-D data over time are the average frequency and dissipation changes over 60 sec intervals of time. In all experiments, solutions were introduced to the quartz crystals at 100 μL/min using an Ismatic IPC High Precision Multichannel Dispenser (Wertheim, Germany) peristaltic pump. When received, the QCM-D sensors were cleaned as suggested by the manufacturer and as described previously.[25]

For QCM-D measurements, SLBs were formed using the bicelle fusion method as described above. Bicelle stock solutions in buffer (0.5 mM; as determined by long-chained lipid concentration) composed of DOPC or mixtures of DOPC and cholesterol, DOPE, DOPS, or DOEPC were diluted to 0.031 mM or 0.16 mM in buffer and introduced to the sensor chamber. Adsorption of bicelles to the SiO_2 surface and subsequent fusion were monitored by QCM-D over time. The formed bilayer was then washed with buffer for at least 20 minutes. Solutions containing 3-oxo-C12-AHL or 3-oxo-C12-HS were then injected into the flow chamber and allowed to interact with the bilayer for 45 minutes. Subsequently, the bilayer was washed with buffer for an additional 45 minutes to observe the desorption of 3-oxo-C12-AHL or 3-oxo-C12-HS from the bilayer over time. Representative QCM-D traces for a single sensor are shown and discussed in

the Supporting Information (Figures S1A, S4, S5, S7, and S11) and data analysis described and included in Figures S1B, 3, 6, 8, and S11 are from 3 or 4 (n=3-4) independent experiments run simultaneously on different crystals. During experiments, the measurement chamber was held at 25 ± 0.5 °C. Immediately following each experiment, the quartz crystal resonators were washed according to the manufacturer's instructions and described previously before storage between measurements.[25]

Preparation of Calcein-Loaded Vesicles. Large unilamellar vesicles (LUVs) loaded with calcein, containing different amounts of cholesterol were prepared using a freeze-thaw and vesicle extrusion procedure as described previously.[25] In brief, desired amounts and compositions of lipids dissolved in chloroform were aliquoted into vials and the chloroform was removed under a stream of dry nitrogen and further dried under vacuum for at least an hour. The dried lipid film was then hydrated with a 70 mM calcein solution in buffer (pH = 7.4) and vortexed vigorously to form a turbid 5 mg/mL suspension of multilamellar vesicles. The resulting vesicle suspension was then frozen and thawed five times by sequential immersion in a iPOH and dry ice bath and a warm water bath (~50 °C) and vortexed vigorously, then passed at least eleven times through a 100 nm PC filter using an Avanti Polar Lipids Mini-prep extruder to produce unilamellar vesicles. After extrusion, the resulting vesicles were washed and separated from external calcein using a hand-packed Sephadex G-50 chromatography column. ^{31}P NMR was used as described in the Supporting Information to quantify the concentration of the resulting purified vesicle solution.

Subsequent calcein leakage assays were performed as previously described using a Tecan Infinite 200 Pro plate reader.[25, 26] In these assays, the vesicle suspensions were diluted 10x into AHL-containing solutions and allowed to sit for at least five minutes. All tests were repeated three

times (n=3) for each batch of vesicles and were performed with three (n=3) independently produced batches of vesicles for a total of nine (n=9) fluorescence measurements. Statistical significance against the buffer control was determined using a one-way ANOVA with all nine normalized replicates for each condition used that was corrected for multiple comparisons using Dunnett's method. The fluorescence intensity for each reading was normalized as described in Equation 1 where: FI is the fluorescence intensity of the test solution, FI_{Buffer} is the fluorescence intensity of the calcein vesicles in buffer as the negative control and, $FI_{TX\text{-}100}$ was the fluorescence intensity of a vesicle solution containing 1% Triton X-100 (which is known to lyse vesicles[48]) as a positive control.

$$Normalized\ Flourescense = \frac{FI - FI_{Buffer}}{FI_{TX-100} - FI_{Buffer}} \quad \text{(Eq. 1)}$$

Results and Discussion

In Chapters 3 and 4 of this thesis, we investigated the influence of AHL head[25] and tail[26] group structure on membrane remodeling in single-component SLBs of DOPC formed using either a vesicle fusion[25] or bicelle formation[26] technique. Other groups have reported that it can be difficult to form some compositionally complex, mixed-lipid SLBs using the vesicle fusion technique[46, 49] and that even single-component bilayers are often non-homogeneous and can contain unruptured vesicles that appear as optical defects.[50] Recent reports by Cho and coworkers demonstrate that more uniform SLBs containing assorted glycerophospholipids and relatively high amounts of cholesterol can be formed on metal oxide substrates using the bicelle formation technique.[45, 46] For the studies described here, we used the bicelle formation technique to produce SLBs composed of either (i) DOPC alone or (ii) multicomponent bilayers composed of mixtures of DOPC with defined amounts of cholesterol, DOPS, or DOPE (Figure 1). We selected this subset

of lipids because they are representative of classes of lipids naturally present in the membranes of mammalian cells and have a variety of impacts on the physicochemical properties of lipid bilayers, including differences in surface charge, lipid packing, and curvature.[2, 6, 43, 44] Additionally, all of these lipids possess two oleic acid tails, and bilayer membranes formed from them are, thus, fluid at room temperature.[51] The studies below were performed using 3-oxo-C12-AHL or 3-oxo-C12-HS to permit characterization of the influence of AHL head group structure (Figure 1) on membrane association and remodeling. 3-oxo-C12-AHL is the principle quorum sensing (QS) signaling molecule used by the pathogen *Pseudomonas aeruginosa*,[52] and thus has relevance to understanding a range of bacterial behaviors that have broad commercial, industrial, and health care impacts.[53-57]

We began our studies by characterizing and validating the formation of DOPC SLBs containing 10 mol% or 30 mol% cholesterol on NaOH-treated glass slides and SiO_2-coated quartz crystals used in the fluorescence microscopy and QCM-D experiments described in sections below. We observed changes in frequency of ~25 Hz and changes in dissipation of less than 0.5 $x10^{-6}$ (as compared to bare SiO_2 crystals; Figure S1), consistent with past studies and suggesting the formation of continuous SLBs.[46] As shown in Figure S2, characterization by fluorescence microscopy revealed SLBs containing 10 mol% cholesterol to be continuous and largely devoid of optical defects (Figure S2B). However, we observed variation in the optical quality of SLBs containing 30 mol% cholesterol; these bilayers sometimes appeared non-homogeneous, with areas of the bilayer having significant optical defects (Figure S2C), and were sometimes observed to be more uniform (Figure S2D). We note that Cho and coworkers determined that 30 mol% cholesterol is the highest cholesterol content that could be consistently incorporated into SLBs using the bicelle formation technique, which could, in part, account the inhomogeneities observed here.[46]

As part of these initial studies, we also formed bilayers composed of mixtures of 75% DOPC and 25% of either (i) DOPE or (ii) DOPS by adapting previously described procedures.[45, 47] For the formation of bilayers containing the zwitterionic lipid DOPE, we found bilayer formation to be more consistent when we used a lower concentration of bicelle solution (0.015 mM vs. 0.031 mM by total long tailed lipid concentration) than was reported to be optimal for the formation of SLBs in past studies using the bicelle method.[45, 47] The DOPE-containing bilayers formed using this approach registered frequency and dissipation shifts of -26.2 ± 0.7 Hz and 0.6 ± 0.05 $x10^{-6}$ compared to a bare SiO_2 quartz crystal (Figure S1). Characterization by optical microscopy revealed non-homogeneous structures with some regions containing continuous bilayers with a relatively low number of optical defects (e.g., Figure S2E) and other areas containing structures that protruded from the bilayer surface (e.g., Figure S2F). These latter structures could result from the negative spontaneous curvature of DOPE lipids[43, 44] and their resulting behaviors during the formation of these low-curvature SLBs. All microscopy observations described below on SLBs of this mixed DOPC/DOPE system were made in regions containing continuous areas of the bilayer.

The formation of DOPC SLBs containing 25 mol% DOPS on SiO_2 surfaces proved more challenging in the simple buffer solutions used to form the SLBs above, as the interactions of anionic bicelles with SiO_2 surfaces is unfavorable due to charge repulsion.[45] We therefore, formed our DOPS-containing SLBs using buffer containing 2 mM $CaCl_2$, as divalent calcium ions can associate with the anionic serine head groups in DOPS and promote adsorption and fusion of the bicelles on the SiO_2 surface.[58] Under these conditions, we observed changes in frequency and dissipation of -25.4 ± 0.8 Hz and 0.2 ± 0.2 $x10^{-6}$ (Figure S1) and the formation of homogeneous bilayers relatively devoid of optical defects by fluorescence microscopy (Figure S2H). We note here that addition of Ca^{2+} during bilayer formation can lead to changes in the physical properties

of anionic bilayers, including the formation of DOPS-rich domains,[15, 39-41] the formation of bilayer curvature,[15, 42] increased lipid packing density,[59, 60] bilayer dehydration,[41, 60, 61] and decrease membrane fluidity.[62] To understand some of the potential impacts of Ca^{2+} in these DOPC/DOPS mixed-lipid SLBs, we also characterized the properties of single-component DOPC SLBs formed in the presence of Ca^{2+} (Figure S1, Figure S2G). We return to a discussion of the potential impacts of Ca^{2+} in these SLBs again in the sections below.

Interactions of 3-oxo-C12-AHL with DOPC Membranes Containing Cholesterol

In a first series of QCM-D studies, we introduced solutions of 3-oxo-C12-AHL to DOPC SLBs containing 10 mol% or 30 mol% cholesterol formed on SiO_2-coated quartz crystal sensors. We selected these cholesterol compositions because 30 mol% cholesterol is at the upper end of the range than can be incorporated into SLBs using the bicelle formation method, and compositions at 10 mol% allowed us to probe the contribution of cholesterol to 3-oxo-C12-AHL induced bilayer reformation at a second, intermediate concentration.[46] Introduction of a 50 μM solution of 3-oxo-C12-AHL to single-component DOPC bilayers yielded changes of frequency and dissipation of -4.0 ± 1.0 Hz and 1.5 ± 0.1 $x10^{-6}$, respectively (see Figures 2 and 5(A-B) for analyses of bilayer reformation from multiple trials after 45 minutes of exposure to 3-oxo-C12-AHL and Figures S3A and S5A for representative time course data). These results are generally consistent with the changes of frequency and dissipation measured upon exposure of DOPC bilayers to solutions of 3-oxo-C12-AHL at 50 μM in our past studies.[25, 26] However, when cholesterol was incorporated into the bilayer, we observed smaller changes in both frequency and dissipation upon exposure to 50 μM 3-oxo-C12-AHL solutions, with changes of (-2.7 ± 0.2 Hz and 0.9 ± 0.3 $x10^{-6}$) and (-2.0 ± 0.3 Hz and 0.8 ± 0.2 $x10^{-6}$) for SLBs containing 10 mol% and 30 mol% cholesterol, respectively

(Figure 2 and Figure S3(B-C)). These smaller changes in frequency and dissipation at higher cholesterol composition were surprising, as previous reports suggested that AHLs had a higher binding capacity to[29] and preferentially interacted with[32] cholesterol containing bilayers, but we note that our results exhibit trends similar to those reported previously for measurements of cholesterol-containing SLBs exposed to other non-ionic amphiphiles. These differences in frequency and dissipation shifts can be understood in terms of the ability of cholesterol to quickly flip-flop across a bilayer to decrease asymmetrical bilayer stresses (*vide infra*).[21]

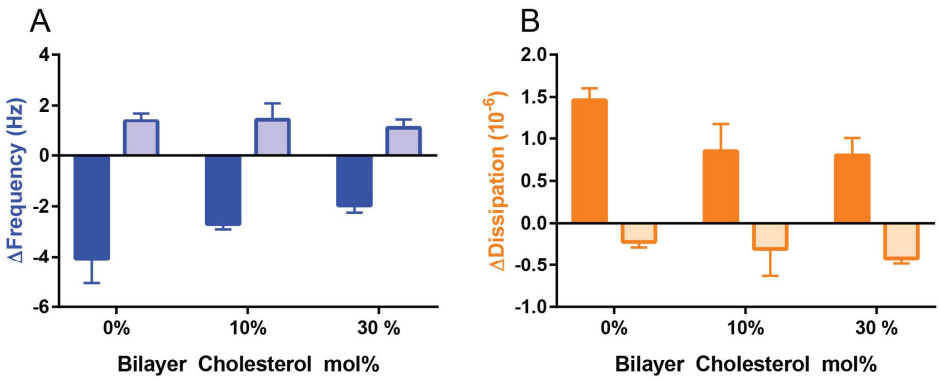


Figure 2: Changes in (A) frequency and (B) dissipation for SLBs with varying cholesterol compositions upon exposure to solutions of 50 μM 3-oxo-C12-AHL for 45 minutes (filled bars) or after 45 minutes of buffer wash (open bars; for the 0% cholesterol bilayers, changes in frequency and dissipation upon washing shown are at 32 minutes, see Supporting Information). The values shown are the means and a single standard deviation of three or four experiments (n= 3-4).

We observed large and visually apparent changes in membrane reformation when otherwise identical experiments were characterized by fluorescence microscopy. Addition of 50 μM solutions of 3-oxo-12-AHL to single-component DOPC SLBs initiated the formation of short tubules, some of which subsequently collapsed into hemispherical caps on the surface of the bilayers (see Figures 3A and 6A for microscopy images after 360 sec of exposure to 3-oxo-C12-

AHL and Figures S4A and S6A for microscopy images at other selected time points). At higher concentrations of 200 µM 3-oxo-C12-AHL, we observed the formation of extended tubule structures hundreds of microns in length; some of these extended tubules collapsed into larger hemispherical caps over time, while others remained on the surface of the bilayer over the duration of the experiment (360 sec; see Figures 3D, 6C, S4B and S6B). Overall, these results are broadly

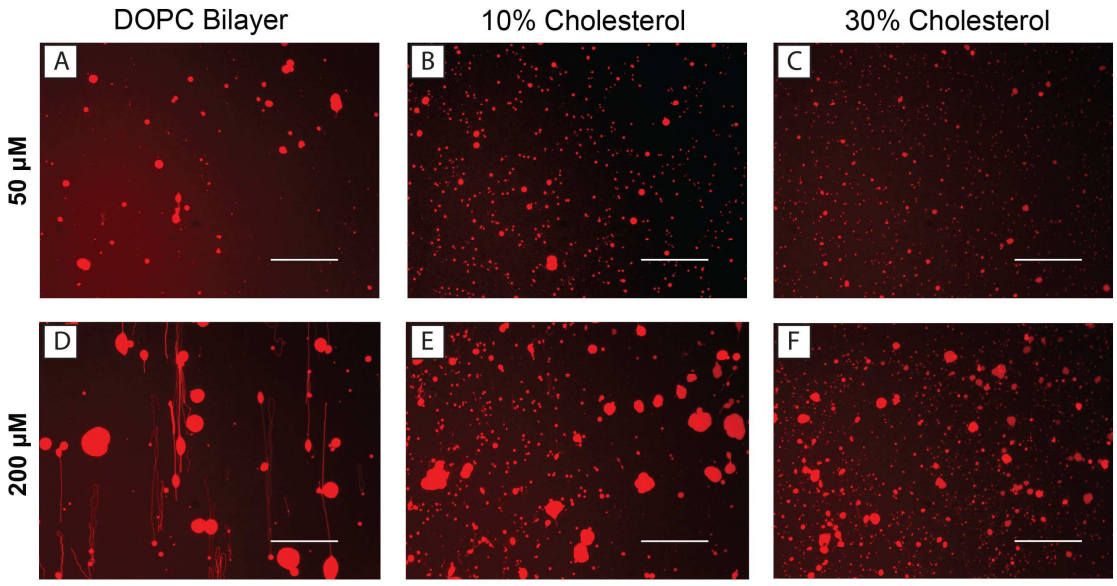


Figure 3: Representative top-down fluorescence micrographs of fluorescently labeled (A,D) DOPC, (B,E) 10% cholesterol or (C,F) 30% cholesterol SLBs after exposure to a continuous flow of (A-C) 50 µM or (D-F) 200 µM 3-oxo-C12-AHL. Images were acquired 360 seconds after the onset of membrane restructuring. The direction of flow in all images was from the bottom to the top of the image. Scale bars are 30 µm.

consistent with those of our past studies on the interactions of 3-oxo-C12-AHL with this single-component DOPC system.[25, 26] In contrast, we observed differences in behavior when 3-oxo-C12-AHL was added to SLBs containing cholesterol. As shown in Figure 3(B-C) and Figure S4A, introduction of 50 µM 3-oxo-C12-AHL to bilayers containing cholesterol also resulted in the formation of tubules on the surface of the bilayer, but these tubules were shorter and thinner and

collapsed or retracted more quickly into hemispherical caps as compared to bilayers that did not contain cholesterol. Similar structures and dynamics were observed when 200 μM 3-oxo-C12-AHL was introduced to the bilayers (Figure 3(E-F), Figure S4B). We note that the final sizes of the hemispherical caps observed in these experiments (e.g., after six min) were generally observed to decrease with increasing cholesterol composition.

As mentioned above, differences in the membrane remodeling observed here upon the addition of 3-oxo-C12-AHL to bilayers of varying cholesterol composition likely result from the short timescales over which cholesterol is able to flip-flop across a bilayer to relieve asymmetrical bilayer stresses.[36, 63] As reported in Chapters 3 and 4 of this thesis, the formation of tubules upon the introduction of an amphiphile to an SLB, and the time-dependent retraction of these features into hemispherical caps, can be understood, at least in part, in terms of the accumulation and subsequent relief of asymmetrical stresses between the leaflets of the bilayer (with a relief of stress leading to a transition from high curvature tubules to lower curvature hemispherical caps).[25, 26] In a cholesterol-free bilayer, this transition would likely be influenced predominantly by the timescale on which flip-flop of the interacting amphiphilic species occurs (we note that phospholipid flip-flop typically occurs on timescales that are much slower than those of single-tailed amphiphiles).[36] For cholesterol-containing bilayers, however, these stresses can also be relieved by the flip-flip of cholesterol across the bilayer.[36] Because flip-flip of cholesterol can occur on relatively fast timescales, we would anticipate (and do observe) transitions from tubules to hemispherical caps to occur more rapidly. Additionally, the negative spontaneous curvature of cholesterol[43] could additionally play a role in the formation of low curvature hemispherical caps as opposed to high curvature extended tubule structures when placed in contact with 3-oxo-C12-AHL, as the spontaneous curvature of surfactants has been described to change the bilayer restructuring

observed.[64] Taken together, the results of our optical microscopy and QCM-D experiments reveal that cholesterol can play a significant role in modulating the interactions of lipid bilayers with 3-oxo-C12-AHL and provide insight into the ways in which timescales of lipid flip-flip can influence interactions with AHLs and subsequent multi-scale responses.

Finally, we note that we reported in Chapters 3 and 4 that 3-oxo-C12-AHL can promote tubule formation in the (unsupported) lipid membranes of GUVs and that treatment of large unilamellar vesicles (LUVs) composed of DOPC with this AHL can lead to low, but statistically significant, levels of leakage of the fluorescent dye calcein encapsulated in the vesicles.[25, 26] We performed a series of experiments to characterize the impact of cholesterol on dye leakage in DOPC LUVs containing 10 mol% and 30 mol% cholesterol. As shown in Figure 4, we observed low levels of calcein leakage in these cholesterol-containing lipid vesicles, corresponding to 5.18 ± 0.77 % and 4.74 ± 1.51% leakage at a concentration of 180 μM 3-oxo-C12-AHL in 10 mol% (Figure 4A) and 30 mol% (Figure 4B) cholesterol vesicles, respectively. These levels of dye leakage are similar to those reported previously for DOPC vesicles (~5% leakage at 180 μM), suggesting that the presence of cholesterol does not affect vesicle leakage substantially. This result was, to some extent, unexpected, as cholesterol has been previously proposed to increase the stability of vesicles in the presence of single-tailed amphiphiles.[18, 65] We note that previous reports have correlated membrane permiabilization to the accumulation of surfactants, and by extension stress, in the outer leaflet of the bilayer. [18, 66, 67] While cholesterol is able to readily alleviate stresses, it may occur on timescales slower than those required to cause leakage, as suggested by the formation of small tubules on the surface of the SLBs. The leakage observed here could therefore occur due to the accumulation of stresses in the bilayer or through a different mechanism.

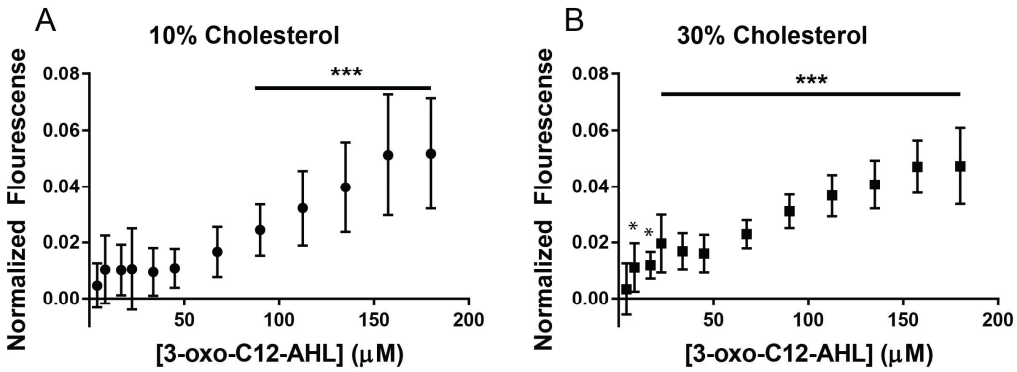


Figure 4: Normalized calcein fluorescence intensity values in a solution containing 100 μM of calcein-loaded DOPC vesicles containing either (A) 10% cholesterol or (B) 30% cholesterol after exposure to solutions of 3-oxo-C12-AHL at various concentrations. Statistical significance compared to a buffer control is indicated for concentrations with the following p values: *p<0.05, ***p<0.001. All points shown are the average and standard deviation of three independent experiments.

Interactions of 3-oxo-C12-AHL and 3-oxo-C12-HS with Bilayers Containing DOPE

We performed an additional series of studies to characterize the interactions of 3-oxo-C12-AHL with SLBs of DOPC containing DOPE. In contrast to DOPC, DOPE is a conical shaped zwitterionic lipid with negative spontaneous curvature (Figure 1),[43, 44] and can promote lipid packing defects when incorporated into bilayers with cylindrical lipids.[6, 37] For these studies, we also included 3-oxo-12-HS, the anionic head group hydrolysis product of 3-oxo-C12-AHL, as a target amphiphile to characterize the influence of head group structure on multi-scale phenomena in this mixed-lipid system.

As shown in Figure 5 and Figure S5(C-D), the introduction of 50 μM solutions of 3-oxo-C12-AHL and 3-oxo-C12-HS to SLBs containing 75% DOPC and 25% DOPE on SiO_2-coated quartz crystal sensors resulted in changes in dissipation and frequency of (-3.2 ± 1.0 Hz and 1.1 ± 0.2 $x10^{-6}$) and (-1.4 ± 0.1 Hz and 0.5 ± 0.1 $x10^{-6}$), respectively. These changes in frequency and

dissipation for 3-oxo-C12-HS solutions are similar to those of DOPC bilayers introduced to this compound under otherwise identical conditions; in contrast, these changes observed for 3-oxo-C12-AHL solutions are lower than those previously observed in DOPC bilayers (Figure 5). Analogous fluorescence microscopy experiments to characterize interactions of 3-oxo-C12-AHL (Figure 6B and Figure S6C) with these DOPE-containing bilayers revealed the immediate and

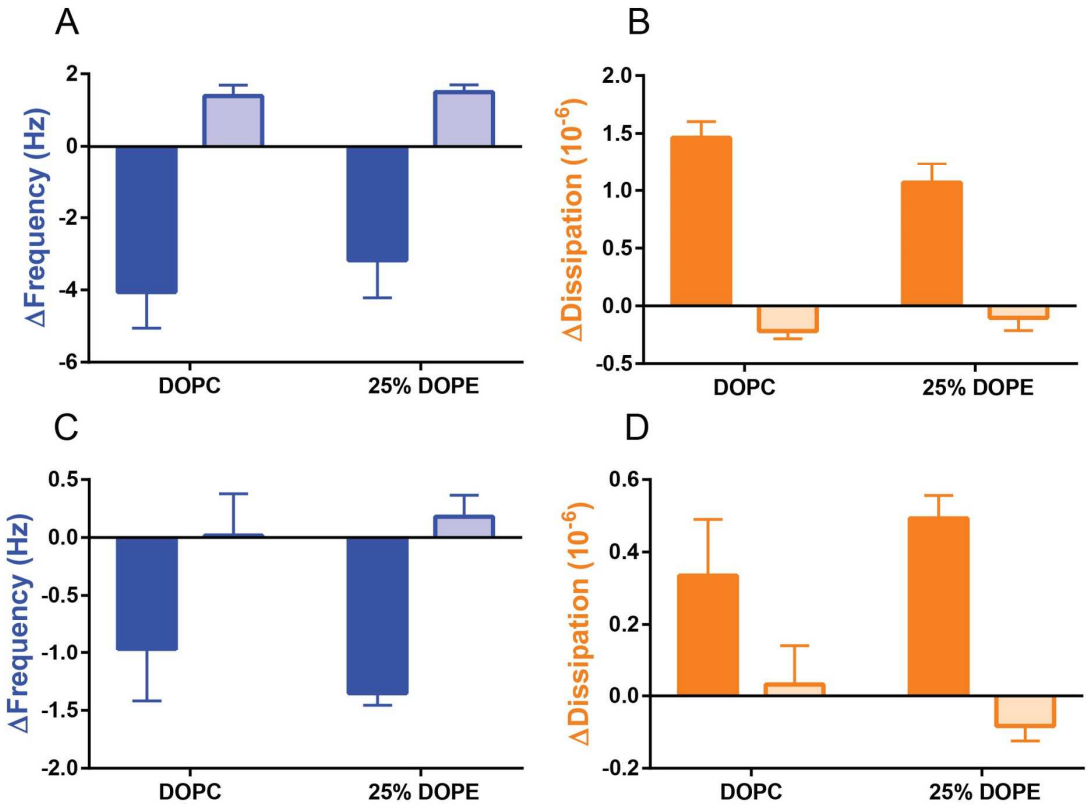


Figure 5: Changes in (A,C) frequency and (B,D) dissipation for SLBs composed of either 100% DOPC or 75% DOPC/25% DOPE after introducing 50 μM solutions of (A,B) 3-oxo-C12-AHL or (C,D) 3-oxo-C12-HS for 45 minutes (filled bars) or after 45 minutes of buffer wash (open bars; for the DOPC bilayers, changes in frequency and dissipation upon washing are shown at 32 minutes, see Supporting Information). The values shown are the means and a single standard deviation of three or four experiments (n = 3-4).

apparently direct formation of hemispherical caps on the surfaces of the bilayers (that is, we did not observe these caps to form by the initial formation and subsequent retraction of extended tubule structures). In contrast, the introduction of 3-oxo-C12-HS at a concentration of 50 μM (Figure 6F and Figure S6C) appeared to lead to the formation of hemispherical caps that appeared to be more protruded from the surface of the bilayer than those reported in our previous studies (as suggested by a visible ring of more intense fluorescence around these structures that is similar in many ways to those observed in other past studies on bilayer reformation).[25, 26, 68] The formation of these more protruded hemispherical caps on the surfaces of bilayers was not observed in our previous studies on the interactions of AHLs with SLBs;[25, 26] additional studies will be required to investigate the formation of these structures more completely and confirm this tentative assignment.

In contrast, at higher concentrations of 200 μM, 3-oxo-C12-AHL formed very short tubules (~10 μm in length) that collapsed, over approximately the first minute of the experiment, into small hemispherical caps that subsequently grew in size over the remaining five minutes of the experiment (Figure 6D and Figure S6D). Overall, the sizes of the hemispherical caps in these mixed-lipid bilayers remained smaller than caps observed to form in single-component DOPC bilayers under otherwise identical conditions (Figure 6C and Figure S6B). At this higher 200 μM concentration, 3-oxo-C12-HS initiated the formation of predominantly short (~10 μm) tubules and some hemispherical caps that extended from the surface of the bilayer (as described above), both of which persisted for the duration of the experiment (Figure 6H and Figure S6D).

The differences in membrane restructuring observed upon the addition of these amphiphiles to DOPE-containing bilayers, relative to those observed in single-component DOPC bilayers, likely arise, at least for 3-oxo-C12-AHL, from lipid packing defects in these mixed-lipid SLBs. As noted above, it is well known that the mixing of conical lipids and cylindrical lipids,

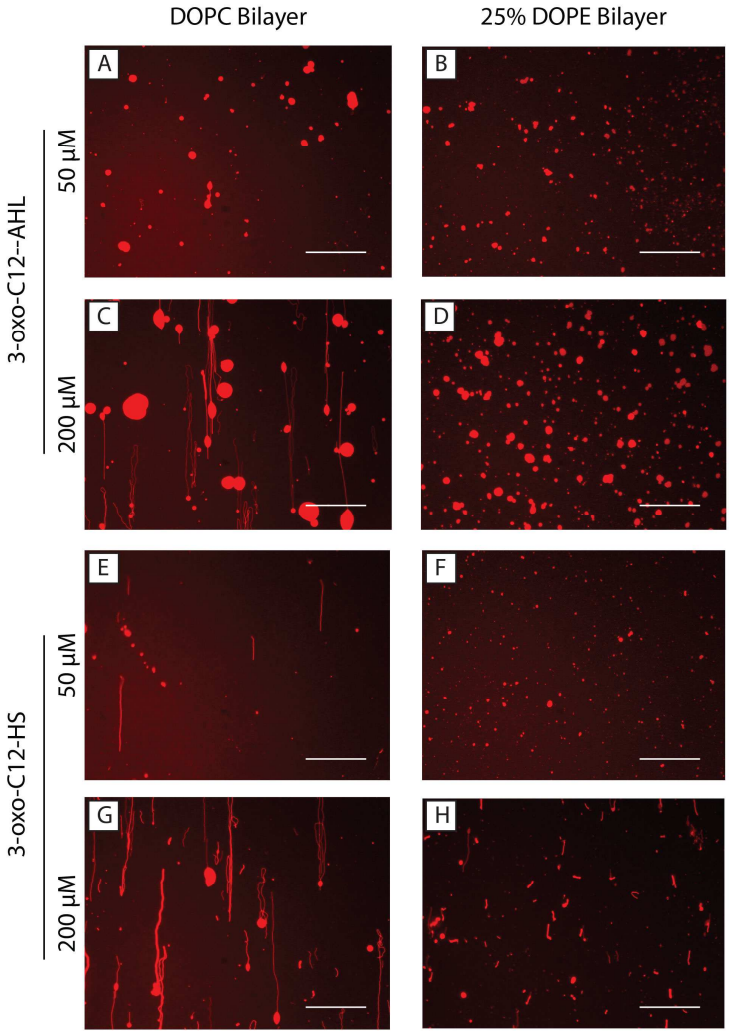


Figure 6: Representative top-down fluorescence micrographs of fluorescently labeled (A,C,E,G) DOPC or (B,D,F,H) 75% DOPC/25% DOPE SLBs after exposure to a continuous flow of (A,B,E,F) 50 µM or (C,D,G,H) 200 µM solutions of (A-D) 3-oxo-C12-AHL or (E-H) 3-oxo-C12-HS in buffer containing $CaCl_2$. Images were acquired 360 seconds after the onset of membrane restructuring. The direction of flow in all images was from the bottom to the top of the image. Scale bars are 30 µm.

especially those with unsaturated aliphatic tails, as used here, can lead to the formation of packing defects.[6, 37] Similar deviations from ideal packing in DSPE-DSPC mixtures have been demonstrated to increase the timescales on which the lipids that compose those membranes are

able to flip-flip across the bilayer.[38, 69] Our past studies on the interactions of AHLs with lipid bilayers, and those of other groups using other synthetic amphiphiles, provide a framework for understanding the formation and associated dynamics of tubules and hemispherical caps in lipid in terms of the timescales over which an adsorbed or intercalated amphiphile is able to translocate across the bilayer (i.e., from the outer leaflet to the inner leaflet) to relieve asymmetrical bilayer stresses.[25, 26] If the presence of lipid packing defects in these DOPE-containing bilayers were able to also increase rates of AHL translocation, this general framework would suggest the possibility that tubules (which are high-curvature structures formed by the initial accumulation of amphiphile in the outer leaflet of the membrane) would transition more rapidly to hemispherical caps (which are lower-curvature structures that result from flip-flop and relief of asymmetrical stress) than they do in bilayers that do not contain such packing defects. The results reported here are consistent with this possibility, as we generally observe faster transitions from tubules to caps in our 3-oxo-C12-AHL experiments with mixed DOPC/DOPE bilayers, as compared to otherwise identical DOPC bilayers. Additional experiments will be required to understand the interactions of these mixed-lipid membranes with 3-oxo-C12-HS, as well as processes and dynamics associated with the apparent formation of potentially more protruded hemispherical caps in the experiments above. We note that our results do not preclude differences in bilayer reformations observed for both 3-oxo-C12-AHL and 3-oxo-C12-HS to potentially result from the negative spontaneous curvature of DOPE, a factor that has previously been suggested to alter the interactions of lipids and surfactants.[64] Additionally, the results of these current experiments do not permit meaningful conclusions about the extent to which packing defects might affect differential rates of translocation of 3-oxo-C12-AHL and 3-oxo-C12-HS across the bilayer.

In a broader context, we note that while the DOPE-containing mixed-lipid system used here is compositionally more complex than the single-component DOPC membranes used in our past studies,[25, 26] it is substantially less complex than lipid membranes in bacterial or mammalian cells.[2] However, packing defects characterized in this mixed-lipid system can serve as models to probe and understand the roles that lipid packing defects and other associated phenomena may play in the transport of agents across cell membranes or other synthetic lipid bilayers comprised of mixtures of cylindrical and conical lipids. The results of these current studies may thus provide useful insight into the roles that lipid packing defects could play in facilitating the translocation of AHLs across these more complex membranes.

Interactions of 3-oxo-C12-AHL and 3-oxo-C12-HS with Charged Bilayers

We conducted a final series of experiments to characterize the interactions of 3-oxo-C12-AHL and 3-oxo-C12-HS with DOPC SLBs containing charged lipids. For these studies, we selected the naturally occurring anionic lipid DOPS (Figure 1) as a model. We note again here that all DOPS-containing SLBs used in experiments described below were formed using the bicelle formation method in buffer containing 2 mM $CaCl_2$ to facilitate the formation of uniform SLBs on anionic SiO_2 surfaces (see Methods for additional details). It has been previously suggested that Ca^{2+} can strongly bind to zwitterionic and anionic bilayers and change the physical properties of both. For example, the addition of Ca^{2+} to single-component DOPC bilayers can decrease the area per lipid molecule,[70] increase membrane thickness,[70, 71]and, at high concentrations, decrease membrane fluidity.[72] In addition to the effects listed above,[41, 59-62] in anionic bilayers, the addition of Ca^{2+} can lead to the formation of anionic lipid domains[15, 39-41] that can introduce curvature into bilayers.[15, 42]

To facilitate more direct comparisons between single-component DOPC and multicomponent DOPC/DOPS bilayers formed in the presence of Ca^{2+}, we first characterized bilayer remodeling in DOPC bilayers in the presence of buffer containing 2 mM $CaCl_2$. As shown in Figures 7 and S7(A,B), introduction of 50 µM solutions of 3-oxo-C12-AHL and 3-oxo-C12-HS to DOPC bilayers in the presence of Ca^{2+} resulted in changes in frequency and dissipation of (-4.1 ± 0.9 Hz and 1.0 ± 0.1 x10^{-6}) and (-0.1 ± 0.1 Hz and 0.2 ± 0.02 x10^{-6}), respectively.

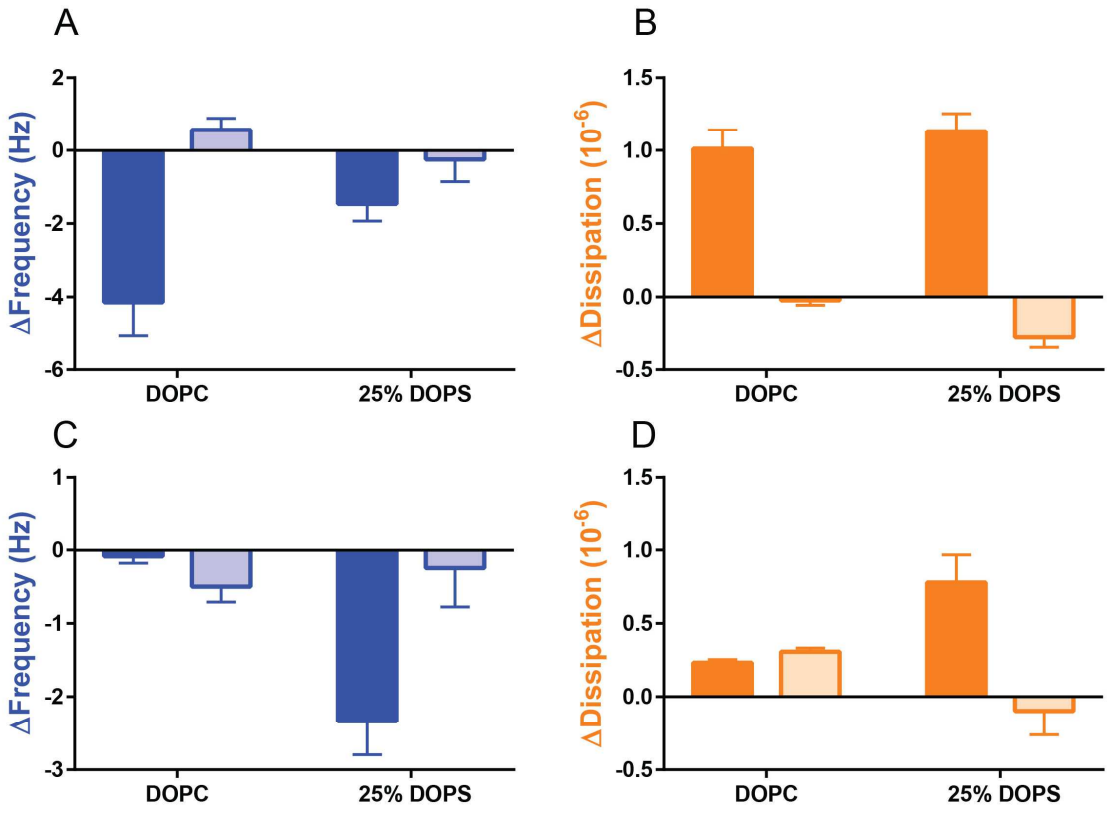


Figure 7: Changes in (A,C) frequency and (B,D) dissipation for SLBs composed of either DOPC or 75% DOPC/25% DOPS after introducing 50 µM solutions of (A,B) 3-oxo-C12-AHL or (C,D) 3-oxo-C12-HS for 45 minutes (filled bars) or after 45 minutes of buffer wash (open bars). The values shown are the means and a single standard deviation of three or four experiments (n = 3-4).

These changes in frequency and dissipation are similar to those observed in the absence of Ca^{2+} under otherwise identical conditions.

Fluorescence micrographs shown in Figures 8(A,C,E,G) and S8(A,B) show that the introduction of non-ionic 3-oxo-C12-AHL to DOPC bilayers in buffer containing $CaCl_2$ at 50 μM or 200 μM led to the formation of tubules that were shorter and that collapsed more quickly into hemispherical caps than observed in DOPC bilayers in the absence of $CaCl_2$. In contrast, introduction of anionic 3-oxo-C12-HS at 50 μM led to no observable membrane restructuring. At higher concentrations of 200 μM, the introduction of 3-oxo-C12-HS led to the formation of hemispherical caps within the first 30 seconds of the experiment and qualitatively less bilayer reformation than that observed in otherwise identical DOPC bilayers in the absence of Ca^{2+}. Taken together, these results demonstrate that the presence of Ca^{2+} leads to changes in the multi-scale remodeling that occurs when these compounds interact with DOPC membranes. It is likely that these changes result from one or more of the impacts of Ca^{2+} on membrane properties discussed above (e.g., decreased membrane fluidity, bilayer thickening, or bilayer compression, etc.)[70-72] and their resulting impacts on the intercalation and subsequent translocation of 3-oxo-C12-AHL or 3-oxo-C12-HS. We note, in this latter context, that it is also possible that, in experiments using 3-oxo-C12-HS, Ca^{2+} ions could also coordinate to the anionic head group and form dimers in solution, thereby changing the solution phase behavior of this compound or, by extension, its interactions with bilayers. We return to this possibility again in the discussion below.

QCM-D experiments in which 3-oxo-C12-AHL and 3-oxo-C12-HS were introduced, at concentrations of 50 μM, to SLBs containing 75 mol% DOPC and 25 mol% DOPS resulted in changes in frequency and dissipation of $(-1.4 \pm 0.5$ Hz and $1.1 \pm 0.1 \times 10^{-6})$ and $(-2.3 \pm 0.5$ Hz and $0.8 \pm 0.2 \times 10^{-6})$, respectively [Figures 7 and S7(C-D)]. This result was surprising, because it

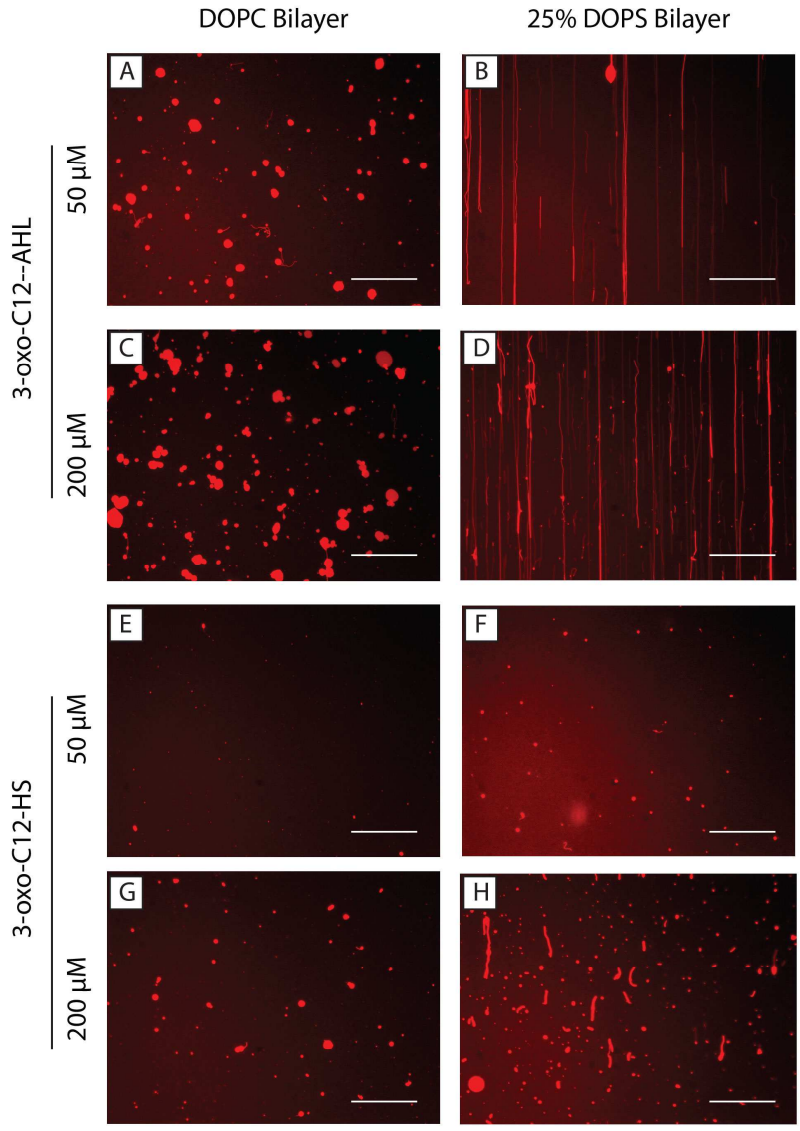


Figure 8: Representative top-down fluorescence micrographs of fluorescently labeled (A,C,E,G) DOPC or (B,D,F,H) 75% DOPC/25% DOPS SLBs after exposure to a continuous flow of (A,B,E,F) 50 µM or (C,D,G,H) 200 µM solutions (A-D) 3-oxo-C12-AHL or (E-H) 3-oxo-C12-HS in buffer containing $CaCl_2$. Images were acquired 360 seconds after the onset of membrane restructuring. The direction of flow in all images was from the bottom to the top of the image. Scale bars are 30 µm.

suggests that, when compared to the DOPC bilayers in the presence of Ca^{2+} discussed above, less 3-oxo-C12-AHL associates with the bilayer (smaller changes in frequency), but that this leads to

otherwise similar amounts of membrane restructuring (larger changes in dissipation). In our past experiments and the results described above, increases in dissipation are generally accompanied by increases in frequency.[25, 26] The results shown in Figure 7 thus hint at the possibility of significant changes in the structures or dynamics of features observed that could occur on the surfaces of these DOPS-containing bilayers (*vide infra*). In contrast, the introduction of 3-oxo-C12-HS to DOPS-containing bilayers resulted in larger changes in frequency and dissipation relative to those observed in single-component DOPC bilayers under otherwise identical conditions. Although the reasons for this are not completely understood, it is possible that increased adsorption or intercalation of this anionic compound to the anionic DOPS component lipids in these mixed bilayers could be facilitated either by (i) the chelation-induced dimerization of 3-oxo-C12-HS by Ca^{2+} ions in solution or (ii) the chelation-induced association of 3-oxo-C12-HS with the serine head group of DOPS on the surface of the bilayer, as also discussed above.[41]

Characterization of interactions of 3-oxo-C12-AHL and 3-oxo-C12-HS with DOPS-containing SLBs by fluorescence microscopy revealed large differences in bilayer remodeling compared to otherwise identical DOPC bilayers. As shown in Figure 8(F,H) and Figure S8(C,D), the introduction of solutions containing 3-oxo-C12-HS to DOPS-containing bilayers led to substantially more membrane reformation than we observed in single-component DOPC bilayers (Figure 8(E,G)), with the formation of hemispherical caps (at concentrations of 50 μM) and a combination of short tubules and hemispherical caps (at concentrations of 200 μM). These large changes in restructuring are generally consistent with the larger changes in frequency and dissipation measured by QCM-D. The increased bilayer reformation observed here could result from complexation of Ca^{2+} to both the DOPS serine head group and the homoserine head group of 3-oxo-C12-HS, as discussed above.[41]

The introduction of 3-oxo-C12-AHL to DOPS-containing bilayers also led to significant differences in the membrane remodeling observed as compared to single-component DOPC bilayers. As shown in Figure 8(B,D) and Figure S8(C,D) introduction of 3-oxo-C12-AHL at concentrations of both 50 and 200 μM led to the formation of long, extended tubule structures (~100 μm in length) on the surface of the bilayer, many of which did not collapse into hemispherical caps during the time course of these experiments (360 sec). These tubules were much longer than those observed on single-component DOPC bilayers in the presence of Ca^{2+}, consistent with the suggestions of substantially different behaviors in this system that arose in our QCM-D measurements described above (Figures 7 and S7C). We note that 3-oxo-C12-AHL is a non-ionic amphiphile, and thus cannot form ionic complexes with Ca^{2+} in the manner proposed and discussed above for experiments involving anionic 3-oxo-C12-HS. It is possible, however, that the differences in restructuring observed using 3-oxo-C12-AHL could result from calcium-induced clustering of DOPS on the surface of the bilayer,[15, 39-41] or from an imbalance of Ca^{2+} on the outer leaflet of the bilayer resulting from a continuous flow of Ca^{2+} across the surface.[15, 42] It is well established that the formation of lipid domains (similar to those observed from calcium induced anionic lipid clustering)[73, 74] or an imbalance of calcium in the two leaflets of DOPS-containing bilayers[15, 42] can result in the formation of bilayer curvature. Either of these effects could, in theory, promote the subsequent formation of high curvature structures (e.g., tubules) on the surface of a bilayer upon contact with added amphiphiles, consistent with the microscopy results reported here. Overall, the results of these studies demonstrate that both lipid composition and other environmental factors (e.g., the presence of Ca^{2+} in the buffer) can lead to changes in the ways that AHLs interact with lipid bilayers and promote subsequent multi-scale phenomena.

As part of the studies reported here, we also characterized the interactions of 3-oxo-C12-AHL and 3-oxo-C12-HS with DOPC SLBs containing the cationic lipid DOEPC (Figure 1). Cationic lipids such as DOEPC are not found naturally in the membranes of mammalian cells,[1, 2] however this broad class of materials is used increasingly for the formulation of lipid-based materials for pharmaceutical applications.[75] To explore the potential interactions of AHLs with DOPC-based, mixed-lipid bilayers containing a cationic lipid, we performed an initial set of experiments using 3-oxo-C12-AHL, 3-oxo-C12-HS, and SLBs comprised of 75 mol% DOPC and 25 mol% DOEPC. We observed remodeling of DOEPC-containing SLBs that was, in general, different from that observed for single-component DOPC SLBs or the anionic DOPS-containing SLBs discussed above. The results of those preliminary studies are included and discussed further in the Supporting Information (Figures S9-11). Although additional experiments will be required to probe and understand the dynamics of these DOEPC-containing membranes more completely, the results of the experiments included here provide further insight into how changes in the physicochemical properties of lipids and lipid membranes can affect their interactions with AHLs.

Summary and Conclusions

We have reported on the influence of membrane composition on multi-scale remodeling that occurs in model mixed-lipid bilayers upon contact with the bacterial quorum sensing signal 3-oxo-C12-AHL and its anionic head group hydrolysis product 3-oxo-C12-HS. As a first step toward understanding the interactions of these important bacterial signals with more complex biological membranes, we investigated interactions of SLBs composed of the phospholipid DOPC either alone or in mixtures containing either cholesterol, DOPE, or DOPS using fluorescence microscopy and QCM-D. Overall, we observed these mixed-lipid membranes to undergo

remodeling events that differ substantially in the nature, extent, and dynamics of bilayer features that form (e.g., tubules and hemispherical caps) compared to features observed to form in single-component DOPC membranes. We attribute these differences, at least in part, to the influence of lipid structure and membrane composition on the relative timescales of molecular (e.g., AHL or constituent lipid) flip-flop,[21, 36] lipid packing defects,[6, 37, 38] lipid phase segregation,[15, 39-41] and the generation of spontaneous curvature[15, 42] in these materials and, thus, differences in the ways that these mixed-lipid bilayers regulate or relieve bilayer stresses that can accumulate upon the adsorption and intercalation of 3-oxo-C12-AHL or 3-oxo-C12-HS.

Many bacteria use 3-oxo-C12-AHL and other AHLs to communicate with each other[22-24] and regulate group behaviors such as virulence factor production,[56] swarming,[76] and biofouling,[77] and a growing body of experimental results suggests that AHLs may also interact with the membranes of mammalian cells and play important roles in regulating host-cell interactions.[29, 32] Each of the individual lipids investigated here is representative of classes of lipids that comprise mammalian cell membranes.[2] The two-component, mixed-lipid membranes investigated here lack the full range of compositional and functional complexity typical of biological membranes, but they present useful models to probe and understand the ways that membrane composition can impact interactions with this class of bacterial signals. Mixed-lipid membranes are also useful for the design of many responsive synthetic materials, including vesicle-based vehicles for drug delivery and supported membranes that can serve as components of environmental sensors.[3, 4, 78] The fundamental studies reported here thus also have the potential to provide guidance for the design of new types of soft materials that can interact with or respond selectively to molecules that bacterial communities use to communicate. Efforts to explore these opportunities are currently underway and will be reported in due course.

Acknowledgements. Financial support for this work was provided by the National Science Foundation through a grant provided to the UW-Madison Materials Research Science and Engineering Center (MRSEC; DMR-1720415). The authors acknowledge the use of instrumentation supported by the NSF through the UW MRSEC (DMR-1720415). C. G. G. was supported in part by a NSF Graduate Research Fellowship.

References

1. Spector, A. A.; Yorek, M. A., Membrane Lipid-Composition And Cellular Function. *J. Lipid Res.* **1985,** *26* (9), 1015-1035.

2. van Meer, G.; de Kroon, A., Lipid map of the mammalian cell. *J. Cell Sci.* **2011,** *124* (1), 5-8.

3. Mura, S.; Nicolas, J.; Couvreur, P., Stimuli-responsive nanocarriers for drug delivery. *Nat. Mater.* **2013,** *12* (11), 991-1003.

4. Lee, Y.; Thompson, D. H., Stimuli-responsive liposomes for drug delivery. *Wiley Interdiscip. Rev. Nanomed. Nanobiotechnol.* **2017,** *9* (5), e1450.

5. Casares, D.; Escriba, P. V.; Rossello, C. A., Membrane Lipid Composition: Effect on Membrane and Organelle Structure, Function and Compartmentalization and Therapeutic Avenues. *Int. J. Mol. Sci.* **2019,** *20* (9), 2167.

6. Bigay, J.; Antonny, B., Curvature, Lipid Packing, and Electrostatics of Membrane Organelles: Defining Cellular Territories in Determining Specificity. *Dev. Cell* **2012,** *23* (5), 886-895.

7. Dimova, R., Recent developments in the field of bending rigidity measurements on membranes. *Adv. Colloid Interface Sci.* **2014,** *208*, 225-234.

8. Subczynski, W. K.; Pasenkiewicz-Gierula, M.; Widomska, J.; Mainali, L.; Raguz, M., High Cholesterol/Low Cholesterol: Effects in Biological Membranes: A Review. *Cell Biochem. Biophys.* **2017,** *75* (3-4), 369-385.

9. Faizi, H. A.; Frey, S. L.; Steinkuhler, J.; Dimova, R.; Vlahovska, P. M., Bending rigidity of charged lipid bilayer membranes. *Soft Matter* **2019,** *15* (29), 6006-6013.

10. Chernomordik, L.; Kozlov, M. M.; Zimmerberg, J., Lipids in Biological Membrane-Fusion. *J. Membr. Biol.* **1995,** *146* (1), 1-14.

11. Storck, E. M.; Ozbalci, C.; Eggert, U. S., Lipid Cell Biology: A Focus on Lipids in Cell Division. *Annu. Rev. Biochem.* **2018,** *87*, 839-869.

12. Paliwal, S. R.; Paliwal, R.; Vyas, S. P., A review of mechanistic insight and application of pH-sensitive liposomes in drug delivery. *Drug Delivery* **2015,** *22* (3), 231-242.

13. Binder, H.; Zschornig, O., The effect of metal cations on the phase behavior and hydration characteristics of phospholipid membranes. *Chem. Phys. Lipids* **2002,** *115* (1-2), 39-61.

14. Javanainen, M.; Melcrova, A.; Magarkar, A.; Jurkiewicz, P.; Hof, M.; Jungwirth, P.; Martinez-Seara, H., Two cations, two mechanisms: interactions of sodium and calcium with zwitterionic lipid membranes. *Chem. Commun.* **2017,** *53* (39), 5380-5383.

15. Graber, Z. T.; Shi, Z.; Baumgart, T., Cations induce shape remodeling of negatively charged phospholipid membranes. *Phys. Chem. Chem. Phys.* **2017,** *19* (23), 15285-15295.

16. Zimmerberg, J.; Kozlov, M. M., How proteins produce cellular membrane curvature. *Nat. Rev. Mol. Cell Biol.* **2006,** *7* (1), 9-19.

17. McMahon, H. T.; Boucrot, E., Membrane curvature at a glance. *J. Cell Sci.* **2015,** *128* (6), 1065-1070.

18. Heerklotz, H., Interactions of surfactants with lipid membranes. *Q. Rev. Biophys.* **2008,** *41* (3-4), 205-264.

19. Yoon, B. K.; Jackman, J. A.; Kim, M. C.; Cho, N. J., Spectrum of Membrane Morphological Responses to Antibacterial Fatty Acids and Related Surfactants. *Langmuir* **2015,** *31* (37), 10223-10232.

20. Yoon, B. K.; Jackman, J. A.; Park, S.; Mokrzecka, N.; Cho, N. J., Characterizing the Membrane-Disruptive Behavior of Dodecylglycerol Using Supported Lipid Bilayers. *Langmuir* **2019,** *35* (9), 3568-3575.

21. Kawakami, L. M.; Yoon, B. K.; Jackman, J. A.; Knoll, W.; Weiss, P. S.; Cho, N. J., Understanding How Sterols Regulate Membrane Remodeling in Supported Lipid Bilayers. *Langmuir* **2017,** *33* (51), 14756-14765.

22. Fuqua, C.; Greenberg, E. P., Listening in on bacteria: Acyl-homoserine lactone signalling. *Nat. Rev. Mol. Cell Biol.* **2002,** *3* (9), 685-695.

23. Waters, C. M.; Bassler, B. L., Quorum sensing: Cell-to-cell communication in bacteria. *Annu. Rev. Cell Dev. Biol.* **2005,** *21*, 319-346.

24. Papenfort, K.; Bassler, B. L., Quorum sensing signal-response systems in Gram-negative bacteria. *Nat. Rev. Microbiol.* **2016,** *14* (9), 576-588.

25. Gahan, C. G.; Patel, S. J.; Chen, L. M.; Manson, D. E.; Ehmer, Z. J.; Blackwell, H. E.; Van Lehn, R. C.; Lynn, D. M., Bacterial Quorum Sensing Signals Promote Large-Scale

Remodeling of Lipid Membranes. *Langmuir* **2021**, https://doi.org/10.1021/acs.langmuir.1c01204.

26. Gahan, C. G.; Van Lehn, R. C.; Blackwell, H. E.; Lynn, D. M., Interactions of Bacterial Quorum Sensing Signals with Model Lipid Membranes: Influence of Acyl Tail Structure on Multi-Scale Response. *Submitted* **2021**.

27. Davis, B. M.; Richens, J. L.; O'Shea, P., Label-Free Critical Micelle Concentration Determination of Bacterial Quorum Sensing Molecules. *Biophys. J.* **2011,** *101* (1), 245-254.

28. Gahan, C. G.; Patel, S. J.; Boursier, M. E.; Nyffeler, K. E.; Jennings, J.; Abbott, N. L.; Blackwell, H. E.; Van Lehn, R. C.; Lynn, D. M., Bacterial Quorum Sensing Signals Self-Assemble in Aqueous Media to Form Micelles and Vesicles: An Integrated Experimental and Molecular Dynamics Study. *J. Phys. Chem. B* **2020,** *124* (18), 3616-3628.

29. Davis, B. M.; Jensen, R.; Williams, P.; O'Shea, P., The Interaction of N-Acylhomoserine Lactone Quorum Sensing Signaling Molecules with Biological Membranes: Implications for Inter-Kingdom Signaling. *PLoS One* **2010,** *5* (10), e13522.

30. Jakubczyk, D.; Barth, C.; Kubas, A.; Anastassacos, F.; Koelsch, P.; Fink, K.; Schepers, U.; Brenner-Weiss, G.; Brase, S., Deuterium-labelled N-acyl-l-homoserine lactones (AHLs)-inter-kingdom signalling molecules-synthesis, structural studies, and interactions with model lipid membranes. *Anal. Bioanal. Chem.* **2012,** *403* (2), 473-482.

31. Barth, C.; Jakubczyk, D.; Kubas, A.; Anastassacos, F.; Brenner-Weiss, G.; Fink, K.; Schepers, U.; Brase, S.; Koelsch, P., Interkingdom Signaling: Integration, Conformation, and Orientation of N-Acyl-L-homoserine Lactones in Supported Lipid Bilayers. *Langmuir* **2012,** *28* (22), 8456-8462.

32. Song, D. K.; Meng, J. C.; Cheng, J.; Fan, Z.; Chen, P. Y.; Ruan, H. F.; Tu, Z. Y.; Kang, N.; Li, N.; Xu, Y.; Wang, X. B.; Shi, F.; Mu, L. B.; Li, T. F.; Ren, W. R.; Lin, X.; Zhu, J.; Fang, X. H.; Amrein, M. W.; Wu, W. H.; Yan, L. T.; Lu, J. H.; Xia, T.; Shi, Y., Pseudomonas aeruginosa quorum-sensing metabolite induces host immune cell death through cell surface lipid domain dissolution. *Nat. Microbiol.* **2019,** *4* (1), 97-111.

33. Yoon, B. K.; Jackman, J. A.; Kim, M. C.; Sut, T. N.; Cho, N. J., Correlating Membrane Morphological Responses with Micellar Aggregation Behavior of Capric Acid and Monocaprin. *Langmuir* **2017,** *33* (11), 2750-2759.

34. Glansdorp, F. G.; Thomas, G. L.; Lee, J. J. K.; Dutton, J. M.; Salmond, G. P. C.; Welch, M.; Spring, D. R., Synthesis and stability of small molecule probes for Pseudomonas aeruginosa quorum sensing modulation. *Org. Biomol. Chem.* **2004,** *2* (22), 3329-3336.

35. Boursier, M. E.; Combs, J. B.; Blackwell, H. E., N-Acyl L-Homocysteine Thiolactones Are Potent and Stable Synthetic Modulators of the RhlR Quorum Sensing Receptor in Pseudomonas aeruginosa. *ACS Chem. Biol.* **2019,** *14* (2), 186-191.

36. Bruckner, R. J.; Mansy, S. S.; Ricardo, A.; Mahadevan, L.; Szostak, J. W., Flip-Flop-Induced Relaxation of Bending Energy: Implications for Membrane Remodeling. *Biophys. J.* **2009,** *97* (12), 3113-3122.

37. Brink-van der Laan, E. V.; Killian, J. A.; de Kruijff, B., Nonbilayer lipids affect peripheral and integral membrane proteins via changes in the lateral pressure profile. *Biochim. Biophys. Acta, Biomembr.* **2004,** *1666* (1-2), 275-288.

38. Anglin, T. C.; Conboy, J. C., Kinetics and Thermodynamics of Flip-Flop in Binary Phospholipid Membranes Measured by Sum-Frequency Vibrational Spectroscopy. *Biochemistry* **2009,** *48* (43), 10220-10234.

39. Ohnishi, S.; Ito, T., Calcium-Induced Phase Separations in Phosphatidylserine-Phosphatidylcholine Membranes. *Biochemistry* **1974,** *13* (5), 881-887.

40. Flynn, K. R.; Martin, L. L.; Ackland, M. L.; Torriero, A. A. J., Real-Time Quartz Crystal Microbalance Monitoring of Free Docosahexaenoic Acid Interactions with Supported Lipid Bilayers. *Langmuir* **2016,** *32* (45), 11717-11727.

41. Melcrova, A.; Pokorna, S.; Pullanchery, S.; Kohagen, M.; Jurkiewicz, P.; Hof, M.; Jungwirth, P.; Cremer, P. S.; Cwiklik, L., The complex nature of calcium cation interactions with phospholipid bilayers. *Sci. Rep.* **2016,** *6*, 38035.

42. Doosti, B. A.; Pezeshkian, W.; Bruhn, D. S.; Ipsen, J. H.; Khandelia, H.; Jeffries, G. D. M.; Lobovidna, T., Membrane Tubulation in Lipid Vesicles Triggered by the Local Application of Calcium Ions. *Langmuir* **2017,** *33* (41), 11010-11017.

43. Churchward, M. A.; Rogasevskaia, T.; Brandman, D. M.; Khosravani, H.; Nava, P.; Atkinson, J. K.; Coorssen, J. R., Specific lipids supply critical negative spontaneous curvature - An essential component of native Ca2+-triggered membrane fusion. *Biophys. J.* **2008,** *94* (10), 3976-3986.

44. Kooijman, E. E.; Chupin, V.; Fuller, N. L.; Kozlov, M. M.; de Kruijff, B.; Burger, K. N. J.; Rand, P. R., Spontaneous curvature of phosphatidic acid and lysophosphatidic acid. *Biochemistry* **2005,** *44* (6), 2097-2102.

45. Sut, T. N.; Jackman, J. A.; Cho, N. J., Understanding How Membrane Surface Charge Influences Lipid Bicelle Adsorption onto Oxide Surfaces. *Langmuir* **2019,** *35* (25), 8436-8444.

46. Sut, T. N.; Park, S.; Choe, Y.; Cho, N. J., Characterizing the Supported Lipid Membrane Formation from Cholesterol-Rich Bicelles. *Langmuir* **2019,** *35* (47), 15063-15070.

47. Kolahdouzan, K.; Jackman, J. A.; Yoon, B. K.; Kim, M. C.; Johal, M. S.; Cho, N. J., Optimizing the Formation of Supported Lipid Bilayers from Bicellar Mixtures. *Langmuir* **2017,** *33* (20), 5052-5064.

48. Lichtenberg, D.; Ahyayauch, H.; Alonso, A.; Goni, F. M., Detergent solubilization of lipid bilayers: a balance of driving forces. *Trends Biochem. Sci.* **2013,** *38* (2), 85-93.

49. Jackman, J. A.; Cho, N. J., Supported Lipid Bilayer Formation: Beyond Vesicle Fusion. *Langmuir* **2020,** *36* (6), 1387-1400.

50. Kim, M. C.; Gunnarsson, A.; Tabaei, S. R.; Hook, F.; Cho, N. J., Supported lipid bilayer repair mediated by AH peptide. *Phys. Chem. Chem. Phys.* **2016,** *18* (4), 3040-3047.

51. Silvius, J. R., Thermotropic Phase Transitions of Pure Lipids in Model Membranes and Their Modifications by Membrane Proteins. In *Lipid-Protein Interactions*, John Wiley & Sons, Inc.: New York, 1982.

52. Welsh, M. A.; Blackwell, H. E., Chemical genetics reveals environment-specific roles for quorum sensing circuits in Pseudomonas aeruginosa. *Cell Chem. Biol.* **2016,** *23*, 361-369.

53. Fuqua, C.; Parsek, M. R.; Greenberg, E. P., Regulation of gene expression by cell-to-cell communication: Acyl-homoserine lactone quorum sensing. *Annu. Rev. Genet.* **2001,** *35*, 439-468.

54. Jensen, P. O.; Givskov, M.; Bjarnsholt, T.; Moser, C., The immune system vs. Pseudomonas aeruginosa biofilms. *FEMS Immunol. Med. Microbiol.* **2010,** *59* (3), 292-305.

55. Reis, R. S.; Pereira, A. G.; Neves, B. C.; Freire, D. M. G., Gene regulation of rhamnolipid production in Pseudomonas aeruginosa - A review. *Bioresour. Technol.* **2011,** *102* (11), 6377-6384.

56. Rutherford, S. T.; Bassler, B. L., Bacterial quorum sensing: its role in virulence and possibilities for its control. *Cold Spring Harb. Perspect. Med.* **2012,** *2* (11), a012427.

57. O'Loughlin, C. T.; Miller, L. C.; Siryaporn, A.; Drescher, K.; Semmelhack, M. F.; Bassler, B. L., A quorum-sensing inhibitor blocks Pseudomonas aeruginosa virulence and biofilm formation. *Proc. Natl. Acad. Sci. U. S. A.* **2013,** *110* (44), 17981- 17986.

58. Richter, R. P.; Brisson, A. R., Following the formation of supported lipid bilayers on mica: A study combining AFM, QCM-D, and ellipsometry. *Biophys. J.* **2005,** *88* (5), 3422-3433.

59. Pedersen, U. R.; Leidy, C.; Westh, P.; Peters, G. H., The effect of calcium on the properties of charged phospholipid bilayers. *Biochim. Biophys. Acta, Biomembr.* **2006,** *1758* (5), 573-582.

60. Sinn, C. G.; Antonietti, M.; Dimova, R., Binding of calcium to phosphatidylcholine-phosphatidylserine membranes. *Colloids Surf., A* **2006,** *282*, 410-419.

61. Dluhy, R. A.; Cameron, D. G.; Mantsch, H. H.; Mendelsohn, R., Fourier-Transform Infrared Spectroscopic Studies of the Effect of Calcium-Ions on Phosphatidylserine. *Biochemistry* **1983,** *22* (26), 6318-6325.

62. Filippov, A.; Oradd, G.; Lindblom, G., Effect of NaCl and $CaCl_2$ on the lateral diffusion of zwitterionic and anionic lipids in bilayers. *Chem. Phys. Lipids* **2009,** *159* (2), 81-87.

63. Bennett, W. F. D.; MacCallum, J. L.; Hinner, M. J.; Marrink, S. J.; Tieleman, D. P., Molecular View of Cholesterol Flip-Flop and Chemical Potential in Different Membrane Environments. *J. Am. Chem. Soc.* **2009,** *131* (35), 12714-12720.

64. Yoon, B. K.; Park, S.; Ma, G. J.; Kolahdouzan, K.; Zhdanov, V. P.; Jackman, J. A.; Cho, N. J., Competing Interactions of Fatty Acids and Monoglycerides Trigger Synergistic Phospholipid Membrane Remodeling. *J. Phys. Chem. Lett.* **2020,** *11* (13), 4951-4957.

65. Apel-Paz, M.; Doncel, G. F.; Vanderlick, T. K., Impact of membrane cholesterol content on the resistance of vesicles to surfactant attack. *Langmuir* **2005,** *21* (22), 9843-9849.

66. Heerklotz, H.; Seelig, J., Leakage and lysis of lipid membranes induced by the lipopeptide surfactin. *Eur. Biophys. J.* **2007,** *36* (4-5), 305-314.

67. Heerklotz, H., Membrane stress and permeabilization induced by asymmetric incorporation of compounds. *Biophys. J.* **2001,** *81* (1), 184-195.

68. Staykova, M.; Arroyo, M.; Rahimi, M.; Stone, H. A., Confined Bilayers Passively Regulate Shape and Stress. *Phys. Rev. Lett.* **2013,** *110* (2), 028101.

69. Allhusen, J. S.; Conboy, J. C., The Ins and Outs of Lipid Flip-Flop. *Acc. Chem. Res.* **2017,** *50* (1), 58-65.

70. Pabst, G.; Hodzic, A.; Strancar, J.; Danner, S.; Rappolt, M.; Laggner, P., Rigidification of neutral lipid bilayers in the presence of salts. *Biophys. J.* **2007,** *93* (8), 2688-2696.

71. Kucerka, N.; Ermakova, E.; Dushanov, E.; Kholmurodov, K. T.; Kurakin, S.; Zelinska, K.; Uhrikova, D., Cation-Zwitterionic Lipid Interactions Are Affected by the Lateral Area per Lipid. *Langmuir* **2021,** *37* (1), 278-288.

72. Kagawa, R.; Hirano, Y.; Taiji, M.; Yasuoka, K.; Yasui, M., Dynamic interactions of cations, water and lipids and influence on membrane fluidity. *J. Membr. Sci.* **2013,** *435*, 130-136.

73. Julicher, F.; Lipowsky, R., Domain-Induced Budding of Vesicles. *Phys. Rev. Lett.* **1993,** *70* (19), 2964-2967.

74. Baumgart, T.; Hess, S. T.; Webb, W. W., Imaging coexisting fluid domains in biomembrane models coupling curvature and line tension. *Nature* **2003,** *425* (6960), 821-824.

75. Zuhorn, I. S.; Engberts, J.; Hoekstra, D., Gene delivery by cationic lipid vectors: overcoming cellular barriers. *Eur. Biophys. J.* **2007,** *36* (4-5), 349-362.

76. Daniels, R.; Reynaert, S.; Hoekstra, H.; Verreth, C.; Janssens, J.; Braeken, K.; Fauvart, M.; Beullens, S.; Heusdens, C.; Lambrichts, I.; De Vos, D. E.; Vanderleyden, J.; Vermant, J.; Michiels, J., Quorum signal molecules as biosurfactants affecting swarming in Rhizobium etli. *Proc. Natl. Acad. Sci. U. S. A.* **2006,** *103* (40), 14965-14970.

77. Davies, D. G.; Parsek, M. R.; Pearson, J. P.; Iglewski, B. H.; Costerton, J. W.; Greenberg, E. P., The involvement of cell-to-cell signals in the development of a bacterial biofilm. *Science* **1998,** *280* (5361), 295-298.

78. Zhou, J.; Loftus, A. L.; Mulley, G.; Jenkins, A. T. A., A Thin Film Detection/Response System for Pathogenic Bacteria. *J. Am. Chem. Soc.* **2010,** *132* (18), 6566-6570.

Supporting Information for Chapter 5

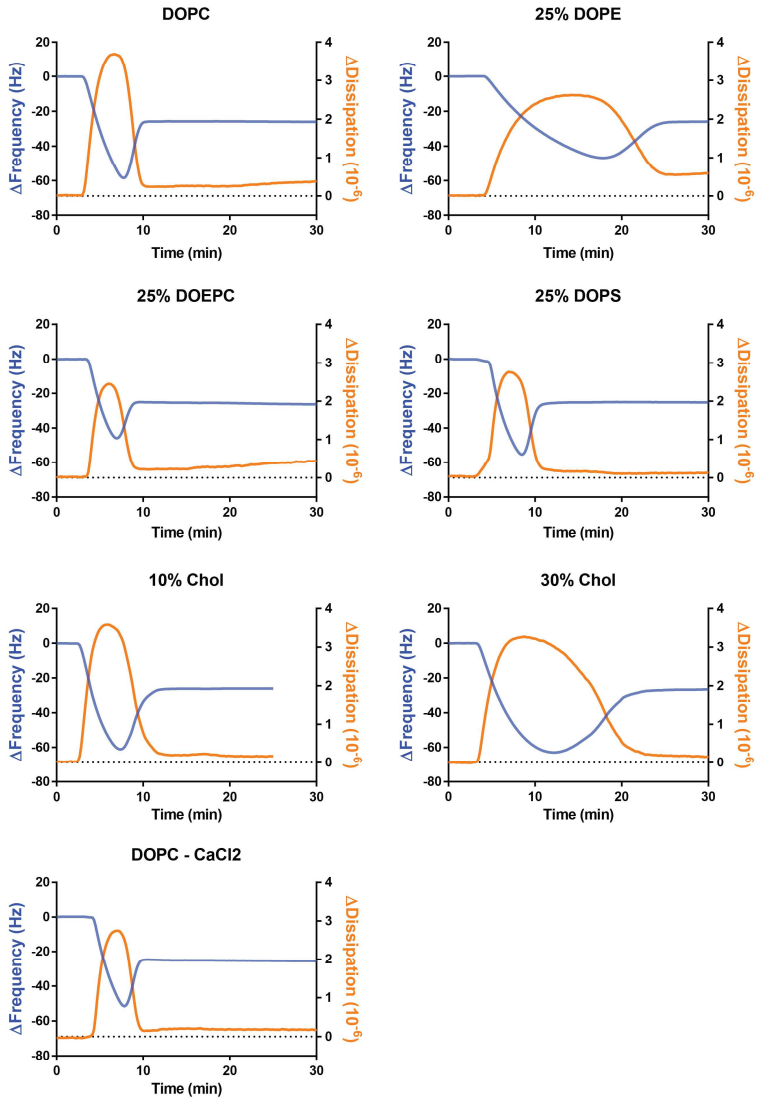


Figure S1A: QCM-D measurements of multicomponent SLB formation on an SiO_2 surface using the bicelle formation technique. Changes in frequency (ΔFrequency, blue lines) and dissipation (ΔDissipation, orange lines) shown are representative of three or four independent experiments. We note that DOPE-containing SLBs were formed at a bicelle concentration of 0.015 mM (see main text), while all others were formed at a concentration 0.31 mM.

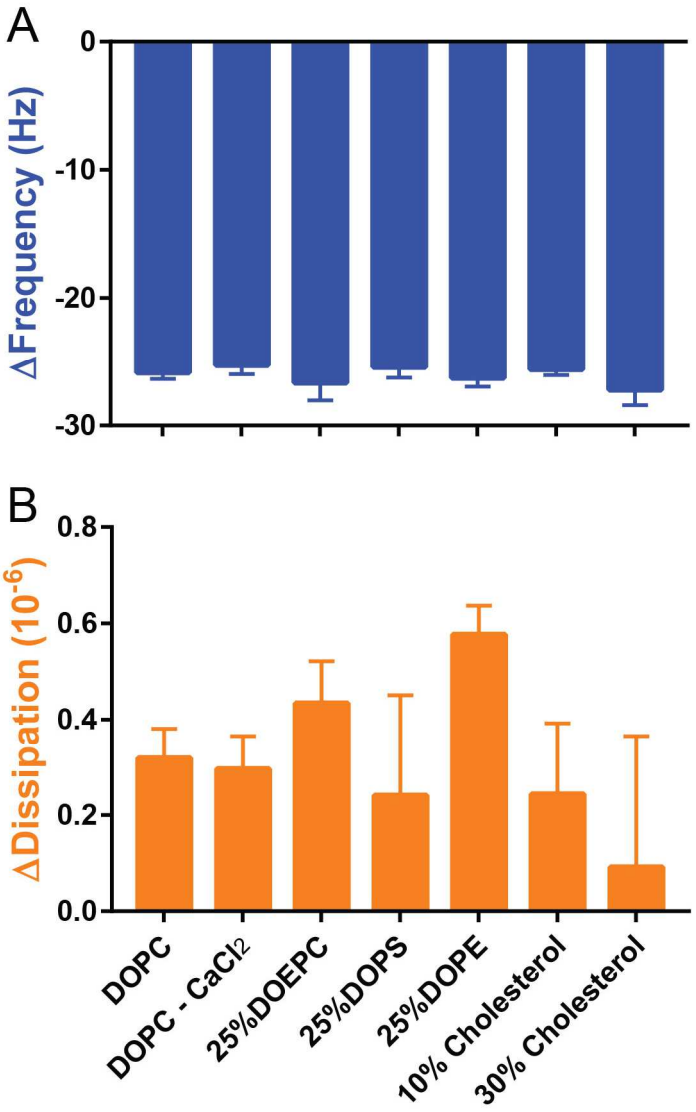


Figure S1B: QCM-D measurements of multicomponent bilayers formed by the bicelle formation technique. Changes in (A) frequency (ΔFrequency) and (B) dissipation (ΔDissipation) going from a bare SiO_2 surface to having an SLB of various compositions on the surface. The values shown are the means and a single standard deviation of three or four experiments (n= 3-4).

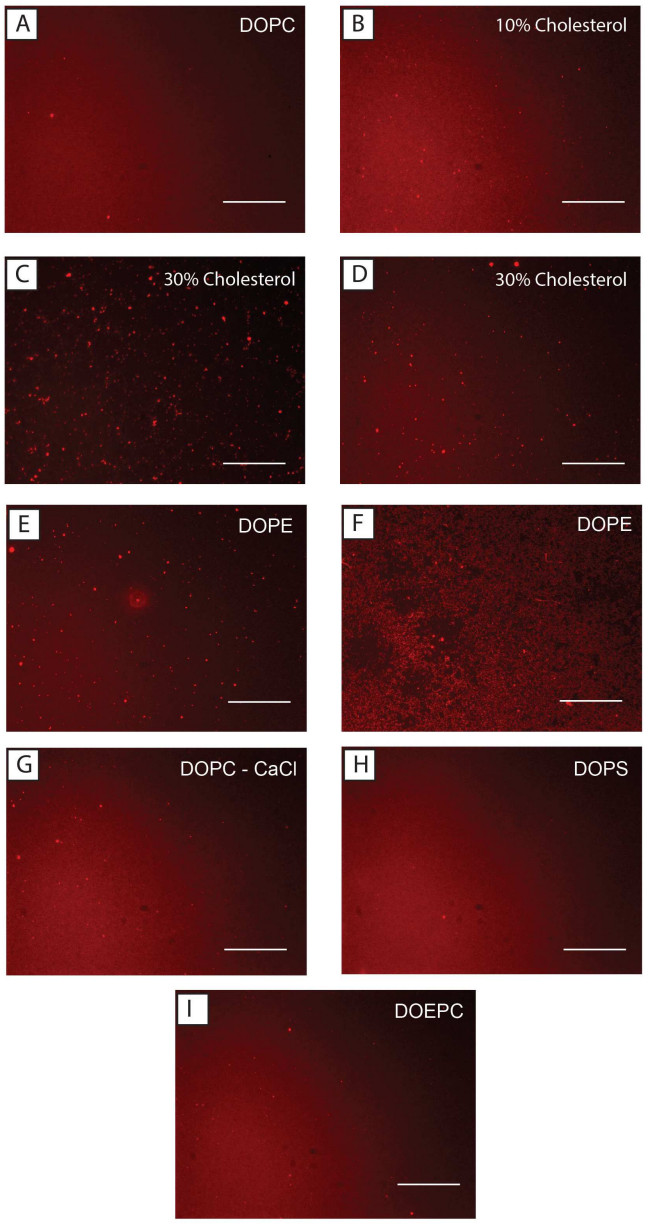


Figure S2: Fluorescence microscopy images of various multicomponent SLBs on an SiO_2 surface formed using the bicelle formation technique. The bilayers shown are composed of (A) 100% DOPC, (B) 90 mol% DOPC/10 mol% cholesterol, (C-D) 70 mol% DOPC/30 mol% cholesterol, (E-F) 75 mol% DOPC/25 mol% DOPE, (G) 100% DOPC in $CaCl_2$-containing buffer, (H) 75 mol% DOPC/25 mol% DOPS in $CaCl_2$-containing buffer and (I) 75 mol% DOPC/25 mol% DOEPC.

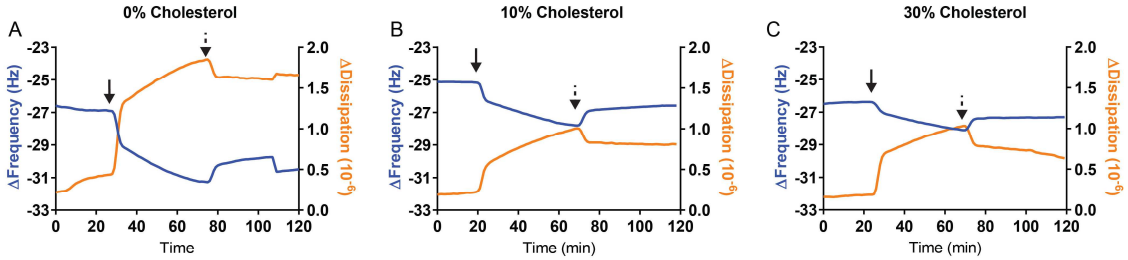


Figure S3: Representative QCM-D measurements of large-scale bilayer reformations in (A) DOPC SLBs, (B) DOPC SLBs containing 10% cholesterol and (C) DOPC SLBs containing 30% cholesterol initiated by the introduction of 3-oxo-C12-AHL solutions at 50 µM. The changes in frequency (ΔFrequency, blue lines) and dissipation (ΔDissipation, orange lines) shown are representative of three or four independent experiments. The initial measurement values (t=0 min) of these experiments corresponds to an SLB on an SiO_2 surface. AHL solutions were introduced at the time indicated by the filled arrow and buffer wash was introduced at the time indicated by the dashed arrow.

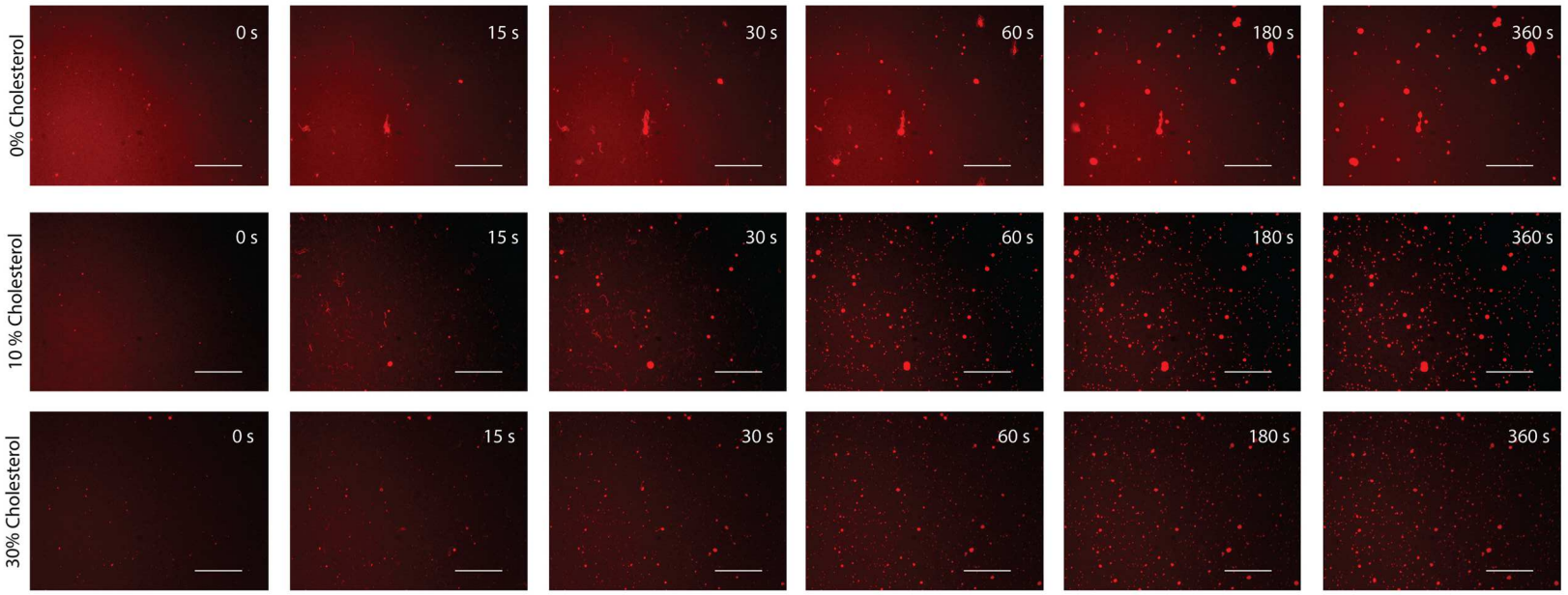


Figure S4A: Representative fluorescence micrographs of fluorescently labeled (*top*) DOPC, (*middle*) 10% cholesterol/DOPC, and (*bottom*) 30% cholesterol/DOPC SLBs after exposure to a continuous flow of 3-oxo-C12-AHL solutions at 50 μM. The images were acquired at time points indicated in the top-right corner of the images after the first membrane restructuring event was observed. The 360-second images shown here are the same as those shown in Figure 3 of the main text. The direction of flow in all of the images was from the bottom to the top of the image. The scale bars represent 30 μM.

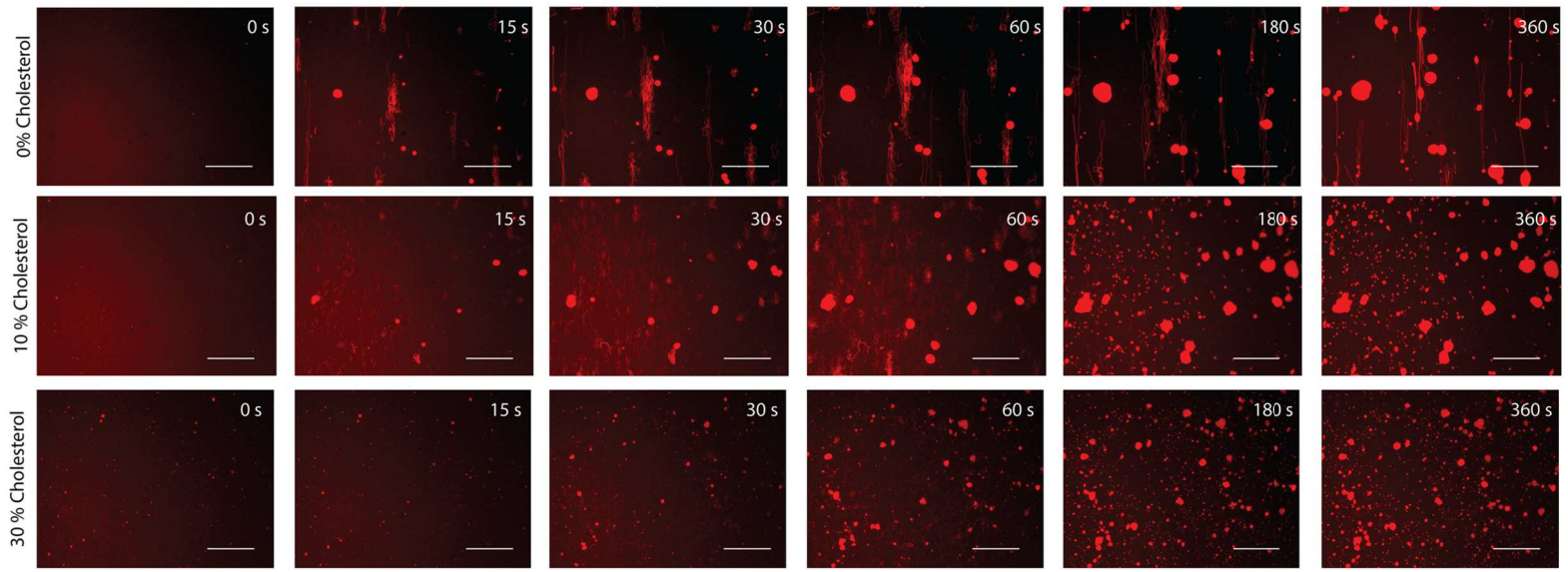


Figure S4B: Representative fluorescence micrographs of fluorescently labeled (*top*) DOPC, (*middle*) 10% cholesterol/DOPC, and (*bottom*) 30% cholesterol/DOPC SLBs after exposure to a continuous flow of 3-oxo-C12-AHL solutions at 200 µM. The images were acquired at time points indicated in the top-right corner of the images after the first membrane restructuring event was observed. The 360-second images shown here are the same as those shown in Figure 3 of the main text. The direction of flow in all of the images was from the bottom to the top of the image. The scale bars represent 30 µM.

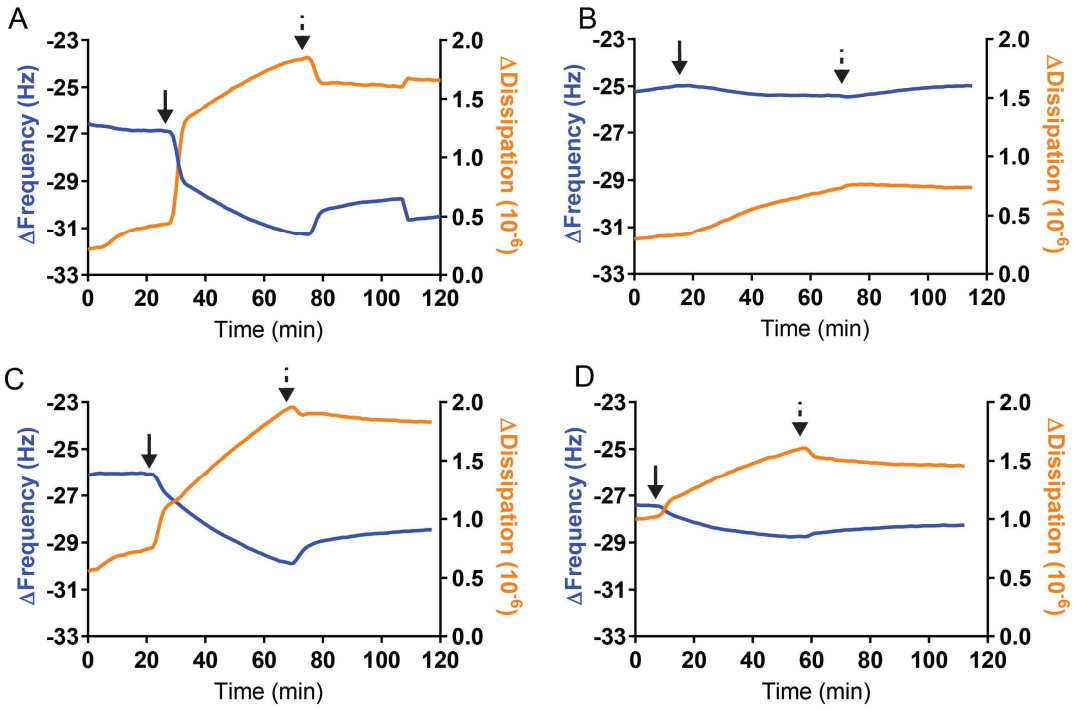


Figure S5: Representative QCM-D measurements of large-scale bilayer reformations in (A-B) DOPC and (C-D) 75 mol% DOPC and 25 mol% DOPE SLBs initiated by the introduction of (A,C) 3-oxo-C12-AHL and (B,D) 3-oxo-C12-HS solutions at 50 μM. The changes in frequency (ΔFrequency, blue lines) and dissipation (ΔDissipation, orange lines) shown are representative of three or four independent experiments. The initial measurement values (t=0 min) of these experiments corresponds to an SLB on an SiO_2 surface. AHL solutions were introduced at the time indicated by the filled arrow and buffer wash was introduced at the time indicated by the dashed arrow.

Note: In the QCM-D measurements shown in Figure S5A for characterization of DOPC bilayers, we observed some instantaneous changes in frequency and dissipation that, upon analysis of other harmonics, not shown here, were determined to be artifacts in the measurements. To avoid contributions of these artifacts in our analysis of frequency and dissipation changes upon buffer washes arising from that experiment, we report changes in frequency and dissipation for these DOCP bilayers between the time right after buffer was introduced to the bilayer (as denoted by the dashed arrow) and the time just before the artifact was observed (determined to be 32 minutes after the introduction of buffer wash).

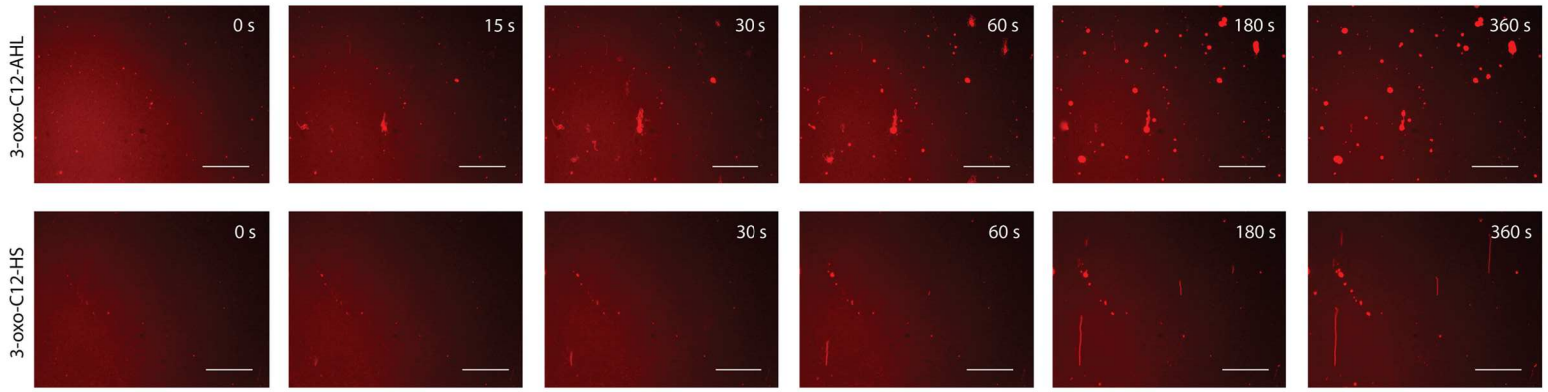


Figure S6A: Representative fluorescence micrographs of fluorescently labeled DOPC SLBs after exposure to a continuous flow of (*top*) 3-oxo-C12-AHL or (*bottom*) 3-oxo-C12-HS solutions at 50 μM. The images were acquired at time points indicated in the top-right corner of the images after the first membrane restructuring event was observed. The 360-second images shown here are the same as those shown in Figure 6 of the main text. The direction of flow in all of the images was from the bottom to the top of the image. The scale bars represent 30 μM.

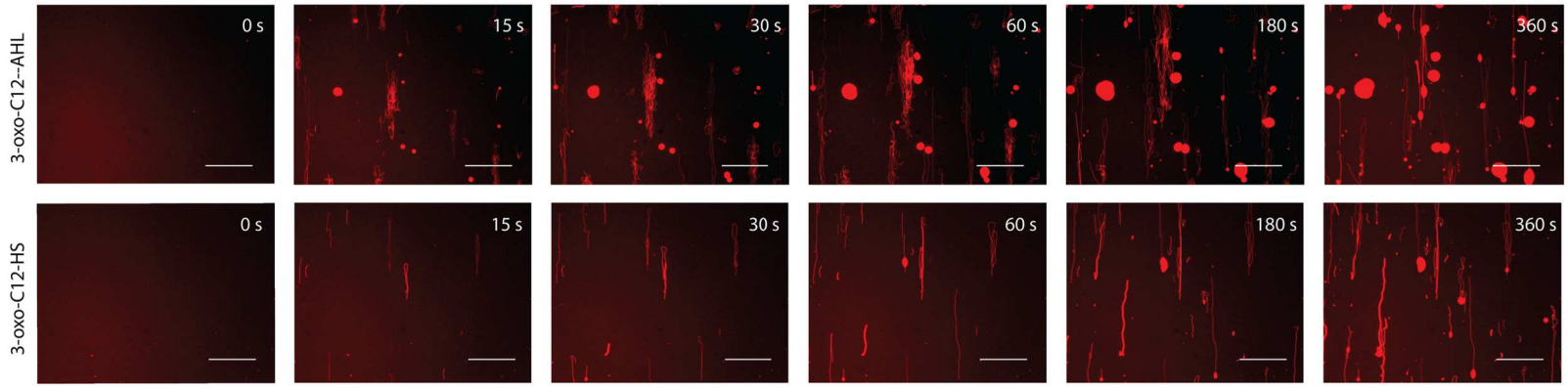


Figure S6B Representative fluorescence micrographs of fluorescently labeled DOPC SLBs after exposure to a continuous flow of (*top*) 3-oxo-C12-AHL or (*bottom*) 3-oxo-C12-HS solutions at 200 μM. The images were acquired at time points indicated in the top-right corner of the images after the first membrane restructuring event was observed. The 360-second images shown here are the same as those shown in Figure 6 of the main text. The direction of flow in all of the images was from the bottom to the top of the image. The scale bars represent 30 μM.

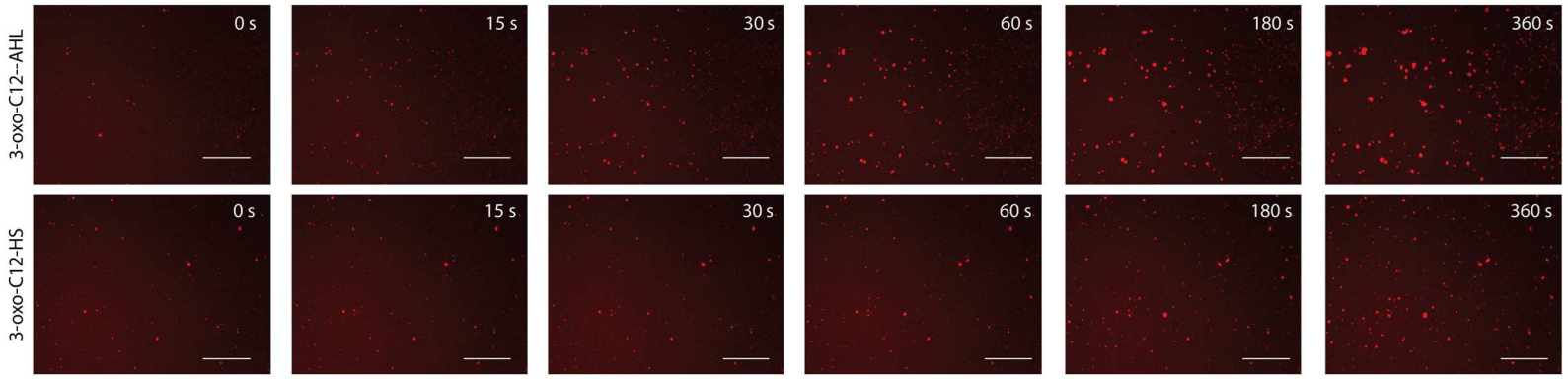


Figure S6C: Representative fluorescence micrographs of fluorescently labeled 75% DOPC/25% DOPE SLBs after exposure to a continuous flow of (*top*) 3-oxo-C12-AHL or (*bottom*) 3-oxo-C12-HS solutions at 50 μM. The images were acquired at time points indicated in the top-right corner of the images after the first membrane restructuring event was observed. The 360-second images shown here are the same as those shown in Figure 6 of the main text. The direction of flow in all of the images was from the bottom to the top of the image. The scale bars represent 30 μM.

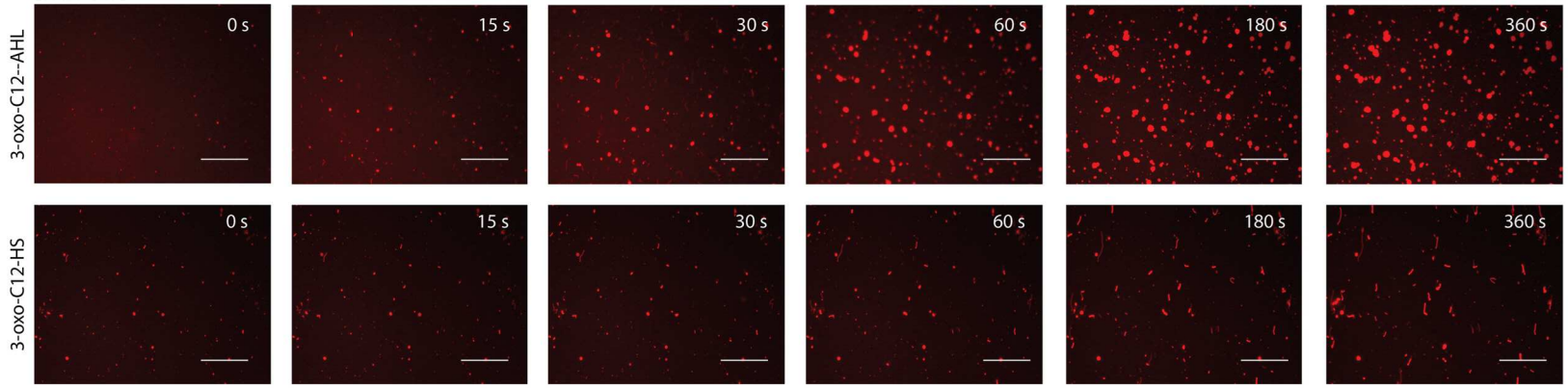


Figure S6D: Representative fluorescence micrographs of fluorescently labeled 75% DOPC/25% DOPE SLBs after exposure to a continuous flow of (*top*) 3-oxo-C12-AHL or (*bottom*) 3-oxo-C12-HS solutions at 200 μM. The images were acquired at time points indicated in the top-right corner of the images after the first membrane restructuring event was observed. The 360-second images shown here are the same as those shown in Figure 6 of the main text. The direction of flow in all of the images was from the bottom to the top of the image. The scale bars represent 30 μM.

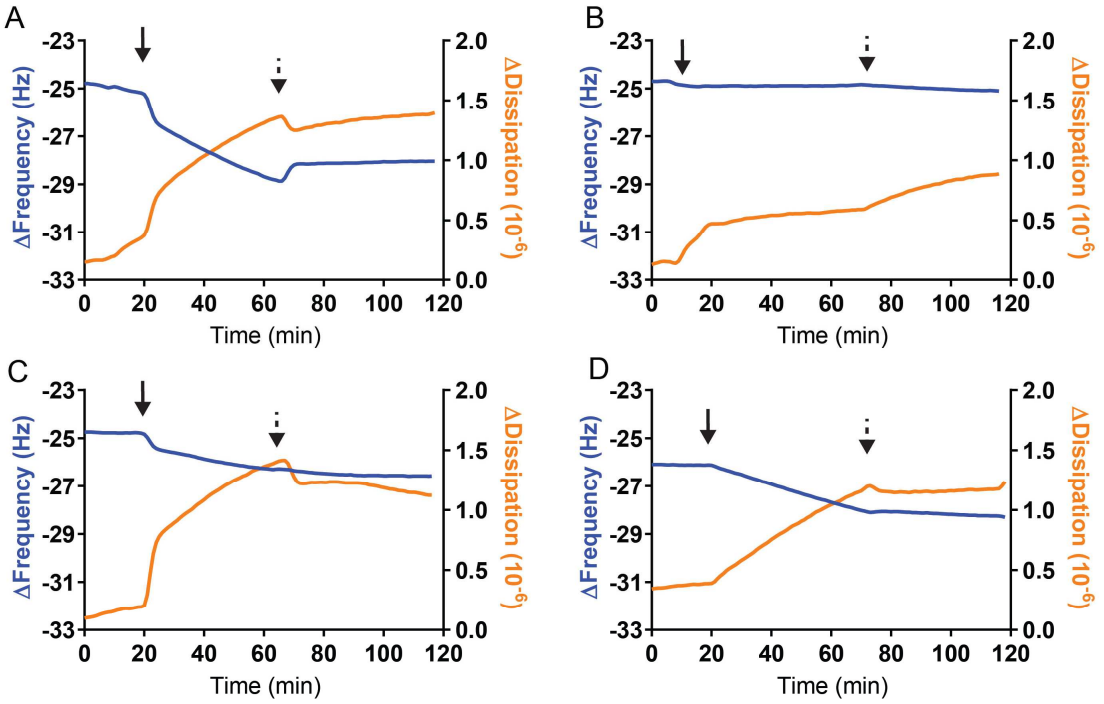


Figure S7: Representative QCM-D measurements of large-scale bilayer reformations in (A-B) 100% DOPC and (C-D) 75 mol% DOPC and 25 mol% DOPS SLBs in $CaCl_2$-containing buffer initiated by the introduction of (A,C) 3-oxo-C12-AHL and (B,D) 3-oxo-C12-HS solutions at 50 µM. The changes in frequency (ΔFrequency, blue lines) and dissipation (ΔDissipation, orange lines) shown are representative of three or four independent experiments. The initial measurement values (t=0 min) of these experiments correspond to an SLB on an SiO_2 surface. AHL solutions were introduced at the time indicated by the filled arrow and buffer wash was introduced at the time indicated by the dashed arrow.

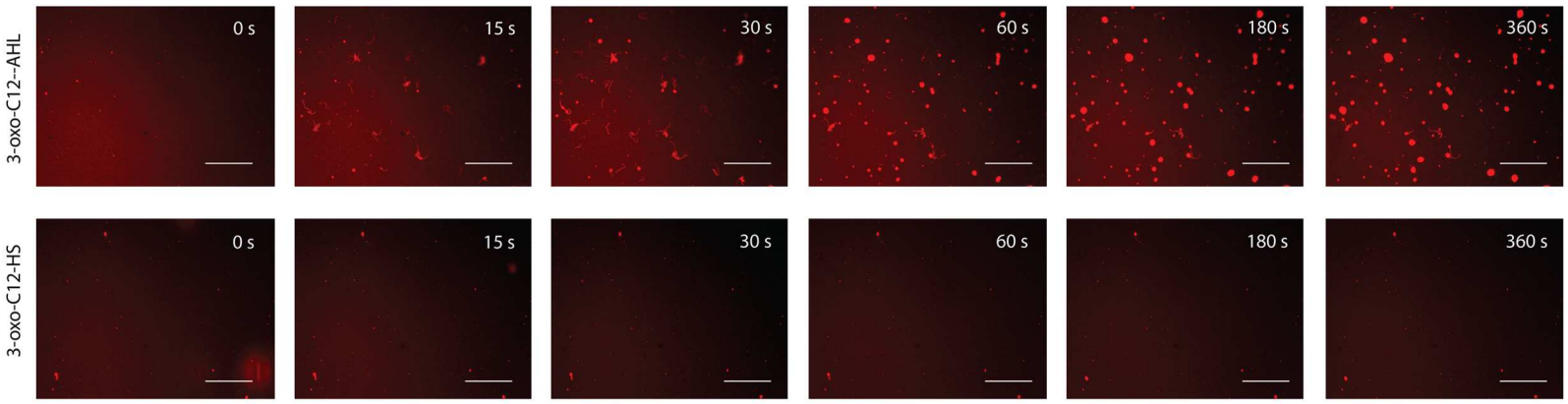


Figure S8A: Representative fluorescence micrographs of fluorescently labeled DOPC SLBs in 2 mM $CaCl_2$-containing buffer after exposure to a continuous flow of (*top*) 3-oxo-C12-AHL or (*bottom*) 3-oxo-C12-HS solutions at 50 µM. The images were acquired at time points indicated in the top-right corner of the images after the first membrane restructuring event was observed. The 360-second images shown here are the same as those shown in Figure 8 of the main text. The direction of flow in all of the images was from the bottom to the top of the image. The scale bars represent 30 µM.

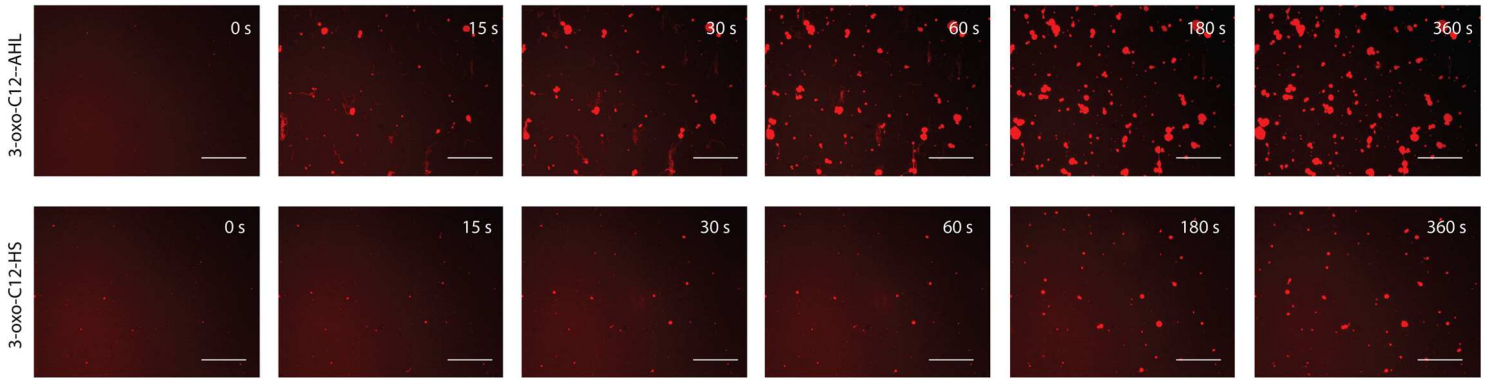


Figure S8B: Representative fluorescence micrographs of fluorescently labeled DOPC SLBs in 2 mM $CaCl_2$-containing buffer after exposure to a continuous flow of (*top*) 3-oxo-C12-AHL or (*bottom*) 3-oxo-C12-HS solutions at 200 μM. The images were acquired at time points indicated in the top-right corner of the images after the first membrane restructuring event was observed. The 360-second images shown here are the same as those shown in Figure 8 of the main text. The direction of flow in all of the images was from the bottom to the top of the image. The scale bars represent 30 μM.

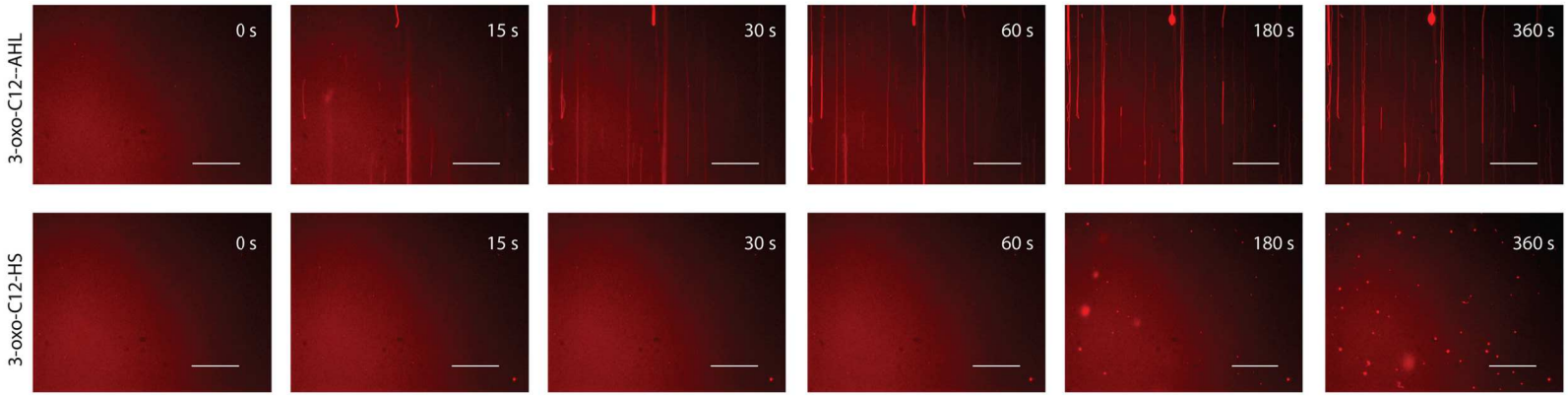


Figure S8C: Representative fluorescence micrographs of fluorescently labeled 75% DOPC/25% DOPS SLBs in 2 mM $CaCl_2$-containing buffer after exposure to a continuous flow of (*top*) 3-oxo-C12-AHL or (*bottom*) 3-oxo-C12-HS solutions at 50 µM. The images were acquired at time points indicated in the top-right corner of the images after the first membrane restructuring event was observed. The 360-second images shown here are the same as those shown in Figure 8 of the main text. The direction of flow in all of the images was from the bottom to the top of the image. The scale bars represent 30 µM.

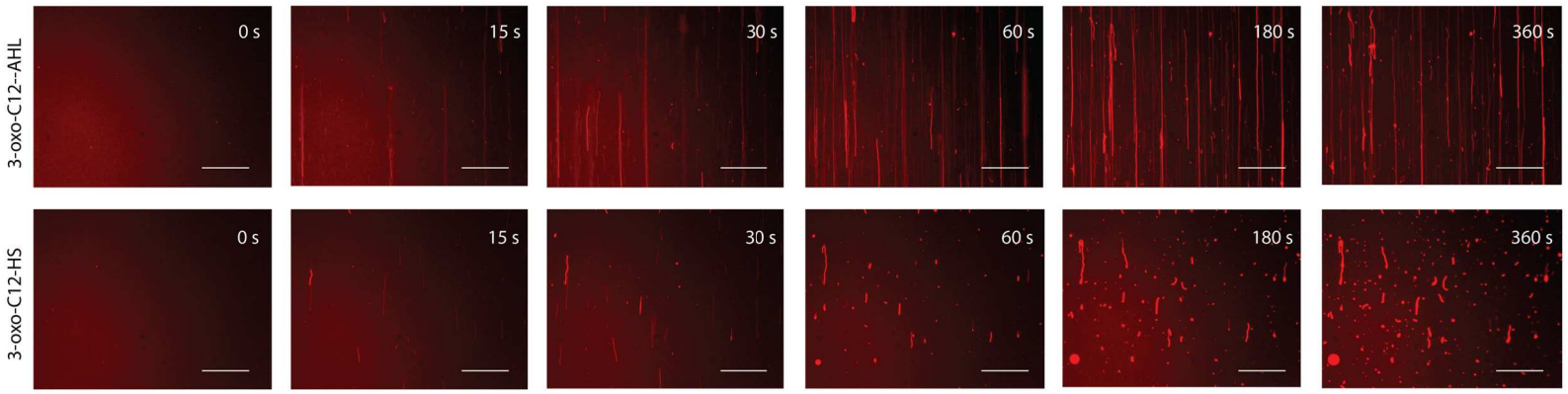


Figure S8D: Representative fluorescence micrographs of fluorescently labeled 75% DOPC/25% DOPS SLBs in 2 mM $CaCl_2$-containing buffer after exposure to a continuous flow of (*top*) 3-oxo-C12-AHL or (*bottom*) 3-oxo-C12-HS solutions at 200 µM. The images were acquired at time points indicated in the top-right corner of the images after the first membrane restructuring event was observed. The 360-second images shown here are the same as those shown in Figure 8 of the main text. The direction of flow in all of the images was from the bottom to the top of the image. The scale bars represent 30 µM.

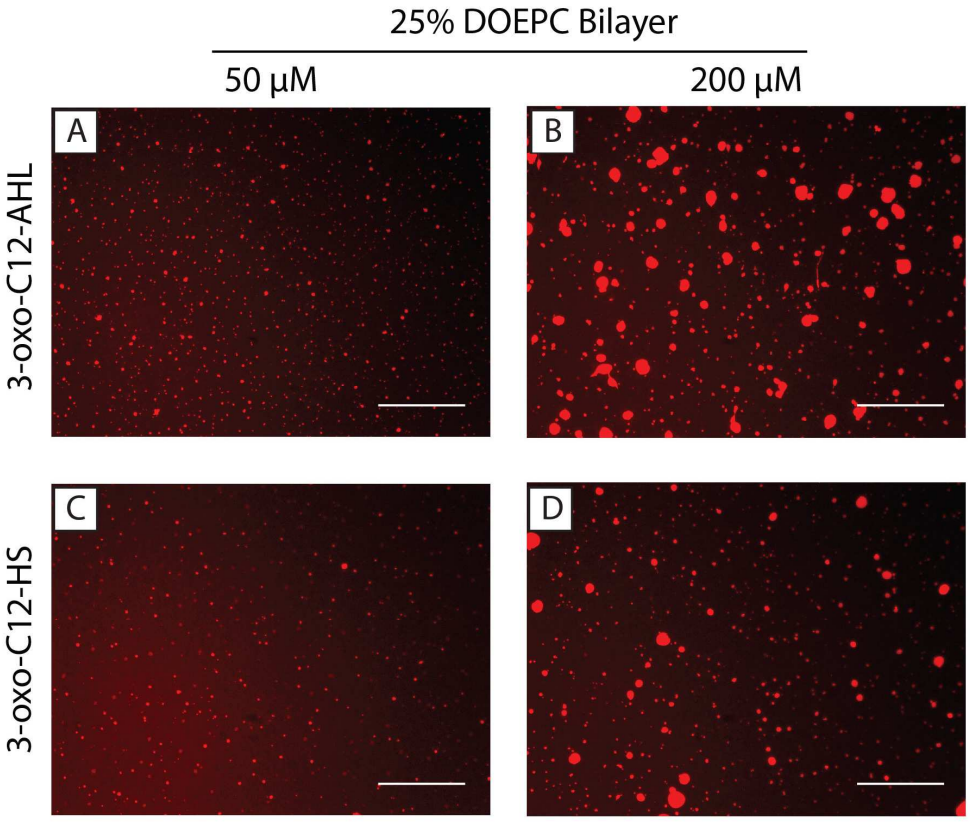


Figure S9: Representative top-down fluorescence micrographs of fluorescently labeled 75 mol% DOPC and 25 mol% DOEPC SLBs after interacting with a continuous flow of (A,C) 50 µM or (B,D) 200 µM solutions of (A-B) 3-oxo-C12-AHL or (C-D) 3-oxo-C12-HS. Images were acquired 360 seconds after the onset of membrane restructuring. The direction of flow in all images was from the bottom to the top of the image. Scale bars are 30 µm.

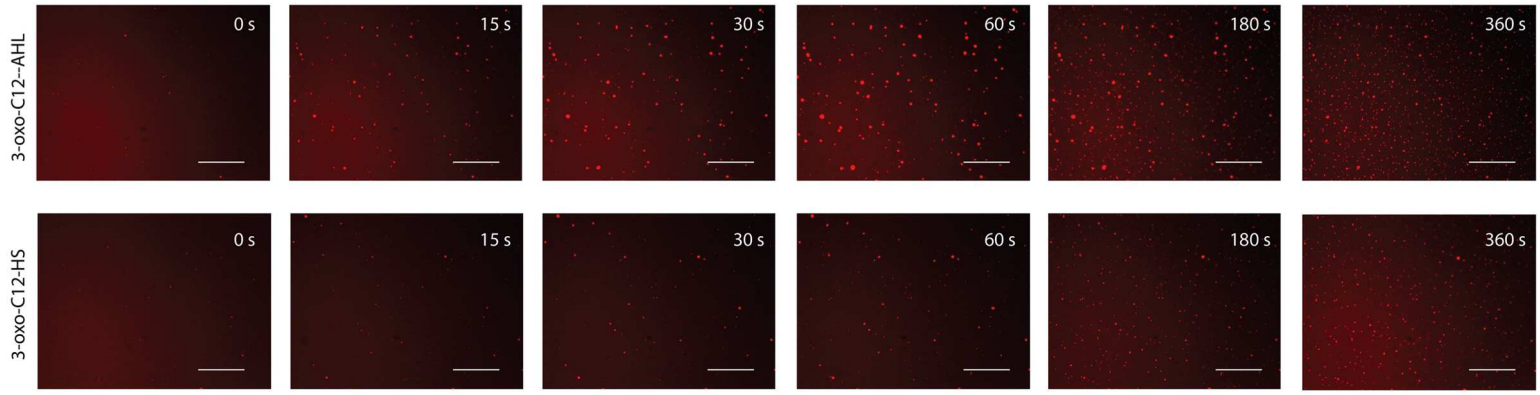


Figure S10A: Representative fluorescence micrographs of fluorescently labeled 75% DOPC/25% DOEPC SLBs after exposure to a continuous flow of (*top*) 3-oxo-C12-AHL or (*bottom*) 3-oxo-C12-HS solutions at 50 μM. The images were acquired at time points indicated in the top-right corner of the images after the first membrane restructuring event was observed. The 360-second images shown here are the same as those shown in Figure S9. The direction of flow in all of the images was from the bottom to the top of the image. The scale bars represent 30 μM.

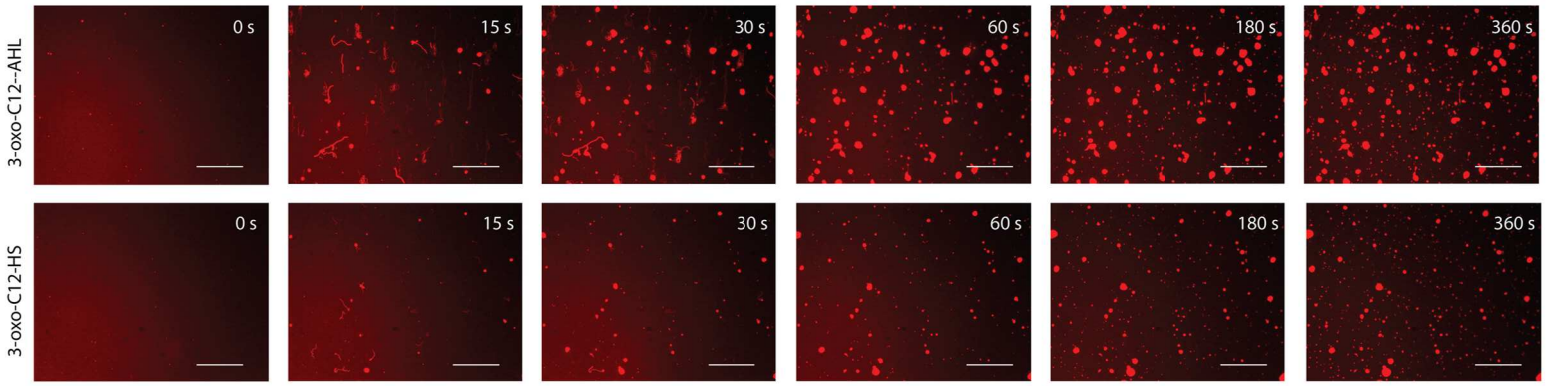


Figure S10B: Representative fluorescence micrographs of fluorescently labeled 75% DOPC/25% DOEPC SLBs after exposure to a continuous flow of (*top*) 3-oxo-C12-AHL or (*bottom*) 3-oxo-C12-HS solutions at 200 μM. The images were acquired at time points indicated in the top-right corner of the images after the first membrane restructuring event was observed. The 360-second images shown here are the same as those shown in Figure S9. The direction of flow in all of the images was from the bottom to the top of the image. The scale bars represent 30 μM.

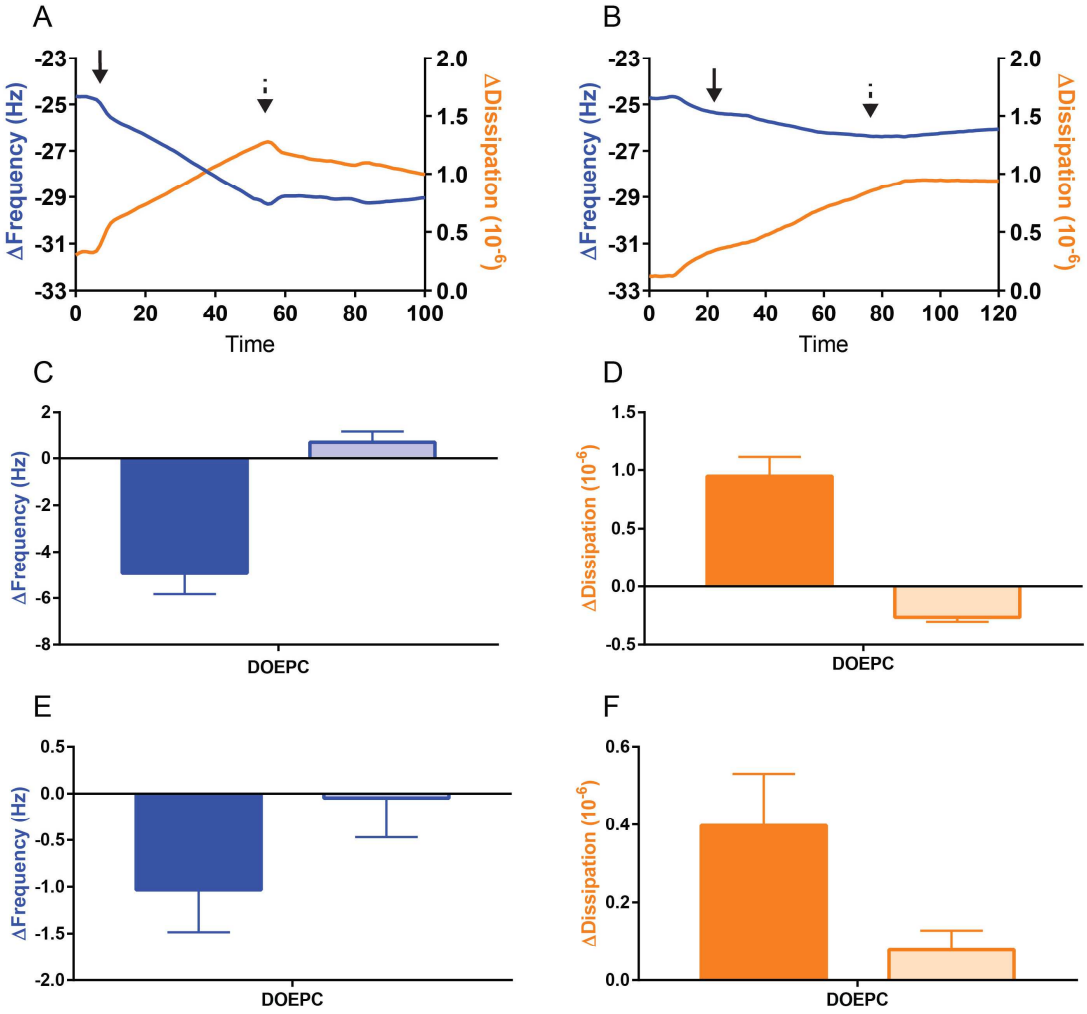


Figure S11: (A-B) Representative QCM-D measurements of large-scale bilayer reformations in 75 mol% DOPC and 25 mol% DOEPC SLBs initiated by the introduction of (A) 3-oxo-C12-AHL and (B) 3-oxo-C12-HS solutions at 50 µM. The changes in frequency (ΔFrequency, blue lines) and dissipation (ΔDissipation, orange lines) shown are representative of three or four independent experiments. The initial measurement values (t=0 min) of these experiments corresponds to an SLB on an SiO_2 surface. AHL solutions were introduced at the time indicated by the filled arrow and buffer wash was introduced at the time indicated by the dashed arrow. Changes in (C, E) frequency and (D, F) dissipation for 75 mol% DOPC and 25 mol% DOEPC SLBs promoted by 50 µM solutions of (C-D) 3-oxo-C12-AHL or (E-F) 3-oxo-C12-HS for 45 minutes (filled bars) or after 45 minutes of buffer wash (open bars). The values shown are the means and a single standard deviation of three or four experiments (n= 3-4).

Interactions of 3-oxo-C12-AHL and 3-oxo-C12-HS with Cationic DOEPC Bilayers

We formed SLBs composed of 75% DOPC and 25% DOEPC, a cationic lipid that differs structurally from DOPC by a single ethyl ether on the phosphate group of the molecule, using methods previously described by Cho.[1] As shown in Figures S1 and S2, we were able to form continuous SLBs that were generally devoid of defects. In an additional set of experiments, we introduced solutions containing 3-oxo-C12-AHL and 3-oxo-C12-HS to SLBs that contained 75% DOPC and 25% DOEPC and observed the response of the bilayer. As shown in Figure S7A and S8A, when we introduced 3-oxo-C12-AHL to these bilayers at 50 μM we observed the immediate formation of hemispherical caps on the surface of the bilayer without the formation of tubules. These hemispherical caps continued to grow in number and size over time. We note that the hemispherical caps observed in these cases are smaller in size and more numerous than those observed in DOPC bilayers under otherwise identical conditions. When we introduced 200 μM 3-oxo-C12-AHL to the bilayer we observed the formation of tubules ~50 μm in length and tubule bundles that collapsed into hemispherical caps similar in size than those observed in otherwise identical DOPC bilayers within the first 90 seconds of their formation (Figure S7B and S8B). When 3-oxo-C12-HS was introduced to the DOEPC-containing bilayers at 50 μM, we observed similar behavior to 3-oxo-C12-AHL at the same concentration, with the immediate formation of hemispherical caps on the surface of the bilayer (Figure S7C and S8A). At 200 μM, we observed 3-oxo-C12-HS to form tubules ~20 μm in length that collapsed into hemispherical caps over the first 30 s of experimentation (Figure S7D and S8B). QCM-D measured changes in frequency and dissipation of (-4.9 ± 0.9 Hz and $0.9 \pm 0.2 \times 10^{-6}$) and ($-1.0 \pm 0.5$ Hz and $0.4 \pm 0.1 \times 10^{-6}$) when 50 μM solutions of 3-oxo-C12-AHL or 3-oxo-C12-HS were introduced to bilayers, respectively (Figure S9). The changes in frequency and dissipation observed for DOEPC-containing bilayers in contact with 3-oxo-C12-HS containing solutions are similar in magnitude to otherwise identical DOPC bilayers. In contrast, 3-oxo-C12-AHL solutions in contact with DOEPC-containing bilayers led to smaller changes in dissipation with similar changes in frequency when compared to otherwise identical DOPC bilayers.

NMR Quantification of Phospholipids. To determine the concentration of phospholipids in stock solutions, quantitative $^{31}P[^{1}H]$ NMR spectroscopy was performed in 90% H_2O and 10% D_2O using a Bruker Avance-400 spectrometer with a BBFO probe. A relaxation delay (D1) of 11s was determined by inversion-recovery pulse sequence experiments. 890 µL of a phospholipid vesicle sample in water was mixed with 10 µL of Triton-X or rhamnolipid solution and 100 µL of a 100 mM triethylphosphine oxide internal standard solution in D_2O. All spectra were referenced relative to the phosphorus peak of the internal standard (~δ65ppm). Acquisition parameters were as follows: PULPROG=zgig30, D1=11s, SW=405ppm, O2P=3.75ppm, NS=64, DS=4, LB=1.[2]

Supplemental references

1. Sut, T. N.; Jackman, J. A.; Cho, N. J., Understanding How Membrane Surface Charge Influences Lipid Bicelle Adsorption onto Oxide Surfaces. *Langmuir* **2019,** *35* (25), 8436-8444.

2. Gahan, C. G.; Patel, S. J.; Chen, L. M.; Manson, D. E.; Ehmer, Z. J.; Blackwell, H. E.; Van Lehn, R. C.; Lynn, D. M., Bacterial Quorum Sensing Signals Promote Large-Scale Remodeling of Lipid Membranes. *Submitted* **2021**.

Chapter 6

Identification of Small Molecules That Strongly Inhibit Bacterial Quorum Sensing Using a High-Throughput Lipid Vesicle Lysis Assay ‡

‡ Portions of this chapter have been submitted for publication as: Polaske T. J.; Gahan C. G.; Nyffeler K. E.; Lynn, D. M.; Blackwell, H. E. "Identification of small molecules that strongly inhibit bacterial quorum sensing using a high-throughput lipid vesicle lysis assay". K. E Nyffeler and I designed and validated the vesicle lysis assay. T. J. Polaske and I collected data replicates that are shown in the thesis chapter. T. J. Polaske performed all high-throughput screening experiments. D. M. Lynn and H. E. Blackwell directed the project.

ABSTRACT: Many of the most common bacterial pathogens use quorum sensing (QS) to regulate virulence and biofilm formation, including *Staphylococcus aureus* and *Pseudomonas aeruginosa*. Chemical strategies to both monitor and block bacterial QS, and thus associated infections, are of significant interest. In this study, we developed a straightforward and robust assay to monitor biosurfactants and lytic agents produced by bacteria under the control of QS. The method is based on the lysis of synthetic lipid vesicles containing the environmentally sensitive fluorescent dye calcein. The assay allows for the facile *in situ* screening of exogeneous compounds capable of altering biosurfactant production by bacteria, and thereby the identification of new structures that could potentially modulate QS pathways, and avoids the constraints of many of the cell-based reporter assays and phenotypic assays commonly used for screening today. Application of this assay in a high-throughput format enabled the screening of a commercial chemical library and the subsequent discovery of five molecules capable of strongly blocking vesicle lysis by *S. aureus.* Two of these compounds were found to almost completely inhibit *agr*-based QS in *S. aureus* and represent the most potent small molecule-derived QS inhibitors to be reported to date in this pathogen. The probes and the methods reported herein will enable both fundamental and applied research in bacterial cell-cell signaling. Moreover, this vesicle lysis assay method should also be broadly applicable to bacteria beyond the two species examined here and useful as a tool to address questions outside those directly pertinent to QS pathways, significantly expanding its potential impact.

Introduction

Bacteria can sense their population densities using low molecular weight signals and alter their behaviors at high cell numbers to act as a group. This cell-to-cell signaling process is called quorum sensing (QS) and its outcomes often have devastating impacts on human and animal health, agriculture, and a range of clinical and industrial environments.[1, 2] *Staphylococcus aureus* and *Pseudomonas aeruginosa* are two notorious pathogens that use QS to regulate toxin production and other behaviors that incur tremendous burdens on human health.[3, 4] *S. aureus* is a Gram-positive bacterium and, once achieving a sufficiently high (i.e., quorate) population, uses the accessory gene regulator (*agr*) QS system to produce protein-based toxins and a suite of peptides, called phenol-soluble modulins (PSMs), that exhibit membrane lytic activity.[5-7] *P. aeruginosa* is a Gram-negative bacterium and uses a set of QS systems (i.e., LuxI/LuxR-type and Pqs) at high cell density to produce an analogous array of protein-based and small-molecule toxins, along with biosurfactants (i.e., rhamnolipids) that can disrupt lipid membranes and kill cells.[8] In this study, we report the application of a robust method to monitor production of lytic agents in these two pathogens. This assay enabled the discovery of new synthetic small-molecule compounds that behave as potent inhibitors of QS and can, thereby, provide a route to preventing the onset of virulence and other undesired behaviors in these organisms.

To date, the scope of compounds available as chemical modulators of QS (QSMs) in *P. aeruginosa* is, in general, limited to analogs of the native *N*-acylated homoserine lactone (AHL) signals used by this species for QS, [9-13] and to a handful of small molecules identified in high-throughput screens against the QS protein receptors LasR [14, 15] and PqsR.[16] The most potent QSMs in the *S. aureus* agr system are peptide-based derivatives of its native QS signal, the auto-inducing peptide (AIP). [17-20] Studies of fungal and bacterial natural products have also identified several

other classes of non-peptidic small molecules that can inhibit QS in *S. aureus*; [21] however, these compounds are considerably less potent than AIP mimetics. Overall, many of the currently known QSMs in both of these species have major limitations related to potency, selectivity, solubility, chemical stability, and/or synthetic accessibility that have prevented their widespread use both as chemical tools and as bases for therapeutic intervention.

Several factors have complicated the discovery and characterization of new synthetic QSMs with improved properties. One factor is the assumption that new compounds identified to target a specific QS system or receptor in conventional cell-based assays using QS reporter gene constructs will ultimately translate directly to QS-linked phenotypes.[13] This assumption is not always true in *S. aureus* and *P. aeruginosa*, however, because additional, and often indirect, pathways can also contribute to the control of virulence phenotypes.[2, 7, 22-24] Conversely, assays based on phenotypic response (e.g., production of toxins, formation of biofilm, motility, etc.) are typically low-throughput and highly environmentally sensitive and, thus, not as well suited for discovery-oriented research. Furthermore, the activity of QSMs in many model laboratory strains used to create QS transcriptional reporter systems for screening campaigns may not be representative of their activities in wild-type isolates. Indeed, a growing number of reports describing the functional role of *S. aureus* and *P. aeruginosa* QS networks in wild-type strains suggests that they can differ substantially from those of common laboratory strains.[25-28]

Here, we report the development and successful implementation of a new assay that is sensitive to, and can report selectively on, the production of QS-regulated virulence factors produced by *S. aureus* and *P. aeruginosa*. Our approach leverages suspensions of large unilamellar vesicles (LUVs) that are stable in bacterial growth media and in the presence of bacteria, but that are readily disrupted by amphiphilic toxins produced by *S. aureus* and *P. aeruginosa* at quorum to

produce a fluorescent signal. This QSM discovery assay is applicable to any *S. aureus* and *P. aeruginosa* strain of interest. The materials required for this assay are accessible and easy to prepare, and this platform is compatible with other methods (e.g., liquid-handling robots and plate readers) commonly used in high-throughput screening assays. This approach thus has the potential to substantially accelerate the pace at which new QSMs are discovered.

We validated this assay in *S. aureus* and *P. aeruginosa* using a range of known QS inhibitors and, to demonstrate the potential of this new platform in the context of discovery, performed high-throughput screens for new inhibitors of lytic phenotypes in *S. aureus* using a small-molecule library containing >25,000 unique chemical structures. This screen identified five compounds that strongly block lysis, two of which were shown to act via *agr*-type QS and represent previously unrecognized chemical QSM scaffolds that are, to our knowledge, the most potent small-molecule inhibitors of *agr*-type QS in *S. aureus*. Our results immediately expand the suite of potential small molecule tools available for investigating *agr*-type QS in *S. aureus* and provide new and general methods for the high-throughput identification of novel QSMs. This assay strategy could be expanded to screen for chemical inhibitors of virulence in a broader range of important pathogens (e.g., *Staphylococcus* sp., *Burkholderia* sp., etc.) that also produce membrane-lytic virulence factors, including in clinical isolates containing bacteria with QS networks that may differ substantially from those observed in common laboratory strains.

Materials and Methods

Materials. 1,2-Dioleoyl-sn-glycerol-3-phosphocholine (DOPC), 1,2-dipalmitoyl-sn-glycerol-3-phosphocholine (DPPC), cholesterol, filter supports, and a Mini extruder were purchased from Avanti Polar Lipids. 1,2-Dipalmitoyl-sn-glycerol-3-phosphoethanolamine (DPPE), dimethyl

sulfoxide (DMSO), sodium hydroxide (NaOH), hydrochloric acid (HCl), sodium chloride (NaCl), triethylphosphine oxide, deuterium oxide (D_2O), calcein, Triton X-100, and Sephadex-G50 column size exclusion chromatography beads were purchased from Sigma. Isopropanol (iPrOH) and tris-base were acquired from Fisher Scientific. Rhamnolipids, 90% pure (commercial mixture of glycolipids isolated from *P. aeruginosa*) were obtained from AGAE Technologies (Corvallis, OR). The small-molecule *agr* inhibitor savirin was purchased from AK Scientific. Polycarbonate extruder filters (100 nm) were purchased from Millipore. Ethylene-diaminetetraacetic acid (EDTA) was acquired from Acros Organics. Concentrated phosphate-buffered saline (PBS) solution (10x) was purchased from Dot Scientific. Luria-Bertani (LB) medium was obtained from Research Products International. Brain heart infusion (BHI) medium was acquired from Teknova. The phenol-soluble modulin PSMα3 was a kind gift from Prof. Samuel H. Gellman (UW–Madison, Madison, WI). Deionization of distilled water was performed using a Milli-Q system yielding water with a resistivity of 18.2 MΩ. All materials were used as received without further purification unless otherwise specified.

Bacterial strains and culture. All bacteria were grown at 37 °C with 200 rpm shaking unless otherwise specified. The strains and plasmids used in this study and their sources are listed in Table S1. *S. aureus* and *P. aeruginosa* were grown in BHI medium and LB medium, respectively. *S. aureus* AH1677 (with an *agr*-YFP reporter plasmid) and *P. aeruginosa* PAO1-PGSC (with a p*lasI*-LVAgfp reporter plasmid) were used as QS transcriptional reporters and grown with 10 μg/mL chloramphenicol and 300 μg/mL carbenicillin, respectively. All other strains were grown without supplemental antibiotic. *S. aureus* RN6390b and *P. aeruginosa* PAO1-PGSC were used as WT strains in vesicle lysis experiments, while *S. aureus* RN9222 and *P. aeruginosa* PAO-JG35 were

used as QS mutants. RN9222 was grown without antibiotic as it was not used as a reporter strain (i.e., it served only as QS mutant). See SI for discussion and analysis of biosurfactants produced by strains in this study (Figure S7, Tables S2 and S3).

Compound handling and preparation. OdDHL and BHL,[29] *S. aureus* AIP and peptide derivatives **1**–**5**,[17-19] and compounds **7**–**9** [30-32] were synthesized using previously described methods. PQS and compound **6** were purchased from Millipore Sigma and AK Scientific respectively. Compounds were stored dry at -20 °C until needed and then dissolved in DMSO. DMSO stock solutions were prepared at concentrations that varied with compound potency and apparent solubility. Final in-well compound concentrations for 96-well vesicle lysis assays, unless noted otherwise, were: 10 μM for AIP, OdDHL, and PQS; 1 mM for BHL; 100 nM for **1**–**4**; 10 μM for **5**; 20 μM for **6**; 100 μM for **7** and **8**; and 200 μM for **9**.

Production of phospholipid vesicles with encapsulated calcein. Large unilamellar vesicles (LUVs) were produced by adapting a freeze-thaw and vesicle extrusion procedure. [33] Briefly, stock solutions of phospholipids (DOPC, DPPC, DPPE, or cholesterol) in chloroform were mixed to the desired lipid compositions (70 mol% DOPC/30 mol% cholesterol for *S. aureus* vesicles or 68 mol% DPPC, 30 mol% cholesterol, 2 mol% DPPE for *P. aeruginosa* vesicles), and the chloroform was removed using an N_2 stream or rotary evaporation followed by drying for at least one hour under vacuum. Self-quenching solutions of calcein were prepared by combining calcein and PBS or a specially prepared calcein buffer (1 mM EDTA, 10 mM Tris-base, and 100 mM NaCl; pH 8) to a calcein concentration of 70 μM. The resulting solutions were titrated with 10 M aqueous NaOH until all calcein was dissolved and the solution reached pH 7.4 or pH 8 for PBS and the

calcein buffer, respectively. The resulting calcein solutions were added to the dried phospholipid films (PBS for *S. aureus* formulations and the calcein buffer for the *P. aeruginosa* formulations) for a final lipid concentration of 5 mg/mL.

The resulting lipid solutions were vortexed vigorously and briefly sonicated in a bath sonicator to form a turbid vesicle suspension. The vesicle suspensions were then freeze-thawed five times by alternately immersing them into an iPrOH/dry ice bath and a warm water bath (~60 °C). Vesicles prepared for continuous time-course experiments were passed at least 5 times through a 100 nm polycarbonate filter using a Mini-prep extruder. Vesicles prepared for the high-throughput screen were passed through the filter 3 times. The resulting vesicles were then separated from external, unloaded calcein using a hand-packed Sephadex-G50 size exclusion chromatography column. The concentration of phospholipid in the solution was quantified using ^{31}P NMR (see SI for detailed protocol), and the phospholipid concentration was adjusted to 2 mM for unsaturated lipid solutions and 1 mM for saturated lipid solutions in their respective buffers. The resulting vesicles were characterized by dynamic light scattering and found to have a hydrodynamic diameter of ~150 nm (Figure S1), which agrees with previous reports describing vesicle production using a similar method.[34]

Microtiter plate vesicle lysis assays. Portions of media (2 or 10 mL) were inoculated with individual bacterial colonies and allowed to shake overnight. From these overnight cultures, subcultures were prepared by diluting the cultures 1:50 (v/v) in fresh BHI for *S. aureus* or 1:100 (v/v) in fresh LB for *P. aeruginosa*. An aliquot of each subculture (178 μL) was added to 20 μL of vesicle suspension and 2 μL of compound solution (dissolved in DMSO at 100x working concentration) in a clear-bottomed, black 96-well microtiter plate (Corning 3904). For controls,

DMSO (vehicle) or Triton X-100 (1% final concentration) was substituted for compound. Plate covers were coated with an aqueous solution of 0.05% Triton X-100 and 20% ethanol[35] to prevent the accumulation of condensation. Plates were incubated in a Biotek Synergy 2 microplate reader running Gen5 1.05 software at 37 °C with shaking at the high-speed setting. Fluorescence (excitation 500 nm, emission 540 nm) and OD_{600} (absorbance at 600 nm) measurements were recorded every 15 minutes for 12 hours. All experiments were performed in technical triplicate in a single microtiter plate. Biological triplicates were then obtained over three days. GraphPad Prism software (v. 9) was used to generate curves and calculate standard error.

High-throughput screening assay and follow-up analyses. Full details of the assay method are provided in the SI. In brief, experimental compounds and positive controls were delivered to 384-well microtiter plates in 2.5 nL of DMSO. An aliquot of diluted cells (50 µL; *S. aureus* RN6390b in BHI medium) containing 0.1 M phospholipid vesicles, for a final compound concentration of 10 µM, was added to plates. Compound **1** (250 nM; positive control) and DMSO (vehicle) were used as the positive and negative controls, respectively. Plates were incubated statically at 37 °C for 24 hours, at which point fluorescence (483 excitation, 530 emission) and OD_{600} measurements were made. Of the 25,280 compounds in the library, 92 (0.36%) resulted in fluorescence emission less than 80% compared to vehicle control. All plates had positive Z'-factors with a median score of 0.42 (Figure S8). A secondary screen of these compounds was performed to confirm fluorescence inhibition, and 16 compounds were selected for follow-up dose-response analyses in the 384-well vesicle lysis assay format. Of these, five compounds were deemed probable inhibitors of biosurfactant production and were selected for further dose-response analysis using the *S. aureus agr* QS YFP reporter. The YFP reporter assay protocol was performed using the method

previously reported by our group.[17] Data from all replicates (biological triplicate of technical triplicates, n = 9) were pooled and GraphPad Prism software (v. 9) was used to generate dose-response curves and calculate IC_{50} values, mean values, and standard error.

Results and Discussion

Lipid vesicles respond selectively to membrane-lytic virulence factors produced at quorum

Past studies by Jenkins and coworkers report lipid vesicle formulations that respond to the presence of amphiphilic virulence factors produced by bacteria.[36-41] In those studies, the authors used vesicles formed from combinations of saturated phospholipids, cholesterol, and an alkyne-containing fatty acid that can be crosslinked via UV light to produce vesicles encapsulating a fluorescent probe (carboxyfluorescein).[36, 38-40] That past work was motivated, in part, by the broad goal of designing fluorescent sensors that could respond to the presence of biosurfactants produced by bacteria and, thus, identify the onset of bacterial virulence. We hypothesized that vesicles that remain stable in the presence of bacteria, but release their contents and produce a signal only upon exposure to membrane-lytic agents produced at quorum, could also provide a straightforward basis for the identification of small molecules that *inhibit* QS. A schematic of the proposed vesicle lysis assay and its application to screening is provided in Figure 1.

S. aureus produces amphipathic peptides called phenol-soluble modulins (PSMs) under the direct control of its *agr* QS system comprised of AgrA-D (Figure 2A). *P. aeruginosa* controls the production of rhamnolipids via the complex interplay of its two LuxI/LuxR QS systems, LasI/R and RhlI/R, and the Pqs QS pathway (Figure 2B). Examples of both of these biosurfactant classes

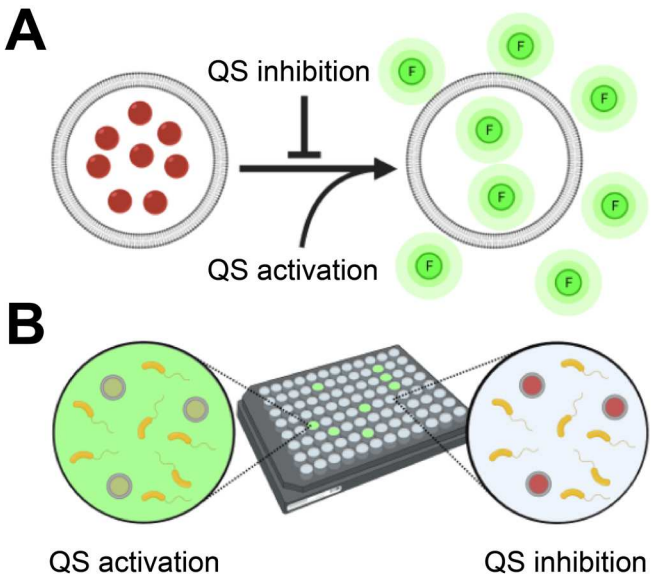


Figure 1. Schematic representations of the vesicle lysis assay developed in this study. (A) When bacteria grow to a sufficient population density and QS is activated, the production of amphiphilic virulence factors leads to the lysis or leakage of lipid vesicles. QS inhibitors prevent the production of virulence factors and inhibit dye leakage. Shown are: (left) a lipid vesicle encapsulating a self-quenching dye (indicated in red); (right) dye leakage in the presence of amphiphilic virulence factors, which results in an increase in solution fluorescence (indicated in green). (B) Schematic showing the implementation of a high-throughput screen, in which changes in the fluorescence of each well are used to identify compounds that inhibit the production of virulence factors.

are shown in Figure 2C and are produced at quorate cell densities and in sufficient extracellular concentrations to permeabilize membranes.[42, 43]

We began our work by identifying simplified lipid vesicle formulations that could respond selectively to membrane-lytic virulence factors, but that would be more accessible and less time-consuming to prepare than prior formulations that required the use of polymerizable lipids or the use of specialized equipment (e.g., a UV oven). For these studies, we incubated LUVs encapsulating the self-quenching fluorescent dye calcein with aliquots of lag phase wild-type (WT) or QS-deficient *S. aureus* and *P. aeruginosa* cultures (see Methods for details related to the preparation and characterization of LUVs). These experiments were conducted in 96-well microtiter plates, and measurements of fluorescence were used to characterize vesicle stability

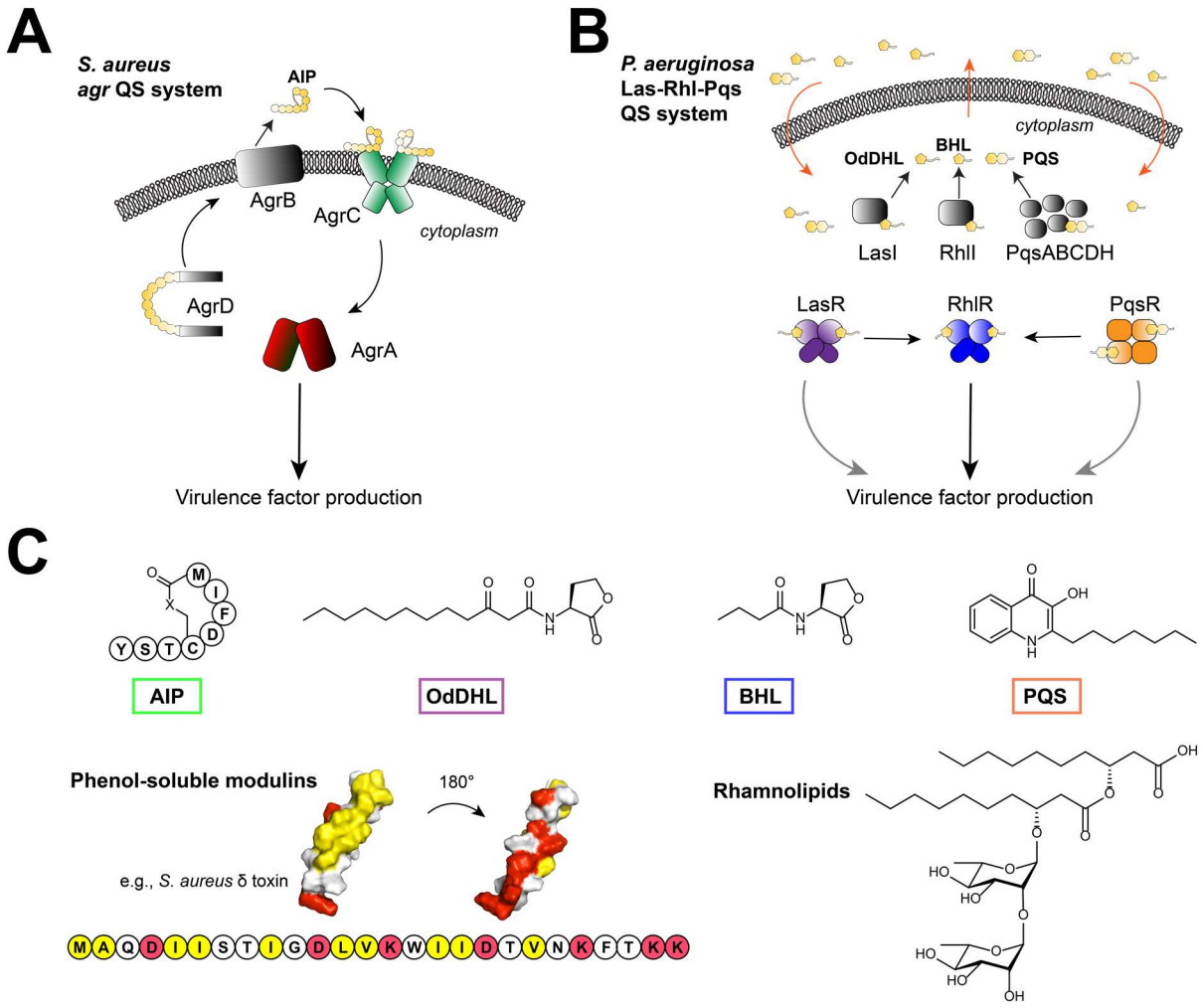


Figure 2. *S. aureus* and *P. aeruginosa* regulate virulence factor production through QS signaling. (A) Schematic of the *S. aureus* accessory gene regulator (*agr*) system. *S. aureus* uses QS to upregulate myriad virulence factors, including phenol soluble modulins (PSMs). (B) Schematic of the Las-Rhl-Pqs *P. aeruginosa* QS system. Rhamnolipid production by *P. aeruginosa* is induced by activation of the LuxI/LuxR-type Rhl QS system. Another LuxI/LuxR-type circuit, Las, is responsible for activation of Rhl, in coordination with the *Pseudomonas* quinolone signaling (PQS) system. (C) The structures of the native QS signaling molecules and relevant amphiphilic virulence factors of both species, including the hemolytic *S. aureus* δ-toxin (one of several PSM types). Colored boxes around compound names indicate cellular targets in panels A and B. AIP and δ-toxin structures are shown with single-letter amino acid codes. Yellow and red shading in δ-toxin indicate hydrophobic and hydrophilic residues, respectively; the two views highlight its overall amphipathic structure. Structure for δ-toxin retrieved from the Protein Data Bank; PDB ID = 2KAM [44]

.

and/or the release of encapsulated calcein over time. The *S. aureus* QS mutant used in these experiments (RN9222, see Table S1 for bacterial strains and plasmids used in this study) lacks the AgrD and AgrB signal processing components of the *agr* system (Figure 2A) and, thus, cannot produce its native AIP. The *P. aeruginosa* QS mutant used here (PAO-JG35) lacks two receptors for AHL signal recognition that are essential transcription factors for their respective regulons (i.e., LasR and RhlR, Figure 2B). As such, these initial screens enabled us to identify lipid vesicle formulations that were stable, and did not release calcein, in the presence of the QS mutants (which cannot produce membrane-lytic virulence factors) and that were unstable, and did release calcein, in the presence of WT organisms (which can produce membrane-lytic compounds at high population densities), as outlined schematically in Figure 1A.

Using this vesicle screening approach, we identified two promising LUV formulations. We found LUVs comprised of 70 mol% of the unsaturated zwitterionic lipid DOPC and 30 mol% cholesterol to respond selectively to WT strains of *S. aureus* (Figure 3A). We also identified formulations comprised of 68 mol% DPPC, 2 mol% DPPE, and 30 mol% cholesterol to respond selectively to WT strains of *P. aeruginosa* (Figure 3B; this formulation was adapted from a formulation previously reported by Jenkins and coworkers).[45] These two vesicle formulations were measured to be ~150 nm in diameter by dynamic light scattering (Figure S1), exhibited sufficient stability, with minimal dye leakage, in bacterial cultures containing the QS-null bacterial strains (and therefore the absence of lytic agents) for 12 hours, and were suitable for all other fundamental and discovery-oriented experiments described below. Control experiments demonstrated that the presence of these vesicles had minimal effects on cell growth over the course of these assays (Figure S2).

The results shown in Figure 3A–B for WT strains versus QS mutants demonstrate that functional QS networks are required for substantial lysis of these vesicle formulations in the presence of either *S. aureus* or *P. aeruginosa*. Because the onset of QS is typically reported to occur at the middle to late log phase of bacterial growth,[46, 47] these results also suggest that vesicle lysis correlates to the times at which quorum is reached in these bacterial cultures.

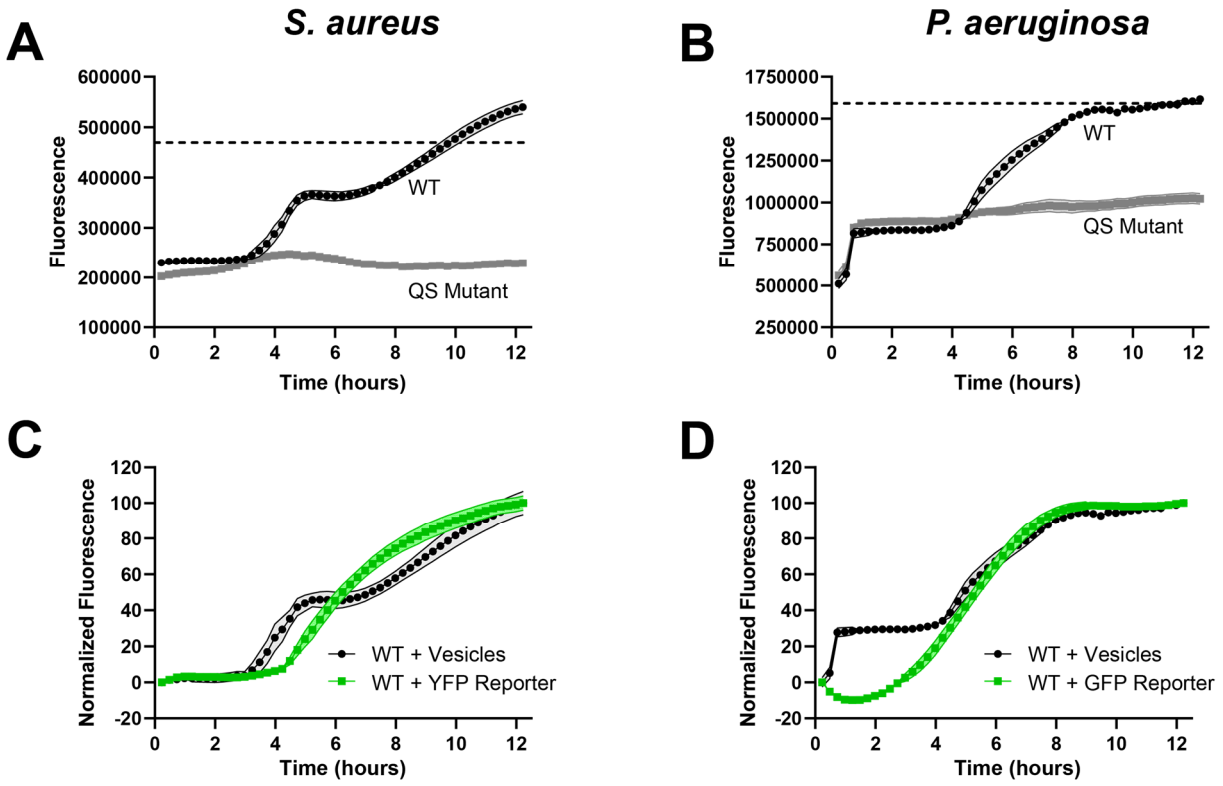


Figure 3. Vesicle lysis occurs in the presence of bacteria. (A–B) Differential vesicle lysis between WT (black) and QS mutant (grey) strains of *S. aureus* (A) and *P. aeruginosa* (B) as measured by fluorescence over time. (C-D) Vesicle lysis (black) induced by WT *S. aureus* (C) and *P. aeruginosa* (D) correlated with QS-onset as determined by transcriptional reporter strains ((green) *S. aureus* containing *agr* reporter plasmid pDB59, producing YFP; *P. aeruginosa* containing p*lasI*-LVAgfp reporter plasmid, producing GFP; see Methods and Table S1 for details). The dashed line in (A, B) indicates fluorescence one hr after addition of the positive lysis control (Triton X-100). Data points represent the mean of all replicates (n = 9). Error bars = SEM (shaded area around data points).

Additional support for this view was provided by the results of experiments performed using WT bacteria containing QS transcriptional reporter plasmids (encoding yellow fluorescent protein

(YFP) in the case of *S. aureus,* and green fluorescent protein (GFP) in the case of *P. aeruginosa*). The panels in Figure 3C–D show comparisons of increases in normalized fluorescence for (i) vesicles incubated with WT strains and (ii) fluorescent protein production in cultures of the *S. aureus* (Figure 3C) and *P. aeruginosa* (Figure 3D) reporter strains. These results reveal the onset of vesicle leakage in experiments using WT bacteria to occur, in general, on time scales similar to those observed for fluorescent protein production (this correlation was more pronounced in the case of *S. aureus*; see Figure 3C). We consider it likely that vesicle lysis was initiated in our WT cultures by the onset of production of membrane-lytic agents—i.e., PSMs (for *S. aureus*) and rhamnolipids (for *P. aeruginosa*). This conclusion is supported by past studies by Jenkins,[39, 40] and by the results of our own experiments in which solutions of authentic samples of either a representative PSM (PSMα3) or rhamnolipid were observed to lyse vesicles in a dose-dependent manner (Figure S3).

Validation of assay method using responsive vesicles and known inhibitors of QS

We conducted a series of experiments to validate the two responsive vesicle formulations identified above as platforms for the identification of inhibitors of QS by adding known QS modulators (structures shown in Figure 4) to cultures of *S. aureus* and *P. aeruginosa* in the presence of vesicles. For experiments with *S. aureus*, we selected the native AIP as an activator, and three inhibitors of the two-component AgrC/AgrA signaling system (Figure 2A). Two of these inhibitors (compounds **1** and **5**), which we reported on previously,[17, 19] are macrocyclic, peptide-based molecules that likely function via competitive inhibition of the AIP ligand:AgrC receptor binding interaction. The third inhibitor, the small molecule **6** (savarin)[48] has been shown to inhibit the *agr* system in *S. aureus* via binding and ostensible inactivation of AgrA, the response regulator

of the transmembrane histidine kinase, AgrC. For experiments with *P. aeruginosa*, we used the native ligands of three of its key QS transcriptional regulators LasR, RhlR, and PqsR (Figure 2B)—i.e., the activators *N*-(3-oxo-dodecanoyl)-L-homoserine lactone (OdDHL), *N*-butyryl-L-homoserine lactone (BHL), and the *Pseudomonas* quinolone signal (PQS), respectively—as well as the LasR antagonist **7** (V-06-018)[14] the potent PqsR antagonist **8** (M64)[16] and the non-native AHL-derived RhlR activator **9.**[49]

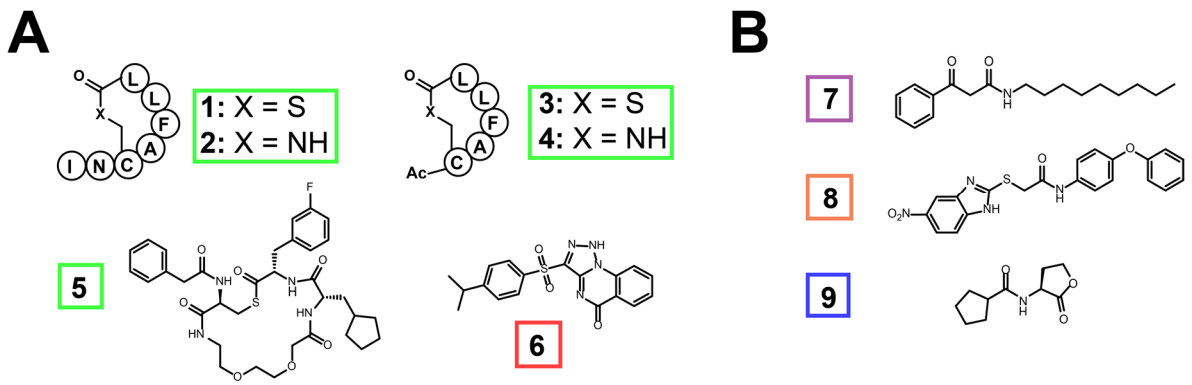


Figure 4. Non-native QSMs of *S. aureus* (A) and *P. aeruginosa* (B) evaluated in this study: Synthetic *S. aureus* QS antagonists (**1**–**6**), *P. aeruginosa* QS antagonists (**7**, **8**), and synthetic QS agonist (**9**). Common compound names: **1**, AIP III D4A; **2**, AIP III D4A amide; **3**, tr. AIP III D2A; **4**, tr. AIP III D2A amide; **5**, Bnc3; **6**, savirin; **7**, V-06-018; **8**, M64. tr.= truncated. Colored boxes indicate the cellular targets color-coded in Figure 2A–B: green = AgrC; red = AgrA; purple = LasR; blue = RhlR; orange = PqsR.

We incubated bacterial cultures containing calcein-loaded vesicles with aliquots of each of these compounds at concentrations needed for near-maximal inhibition or activation (as reported in previous studies) and monitored changes in fluorescence of the cultures over 12 hours (Figure 5). We also conducted parallel control experiments using a QS mutant strain to determine whether observed changes in vesicle permeabilization were a result of bacterial production of membrane-lytic factors and not the potential surface/membrane activity of these QS inhibitors. For

experiments using *S. aureus*, inhibitors **1** and **6** wholly abrogated vesicle lysis (Figure 5A; blue and purple curves), consistent with their ability to nearly completely quench *agr* activity. The addition of inhibitor **5** suppressed dye release, relative to vehicle controls containing no inhibitor, over 12 hours, yet we observed a steady increase in fluorescence during the course of these experiments (red curve), suggesting that *agr* activity was not completely blocked under the conditions used here. The reasons for this reduced activity for **5** are not completely understood. It is possible that this result may reflect an intrinsic inability of this compound to fully inhibit the *agr* system, with a basal amount of *agr* activity allowing for low levels of PSM to accumulate and affect low levels of membrane disruption. This result could also, however, arise from the sequestration of this inhibitor resulting from interactions with the vesicles, aggregation, and/or degradation, each of which would reduce *in situ* concentrations and affect inhibitory activity.

Turning to a QS agonist, we observed that the exogenous addition of native AIP triggered calcein leakage approximately two hours earlier in the WT organism relative to the vehicle control (Figure 5B), even though the culture remained in the lag/early exponential phase of growth (Figure S4B). This result is consistent with the production of membrane-lytic virulence factors in sub-quorate populations of bacteria treated with strong *agr* agonists (i.e., prematurely forcing group behavior) and suggests that temporal dynamics associated with vesicle leakage could also be used to screen for and identify new agonists of QS in *S. aureus.* Finally, we note that none of the compounds investigated here affected calcein leakage when incubated with the *agr*-null strain (i.e., QS mutant, Figure S4A), confirming that the results shown in Figure 5A–B result from compound/*agr* system interactions and not any other direct physicochemical influence of these compounds on membrane permeability. The native AIP and peptide analogs **1** and **5** had minimal

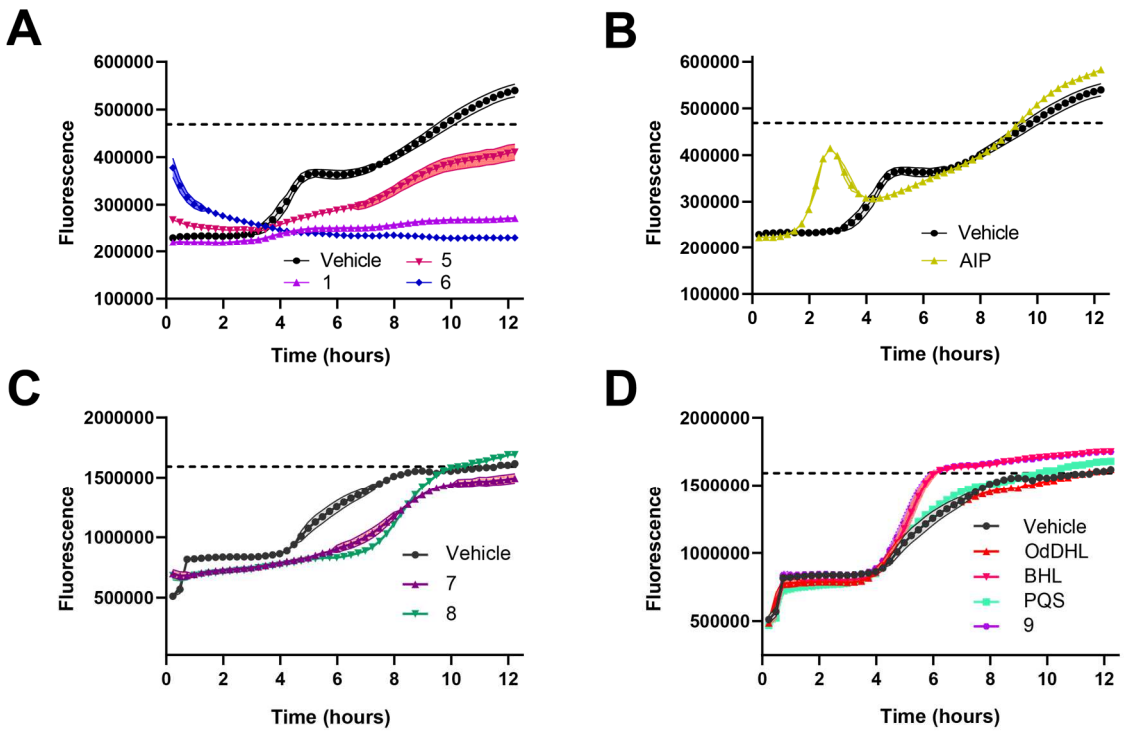


Figure 5. Vesicle lysis is strongly influenced by exogenously added QSMs. Fluorescence was monitored for 12 hr after incubation of lag phase WT bacteria with vesicle suspensions and QSMs. (A) QS inhibitors **1**, **5**, and **6** repress vesicle lysis in *S. aureus*, whereas (B) the native AIP induces early lysis. (C) QS inhibitors **7** and **8** delay the onset of vesicle lysis by approximately 2 hr in *P. aeruginosa*. (D) RhlR activators BHL and **9** facilitate vesicle lysis in *P. aeruginosa*, while the native agonists of LasR and RhlR, OdDHL and PQS, had no observable effect. The dashed line indicates fluorescence 1 hr after addition of the positive lysis control (Triton X-100). Vehicle = DMSO. Data points represent the mean of all replicates (n = 9). Error bars = SEM (shaded area around data points).

impact on cell growth; small molecule **6** showed some effects on growth at later time points (Figures S4B and S4C).

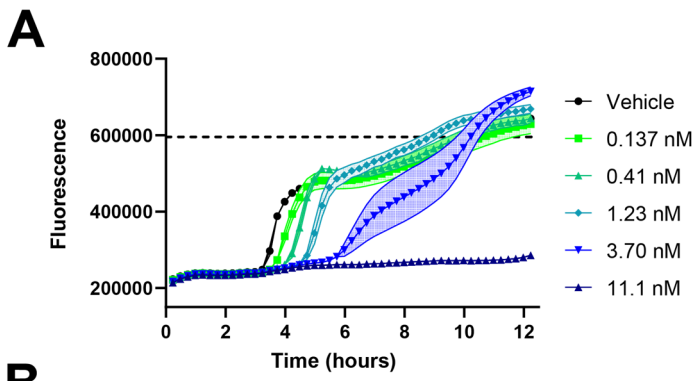
The overall trends in experiments using *P. aeruginosa* and our vesicle lysis assay were similar to those observed above; however, the influence of QS inhibitors used in this organism on calcein leakage was generally more complex, and thus more difficult to interpret, than those observed in *S. aureus.* Inspection of the results in Figure 5C reveals that LasR antagonist **7** and PqsR antagonist **8** (Figure 4) significantly delayed vesicle lysis by approximately two hours

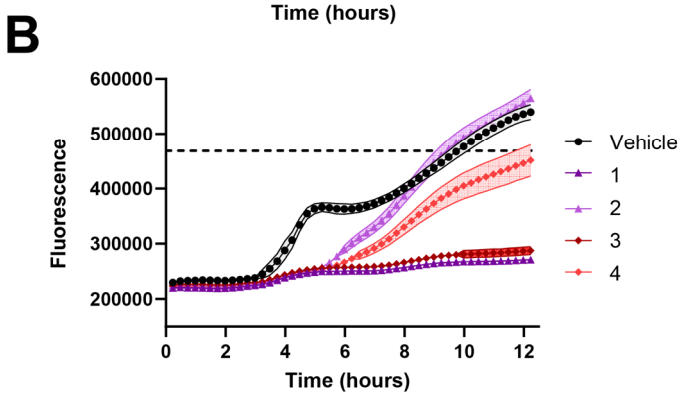
relative to vehicle controls, but that, in both cases, fluorescence continued to increase over the course of 12 hours. Interestingly, the influence of the addition of QS agonists varied based on their target receptors in this organism. For example, the native LasR agonist OdDHL and PqsR agonist PQS (Figure 4) had no observable influence on levels of fluorescence (Figure 5D; red and green curves), in contrast to the addition of a QS agonist in the presence of *S. aureus* (Figure 5B). However, treatment with the native RhlR agonist BHL and non-native RhlR agonist **9** resulted in an earlier onset of dye leakage (Figure 5D; pink and purple curves). We note that both the Las and Pqs systems play roles in activation of the Rhl system, and that Rhl plays a key role in the regulation of rhamnolipid production in *P. aeruginosa*.[50] These results are thus consistent with past reports from our group on the interplay of the Las-Rhl-Pqs signaling network and its impact on the production of rhamnolipids.[51] Finally, we note that the native QS signaling molecules and compounds **7–9** had negligible effects on either calcein leakage (in the presence of QS mutants, Figure S5A) or bacterial growth (Figures S5B and S5C), although compound **7** was observed to inhibit growth mildly at later time points.

We conducted an additional series of experiments to characterize the sensitivity of vesicle lysis in bacterial cultures to changes in the concentrations and potencies of added QS inhibitors. High sensitivity to these differences would increase the utility of this assay for a range of screening applications. For these experiments, we focused our efforts on characterization in cultures of *S. aureus,* as we had ready access to a suite of structurally related *agr* inhibitors with well-understood activity profiles previously identified by our group (i.e., **1–4**; Figure 4).[17-19] We also reasoned that the results for this organism would be easier to interpret than those arising from experiments with *P. aeruginosa* in view of its more complex and inter-regulated QS network (*vide supra*). Calcein-loaded vesicles were incubated with WT *S. aureus* and 3-fold dilutions of QS inhibitor **1**, starting

at a concentration of 100 nM. Increasing concentrations of **1** were observed to lead to increases in the times required for the onset of calcein leakage (Figure 6A). We also examined whether vesicle leakage could be used to identify differences in the potencies of the four structurally similar *agr* inhibitors (**1**–**4**). For these experiments, all compounds were tested at equivalent concentrations of 100 nM. Inspection of Figure 6B reveals the more potent inhibitors **1** and **3** completely prevent calcein leakage, whereas their less potent amide-bridged analogs **2** and **4** resulted only in a delayed response. At 12 hr, we observed a clear correlation between compound potency (as determined previously using cell-based transcriptional reporter assays) and fluorescence as a measure of vesicle lysis (Figure 6C).

When combined, the results of the experiments above demonstrate that the presence (or absence) of calcein leakage can be used to identify the presence (or absence) of inhibitors or agonists of QS in cultures of *S. aureus* and *P. aeruginosa*. In addition, the vesicle lysis assay can be used to report the relative amounts and potencies of QS inhibitors. Our results support the view that the ability of this materials platform to discriminate and report on QS is a result of the sensitivity of calcein leakage to the production of membrane-lytic virulence factors in these organisms, and suggest that the timing and the magnitude of calcein leakage may also convey useful information related to potency or other dynamics in these systems. Overall, the impacts of added QS inhibitors and activators on calcein leakage are more straightforward to interpret in cultures of *S. aureus* (at least under the conditions evaluated in this study) relative to *P. aeruginosa.* However, decreases in calcein fluorescence of the cultures induced by QS inhibitors in the latter are significant and can still be observed in Figure 5. In the section below, we focus our attention on *S. aureus* to exploit our vesicle leakage assay to conduct high-throughput screens and identify new chemical inhibitors of QS in this pathogen (shown schematically in Figure 1B).





C

	IC_{50} (nM)	Fluorescence (at 12 hr; a.u./10^3)
1	0.485	270
2	1.20	560
3	0.257	290
4	1.50	450

Figure 6. The timing and magnitude of vesicle lysis is dependent on QSM concentration and potency. (A) Fluorescence as measured over time for a *S. aureus*-vesicle mixture treated with QS antagonist **1** at varying concentrations. (B) Fluorescence as measured over time for a *S. aureus*-vesicle mixture treated with QS inhibitors **1**–**4** at 100 nM; **1**–**4** are structurally related compounds with similar, yet distinct, IC_{50} values in cell-based reporter assays. The dashed lines indicate fluorescence one hr after addition of the positive lysis control (Triton X-100). Vehicle = DMSO. Data points represent the mean of all replicates (n = 9). Error bars = SEM (shaded area around data points). (C) IC_{50} values for **1**–**4** in cell-based reporter assays (reproduced from (Tal-Gan et al., 2016)) correlate with vesicle leakage as measured by fluorescence after 12 hr (a.u. = arbitrary units).

A high-throughput screen identifies novel and potent small-molecule inhibitors of agr*-type QS*

We conducted a final series of experiments to explore the feasibility of using the vesicle leakage assay described above as a platform for the high-throughput screening and identification of new small-molecule inhibitors of *agr*-type QS in *S. aureus.* For these experiments, we used WT

S. aureus and the 70% DOPC/30% cholesterol vesicles characterized above, and the assay was re-optimized for use in an automated, 384-well microtiter plate format (see Methods). We selected *agr* inhibitor **1** (Figure 4) as a positive control for these studies and screened a commercially available small molecule library of 25,280 compounds (at concentrations of 10 μM; see Methods and SI for details). Each microtiter plate contained positive (250 nM **1**) and negative (DMSO vehicle) controls in addition to 320 wells containing experimental compounds. After the addition of an aliquot of a vesicle/cell mixture, plates were incubated statically for 24 hr at 37 °C, at which point fluorescence and optical density readings were acquired.

These high-throughput assays identified 92 compounds that resulted in <80% fluorescence emission relative to the vehicle control (Figure 7A). Subsequent dose-response analysis of these initial hits using the vesicle leakage assay identified five compounds with strong activity profiles, with three compounds able to completely block vesicle lysis at concentrations >10 μM (Figure 7B). The abilities of these lead hit compounds to target *agr* in *S. aureus* was evaluated using an *agr* transcriptional reporter assay (Figure 7C), revealing two compounds (the pyrazolopyrimidine **10** and thiazolopyridine derivative **11**, Figure 7D) as near-maximal *agr* inhibitors. We note that compounds **10** and **11** are approximately 5–10 times more potent than compound **6** in the reporter assay (**10** (IC_{50} = 0.5 μM) and **11** (IC_{50} = 0.7 μM) vs. **6** (IC_{50} = 5.5 μM)), which is one of the strongest small-molecule inhibitors of QS reported to date in *S. aureus*,[48] and that these two compounds do not inhibit cellular growth. Both **10** and **11** are low molecular weight (MW < 500 g/mol), readily soluble in DMSO and aqueous solutions, contain no obvious reactive sites that could potentially lead to compound degradation, and are readily amenable to synthetic modification. We note that while compound **10** and its analogs have been reported to be agonists

of the human apelin receptor,[52] a G protein-coupled receptor unrelated to the *agr* system, neither compound **10** nor **11** has previously been reported to influence bacterial QS.

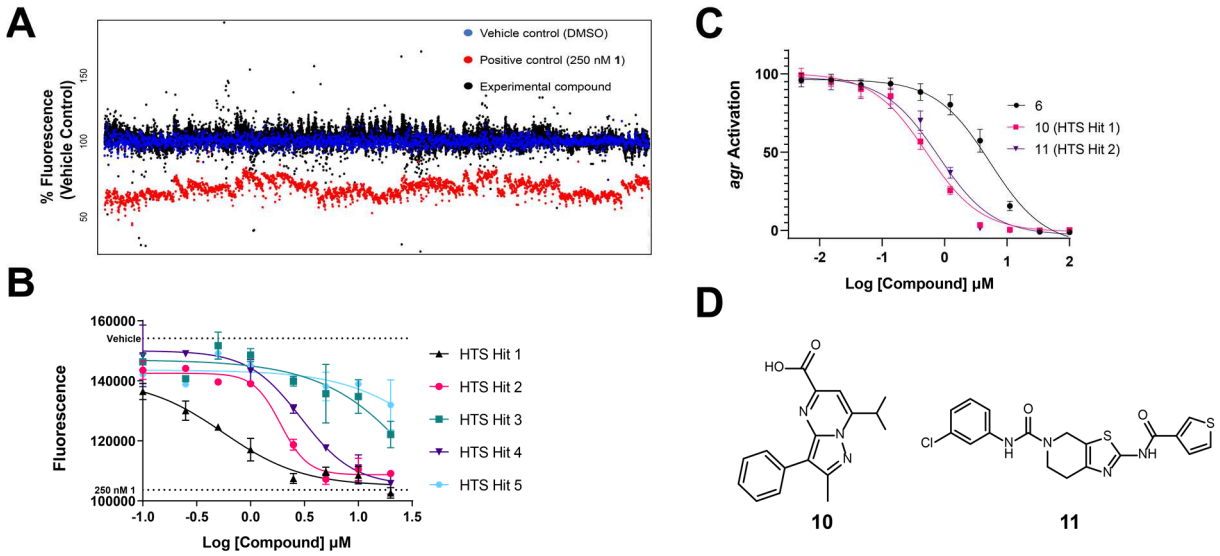


Figure 7. Summary of high-throughput screening results. (A) A scatter plot was generated for the primary screen of experimental compounds. Experimental compounds (black) that resulted in less than 80% fluorescence relative to vehicle controls (blue) were selected for secondary screening to confirm activity. Positive controls (red) typically yielded fluorescence values between 50% and 70% of the vehicle controls. (B) Dose-response analysis of select high-throughput screening (HTS) hit compounds using the vesicle leakage assay. Of the 14 compounds selected for dose-response analysis, five indicated probable inhibition of biosurfactant production and were subjected to further analysis using an *agr* YFP transcriptional reporter. Error bars indicate SD. Vehicle and positive controls (dashed lines) are also shown. (C) Dose-response analysis for high-throughput screen (HTS) hit compounds 1 and 2 using an *agr* YFP transcriptional reporter. Error bars indicate SEM. (D) Structure of novel *agr* inhibitors **10** and **11** identified using this high-throughput screen.

The potency, efficacy, and small-molecule nature of compounds **10** and **11** make them valuable additions to the available toolbox of *agr* inhibitors. Additional characterization of these compounds, including delineating their mechanisms of *agr* inhibition and exploration of potential structure-activity relationships that could be useful for the generation of new synthetic derivatives, is currently underway and will be reported in due course. While we immediately recognized and have focused here on the utility of **10** and **11**, we note that three additional hit compounds (HTS

hits 3–5, Figure 7B) were active in our cell-based *agr* transcriptional reporter assay (albeit not to the extent of **10** and **11**; Figure S6), and the activity profiles of these compounds also warrant additional scrutiny. In the context of this current study, however, the identification of **10** and **11** as potent, small-molecule based *agr* inhibitors underscores the utility of our vesicle leakage assay as an accessible and high-throughput platform for the discovery of novel QSMs.

Summary and Conclusions

We have developed a vesicle lysis assay that allows for the facile monitoring of QS activity in common bacterial pathogens, as manifest by the production of biosurfactants associated with virulence, and the application of this assay to discover novel molecules capable of blocking QS activity. The assay method uses suspensions of LUVs that are readily disrupted by amphiphilic toxins produced by *S. aureus* and *P. aeruginosa* at high cell densities, resulting in the production of a readily measurable fluorescence signal. This signal serves as a marker for an active QS system; a suite of known QSMs was found to either block or amplify this signal in a dose- and potency-dependent manner. This assay can be miniaturized to be compatible with conventional high-throughput screening methods and allowed us to screen a sizable commercial library of small molecules for modulation of vesicle lysis in the presence of *S. aureus*. Notably, the results of the high-throughput lysis assay, followed by cell-based secondary assays for *agr* activity, identified two new QS inhibitors in *S. aureus* with potencies an order of magnitude higher than the current lead small-molecule *agr* inhibitor, savirin (**6**). These results strongly support the use of the vesicle lysis assay for the straightforward identification of new QSMs in this formidable pathogen. Moreover, they provide two powerful chemical tools for the study of QS in *S. aureus* that sidestep several limitations associated with current chemical tools available to study and dissect QS.

Acknowledgements

Financial support for this work was provided by the NIH (R21 AI135745) and a grant provided by the UW−Madison Materials Research Science and Engineering Center (MRSEC; DMR-1720415). The authors acknowledge the use of instrumentation supported by the NSF through the UW MRSEC. T.J.P. and K.E.N. were supported in part by the UW−Madison NIH Chemistry−Biology Interface Training Program (T32 GM008505). C.G.G. was supported in part by an NSF Graduate Research Fellowship. NMR and MS characterization was performed in facilities in the Department of Chemistry at UW−Madison that are supported by the NSF (CHE-0342998 and CHE-9974839, respectively). High-throughput screening was performed at the UW Carbone Cancer Center (UWCCC) Small Molecule Screening Facility that is supported by the NIH (P30 CA014520). We thank Dr. Gene Ananiev and Song Guo of the UWCCC for their expert guidance with the high-throughput experiments, Dr. Korbin West for assistance with PSM identification, and Christopher Eom and Dr. M. R. Lee for assistance with NMR quantification experiments. Figure 1 were created with BioRender.com.

References

1. Camilli, A.; Bassler, B. L., Bacterial small-molecule signaling pathways. *Science* **2006,** *311* (5764), 1113-1116.

2. Whiteley, M.; Diggle, S. P.; Greenberg, E. P., Progress in and promise of bacterial quorum sensing research. *Nature* **2017,** *551* (7680), 313-320.

3. Lyon, G. J.; Mayville, P.; Muir, T. W.; Novick, R. P., Rational design of a global inhibitor of the virulence response in Staphylococcus aureus, based in part on localization of the site of inhibition to the receptor-histidine kinase, AgrC. *Proc. Natl. Acad. Sci. U. S. A.* **2000,** *97* (24), 13330-13335.

4. Rutherford, S. T.; Bassler, B. L., Bacterial quorum sensing: its role in virulence and possibilities for its control. *Cold Spring Harb. Perspect. Med.* **2012,** *2* (11), a012427.

5. Thoendel, M.; Kavanaugh, J. S.; Flack, C. E.; Horswill, A. R., Peptide signaling in the staphylococci. *Chem. Rev.* **2011,** *111* (1), 117-151.

6. Le, K. Y.; Otto, M., Quorum-sensing regulation in staphylococci-an overview. *Front. Microbiol.* **2015,** *6*, 1174.

7. Wang, B.; Muir, T. W., Regulation of Virulence in *Staphylococcus aureus:* Molecular Mechanisms and Remaining Puzzles. *Cell Chem. Biol.* **2016,** *23* (2), 214-224.

8. Fuqua, C.; Parsek, M. R.; Greenberg, E. P., Regulation of gene expression by cell-to-cell communication: Acyl-homoserine lactone quorum sensing. *Annu. Rev. Genet.* **2001,** *35*, 439-468.

9. Amara, N.; Mashiach, R.; Amar, D.; Krief, P.; Spieser, S. A. H.; Bottomley, M. J.; Aharoni, A.; Meijler, M. M., Covalent Inhibition of Bacterial Quorum Sensing. *J. Am. Chem. Soc.* **2009,** *131* (30), 10610-10619.

10. Hodgkinson, J. T.; Galloway, W.; Wright, M.; Mati, I. K.; Nicholson, R. L.; Welch, M.; Spring, D. R., Design, synthesis and biological evaluation of non-natural modulators of quorum sensing in Pseudomonas aeruginosa. *Org. Biomol. Chem.* **2012,** *10* (30), 6032-6044.

11. O'Loughlin, C. T.; Miller, L. C.; Siryaporn, A.; Drescher, K.; Semmelhack, M. F.; Bassler, B. L., A quorum-sensing inhibitor blocks Pseudomonas aeruginosa virulence and biofilm formation. *Proc. Natl. Acad. Sci. U. S. A.* **2013,** *110* (44), 17981- 17986.

12. Moore, J. D.; Rossi, F. M.; Welsh, M. A.; Nyffeler, K. E.; Blackwell, H. E., A Comparative Analysis of Synthetic Quorum Sensing Modulators in Pseudomonas aeruginosa: New Insights into Mechanism, Active Efflux Susceptibility, Phenotypic Response, and Next-Generation Ligand Design. *J. Am. Chem. Soc.* **2015,** *137* (46), 14626-14639.

13. Welsh, M. A.; Blackwell, H. E., Chemical probes of quorum sensing: from compound development to biological discovery. *FEMS Microbiol. Rev.* **2016,** *40* (5), 774-794.

14. Muh, U.; Schuster, M.; Heim, R.; Singh, A.; Olson, E. R.; Greenberg, E. P., Novel *Pseudomonas aeruginosa* quorum-sensing inhibitors identified in an ultra-high-throughput screen. *Antimicrob. Agents Chemother.* **2006,** *50* (11), 3674-3679.

15. Muh, U.; Hare, B. J.; Duerkop, B. A.; Schuster, M.; Hanzelka, B. L.; Heim, R.; Olson, E. R.; Greenberg, E. P., A structurally unrelated mimic of a Pseudomonas aeruginosa acyl-homoserine lactone quorum-sensing signal. *Proc. Natl. Acad. Sci. U. S. A.* **2006,** *103* (45), 16948-16952.

16. Starkey, M.; Lepine, F.; Maura, D.; Bandyopadhaya, A.; Lesic, B.; He, J.; Kitao, T.; Righi, V.; Milot, S.; Tzika, A.; Rahme, L., Identification of anti-virulence compounds that disrupt quorum-sensing regulated acute and persistent pathogenicity. *PLoS Pathog.* **2014,** *10* (8), e1004321.

17. Tal-Gan, Y.; Stacy, D. M.; Foegen, M. K.; Koenig, D. W.; Blackwell, H. E., Highly potent inhibitors of quorum sensing in *Staphylococcus aureus* revealed through a systematic synthetic study of the group-III autoinducing peptide. *J. Am. Chem. Soc.* **2013,** *135* (21), 7869-7882.

18. Tal-Gan, Y.; Ivancic, M.; Cornilescu, G.; Yang, T.; Blackwell, H. E., Highly Stable, Amide-Bridged Autoinducing Peptide Analogues that Strongly Inhibit the AgrC Quorum Sensing Receptor in Staphylococcus aureus. *Angew. Chem. Int. Ed.* **2016,** *55* (31), 8913-8917.

19. Vasquez, J. K.; Blackwell, H. E., Simplified Autoinducing Peptide Mimetics with Single-Nanomolar Activity Against the Staphylococcus aureus AgrC Quorum Sensing Receptor. *ACS Infect. Dis.* **2019,** *5* (4), 484-492.

20. Xie, Q.; Wiedmann, M. M.; Zhao, A.; Pagan, I. R.; Novick, R. P.; Suga, H.; Muir, T. W., Discovery of quorum quenchers targeting the membrane-embedded sensor domain of the Staphylococcus aureus receptor histidine kinase, AgrC. *Chem. Commun.* **2020,** *56* (76), 11223-11226.

21. Horswill, A. R.; Gordon, C. P., Structure-Activity-Relationship Studies of Small Molecule Modulators of the Staphylococcal Accessory Gene Regulator. *J. Med. Chem.* **2019,** *63* (6), 2705-2730.

22. Schuster, M.; Peter Greenberg, E., A network of networks: Quorum-sensing gene regulation in Pseudomonas aeruginosa. *Int. J. Med. Microbiol.* **2006,** *296* (2), 73-81.

23. Rasko, D. A.; Sperandio, V., Anti-virulence strategies to combat bacteria-mediated disease. *Nat. Rev. Drug. Discov.* **2010,** *9* (2), 117-128.

24. Jenul, C.; Horswill, A. R., Regulation of Staphylococcus aureus Virulence. *Microbiol. Spectrum* **2019,** *7* (2), 10.1128/microbiolspec.GPP3-0031-2018.

25. Yarwood, J. M.; Schlievert, P. M., Quorum sensing in Staphylococcus infections. *J. Clin. Invest.* **2003,** *112* (11), 1620-1625.

26. Traber, K. E.; Lee, E.; Benson, S.; Corrigan, R.; Cantera, M.; Shopsin, B.; Novick, R. P., agr function in clinical Staphylococcus aureus isolates. *Microbiology* **2008,** *154* (Pt 8), 2265-2274.

27. Hoffman, L. R.; Kulasekara, H. D.; Emerson, J.; Houston, L. S.; Burns, J. L.; Ramsey, B. W.; Miller, S. I., Pseudomonas aeruginosa lasR mutants are associated with cystic fibrosis lung disease progression. *J. Cystic Fibrosis* **2009,** *8* (1), 66-70.

28. Feltner, J. B.; Wolter, D. J.; Pope, C. E.; Groleau, M.-C.; Smalley, N. E.; Greenberg, E. P.; Mayer-Hamblett, N.; Burns, J.; Déziel, E.; Hoffman, L. R.; Dandekar, A. A., LasR Variant Cystic Fibrosis Isolates Reveal an Adaptable Quorum-Sensing Hierarchy in Pseudomonas aeruginosa. *mBio* **2016,** *7* (5), e01513-16.

29. Hodgkinson, J. T.; Galloway, W. R. J. D.; Casoli, M.; Keane, H.; Su, X.; Salmond, G. P. C.; Welch, M.; Spring, D. R., Robust routes for the synthesis of N-acylated-l-homoserine lactone (AHL) quorum sensing molecules with high levels of enantiomeric purity. *Tetrahedron Lett.* **2011,** *52* (26), 3291-3294.

30. Welsh, M. A.; Blackwell, H. E., Chemical genetics reveals environment-specific roles for quorum sensing circuits in Pseudomonas aeruginosa. *Cell Chem. Biol.* **2016,** *23*, 361-369.

31. Boursier, M. E.; Moore, J. D.; Heitman, K. M.; Shepardson-Fungairino, S. P.; Combs, J. B.; Koenig, L. C.; Shin, D.; Brown, E. C.; Nagarajan, R.; Blackwell, H. E., Structure-Function Analyses of the N-Butanoyl L-Homoserine Lactone Quorum-Sensing Signal Define Features Critical to Activity in RhIR. *ACS Chem. Biol.* **2018,** *13* (9), 2655-2662.

32. Manson, D. E.; O'Reilly, M. C.; Nyffeler, K. E.; Blackwell, H. E., Design, Synthesis, and Biochemical Characterization of Non-Native Antagonists of the Pseudomonas aeruginosa Quorum Sensing Receptor LasR with Nanomolar IC50 Values. *ACS Infect. Dis.* **2020,** *6* (4), 649-661.

33. Mayer, L. D.; Hope, M. J.; Cullis, P. R., Vesicles of variable sizes produced by a rapid extrusion procedure. *Biochim. Biophys. Acta* **1986,** *858* (1), 161-168.

34. Lapinski, M. M.; Castro-Forero, A.; Greiner, A. J.; Ofoli, R. Y.; Blanchard, G. J., Comparison of liposomes formed by sonication and extrusion: Rotational and translational diffusion of an embedded chromophore. *Langmuir* **2007,** *23* (23), 11677-11683.

35. Brewster, J. D., A simple micro-growth assay for enumerating bacteria. *J. Microbiol. Methods* **2003,** *53* (1), 77-86.

36. Zhou, J.; Loftus, A. L.; Mulley, G.; Jenkins, A. T. A., A Thin Film Detection/Response System for Pathogenic Bacteria. *J. Am. Chem. Soc.* **2010,** *132* (18), 6566-6570.

37. Zhou, J.; Tun, T. N.; Hong, S. H.; Mercer-Chalmers, J. D.; Laabei, M.; Young, A. E. R.; Jenkins, A. T. A., Development of a prototype wound dressing technology which can detect and report colonization by pathogenic bacteria. *Biosens. Bioelectron.* **2011,** *30* (1), 67-72.

38. Marshall, S. E.; Hong, S. H.; Thet, N. T.; Jenkins, A. T. A., Effect of Lipid and Fatty Acid Composition of Phospholipid Vesicles on Long-Term Stability and Their Response to Staphylococcus aureus and Pseudomonas aeruginosa Supernatants. *Langmuir* **2013,** *29* (23), 6989-6995.

39. Laabei, M.; Jamieson, W. D.; Lewis, S. E.; Diggle, S. P.; Jenkins, A. T. A., A new assay for rhamnolipid detection-important virulence factors of Pseudomonas aeruginosa. *Appl. Microbiol. Biotechnol.* **2014,** *98* (16), 7199-7209.

40. Laabei, M.; Jamieson, W. D.; Massey, R. C.; Jenkins, A. T. A., Staphylococcus aureus Interaction with Phospholipid Vesicles – A New Method to Accurately Determine Accessory Gene Regulator (agr) Activity. *PLoS One* **2014,** *9* (1), e87270.

41. Zhou, J.; Yao, D. Y.; Qian, Z. Y.; Hou, S.; Li, L. H.; Jenkins, A. T. A.; Fan, Y. B., Bacteria-responsive intelligent wound dressing: Simultaneous In situ detection and inhibition of bacterial infection for accelerated wound healing. *Biomaterials* **2018,** *161*, 11-23.

42. Ortiz, B. J.; Boursier, M. E.; Barrett, K. L.; Manson, D. E.; Amador-Noguez, D.; Abbott, N. L.; Blackwell, H. E.; Lynn, D. M., Liquid Crystal Emulsions That Intercept and Report on Bacterial Quorum Sensing. *ACS Appl. Mater. Interfaces* **2020,** *12* (26), 29056-29065.

43. Otto, M., Phenol-soluble modulins. *Int. J. Med. Microbiol.* **2014,** *304* (2), 164-169.

44. Loureiro-Ferreira, N., Rodrigues, J., Brito, R.M.M, NMR structure of delta-toxin from Staphylococcus aureus in CD3OH. 2008.

45. Thet, N. T.; Hong, S. H.; Marshall, S.; Laabei, M.; Toby, A.; Jenkins, A., Visible, colorimetric dissemination between pathogenic strains of Staphylococcus aureus and Pseudomonas aeruginosa using fluorescent dye containing lipid vesicles. *Biosens. Bioelectron.* **2013,** *41*, 538-543.

46. Novick, R. P., Autoinduction and signal transduction in the regulation of staphylococcal virulence. *Mol. Microbiol.* **2003,** *48* (6), 1429-1449.

47. Schuster, M.; Lostroh, C. P.; Ogi, T.; Greenberg, E. P., Identification, Timing, and Signal Specificity of Pseudomonas aeruginosa Quorum-Controlled Genes: a Transcriptome Analysis. *J. Bacteriol.* **2003,** *185* (7), 2066-2079.

48. Sully, E. K.; Malachowa, N.; Elmore, B. O.; Alexander, S. M.; Femling, J. K.; Gray, B. M.; DeLeo, F. R.; Otto, M.; Cheung, A. L.; Edwards, B. S.; Sklar, L. A.; Horswill, A. R.; Hall, P. R.; Gresham, H. D., Selective chemical inhibition of agr quorum sensing in *Staphylococcus aureus* promotes host defense with minimal impact on resistance. *PLoS Pathog.* **2014,** *10* (6), e1004174.

49. Eibergen, N. R.; Moore, J. D.; Mattmann, M. E.; Blackwell, H., Potent and Selective Modulation of the RhlR Quorum Sensing Receptor by Using Non-native Ligands: An Emerging Target for Virulence Control in Pseudomonas aeruginosa. *ChemBioChem* **2015,** *16* (16), 2348-2356.

50. Schuster, M.; Greenberg, E. P., LuxR-Type Proteins in Pseuodomonas aeruginosa Quorum Sensing: Distinct Mechanisms with Global Implications. In *Chemical Communication among Bacteria*, ASM Press: Washington, DC, 2008; pp 133-144.

51. Welsh, M. A.; Eibergen, N. R.; Moore, J. D.; Blackwell, H. E., Small Molecule Disruption of Quorum Sensing Cross-Regulation in Pseudomonas aeruginosa Causes Major and Unexpected Alterations to Virulence Phenotypes. *J. Am. Chem. Soc.* **2015,** *137* (4), 1510-1519.

52. Smith, L. H. L. J., CA, US), Pinkerton, Anthony B. (La Jolla, CA, US), Hershberger, Paul (La Jolla, CA, US), Maloney, Patrick (La Jolla, CA, US), Mcanally, Danielle (La Jolla, CA, US) Apelin Receptor Agonists and Methods of Use Thereof. 2018.

Supporting Information for Chapter 6

Table S1. Bacterial strains and plasmids used in this study.

	Description	**Reference or Source**
Staphylococcus aureus		
RN6390b	Wild-type, *agr* group I (NTCC 8325 cured of prophages)[1]	Novick[2]
RN9222	RN6911 with pRN7062, QS mutant	Lyon *et al*.[3]
RN6911	*agr*::*tetM* (agr-null), from RN6390	Novick *et al*.[1]
AH1677	USA300 LAC with pDB59	Kirchdoerfer *et al*.[4]
Pseudomonas aeruginosa		
PAO1-PGSC	Wild-type	Pseudomonas Genetic Stock Center
PAO-JG35	*ΔlasR*::Tc^R *ΔrhlR*, Tc^R, from PAO1-PGSC, QS mutant	Gerdt and Blackwell[5]
Plasmids		
pDB59	*P3-yfp*$_{10B}$ transcriptional fusion, Cm^R	Yarwood *et al*.[6]
pRN7062	Contains *agrCA* and *P3-blaZ* transcriptional fusion, Erm^R	Lyon *et al*.[3]
p*lasI*-LVAgfp	p*lasI*-LVAgfp transcriptional fusion, Amp^R	De Kievit *et al*.[7]

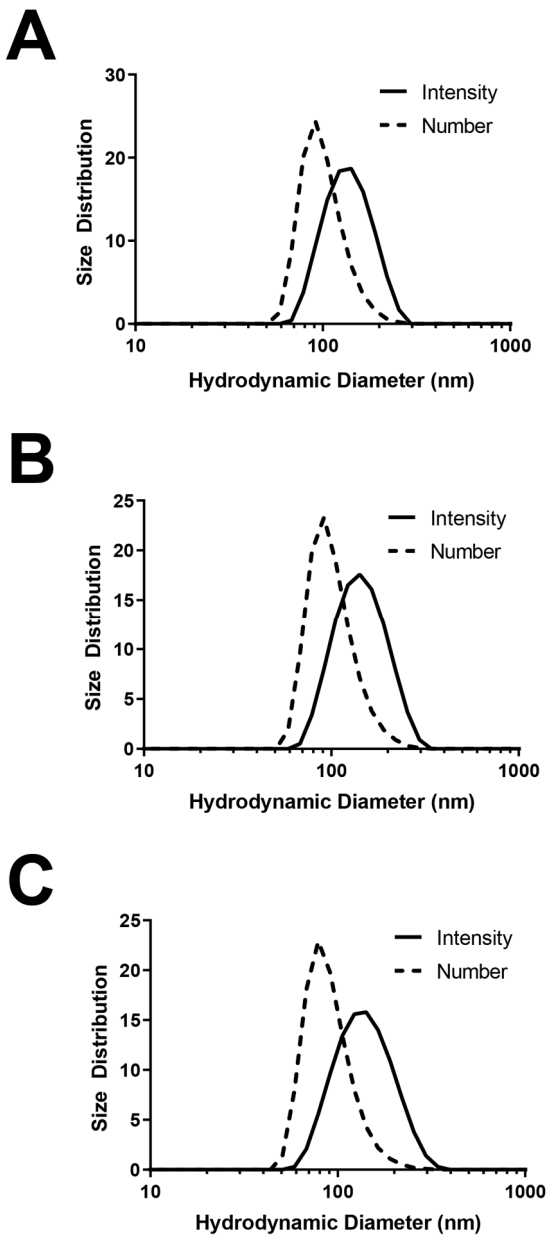


Figure S1. Results of dynamic light scattering (DLS) analysis of the calcein-loaded vesicle formulations used in this study. Intensity and number average size distributions for vesicles composed of (A) 68% DPPC, 30% cholesterol, and 2% DPPE and (B–C) 70% DOPC and 30% cholesterol passed through a 100 nm polycarbonate membrane either (B) 3 times (representative of vesicles used in high-throughput assays) or (A,C) 7 times (representative of vesicles used in continuous time course experiments). These DLS results demonstrate that the vesicles used in this study are ~150 nm in diameter. Size distributions shown are the average of three independent measurements of a single vesicle sample.

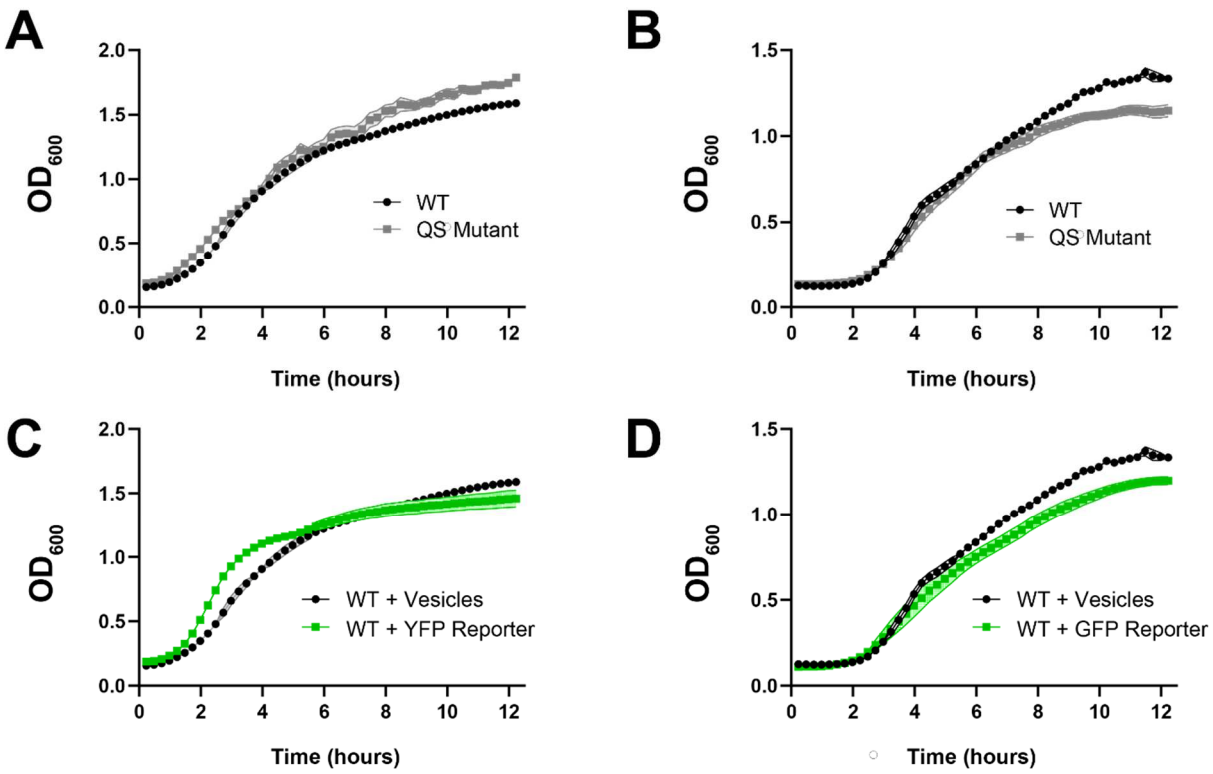


Figure S2. Growth curves for bacteria incubated in the presence of calcein-loaded vesicles. (A) Growth curves for *S. aureus* WT and an agr-null strain (*S. aureus* QS mutant). (B) Growth curves for *P. aeruginosa* WT and a Δ*lasRrhlR* strain (*P. aeruginosa* QS mutant). (C) Growth curves for *S. aureus* WT with vesicles and *S. aureus* WT containing a YFP QS reporter plasmid (pDB59). (D) Growth curves for *P. aeruginosa* WT with vesicles and *P. aeruginosa* WT containing a GFP QS reporter plasmid (p*lasI*-LVAgfp). Data points represent the mean of all replicates (n = 9). Error bars = SEM (shaded area around data points). See Methods for assay protocols and Table S1 for details of strains and plasmids used.

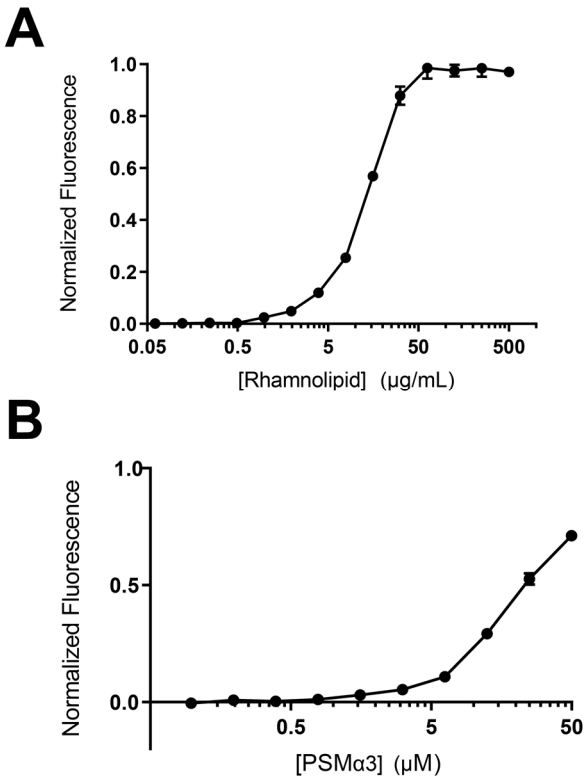


Figure S3. Normalized calcein fluorescence intensity values for (A) rhamnolipid introduced to 68% DPPC, 30% cholesterol, 2% DPPE vesicles containing calcein in calcein buffer (the vesicles used for experiments with *P. aeruginosa*) at various concentrations and (B) PSMα3 introduced to 70% DOPC, 30% cholesterol vesicles containing calcein in PBS (the vesicles used for experiments with *S. aureus*) at various concentrations. In all measurements, the lipid concentration of the vesicles was held constant at 100 μM for *P. aeruginosa* vesicles or 200 μM for *S. aureus* vesicles. All points shown are the mean and SD of three measurements of a single technical replicate. In both plots, some error bars are obscured by the sizes of the data points. See Methods for details of each vesicle formulation.

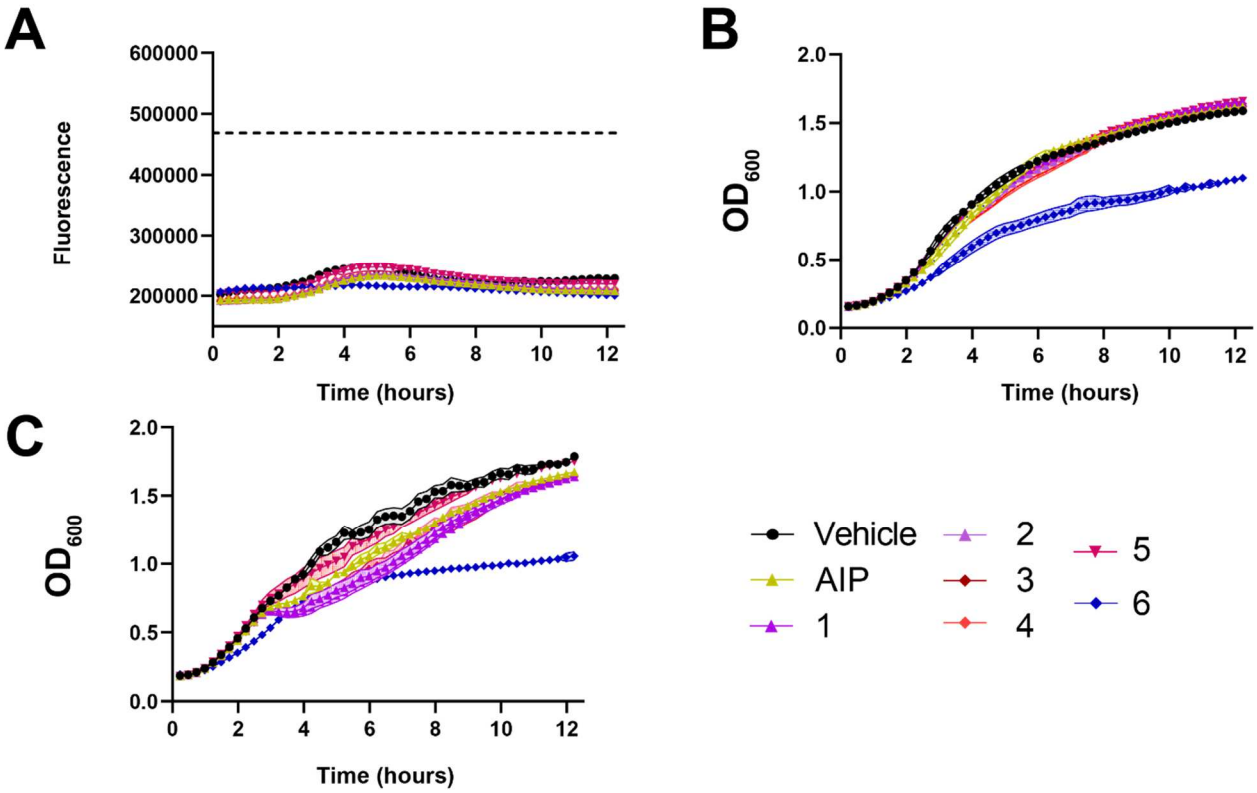


Figure S4. Effects of exogenously added AIP and compounds **1**–**6** on vesicle lysis and *S. aureus* growth. Compounds and corresponding colors/symbols are shown at lower right. (A) Fluorescence curves for vesicles incubated with the *S. aureus* QS mutant + vehicle and/or compounds. The dashed line indicates fluorescence 1 hr after addition of Triton X-100 (positive control for complete vesicle lysis). Compounds did not have a noticeable effect on vesicle lysis. (B) Growth curves for *S. aureus* WT incubated with vesicles + vehicle/compounds. (C) Growth curves for the *S. aureus* QS mutant incubated with vesicles + vehicle/compounds. Data points represent the mean of all replicates (n = 9). Error bars = SEM (shaded area around data points). See Methods for full details of assays.

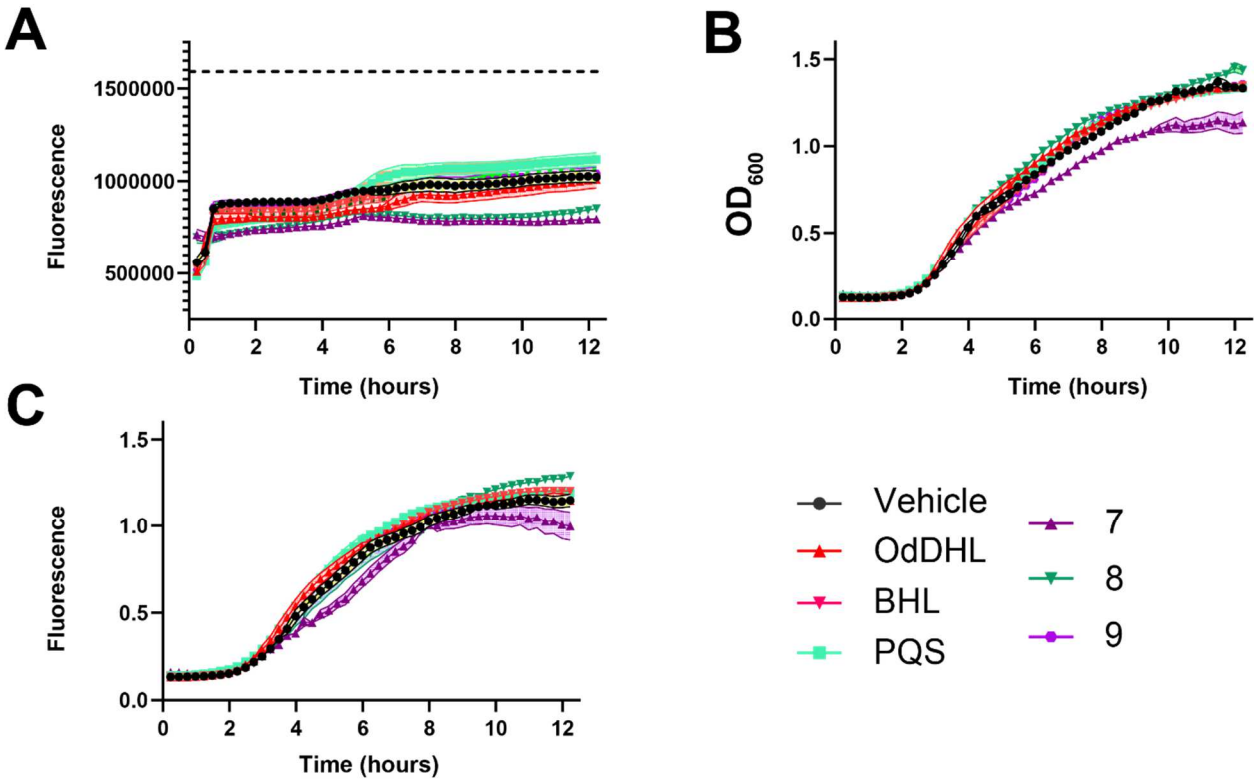


Figure S5. Effects of exogenously added native QS signaling molecules (OdDHL, BHL, and PQS) and compounds **7–9** on vesicle lysis and *P. aeruginosa* growth. Compounds and corresponding colors/symbols are shown at lower right. (A) Fluorescence curves for vesicles incubated with the *P. aeruginosa* QS mutant + vehicle and/or compounds. The dashed line indicates fluorescence 1 hr after addition of Triton X-100 (positive control for complete vesicle lysis). Compounds did not have a noticeable effect on vesicle lysis. (B) Growth curves for WT *P. aeruginosa* incubated with vesicles + vehicle/compounds. (C) Growth curves for the *P. aeruginosa* QS mutant incubated with vesicles + vehicle/compounds. Data points represent the mean of all replicates (n = 9). Error bars = SEM (shaded area around data points). See Methods for full details of assays.

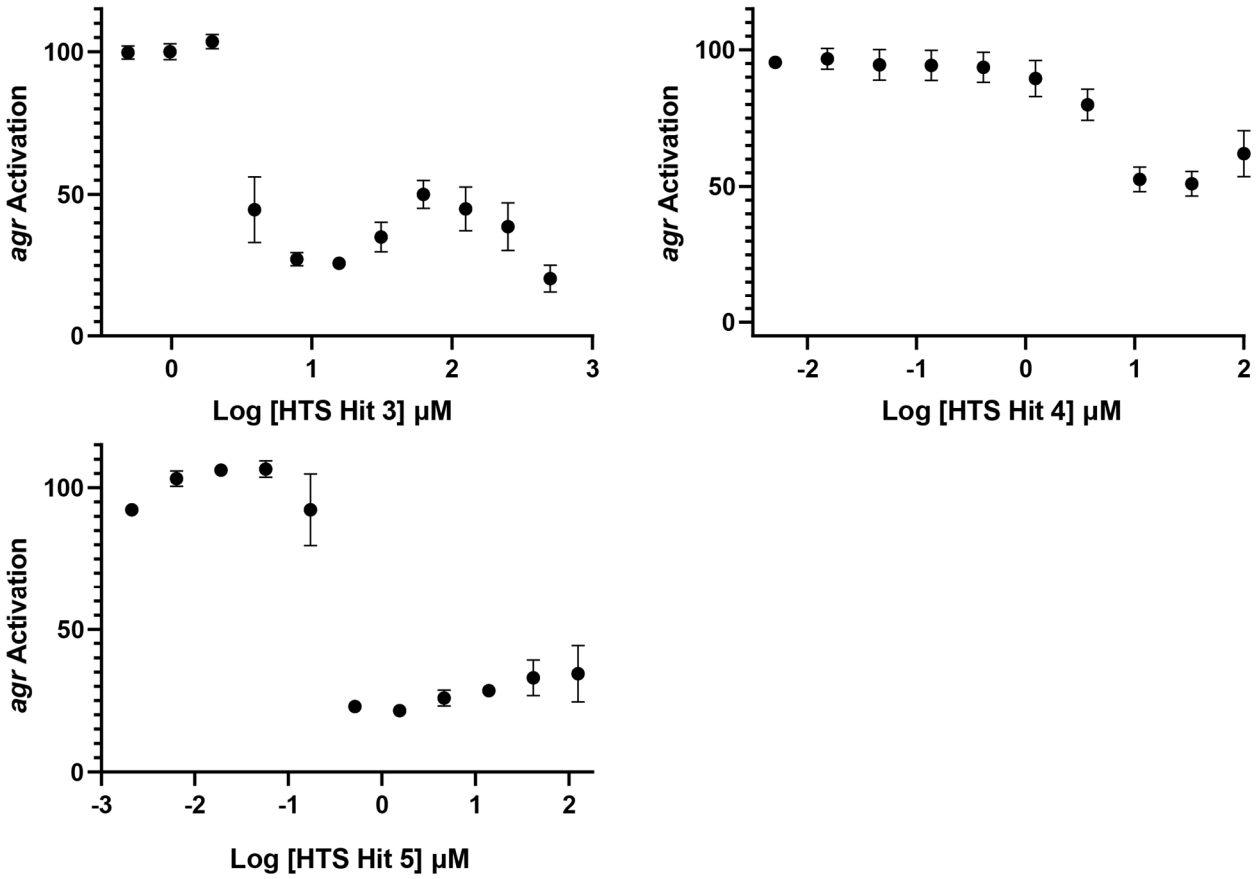


Figure S6. Dose-response *agr* inhibition data for high-throughput screen (HTS) hit compounds 3–5 in the *S. aureus agr* reporter strain containing a YFP QS plasmid (pDB59). Data points represent the mean of all replicates (n = 9). Error bars = SEM. See Methods for details of reporter assay.

Identification of biosurfactants in *P. aeruginosa* and *S. aureus*. *P. aeruginosa* PAO1, the parent strain of the WT *P. aeruginosa* strain used here (PAO1-PGSC), is well known to produce rhamnolipid,[8] and we demonstrated in a prior study that *P. aeruginosa* PAO1 produces rhamnolipid.[9] As the WT *S. aureus* strain used here, RN6390, may not produce functional PSMα3,[10] a highly lytic PSM, we sought to investigate the levels and identities of the PSMs produced by this strain. Subcultures (10 mL) of *S. aureus* WT and the *S. aureus* QS mutant were grown overnight by diluting a previous overnight culture 1:50 into fresh BHI medium. This subculture was centrifuged at 16,100 g for 5 minutes. The supernatant was then passed through a PerkinElmer polytetrafluoroethylene (PTFE) syringe filter with 0.45 μm pore size. Using reversed-phase high performance liquid chromatography (RP-HPLC) and MS/MS analyses, we were able to identify both formylated and non-formylated δ-toxin, a 26 residue PSM, in the *S. aureus* WT supernatant (Figure S7). Neither of these PSM species were observed in supernatant of the *S. aureus* QS mutant. δ-toxin is commonly isolated from *S. aureus* as a mixture of formylated and non-formylated variants, with the former predominating.[11] As δ-toxin was the predominant PSM class isolated from this WT strain, and this PSM is well known to be associated with *S. aureus* lytic phenotypes,[12, 13] these results are consistent with δ-toxin being a causative agent of vesicle lysis upon incubation with WT *S. aureus* in the current study.

RP-HPLC analysis of *S. aureus* supernatants was performed using Shimadzu system equipped with a SCL-10Avp system controller, a DGU-14A degasser, LC-20AT solvent delivery unit, a SIL-10AF autosampler, a CTO-10AS column oven equipped with a manual injector, a SPD-M10A UV-Vis diode array detector, and a FRC-10A fraction collector was used. Solvent A was 18 MΩ water with 0.1% TFA, and solvent B was HPLC-grade acetonitrile with 0.1% TFA. The column was a Kromasil Eternity C18 column (10 mm x 250 mm, 5 mm particle size with 100 Å

pore size). A linear gradient of 0% solvent B → 100% solvent B at 5 mL/min flow rate was run for 41 min. A 4 mL sample of the filtered supernatant was injected. Two fractions corresponding to peaks observed between 30 and 45 minutes (Figure S7 *top*) were collected, lyophilized, and further analyzed with a Bruker impact II ESI-Q-TOF mass spectrometer equipped with a Thermo UltiMate 3000 HPLC (with reverse-phase [C18] column). Solvent A was 18 MΩ water with 0.1% formic acid, and solvent B was HPLC-grade acetonitrile with 0.1% formic acid. A linear gradient of 0% solvent B → 100% solvent B at 300 µL/min flow rate was run for 50 min. MS/MS analysis of the two fractions revealed the presence of formylated δ-toxin (at the N-terminal Met residue) and non-formylated δ-toxin as the predominant species (Figure S7 *bottom*; Tables S2 and S3).

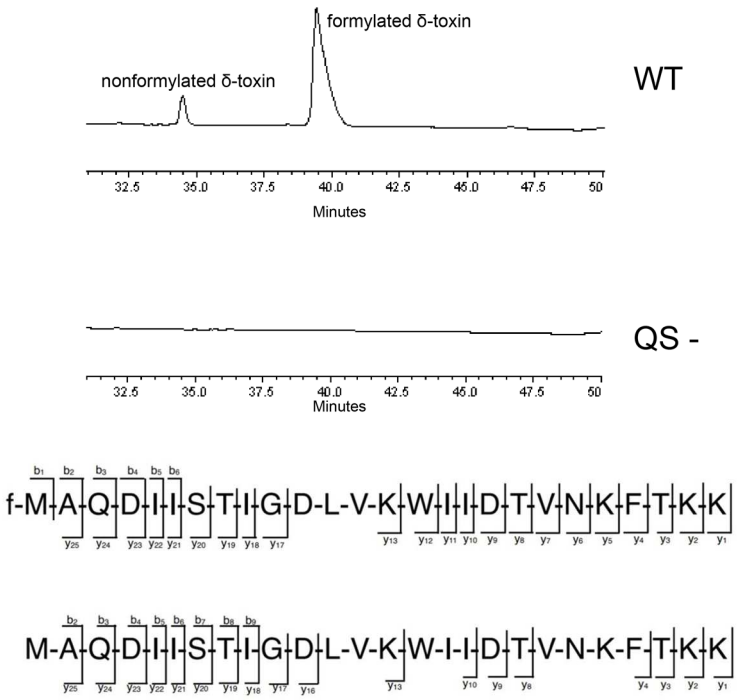


Figure S7. *(Top)* Portions of the analytical RP-HPLC traces corresponding to PSMs from the analyses of the supernatants of WT *S. aureus* and QS mutant *S. aureus* strains. *(Bottom)* Sequences and b-/y- fragment ions obtained via MS/MS analysis of N-terminal formylated and non-formylated δ-toxin samples (single letter amino acid codes used; f = formyl).

Table S2. MS/MS data for formylated δ-toxin.

$[M+H]^+$ = 3005.64 calculated; 3005.63 observed				
b ions			*y ions*	
Calc.	**Obs.**	**Residue**	**Calc.**	**Obs.**
160.04	160.04	1 M 26		
231.08	231.08	2 A 25	2846.60	2846.59
359.14	359.14	3 Q 24	2775.57	2775.55
474.17	474.16	4 D 23	2647.51	2647.50
587.25	587.25	5 I 22	2532.48	2532.47
700.33	700.33	6 I 21	2419.40	2419.39
787.37	na	7 S 20	2306.31	2306.30
888.41	na	8 T 19	2219.28	2219.27
1001.50	na	9 I 18	2118.23	2118.22
1058.52	na	10 G 17	2005.15	2005.14
1173.55	na	11 D 16	1948.13	na
1286.63	na	12 L 15	1833.10	na
1385.70	na	13 V 14	1720.02	na
1513.79	na	14 K 13	1620.95	1620.95
1699.87	na	15 W 12	1492.85	1492.85
1812.96	na	16 I 11	1306.77	1306.77
1926.04	na	17 I 10	1193.69	1193.68
2041.07	na	18 D 9	1080.61	1080.60
2142.12	na	19 T 8	965.58	965.57
2241.18	na	20 V 7	864.53	864.53
2355.23	na	21 N 6	765.46	765.46
2483.32	na	22 K 5	651.42	651.41
2630.39	na	23 F 4	523.32	523.32
2731.44	na	24 T 3	376.26	376.25
2859.53	na	25 K 2	275.21	275.21
		26 K 1	147.11	147.11

Table S3. MS/MS data for non-formylated δ-toxin.

$[M+H]^+$ = 2977.64 calculated; 2977.65 observed				
b ions			*y ions*	
Calc.	**Obs.**	**Residue**	**Calc.**	**Obs.**
132.05	132.00	1 M 26		
203.09	203.09	2 A 25	2846.60	2846.61
331.14	331.14	3 Q 24	2775.57	2775.57
446.17	446.17	4 D 23	2647.51	2647.51
559.26	559.26	5 I 22	2532.48	2532.40
672.34	672.34	6 I 21	2419.40	2419.40
759.37	759.37	7 S 20	2306.31	2306.32
860.42	860.47	8 T 19	2219.28	2219.29
973.50	973.50	9 I 18	2118.23	2118.24
1030.52	na	10 G 17	2005.15	2005.16
1145.55	na	11 D 16	1948.13	1948.14
1258.64	na	12 L 15	1833.10	na
1357.70	na	13 V 14	1720.02	na
1485.80	na	14 K 13	1620.95	1620.96
1671.88	na	15 W 12	1492.85	na
1784.96	na	16 I 11	1306.77	na
1898.05	na	17 I 10	1193.69	1193.69
2013.07	na	18 D 9	1080.61	1080.60
2114.12	na	19 T 8	965.58	965.58
2213.19	na	20 V 7	864.53	na
2327.23	na	21 N 6	765.46	na
2455.33	na	22 K 5	651.42	na
2602.40	na	23 F 4	523.32	523.33
2703.44	na	24 T 3	376.26	376.26
2831.54	na	25 K 2	275.21	275.20
		26 K 1	147.11	147.11

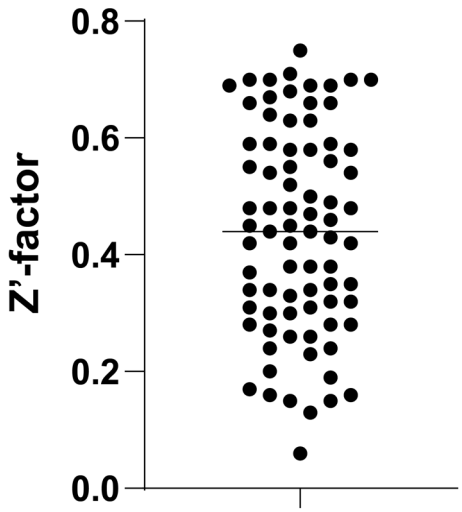


Figure S8. Z'-factors of all 79 microtiter plates used in the high-throughput screen. All plates had positive Z'-factors with a median value of 0.42 (black bar). Z'-factors were calculated according to previously established methods.[14] See Methods and below for details of high-throughput screening assay protocol.

NMR quantification of concentrations of phospholipids in vesicles. The concentration of phospholipids in stock solutions of vesicles was determined using our previously reported method based on quantitative $^{31}P[^{1}H]$ NMR spectroscopy.[15] All experiments were performed in 90% H_2O and 10% D_2O using a Bruker Avance-400 spectrometer with a BBFO probe. A relaxation delay (D1) of 11 s was determined by inversion-recovery pulse sequence experiments. A phospholipid vesicle sample (890 µL in water) was mixed with 10 µL of Triton X-100 or rhamnolipid solution (to fully lyse the vesicles), and 100 µL of a triethylphosphine oxide (TPO) solution (100 mM in D_2O) was added as an internal standard. Integrations for phospholipid peaks were performed relative to the phosphorus peak of TPO (δ ~65 ppm). NMR acquisition parameters were as follows: PULPROG (pulse program) = zgig30, D1 (relaxation delay) = 11 s, SW (sweep width) = 405 ppm, O2P (transmitter frequency of f2 channel) = 3.75 ppm, NS (number of scans) = 64, DS (number of dummy scans) = 4, LB (line broadening factor) = 1.

High-throughput screening and follow-up analysis protocols. Experimental compounds and positive control **1** were delivered in 2.5 nL aliquots of DMSO with an Echo 550 liquid handler (LabCyte Inc.) into black 384-well microtiter plates (Corning). All experimental compounds were tested at 10 μM; positive control **1** was tested at 250 nM. Overnight cultures (2 mL) of WT *S. aureus* (RN6390b) were grown at 37 °C with shaking at 200 rpm. These cultures were diluted 1:500 (v/v) in fresh BHI medium, at which point vesicle solutions were added to a final concentration of 1 mM phospholipid (as determined by ^{31}P NMR analyses). This vesicle-cell mixture was then added to the 384-well microtiter plates with a Multidrop 384 liquid-dispensing robot (Thermo Scientific) for a total volume of 50 μL per well. Plates were incubated statically for ~24 hr at 37 °C, at which point fluorescence (excitation 483, emission 530) and OD_{600} (absorbance at 600 nm) measurements were made using a CLARIOstar® *Plus* microtiter plate reader (BMG Labtech) running MARS data analysis software. Scatter plots were generated using the Collaborative Drug Discovery Vault informatics platform. The dose-response experiment using the vesicle lysis assay was performed in a 384-well plate in technical duplicate with compound concentrations of 0.1, 0.25, 0.5, 1, 2.5, 5, 10, and 20 μM. Dose-response curves were generated using variable slope (4 parameter) non-linear regression analysis for compound inhibition using GraphPad Prism software (v. 9).

Analysis of the QS modulatory activity of the HTS hits and **6** (savirin) was performed using the *S. aureus* YFP transcriptional reporter strain. HTS hits were purchased directly from Life Chemicals, Inc. DMSO stock solutions (10 mM) of each compound were prepared and stored at -20 °C. Serial dilutions (1:3) were prepared from the stock solutions in DMSO, and 2 μL aliquots of the resulting dilutions were added to the wells of black 96-well microtiter plates (Corning).

Overnight cultures of the *S. aureus* reporter strain (2 mL) were grown at 37 °C with shaking at 200 rpm. Cultures were diluted 1:50 (v/v) into fresh BHI medium, and 198 µL of this diluted culture were added to each well containing compound, for a total volume of 200 µL per well. All plates contained a vehicle control consisting of 2 µL of DMSO and 198 µL of culture and a media control consisting of 200 µL BHI. Plates were incubated for ~24 hours at 37 °C with shaking at 200 rpm. Fluorescence (excitation 510, emission 544) and OD_{600} measurements were acquired with a PerkinElmer EnVision microtiter plate reader running Envision Manager software. Background fluorescence from BHI control was subtracted from raw fluorescence reads, OD_{600} corrected, and finally normalized to vehicle control. Dose-response curves and IC_{50} values were generated using 3-parameter non-linear regression analysis for compound inhibition using GraphPad Prism software (v. 9). All compounds were tested in technical triplicate with at least 3 biological replicates.

Supplemental References

1. Novick, R. P.; Ross, H. F.; Projan, S. J.; Kornblum, J.; Kreiswirth, B. N.; Moghazeh, S., Synthesis of staphylococcal virulence factors is controlled by a regulator RNA molecule. *EMBO J.* **1993,** *12* (10), 3967-3975.

2. Novick, R. P., Properties of a Cryptic High-Frequency Transducing Phage in *Staphylococcus aureus*. *Virology* **1967,** *33*, 155-166.

3. Lyon, G. J.; Mayville, P.; Muir, T. W.; Novick, R. P., Rational design of a global inhibitor of the virulence response in *Staphylococcus aureus*, based in part on localization of the site of inhibiton to the receptor-histidine kinase, AgrC. *Proc. Natl. Acad. Sci. U S A* **2000,** *97* (24), 13330-13335.

4. Kirchdoerfer, R. N.; Garner, A. L.; Flack, C. E.; Mee, J. M.; Horswill, A. R.; Janda, K. D.; Kaufmann, G. F.; Wilson, I. A., Structural basis for ligand recognition and discrimination of a quorum-quenching antibody. *J. Biol. Chem.* **2011,** *286* (19), 17351-17358.

5. Gerdt, J. P.; Blackwell, H. E., Competition studies confirm two major barriers that can preclude the spread of resistance to quorum-sensing inhibitors in bacteria. *ACS Chem. Biol.* **2014,** *9* (10), 2291-2299.

6. Yarwood, J. M.; Bartels, D. J.; Volper, E. M.; Greenberg, E. P., Quorum sensing in Staphylococcus aureus biofilms. *J. Bacteriol.* **2004,** *186* (6), 1838-1850.

7. De Kievit, T. R.; Gillis, R.; Marx, S.; Brown, C.; Iglewski, B. H., Quorum-sensing genes in Pseudomonas aeruginosa biofilms: their role and expression patterns. *Appl. Environ. Microbiol.* **2001,** *67* (4), 1865-1873.

8. Davey, M. E.; Caiazza, N. C.; O'Toole, G. A., Rhamnolipid surfactant production affects biofilm architecture in Pseudomonas aeruginosa PAO1. *J. Bacteriol.* **2003,** *185* (3), 1027-1036.

9. Ortiz, B. J.; Boursier, M. E.; Barrett, K. L.; Manson, D. E.; Amador-Noguez, D.; Abbott, N. L.; Blackwell, H. E.; Lynn, D. M., Liquid Crystal Emulsions That Intercept and Report on Bacterial Quorum Sensing. *ACS Appl. Mater. Interfaces* **2020,** *12* (26), 29056-29065.

10. Bæk, K. T.; Frees, D.; Renzoni, A.; Barras, C.; Rodriguez, N.; Manzano, C.; Kelley, W. L., Genetic Variation in the Staphylococcus aureus 8325 Strain Lineage Revealed by Whole-Genome Sequencing. *PLoS One* **2013,** *8* (9), e77122.

11. Somerville, G. A.; Cockayne, A.; Durr, M.; Peschel, A.; Otto, M.; Musser, J. M., Synthesis and deformylation of Staphylococcus aureus delta-toxin are linked to tricarboxylic acid cycle activity. *J. Bacteriol.* **2003,** *185* (22), 6686-6694.

12. Otto, M., Phenol-soluble modulins. *Int. J. Med. Microbiol.* **2014,** *304* (2), 164-169.

13. Laabei, M.; Jamieson, W. D.; Yang, Y.; van den Elsen, J.; Jenkins, A. T. A., Investigating the lytic activity and structural properties of Staphylococcus aureus phenol soluble modulin (PSM) peptide toxins. *Biochim. Biophys. Acta, Biomembr.* **2014,** *1838* (12), 3153-3161.

14. Zhang, J.-H.; Chung, T. D. Y.; Oldenburg, K. R., A Simple Statistical Parameter for Use in Evaluation and Validation of High Throughput Screening Assays. *J. Biomol. Screening* **1999,** *4* (2), 67-73.

15. Gahan, C. G.; Patel, S. J.; Chen, L. M.; Manson, D. E.; Ehmer, Z. J.; Blackwell, H. E.; Van Lehn, R. C.; Lynn, D. M., Bacterial Quorum Sensing Signals Promote Large-Scale Remodeling of Lipid Membranes. *Langmuir* **2021**, https://doi.org/10.1021/acs.langmuir.1c01204.

Chapter 7

Sustained Release of a Synthetic Autoinducing Peptide Mimetic Strongly Attenuates MRSA Infections *In Vivo*‡

‡ Portions of this chapter have been submitted for publication as: West, K. H. J.; Gahan, C. G.; Kierski, P. R.; Calderon, D. F.; Czuprynski, C. J.; McAnulty, J. F.; Lynn D. M; Blackwell, H. E. "Sustained Release of a Synthetic Autoinducing Peptide Mimetic Strongly Attenuates MRSA Infections *In Vivo*". K. H. J. West deigned and performed experiments related to compound sequestration and other bacterial laboratory experiments. I fabricated and characterized the loaded PLA microparticles and assisted in discussion and data analysis. K. H. J. West, P. R. Kierski and D. F. Calderon designed and performed all in vivo experiments. C. J. Czuprynski, J. F. McAnulty, D. M. Lynn and H. E. Blackwell directed the project.

ABSTRACT: There is significant and growing interest in the development of approaches to the treatment of bacterial infections that have the potential to block virulence without creating selective pressures that lead to antimicrobial resistance. Quorum sensing (QS) regulates key virulence behaviors in many common bacterial pathogens. Here, we report the development of an 'anti-virulence' strategy that exploits the activity of potent synthetic inhibitors of *S. aureus agr*-type QS. We identify peptide-based inhibitors of QS that are resistant to sequestration or degradation by components of murine tissue, and demonstrate that encapsulation of a lead inhibitor in degradable polymer microparticles substantially inhibits *agr*-based QS *in vitro* over at least seven days. Using a murine dermonecrosis abscess model, we demonstrate that this synthetic inhibitor attenuates methicillin-resistant *S. aureus* (MRSA) infections *in vivo*, and that our controlled release strategy significantly improved outcomes compared to mice that received a single-dose bolus administration of the inhibitor. Our results present an effective and potentially modular approach to controlling bacterial virulence *in vivo* by providing new tools for addressing connections between bacterial QS and infection, and could help guide the development of new approaches to target QS inhibition as a therapeutic strategy.

Introduction

Hospital-acquired infections present a sustained and increasingly critical health threat. *Staphylococcus aureus,* an opportunistic Gram-positive pathogen, currently causes over 100,000 hospital-acquired infections per year in the US alone, with nearly 20,000 of those infections becoming fatal.[1] A major barrier to combating *S. aureus* infections is the emergence of widespread resistance to conventional antibiotics, with strains such as the persistent and hardy methicillin-resistant *S. aureus* (MRSA) plaguing healthcare systems worldwide.[2-4] This emerging antibiotic crisis has motivated researchers to explore alternative, non-biocidal approaches to treat and clear bacterial infections. So-called 'anti-virulence' strategies are of particular interest in this context, as they aim to reduce the severity of an infection without killing the infective organism. By doing so, they reduce selective pressures that ultimately lead to resistance and potentially allow a host's immune response to naturally clear the infection.[5-7]

Quorum sensing (QS) is a cell-cell communication system used by bacteria that relies on the production and reception of chemical signals.[8] Because many human pathogens use QS to regulate the production of virulence factors that lead to or further sustain infections, QS presents an attractive target for the development of new anti-virulence approaches.[8-10] QS in *S. aureus* and other related Gram-positive bacteria is governed by the accessory gene regulator (*agr*) QS system, which utilizes an autoinducing peptide (AIP) as its signaling molecule. The *agr* system is now widely understood to be a major regulator of virulence in *S. aureus*, controlling biofilm formation and the production of hemolysins and toxic shock syndrome toxin, among many other virulence factors.[11-13] In recent years, chemical inhibition of the *agr* system has proven effective in attenuating *S. aureus* virulence phenotypes in bacterial cultures.[14-18] Several reports have demonstrated that *agr*-based QS can be strongly antagonized by a range of synthetic small-

molecules,[15, 17, 19] natural products (or their derivatives),[20-25] and macromolecular agents.[26-28] To date, peptide-based *agr* inhibitors represent the most potent and efficacious QS blockers known in *S. aureus*.[12, 14, 18, 29-30]

The ability of certain *agr* inhibitors to attenuate *S. aureus* infections *in vivo* has been investigated in past studies using murine models. As an example, co-injection of non-cognate native AIPs with *S. aureus* has been reported to inhibit *agr* activity in an abscess model by competing with the cognate AIP during infection, preventing *agr* activation and thereby reducing abscess formation.[31-32] These results are exciting in view of the well characterized cross-activity between many *agr* systems and non-cognate AIPs.[13, 18, 33] However, native AIPs have short half-lives *in vivo* (~ 4 hours)[31] and are susceptible to interference with or sequestration by host proteins.[26-27, 34] Small-molecule[15, 19] and natural product-based[20-22] *agr* inhibitors can also attenuate *S. aureus* infection *in vivo*; however, the lower potencies of these agents often requires larger quantities of compound to be administered (e.g., on the order of micrograms per animal), and the mechanisms by which some of these inhibitors function is not yet well understood.[20-21] Many important questions remain to be answered before inhibition of the *agr* system can be deployed *in vivo* as an effective anti-virulence strategy. For example, while inhibition of *agr* blocks the production of toxins and exoproducts that are part of acute *S. aureus* infections,[14, 35] inhibition of *agr* has also been shown to induce biofilm formation (a growth state common in chronic infections) in a limited set of *in vivo* studies.[36-37] In addition, many of the most potent synthetic QS modulators are thioester-linked peptide macrocycles[14, 18, 29] that, like their native AIP counterparts, have short half-lives, low solubilities in biologically-relevant media, and are prone to sequestration or degradation by serum proteins.[26-27, 34]

In this study, we report the identification of a stable and exceptionally potent synthetic peptide-based inhibitor of the *agr* system that attenuates *S. aureus* infections in a murine dermonecrosis abscess model. We first identified synthetic QS inhibitors that are resistant to interference by host tissue sequestration and degradation using an initial *ex vivo* screen, and then investigated the ability of a lead compound to attenuate *S. aureus* infection *in vivo.* Our results demonstrate that this inhibitor can substantially reduce the severity of infection, and that delivery of this inhibitor using degradable polymers can prolong release and significantly improve infection outcomes relative to mice receiving a single bolus administration of the inhibitor. The results of this proof-of-concept study present an effective and potentially modular anti-virulence approach to controlling bacterial infections *in vivo* in a well-studied wound model. In a broader context, this work also provides new and useful chemical/material tools that could be used to address fundamental connections between QS and *S. aureus* infection. With further development, this effort could provide a pathway toward new approaches that target QS as a therapeutic strategy.

Materials and Methods

Reagents, strains, and general methods. Poly (DL-lactide-co-glycolide) (PLG; lactide:glycolide, 50:50; 30–60 kDa), *N*,*N*-dimethylformamide (DMF), tetrahydrofuran (THF), and dimethylsulphoxide (DMSO) were purchased from Sigma-Aldrich and used as received. Phosphate-buffered saline (PBS, 10x solution) was purchased from Dot Scientific and diluted 10x into water and titrated to pH 7.4 before use. Deionization of distilled water was performed using a Milli-Q system, yielding 18.2 MΩ water. The USA300 LAC MRSA strain AH1677[60] was used for reporter assays and general *in vivo* dermonecrosis assays. The *S. aureus* wild-type lab strain RN6390B[61] and the *Δagr* RN9222[62] strain were used only to examine *agr* dependence for abscess

formation in the dermonecrosis model. All strains were cultured with brain heart infusion (BHI, Teknova) medium and incubated at 37 °C with shaking at 200 rpm, with AH1677 cultures supplemented with 10 μg/mL chloramphenicol.

No unexpected or unusually high safety hazards were encountered in the course on this work.

Instrumentation and related considerations. Top-down scanning electron micrographs were acquired using a LEO-1550 VP field-emission SEM operated with an accelerating voltage of 1.0 kV. Microparticle diameters were measured using ImageJ version 1.52a software. Solution fluorescence and absorbance in bacterial cultures was measured using a BioTek Synergy 2 plate reader using Gen5 software. RP-HPLC was performed on a Shimadzu system with a SCL-10Avp controller, a DGU-20A5 degasser, a LC-20AT solvent delivery unit, a SIL-10AF autosampler, a CO-20A column oven with a manual injector, a SPD-M20A UV-Vis diode array detector, and analytical Kromasil Eternity C18 column (4.6 mm by 250 mm, with a 5 mm particle size and 100 Å pore size). Solvent A was water with 0.1% trifluoroacetic acid and solvent B was acetonitrile with 0.1% trifluoroacetic acid. A linear gradient was used to analyze peptides and solutions, beginning at 10% solvent B and ramping to 95% solvent B over 27 min at a flow rate of 1 mL/min.

Fluorescence-based bacterial reporter assay. Compound activity screening was performed as previously described using *S. aureus* AH1677.[39] GraphPad Prism 7 was used for statistical analysis of the resulting data. Supernatants from microparticle release experiments were subjected to this reporter assay with the following modifications: supernatant was serially diluted into PBS, and 20 μL aliquots of each dilution were transferred to a black 96-well microtiter plate and incubated with

180 µL of bacterial culture. Each plate contained additional controls for data processing: a PBS control (20 µL) and a tr AIP-III D2A control (100 nM final concentration, 2 µL of 10 µM tr AIP-III D2A stock solution in DMSO and 18 µl PBS).

***Ex vivo* tissue sequestration assay.** In 1.5 mL microcentrifuge tubes, 1 mM DMSO stock solutions of compounds were diluted in PBS to 10,000x their respective IC_{50} values in a total volume of 500 µL, along with a PBS control without any compound. A mouse tissue sample was bath sonicated for 5 minutes (and, if appropriate, incubated at 80 °C for 15 min then cooled in ice bath for 5 min) and transferred into each microcentrifuge tube. The tubes were vortexed, and 10 µL aliquots were stored in a chemical resistant microtiter plate in a -20 °C freezer. The microcentrifuge tubes were incubated at 37 °C with shaking at 200 rpm until the next time point was reached, at which point the tubes were removed, vortexed, and additional 10 µL aliquots were taken. This process was repeated for all the time points. After the final time point, 2 µL of each aliquot, or a 1:10 dilution of each aliquot, was transferred to a black 96-well microtiter plate and tested using the fluorescence reporter assay detailed above.

Fabrication of tr AIP-III D2A-loaded PLG microparticles. A 0.8 mM solution of tr AIP-III D2A in DMF was diluted with THF to produce a THF:DMF solvent system (3:1, v/v) resulting in a final tr AIP-III D2A concentration of 0.2 mM. A 60 mg/mL solution of PLG in THF:DMF (3:1, v/v) was prepared and allowed to stir until the polymer was dissolved. Electro-spraying of the microparticles was conducted on a custom-built electro-spraying device with a digital syringe pump (Harvard Bioscience Co.) at a flow rate of 1.0 mL/hr. A 15 cm working distance separated a blunt 20G needle and the 10 x 10 cm grounded aluminum foil sample collector. The produced

microparticles were harvested from the surface of the aluminum foil using an eyelash applicator brush, followed by immersion of the brush in water and sonicating to create a microparticle suspension. The suspension was then lyophilized to produce dry microparticles.

Characterization of peptide loading of PLG microparticles. Microparticles were dissolved in DMSO (20 mg/mL) and then precipitated into water by mixing 100 μL of the DMSO solution into 900 μL of water. The suspension was centrifuged at 5,000 g for 5 min, and the resulting supernatant was analyzed by analytical RP-HPLC to determine the amount of peptide in the microparticles.

Characterization of peptide-loaded PLG microparticle release profiles. PLG microparticles (10 mg) were immersed in 1 mL of PBS. The particles were sonicated to suspend them in solution and allowed to incubate while rotating at room temperature. At predetermined time points, the microparticles were centrifuged at 5,000 g for 5 min and the supernatant was removed and replaced. Each supernatant sample was immediately frozen and stored at -20 °C until analysis. At time of analysis, supernatant samples were thawed and centrifuged at 16,000 g for 5 min to remove any solid polymer debris that may have been isolated with the supernatant. The concentrations of the peptides released at each timepoint were measured using the microparticle-modified bacterial reporter assay described above. After 21 days of incubation in buffer, the remaining polymer solids were characterized to determine the amount of unreleased peptide using the dissolution and analytical RP-HPLC method described above.

Murine abscess infection model. The infection assay protocol was modified from that of Sully *et al.*[15] Briefly, cultures of the appropriate *S. aureus* strain were grown overnight in BHI medium and

diluted in sterile PBS to an OD_{600} corresponding to $2x10^8$ CFU/mL. For experiments on peptide in solution, DMSO (1%, control) or peptide in DMSO solution (50 μM or 500 nM) were added to $2x10^8$ CFU/mL culture to reach an appropriate desired concentration. For PLG microparticle experiments, $2x10^8$ CFU/mL culture was added to lyophilized microparticle tubes to reach a concentration of 20 mg/mL particles. Cultures were vortexed to mix and then 50 μL were injected subcutaneously into the shaved flank of age- and sex-matched C57BL/6 mice. Body weight was recorded at time of injection and monitored over the course of the experiment. Images of lesions were taken on days 1, 3, 5, and 7, and analyzed using ImageJ to determine lesion area. GraphPad Prism 7 was used to obtain statistical information about the abscess sizes. All experimental protocols were approved by the Institutional Animal Care and Use Committee at UW–Madison and conformed to the NIH Guide for the Care and Use of Laboratory Animals, 8th edition (2011).

Results and Discussion

Ex vivo screening reveals two stable and highly potent synthetic inhibitors of agr

We began our studies by focusing on a set of six synthetic peptide-based inhibitors of the *S. aureus agr* system on which we reported previously (Figure 1).[14, 38-39] This family of inhibitors comprises thioester- and amide-containing full or tail-truncated (tr) structural mimics of native AIP signals used by *S. aureus*, all of which are highly potent and efficacious at blocking *agr* activity, as measured in cell-based reporter gene assays and QS phenotypic assays (i.e., hemolysin and other toxin production). None of the compounds investigated in this study affect *S. aureus* growth at concentrations up to 10 μM.

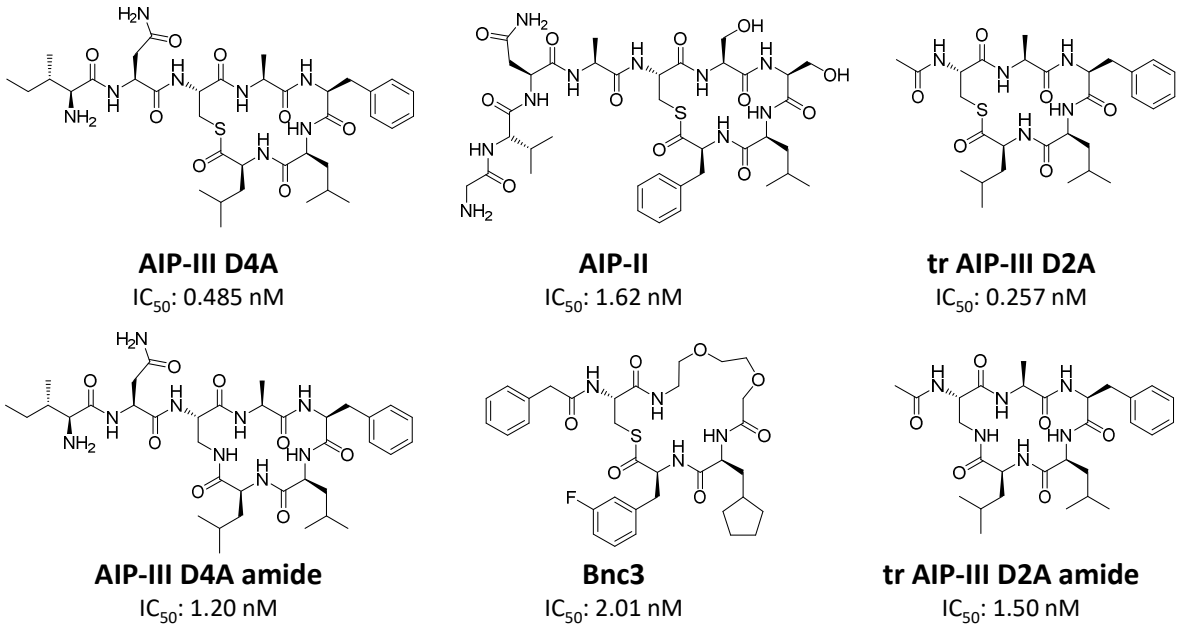


Figure 1. Chemical structures and potency values for QS inhibitors evaluated in this study. Potency values are from previous reports (see references 14 and 38-39) and were determined by dose-dependent inhibition of compounds in cell-based reporter assays in wild-type *S. aureus* (group-I).

A series of exploratory experiments with one of our most potent inhibitors (AIP-III D4A; Figure 1) showed only a limited benefit on wound healing in a murine open-wound model of *S. aureus* infection, even at relatively high concentrations (e.g., at 10 μM; >20,000-fold above the IC_{50} of this compound in culture).[14] We considered the possibility that this disappointing outcome could result from inactivation of this inhibitor *in vivo*. Prior reports revealed native AIPs to be relatively short-lived *in vivo* (as highlighted above),[31] likely due to sequestration by proteins in serum (e.g., apolipoprotein B; ApoB)[26-27, 34] or other proteins that can degrade native AIP signals. We therefore developed an *ex vivo* assay (Figure S1) to evaluate this inhibitor in the presence of murine tissue samples (~6 mm in diameter; 1 mm thick; acquired via a tissue punch of C57BL/6-type mouse epidermis; see Methods). AIP-III D4A was incubated in the presence of tissue punches at 4.85 μM in PBS for 24 hours. Portions of the supernatant were removed over time, diluted 100-

fold, and added to a *S. aureus agr* fluorescence reporter strain to measure inhibitor activity (see Methods). This reporter strain produces native AIP at wild-type levels, activating the *agr* system at quorate cell densities and inducing expression of yellow fluorescent protein (YFP). The level of YFP fluorescence thus serves as a proxy for *agr* activity, and the efficacy of added inhibitors can be measured by reductions in fluorescence.

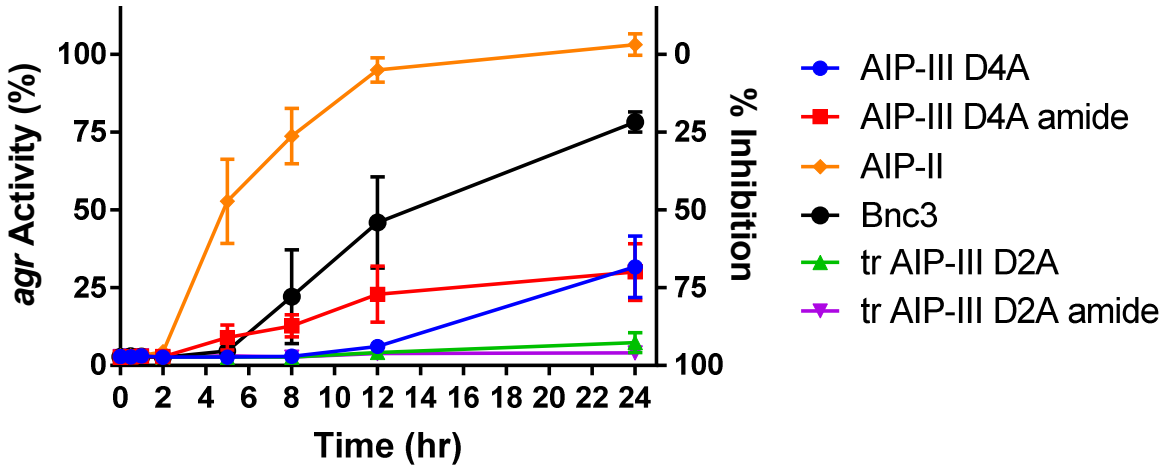


Figure 2. Time course of *S. aureus agr* activity for compounds incubated with mouse tissue. *agr* activity was measured using a fluorescent reporter assay. Values shown are the average and SEM of three (n=3) independent *ex vivo* experiments.

We found that AIP-III D4A was no longer capable of fully inhibiting *S. aureus agr* activity (Figure 2, blue line) after 24 hours of *ex vivo* incubation with mouse tissue, even at the relatively high concentration used in this experiment (~10,000-fold its IC_{50}). The roughly 25% loss of *agr* inhibition at 24 hours corresponds to approximately 150 nM of free and active compound remaining in solution (as determined from a previous dose-response assay).[14] This substantial reduction represents an ~95% loss of active compound. We have previously shown that AIPs in general are modestly stable to thioester hydrolysis in PBS (~20% hydrolysis after 24 hours).[38] A

control study performed with AIP-III D4A in the absence of mouse tissue revealed no loss of inhibitory activity in 24 hr (Figure S2). Taken together, these results suggest that AIP-III D4A is degraded or sequestered by components of mouse tissue. Subsequent experiments demonstrated that this loss of activity could be prevented by heat treating the tissue sample at 80 °C for 15 min prior to the addition of AIP-III D4A (Figure S3; see Methods), suggesting that loss of activity likely involves a tissue protein or other component that is rendered irreversibly non-functional by heat.

We used this *ex vivo* assay to identify synthetic inhibitors that were stable to components of murine skin tissue. The results of a screen of all six inhibitors shown in Figure 1 at concentrations 10,000-fold above their respective IC_{50} values is illustrated in Figure 2. Inspection of these results reveals several useful structure-function relationships. AIP-II (a native *S. aureus* AIP; orange curve) and Bnc3 (a synthetic peptidomimetic based on AIP-II; black curve)[39] lost nearly all antagonistic activity within 24 hours, far exceeding the 25% loss in inhibitory activity observed for the synthetic AIP-III mimic, AIP-III D4A. AIP-III D4A amide (red curve),[38] an analog of AIP-III D4A in which the thioester is replaced with a more hydrolytically-stable amide linkage, exhibited a loss of activity that was similar in magnitude to that of AIP-III D4A (blue curve). This result suggests that the loss of activity of AIP-III D4A in the experiments above was not a result of accelerated thioester hydrolysis. In stark contrast to these results, tr AIP-III D2A[14] (green curve) and tr AIP-III D2A amide (purple curve),[38] which are truncated (tr) versions of AIP-III D4A in which the exocyclic tail is replaced with acetyl group, retained essentially full activity after 24 hours of incubation with murine tissue.

The reason for the surprisingly high retention of activity by these truncated compounds is unclear; however, we note that the absence of the two amino acid tail and the lack of a free amine

terminus alter the polarity, amphipathic nature, and solution-phase conformation of these compounds,[40] which could substantially impact interactions with proteins present in skin tissue. Additional experiments in which AIP-III D4A and tr AIP-III D2A were incubated with ApoB—an apolipoprotein commonly found in skin and blood[41-42] that was reported to bind to and sequester AIPs [26-27]—provided additional support for this view. When we incubated AIP-III D4A with ApoB for three hours, we observed a significant (~80%) decrease in AIP-III D4A recovered by analytical HPLC (Figure S4A). In contrast, we observed essentially no loss of tr AIP-III D2A when it was incubated with ApoB under identical conditions (Figure S4B). Although additional experiments will be required to more fully understand the basis for the increased stability of these truncated compounds, this *ex vivo* screen identified two surprisingly stable and potent candidates for further evaluation *in vivo*. We selected tr AIP-III D2A for use in all subsequent studies described below on the basis of its greater potency in culture (IC_{50} = 0.257 nM; Figure 1).

tr AIP-III D2A substantially reduces abscess formation in a murine dermonecrosis model

We next evaluated the ability of tr AIP-III D2A to attenuate *S. aureus* infection using a murine dermonecrosis abscess model.[43] This model and related infection models have been used in past studies to characterize the role of *agr* activity in *S. aureus* infections using *agr* mutant strains,[15-16, 21] non-cognate native AIPs,[16, 31-32] and small-molecule chemical tools that inhibit *S. aureus* QS.[15, 20-21] In this model, lesion development is evaluated over time by imaging the animals on predetermined days and measuring the areas of visible lesions. To validate this model in our hands, we first compared abscess formation in mice inoculated with a common lab *S. aureus* strain or with a mutant (Δ*agr*) lacking a functional *agr* system (see Methods). We observed significantly larger abscesses to develop in mice inoculated with the wild-type strain than in mice inoculated

with the Δ*agr* strain (Figure S5). This result is comparable to previous reports indicating that the absence of *agr* activity attenuates infection.[15-16, 21, 31]

We then co-injected 1.5 μg of tr AIP-III D2A or a vehicle control solution (DMSO with no inhibitor) and a culture of USA300 LAC MRSA and monitored infection over the course of a week using the murine abscess model. The total molar amount of compound injected in these experiments was either similar to or less than amounts used to evaluate other QS inhibitors *in vivo* in past studies.[15-16, 21] Lesions were imaged 1, 3, 5, and 7 days after inoculation, and representative images of mice in treated groups and untreated vehicle control groups are shown in Figure 3A. Treatment with tr AIP-III D2A significantly reduced the sizes of lesions on each day relative to vehicle controls (Figure 3B), with only half of the inhibitor-treated mice showing visible lesions seven days after infection, as opposed to 90% of the vehicle control group (see SI for pictures of the abscesses of all mice in this study on day 7). These results indicate that bolus administration of tr AIP-III D2A can substantially diminish the severity of *S. aureus* infections in this mouse model. These results constitute the first demonstration of inhibitory activity *in vivo* using this class of synthetic *agr* inhibitors based on native AIP-III, and are consistent with *agr* inhibition as the likely cause for attenuation.

We conducted additional experiments to investigate the ability of tr AIP-III D2A to inhibit *S. aureus* infections in this model when loaded into degradable polymer microparticles. For these studies, we adapted a previously reported electrospraying protocol[44] to fabricate pseudo-spherical microparticles of PLG (lactide:glycolide (50:50); 30–60 kDa; see Methods), with diameters of 1.48 (± 0.38) μm (as characterized by SEM; see Figure 4A and Figure S6) that were sized appropriately to fit through the 25 gauge needles used in our *in vivo* experiments.

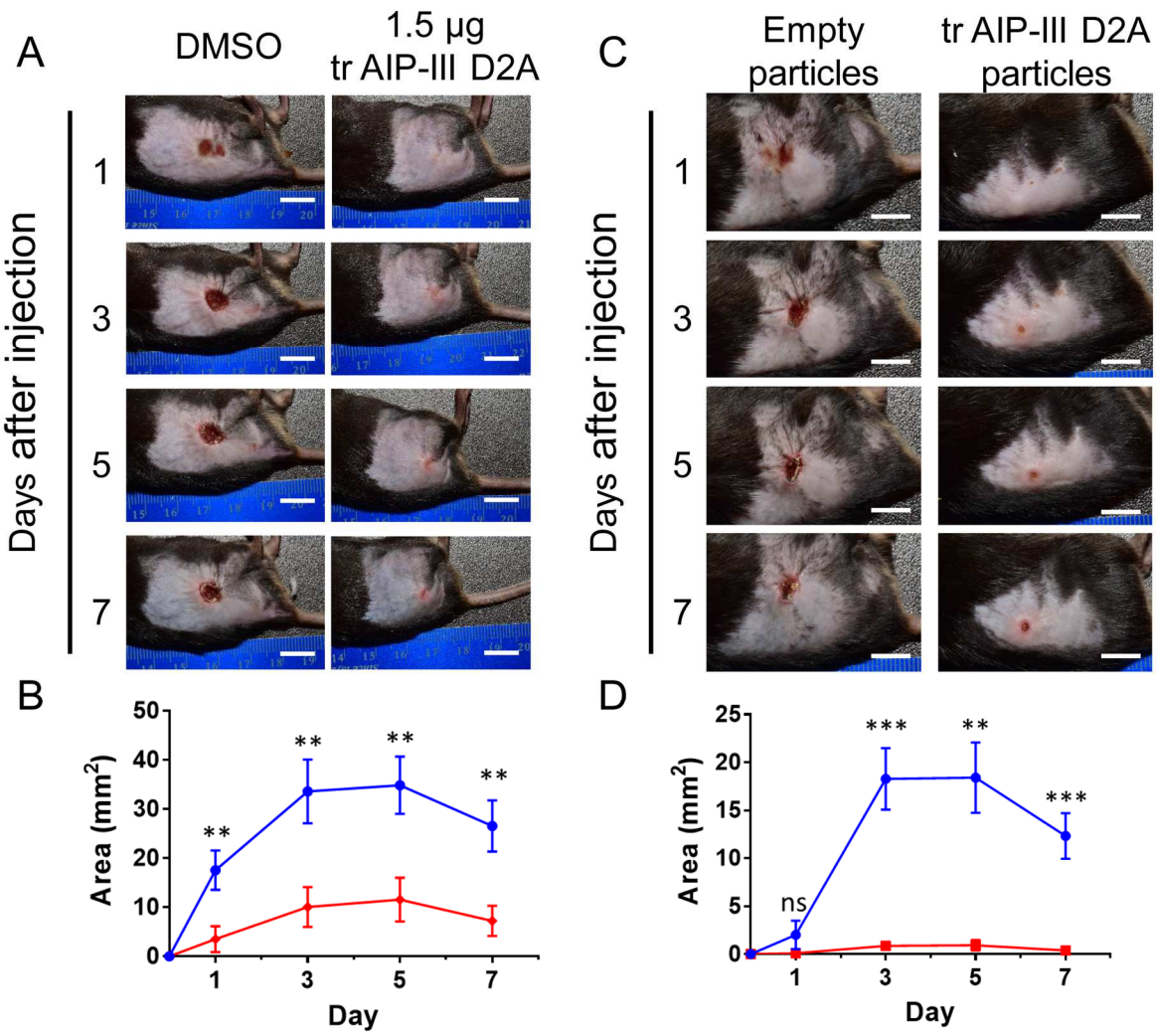


Figure 3. Abscess attenuation due to tr AIP-III D2A delivered as a bolus in solution (A–B) or delivered in 1 mg of PLG microparticles (C–D). (A) Representative images for the DMSO vehicle and compound-treated groups. (B) Average abscess size with SEM for vehicle group (blue line, n=10) and compound-treated group (red line, n=10). (C) Representative images for groups treated with empty, non-loaded microparticles and compound-loaded microparticles. (D) Average abscess size with SEM for empty microparticle group (blue line, n=9) and compound-loaded microparticle group (red line, n=10). Statistical analysis with Mann-Whitney test, **p < 0.01, ***p < 0.001.

These microparticles were measured to contain 0.71 (± 0.14) nmol of peptide/mg polymer as determined using analytical HPLC (see Methods and Figure S7), or approximately 21% of the maximum theoretical loading of peptide using this fabrication approach. These particles released approximately 22 pmol of tr AIP-III D2A per mg of particle into solution over 21 days when

incubated in PBS, with a large burst release over the first 24 hours (Figure 4B; as determined using a biological reporter assay; see Methods, Equations S1–S2, and the SI for additional information related to these experiments). We estimate this amount to correspond to less than 1% of the total loaded peptide, suggesting that these particle formulations could be used to promote release over much longer time periods than those evaluated here.

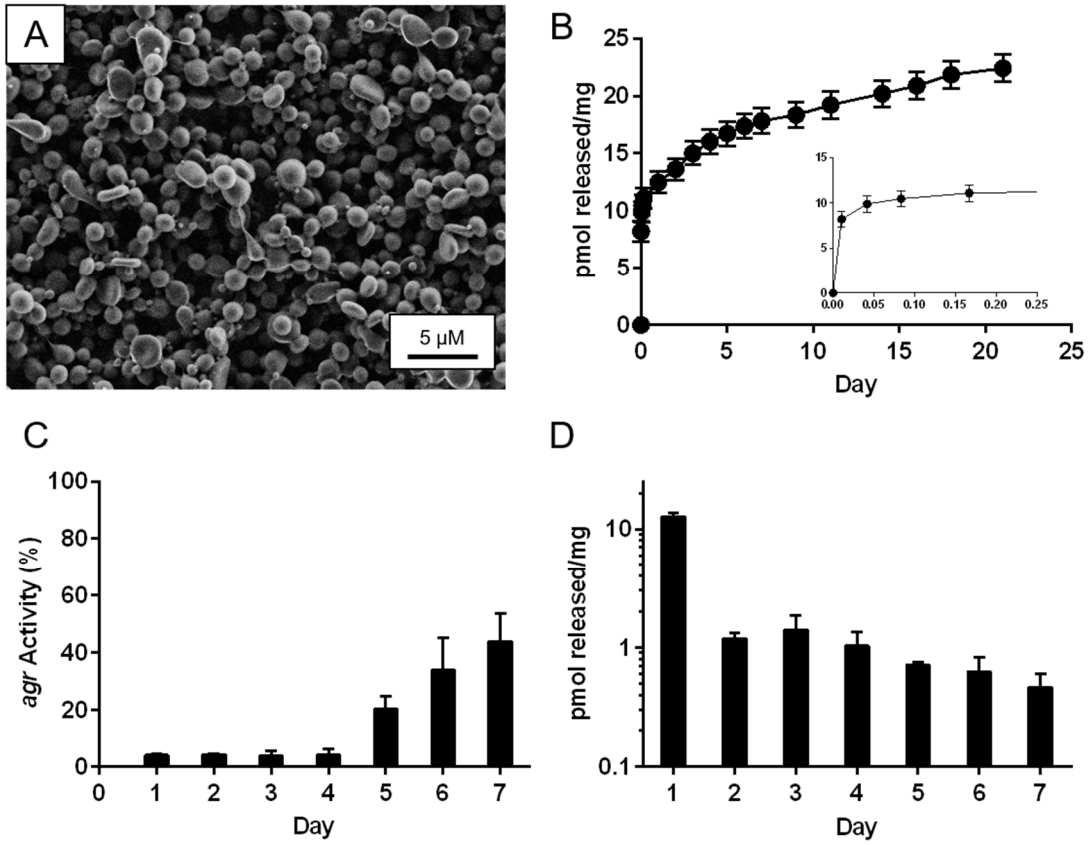


Figure 4. Characterization of PLG microparticles loaded with tr AIP-III D2A. (A) Top-down SEM images of tr AIP-III D2A-loaded PLG microparticles fabricated by electrospraying. (B) The normalized cumulative release of tr AIP-III D2A from the PLG microparticles over three weeks. (C) The *agr* activity of the *S. aureus* reporter incubated with undiluted aliquots acquired each day from the release experiments. (D) The normalized release of tr AIP-III D2A from the PLG microparticles each day. The values shown in (B–D) are the average and single standard deviation for three (n=3) independent release experiments.

Characterization of released inhibitor using our *S. aureus* fluorescent *agr* reporter strain (see Methods and Figure S8) revealed that (i) tr AIP-III D2A retained its biological activity upon

release from PLG and (ii) sufficient amounts were released for each of the first four days to fully inhibit *agr* activity. Amounts released in each subsequent 24-hour time period did not completely inhibit *agr* activity, but substantial inhibition was observed out to day 7 under the conditions evaluated here (Figure 4C–D, Figure S9). We note that it should be straightforward to further modify and optimize the loading and release profiles of these particles by adjusting the chemical and physical properties of PLG and/or process parameters used to fabricate the particles.[45-48] The sizes, loadings, and release profiles of the particles reported here were sufficient for all subsequent proof-of-concept experiments in mice described below.

Using the mouse abscess model, we co-injected *S. aureus* culture and either (i) 1 mg of tr AIP-III D2A-loaded microparticles (~720 ng of inhibitor total) or (ii) 1 mg of unloaded (no inhibitor) microparticles into mice. Representative images from these experiments are shown in Figure 3C. We observed lesions that were significantly smaller for the inhibitor-loaded particle group, as compared to the empty particle group on every day other than day 1 (Figure 3D). Comparing the final abscess sizes on day 7, only a single mouse out of 10 from the inhibitor-loaded particle-treated group had an observable lesion (2.89 mm^2). In contrast, nearly 80% of the mice in the control group (no inhibitor) had lesions with an average size of 15.8 mm^2 (see SI for images of the abscesses of all mice in this study on day 7). We conclude on the basis of these results that the polymer microparticles release tr AIP-III D2A in a form that remains biologically active *in vivo*, and that this controlled release strategy yields a concentration profile at the site of infection over a seven-day period that is sufficient to inhibit bacterial virulence at levels comparable to, if not better than, those observed in the single-dose, bolus administration *in vivo* experiments described above.

The results shown in Figure 3 not only demonstrate that tr AIP-III D2A can provide significant protection against *S. aureus* infection, but also suggest that well understood advantages of strategies for the localized and controlled release of active agents used in other scenarios[49-51] can provide additional practical benefits in this context. Specifically, we note that the amount of compound released over the course of 7 days in the microparticle-treated mice in the experiments above (Figure 3C) is approximately 100-fold less than the amount that was administered in the single-dose, bolus administration experiment (Figure 3A). This outcome is further consistent with the well-established ability of controlled release approaches to substantially improve therapeutic outcomes at reduced loadings of active agent.[49-51]

To obtain a side-by-side comparison of the efficacies of a single-dose, bolus administration of tr AIP-III D2A to the microparticle formulation when the total amounts of inhibitor estimated to be available at the infection site were comparable, we performed a final series of *in vivo* experiments. On the basis of the release profile shown in Figure 4B, we estimate 18 pmol (11 ng) of tr AIP-III D2A to be released from 1 mg of particles over 7 days. We therefore compared the efficacy of our inhibitor-loaded particles directly to an approximately similar amount of inhibitor (25 pmol, or 15 ng) administered as a single-dose, bolus injection. As shown in Figure 5, a single bolus dose of tr AIP-III D2A did not attenuate *S. aureus* infection at any time point as compared to control mice ($p > 0.05$; Kruskal-Wallis test). In contrast, the tr AIP-III D2A-loaded microparticles substantially reduced abscess size at each time point ($p < 0.05$ for day 5, $p < 0.01$ for days 1, 3, and 7; Kruskal-Wallis test), consistent with the results of the experiments above (Figure 3C–D). This result strongly underscores potential benefits arising from the sustained release of inhibitor in preventing abscess formation by *S. aureus*. We attribute the superior performance of the controlled release formulation to its ability to sustain effective locally high

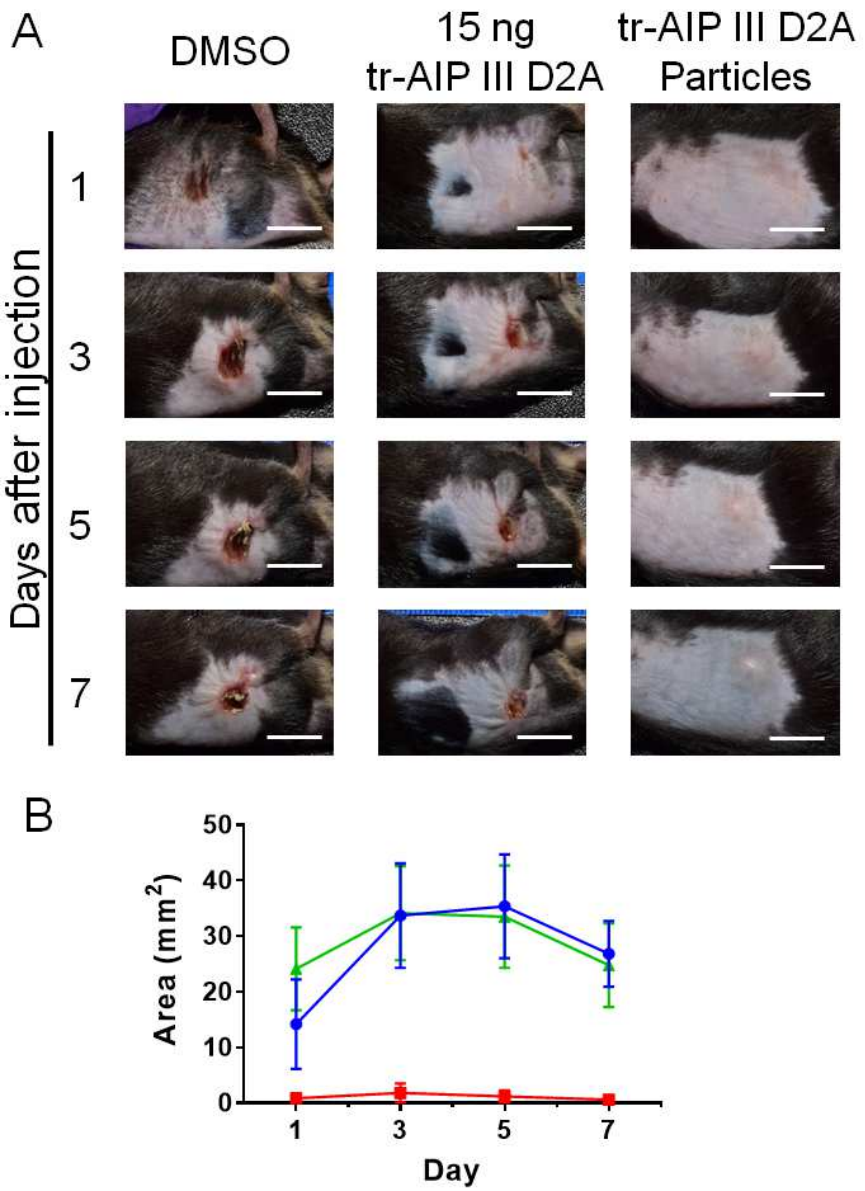


Figure 5. Side-by-side comparison of abscess formation after treatment with tr AIP-III D2A in solution vs. PLG microparticles. (A) Representative images from mice treated with vehicle, a solution of compound, or compound loaded in microparticles. (B) Average abscess size with SEM of mice treated with vehicle (green, n=8), 15 ng of tr AIP-III D2A in solution (blue line, n=8), or with 1 mg of microparticles (red line, n=8). Data analyzed with Kruskal-Wallis test.

concentrations of inhibitor in the immediate vicinity of the infection site. Conversely, the bolus administration of soluble inhibitor can rapidly drain or diffuse away from the injection site,

reducing the local concentration of inhibitor below what is needed to reduce the severity of infection.

Summary and Conclusions

Our results demonstrate (i) the ability of a potent truncated synthetic peptide inhibitor of *S. aureus* QS to attenuate bacterial virulence *in vivo* and (ii) an efficacious controlled release strategy for reducing bacterial infection using this anti-virulence approach. These results were enabled by the *ex vivo* screening of *S. aureus agr*-inhibitors to identify compounds resistant to inactivation by components present in mouse tissue. We identified a lead compound, tr AIP-III D2A, that nearly completely blocks MRSA infection in a mouse dermonecrosis abscess model following a single-dose bolus administration of inhibitor, or by injection of polymer microparticles that sustain the local release of active inhibitor at the infection site. Our results demonstrate significantly greater efficacy using the polymer microparticle approach, underscoring the potential strategic value of using sustained-release strategies for the administration of QS inhibitors and the development of new anti-virulence approaches to combat bacterial infections *in vivo*.

The results of this study are important for several reasons. First, we demonstrate the ability of a lead *agr* inhibitor—one of the most potent known inhibitors of *S. aureus* QS in culture—to strongly block bacterial infection *in vivo*. Second, our results reveal tail truncation of two AIP-derived mimetics to be an effective strategy to eliminate interference by host tissue, in sharp contrast to inhibition of similar native AIPs and their close analogs. This observation underpins the efficacy and potency of these compounds *in vivo* and provides guidance that will prove useful for the design and discovery of new inhibitors suitable for use *in vivo*. Third, our results demonstrate that controlled release strategies can improve the therapeutic potential of these

truncated inhibitors and reduce to nanograms the total amount of compound required to attenuate infection *in vivo*. Notably, these findings represent more than an order of magnitude improvement compared to previous *in vivo* analyses that required the administration of microgram quantities of less-potent *agr* inhibitors for efficacy in similar infection models.[15, 20-22, 31] Past studies have investigated strategies for the encapsulation of bacterial QS inhibitors into materials and the testing of these approaches *in vitro* and *ex vivo*.[52-58] The results of this current study represent, to our knowledge, the first report of the successful application of a controlled release QS inhibition strategy to abate bacterial infection *in vivo*.

More broadly, the discovery of stable and highly potent inhibitors and the identification of strategies that enable controlled release and local availability of these agents during infection provide powerful tools, alone or in combination, to address a range of important fundamental questions. These include the role of *agr* QS in long-term chronic infections or the emergence of spontaneous QS mutants commonly isolated from patients with such infections.[5, 35, 59] These tools also provide a foundation for the development of new types of materials (e.g., surface coatings) that could more effectively attenuate bacterial virulence in or around implantable or indwelling medical devices, or on other commercial surfaces on which *S. aureus* colonization and infections are endemic. Looking beyond *S. aureus,* the approach reported here should also be readily applicable to other combinations of QS inhibitors and polymers, significantly expanding the utility of chemical methods to explore and modulate QS pathways and outcomes, and thus has implications for new therapeutic interventions.

Acknowledgements

Financial support for this work was provided by the NIH (R21 AI135745), the Wisconsin Alumni Research Foundation (WARF) UW2020 Program, and the NSF through a grant provided to the UW–Madison Materials Research Science and Engineering Center (MRSEC; DMR-1720415). The authors acknowledge the use of instrumentation supported by the NSF through the UW MRSEC (DMR-1720415). K. H. J. W. was supported in part by the UW–Madison NIH Chemistry–Biology Interface Training Program (T32 GM008505). C. G. G. was supported in part by a NSF Graduate Research Fellowship. J. F. M. and C. J. C. acknowledge the Walter and Martha Renk Endowed Laboratory for Food Safety and the UW–Madison Food Research Institute. We thank Prof. Alexander Horswill (University of Colorado Medical School) for *S. aureus* strains and Prof. Tom Turng (UW–Madison) for providing access to electrospraying instrumentation, and acknowledge support for those facilities provided by the Wisconsin Institutes of Discovery and the Vice Chancellor for Research and Graduate Education at UW–Madison.

References

1. Kourtis, A. P.; Hatfield, K.; Baggs, J.; Mu, Y.; See, I.; Epson, E.; Nadle, J.; Kainer, M. A.; Dumyati, G.; Petit, S.; Ray, S. M.; Emerging Infections Program MRSA author group; Ham, D.; Capers, C.; Ewing, H.; Coffin, N.; McDonald, L. C.; Jernigan, J.; Cardo, D., Vital Signs: Epidemiology and Recent Trends in Methicillin-Resistant and in Methicillin-Susceptible *Staphylococcus aureus* Bloodstream Infections - United States. *MMWR Morb. Mortal. Wkly. Rep.* **2019,** *68* (9), 214-219.

2. Tong, S. Y.; Davis, J. S.; Eichenberger, E.; Holland, T. L.; Fowler, V. G., Jr., *Staphylococcus aureus* infections: epidemiology, pathophysiology, clinical manifestations, and management. *Clin. Microbiol. Rev.* **2015,** *28* (3), 603-661.

3. David, M. Z.; Daum, R. S., Community-associated methicillin-resistant *Staphylococcus aureus*: epidemiology and clinical consequences of an emerging epidemic. *Clin. Microbiol. Rev.* **2010,** *23* (3), 616-687.

4. Klein, E.; Smith, D. L.; Laxminarayan, R., Hospitalizations and deaths caused by methicillin-resistant *Staphylococcus aureus*, United States, 1999-2005. *Emerg. Infect. Dis.* **2007,** *13* (12), 1840-1846.

5. Ford, C. A.; Hurford, I. M.; Cassat, J. E., Antivirulence Strategies for the Treatment of *Staphylococcus aureus* Infections: A Mini Review. *Front. Microbiol.* **2020,** *11*, 632706.

6. Dickey, S. W.; Cheung, G. Y. C.; Otto, M., Different drugs for bad bugs: antivirulence strategies in the age of antibiotic resistance. *Nat. Rev. Drug Discov.* **2017,** *16* (7), 457-471.

7. Allen, R. C.; Popat, R.; Diggle, S. P.; Brown, S. P., Targeting virulence: can we make evolution-proof drugs? *Nat. Rev. Microbiol.* **2014,** *12* (4), 300-308.

8. Whiteley, M.; Diggle, S. P.; Greenberg, E. P., Progress in and promise of bacterial quorum sensing research. *Nature* **2017,** *551* (7680), 313-320.

9. Azimi, S.; Klementiev, A. D.; Whiteley, M.; Diggle, S. P., Bacterial Quorum Sensing During Infection. *Annu. Rev. Microbiol.* **2020,** *74*, 201-219.

10. LaSarre, B.; Federle, M. J., Exploiting quorum sensing to confuse bacterial pathogens. *Microbiol. Mol. Biol. Rev.* **2013,** *77* (1), 73-111.

11. Novick, R. P.; Geisinger, E., Quorum Sensing in Staphylococci. *Annu. Rev. Genet.* **2008,** *42*, 541-564.

12. Wang, B.; Muir, T. W., Regulation of Virulence in *Staphylococcus aureus:* Molecular Mechanisms and Remaining Puzzles. *Cell Chem. Biol.* **2016,** *23* (2), 214-224.

13. Thoendel, M.; Kavanaugh, J. S.; Flack, C. E.; Horswill, A. R., Peptide Signaling in the Staphylococci. *Chem. Rev.* **2011,** *111* (1), 117-151.

14. Tal-Gan, Y.; Stacy, D. M.; Foegen, M. K.; Koenig, D. W.; Blackwell, H. E., Highly potent inhibitors of quorum sensing in *Staphylococcus aureus* revealed through a systematic synthetic study of the group-III autoinducing peptide. *J. Am. Chem. Soc.* **2013,** *135* (21), 7869-7882.

15. Sully, E. K.; Malachowa, N.; Elmore, B. O.; Alexander, S. M.; Femling, J. K.; Gray, B. M.; DeLeo, F. R.; Otto, M.; Cheung, A. L.; Edwards, B. S.; Sklar, L. A.; Horswill, A. R.; Hall, P. R.; Gresham, H. D., Selective chemical inhibition of agr quorum sensing in *Staphylococcus aureus* promotes host defense with minimal impact on resistance. *PLoS Pathog.* **2014,** *10* (6), e1004174.

16. Mayville, P.; Ji, G.; Beavis, R.; Yang, H.; Goger, M.; Novick, R. P.; Muir, T. W., Structure-activity analysis of synthetic autoinducing thiolactone peptides from *Staphylococcus aureus* responsible for virulence. *Proc. Natl. Acad. Sci. U. S. A.* **1999,** *96* (4), 1218-1223.

17. Salam, A. M.; Quave, C. L., Targeting Virulence in *Staphylococcus aureus* by Chemical Inhibition of the Accessory Gene Regulator System In Vivo. *mSphere* **2018,** *3* (1), e00500-17.

18. Horswill, A. R.; Gordon, C. P., Structure-Activity Relationship Studies of Small Molecule Modulators of the Staphylococcal Accessory Gene Regulator. *J. Med. Chem.* **2020,** *63* (6), 2705-2730.

19. Kuo, D.; Yu, G.; Hoch, W.; Gabay, D.; Long, L.; Ghannoum, M.; Nagy, N.; Harding, C. V.; Viswanathan, R.; Shoham, M., Novel quorum-quenching agents promote methicillin-resistant *Staphylococcus aureus* (MRSA) wound healing and sensitize MRSA to beta-lactam antibiotics. *Antimicrob. Agents Chemother.* **2015,** *59* (3), 1512-1518.

20. Todd, D. A.; Parlet, C. P.; Crosby, H. A.; Malone, C. L.; Heilmann, K. P.; Horswill, A. R.; Cech, N. B., Signal Biosynthesis Inhibition with Ambuic Acid as a Strategy To Target Antibiotic-Resistant Infections. *Antimicrob. Agents Chemother.* **2017,** *61* (8), e00263-17.

21. Parlet, C. P.; Kavanaugh, J. S.; Crosby, H. A.; Raja, H. A.; El-Elimat, T.; Todd, D. A.; Pearce, C. J.; Cech, N. B.; Oberlies, N. H.; Horswill, A. R., Apicidin Attenuates MRSA Virulence through Quorum-Sensing Inhibition and Enhanced Host Defense. *Cell Rep.* **2019,** *27* (1), 187-198 e6.

22. Daly, S. M.; Elmore, B. O.; Kavanaugh, J. S.; Triplett, K. D.; Figueroa, M.; Raja, H. A.; El-Elimat, T.; Crosby, H. A.; Femling, J. K.; Cech, N. B.; Horswill, A. R.; Oberlies, N. H.; Hall, P. R., omega-Hydroxyemodin limits *Staphylococcus aureus* quorum sensing-mediated pathogenesis and inflammation. *Antimicrob. Agents Chemother.* **2015,** *59* (4), 2223-2235.

23. Nielsen, A.; Mansson, M.; Bojer, M. S.; Gram, L.; Larsen, T. O.; Novick, R. P.; Frees, D.; Frokiaer, H.; Ingmer, H., Solonamide B inhibits quorum sensing and reduces *Staphylococcus aureus* mediated killing of human neutrophils. *PLoS One* **2014,** *9* (1), e84992.

24. Brango-Vanegas, J.; Martinho, L. A.; Bessa, L. J.; Vasconcelos, A. G.; Placido, A.; Pereira, A. L.; Leite, J.; Machado, A. H. L., Synthesis of novel sulfide-based cyclic peptidomimetic analogues to solonamides. *Beilstein J. Org. Chem.* **2019,** *15*, 2544-2551.

25. Piewngam, P.; Zheng, Y.; Nguyen, T. H.; Dickey, S. W.; Joo, H. S.; Villaruz, A. E.; Glose, K. A.; Fisher, E. L.; Hunt, R. L.; Li, B.; Chiou, J.; Pharkjaksu, S.; Khongthong, S.; Cheung, G. Y. C.; Kiratisin, P.; Otto, M., Pathogen elimination by probiotic *Bacillus* via signalling interference. *Nature* **2018,** *562* (7728), 532-537.

26. Peterson, M. M.; Mack, J. L.; Hall, P. R.; Alsup, A. A.; Alexander, S. M.; Sully, E. K.; Sawires, Y. S.; Cheung, A. L.; Otto, M.; Gresham, H. D., Apolipoprotein B is an innate barrier against invasive *Staphylococcus aureus* infection. *Cell Host Microbe* **2008,** *4* (6), 555-566.

27. Elmore, B. O.; Triplett, K. D.; Hall, P. R., Apolipoprotein B48, the Structural Component of Chylomicrons, Is Sufficient to Antagonize *Staphylococcus aureus* Quorum-Sensing. *PLoS One* **2015,** *10* (5), e0125027.

28. Da, F.; Yao, L.; Su, Z.; Hou, Z.; Li, Z.; Xue, X.; Meng, J.; Luo, X., Antisense locked nucleic acids targeting *agrA* inhibit quorum sensing and pathogenesis of community-associated methicillin-resistant *Staphylococcus aureus*. *J. Appl. Microbiol.* **2017,** *122* (1), 257-267.

29. Lyon, G. J.; Wright, J. S.; Muir, T. W.; Novick, R. P., Key determinants of receptor activation in the *agr* autoinducing peptides of *Staphylococcus aureus*. *Biochemistry* **2002,** *41* (31), 10095-10104.

30. Xie, Q.; Wiedmann, M. M.; Zhao, A.; Pagan, I. R.; Novick, R. P.; Suga, H.; Muir, T. W., Discovery of quorum quenchers targeting the membrane-embedded sensor domain of the *Staphylococcus aureus* receptor histidine kinase, AgrC. *Chem. Commun. (Camb.)* **2020,** *56* (76), 11223-11226.

31. Wright, J. S., 3rd; Jin, R.; Novick, R. P., Transient interference with staphylococcal quorum sensing blocks abscess formation. *Proc. Natl. Acad. Sci. U. S. A.* **2005,** *102* (5), 1691-1696.

32. Brown, M. M.; Kwiecinski, J. M.; Cruz, L. M.; Shahbandi, A.; Todd, D. A.; Cech, N. B.; Horswill, A. R., Novel Peptide from Commensal *Staphylococcus simulans* Blocks Methicillin-Resistant *Staphylococcus aureus* Quorum Sensing and Protects Host Skin from Damage. *Antimicrob. Agents Chemother.* **2020,** *64* (6), e00172-20.

33. Ji, G.; Beavis, R.; Novick, R. P., Bacterial interference caused by autoinducing peptide variants. *Science* **1997,** *276* (5321), 2027-2030.

34. Yarwood, J. M.; McCormick, J. K.; Paustian, M. L.; Kapur, V.; Schlievert, P. M., Repression of the *Staphylococcus aureus* accessory gene regulator in serum and *in vivo*. *J. Bacteriol.* **2002,** *184* (4), 1095-1101.

35. Cheung, G. Y. C.; Bae, J. S.; Otto, M., Pathogenicity and virulence of *Staphylococcus aureus*. *Virulence* **2021,** *12* (1), 547-569.

36. Schilcher, K.; Horswill, A. R., Staphylococcal Biofilm Development: Structure, Regulation, and Treatment Strategies. *Microbiol. Mol. Biol. Rev.* **2020,** *84* (3).

37. Le, K. Y.; Dastgheyb, S.; Ho, T. V.; Otto, M., Molecular determinants of staphylococcal biofilm dispersal and structuring. *Front. Cell. Infect. Microbiol.* **2014,** *4*, 167.

38. Tal-Gan, Y.; Ivancic, M.; Cornilescu, G.; Yang, T.; Blackwell, H. E., Highly Stable, Amide-Bridged Autoinducing Peptide Analogues that Strongly Inhibit the AgrC Quorum Sensing Receptor in *Staphylococcus aureus*. *Angew. Chem. Int. Ed. Engl.* **2016,** *55* (31), 8913-8917.

39. Vasquez, J. K.; Blackwell, H. E., Simplified Autoinducing Peptide Mimetics with Single-Nanomolar Activity Against the *Staphylococcus aureus* AgrC Quorum Sensing Receptor. *ACS Infect. Dis.* **2019,** *5* (4), 484-492.

40. Tal-Gan, Y.; Ivancic, M.; Cornilescu, G.; Cornilescu, C. C.; Blackwell, H. E., Structural characterization of native autoinducing peptides and abiotic analogues reveals key features essential for activation and inhibition of an AgrC quorum sensing receptor in *Staphylococcus aureus*. *J. Am. Chem. Soc.* **2013,** *135* (49), 18436-18444.

41. Mommaas, M.; Tada, J.; Ponec, M., Distribution of low-density lipoprotein receptors and apolipoprotein B on normal and on reconstructed human epidermis. *J. Dermatol. Sci.* **1991,** *2* (2), 97-105.

42. Feingold, K. R.; Elias, P. M.; Mao-Qiang, M.; Fartasch, M.; Zhang, S. H.; Maeda, N., Apolipoprotein E deficiency leads to cutaneous foam cell formation in mice. *J. Invest. Dermatol.* **1995,** *104* (2), 246-250.

43. Bunce, C.; Wheeler, L.; Reed, G.; Musser, J.; Barg, N., Murine Model of Cutaneous Infection with Gram-Positive Cocci. *Infect. Immun.* **1992,** *60* (7), 2636-2640.

44. Almeria, B.; Deng, W.; Fahmy, T. M.; Gomez, A., Controlling the morphology of electrospray-generated PLGA microparticles for drug delivery. *J. Colloid Interface Sci.* **2010,** *343* (1), 125-133.

45. Anderson, J. M.; Shive, M. S., Biodegradation and biocompatibility of PLA and PLGA microspheres. *Adv. Drug Deliv. Rev.* **1997,** *28* (1), 5-24.

46. Tracy, M. A.; Ward, K. L.; Firouzabadian, L.; Wang, Y.; Dong, N.; Qian, R.; Zhang, Y., Factors affecting the degradation rate of poly(lactide-co-glycolide) microspheres in vivo and in vitro. *Biomaterials* **1999,** *20* (11), 1057-1062.

47. Makadia, H. K.; Siegel, S. J., Poly Lactic-co-Glycolic Acid (PLGA) as Biodegradable Controlled Drug Delivery Carrier. *Polymers* **2011,** *3* (3), 1377-1397.

48. Uhrich, K. E.; Cannizzaro, S. M.; Langer, R. S.; Shakesheff, K. M., Polymeric systems for controlled drug release. *Chem. Rev.* **1999,** *99* (11), 3181-3198.

49. Mitragotri, S.; Burke, P. A.; Langer, R., Overcoming the challenges in administering biopharmaceuticals: formulation and delivery strategies. *Nat. Rev. Drug Discov.* **2014,** *13* (9), 655-672.

50. Tibbitt, M. W.; Dahlman, J. E.; Langer, R., Emerging Frontiers in Drug Delivery. *J. Am. Chem. Soc.* **2016,** *138* (3), 704-717.

51. Fenton, O. S.; Olafson, K. N.; Pillai, P. S.; Mitchell, M. J.; Langer, R., Advances in Biomaterials for Drug Delivery. *Adv. Mater.* **2018**, e1705328.

52. Kratochvil, M. J.; Yang, T.; Blackwell, H. E.; Lynn, D. M., Nonwoven Polymer Nanofiber Coatings That Inhibit Quorum Sensing in *Staphylococcus aureus*: Toward New Nonbactericidal Approaches to Infection Control. *ACS Infect. Dis.* **2017,** *3* (4), 271-280.

53. Kratochvil, M. J.; Tal-Gan, Y.; Yang, T.; Blackwell, H. E.; Lynn, D. M., Nanoporous Superhydrophobic Coatings that Promote the Extended Release of Water-Labile Quorum Sensing Inhibitors and Enable Long-Term Modulation of Quorum Sensing in *Staphylococcus aureus*. *ACS Biomater. Sci. Eng.* **2015,** *1* (10), 1039-1049.

54. Broderick, A. H.; Stacy, D. M.; Tal-Gan, Y.; Kratochvil, M. J.; Blackwell, H. E.; Lynn, D. M., Surface coatings that promote rapid release of peptide-based AgrC inhibitors for attenuation of quorum sensing in *Staphylococcus aureus*. *Adv. Healthc. Mater.* **2014,** *3* (1), 97-105.

55. Broderick, A. H.; Breitbach, A. S.; Frei, R.; Blackwell, H. E.; Lynn, D. M., Surface-mediated release of a small-molecule modulator of bacterial biofilm formation: a non-bactericidal approach to inhibiting biofilm formation in *Pseudomonas aeruginosa*. *Adv. Healthc. Mater.* **2013,** *2* (7), 993-1000.

56. Singh, N.; Romero, M.; Travanut, A.; Monteiro, P. F.; Jordana-Lluch, E.; Hardie, K. R.; Williams, P.; Alexander, M. R.; Alexander, C., Dual bioresponsive antibiotic and quorum sensing inhibitor combination nanoparticles for treatment of *Pseudomonas aeruginosa* biofilms *in vitro* and *ex vivo*. *Biomater. Sci.* **2019,** *7* (10), 4099-4111.

57. Lu, H. D.; Spiegel, A. C.; Hurley, A.; Perez, L. J.; Maisel, K.; Ensign, L. M.; Hanes, J.; Bassler, B. L.; Semmelhack, M. F.; Prud'homme, R. K., Modulating *Vibrio cholerae* quorum-sensing-controlled communication using autoinducer-loaded nanoparticles. *Nano Lett.* **2015,** *15* (4), 2235-2241.

58. Nafee, N.; Husari, A.; Maurer, C. K.; Lu, C.; de Rossi, C.; Steinbach, A.; Hartmann, R. W.; Lehr, C. M.; Schneider, M., Antibiotic-free nanotherapeutics: ultra-small, mucus-penetrating solid lipid nanoparticles enhance the pulmonary delivery and anti-virulence efficacy of novel quorum sensing inhibitors. *J. Control. Release* **2014,** *192*, 131-140.

59. Traber, K. E.; Lee, E.; Benson, S.; Corrigan, R.; Cantera, M.; Shopsin, B.; Novick, R. P., *agr* function in clinical *Staphylococcus aureus* isolates. *Microbiology* **2008,** *154* (Pt 8), 2265-2274.

60. Kirchdoerfer, R. N.; Garner, A. L.; Flack, C. E.; Mee, J. M.; Horswill, A. R.; Janda, K. D.; Kaufmann, G. F.; Wilson, I. A., Structural basis for ligand recognition and discrimination of a quorum-quenching antibody. *J. Biol. Chem.* **2011,** *286* (19), 17351-17358.

61. Novick, R. P., Genetic systems in Staphylococci. *Methods Enzymol.* **1991,** *204*, 589-636.

62. Lyon, G. J.; Mayville, P.; Muir, T. W.; Novick, R. P., Rational design of a global inhibitor of the virulence response in *Staphylococcus aureus,* based in part on localization of the site of inhibition to the receptor-histidine kinase, AgrC. *Proc. Natl. Acad. Sci. U. S. A.* **2000,** *97* (24), 13330-13335.

Supporting Information for Chapter 7

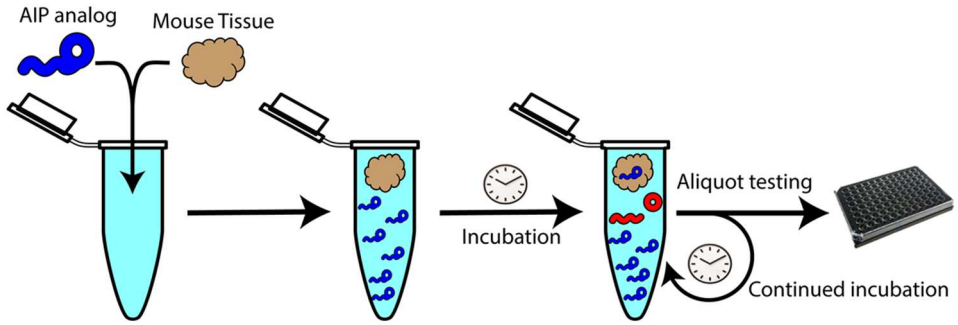


Figure S1: A schematic of *ex vivo* experimental system to examine compound activity incubated at 10,000-fold IC_{50} in presence of mouse tissue.

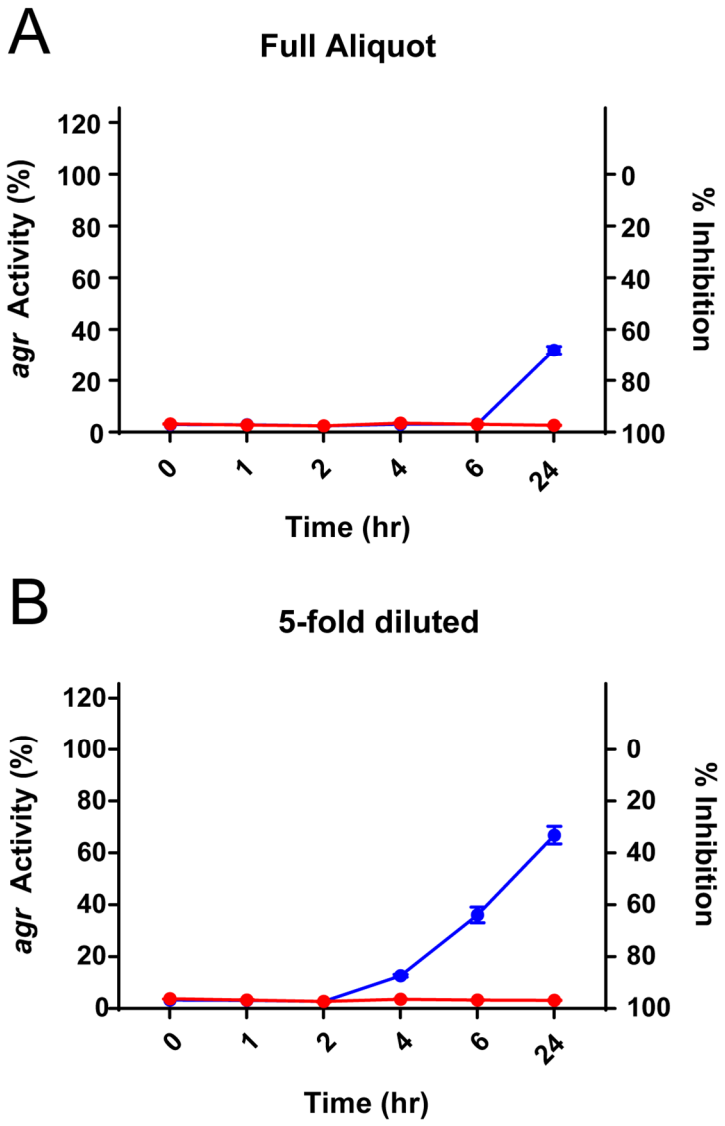


Figure S2: Activity of *S. aureus agr*-I fluorescence reporter strain when exposed to supernatant of AIP-III D4A incubated in PBS in the presence (blue line) or absence (red line) of mouse tissue sample. Both a full aliquot (A) and a 5-fold dilution (B) were assayed. The values shown are the average and SEM of three (n=3) technical replicates. Some error bars are obscured due to the size of the data point.

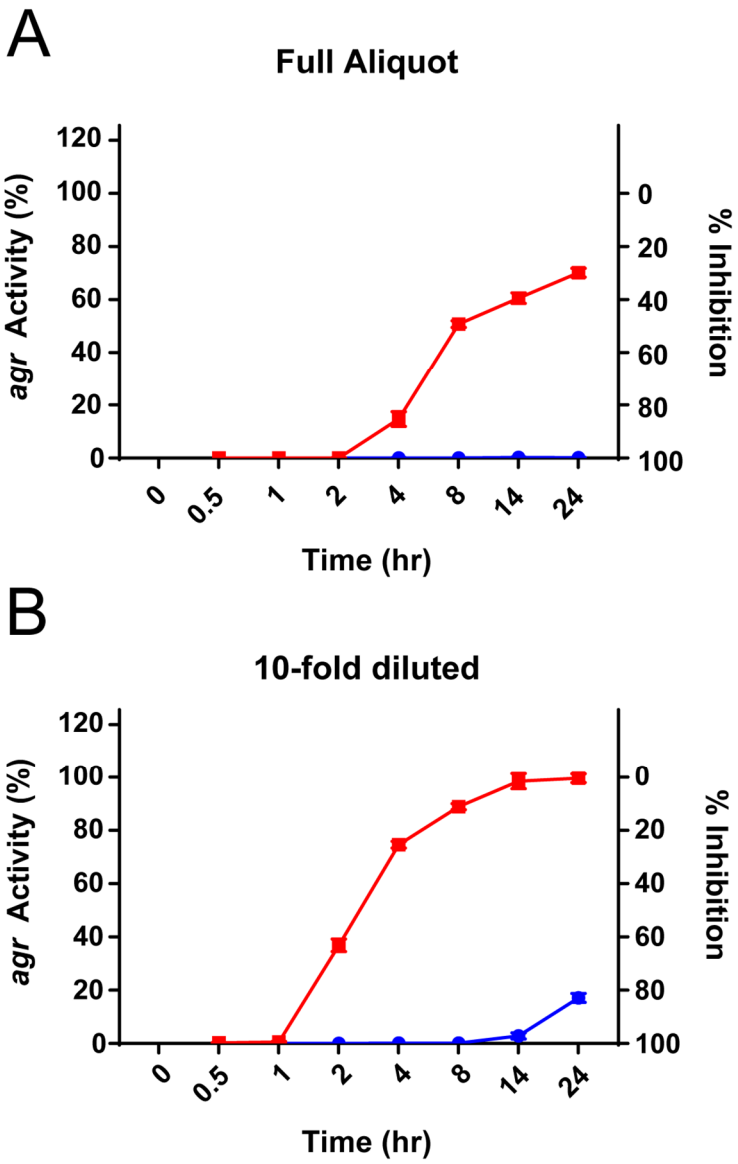


Figure S3: Activity of AIP-III D4A in *S. aureus agr*-I fluorescent reporter strain when exposed to either heat denatured mouse tissue (blue) or a control tissue (red). Both a full aliquot (A) and a 10-fold dilution (B) were assayed. The values shown are the average and SEM of three (n=3) technical replicates. Some error bars are obscured due to the size of the data point.

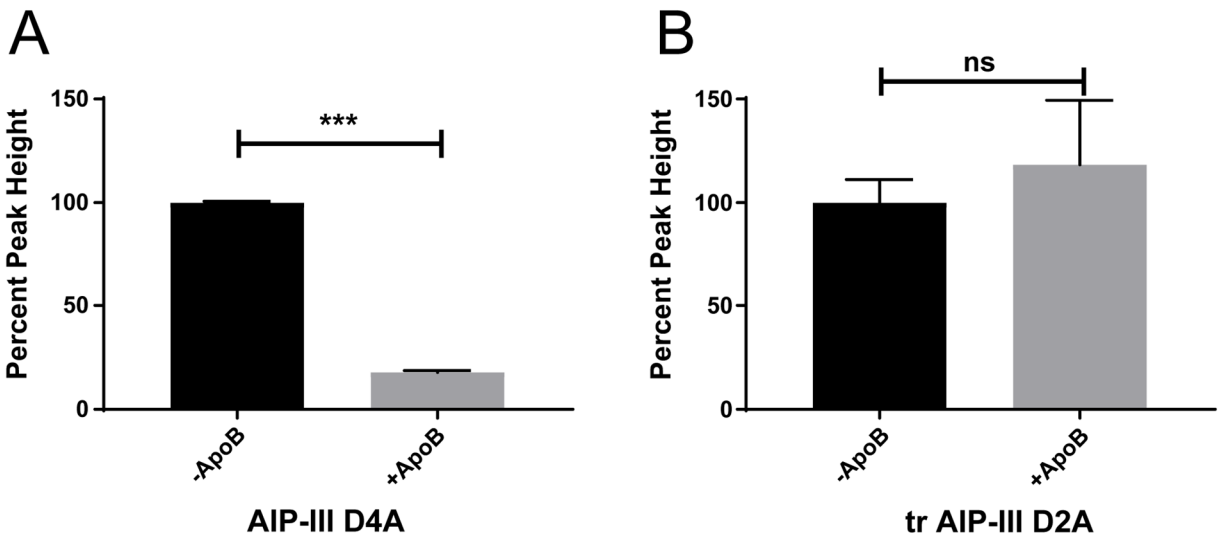


Figure S4: Examination of interactions of AIP-III D4A and tr AIP-III D2A with ApoB as analyzed via analytical RP-HPLC. The peak for AIP-III D4A (A) was substantially reduced (***, $p<0.001$, unpaired t-test) in the presence of ApoB, while there was no significant effect on the peak corresponding to tr AIP-III D2A (B) in the presence of ApoB. Peak heights were normalized to the average peak height of controls lacking ApoB. Analytical RP-HPLC analysis performed in duplicate (n=2). Data represented as mean and SEM.

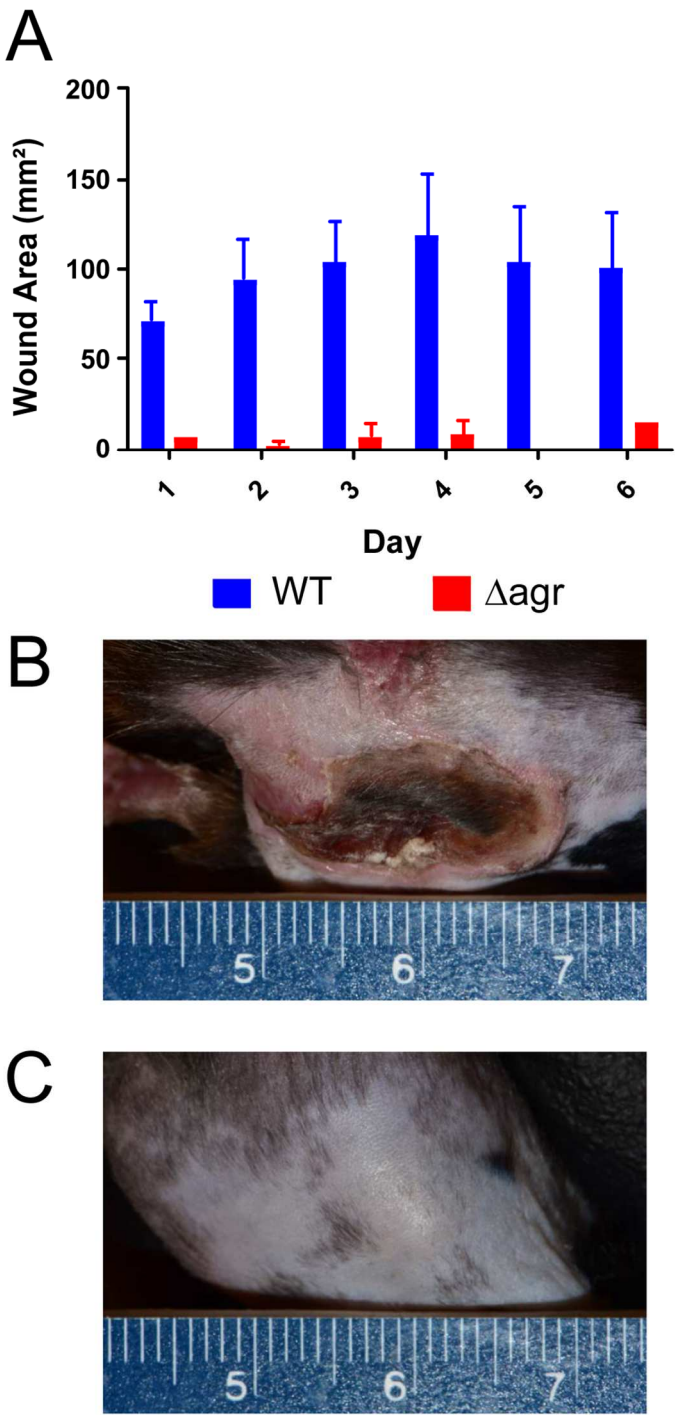


Figure S5: Infection abscess analysis of mice inoculated with wild-type and *Δagr S. aureus*. (A) Observed abscess size for mice receiving either a wild-type strain of *S. aureus* (RN6390B, n=6) or an *Δagr* mutant of this strain (RN9222, n=6). Values shown represent averages and SEM. Representative images of mice from (B) wild-type infected group and (C) *Δagr* infected group. Ruler indicates centimeters.

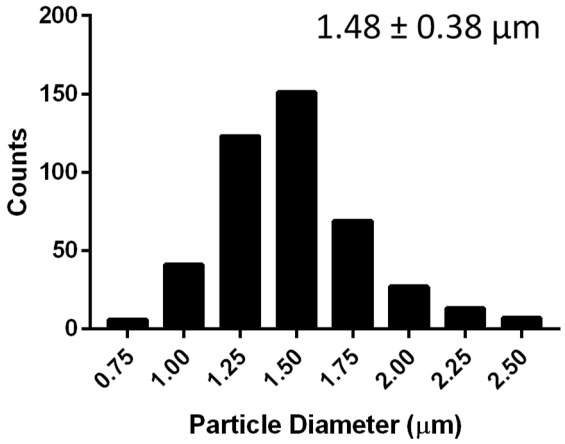


Figure S6: PLG microparticle size histogram as measured by SEM. The average particle diameter was 1.48 ± 0.38 µm. Particle diameters measured by the minor axis of elliptically-shaped particles. The histogram shows measurements for (n=450) microparticles (150 particles were counted from three independent samples).

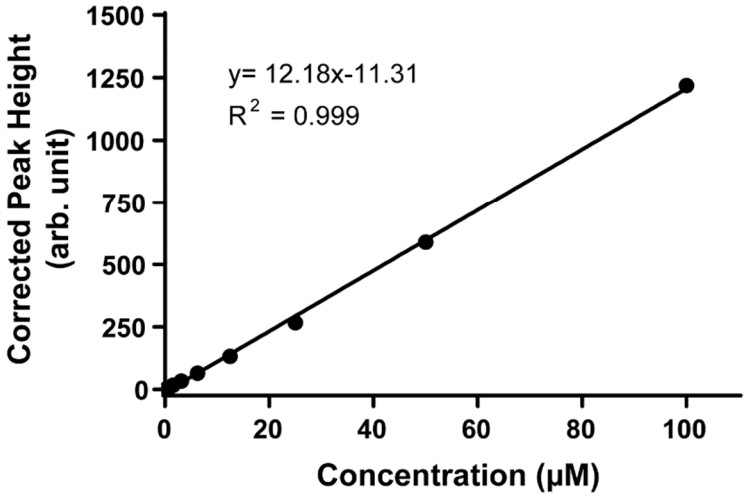


Figure S7: HPLC standard curve for tr-AIP III D2A. Serially diluted tr AIP-III D2A was analyzed by RP-HPLC to determine relationship between peak height and concentration.

Discussion of peptide quantification.

We utilized Equation S1, the four-parameter logistic regression model, to model the dose-response activity of our inhibitory compounds in *S. aureus agr* reporter assays. By rearranging the variables into Equation S2, using the observed activity level of samples with unknown concentrations in our reporter assays, we can then estimate the concentration of the compound in samples from our other assays (i.e., compound release from microparticles). Activity values between 20–80% were used to estimate compound concentration.

- Y = *agr* activity level
- X = Compound concentration in nanomolar
- T = Top (upper) plateau of activity in model
- B = Bottom (lower) plateau of activity in model
- H = Hill slope
- IC_{50} = Inhibitory Concentration at 50% activity

Equation S1:

$$Y = B + \frac{T - B}{1 + \left(\frac{X}{IC_{50}}\right)^{H}}$$

Equation S2:

$$X = IC_{50}\left(\frac{T - B}{Y - B} - 1\right)^{1/H}$$

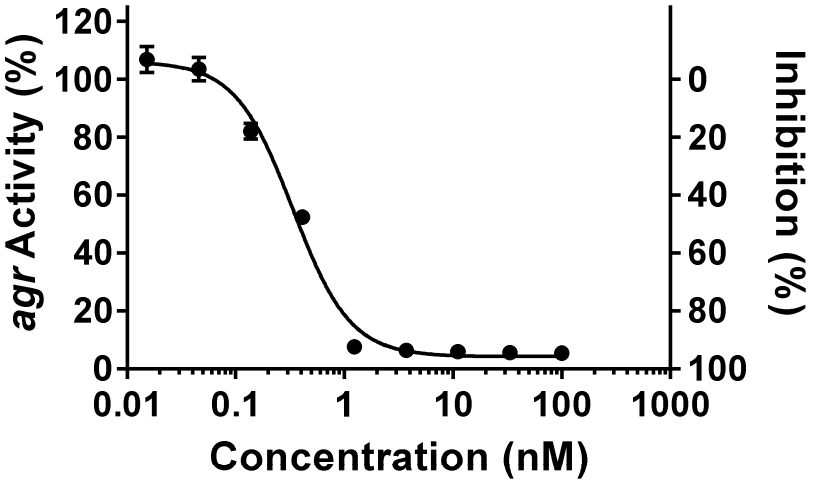


Figure S8: Dose-response inhibition curve for tr AIP-III D2A following the microparticle-modified *S. aureus agr* fluorescence reporter assay. The values shown are the average and SEM of three (n=3) independent technical and biological replicates. The following parameters were observed for this dose response analysis: T=106.1, B=4.293, IC_{50}=0.3353, H=1.648. These values were used in Equation S2 to quantify concentration of compound released in microparticle characterization experiments.

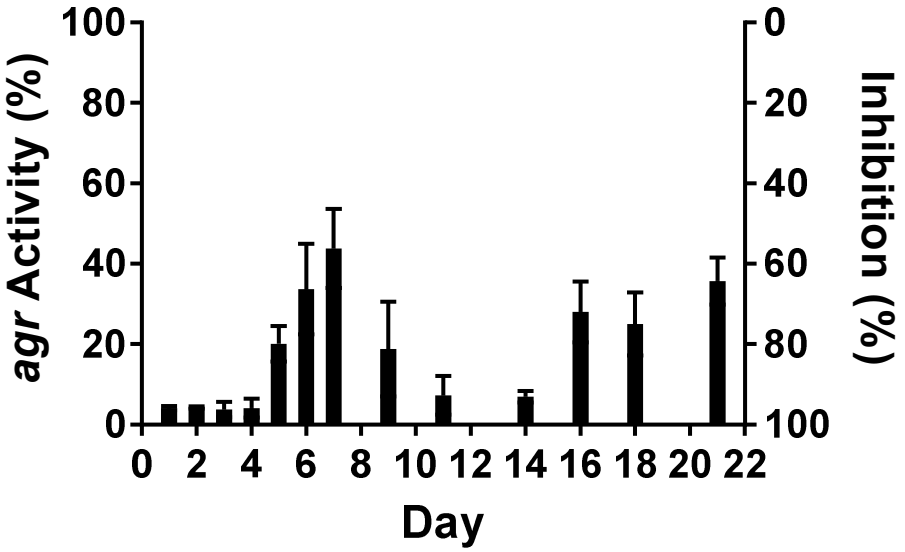
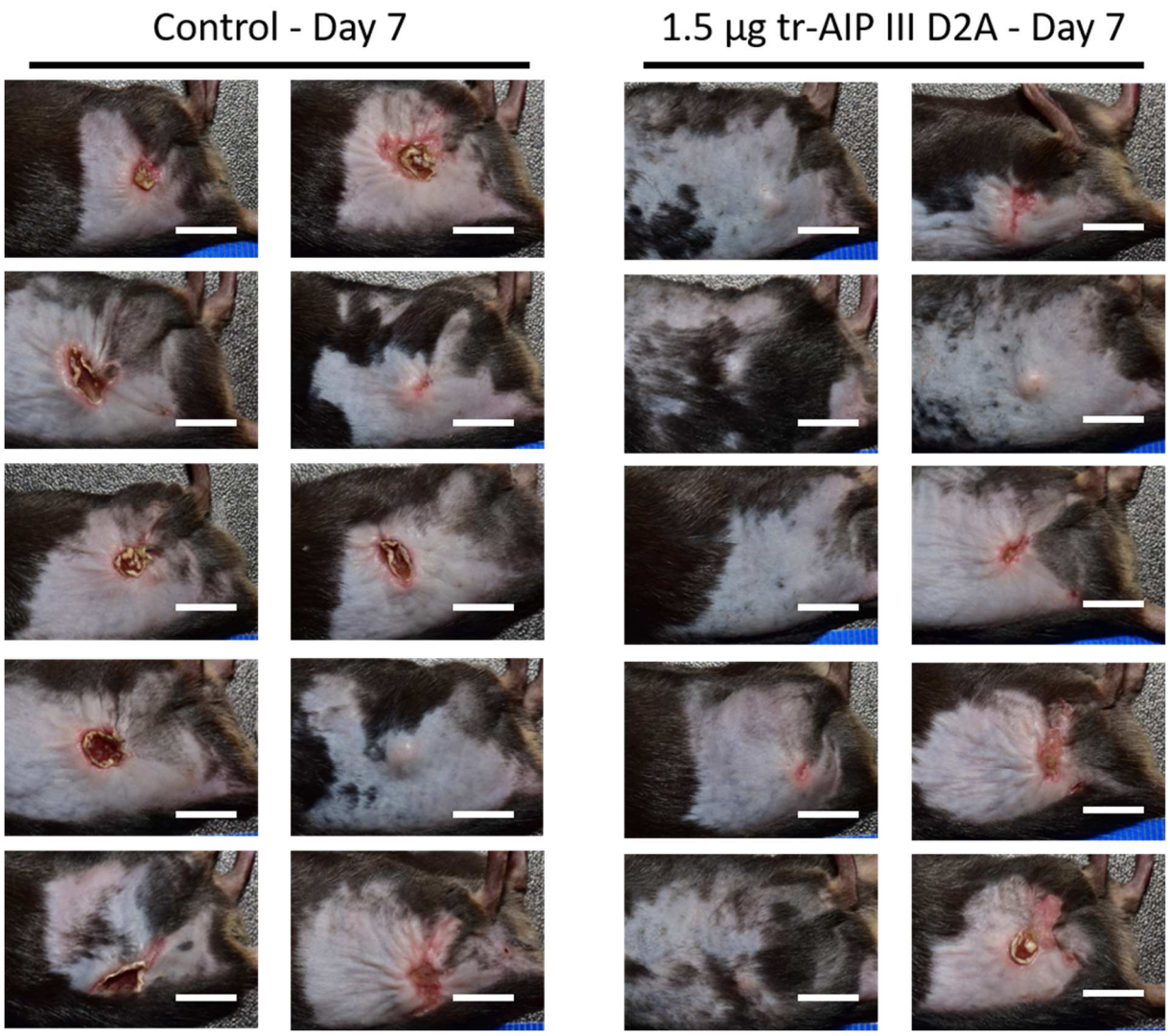


Figure S9: Activity of supernatants isolated over time in release experiments from tr AIP-III D2A-loaded PLG microparticles. Compound activity measured using the *S. aureus agr*-I fluorescence reporter. Supernatants were diluted 10-fold into reporter strain culture for each timepoint. The values shown are the average and single standard deviation of three (n=3) independent technical and material replicates.

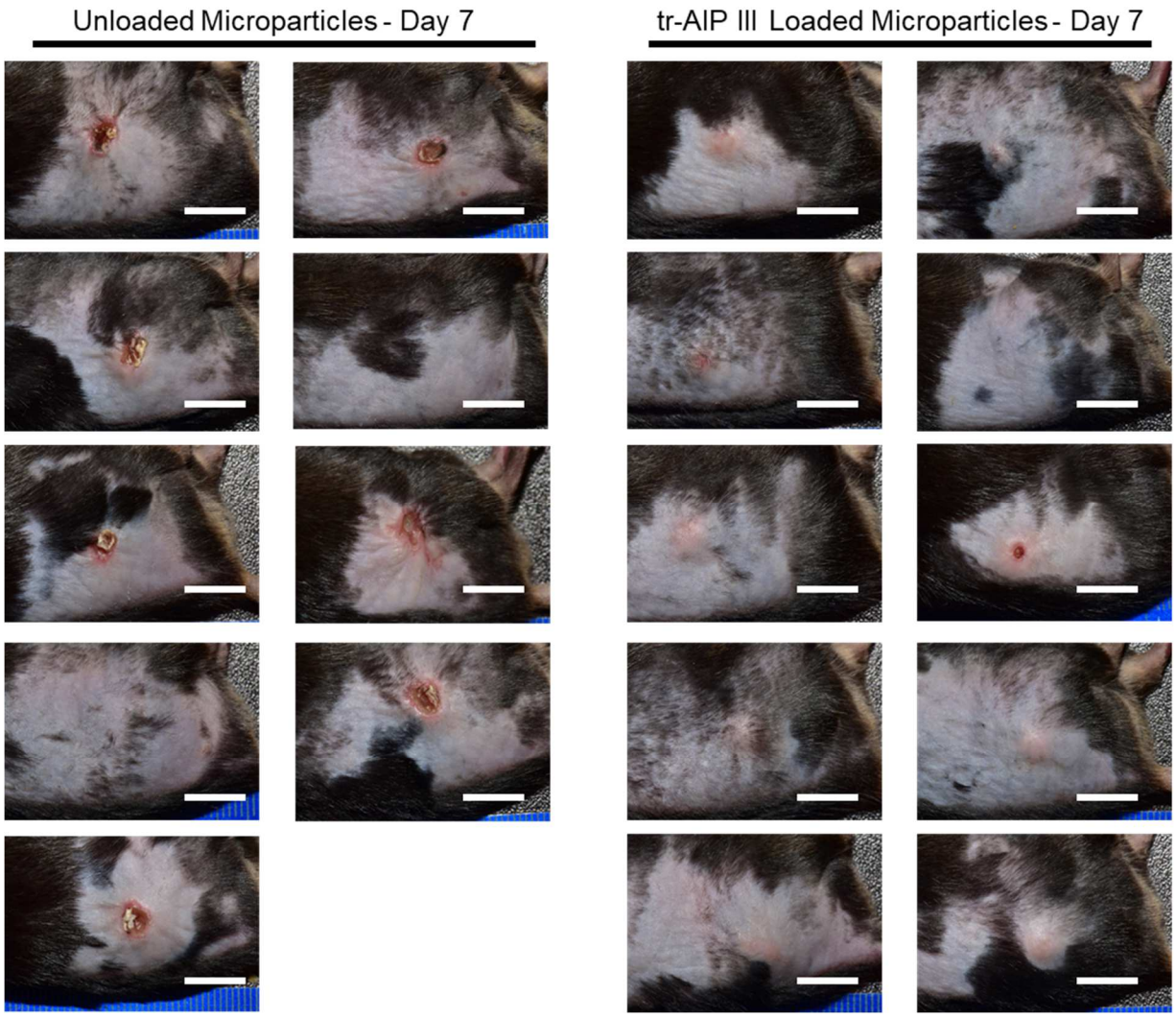
Images of mouse lesions from day 7 of abscess experiments.

1.5 µg tr AIP-III D2A vs. DMSO vehicle control experiment:



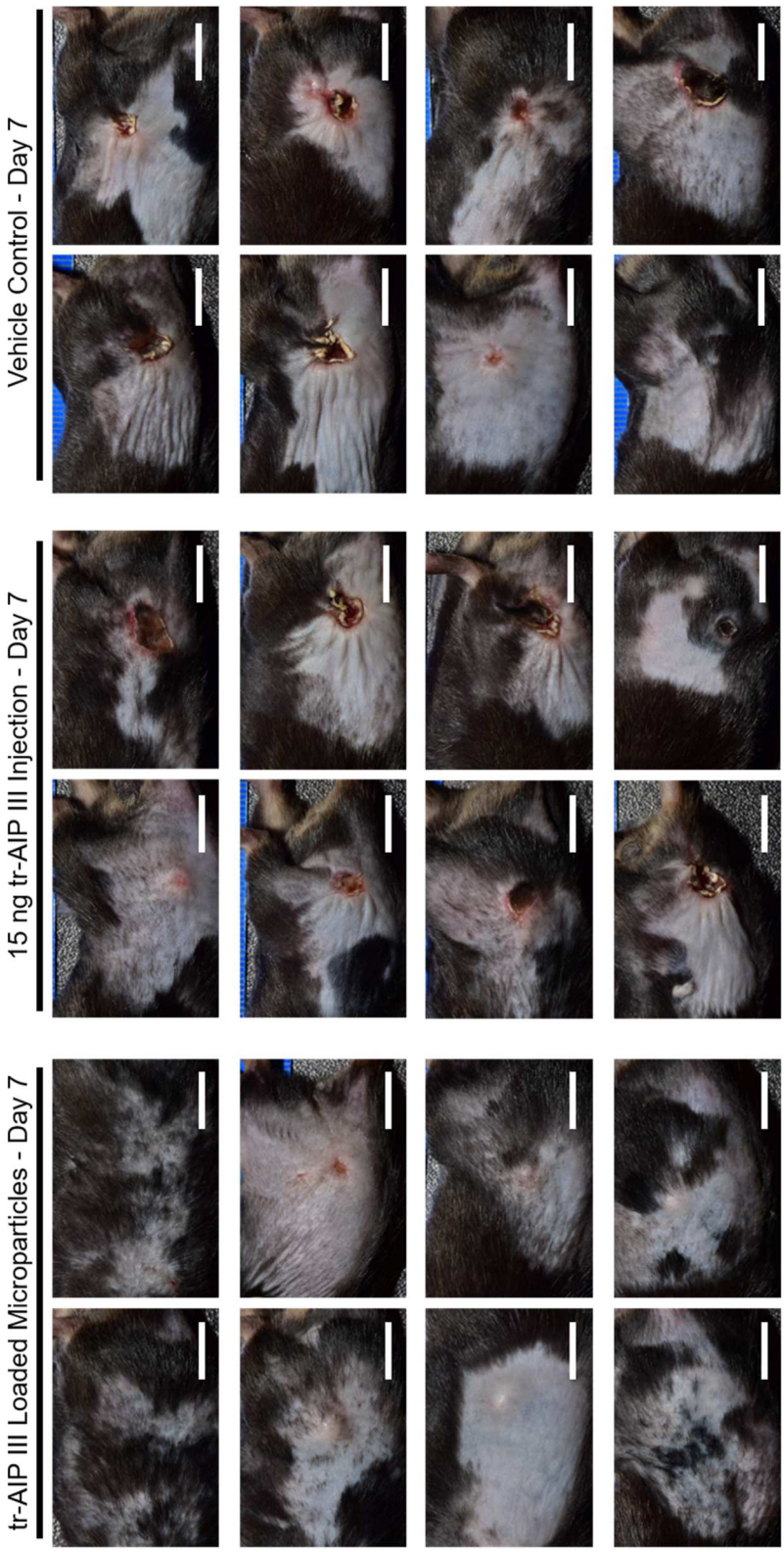
White bar = 1 cm.

1 mg tr AIP-III D2A particles vs. empty PLG particles experiment:



White bar = 1 cm.

1 mg tr AIP-III D2A particles vs. 15 ng tr AIP-III D2A vs. DMSO vehicle experiment:



White bar = 1 cm.

Chapter 8

Membrane Remodeling and Stimulation of Aggregation Following α-Synuclein Adsorption to Phosphotidylserine Vesicles

‡ Portions of this chapter have been previously published as: Hoover, B. M.; Shen, Z.; Gahan, C. G.; Lynn, D. M.; Van Lehn, R. C.; Murphy, R. M.; Membrane Remodeling and Stimulation of Aggregation Following α-Synuclein Adsorption to Phosphotidylserine Vesicles. *J. Phys. Chem. B* **2021**, *125, 6*, 1582-1594. B. M. Hoover prepared materials, performed fluorescence, NTA and CD experiments. Z. Shen developed and ran simulations and analyzed results. I performed TEM experiments. D. M. Lynn, R. C. Van Lehn and R. M. Murphy directed the project.

ABSTRACT: Alpha-synuclein is an intrinsically disordered protein abundant in presynaptic terminals in neurons and in synaptic vesicles. Alpha-synuclein's interaction with lipid bilayers is important not only for its normal physiological function but also in its pathological aggregation and deposition as Lewy bodies in Parkinson's disease. Alpha-synuclein binds preferentially to lipids with acidic head groups and to high-curvature vesicles and can modulate membrane curvature. The relationship between the protein's role as a membrane curvature sensor and generator, and the role of membranes in facilitating its aggregation, remains unknown. We investigated the interaction of alpha-synuclein with vesicles of 1,2-dioleoyl-sn-glycero-3-phospho-L-serine (DOPS) or 1,2-dilauroyl-sn-glycero-3-phospho-L-serine (DLPS). Using nanoparticle tracking along with electron microscopy, we demonstrate that alpha-synuclein induces extensive vesicle disruption and membrane remodeling into discoids, tubules, and ribbons with DLPS vesicles, but not DOPS. Coarse-grained molecular dynamics simulations revealed that adsorption of alpha-synuclein to DLPS but not DOPS vesicles induced vesicle elongation and redistribution of protein to regions of higher curvature, a process that could drive protein aggregation. In agreement with this hypothesis, DLPS but not DOPS strongly stimulated alpha-synuclein aggregation. Our results provide new insights into the critical contribution of bilayer stability in the membrane response to alpha-synuclein adsorption, and in stimulation of aggregation.

Introduction

Parkinson's disease is the second most common neurodegenerative disorder in the world, with an estimated 1 million patients in the United States and 10 million worldwide [1,2]. One defining characteristic of Parkinson's is the appearance of Lewy bodies, abnormal intraneuronal deposits comprised primarily of a 14 kDa protein, α-synuclein (aSyn), and lipid [3–6]. In Lewy bodies, aSyn is found as insoluble aggregates with a fibrillar morphology and cross-β sheet structure typical of amyloid [6]. In vitro, the protein spontaneously aggregates into amyloid fibrils under certain conditions, such as with agitation or at acidic pH [7, 8], by a nucleation-elongation mechanism [9].

In solution, aSyn is intrinsically disordered but adopts an elongated or broken α-helical secondary structure upon adsorption to lipid bilayers [10–12]. Generally, the amphipathic helix preferentially binds to lipid surfaces containing acidic headgroups [10, 11], to unsaturated lipids [13], to membranes in the liquid disordered phase [14, 15], and to vesicles with high curvature [11, 14]. Packing defects in the lipid bilayer, such as those introduced by high-curvature or conical lipid components, facilitate strong aSyn binding [16, 17]. More broadly, the conserved amphipathic helix motif among the synuclein family of proteins has been identified as a region capable of both curvature sensing and curvature generation[17–20]. The latter action is believed to occur by lateral expansion of lipid headgroups via a wedging mechanism [17–20].

While it is generally accepted that aSyn binding to biological membranes is essential for the protein to carry out its physiological function, interaction of the protein with lipid interfaces has also been found to promote its pathological aggregation under some circumstances [15, 21–25]. For example, it has been demonstrated that lipid membranes composed of DMPS (1,2-dimyristoyl-sn-glycero-3-phospho-L-serine) stimulated the aggregation of aSyn [15, 24]. A decrease in the acyl chain length from DMPS (14:0) to DLPS (12:0) was found to further increase the rate of aSyn

aggregation. By contrast, DOPS (18:1) vesicles did not stimulate protein aggregation, a finding attributed to its lower solubility [15]. The lipid surface can support a high local concentration of aSyn molecules, suggesting that protein crowding due to adsorption to the membrane may trigger aggregation. However, the stoichiometry and affinity of aSyn-vesicle binding was comparable for DOPS, DMPS, and DLPS vesicles [15], suggesting that mechanisms beyond protein enrichment at the membrane surface must affect whether a specific lipid chemistry will stimulate aSyn aggregation.

The ability of aSyn to disrupt and promote changes in membrane shape and curvature has been well established for membranes comprised of lipids with acidic phosphatidyl-glycerol (PG) head groups. Co-incubation of aSyn with model membranes consisting of POPG (1-palmitoyl-2-oleoyl-sn-glycero-3-phospho-1'-rac-glycerol), DMPG, and DLPG have been reported to disrupt vesicle integrity, resulting in conversion of spherical liposomes into a rich diversity of morphologies including tubules, cylindrical micelles and thick bilayer tubes [18, 20, 26, 27], a process known as membrane remodeling. Membrane remodeling by aSyn has also been demonstrated with POPS and the zwitterionic POPC [27, 28]; the latter case is somewhat surprising because the affinity of aSyn for POPC is low and aSyn remained in a disordered (non α-helical) conformation. It has been previously suggested that aSyn-mediated membrane remodeling might influence aggregation under some circumstances [27, 28]. For example, POPG tubules stimulated aSyn aggregation at high protein:lipid ratio [27], whereas POPC inhibited amyloid formation (28). These studies were conducted using mechanical agitation [27, 28], a treatment that accelerates aSyn aggregation in the absence of lipids.

In this investigation, we explored the role of aSyn-mediated membrane remodeling under quiescent conditions and at neutral pH. At these conditions, aSyn alone is not prone to aggregate;

thus, the choice of these conditions allows any membrane remodeling to be isolated from confounding effects of aSyn aggregation or mechanical agitation. We chose PS because it is the predominant acidic head group in mammalian membranes, and for direct comparison to a previous study in which PS lipid-mediated acceleration of aSyn aggregation was shown to be strongly and inversely dependent on acyl chain length, with greater stimulation of aggregation as chain length decreased [15, 24]. In that work, aSyn aggregation was posited to occur on the membrane surface, without disruption of the lipid vesicles, and neither vesicle stability nor membrane remodeling were specifically interrogated [15]. Acyl chain length is physiologically relevant, because peroxidation of polyunsaturated lipids shortens hydrocarbon chains, causing changes in membrane fluidity, increases in transport to other organelles, and cell damage [24].

We used nanoparticle tracking analysis (NTA) to monitor changes in the properties of large unilamellar vesicles (LUVs) of DOPS (18:1) or DLPS (12:0) in the presence of aSyn. NTA is particularly useful for these studies as the technique allows simultaneous detection of particle size and particle number concentration over minutes to hours, in aqueous buffers, without the need for labels or dyes. With these data, along with images obtained by transmission electron microscopy (TEM), we demonstrate that the interaction of aSyn with DOPS LUVs induced a morphological change from spherical to ellipsoidal, but without significant vesicle lysis, fusion, or tubulation. In sharp contrast, interaction of aSyn with DLPS resulted in membrane remodeling into a polydisperse mixture of discoids, tubules and helical ribbons, a process that continued for hours. Coarse-grained molecular dynamics simulations revealed that adsorption of aSyn to DLPS, but not DOPS, induced vesicle elongation that generated regions of high membrane curvature, leading to a preferential redistribution of aSyn molecules to the vesicle poles. These simulations provide insight into the mechanism by which aSyn induces major membrane remodeling in DLPS, and

may also explain how membrane remodeling could cause a high local protein concentration that may stimulate aggregation. Consistent with this hypothesis as well as previously published work, aSyn aggregation was much faster in the presence of DLPS compared to DOPS. Thus, the active response of lipid bilayers to aSyn adsorption depends on bilayer stability, and in turn membrane remodeling stimulates aSyn aggregation. Taken together, our results provide insight into α-synuclein's roles in membrane remodeling and membrane-mediated aggregation, thus connecting the protein's normal physiological function with its pathological.

Materials and Methods

Purification of aSyn and lipid preparation. Wild-type aSyn was purified as described [29]. Lipids purchased from Avanti Polar Lipids Inc. (Alabaster, AL) were prepared in glass tubes under a gentle stream of nitrogen and evaporated overnight. Multi-lamellar vesicles (MLVs) were prepared by rehydration into phosphate-buffered saline (PBS: 10 mM NaH_2PO_4/ Na_2HPO_4, 100 mM NaCl pH 7.4). Large unilamellar vesicles (LUVs) were prepared by extrusion through a 100 nm or 50 nm polycarbonate membrane on a hotplate set above the phase transition temperature of the lipids. All experiments were conducted in PBS unless otherwise stated.

Vesicle clearance assay. Vesicle clearance of MLVs at protein:lipid (P:L) molar ratios of 1:40, 1:20, and 1:10 were monitored using a spectrophotometer (Eppendorf) at a wavelength of 500 nm at room temperature. Total lipid concentration was 600 μM. Experimental details are provided in Supporting Information.

Carboxyfluorescein dye leakage assay. 5-6-carboxyfluorescein was encapsulated in 100 nm diameter LUVs, and dye leakage from vesicles (100 μM lipid) due to addition of aSyn (protein:lipid ratios of 1:1, 1:10 and 1:100) was monitored by excitation at 470 nm and emission at 525 nm using a QuantaMaster spectrofluorometer (PTI, Birmingham, NJ). Dye leakage was calculated as described in Supporting Information.

Dynamic light scattering. aSyn (150 μM) and 100 nm DLPS vesicles (150 μM) in PBS were separately filtered through a 0.22-μm syringe filter (Millipore) before mixing into a precleaned quartz cuvette. The cuvette was placed into a bath containing refractive index matching decahydronaphthalene (Sigma) and equilibrated to 23°C. Measurements were taken at 90° scattering angle using a Brookhaven BI-200SM and Innova 90C (Coherent, Inc.) 488 nm, 150 mW argon laser. Autocorrelation data were collected for 5 min following 24 h of co-incubation. CONTIN fit to the autocorrelation function was used to determine a scattered intensity size distribution.

Nanoparticle tracking analysis. The kinetics of the interaction of aSyn with LUVs and the measurement of the hydrodynamic size and particle number concentration of DOPS or DLPS LUVs alone or with aSyn were monitored by NTA. All measurements were collected with a Nanosight LM10 (Nanosight) equipped with a 405 nm laser at room temperature for P:L molar ratios of 1:100, 1:10, and 1:1 for 5 hours. Liposome samples were diluted to 6 x 10^9 liposomes/mL in 0.02 μm filtered PBS and mixed at P:L molar ratios of 1:1, 1:10, and 1:100 to obtain a concentration of approximately 3 x 10^9 liposomes/mL at the start of data collection. Samples were injected directly into the sample chamber using LuerLok syringes (BD). The camera level was

maintained at a setting of 14. Video tracking was acquired for 30 second time intervals with five measurements for each sample. Measurements were repeated once per hour for five hours. Analysis of the particle concentration, mean size, and standard deviation of particle tracks was conducted using NTA 3.0 software using a detection threshold of 5. Additional information and calculations are provided in the Supporting Information.

Transmission EM. Samples were stained with a 2% solution of uranyl acetate on a 400 mesh copper grid. The grid was air dried and imaged with a Techni T12 TEM at 120 V accelerating voltage at 1 second exposure time on a Gatan 4k Ultrascan CCD camera.

Coarse-grained molecular dynamics simulations. Simulations were performed using the BMW MARTINI force field, which combines approximately four non-hydrogen atoms into single beads to model the interactions of protein, water, and lipids [30, 31]. Simulations were performed at constant number of particles, pressure, and temperature using GROMACS 2016. All simulations were performed at 87°C to increase sampling without significantly influencing aSyn-bilayer interactions [32–34] and to decrease the bending rigidities of both membranes because BMW MARTINI overestimates lipid mechanical properties [31, 35, 36]. Similar elevated temperature simulations have been previously employed to model bilayer phenomena, including peptide partitioning into bilayers [32, 34]. aSyn-vesicle systems were equilibrated for 120 ns followed by a production run of 300 ns. aSyn-bilayer systems were equilibrated for 200 ns followed by a production run of 700 ns. Both simulation workflows were repeated twice for each bilayer composition using different initial velocities aSyn configurations. Detailed simulation methods are given in the Supporting Information.

Thioflavin-T (ThT) assay. Kinetics of aggregation were monitored under two solution conditions: PBS and PB (20 mM NaH_2PO_4/ Na_2HPO_4, pH 6.5). aSyn and lipid were mixed at a 1:10 P:L molar ratio and incubated at 37°C in PBS for 8 days, or at 30°C in PB for 48 h. Aliquots containing 2 μM of protein were mixed with 10 μM of ThT and measured once per day. aSyn concentration was 100 μM in PBS and 80 μM in PB. Fluorescence emission was monitored at an excitation of 440 nm and emission from 485 nm using a QuantaMaster spectro-fluormeter (PTI, Birmingham, NJ). An average of three independently prepared replicates and their standard error were determined by subtraction of the background fluorescence for a sample containing buffer only. The low background fluorescence at 0h was subtracted from each later time point for each sample. For pelleted samples, 5 uL of resuspended pellet was mixed with 10 μM of ThT and the background with buffer alone subtracted from the raw intensity.

Circular dichroism (CD) spectroscopy. aSyn and lipid were mixed at 1:10 P:L molar ratio, 80 μM protein, in PB and incubated for 48h at 30°C. Samples were ultracentrifuged at 90 krpm for 30 minutes at 4°C. The pellet was resuspended in PB. CD spectra of the supernatant, pellet and background buffer were recorded between 185-340 nm using an Aviv model 420 CD spectrometer. Data were acquired at room temperature with an averaging time of 5 seconds per wavelength. The molar protein concentration of the supernatant was determined by absorbance and that of the pellet by mass balance. The background buffer baseline was subtracted from the raw data and normalized by molar ellipticity.

Results

Results are presented in the following order. We first present experimental data demonstrating that addition of monomeric aSyn induces much greater membrane disruption and remodeling of DLPS compared to DOPS vesicles. Next, coarse-grained molecular dynamic simulations are used to help elucidate the mechanisms underlying the experimentally-observed differences in vesicle response to aSyn. Finally, we provide experimental data that correlates greater membrane remodeling of DLPS by aSyn to a greater potential of DLPS versus DOPS vesicles to induce aggregation of aSyn, an outcome that can be explained by protein-crowding phenomena identified by simulation.

The acyl-chain length of PS lipids strongly affects vesicle clearance in the presence of aSyn.

aSyn is well known to bind strongly to phospholipids with acidic head groups, and under certain conditions, the binding leads to a loss of membrane integrity. Specifically, aSyn disrupts POPG multilamellar vesicles (MLVs), as detected by a decrease in turbidity over time using a vesicle clearance assay [18, 37, 38]. The most prevalent acidic phospholipid in mammalian cell membranes is PS [39]. To determine whether aSyn disrupts PS membranes, we prepared MLVs of DOPS or DLPS (600 μM) with varying concentrations of aSyn and compared their vesicle clearance rates. Both lipids are in the fluid phase because the transition temperatures T_m are below the experimental temperature (T_m = 16°C for DLPS versus -11°C for DOPS). As shown in Figure 1, DOPS MLVs remained stable, while the turbidity of DLPS MLVs decreased rapidly with increasing aSyn concentration. This effect is not due to differences in the affinity of aSyn binding to DLPS versus DOPS, as the K_D's are similar [15].

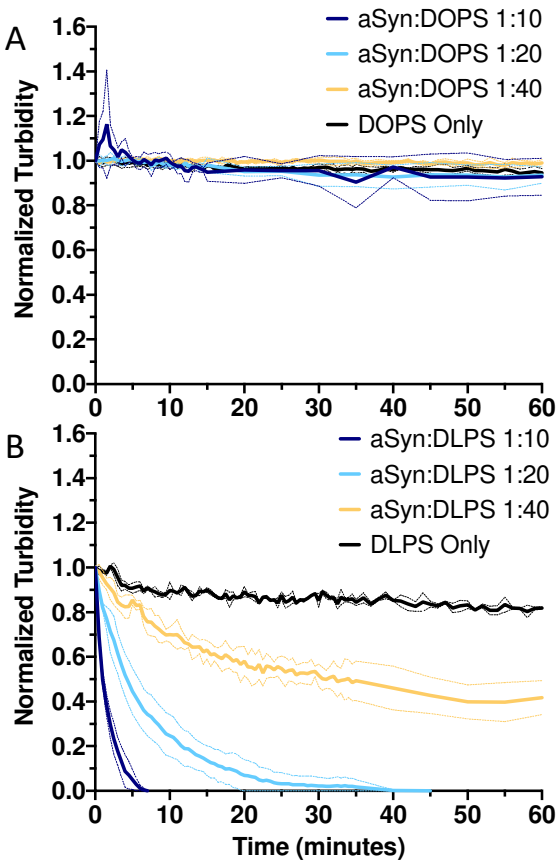


Figure 1. Propensity of aSyn to clear turbidity of solutions containing MLVs of model membranes. (A) Co-incubation of aSyn with DOPS MLVs. (B) Co-incubation of aSyn with DLPS MLVs. Experiments were conducted in PBS (10 mM phosphate buffer, 100 mM NaCl, pH 7.4) at 600 µM lipids with aSyn added at 1:40 to 1:10 P:L molar ratio at room temperature, above the phase transition temperature of both lipids. Data points indicate the average of three independent replicates and shading indicates the standard deviation.

aSyn induces modest changes in DOPS liposome shape and permeability without affecting liposome stability

Carboxyfluorescein (CF) was encapsulated in 100 nm DOPS large unilamellar vesicles (LUVs) and dye leakage was monitored by fluorescence following aSyn addition. Integrity of DOPS membranes was largely retained in the absence of protein (Figure S1). Addition of aSyn increased the rate of dye leakage in a concentration-dependent manner; dye leakage was gradual and incomplete, indicating the formation of transient and/or small pores, or a subtle rearrangement

of the protein-lipid interface upon protein adsorption [40, 41]. TEM images were obtained of 100 nm DOPS LUVs alone or incubated for 5 h with aSyn at a protein:lipid (P:L) ratio of 1:10. DOPS LUVs alone were spherical, with a collapsed appearance typical of TEM images of unilamellar vesicles (Figure 2A). Binding of aSyn to DOPS induced changes in vesicle shape from spherical to prolate ellipsoidal (Figures 2B, 2C and 2D, white arrows).

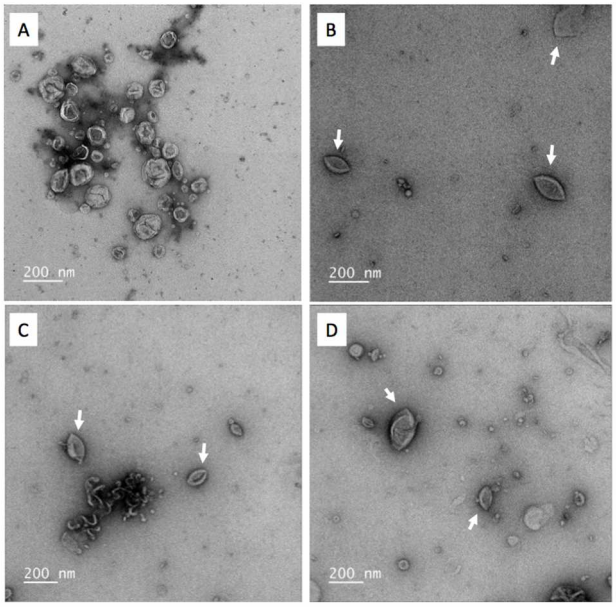


Figure 2. Effect of co-incubation of aSyn with DOPS membranes. Samples were prepared in PBS (pH 7.4). (A) TEM of DOPS LUVs alone or (B-D) with added aSyn at a 1:10 P:L molar ratio following 5 h of co-incubation at room temperature. Arrows indicate prolate ellipsoidal 'football' vesicles. Images were taken from two independent replicates.

To quantify changes in vesicle properties following the addition of aSyn, we used Nanoparticle Tracking Analysis (NTA). In NTA, the Brownian motion of individual particles in solution is tracked to obtain the hydrodynamic diameter of an equivalent sphere, D_{sphere}. The technique allows simultaneous measurement of the particle-by-particle size distribution as well as total particle number concentration. The minimum detection threshold for biological material is ~30 nm [42, 43], so monomeric aSyn (D_{sphere} ~5-6 nm) [44] is undetectable, and only the liposome or

liposome-protein complex is sampled. A stock solution of DOPS LUVs of nominal 100 nm diameter was diluted to a particle number concentration optimal for analysis (3 x 10^9 liposomes/mL, ~ 500 nM lipid) [29]. The number-weighted mean value of D_{sphere} of liposomes in the absence of protein was 103 ± 17 nm, averaged over three independently prepared replicates. Because the vesicle diameter and particle concentration varied somewhat for each independently-prepared liposome solution, we normalized each subsequent measurement to the liposome-only value for that preparation. Samples of DOPS LUVs with aSyn at P:L molar ratios of 1:100, 1:10, and 1:1 were prepared and analyzed, with data collection continuing for 5 h. Mean normalized D_{sphere} increased immediately upon addition of aSyn, with little to no additional change thereafter (Figure 3A). As the P:L ratio increased from 1:100, 1:10 and 1:1, D_{sphere} increased by approximately 7 nm, 12 nm and 16 nm, respectively. The size of the increase is calculated for a single liposome preparation, with the increase similar across independently prepared liposome solutions despite some variability in absolute liposome size between different preparations. A representative particle-by-particle size distribution is shown in Figure S2, exhibiting a unimodal distribution with a shift towards larger diameter upon aSyn addition. There was no change in liposome number concentration upon addition of aSyn (Figure 3B), indicating that the liposomes remained stable, with no indication of vesicle fusion or breakup.

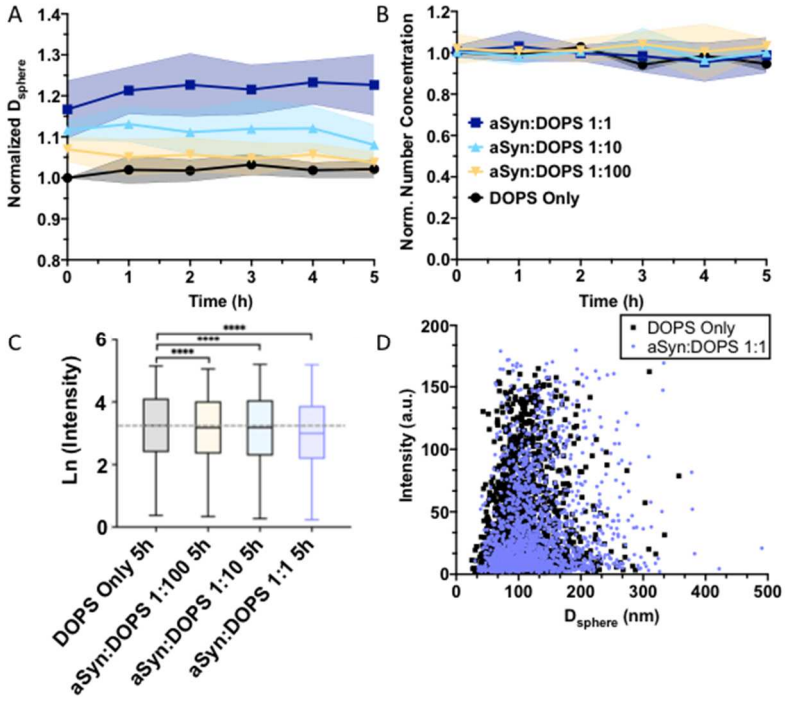


Figure 3. NTA analysis of DOPS LUVS (100 nm nominal size) alone or incubated with aSyn at 1:100, 1:10 or 1:1 P:L molar ratios. Samples were prepared in PBS and measurements taken at room temperature. (A) Number-averaged mean hydrodynamic diameter, normalized to LUVs alone at t = 0. Data points are the average of 3 replicates and shading indicates the standard deviation. (B) Normalized particle number concentration. (C) Representative box-and-whiskers plot of the scattered intensity distribution for size range between 75-125 nm following 5h of co-incubation ****p < 0.0001 (unpaired two-tailed t test). Approximately 8,000 particles per condition were tracked. (D) Representative comparison of particle size and scattered intensity distribution for DOPS alone (black) and with aSyn at 1:1 molar ratio (purple) after 5h.

We evaluated whether the increase in D_{sphere} was fully accounted for by adsorption of aSyn to the interface. It is generally accepted that aSyn adopts an α-helical conformation upon binding to lipid bilayers and that the bulk of the protein rests on the surface of the membrane [45, 46], sampling between an extended single helix or a broken helix conformation [47]. We estimated the thickness of a monolayer of aSyn bound to liposomes to be that of an α-helix (~1.2 nm) [48], with a small unknown additional contribution from the disordered C-terminal tail [49]. Thus, aSyn adsorption as a monolayer to the surface should increase D_{sphere} of liposomes by only ~3 nm, insufficient to

explain the entire observed 7-16 nm increase. We wondered whether the 'excess' increase in D_{sphere} (beyond that expected by adsorption) could be explained by the aSyn-mediated induction of a shape change from spherical to ellipsoidal that was observed in TEM images. To test this, we measured the dimensions of 45 liposomes in the absence of aSyn (Figure 2A) and obtained a diameter of 94 ± 27 nm. Next, the major and minor axial dimensions of 20 prolate ellipsoids formed in the presence of aSyn, similar to those observed in Figures 2B, 2C and 2D, were measured to be 130-175 nm and 75-100 nm, respectively. Using a model for the hydrodynamic diameter of prolate ellipsoids (SI), we calculated D_{sphere} = 110 ± 40 nm, or an increase of 16 nm in the mean hydrodynamic diameter. This result is in good agreement with the increase in diameter measured by NTA following the addition of protein. We repeated the NTA experiment with DOPS liposomes extruded through a 50 nm membrane and observed a comparable trend, but with a smaller increase in size (Figure S3). If adsorption alone without a shape change could account for the increase in D_{sphere}, then the size of the increase should be independent of the LUV diameter. This result is consistent with our interpretation of NTA and TEM data, that adsorption of aSyn to DOPS liposomes induces a change in shape from spherical to slightly ellipsoidal.

NTA provides not only size and number information but also intensity of scattered light on a particle-by-particle basis. The intensity distribution of the incident light is broad because the beam is Gaussian. The scattered intensity per particle I_p varies with the intensity of the incident beam I_0, and is a function of particle molecular weight M, refractive index increment dn/dc, and particle scattering factor $P(q)$, which depends on particle shape and dimensions [50, 51],

$$I_p \propto I_0 \times M^2 \, x \left(\frac{dn}{dc}\right)^2 x \, P(q)$$

Eq. 1

Upon aSyn binding to liposomes, I_p should increase because M of the protein-liposome complex is greater than that of liposome alone, and because dn/dc for protein (0.19 ml/g) [52] is larger than for lipid (0.16 ml/g) [53]. Countering this effect, a change in shape from spherical to ellipsoid reduces $P(q)$ and therefore decreases I_p; we calculated a ~10% reduction in $P(q)$ based on the dimensions from TEM (SI). We analyzed scattering from ~8,000 particles with D_{sphere} between 75-125 nm. We observed a small but statistically significant decrease in the mean intensity of the population for DOPS+aSyn relative to DOPS only (Figures 3C and 3D, Figures S4 and S5), consistent with the change in vesicle shape from spherical to ellipsoidal.

Taken together, dye leakage, NTA, and TEM results show that aSyn modestly increases membrane permeability of DOPS LUVs and changes the shape from spherical to ellipsoidal, but does not cause vesicle breakup or major vesicle disruption.

aSyn substantially disrupts and remodels DLPS liposomes

We verified by NTA that DLPS LUVs were formed during extrusion of lipids with a measured diameter of ~100 nm (not shown). However, we were unable to encapsulate CF inside DLPS vesicles, indicating that DLPS vesicles are inherently less cohesive than DOPS vesicles. Lack of dye retention has also been reported for DLPC membranes [54], and is attributable to the lipid's finite solubility (100 nM) [15].

We diluted DLPS LUVs to approximately 3 x 10^9 liposomes/mL, (~ 500 nM lipid) and investigated their properties by NTA. Whereas DOPS vesicles were stable upon dilution, the size and number concentration of DLPS vesicles slowly decreased over several hours (Figure 4A-B, black). This outcome is consistent with partial dissociation of liposomes upon dilution due to the finite DLPS solubility. We then measured the effect of aSyn addition on DLPS LUVs, for P:L

molar ratios of 1:100, 1:10 and 1:1. Whereas vesicle size increased with aSyn addition for DOPS, the normalized D_{sphere} decreased slightly over time for both DLPS alone and at 1:100 and 1:10 P:L (Figure 4A). At 1:1 P:L, D_{sphere} was nearly constant with time but there was high variability in the data. Also, in sharp contrast to the unchanging particle number concentration upon addition of aSyn to DOPS, particle number concentration decreased significantly with time, with the rate of change increasing with protein concentration and the decrease continuing over the entire 5 h measurement period (Figure 4B). Particle size distributions of DLPS with and without aSyn revealed overall similar size distributions but with the addition of a few very large particles at 1:1 P:L following 5 h (Figure S6). Mean I_p decreased significantly as P:L molar ratio increased (Figure 4C, Figure S7&S8); the change was much greater for DLPS than for DOPS. The decrease in I_p is also apparent in the intensity distribution plot (Figure 4D), and was time-dependent at all P:L molar ratios (Figure S8).

TEM images of mixtures of aSyn with DLPS were obtained to assist with further interpretation of NTA results. These images revealed a striking morphological diversity, including twisted and helical ribbons (Figures 5A, 5B and 5C), tubules (Figure 5D), and discoids (Figures 5E, 5F and 5G), all of which were absent in control vesicles (Figure 5H). The most numerous objects were flattened discoids ~30 nm in diameter and 5 nm in thickness (Figures 5E, 5F and 5G). Tubules (Figure 5D) were typically 10-20 nm in diameter with contour lengths ranging between 300-700 nm. Larger structures (~1.5 μm in length) were rare but consistently observed in multiple preparations.

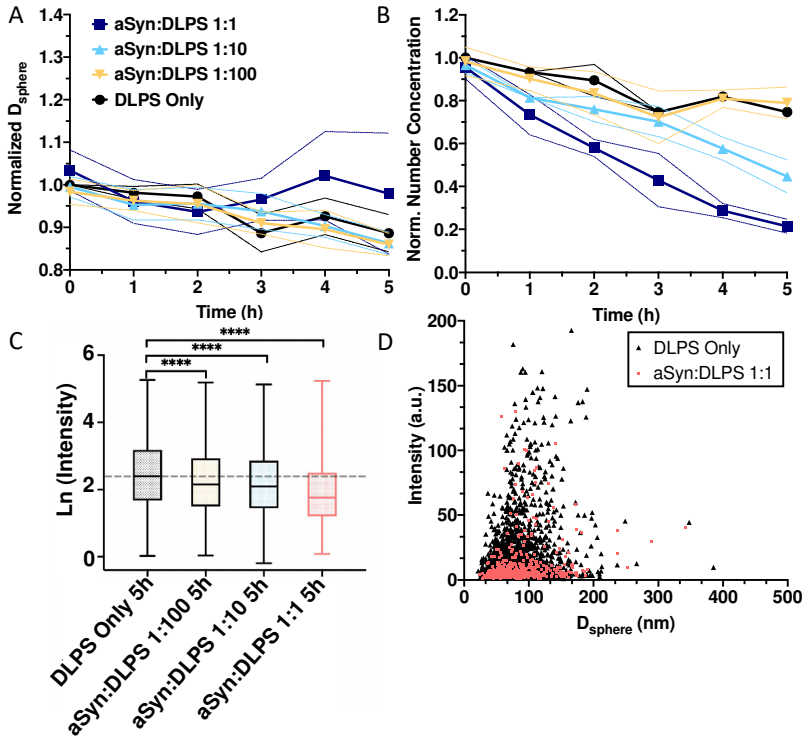


Figure 4. NTA analysis of DLPS LUVS (100 nm nominal size) alone or incubated with aSyn at 1:100, 1:10 or 1:1 P:L molar ratios. Samples were prepared in PBS and measurements taken at room temperature. (A) Number-averaged mean hydrodynamic diameter, normalized to LUVs alone at $t = 0$. Data points are average of 3 replicates and shading indicates standard deviation. (B) Normalized particle number concentration. (C) Representative box-and-whiskers plot of the scattered intensity distribution following 5h of co-incubation. Approximately 15,000 DLPS vesicles in the absence of lipid were tracked and compared with ~14,500 (P:L 1:100), ~9,700 (P:L 1:10), and ~4,400 (P:L 1:1) particles ****p < 0.0001 (unpaired two-tailed t test). (D) Representative comparison of particle size and scattered intensity distribution for DLPS alone and with aSyn at 1:1 molar ratio after 5h.

As a negative control, addition of bovine serum albumin did not cause any vesicle remodeling or shape change in DLPS or DOPS, as assessed by both TEM and NTA (Figure S9). This result indicates that vesicle remodeling is specific to aSyn and not a general property of protein interaction with these vesicles.

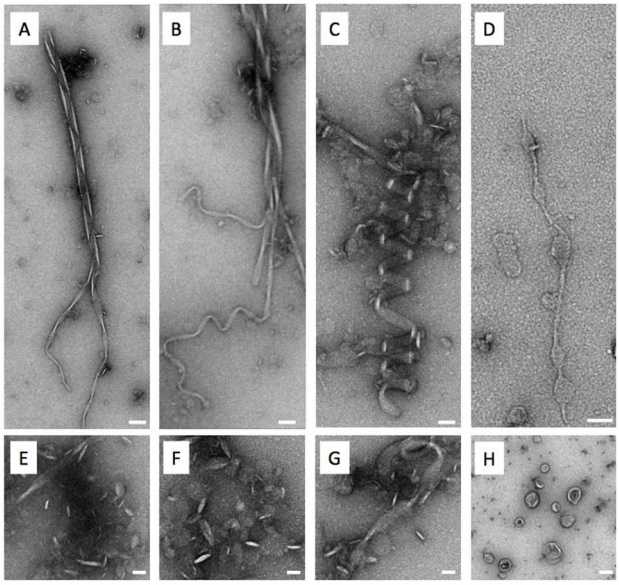


Figure 5. Effect of co-incubation of aSyn with DLPS membranes. (A-B) TEM images exhibiting large twisted and helical ribbons. Scale bar is 100 nm. (C) Helical ribbon. Scale bar is 50 nm. (D) Thin tubules. Scale bar is 100 nm. (E-G) Discoid shapes. Scale bar is 50 nm. (H) DLPS vesicles in the absence of aSyn. Scale bar is 100 nm. Samples were prepared in PBS and incubated for 5 h at room temperature. Images were taken from two independent replicates.

We tested whether the decrease in particle number concentration as measured by NTA could be attributed to vesicle breakup into small discoids. We obtained dimensions of 47 discoids from TEM images and calculated D_{sphere} for these particles to be 27±7 nm (SI), a size slightly below the minimum size detection threshold of the instrument of about 30 nm. We confirmed this detection threshold using IgM, an oblate ellipsoid with hydrodynamic diameter of ~28 nm [29]. To find additional evidence for the existence of these smaller particles, we measured the size distribution of aSyn-DLPS mixtures using dynamic light scattering (DLS), a technique that provides average rather than particle-by-particle size measurements, but is sensitive to much smaller particles compared to NTA. An analysis of the autocorrelation function indeed revealed a bimodal size distribution with peaks centered near 25 nm and 100 nm (Figure S10). Taken

together, this analysis supports our interpretation that the NTA-measured decrease in particle number concentration can be attributed, at least in part, to breakup into small discoids.

We next considered the tubules. To estimate their hydrodynamic properties from dimensions derived from TEM images, we used a semiflexible (wormlike) chain model. We measured contour lengths of 300-700 nm and diameters of 10-20 nm (SI), yielding an estimate of D_{sphere} of 60-100 nm, in reasonably good agreement with the particle sizes detected by NTA as well as the second peak in the particle size distribution obtained by DLS. From tubule dimensions, we calculated the number of lipids per tubule, as well as the number of lipids in a 100 nm-diameter sphere, and concluded that a tubule could form by remodeling of a single vesicle (SI). To interpret the decrease in I_p upon addition of aSyn (Figure 4C), we calculated $P(q)$ of 0.36 to 0.64 for tubules of 300-700 nm length, compared to 0.98 for LUVs (SI). The slow continuing decrease in I_p with time (Figure S8), suggests that aSyn remodeling of LUVs to tubules occurs slowly and continues for hours.

The hydrodynamic properties of the rare helices and ribbons are difficult to calculate; as a rough estimate we calculated D_{sphere} ~375 nm using a hollow cylinder model for the morphology shown in Figure 5A, which has a length of ~1500 nm and diameter of ~70 nm. There are indeed a few particles detected by NTA that are in this size range. Given the large dimensions of these particles, they must arise from fusion of many vesicles, which would also lead to a decrease in number concentration. As a final note, we have previously observed that thin, highly elongated particles are undercounted by NTA, a phenomenon that can be explained by interference effects [50, 51], which would also lead to a decrease in number concentration over time.

Taken together, our combined data are consistent with a remarkable degree of aSyn-induced remodeling of DLPS vesicles into a diversity of morphologies ranging from discoids (a

product of vesicle breakup) to tubules (vesicle rearrangement) to large ribbons and coils (vesicle fusion and restructuring). Moreover, membrane remodeling is a slow process that continues over hours.

Coarse-grained simulations identify differences in aSyn interactions with DOPS versus DLPS

We performed coarse-grained molecular dynamics (MD) simulations using the BMW MARTINI force field to gain molecular insight into the interactions of aSyn monomers with DOPS and DLPS vesicles. This force field permitted simulations of sufficiently large system sizes to observe membrane remodeling while reproducing electrostatics effects that could influence aSyn binding [30, 31, 55]. BMW MARTINI has also been shown to reproduce membrane adsorption behavior observed in more detailed all-atom simulations and experiments [31, 56, 57]. We first modeled aSyn binding to small vesicles to determine if the simulations predict morphology changes that were consistent with our experiments. We self-assembled single-component DOPS and DLPS vesicles (diameters of 9.6 and 9.8 nm, respectively) in the absence of aSyn, then placed 10 evenly spaced aSyn monomers in solution 2 nm from the outer leaflet of each vesicle (Figure 6A and 6D, Figure S11) and allowed the monomers to adsorb to the vesicles in unbiased MD simulations. Simulation of the larger vesicles used in experiments (~100 nm) while maintaining a chemically specific force field such as MARTINI is not computationally tractable. As controls, we also simulated DOPS and DLPS vesicles in the absence of aSyn with the same simulation parameters. All simulation systems (described in SI and Table S1) were simulated twice with different initial configurations and velocities.

The simulations revealed that all 10 aSyn monomers rapidly bind to both vesicles. aSyn binding led to minimal change in the structure of a DOPS vesicle compared to the control (Figure

6B) and the aSyn monomers distributed in clusters with no apparent order on the vesicle surface. The monomer distribution for the final simulation configuration is illustrated by stereographic projections that plot the center-of-mass (COM) positions of the monomers relative to the equatorial plane of the vesicle (Figure 6E). In contrast, aSyn binding induced the elongation of a DLPS vesicle and the accumulation of monomers at the poles of the elongated structure (Figures 6C and 6F). To quantify the extent of deformation of each vesicle from a sphere, we compared the meridional and equatorial eccentricities (Figure S12, Table S2), calculated as $e = \sqrt{1 - b^2/a^2}$, where a and b represent the semi-major and minor axes, respectively. The meridional eccentricity of the DLPS vesicle (0.78 ± 0.01) was much greater than that of the DLPS vesicle in the absence of aSyn (0.49 ± 0.06), while the equatorial eccentricity (0.34 ± 0.08) is similar to that in the absence of aSyn (0.32 ± 0.09). Both the meridional (0.59 ± 0.03) and equatorial (0.36 ± 0.08) eccentricities of the DOPS vesicle increased compared to the DOPS vesicle control (0.38 ± 0.06 and 0.25 ± 0.07, respectively), but to a much lesser degree than the increase of meridional eccentricity of the DLPS vesicle. These results confirm that aSyn binding slightly perturbs the structure of DOPS while significantly elongating the DLPS vesicle. While the simulated vesicles are substantially smaller than those studied experimentally in order to be computationally tractable, these simulation findings are consistent with our experimental observations of a minor deformation of DOPS vesicles and the more pronounced remodeling of DLPS vesicles.

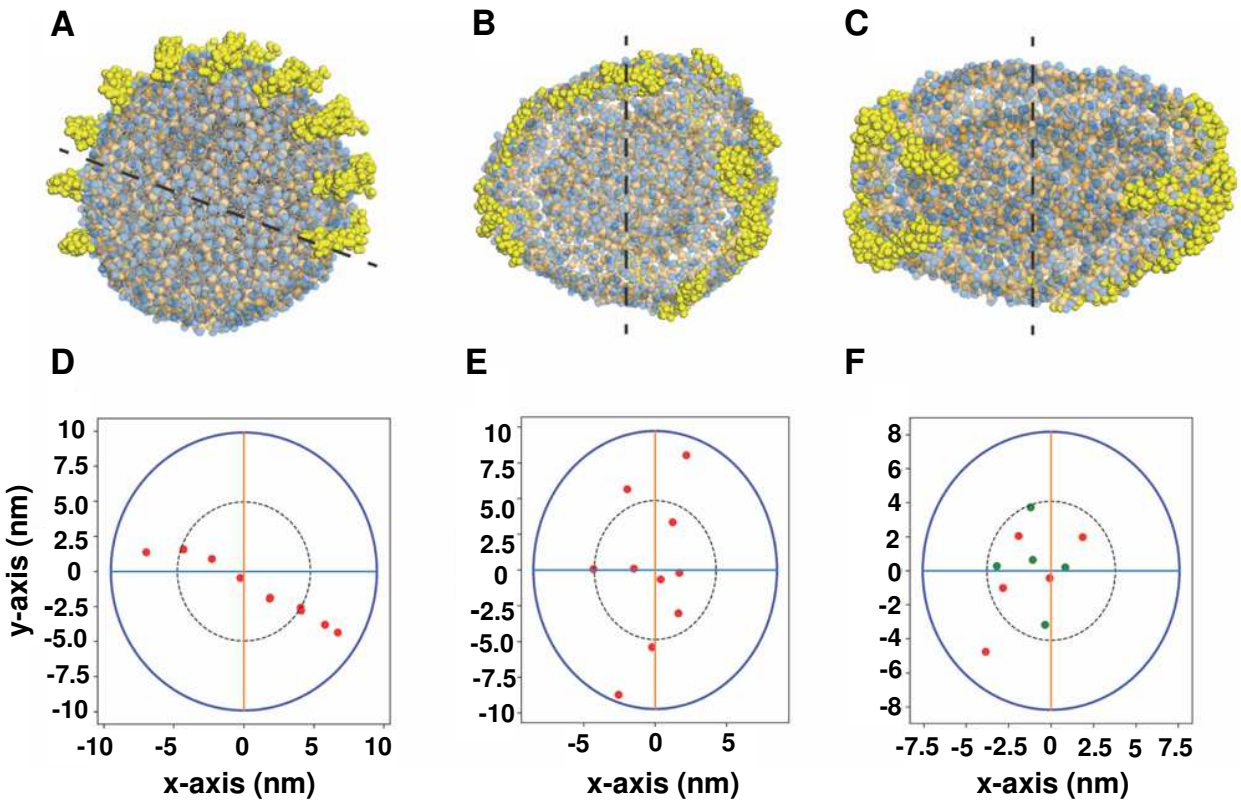


Figure 6. MD simulations of aSyn interaction with DOPS or DLPS vesicles. (A) Initial configuration of 10 aSyn monomers placed near a vesicle surface. (B) DOPS vesicle after equilibration. (C) DLPS vesicle after equilibration. The dashed lines in (B) and (C) indicate the equatorial plane of each vesicle. (D-F) Stereographic projections of the location of the 10 aSyn monomers with respect to the equatorial plane for the simulation snapshots in (A-C). In (F), aSyn monomers above and below the equatorial plane are labeled with green and red points, respectively.

We hypothesized that the difference in the morphology in DOPS vesicles versus DLPS upon adsorption of aSyn arose because of differences in the curvature induced by aSyn binding. To interrogate this hypothesis, we modeled the interactions of a single aSyn monomer with a planar DOPS or DLPS bilayer. To quantify induced curvature, we calculated the change in the time-averaged height of the lipid surface near the bound aSyn monomer (SI). aSyn binding to a planar DOPS bilayer increased the height of the lipid interface around the bound protein parallel to its long axis (Figure S13, Figure S14, Table S3). This result indicates that aSyn induces local positive

curvature in flat DOPS bilayers, consistent with previous reports [37], suggesting that aSyn preferentially binds to positively curved and not flat DOPS bilayers which would tend to stabilize the spherical vesicles. On the other hand, aSyn binding to a planar DLPS membrane led to a smaller increase in the height of the lipid interface relative to the DOPS results, indicating a preference for flatter bilayers with less positive curvature. The response of planar bilayers to aSyn adsorption explains the behavior observed in the vesicle simulations: aSyn binding to the DLPS bilayer flattens the local bilayer curvature, thus driving elongation, because elongation flattens the bilayer along one axis.

The simulations also suggest that aSyn monomers preferentially, although not exclusively, accumulate at the poles of elongated DLPS vesicles (Figure 6C). However, this accumulation was less apparent in a second simulation (Figure S15). We performed additional simulations in which a single monomer diffused on a DLPS vesicle that was restrained in an elongated conformation (Figure S16). In two independent simulations, the monomer aligned its long axis parallel to the long axis of the elongated vesicle and diffused toward the pole. These simulations confirm that the accumulation of aSyn monomers at the poles reflects curvature sensing rather than direct monomer-monomer interactions. Combined, these simulations suggest that there are two apparently contradictory outcomes of aSyn-DLPS interactions: aSyn adsorption tends to flatten and therefore elongate DLPS vesicles, but on the other hand adsorbed aSyn tends to migrate towards the highly curved poles. In the simulation snapshots of Figure S14, migration of an aSyn monomer leads to the disordered tail region (green) binding to the highly curved pole, in agreement with recent simulations indicating that the disordered tail can contribute to curvature [58]. Together, these observations suggest that curvature generation versus curvature sensing could emerge from different conformations of bound aSyn monomers.

Aggregation of aSyn is stimulated by DLPS but not DOPS

Simulation results suggest that aSyn binding can trigger vesicle shape change in DLPS and local accumulation of aSyn monomers at regions of high curvature, which might lead to aggregation. Several groups have shown that, under certain conditions, lipids can accelerate aSyn aggregation [15, 21, 22, 24, 25]. Of particular relevance, Galvagnion et al. reported that DLPS but not DOPS induced aggregation of aSyn at pH 6.5 in the absence of added salt, while DMPS was intermediate in its ability to cause aSyn aggregation [15]. We incubated aSyn with DOPS, DMPS or DLPS LUVs and tested for the formation of amyloid fibrils using the thioflavin T (ThT) fluorescence assay. Samples were incubated in PBS (pH 7.4, 100 mM NaCl) at 30°C and at 37°C. At 30°C we did not observe any aggregation during the course of the study. At 37°C after 168h, a significant increase in ThT fluorescence was observed in DLPS, a smaller increase in DMPS, and virtually no increase in DOPS, while the protein-only control remained ThT-negative (Figure 7A). We repeated the experiment in PB (pH 6.5, 0 mM NaCl) and 30°C, to mimic the conditions used in previously published work [15]. Lowering the salt concentration and pH increased the rate of aggregation significantly as expected, but did not change the order of lipid dependence (Figure 7B). TEM images were taken of aSyn in the presence of DOPS, DMPS, and DLPS after 4, 24 or 48 h of incubation in PB (Figures 7C, 7D and 7E, Figure S17). With DOPS vesicles, the TEM images revealed some incipient tubulation at 5 h and disruption of intact vesicles at 48 h, but no large ribbons or helical coils were observed (Figure 7C). In contrast, with DLPS, significant membrane lysis was evident at 5 h alongside examples of twisted and helical ribbons, with a higher frequency at 24 h (Figure 7E). Similar morphologies, although less frequent, were observed with DMPS (Figure 7D). Comparable morphologies and positive ThT fluorescence were also observed

in aSyn mixed with DLPG liposomes (Figure S18). Thus, there is a strong correlation between the appearance of twisted and helical ribbons and an increase in ThT fluorescence.

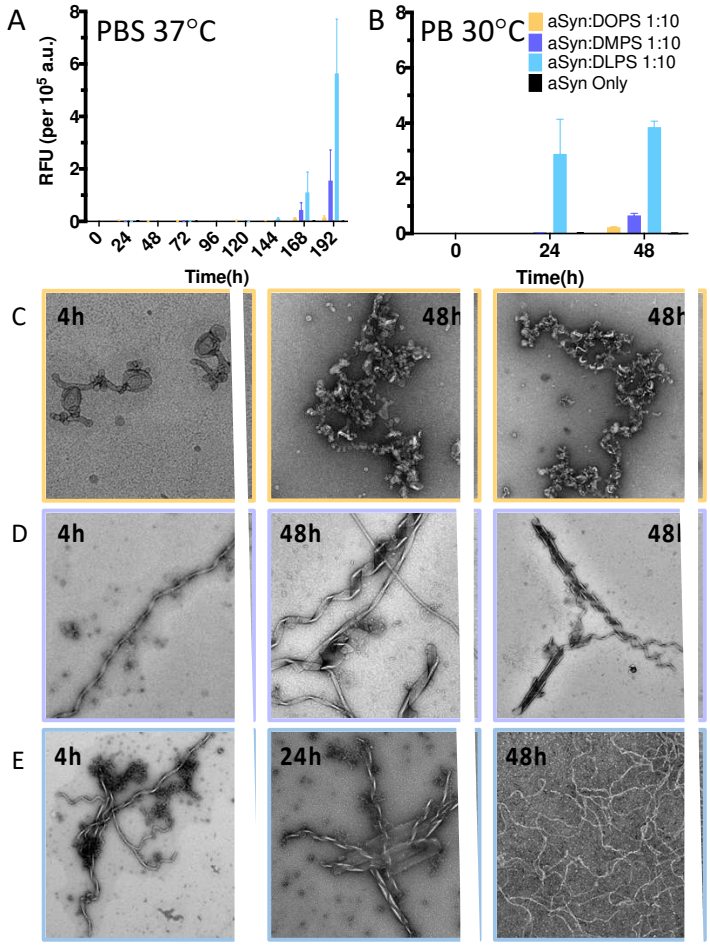


Figure 7. Aggregation propensity and morphology of aSyn incubated in the presence of model membranes. A) ThT fluorescence of aSyn alone (black, 100 μM) or with DOPS (orange), DMPS (purple), DLPS (blue) at a P:L molar ratio of 1:10 in PBS. (B) ThT fluorescence for the same P:L molar ratio (80 μM: 800 μM) in PB (pH 6.5). Data represents the average of three independent replicates and error bars indicate the standard error of the mean. (C-E) TEM images showing representative examples of morphologies observed in the presence of (C) DOPS, (D) DMPS, and (E) DLPS at the indicated time points in PB. Scale bars are 100 nm in all images.

Identically prepared samples were incubated for 48 h. Samples were centrifuged, then the resuspended pellet and supernatant were analyzed separately for protein and lipid content (Table S4, Figure S19), imaged by TEM (Figures 8A, 8B, 8C and 8D) and analyzed for secondary structure by circular dichroism (CD, Figure 8E). The resuspended DOPS pellet contained primarily

intact vesicles with some minor tubulation (Figure 8A). CD spectra were consistent with α-helical secondary structure (Figure 8E), typical of aSyn bound to lipid vesicles (59), and the ThT signal was weak, indicating that the vast majority of aSyn remains lipid-bound in a non-fibrillar form with DOPS. With DLPS, about 10% of protein and lipid were found in the pellet (Table S4). The resuspended pellet contained a polydisperse mixture of morphologies including tubules, ribbons and tapes (Figures 8C and 8D); CD spectra exhibited a broad minimum at ~215-218 nm (Figure 8E), characteristic of β-sheet secondary structure that is typical of amyloid aggregates [59], and the pellet was strongly ThT-positive. In contrast, no coils, ribbons or sheets were observed in the DLPS supernatant (Figure S19C), and CD spectra of the supernatant indicated an α-helical conformation (Figure S19D). This result indicates that a fraction of aSyn is responsible for fibril formation in the presence of DLPS vesicles, while most of the protein remains lipid-bound but not aggregated. Thus, the presence of tubules, ribbons and tapes is associated with the formation of β-sheet and amyloid (ThT-positive) structures. Similarly, the resuspended DMPS pellet contained twisted and helical ribbons (Figure 8B) and CD spectra as well as ThT fluorescence indicated β-sheet secondary structure (Figure 8E), again demonstrating a strong correlation between aSyn-induced membrane remodeling and the conversion of aSyn to β-sheet amyloid aggregates.

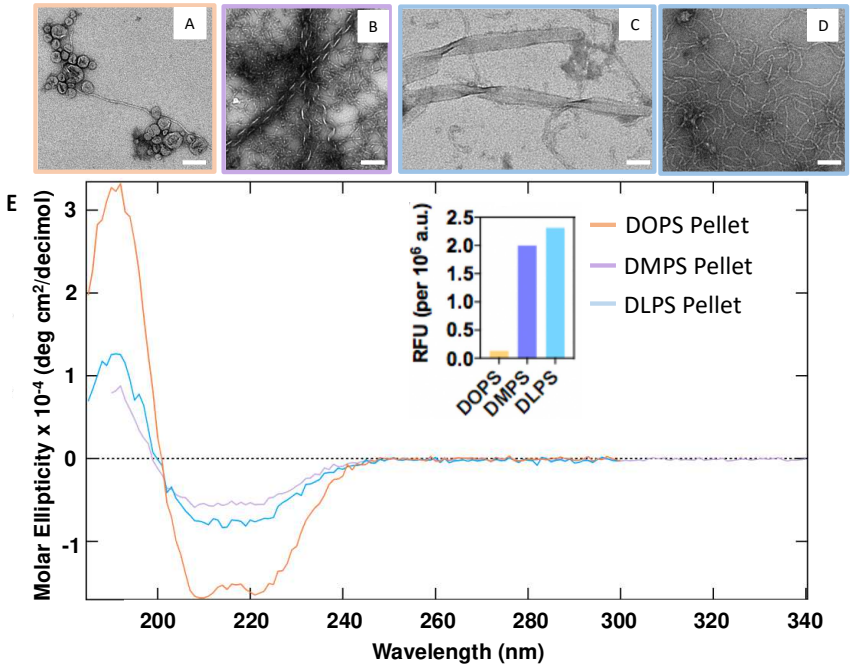


Figure 8. TEM images and CD spectra of resuspended pellets following co-incubation of aSyn and vesicles. (A-D) Samples (P:L 1:10) were incubated in PB for 48 h at 30°C and pelleted by ultracentrifugation. Supernatant was removed and pellets resuspended. TEM images of aSyn with DOPS (orange), DMPS (purple), and DLPS (blue). Scale bar is 100 nm for (A, B and D) and 50 nm for (C). (E) Circular dichroism spectra. Inset shows ThT fluorescence of the pellet following CD.

Discussion

Our investigation was motivated by reports that aSyn aggregation was strongly promoted by DLPS but not DOPS vesicles, despite similar adsorption properties [15]. Using both experiment and simulation, we studied the response of DLPS and DOPS vesicles to aSyn adsorption, prior to the onset of aSyn aggregation. Because of its shorter acyl chain and greater lipid solubility, DLPS vesicles are unstable compared to DOPS vesicles, as evidenced by their inability to encapsulate dye and the slow decrease in vesicle number upon dilution even in the absence of aSyn (Figure 4B). We hypothesized that the lower intrinsic stability of DLPS vesicles would lead to a much stronger remodeling response to aSyn. Indeed, as shown by a combination of NTA, TEM and dye

leakage assays, the interaction of aSyn with DOPS LUVs resulted in a modest change in vesicle shape from spherical to ellipsoidal, but without significant vesicle fusion, tubulation or lysis. In sharp contrast, interaction of aSyn with DLPS LUVs led to formation of a rich heterogeneity of morphologies, including discoids, tubules, and large twisted and helical ribbons.

A novel feature of our work is the combination of NTA and TEM to investigate the response of liposomes to aSyn. Advantageous features of NTA are that the kinetics of membrane remodeling can be followed over time, and information on vesicle size, number and shape is obtained simultaneously, in real time, and without the use of labels, dyes or other reagents. Through NTA, we observed that the increase in size of DOPS LUVs upon addition of aSyn was essentially instantaneous, and vesicle size did not change further over five hours. The constant particle number concentration, as well as the immediate change to a lower scattering intensity, is consistent with a small shift in particle morphology from spherical to ellipsoidal upon aSyn adsorption to DOPS, as evidenced by TEM images. On the other hand, membrane remodeling of DLPS is an extensive and slow process that continues unabated over several hours, a conclusion consistent with the continued decrease over time in measured particle number concentration (Figure 4B) and scattered intensity (Figure S8). Discoids and tubules were the most numerous remodeled species in mixtures of aSyn with DLPS (Figure 5D-F, Figure S10). Discoids are likely the product of pinching off patches of membrane, while tubules likely arise from major restructuring of a single vesicle (SI).

Through coarse-grained MD simulations, we identified a mechanism by which aSyn induces greater remodeling in DLPS compared to DOPS vesicles, recognizing that simulations can capture only the earliest steps in the remodeling process. Specifically, aSyn binding generated greater positive curvature in planar DOPS bilayers compared to DLPS bilayers, which indicates

that aSyn would tend to stabilize sphericity in DOPS to a greater extent than DLPS. Indeed, aSyn binding to spherical DLPS vesicles led to elongation of vesicles to create a long axis with a reduced radius of curvature. The more dramatic remodeling of DLPS compared to DOPS is facilitated by the lower bending rigidity of DLPS bilayers due to its shorter tail. These lipid-dependent curvature preferences are consistent with the dominant remodeled DLPS structures observed by TEM: tubules and discoids have reduced curvature along one (tubule) or two (discoid) axes compared to spheres. Interestingly, aSyn monomers were found to preferentially redistribute towards the higher curvature poles of the elongated DLPS vesicles, with migration to the pole associated with an oriented binding of the disordered tail region. Thus, our simulations indicate that aSyn monomers act as both curvature *modifiers* to drive lipid-dependent membrane remodeling processes [60] and as curvature *sensors* to facilitate protein-mediated crowding. These results are in broad agreement with MD simulations of other curvature-sensing and generating proteins; for example, one study showed that N-BAR domains exhibited a preference for curvature and, at ~50% bound protein density, led to significant local protein crowding [61]. Although more detailed investigations are required to confirm the mechanism underlying these phenomena, these observations suggest that curvature generation versus curvature sensing could emerge from different conformations of bound aSyn monomers, which also may contribute to diverse remodeled structures observed experimentally.

In addition to numerous discoids and tubules in the DLPS samples, we observed larger structures such as sheets, twisted and helical ribbons, and nanotubes (Figures 5A, B and 5C, Figure 7E, Figure S17). These morphologies occurred only in the presence of aSyn, and resemble aggregates formed from self-assembling peptides [62] and selected peptide sequences from amyloidogenic proteins [63, 64], including an amphiphilic 8-residue peptide of aSyn [65]. Generally, the

ribbons, tubes and sheets appeared prior to the detection of amyloid by ThT. TEM, CD and ThT results provide a strong linkage between the formation of these morphologies, adoption of β-sheet secondary structure, and amyloid formation (Figure 8). Although we did not directly test whether the aggregates we observed contained both lipid and protein, the similarity in the fraction of protein and lipid in pelletable fractions (Table S4) suggests that co-assembly likely underlies their formation. These results are consistent with recent studies that have also demonstrated co-assembly of protein and lipid after prolonged incubation [27, 66]. Compositional and structural characterization of the discoids, tubules and large ribbons and coils formed upon co-incubation of aSyn and DLPS is beyond the scope of the current investigation, but would provide further insight into their nature and mechanism of formation.

Local enrichment of protein molecules by adsorption to surfaces is one mechanism by which aSyn aggregation might be accelerated. Experimental support for this hypothesis has been inferred from NMR data that showed molecular crowding of aSyn on the surface of flat nanodiscs, resulting in close spatial proximity of the NAC region that is necessary for aggregation [67]. Our simulations point to a story in which aggregation arises from active responses of aSyn and lipid vesicle to each other. Adsorption of aSyn to a lipid vesicle of low bending rigidity like DLPS drives vesicle elongation, producing regions of variable curvature. Then, the protein redistributes to, and concentrates in, the polar regions of the elongated vesicle. In other words, membrane remodeling induced by aSyn provides the conditions that lead to aSyn crowding and then, presumably, aSyn aggregation.

Whether membrane-remodeling stimulation of aSyn aggregation is a general phenomenon remains an open question. A strong correlation between reduced vesicle integrity (greater lipid solubility) and increased stimulation of aSyn aggregation was observed with PS lipids of variable

chain length, but membrane remodeling was not interrogated and it was assumed that aggregation occurred on stable vesicle surfaces [24]. Vesicle clearance, tubulation, and vesicle leakage were reported upon addition of aSyn to POPG but not POPC [18, 19], but aSyn aggregation was not measured in that study. Similarly, micelles, tubules and discoids were observed with PG vesicles, with morphological differences depending on protein:lipid ratio and length of the acyl chain [26], but again aggregation was not explored. In pioneering work, Lee and coworkers directly explored the relationship between membrane remodeling and aSyn aggregation [27, 28]. Briefly, POPG and POPS were remodeled by aSyn into micellar tubules, and POPG tubules stimulated aSyn aggregation at high but not low protein:lipid ratios; POPS was not tested for its effect on aggregation [27]. In another study, these researchers reported an inverse relationship between membrane remodeling and aSyn aggregation: specifically, vesicles of POPC but not POPC/POPA were tubulated by aSyn, whereas aSyn aggregation was inhibited by POPC and stimulated by POPC/POPA [28]. Interestingly, the binding affinity of aSyn for POPC is much weaker than for lipids with acidic head groups, and aSyn remained disordered and not α-helical when mixed with POPC, so aSyn-induced tubulation of POPC was a somewhat surprising result. The underlying reason for the different relationship between membrane remodeling and aSyn aggregation stimulation in that work versus in our work is unknown. One possible difference is the difference in head group charge, since PA and PS are acidic but PC is zwitterionic. Another is that Lee and coworkers used mechanical agitation which promotes aSyn aggregation in the absence of lipids [8, 68, 69], whereas our experiments were conducted quiescently, under conditions where aSyn alone did not aggregate. In preliminary studies, we observed disruption of DOPS LUVs increased strongly with an increase in shaking intensity, and this disruption correlated with an increase in ThT fluorescence when co-incubated with aSyn (Hoover and Murphy, unpublished observations).

Taken together, our results demonstrate aSyn-mediated membrane remodeling as a precursor to membrane-mediated aSyn aggregation. Phospholipid compositions that reduce bilayer rigidity and membrane stability could facilitate active aSyn-mediated membrane remodeling, likely a key feature of the protein's normal biological function, but may also conversely facilitate pathological aggregation. Thus, age-related changes in lipid composition, such as a greater abundance of shorter fatty acid tails, that lead to reduction in membrane integrity may be important contributors to aSyn aggregation and Parkinson's disease etiology. In agreement with this view, it has recently been identified that Lewy body pathology is characterized by a much larger lipid content than previously thought [3, 4], with an abundance of vesicular structures, dysmorphic organelles, membranous fragments and crowding of aSyn and lipid in Lewy bodies and neurites [5]. Describing the process by which lipid and protein are re-organized into the morphologies identified in this study will be important in understanding the role of lipid in modulating aSyn aggregate structure and pathology *in vivo*.

Conclusions

Using nanoparticle tracking analysis along with electron microscopy, we demonstrate that the response of phosphatidylserine vesicles to adsorption of aSyn is strongly dependent on the acyl chain length. Incubation of aSyn with DOPS vesicles led rapidly to minor changes in vesicle shape from spherical to prolate ellipsoid. In contrast, aSyn dramatically remodeled DLPS vesicles into a diversity of discoids, tubules, ribbons and sheets, in a process that continued for hours. Simulations revealed that adsorption of aSyn to DLPS but not DOPS caused a marked elongation of vesicles, followed by preferential redistribution of the monomers to the highly-curved polar regions of the elongated vesicles, resulting in high localized protein concentrations supportive of accelerated

aggregation. We observed unusual morphologies of twisted and helical ribbons and sheets in mixtures of aSyn and DLPS well before fluorescence detection of amyloid aggregates. Our experimental and computational work challenge the prevailing hypothesis that acidic lipid vesicles nucleate aSyn aggregation by passively providing a surface for protein concentration. Our results point to a more complex story, in which aggregation requires *active* responses of aSyn and membrane to each other. Lipid compositions with lower bending rigidity might facilitate aSyn-mediated membrane remodeling as a part of aSyn's normal role in synaptic vesicle trafficking, but may conversely also facilitate pathological aggregation via the concerted action of its curvature generating and sensing roles. These findings provide new insights into the mechanism by which aSyn-induced membrane remodeling, not simply membrane adsorption, drives lipid-bilayer stimulation of protein aggregation.

Acknowledgements Funding for this work was provided by the National Science Foundation CBET-1703237 and the William F. Vilas Trust of the University of Wisconsin. Computational work used the Extreme Science and Engineering Discovery Environment (XSEDE), which is supported by National Science Foundation grant number ACI-1548562.

References

1. Rocca, W.A. The burden of Parkinson's disease: a worldwide perspective. *The Lancet Neurology* **2018,** *1,* 928–929.

2. Ball, N.; Teo, W.-P.; Chandra, S.; Chapman, J. Parkinson's disease and the environment. *Front. Neurol.* **2019**, *10*, 218.

3. Spillantini, M.G.; Schmidt, M.L.; Lee, V.M.-Y.; Trojanowski, J.Q.; Jakes, R.; Goedert, M. α-Synuclein in Lewy bodies. *Nature* **1997,** *388,* 839–840.

4. Spillantini, M.G., Crowther, R.A.; Jakes, R.; Hasegawa, M.; Goedert, M. Alpha-synuclein in filamentous inclusions of Lewy bodies from Parkinson's disease and dementia with lewy bodies. *Proc. Natl. Acad. Sci. U.S.A.* **1998,** *95*, 6469–6473.

5. Shahmoradian, S.H.; Lewis, A.J.; Genoud, C.; Hench, J.; Moors, T.E.; Navarro, P.P.; Castaño-Díez, D.; Schweighauser, G.; Graff-Meyer, A.; Goldie, K.N., et al. Lewy pathology in Parkinson's disease consists of crowded organelles and lipid membranes. *Nature Neurosci*. **2019**, *22*, 1099–1109.

6. Araki, K.; Yagi, N.; Aoyama, K.; Choong, C.-J.; Hayakawa, H.; Fujimura, H.; Nagai, Y.; Goto, Y.; Mochizuki, H. Parkinson's disease is a type of amyloidosis featuring accumulation of amyloid fibrils of α-synuclein. *Proc. Natl. Acad. Sci. USA*. **2019**, *116*, 17963–17969.

7. Uversky, V.N.; Li, J.; Souillac, P.; Millett, I.S.; Doniach, S.; Jakes, R.; Goedert, M.; Fink, A.L. Biophysical properties of the synucleins and their propensities to fibrillate: inhibition of α-synuclein assembly by β- and γ-synucleins. *J. Biol. Chem.* **2002**, *277*, 11970–11978.

8. Buell, A.K.; Galvagnion, C.; Gaspar, R.; Sparr, E.; Vendruscolo, M.; Knowles, T.P.J.; Linse, S.; Dobson, C.M. Solution conditions determine the relative importance of nucleation and growth processes in α-synuclein aggregation. *Proc. Natl. Acad. Sci. USA*. **2014**, *111*, 7671–7676.

9. Uversky, V.N. A protein-chameleon: conformational plasticity of α-synuclein, a disordered protein involved in neurodegenerative disorders. *J. Biomolec. Struct. Dynam*. **2003,** *21*, 211–234.

10. Jo, E.; McLaurin, J.; Yip, C.M.; St. George-Hyslop, P.; Fraser, P.E. α-Synuclein membrane interactions and lipid specificity. *J. Biol. Chem.* **2000**, *275*, 34328–34334.

11. Davidson, W.S.; Jonas, A.; Clayton, D.F.; George, J.M. 1998, Stabilization of α-synuclein secondary structure upon binding to synthetic membranes. *J. Biol. Chem.* **1998,** *273*, 9443–9449.

12. Georgieva, E.R.; Ramlall, T.F.; Borbat, P.P.; Freed, J.H.; Eliezer, D. 2010. The lipid-binding domain of wild type and mutant α-synuclein: compactness and interconversion between the broken and extended helix forms. *J. Biol. Chem.* **2010**, *285*, 28261–28274.

13. Shvadchak, V.V.; Falomir-Lockhart, L.J.; Yushchenko, D.A.; Jovin, T.M. Specificity and kinetics of α-synuclein binding to model membranes determined with fluorescent excited state intramolecular proton transfer (ESIPT) probe. *J. Biol. Chem.* **2011**, *286*, 13023–13032.

14. Middleton, E.R.; Rhoades, E. Effects of curvature and composition on α-synuclein binding to lipid vesicles. *Biophys. J*. **2010**, *99*, 2279–2288.

15. Galvagnion, C.; Brown, J.W.P.; Ouberai, M.M.; Flagmeier, P.; Vendruscolo, M.; Buell, E. Sparr, A.K.; Dobson, C.M. Chemical properties of lipids strongly affect the kinetics of the membrane-induced aggregation of α-synuclein. *Proc. Natl. Acad. Sci. USA*. **2016**, *113*, 7065–7070.

16. Nuscher, B.; Kamp, F.; Mehnert, F.; Odoy, F.; Haass, C.; Kahle, P.J.; Beyer, K. α-Synuclein has a high affinity for packing defects in a bilayer membrane: a thermodynamics study. *J. Biol. Chem.* **2004**, *279*, 21966–21975.

17. Ouberai, M.M.; Wang, J.; Swann, M.J.; Galvagnion, C.; Guilliams, T.; Dobson, C.M.; Welland, M.E. α-Synuclein senses lipid packing defects and induces lateral expansion of lipids leading to membrane remodeling. *J. Biol. Chem.* **2013**, *288*, 20883–20895.

18. Varkey, J.; Isas, J.M.; Mizuno, N.; Jensen, M.B.; Bhatia, V.K.; Jao, C.C.; Petrlova, J.; Voss, J.C.; Stamou, D.G.; Steven, A.C.; Langen, R. Membrane curvature induction and tubulation are common features of synucleins and apolipoproteins. *J. Biol. Chem.* **2010**, *285*, 32486–32493.

19. O'Leary, E.I.; Lee, J.C. Interplay between α-synuclein amyloid formation and membrane structure. *Biochim. Biophys. Acta Prot. Proteom*. **2019**, *1867*, 483–491.

20. Westphal, C.H.; Chandra, S.S. Monomeric synucleins generate membrane curvature. *J. Biol. Chem.* **2013**, *288*,1829–1840.

21. Grey, M.; Linse, S.; Nilsson, H.; Brundin, P.; Sparr, E. Membrane interaction of α-synuclein in different aggregation states. *J. Parkinson's Dis*. **2011**, *1*, 359–371.

22. Grey, M.; Dunning, C.J.; Gaspar, R.; Grey, C.; Brundin, P.; Sparr, E.; Linse, S. Acceleration of α-synuclein aggregation by exosomes. *J. Biol. Chem.* **2015**, *290*, 2969–2982.

23. Gaspar, R.; Pallbo, J.; Weininger, U.; Linse, S.; Sparr. E. 2018. Ganglioside lipids accelerate α-synuclein amyloid formation. *Biochim. Biophys. Acta Prot. Proteom*. **2018**, *1866*, 1062–1072.

24. Galvagnion, C.; Buell, A.K.; Meisl, G.; Michaels, T.C.T.; Vendruscolo, M.; Knowles, T.P.J.; Dobson, C.M. Lipid vesicles trigger α-synuclein aggregation by stimulating primary nucleation. *Nature Chem. Biol*. **2015**, *11*, 229–234.

25. Zhu, M.; Li, J.; Fink, A.L. The association of α-synuclein with membranes affects bilayer structure, stability, and fibril formation. *J. Biol. Chem.* **2003**, *278*, 40186–40197.

26. Mizuno, N.; Varkey, J.; Kegulian, N.C.; Hegde, B.G.; Cheng, N.; Langen, R.; Steven, A.C. Remodeling of lipid vesicles into cylindrical micelles by α-synuclein in an extended α-helical conformation. *J. Biol. Chem.* **2012**, *287*, 29301–29311.

27. Jiang, Z.; Flynn, J.D.; Teague, W.E.; Gawrisch, K.; Lee, J.C. Stimulation of α-synuclein amyloid formation by phosphatidylglycerol micellar tubules. *Biochim. Biophys. Acta Biomembranes*. **2018**, *1860*, 1840–1847.

28. Jiang, Z.; de Messieres, M.; Lee, J.C. Membrane remodeling by α-synuclein and effects on amyloid formation. *J. Am. Chem. Soc.* **2013**, *135*, 15970–15973.

29. Hoover, B.M.; Murphy, R.M. Evaluation of nanoparticle tracking analysis for the detection of rod-shaped particles and protein aggregates. *J. Pharm. Sci*. **2020**, *109*, 452–463.

30. Wu, Z.; Cui, Q.; Yethiraj, A. A new coarse-grained model for water: the importance of electrostatic interactions. *J. Phys. Chem. B*. **2010**, *114*, 10524–10529.

31. Wu, Z.; Cui, Q.; Yethiraj, A. A new coarse-grained force field for membrane–peptide simulations. *J. Chem. Theory Comput.* **2011**, *7*, 3793–3802.

32. Ulmschneider, J.P.; Smith, J.C.; White, S.H.; Ulmschneider, M.B. In silico partitioning and transmembrane insertion of hydrophobic peptides under equilibrium conditions. *J. Am. Chem. Soc.* **2011**, *133*, 15487–15495.

33. Noé, F.; Schütte, C.; Vanden-Eijnden, E.; Reich, L.; Weikl, T.R. Constructing the equilibrium ensemble of folding pathways from short off-equilibrium simulations. *Proc. Natl. Acad. Sci. USA*. **2009**, *106*, 19011–19016.

34. Chng, C.-P. Effect of simulation temperature on phospholipid bilayer–vesicle transition studied by coarse-grained molecular dynamics simulations. *Soft Matter*. **2013**, *9*, 7294.

35. Brandt, E.G.; Braun, A.R.; Sachs, J.N.; Nagle, J.F.; Edholm, O. Interpretation of fluctuation spectra in lipid bilayer simulations. *Biophys. J.* **2011**, *100*, 2104–2111.

36. Pan, J.; Tristram-Nagle, S.; Kučerka, N.; Nagle, J.F. Temperature dependence of structure, bending rigidity, and bilayer interactions of dioleoylphosphatidylcholine bilayers. *Biophys. J*. **2008**, *94*, 117–124.

37. Braun, A.R.; Lacy, M.M.; Ducas, V.C.; Rhoades, E.; Sachs, J.N. α-Synuclein-induced membrane remodeling is driven by binding affinity, partition depth, and interleaflet order asymmetry. *J. Am. Chem. Soc.* **2014**, *136*, 9962–9972.

38. Braun, A.R.; Lacy, M.M.; Ducas, V.C.; Rhoades, E.; Sachs, J.N. α-Synuclein's uniquely long amphipathic helix enhances its membrane binding and remodeling capacity. *J. Membrane Biol*. **2017**, *250*, 183–193.

39. Kim, H.-Y.; Huang, B.X.; Spector, A.A. Phosphatidylserine in the brain: Metabolism and function. *Prog. Lipid Res*. **2014**, *56*, 1–18.

40. Almeida, P.F.; Pokorny, A. Mechanisms of antimicrobial, cytolytic, and cell-penetrating peptides: From kinetics to thermodynamics. *Biochem.* **2009**, *48*, 8083–8093.

41. Apellániz, B.; Nieva, J.L.; Schwille, P.; García-Sáez, A.J. All-or-none versus graded: Single-vesicle analysis reveals lipid composition effects on membrane permeabilization. *Biophys. J.* **2010**, *99*, 3619–3628.

42. Filipe, V.; Hawe, A.; Jiskoot, W. Critical evaluation of nanoparticle tracking analysis (NTA) by nanosight for the measurement of nanoparticles and protein aggregates. *Pharm. Res*. **2010**, *27*, 796–810.

43. Dragovic, R.A.; Gardiner, C.; Brooks, A.S.; Tannetta, A.S.; Ferguson, D.J.P.; Hole, P.; Carr, B.; Redman, C.W.G.; Harris, A.L.; Dobson, P.J., et al. Sizing and phenotyping of cellular vesicles using nanoparticle tracking analysis. *Nanomedicine: Nanotechnol. Biol. Med*. **2011,** *7*, 780–788.

44. Gang, H.; Galvagnion, C.; Meisl, G.; Müller, T.; Pfammatter, M.; Buell, A.K.; Levin, A.; Dobson, C.M.; Mu, B.; Knowles, T.P.J. Microfluidic diffusion platform for characterizing the sizes of lipid vesicles and the thermodynamics of protein–lipid interactions. *Anal. Chem.* **2018**, *90*, 3284–3290.

45. Burré, J.; Sharma, M.; Südhof, T.C. α-Synuclein assembles into higher-order multimers upon membrane binding to promote SNARE complex formation. *Proc. Natl. Acad. Sci. USA*. **2014**, *111*, E4274–E4283.

46. Jao, C.C.; Hegde, B.G.; Chen, J.; Haworth, I.S.; Langen, R. Structure of membrane-bound -synuclein from site-directed spin labeling and computational refinement. *Proc. Natl. Acad. Sci. USA*. **2008**, *105*, 19666–19671.

47. Pfefferkorn, C.M.; Jiang, Z.; Lee, J.C. Biophysics of α-synuclein membrane interactions. *Biochim. Biophys. Acta Biomem*. **2012**, *1818*,162–171.

48. Nelson, D.L.; Cox, M.M.; A.A. Hoskins. *Lehninger: Principles of Biochemistry*. Eighth edition. W. H. Freeman, New York, N. Y. 2021.

49. Dikiy, I.; Eliezer, D. Folding and misfolding of alpha-synuclein on membranes. *Biochim. Biophys. Acta Biomem*. **2012**, *1818*, 1013–1018.

50. Yang, D.T.; Lu, X.; Fan, Y.; Murphy, R.M. Evaluation of nanoparticle tracking for characterization of fibrillar protein aggregates. *AIChE J.* **2014**, *60*, 1236–1244.

51. Murphy, R. M.; Lee, C. C. In Misbehaving Proteins: Protein (Mis)folding, Aggregation, and Stability. Murphy, R. M.; Tsai, A. M., Eds. Springer, New York, N.Y. 2006; pp 147-165.

52. Zhao, H.; Brown, P.H.; Schuck, P. 2011. On the distribution of protein refractive index increments. *Biophys. J*. **2011**, *100*, 2309–2317.

53. Theisen, A. *Refractive Increment Data-Book for Polymer and Biomolecular Scientists*. Nottingham University Press, Nottingham, U.K. 2000.

54. Mathai, J.C.; Tristram-Nagle, S.; Nagle, J.F.; Zeidel, M.L. Structural determinants of water permeability through the lipid membrane. *J. Gen. Physiol*. **2008**, *131*, 69–76.

55. Wu, Z.; Cui, Q.; Yethiraj, A. Why do arginine and lysine organize lipids differently? Insights from coarse-grained and atomistic simulations. *J. Phys. Chem. B*. **2013**, *117*, 12145–12156.

56. Sheavly, J.K.; Pedersen, J.A.; Van Lehn, R.C. Curvature-driven adsorption of cationic nanoparticles to phase boundaries in multicomponent lipid bilayers. *Nanoscale* **2019**, *11*, 2767–2778.

57. Das, M.; Dahal, U.; Mesele, O.; Liang, D.; Cui, Q. Molecular dynamics simulation of interaction between functionalized nanoparticles with lipid membranes: Analysis of coarse-grained models. *J. Phys. Chem. B*. **2019**, *123*, 10547–10561.

58. Caparotta, M.; Bustos, D.M.; Masone, D. Order–disorder skewness in alpha-synuclein: a key mechanism to recognize membrane curvature. *Phys. Chem. Chem. Phys.* **2020**, *22*, 5255–5263.

59. Greenfield, N.J. Using circular dichroism spectra to estimate protein secondary structure. *Nat Protoc*. **2006**, 1, 2876–2890.

60. West, A.; Brummel, B.E.; Braun, A.R.; Rhoades, E.; Sachs, J.N. Membrane remodeling and mechanics: Experiments and simulations of α-synuclein. *Biochim. Biophys. Acta Biomembranes*. **2016**, *1858*, 1594–1609.

61. Simunovic, M.; Srivastava, A.; Voth, G.A. Linear aggregation of proteins on the membrane as a prelude to membrane remodeling. *Proc. Nat. Acad. Sci. USA* **2013**, *110*, 20396–20401.

62. Dehsorkhi, A.; Castelletto, V.; Hamley, I.W. Self-assembling amphiphilic peptides. *J. Pept. Sci.* **2014**, *20*, 453–467.

63. Adamcik, J.; Mezzenga; R. Amyloid polymorphism in the protein folding and aggregation energy landscape. *Angew. Chem. Int. Ed.* **2018**, *57*, 8370–8382.

64. Reynolds, N.P.; Adamcik, J.; Berryman, J.T.; Handschin, S.; Zanjani, A.A.H.; Li, W.; Liu, K.; Zhang, A.; Mezzenga. R. Competition between crystal and fibril formation in molecular mutations of amyloidogenic peptides. *Nature Commun*. **2017**, *8*, 1338.

65. Morris, K.L.; Zibaee, S.; Chen, L.; Goedert, M.; Sikorski, P.; Serpell, L.C. The structure of cross-β tapes and tubes formed by an octapeptide, αSβ1. *Angew. Chem. Int. Ed.* **2013**, *52*, 2279–2283.

66. Galvagnion, C.; Topgaard, D.; Makasewicz, K.; Buell, A.K.; Linse, S.; Sparr, E.; Dobson, C.M. Lipid dynamics and phase transition within α-synuclein amyloid fibrils. *J. Phys. Chem. Lett.* **2019**, *10*, 7872–7877.

67. Viennet, T.; Wördehoff, M.M.; Uluca, B.; Poojari, C.; Shaykhalishahi, H.; Willbold, D.; Strodel, B; Heise, H.; Buell, A.K.; Hoyer, W.; Etzkorn, M. Structural insights from lipid-bilayer nanodiscs link α-synuclein membrane-binding modes to amyloid fibril formation. *Commun Biol*. **2018**, 1, 44.

68. Campioni, S.; Carret, G.; Jordens, S.; Nicoud, L. ; Mezzenga, R.; Riek, R. The presence of an air–water interface affects formation and elongation of α-synuclein fibrils. *J. Am. Chem. Soc.* **2014**, *136*, 2866–2875.

69. Kiskis, J.; Horvath, I.; Wittung-Stafshede, P.; Rocha, S. Unraveling amyloid formation paths of Parkinson's disease protein α-synuclein triggered by anionic vesicles. *Quart. Rev. Biophys.* **2017**, *50*:e3.

Supplemental Information for Chapter 8

Supplemental Experimental Methods

Carboxyfluorescein dye leakage. 5-6-carboxyfluorescein (CF) (100 mM) was used to measure liposome integrity as previously described [1,2]. Briefly, lipids were resuspended in quenched CF and samples were incubated at 40°C for 30 minutes. Each sample was sonicated for 30 minutes in an ice-water bath using a probe-tip sonicator and centrifuged for 5 minutes at 10,000 x g. Samples were frozen and thawed 5 times using an ethanol/dry ice bath and then extruded 21 times through a 100-nm polycarbonate membrane using an Avanti Mini-Extruder (Avanti Lipids) on a hot plate set to 40°C. Vesicles were separated from free CF using Sephadex G-25 PD-10 columns (GE Healthcare). Dye leakage was monitored at an excitation of 470 nm and emission of 525 nm using a QuantaMaster spectrofluormeter (PTI, Birmingham, NJ). Vesicles (100 μM) were mixed with aSyn in protein:lipid (P:L) molar ratios of 1:1, 1:10, and 1:100. Fluorescence measurements were recorded for 60 minutes. Triton X-100 (Sigma) (0.1% vol/vol) was used to obtain the maximum fluorescence (f_{max}) at the end of data collection. The background fluorescence at time 0 (f_0) and leakage in the absence of protein was subtracted from the raw data. Total percentage of dye leakage was calculated using the equation $f_{normalized} = (f_x\text{-}f_0)/(f_{max} - f_0)$ x 100.

Dynamic Light Scattering (DLS). aSyn (150 μM) and 100 nm DLPS vesicles (150 μM) in PBS were separately filtered through a 0.22-μm syringe filter (Millipore) before mixing into a precleaned quartz cuvette. The cuvette was placed into a bath containing refractive index matching decahydronaphthalene (Sigma) and equilibrated to 23°C. Measurements were taken at 90° scattering angle using a Brookhaven BI-200SM and Innova 90C (Coherent, Inc.) 488 nm, 150 mW argon laser. Autocorrelation data were collected for 5 min following 24h of co-incubation.

CONTIN fit to the autocorrelation function was used to determine a scattered intensity size distribution [3].

Stewart Assay. Relative lipid concentrations in the supernatant and pellet were determined by the Stewart assay[4]. Briefly, 2 mL of ferrothiocyanate was mixed with 2 mL of chloroform. Samples were added and mixed vigorously and then centrifuged at 1000 rpm for 5 minutes. To determine lipid concentrations a standard curve was generated from DOPS between 0.01 mg and 0.1 mg in duplicate, and the absorbance of samples was measured at 452 nm and compared. Supernatant and pellet fractions were measured at the same wavelength and the percentage of lipid in the supernatant and pellet was determined.

Supplemental Simulations Methods

Coarse-Grained Molecular Dynamics Simulations. Coarse-grained molecular dynamics (MD) simulations were performed using the BMW MARTINI force field, which combines approximately four non-hydrogen atoms into single beads to model the interactions of protein, water, and lipids. Simulations were performed using GROMACS 2016 [5]. Equations of motion were integrated using the leapfrog algorithm with a time step of 20 fs. All simulations used the force field cutoffs and parameters recommended by the BMW MARTINI developers.

Simulations were performed to model the adsorption of aSyn to DOPS and DLPS vesicles and planar bilayers. 2048 lipid molecules were used in all systems. The 140 amino acids of aSyn (PDB ID: 1XQ8) were represented by 272 coarse-grained beads. The secondary structure of aSyn was selected as a broken alpha helix, where the residues 3-37 and 45-92 were modeled as alpha helices and the other residues as random coils [6]. The secondary structure was constrained during

the simulations because aSyn is known to maintain alpha-helical structures upon bilayer adsorption. The components of all systems are listed in Table S1.

We selected the BMW MARTINI force field because the original MARTINI force field lacks a dipole on its water molecules and assumes of a system-wide dielectric constant of 15, and thus is unreliable for highly charged systems like the anionic bilayers studied here[7]. Prior work has found that the polarizable water model used with MARTINI can also lead to spurious results for interfacial adsorption [8,9]. Consequently, we chose BMW MARTINI to more accurately model the electrostatic interactions between aSyn residues and charged lipids. Since the BMW MARTINI force field overestimates bilayer mechanical properties [10], including the area compressibility modulus, bending rigidity, and line tension, we performed all simulations (unless otherwise noted) at an elevated temperature of 360 K to reduce the bending rigidity and enhance sampling. The bending rigidities of DOPS at 360K and 300K were calculated from simulations to be 8.4±1.1 x 10^{-20} J and 9.4 ±1.7 x 10^{-20} J, respectively. The value at 360K is similar to the experimental value of the bending rigidity of DOPC at 300K, which has been measured to be 8.22 x 10^{-20} J and is estimated to be comparable to the bending rigidity of DOPS due to the similar tail groups[11]. For DLPS, bending rigidities were calculated to be 7.6±0.6 and 8.1±0.8 x 10^{-20} J at 360K and 300K, respectively. To our knowledge there are no experimental data for the bending rigidity of DLPS, although decreasing the tail length of lipids with PC head groups decreases experimentally determined bending rigidities in agreement with these calculations[11].

To test the effect of temperature on vesicle elongation, we simulated the vesicle systems with 10 aSyn monomers adsorbed on the surface at temperatures ranging 300-360 K in 20 K intervals. For these simulations, we used the standard MARTINI force field with 10% of the water beads set as “antifreeze” beads to prevent spurious ion or water clustering. We quantify elongation

based on the meridonal and equatorial eccentricities after 300 ns of simulation time, which we found to be sufficient for convergence at all temperatures. Table S2 shows both eccentricities as a function of temperature. The meridional eccentricities at 360K are 0.76 $\pm$ 0.02 and 0.62 $\pm$ 0.04 for DLPS and DOPS, respectively, which are within error of the values obtained from simulations using BMW MARTINI (0.78 $\pm$ 0.01 and 0.59 $\pm$ 0.03, respectively). These similar values obtained by the two force fields suggests that we can determine the effect of temperature by using the regular MARTINI force field, which is more computationally efficient than BMW MARTINI. The snapshots in Figure S11 further highlight that aSyn monomers accumulate at the poles of elongated DLPS vesicles but do not induce elongation or aggregate for DOPS vesicles in agreement with the BMW MARTINI simulations. The meridional eccentricities of DLPS are greater than those of DOPS for all temperatures (with no consistent differences in equatorial eccentricites). We also observe that the difference between the meridonal and equatorial eccentricities is consistently higher for DLPS than DOPS, although this difference is less pronounced at lower simulation temperatures. Together, these two observations indicate that the greater elongation of DLPS than DOPS vesicles is not dependent on the simulation temperature.

Planar bilayers were composed of 1024 DOPS or DLPS molecules in each leaflet and had initial dimensions of 25 x 25 x 25 nm^3. A single aSyn monomer was initially placed ~2 nm above the upper leaflet of the bilayer and associated counterions were added to solution. Each aSyn-bilayer system was equilibrated in the *NPT* ensemble at 1 bar and 360 K using a Berendsen thermostat and a semi-isotropic Berendsen barostat[12] for 200 ns, followed by a production run of 700 ns using a Nosé-Hoover thermostat [13,14] and a semi-isotropic Parrinello-Rahman barostat [15,16] with time constants of 4 ps. The entire workflow was repeated twice for each bilayer composition, using different initial aSyn configurations. During these simulations, aSyn monomers partially

inserted into the bilayer; insertion depths are listed in Table S3. To characterize key interactions that influence insertion, we generated maps (Figure S13) that count the time-averaged number of contacts between aSyn residues and lipid head and tail groups. A contact was counted if a protein side chain bead was within 0.5 nm of either a lipid head group bead or lipid tail group bead. In both bilayers, the most probable interactions are between negatively charged lipid phosphate beads (PO4) and positively charged beads in the two helices of the protein (residue numbers 6, 10, 23, 43, 45, 58, 80, 96, and 97 which are all cationic lysine or arginine residues) as expected based on their opposing charges.

The initial configurations of the DOPS and DLPS vesicles were generated by inserting additional water molecules on the x- and y- boundaries of the equilibrated bilayers described above, resulting in x-y dimensions of 35 x 35 nm^2. This procedure results in a free boundary between the bilayer and water. The aSyn monomer added for the aSyn-bilayer simulations was then removed and the bilayer was simulated for 150 ns in an anisotropic *NPT* ensemble using a Berendsen thermostat and barostat at 1 bar and 300 K, resulting in vesicle self-assembly. Self-assembly at a lower temperature ensures reasonable vesicle structural properties. The resulting DOPS and DLPS vesicle diameters were ~9.6 nm and ~8.9 nm, respectively. 10 aSyn monomers were then evenly distributed on the outer layer of each vesicle. We also performed control simulations of vesicles in the absence of aSyn to identify effects associated with aSyn binding. The aSyn-vesicle systems were equilibrated in an anisotropic *NPT* ensemble at 1 bar and 300 K for 120 ns (Berendsen thermostat and barostat with time constants of 2 ps), followed by a production run in the *NVT* ensemble at 360 K for 300 ns using a Nosé-Hoover thermostat with a time constant of 4 ps. 300 ns was sufficient for vesicle structural parameters to plateau (Figure

S12). All aSyn-vesicle systems were modeled twice, starting from different initial velocities and aSyn configurations.

Simulations were also performed to study the diffusion of individual aSyn monomers on the outer leaflet of an elongated DLPS vesicle. In these simulations, 9 of the 10 aSyn monomers (excluding one of the two highlighted monomers) and their associated counterions were removed from the final configuration of the aSyn-vesicle production trajectory, leaving a single bound aSyn monomer and elongated DLPS vesicle that was used as a new initial configuration (simulation components are listed as DLPS Vesicle 3 in Table S1). The two possible monomers which were retained in the simulations were selected based on their proximity to the center of the elongated vesicle. The two test monomers are drawn as pink and orange in Figure S15B. The elongated shape of the DLPS vesicle was maintained by restraining the phosphate beads at the two poles to their initial positions using a force constant of 1000 kJ/(mol nm^2) in each Cartesian direction. In the first replica of this protocol (using the pink monomer in Figure S15B), the first simulation was performed for 260 ns with 100 phosphate beads at each pole restrained (Figure S16A). After the aSyn monomer moved close to the restrained beads at one pole (Figure S16B), a second simulation was performed for 240 ns with 30 phosphate beads at each pole restrained (Figure S16C). Again, the aSyn monomer moved closer to the pole (Figure S16D). A third simulation was then conducted for 240 ns with 24 phosphate beads restrained (Figure S16E), and no further migration was observed. In the second replica of this protocol (using the orange monomer in Figure S15B), only one simulation was performed for 260 ns with 100 phosphate beads at each pole restrained (Figure S16G). This series of simulations indicates that aSyn monomers diffuse toward the higher curvature poles of the elongated vesicle independent of the number of restrained DLPS lipids. All

diffusion simulations were performed in the *NVT* ensemble at 360 K using a Nosé-Hoover thermostat with a time constant of 4 ps.

Simulation Analysis.

Vesicle eccentricities: In order to calculate the eccentricities of vesicles, the lengths of the three principle axes of an ellipsoid were fitted using the coordinates of phosphate beads of the outer vesicle leaflet (Figure S12). The eccentricities from the last 150 ns of the aSyn-vesicle production trajectories were averaged to obtain the values reported in the main text and Figure S12.

aSyn insertion depth: The insertion depth of an aSyn monomer on a planar DLPS or DOPS bilayer (Table S3) was defined as the z-component of the distance between the center of mass (COM) of the first 99 residues of aSyn and the COM of the phosphate beads of the upper leaflet.

Bilayer height: The midplane height of a planar bilayer, $h(x, y)$, was defined based on the z-positions of the phosphate beads. For each simulation configuration, the z-positions of lipids in the upper and lower leaflets were interpolated using cubic splines onto a square grid (each point separated by 0.2 nm) that spanned the x-y plane. The midplane height was then defined at each grid point as the average of the upper and lower leaflet z-positions. To maintain a consistent coordinate system relative to a bound aSyn monomer, the COM of the first 99 residues of aSyn were defined as the origin of the coordinate system and the coordinates of all beads were rotated for each simulation configuration to align the long axis of the monomer with the x-axis. The midplane height was then time-averaged using the last 200 ns of the aSyn-bilayer production trajectories and used to generate the height contour maps in Figure S14, as well as the insertion depth and area per lipid in Table S3.

Bending rigidity: The bending rigidities of the DLPS and DOPS bilayers were calculated in the absence of aSyn from the power spectrum of the height fluctuations $\langle|h(\boldsymbol{q})|^2\rangle$, which is given by $\langle|h(\boldsymbol{q})|^2\rangle = \frac{k_B T}{K_c q^4}$, where h is the bilayer surface height, $\boldsymbol{q}$ is the wavenumber in nm^{-1}, K_c is the bending rigidity, k_B is the Boltzmann's constant, and T is the temperature[17]. The values of $q^4\langle|h(\boldsymbol{q})|^2\rangle$ with wavelength greater than twice the bilayer thickness (> 6.8 nm and > 9.8 nm for DLPS and DOPS, respectively) were averaged to determine the K_c.

Supplemental Analysis of Particle Shapes

Spheres. Scattering from liposomes is well described by $P(q)_{sphere}$ of a solid sphere with radius R <100 nm[18], given by the expression:

$$P(q)_{sphere} = 9\left[\frac{\sin x - x\cos x}{x^3}\right]^2$$

(Eq. S1)

where $x = qR$, $q = (4\pi n/\lambda)sin(\theta/2)$, n = solvent refractive index, λ = wavelength of incident beam and θ = scattering angle. We used θ = 90° for all calculations; for NTA the scattering angle is between 70 and 100° [19].

Prolate ellipsoids. aSyn:DOPS complexes were modeled as prolate ellipsoids. The equivalent hydrodynamic diameter D_{sphere} for prolate ellipsoids was calculated from [20]:

$$D_{sphere} = \frac{l\sqrt{r^2-1}}{r}\frac{1}{ln\,[r+\sqrt{r^2-1}]} \text{ for (r > 1)}$$

(Eq. S2)

where *r* and *l* represent the axial ratio (major axis to minor axis) and major axis of the ellipsoid, respectively. *P(q)* for ellipsoids is given by [21]:

$$P(q)_{ellipsoid} = \int_0^{\pi/2} [\Phi(qR')]^2 \sin(\alpha)\, d\alpha$$

(Eq. S3)

where

$$R' = R(\sin^2 \alpha + l^2 \cos^2 \alpha)^{1/2}$$

and

$$\Phi(qR') = \frac{3[\sin qR' - qR' \cos qR']}{qR'^3}$$

where *R* is the equatorial radius, l is the axial ratio, and α is the angle of integration.

Discoids. Discoid particles were observed in TEM images of mixtures of aSyn with DLPS. The diameter d_{disk} and thickness *t* of 47 particles were measured, yielding a distribution centered around d_{disk} = 33 ± 8 and t = 6 ± 3 nm. The equivalent hydrodynamic diameter of discoids was calculated from [22,23]:

$$D_{sphere} = \frac{3d_{disk}}{4}\left\{[1+\alpha^2]^{1/2} + \frac{1}{\alpha}\ln\left[\alpha + [1+\alpha^2]^{1/2}\right] - \alpha\right\}^{-1}$$

(Eq. S4)

where $\alpha = t/d_{disk}$, yielding a distribution with a mean value of 27 ± 7 nm (Figure S10B).

Tubules. Tubules, observed in TEM images of mixtures of aSyn with DLPS, were typically 10-20 nm in diameter with lengths ranging between 300-700 nm (Figure 5D). We checked whether DLPS tubules could have been produced by remodeling of a single 100 nm LUV. The number of lipid molecules in a cylindrical body capped by two hemispheres is:

$$N_{lipid} = \frac{2\pi rL + 2\pi(r-h)L + 4\pi r^2 + 4\pi(r-h)^2}{a}$$

(Eq. S5)

where r is the radius, L is the length of the cylindrical body, h is the bilayer thickness, and a is the area per lipid molecule, respectively. For a DLPS tubule of L = 700 nm and r ~ 5 nm (Figure 5D), N_{lipid} = 5 x 10^4, equivalent to a spherical liposome of 72 nm in diameter (Eq. S1).

For estimating hydrodynamic properties, tubules were modeled as semiflexible (wormlike) chains. We assumed a chain diameter of d_c = 10 nm and estimated the persistence length by TEM to be ~35 nm. For wormlike chains, the Kuhn statistical length l_k is double the persistence length, or l_k = 70 nm. Contour lengths, L_c, were measured for 13 particles and ranged from 300-700 nm. D_{sphere} for semiflexible chains was calculated as described [24,25]:

$$\frac{L_C}{D_{sphere}} = A_1\left(\frac{L_C}{l_k}\right)^{0.5} + A_2 + A_3\left(\frac{L_C}{l_k}\right)^{-0.5} + A_4\left(\frac{L_C}{l_k}\right)^{-1} + A_5\left(\frac{L_C}{l_k}\right)^{-1.5}$$

(Eq. S6)

for $L_C/l_k > 2.278$. The coefficients A_i are given by Yamakawa and Fuiji [25].

The calculated value for D_{sphere} ranged from 60-100 nm, in good agreement with the size distribution measured by NTA. $P(q)$ for a semiflexible chain is given as [26,27]:

$$P(q)_{tubule} = \frac{2}{L_c}\int_0^{L_c}(L_c - t) \times exp\left(-\frac{1}{6}q^2 l_k \times tf(t)\right) \times \frac{\sin(q \times tg(t))}{q \times tg(t)}\,dt \quad \text{(Eq. S7)}$$

where the functions $f(t)$ and $g(t)$ are defined elsewhere[27]. We calculated a $P(q)_{tubule}$ between 0.36 and 0.64 for this length range between contour lengths of 700-300 nm.

Cylindrical particles. Some large complex structures including helical and twisted ribbons were observed in aSyn-DLPS mixtures. We modeled them simply as long cylindrical particles, which are well described by Broersma's relations [28]:

$$D_T = \frac{k_B T}{3\pi\eta L}[\delta - (1/2)(\gamma_1 + \gamma_2)]$$

(Eq. S8)

$$\gamma_1 = 0.807 + \frac{0.15}{\delta} + \frac{13.5}{\delta^2} - \frac{37}{\delta^3} + \frac{22}{\delta^4}$$

$$\gamma_2 = -0.194 + \frac{0.15}{\delta} + \frac{8.1}{\delta^2} - \frac{18}{\delta^3} + \frac{9}{\delta^4}$$

$$\text{with } \delta = \ln(2L/d)$$

and the Stokes-Einstein relationship:

$$D_{sphere} = \frac{k_B T}{3\pi\eta D_t}$$

(Eq. S9)

where L is the cylinder length, d is the diameter, k_B is the Boltzmann constant, T is the temperature and η is the solvent viscosity. For a representative structure shown in Figure 5A, we measured L ~ 1500 nm and d ~ 70 nm, corresponding to D_{sphere} = 374 nm. To determine the shape factor, we modeled cylindrical particles using an expression for hollow cylinders [29]:

$$P(q)_{ribbbon} = \int_0^1 \left(\frac{1}{1-(R_2/R_1)}\right)^2 \left[\frac{2J_1(qR_1(1-t^2)^{1/2})}{qR_1(1-t^2)^{1/2}} - \frac{(R_2/R_1)^2 2J_1(qR_1(1-t^2)^{1/2})}{qR_2(1-t^2)^{1/2}}\right]^2 \left(\frac{\sin(qLt/2)}{qLt/2}\right)^2 dt$$

(Eq. S10)

Where R_1, R_2, and L are the inner, outer radius and length of the cylinder, respectively, and $J_1(t)$ is the Bessel function of the first order. While it is difficult to estimate the thickness of the ribbons, by TEM they are thin (~5 nm) by measuring the edge of the tip of the helical ribbon shown in Figure 5A. Thus, we estimated that R_1 and R_2 were approximately 30 and 35 nm, respectively. Using a length of ~1500 nm, we calculated a $P(q)_{ribbon}$ of 0.01. Hollow cylinders scatter weakly for their size given their extended shape and water filled interior.

Table S1: Number of molecules of lipid, aSyn, water, Na+, and Cl- in each bilayer and vesicle system, as well as simulation run times.

	System								
	DOPS Bilayer 1	DOPS Bilayer 2	DLPS Bilayer 1	DLPS Bilayer 2	DLPS Vesicle (no aSyn)	DLPS Vesicle 1/2	DOPS Vesicle (no aSyn)	DOPS Vesicle 1/2	DLPS Vesicle 3
DOPS	2048	2048	2048	2048	2048	2048	2048	2048	2048
α-Syn	1	1	1	1	0	10	0	10	1
Water	98662	98674	105560	105557	220259	219532	202368	201243	219532
Na+	2485	2485	2587	2587	2578	2668	2476	2566	2587
Cl-	428	428	530	530	530	530	428	428	530
Equilibration time (ns)	200	200	200	200	120	120	120	120	N/A
Production Time (ns)	700	700	700	700	300	300	300	300	260-740

Table S2: Effect of temperature on eccentricity.

Lipid Type	**Temperature (K)**	**Meridional**	**Equatorial**
DLPS	300	0.51±0.06	0.38±0.09
DLPS	320	0.45±0.06	0.30±0.08
DLPS	340	0.64±0.03	0.51±0.09
DLPS	360	0.76±0.02	0.37±0.09
DOPS	300	0.45±0.07	0.33±0.09
DOPS	320	0.38±0.06	0.27±0.08
DOPS	340	0.51±0.05	0.36±0.09
DOPS	360	0.62±0.04	0.38±0.09

Table S3: aSyn insertion depth, area per lipid, and bending rigidity of each lipid bilayer systems.

Lipid Type	**System**	**Temperature (K)**	**Insertion Depth (nm)**	**Area per Lipid (nm^2)**	**Bending Rigidity (10^{-20} J)**
DLPS	Replica 1	360	-0.22±0.34	0.66±0.002	7.95±0.83
	Replica 2		0.27±0.28	0.66±0.002	7.26±0.29
DOPS	Replica 1		0.26±0.27	0.70±0.00	8.42±1.08
	Replica 2		0.48±0.27	0.70±0.00	8.35±1.20
DLPS	Replica 1	300	0.08±0.21	0.60±0.002	8.69±0.98
	Replica 2		0.02±0.22	0.60±0.002	7.48±0.54
DOPS	Replica 1		-0.01±0.23	0.64±0.002	11.25±2.01
	Replica 2		0.21±0.16	0.64±0.002	7.57±1.47

Table S4: Distribution of lipid and protein between supernatant and pellet following ultracentrifugation. Samples were prepared in PB at 1:10 P:L molar ratio and incubated for 48 h at 30°C before separation by ultracentrifugation.

	Lipid		Protein	
Lipid	Supernatant	Pellet	Supernatant	Pellet
DOPS	26%	74%	50%	50%
DMPS	undetectable	100%	29%	71%
DLPS	91%	9%	87%	13%

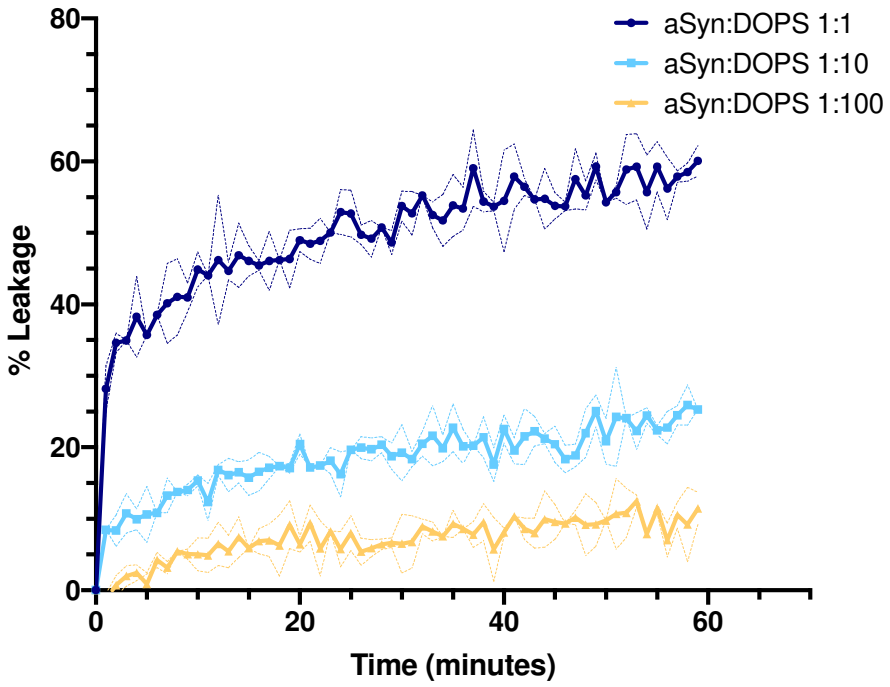


Figure S1: Carboxyfluorescein leakage from DOPS LUVs by aSyn. Samples were prepared at 1:100 (yellow), 1:10 (light blue) or 1:1 (blue) P:L molar ratio in PBS. Dye leakage was monitored by fluorescence. Baseline leakage from DOPS vesicles in the absence of protein was subtracted and the data were normalized to maximum fluorescence released with Triton X-100. Data points indicate the average of three replicates and shading indicates the standard deviation.

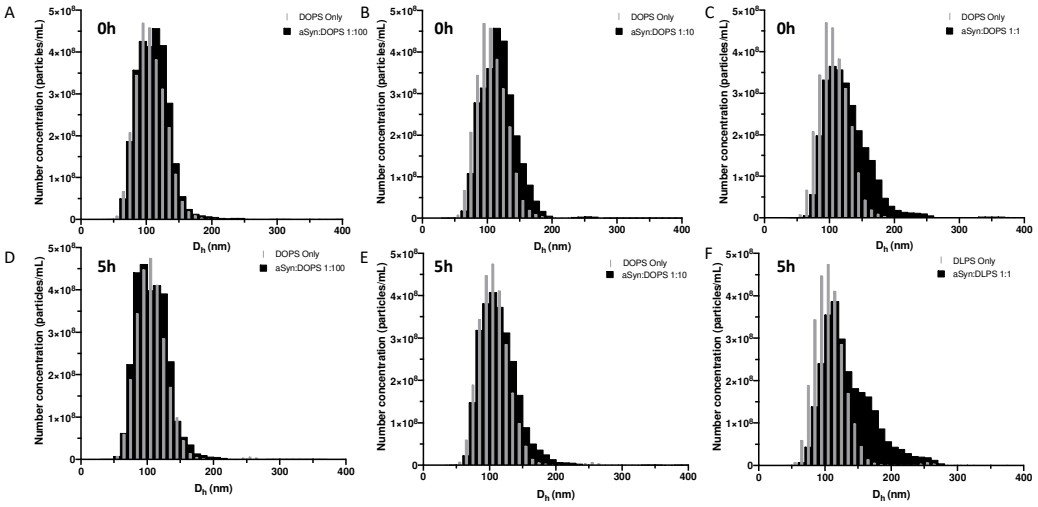


Figure S2: Size distributions for DOPS LUVs mixed with aSyn. Samples were prepared with aSyn and 100 nm DOPS LUVs at 1:100, 1:10 or 1:1 P:L molar ratios in PBS. Particle-by-particle size distributions were collected by NTA immediately after preparation and after 5h incubation at room temperature. Mixtures of aSyn and DOPS (black) are compared to DOPS liposomes only (grey). The size distribution shifted towards greater hydrodynamic diameter with increasing protein and increasing time. Total number concentration remained essentially constant over 5 h (Figure 3B). All plots shown are representative distributions of a single replicate from three independent replicates.

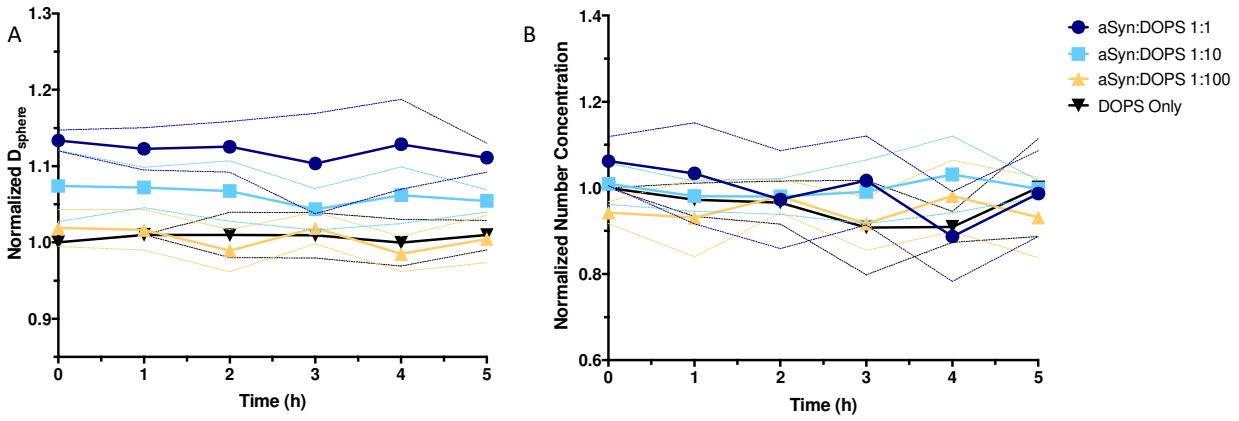


Figure S3: NTA of 50 nm (nominal) DOPS LUVs with aSyn in PBS. (A) Mean hydrodynamic diameter of 50 nm DOPS vesicles mixed with aSyn at 1:100, 1:10 or 1:1 P:L molar ratio. Data are normalized to vesicles alone at $t = 0$. The mean diameter of vesicles of three independent replicates was 65 ± 5 nm. D_{sphere} increased by 2 ± 1 nm, 5 ± 3 nm, and 9 ± 1 nm for P:L of 1:100, 1:10, and 1:1, respectively. These increases were smaller for 50 nm liposomes than for 100 nm liposomes. If a monolayer of adsorbed aSyn were responsible for the increase in D_{sphere}, we would have expected the same size increase independent of the LUV diameter. (B) Particle number concentration of 50 nm DOPS vesicles mixed with aSyn at 1:100, 1:10 or 1:1 P:L molar ratio. Data are normalized to vesicles alone at $t = 0$. Data points are the average of 3 independent replicates and shading indicates standard deviation. As with 100 nm LUVs, there was no significant change in liposome number.

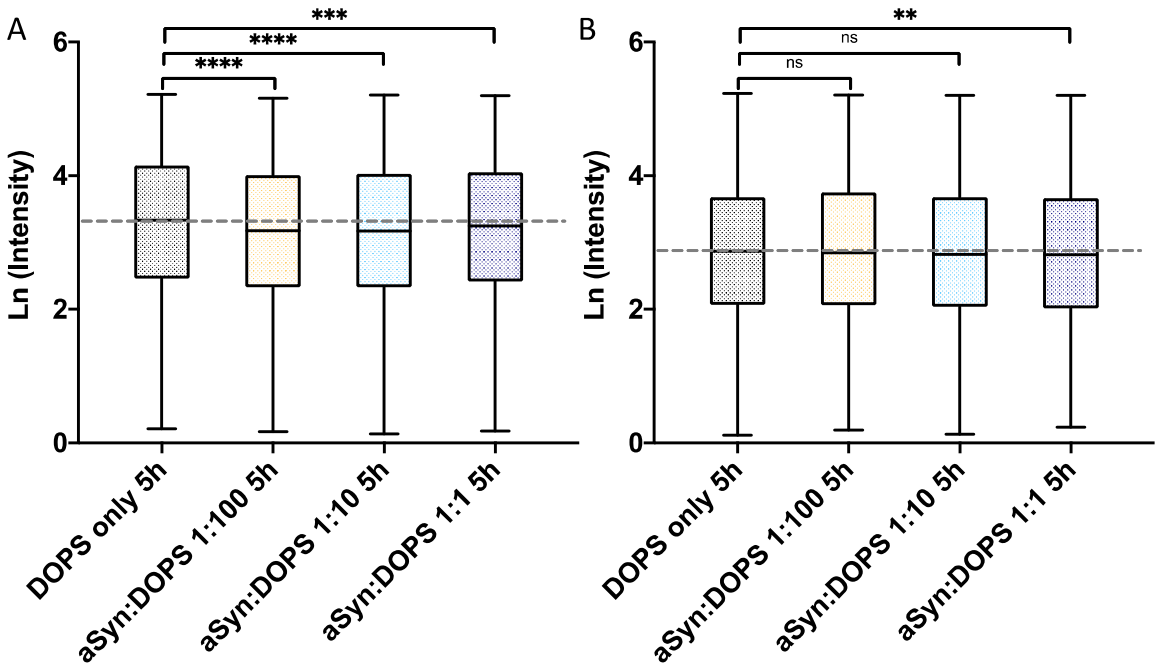


Figure S4: Box and whiskers plot of the scattered intensity distribution for size range between 75-125 nm following 5h of co-incubation with DOPS vesicles for two additional independent replicates. (A) Approximately 7,200 DOPS vesicles in the absence of lipid were tracked and compared with ~7,400 (P:L 1:100), ~7,300 (P:L 1:10), and ~5,600 (P:L 1:1) particles. (B) About 7,000 DOPS vesicles in the absence of lipid were tracked and compared with ~7,800 (P:L 1:100), ~7,700 (P:L 1:10), and ~7,800 (P:L 1:1) particles. *ns* not significant, ** $p < 0.01$, *** $p < 0.001$, and ****$p < 0.0001$, unpaired two-tailed t test.

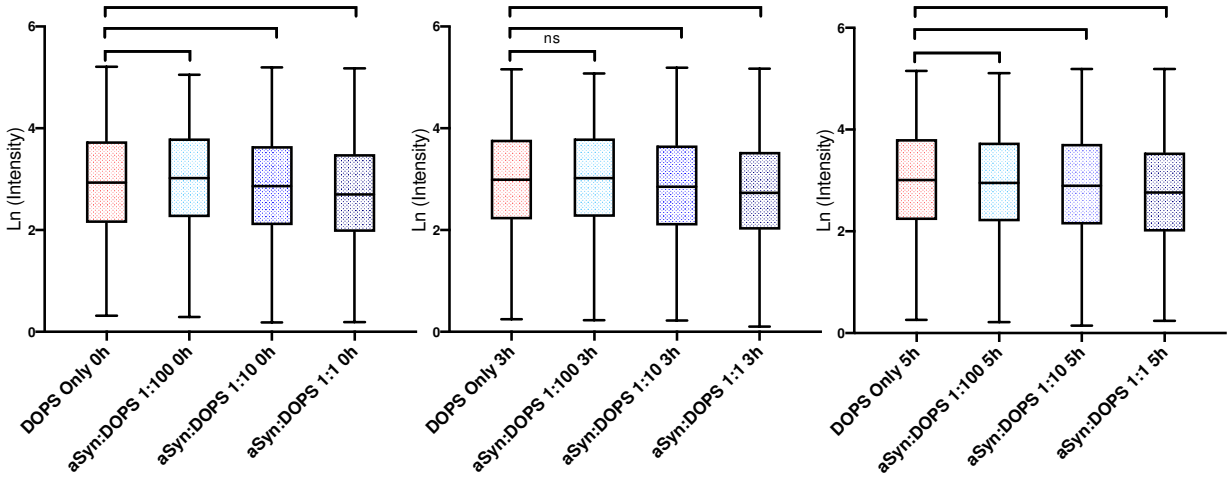


Figure S5: Box and whiskers plots showing scattered intensity distribution per particle for DOPS alone compared with aSyn added at P:L molar ratios of 1:100, 1:10, and 1:1 at 0 h, 3 h and 5 h. *ns*, not significant, * $p < 0.05$, *** $p < 0.001$, and ****$p < 0.0001$ (unpaired two-tailed t test). Dotted line shows the mean scattered intensity per particle for DOPS vesicles in the absence of added protein. All plots shown are representative distributions of a single replicate from three independent replicates.

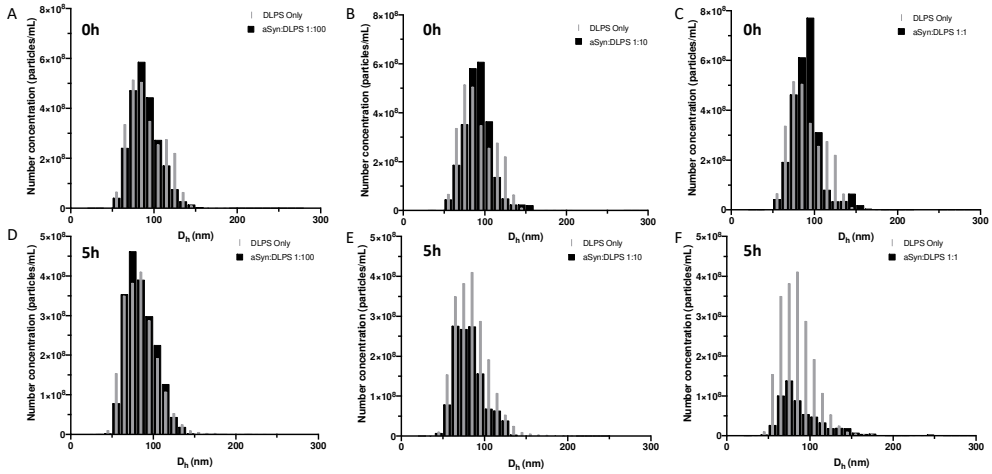


Figure S6: Size distributions for DLPS LUVs mixed with aSyn. Samples were prepared with aSyn and 100 nm DLPS LUVs at 1:100, 1:10 or 1:1 P:L molar ratios in PBS. Particle-by-particle size distributions were collected by NTA immediately after preparation and after 5 h incubation at room temperature. Mixtures of aSyn with DLPS (black) are compared to DLPS liposomes only (gray). The total number concentration of DLPS LUVs decreased over time following protein addition. The mean hydrodynamic diameter was approximately invariant with protein concentration and time, although at the highest P:L ratio the distribution became somewhat broader with the appearance of a few very large particles. All plots shown are representative distributions of a single replicate from three independent replicates.

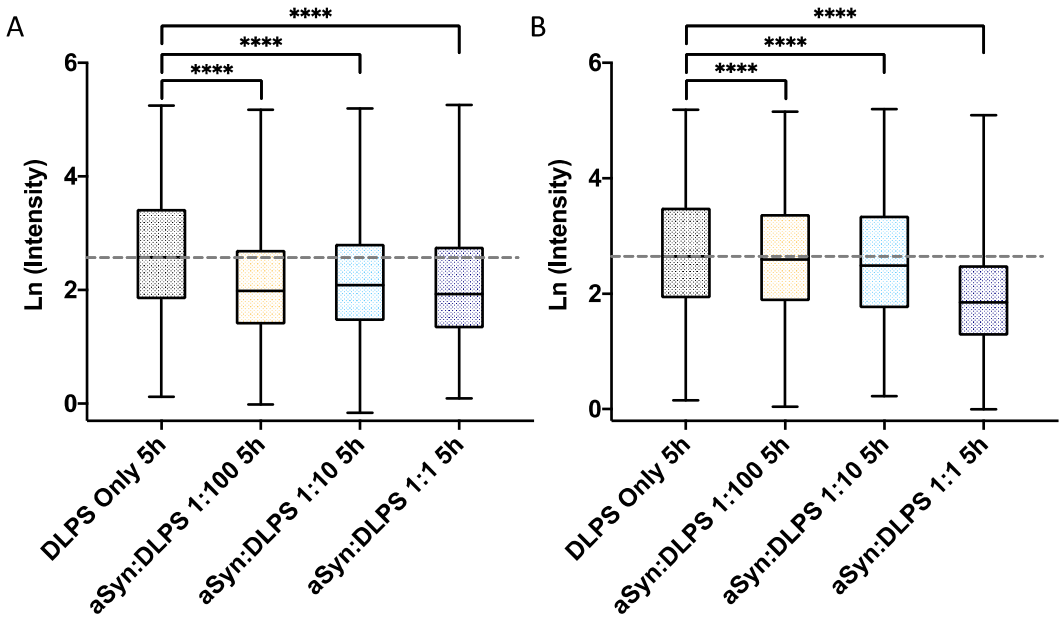


Figure S7: Box and whiskers plot of the scattered intensity distribution following 5h of co-incubation with DLPS vesicles for two additional independent replicates. (A) Approximately 16,700 DLPS vesicles in the absence of lipid were tracked and compared with ~8,200 (P:L 1:100), ~7,800 (P:L 1:10), and ~4,900 (P:L 1:1) particles. (B) About 15,200 DLPS vesicles in the absence of lipid were tracked and compared with ~16,300 (P:L 1:100), ~10,400 (P:L 1:10), and ~4,200 (P:L 1:1) particles. ****$p < 0.0001$, unpaired two-tailed t test.

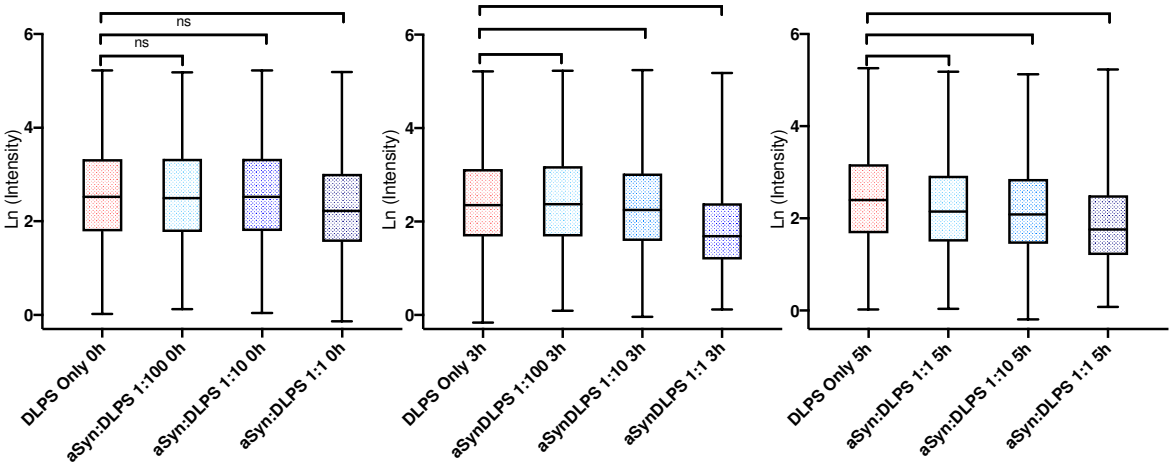


Figure S8: Box and whiskers plots showing scattered intensity distribution per particle for DLPS alone compared with aSyn added at P:L molar ratios of 1:100, 1:10, and 1:1 at 0 h, 3 h and 5 h. *ns*, not significant, ** $p < 0.01$, *** $p < 0.001$, and ****$p < 0.0001$ (unpaired two-tailed t test). Dotted line shows the mean scattered intensity per particle for DLPS vesicles in the absence of added protein. All plots shown are representative distributions of a single replicate from three independent replicates.

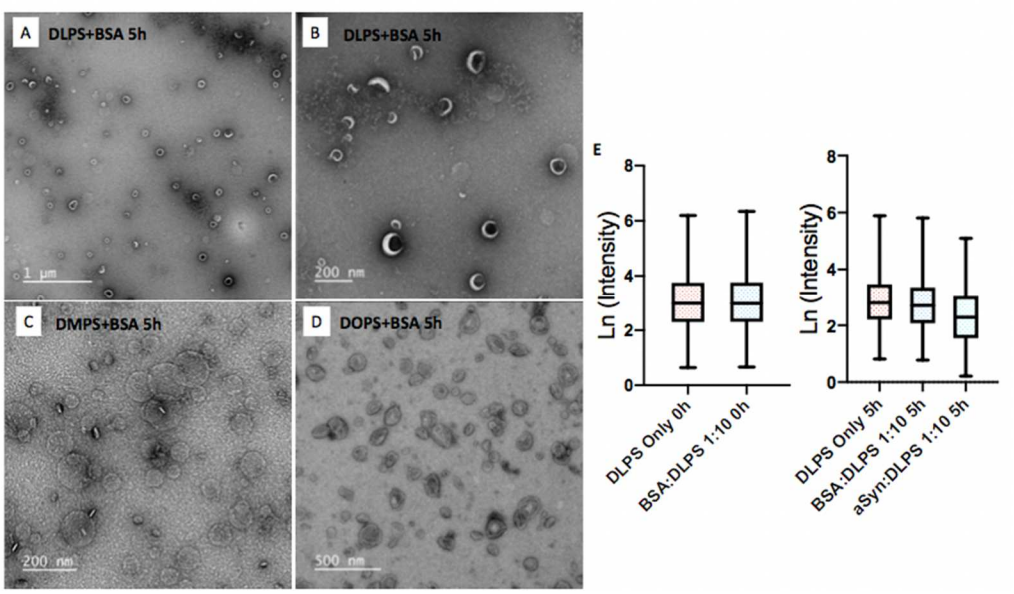


Figure S9: Control experiments with BSA and liposomes. BSA is known to adsorb to PS lipid surfaces and induces dye leakage from vesicles [30]. BSA and DOPS, DMPS or DLPS LUVs were incubated in PBS at 1:10 P:L molar ratio. (A-D) Representative TEM images showing that vesicles largely retained their spherical shape and size following incubation with BSA. No tubules, helical ribbons or coils were observed with DLPS. (E) Scattered intensity per particle with DLPS alone or incubated with BSA or aSyn at 1:10 P:L molar ratio of 1:10. There is no statistically significant change in the mean intensity of the distribution with addition of BSA, in contrast to the change with addition of aSyn. We conclude that the extensive membrane remodeling of DLPS is specific to aSyn.

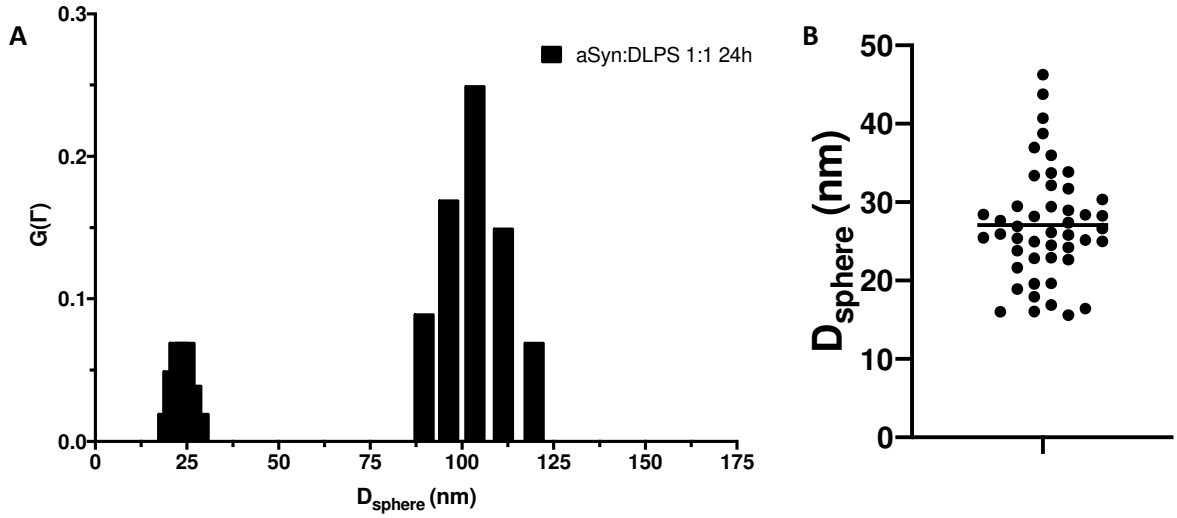


Figure S10: DLS of aSyn incubated with DLPS at a 1:1 P:L molar ratio for 24 h. (A) CONTIN analysis of the scattering size distribution, showing a bimodal distribution centered at ~ 25 nm and ~ 100 nm. (B) Hydrodynamic diameter of discoid particles measured by TEM using equation S7, demonstrating consistency between DLS and TEM estimates of discoid particle size of ~25 nm. The discoids are too small to be detected by NTA. The peak detected by DLS centered at 100 nm is consistent with NTA particle size as well as estimates of D_{sphere} for tubules from TEM images.

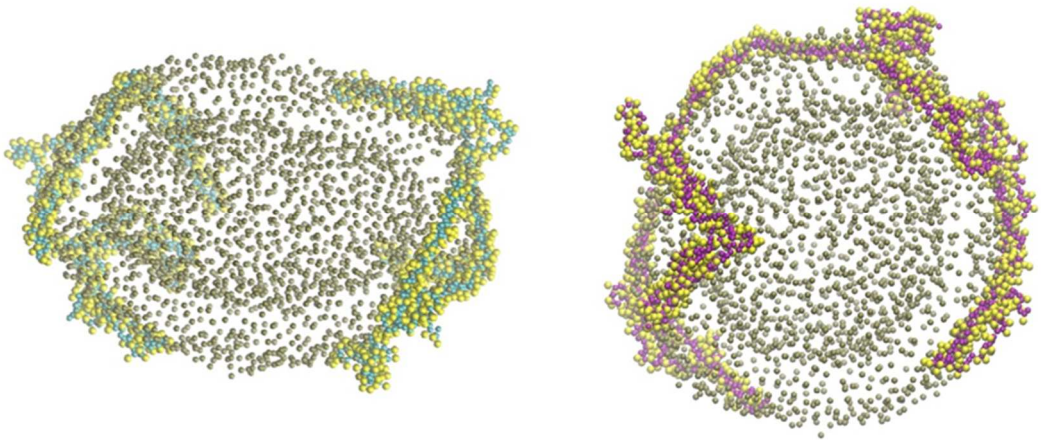


Figure S11. Snapshots from simulations of 10 aSyn monomers after adsorption to DLPS (left) and DOPS (right) vesicles, respectively, at 360 K using the standard MARTINI force field with anti-freeze water beads. The aSyn monomers elongate the DLPS vesicle and accumulate near the poles, whereas the DOPS vesicle remains spherical. These results are consistent with observations from the BMW MARTINI force field.

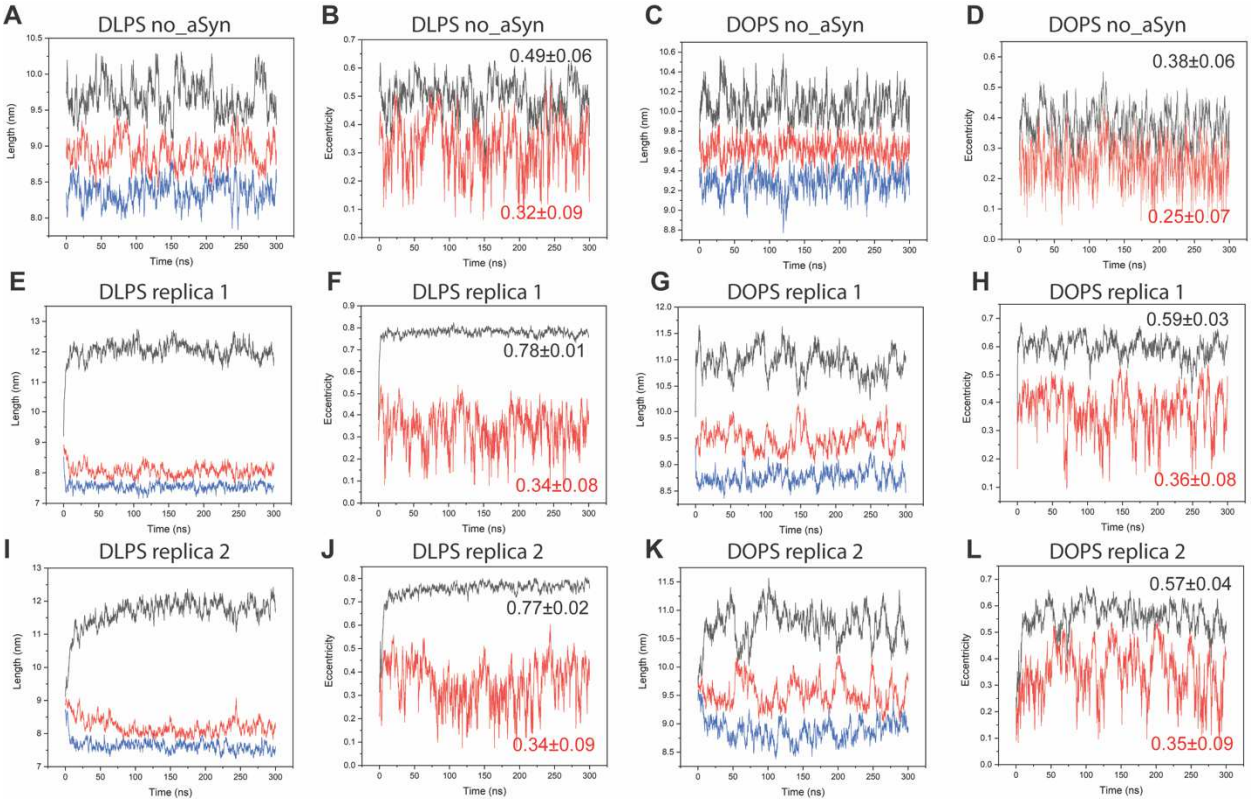


Figure S12: (A) Lengths of the three principle axes of a DLPS vesicle in the absence of aSyn as a function of time in ns. The black, red, and blue curves correspond to the longest, median, and the shortest axes, respectively. (B) Changes of meridional (black curve) and equatorial (red curve) eccentricities of a DLPS vesicle in the absence of aSyn as a function of time in ns. (C), (E), (G), (I), (J) are changes of three principle axes of a DOPS vesicle in the absence of aSyn, a DLPS vesicle in the presence of 10 aSyn, a DOPS vesicle in the presence of 10 aSyn, a second DLPS vesicle in the presence of 10 aSyn, a second DOPS vesicle in the presence of 10 aSyn, respectively. (D), (F), (H), (J), and (L) are changes of meridional and equatorial eccentricities of a DOPS vesicle in the absence of aSyn, a DLPS vesicle in the presence of 10 aSyn, a DOPS vesicle in the presence of 10 aSyn, a second DLPS vesicle in the presence of 10 aSyn, a second DOPS vesicle in the presence of 10 aSyn, respectively.

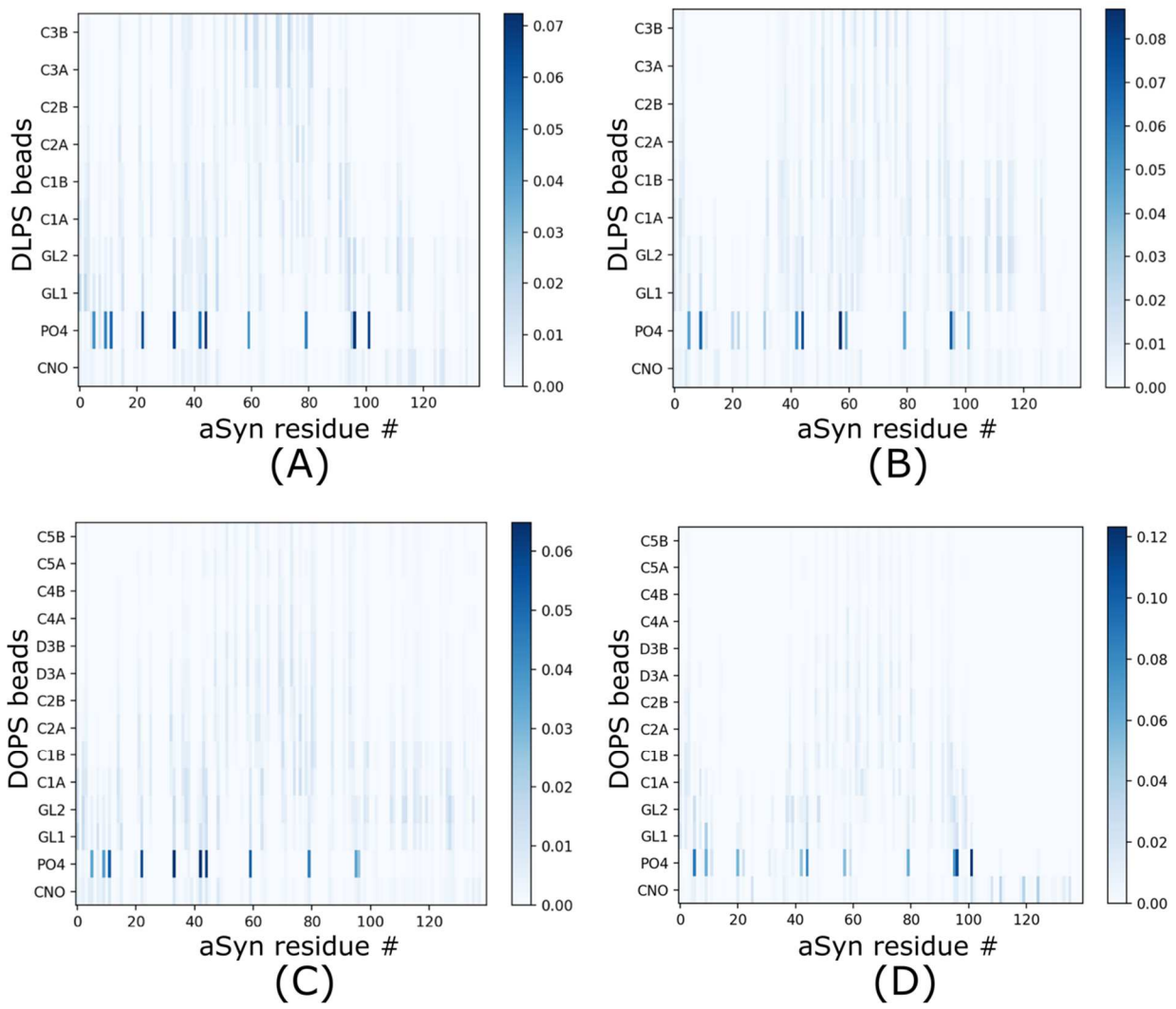


Figure 13. Contact maps for interactions between aSyn side chain beads and lipid beads. The color bar indicates the time-averaged number of contacts, with larger values indicating a higher likelihood that two beads are in contact. (A) and (B) show contacts with DLPS bilayers from two independent simulations. (C) and (D) show contacts with DOPS bilayers from two independent simulations. In all cases, contacts are primarily between negatively charged PO4 beads in the lipids and positively charged aSyn residues.

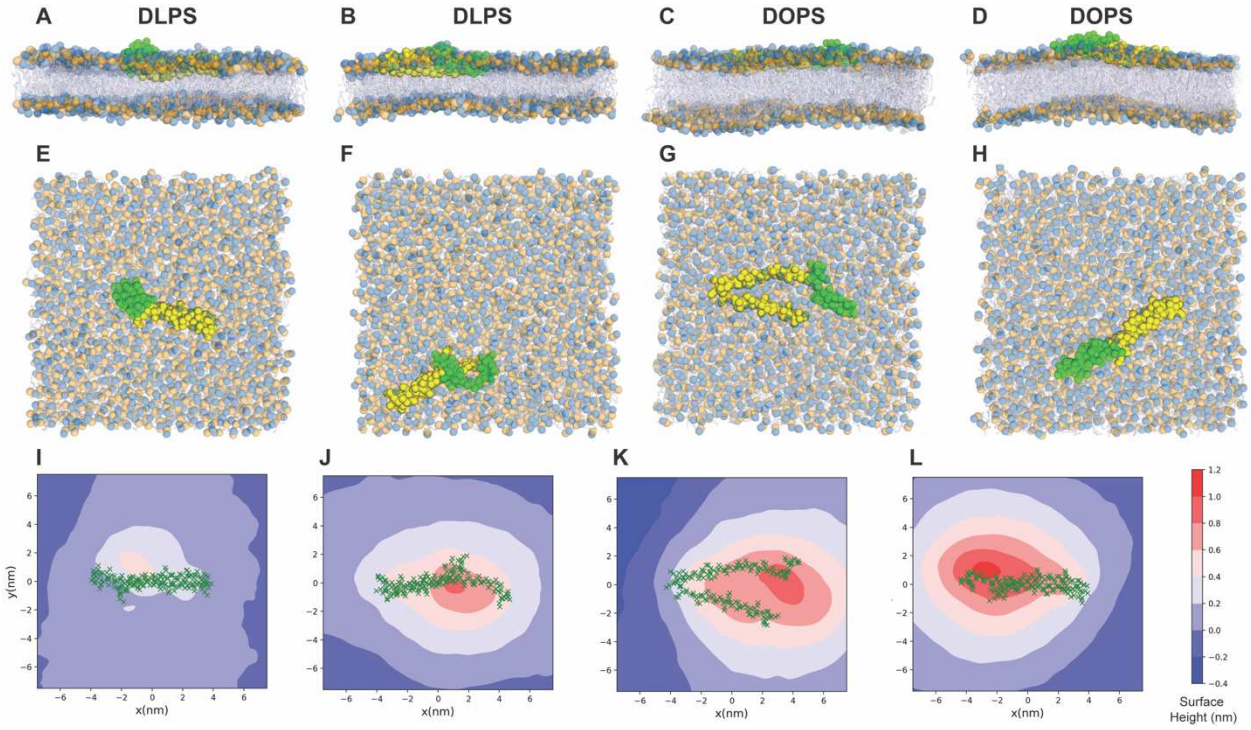


Figure S14: Side view (A-D) and top-down (E-H) view of the two replicas of the DLPS (A, B, E, F) and DOPS (C, D, G, H) bilayer systems. For clarity, only headgroup beads of DOPS or DLPS are shown (phosphate in orange and serine in blue). The first 99 amino acids of aSyn are shown in yellow and the tail beads are in green. (I) and (J) show time-averaged height contours indicating deviations in the height of the bilayer midplane at each *x*-*y* position relative to the average height of the bilayer midplane. Contours are shown for the two DLPS bilayer replicas. The projected positions of the first 99 amino acids (the first 190 beads) of aSyn are displayed as green crosses using the positions from the final configuration of the production simulation. The *x*-axis is aligned with the long axis of the first 99 amino acids. (K) and (L) show averaged height contours indicating deviations in the height of the bilayer midplane for the two DOPS bilayer replicas. The color bar is the same for (I)-(L).

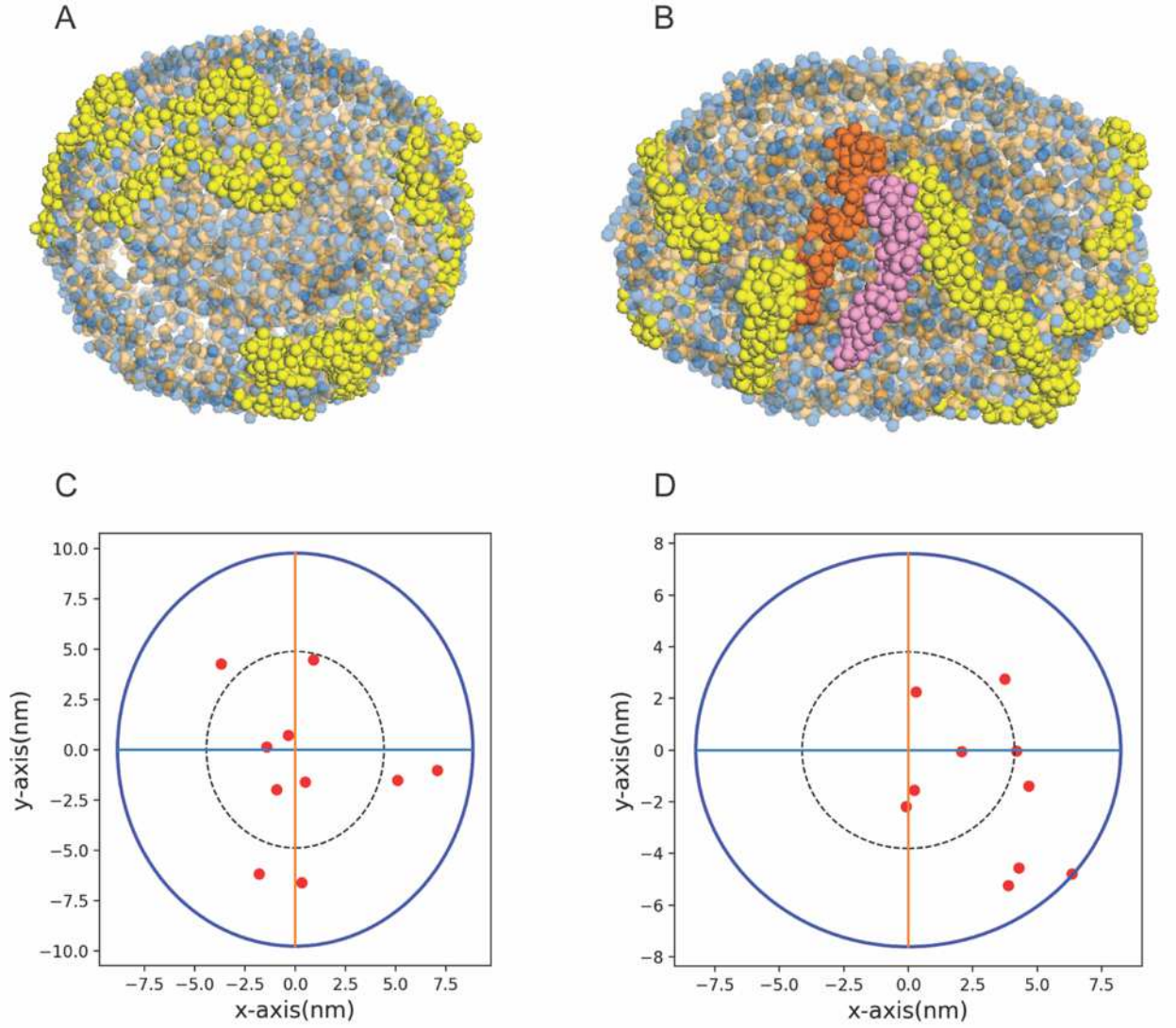


Figure S15: (A) Snapshot of the second replica of a DOPS vesicle with 10 aSyn monomers after the production simulation. (B) Snapshot of the second replica of a DLPS vesicle with 10 aSyn monomers after the production simulation. (C-D) Stereographic projections of the location of the 10 aSyn monomers with respect to the equatorial plane for the simulation snapshots in (A and B).

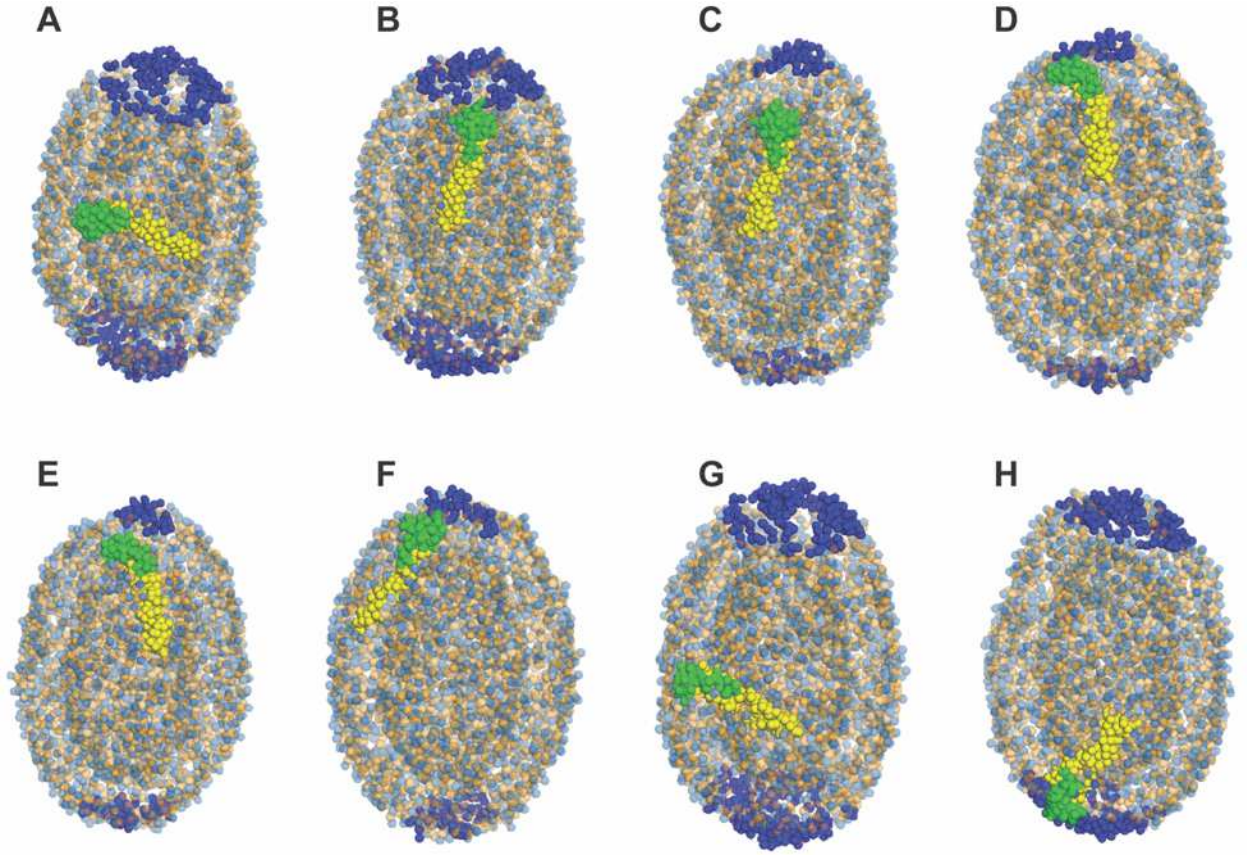


Figure S16: (A) Snapshot of the initial position of an aSyn monomer on an elongated DLPS vesicle (extracted from the second simulation replica of the DLPS vesicle with 10 aSyn monomers and drawn as the pink monomer in Figure S15. 100 phosphate beads are restrained at each pole and indicated in blue. (B) Snapshot of final position of the aSyn monomer on the elongated vesicle. (C) Same configuration as (B) but with only 30 restrained phosphate beads. This configuration was used as the initial position for a second simulation. (D) Snapshot of final position of this aSyn monomer from the second simulation. (E) Same configuration as (D) but with only 24 restrained phosphate beads, which was used as the initial position for a third simulation. (F) Snapshot of the final position of the aSyn monomer from the third simulation. (G) Snapshot of the initial position of an aSyn monomer on an elongated DLPS vesicle (extracted from the second simulation replica of the DLPS vesicle with 10 aSyn monomers and drawn as the orange monomer in Figure S15. 100 phosphate beads are restrained at each pole and indicated in blue. (H) Snapshot of final position of the aSyn monomer from (G) on the elongated vesicle.

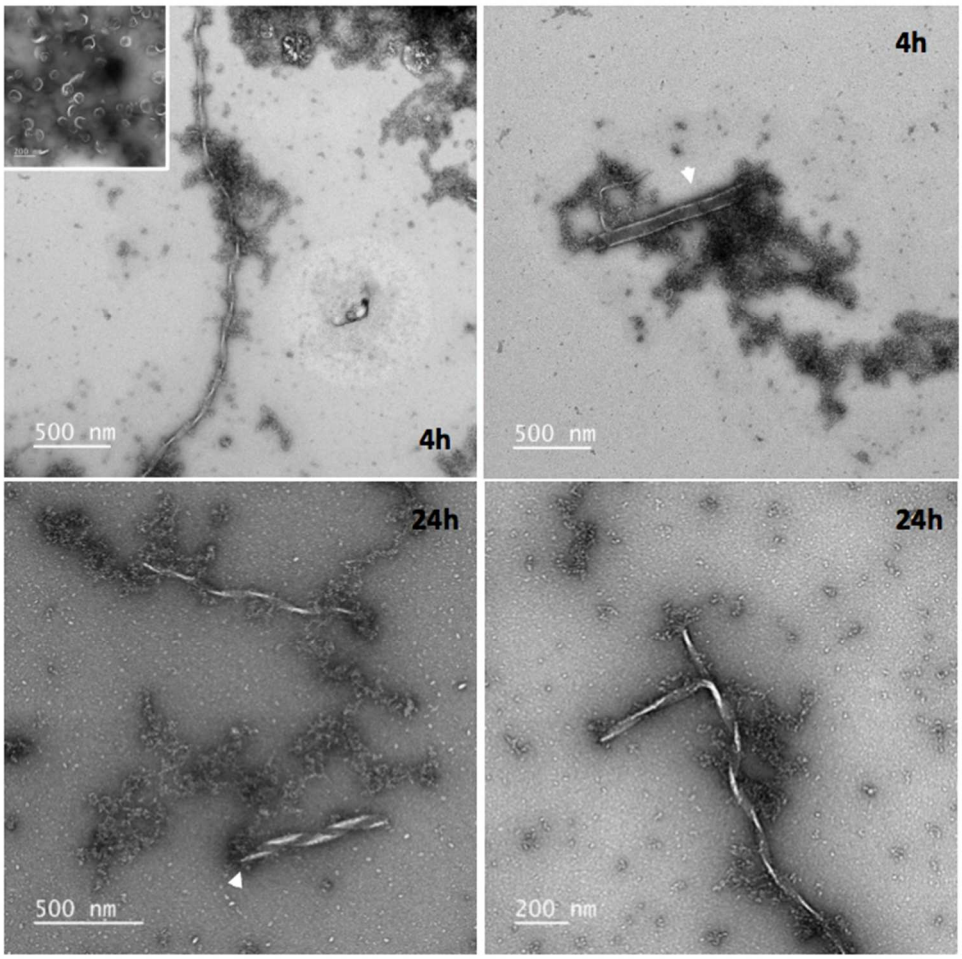


Figure S17: Additional TEM images revealing the presence of twisted and helical ribbons and nanotubes (arrow heads) after incubation of aSyn with DLPS vesicles. Samples were prepared at 1:10 P:L molar ratio in PB at 30°C and imaged after 4h (top panel) and 24h (bottom panel). Inset shows lipid only control after 4h at 30°C.

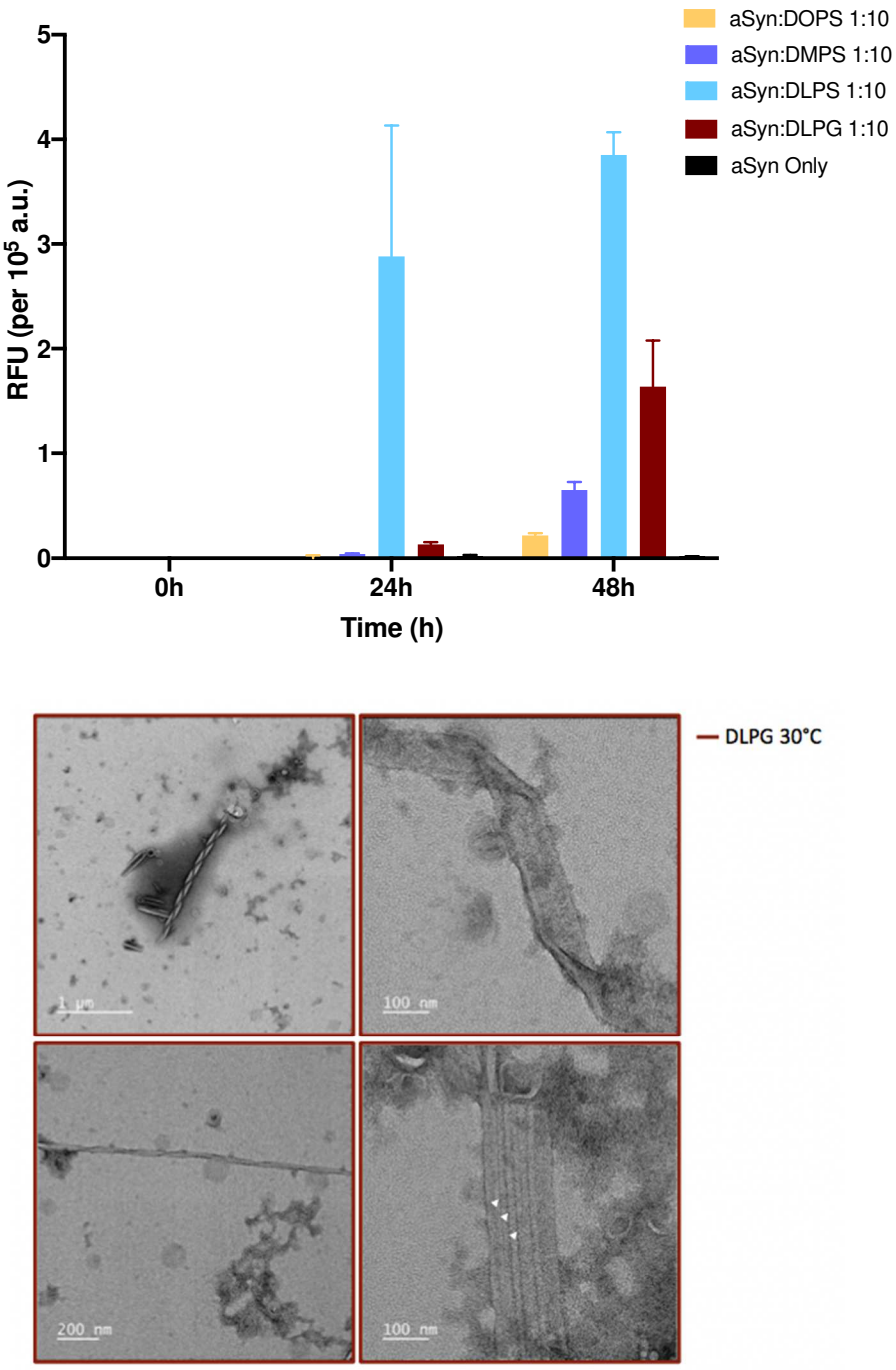


Figure S18: Aggregation of aSyn in the presence of DOPS, DMPS, DLPS, or DLPG vesicles (80 µM aSyn: 800 µM lipid), with incubation at 30°C in PB. (A) ThT fluorescence measurement of kinetics of amyloid formation. (B) Representative TEM images of aSyn with DLPG vesicles following 72h of incubation, revealing coiled ribbons and wide (~100 nm) sheets. White arrows indicate appearance of a lamellar pattern [31].

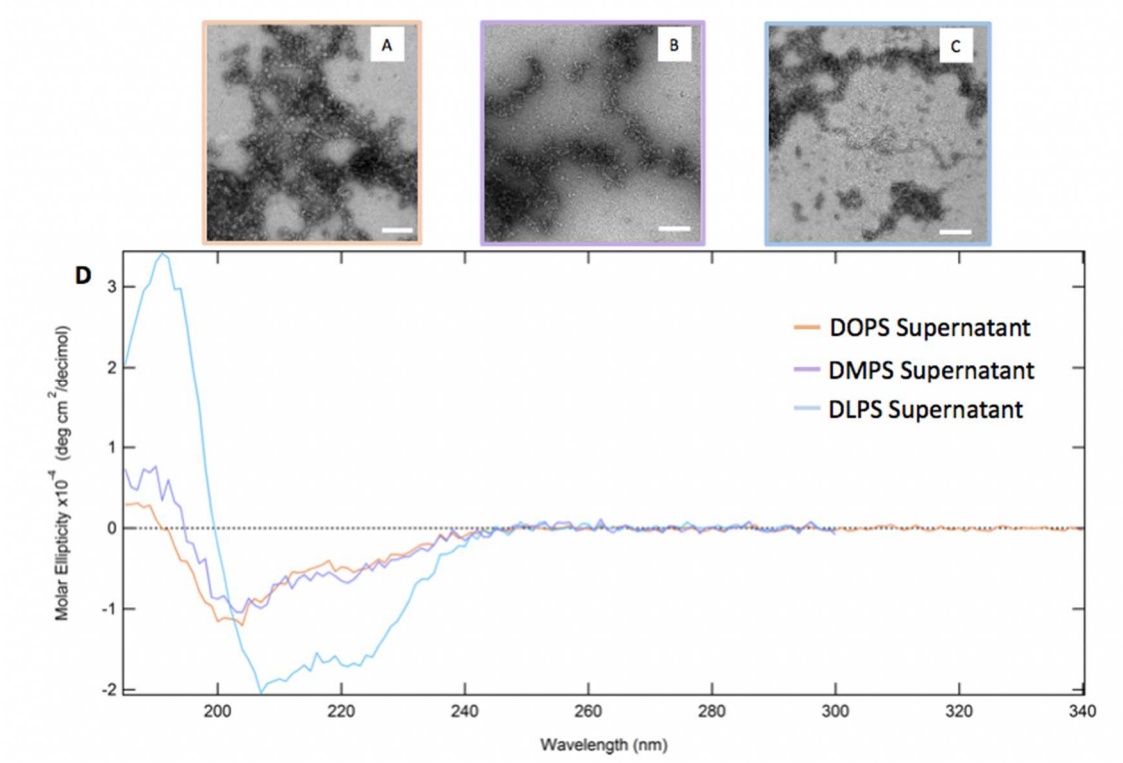


Figure S19: Analysis of supernatant, prepared by incubation at 1:10 P:L molar ratio in PB at 30°C for 48 h followed by separation by ultracentrifugation. The distribution of protein and lipid in supernatant and pellet is shown in Table S4. (A) Representative TEM image of supernatant of mixtures of aSyn and DOPS, revealing examples of what appears to be lysed membranes. Approximately 50% of protein and 26% of lipid was recovered in supernatant. Scale bars are 50 nm. (B) Representative TEM image of

supernatant of mixtures of aSyn and DMPS. Approximately 29% of protein and negligible lipid was recovered in supernatant. (C) Representative TEM image of supernatant of mixtures of aSyn and DLPS, showing an example of tubule formation and lysed membranes. Approximately 90% of protein and lipid was recovered in supernatant. (D) Circular dichroism spectra of supernatants, indicating disordered conformations for aSyn with DOPS and DMPS and α-helical secondary structure of aSyn in the DLPS supernatant.

Supplemental References

1. Ferdani, R.; Li, R.; Pajewski, R.; Pajewska, J.; Winter, R. K.; Gokel, G. W. Transport of chloride and carboxyfluorescein through phospholipid vesicle membranes by heptapeptide amphiphiles. *Org. Biomolec. Chem.* **2007,** *5*, 2423.

2. Bergstrom, C. L.; Beales, P. A.; Lv, Y.; Vanderlick, T. K.; Groves, J. T. Cytochrome c causes pore formation in cardiolipin-containing membranes. *Proc. Natl. Acad. Sci. U.S.A.* **2013**, *110*:6269–6274.

3. Pecora, R. Dynamic light scattering measurement of nanometer particles in liquids. *J. Nanoparticle Res*. **2000**, *2*:123–131.

4. Stewart, J. C. M. Colorimetric determination of phospholipids with ammonium ferrothiocyanate. *Anal. Biochem*. **1980**, *104*:10–14.

5. Abraham, M. J.; Murtola, T.; Schulz, R.; Páll, S.; Smith, J. C.; Hess, B.; Lindahl, E. GROMACS: High performance molecular simulations through multi-level parallelism from laptops to supercomputers. *SoftwareX*. **2015**, *1–2*:19–25.

6. Ulmer, T. S.; Bax, A.; Cole, N. B.; Nussbaum, R. L. Structure and dynamics of micelle-bound human α-synuclein. *J. Biol. Chem*. **2005**, *280*:9595–9603.

7. Yesylevskyy, S. O.; Schäfer, L. V.; Sengupta, D.; Marrink, S. J.; Schaefer, L. V.; Sengupta, D.; Marrink, S. J. Polarizable water model for the coarse-grained MARTINI force field. *PLoS Comp. Biol.*, **2010,** *6*,1–17.

8. Sheavly, J.K.; Pedersen, J.A.; Van Lehn, R.C. Curvature-driven adsorption of cationic nanoparticles to phase boundaries in multicomponent lipid bilayers. *Nanoscale* **2019**, *11*, 2767–2778.

9. Das, M.; Dahal, U.; Mesele, O.; Liang, D.; Cui, Q. Molecular dynamics simulation of interaction between functionalized nanoparticles with lipid membranes: Analysis of coarse-grained models. *J. Phys. Chem. B*. **2019**, *123*, 10547–1056

10. Wu, Z.; Cui, Q.; Yethiraj, A. A new coarse-grained force field for membrane–peptide simulations. *J. Chem. Theory Comput.* **2011**, *7*, 3793–3802.

11. Rawickz, W.; Olbrich, K. C.; McIntosh, T.; Needham, D.; Evans, E. Effect of chain length and unsaturation on elasticity of lipid bilayers. *Biophys. J. **2000**, 79*:328-339.

12. Berendsen, H. J. C.; Postma, J. P. M.; van Gunsteren, W. F.; DiNola, A.; Haak, J. R. Molecular dynamics with coupling to an external bath. *J. Chem. Phys*. **1984**, *81*:3684–3690.

13. Nosé, S. A molecular dynamics method for simulations in the canonical ensemble. *Molec. Physics*. **1984**, *52*:255–268.

14. Hoover, W. G. Canonical dynamics: Equilibrium phase-space distributions. *Physical Review A*. **1985**, *31*:1695–1697

15. Parrinello, M.; Rahman, A. Polymorphic transitions in single crystals: A new molecular dynamics method. *J. Appl. Phys*. 1981, *52*:7182–7190.

16. Nosé, S.; Klein, M. L. Constant pressure molecular dynamics for molecular systems. *Molecular Physics*. **1983**, *50*:1055–1076.

17. Watson, M. C.; Brandt, E. G.; Welch, P. M.; Brown, F. L. H. Determining biomembrane bending rigidities from simulations of modest size. *Phys. Rev. Lett*. **2012**, 10.1103/PhysRevLett.109.028102

18. Matsuzaki, K.; Murase, O.; Sugishita, K.; Yoneyama, S.; Akada, K.; Ueha, M.; Nakamura, A.; Kobayashi, S. Optical characterization of liposomes by right angle light scattering and turbidity measurement. *Biochim. Biophys. Acta (BBA) - Biomem*. **2000**, *1467*:219–226.

19. Gallego-Urrea, J. A.; Tuoriniemi, J.; Hassellöv, M. Applications of particle-tracking analysis to the determination of size distributions and concentrations of nanoparticles in environmental, biological and food samples. *TrAC Trends Anal. Chem*. **2011**, *30*:473–483.

20. Jennings, B. R.; Parslow, K. Particle size measurement: The equivalent spherical diameter. *Proc. Royal Soc. A: Math. Phys. Eng. Sci*. **1988**, *419*:137–149.

21. Pedersen, J. S. Analysis of small-angle scattering data from colloids and polymer solutions: modeling and least-squares fitting. *Adv. Coll. Interface Sci*. **1997**, *70*:171–210.

22. Johnsson, M.; Edwards, K. Liposomes, disks, and spherical micelles: Aggregate atructure in mixtures of gel phase phosphatidylcholines and poly(ethylene glycol)-phospholipids. *Biophys. J*. **2003**, *85*:3839–3847.

23. Mazer, N. A.; Benedek, G. B.; Carey, M. C. Quasielastic light-scattering studies of aqueous biliary lipid systems. Mixed micelle formation in bile salt-lecithin solutions. *Biochem*. **1980**, *19*:601–615.

24. Amorós, D.; Ortega, A.; García de la Torre, J. Hydrodynamic properties of wormlike macromolecules: Monte Carlo simulation and global analysis of experimental data. *Macromol*. **2011**, *44*:5788–5797.

25. Yamakawa, H.: Fujii, M. Translational friction coefficient of wormlike chains. *Macromol*. **1973**, *6*:407–415.

26. Koyama, R. Light scattering of stiff chain polymers. *J. Phys. Soc. Japan*. **1973**, *34*:1029–1038.

27. Shen, C. L.; Fitzgerald, M. C.; Murphy, R. M. Effect of acid predissolution on fibril size and fibril flexibility of synthetic beta-amyloid peptide. *Biophys. J*. **1994**, *67*:1238–1246.

28. Tsay, J. M.; Doose, S.; Weiss, S. Rotational and translational diffusion of peptide-coated CdSe/CdS/ZnS nanorods studied by fluorescence correlation spectroscopy. *J. Am. Chem. Soc*. **2006**, *128*:1639–1647.

29. Lu, K.; Jacob, J.; Thiyagarajan, P.; Conticello, V. P.; Lynn, D. G. Exploiting amyloid fibril lamination for nanotube self-assembly. *J. Am. Chem. Soc*. **2003**, *125*:6391–6393.

30. Schroit, A. J.; Fidler, I. J. Effects of liposome structure and lipid composition on the activation of the tumoricidal properties of macrophages by liposomes containing muramyl dipeptide. *Cancer Res.* **1982**, *42*:161–167.

31. Pallbo, J.; Sparr, E.; Olsson, U. Aggregation behavior of the amyloid model peptide NACore. *Quart. Rev. Biophys*. **2019**, 10.1017/S003358351

Chapter 9

Polymer Coatings Comprised Entirely of Soft and Semi-Permeable Microcapsules‡

‡ Portions of this chapter have been published as: Gahan, C. G.; Guo, X.; Manna, U.; Lynn, D. M. "Polymer Coatings Comprised Entirely of Soft and Semi-Permeable Microcapsules" *ACS Appl. Polym. Mater.* **2021.** X. Guo and I designed and performed all experiments related to the fabrication and characterization of multiplayer assemblies of polymer capsules. U. Manna performed early guiding experiments. D. M. Lynn directed the project.

ABSTRACT: We report the fabrication and characterization of surface coatings that consist entirely of networks of hollow and semi-permeable polymeric microcapsules. These assemblies incorporate many useful functions of individual microcapsules into coatings with unique compartmentalized structures. Iterative immersion of substrates into suspensions of microparticles coated with polymer multilayers presenting either (i) amine or (ii) amine-reactive azlactone functionality resulted in the reactive/covalent layer-by-layer assembly of coatings of colloidal particles. Removal of particle cores yielded compartmentalized coatings consisting of semi-permeable hollow capsules that were physically stable in aqueous media and upon drying and rehydration. Confocal microcopy and SEM revealed these assemblies to have disordered structures with some apparent hints of stratification resulting from the iterative assembly process. Residual azlactone groups in the capsule walls enabled tailoring of interfacial properties and controlled release behaviors by treatment with hydrophobic or hydrophilic amines. Fabrication of hollow-capsule assemblies on sacrificial substrates permitted triggered delamination and subsequent transfer of these coatings to secondary surfaces. The coatings reported here are mixtures of two different kinds of hollow reactive capsules. This iterative approach could be also used to design coatings comprising many different types of capsules with different properties (e.g., different types of encapsulated cargo or degrees of permeability). The structures and properties of these hollow-capsule coatings could thus prove useful in many applied contexts, ranging from catalysis and controlled release to the development of soft-material coatings with tunable interfacial or mechanical properties.

Introduction

Hollow polymer microcapsules are important in a range of fundamental and applied contexts, ranging from tools for basic research to new types of vehicles or containers for drug delivery and catalysis. Many different methods can be used to fabricate polymeric microcapsules, including approaches based on microfluidics,[1-4] phase separation,[5-8] interfacial polymerization,[9-13] and layer-by-layer assembly.[14-19] Of these approaches, layer-by-layer (LbL) assembly, in which sacrificial colloidal particles are iteratively coated with layers of polymer prior to subsequent dissolution of the underlying core, has proven particularly versatile because it enables a broad range of control over capsule structure and function (e.g., capsule size, wall thickness, internal or external functionality, permeability, mechanical properties, encapsulation/release properties, etc.) by judicious choice of polymer-based building blocks and assembly conditions.[14-26] This versatility has led to many exciting potential applications of multilayer capsules.[22,24,27-30] In most cases, polymer microcapsules are designed to be used as free-floating suspended 'containers', or are immobilized individually on surfaces and, in general, are designed to interact with their environments in isolation. In this paper, we report the fabrication of surface coatings consisting of networks of interconnected assemblies of hollow polymer microcapsules; these coatings incorporate several useful properties or functions of individual polymer microcapsules into uniform and conformal polymer coatings with unique, compartmentalized internal structures.

The work reported here was motivated by past work demonstrating that amine-containing polymer multilayer capsules could be immobilized on amine-reactive surfaces.[31] In that work, hollow polymer capsules were fabricated by the reactive layer-by-layer assembly of poly(2-vinyl-4,4-dimethylazlactone) (PVDMA; a polymer containing amine-reactive azlactone functionality) and poly(ethyleneimine) (PEI; a polymer containing amine functionality) on sacrificial

microparticle templates that could subsequently be etched and removed.[31] That reactive approach leads to capsules that can be readily functionalized after fabrication and that are physically stable in a wide variety of harsh environments (including at high ionic strength and at high surfactant concentrations).[31-33] It occurred to us that residual amine functionality on the surfaces of those immobilized capsules could also be used to support the reactive deposition of additional azlactone-functionalized capsules, and that this iterative approach could, potentially, be used to design new types of networks or coatings comprised entirely of hollow polymer capsules.

Here, we report a template-based approach to the design of coatings comprised of hollow, semi-permeable polymeric capsules. Our approach is based on the iterative exposure of surfaces to suspensions of model $CaCO_3$ microparticles coated with nanoscale amine- or azlactone-functionalized polymer multilayers. We demonstrate that subsequent removal of the sacrificial cores in these materials yields compartmentalized networks of interconnected hollow capsules that are physically stable in aqueous environments and able to host cargo for extended time periods. Characterization by confocal microscopy and scanning electron microscopy reveal these capsule assemblies to have relatively disordered structures consistent with an iterative, kinetically trapped assembly process driven by covalent interactions. The azlactone functionality remaining in these coatings allows tailoring of the interfacial properties and controlled release behaviors of these materials by post-fabrication functionalization with amine-containing compounds. Finally, we demonstrate that these novel capsule assemblies can be lifted off of their underlying substrates to produce free-floating films that can be subsequently transferred onto secondary surfaces.

The structures of these hollow-capsule assemblies differ from those of porous materials fabricated by the deposition of polymers on close-packed spherical templates, which typically leads to materials with open-cell structures.[34-36] These materials also differ substantially in

structure, form, and scale from previously reported LbL films that contain embedded liposomal structures[37-42] or hydrogel microparticles.[43-45] Those and other related materials[46,47] are also sub-compartmentalized and have been investigated as hosts for agents in a broad range of applied contexts, but have structures and properties that are different from the coatings reported here, which consist entirely of interconnected and hollow microscale polymer capsules. In this latter context, the materials reported here are similar, in some ways, to recently reported 'protocellular' materials and, more broadly, to other micro-compartmentalized structures assembled from aggregates of semi-permeable protein/polymer or lipid vesicles.[48-50] The methods reported here enable the design of capsule assemblies composed of mixtures of multiple different types of capsules with different physical properties or contents, and could thus prove useful in contexts ranging from drug delivery and catalysis to new and general methods for the design of novel and responsive soft material coatings.

Materials and Methods

Materials. 2,2´-Azoisobutyronitrile (AIBN), branched poly(ethyleneimine) (PEI, M_W ~25,000 Da), fluorescein isothiocyanate-dextran (FITC-Dextran, M_W ~2000 kDa), cystamine hydrochloride purum (≥98.0%), acetonitrile, tetrahydrofuran (THF), dimethyl sulfoxide (DMSO), calcein, calcium chloride, sodium carbonate, and acetone were purchased from Sigma-Aldrich (Milwaukee, WI). Cystamine was prepared, as described previously, by deprotonation of cystamine hydrochloride.[51] Tetramethylrhodamine (TMR) cadaverine was purchased from Setareh Biotech. 6-Aminofluorescein was obtained from Tokyo Chemical Industry (Tokyo, Japan). Ethylenediaminetetraacetic acid trisodium salt hydrate (EDTA), 3-(dimethylamino)propylamine (DMAPA, 99%) and glutathione (GSH, 98%, reduced) was acquired from Acros Organics (New

Jersey, USA). Phosphate-buffered saline (PBS) 10x was obtained from Dot Scientific (Burton, MI) and diluted in MilliQ water before use. Methanol was obtained from Macron Fine Chemicals (Center Valley, PA). Test grade n-type silicon wafers were purchased from Silicon Materials, Inc. (Glenshaw, PA). Glass coverslips and Lab-Tek II Chamber slides were obtained from Fisher Scientific (Rochester, NY). 2-Vinyl-4,4-dimethylazlactone (VDMA) was a kind gift from Dr. Steven M. Heilmann (3M Corporation, Minneapolis, MN). Poly(2-vinyl-4,4-dimethylazlactone) (PVDMA, M_W ~31,600; $Đ$ = 7.2) was synthesized by polymerization of VDMA, as reported previously.[52] PVDMA labeled with TMR (1 mol%; referred to as $PVDMA_{TMR}$ from here on) and 6-aminofluororescein (5 mol%; $PVDMA_{FL}$) was synthesized as described previously.[52] Distilled water was deionized using a Milli-Q system (Millipore, Bedford, MA) to give water having a resistivity of 18.2 MΩ. All materials were used as received without further purification unless otherwise noted.

General Considerations. Fluorescence and bright-field microscopy images were acquired using an Olympus IX71 inverted microscope (Center Valley, PA) using a 4x, 20x, or 60x objective lens. Laser-scanning confocal microscopy (LSCM) was performed using a Leica SP8 3X STED super-resolution confocal microscope and processed using Leica Instruments Software or a Nikon AR1S HD confocal microscope and processed using Nikon Elements Software. Scanning electron microscopy (SEM) images were acquired using methods similar to those described previously.[32] Measurements of solution fluorescence were made using a Tecan Infinite 200 Pro plate reader.

Coating of Planar Substrates. Glass or silicon substrates were cleaned using methods similar to those described previously.[53] Polymer solutions were prepared in acetone (20 mM; with respect to

repeat unit molecular weight). Coatings were deposited layer-by-layer on substrates according to a previously reported procedure[54] to give PEI/PVDMA films ~40 nm thick having a final nominal layer of PVDMA. Redox-degradable coatings were fabricated using a similar procedure reported previously[55] to deposit 45 bilayers of PVDMA and cystamine, yielding films ~200 nm thick and having a final nominal layer of azlactone-containing PVDMA. Films were dried under a stream of air and then either used immediately or under vacuum until use.

Fabrication of Coated Particles. Spherical $CaCO_3$ microparticles with average diameters of ~3-5 μm, either unloaded or loaded with the fluorophores FITC-Dextran (~2000 kDa) or calcein, were fabricated using a method described previously.[56] Loaded particles were prepared by dissolving 1 mg/mL of FITC-Dextran or calcein into a $CaCl_2$ solution. Microparticles were rinsed using acetone prior to coating. PEI, $PVDMA_{FL}$, and $PVDMA_{TMR}$ were dissolved in acetone (20 mM with respect to the polymer repeat unit). Coated particles and hollow capsules were fabricated using methods reported previously,[32] using solutions of $PVDMA_{FL}$ for coated particles terminated with PEI or $PVDMA_{TMR}$ for those terminated with PVDMA. Additional layers were added until the appropriate number of layer pairs (four for PVDMA-terminated particles and four and a half for PEI-terminated particles) were deposited. After fabrication was complete, the coated particles were washed twice using DMSO and then re-suspended in DMSO.

Layer-by-Layer Assembly of Films of Coated Particles. Multilayer assemblies of PEI/PVDMA-coated particles were fabricated in Lab-Tek II chamber slides. Briefly, glass or silicon surfaces coated with PEI/PVDMA films (with PVDMA as the outermost layer) were cut into ~8 mm × 15 mm rectangles to fit into the chambers. Suspensions (5 mg/mL; 600 μL) of

PEI/PVDMA$_{FL}$- or PEI/PVDMA$_{TMR}$-coated particles were then added into each chamber. The first layer of coated particles was deposited by submerging the substrates into the suspension of primary amine-containing PEI/PVDMA$_{FL}$-coated particles. The coated particles were allowed to settle onto substrates for 10 min, agitated, and allowed to settle for an additional 5 min to react with the amine-reactive surfaces. The substrates were then removed from the suspension and dipped into a DMSO rinse solution, followed by rinsing in a stream of DMSO, to remove any loosely bound particles from the surface. The second layer of particles was added to the assemblies by submerging the substrates into the suspension of amine-reactive PEI/PVDMA$_{TMR}$-coated particles and allowing the particles to settle on the substrate surface for 10 min, and then agitating and allowing them to settle for an additional 5 min to react with the primary amine-containing particles. DMSO was then used to rinse the substrates, as described above. This process of submerging the substrates in alternating suspensions of PEI/PVDMA$_{FL}$- and PEI/PVDMA$_{TMR}$-coated particles (with a DMSO rinse in between) was repeated until four layers (or some other desired number of layers) of coated particles had been deposited on the surface. The substrates coated with multilayer assemblies of particles were then rinsed with DMSO and methanol and dried under a stream of air. For experiments using materials formed by nonspecific interactions between coated particles, PEI/PVDMA$_{TMR}$-coated particles were treated with 3-dimethylaminopropylamine (DMAPA) in THF (20 mM) for 1 hr prior to assembly,[31] rinsed with THF, and re-suspended in DMSO. Substrates coated with multilayer assemblies of coated particles were analyzed by fluorescence microscopy and SEM after 1, 2, and 4 layers of deposition. The substrates were dried under vacuum prior to SEM imaging. Cross-sectional SEM images of coated particles were acquired from cross-sections after fracturing the substrates.

Fabrication of Multilayer Assemblies of Hollow Capsules. The $CaCO_3$ cores of the multilayer assemblies of coated particles described above were etched by treatment with a 0.2 M solution of EDTA for 30 min. Substrates coated with the resulting assemblies of hollow capsules were rinsed with water three times and analyzed by fluorescence and confocal microscopy while submerged in water. The samples were then removed from water, dried under vacuum, and characterized in a similar manner as described above.

Lift-off and Transfer of Hollow Capsule Assemblies. Assemblies of polymer-coated microparticles were fabricated as described above on substrates coated with previously reported amine-reactive polymer multilayers that undergo triggered degradation in response to reducing agents.[55] These assemblies were then submerged in a 100 mM solution of EDTA (PBS; pH=7.4) to dissolve the $CaCO_3$ templates. Subsequently, an equal volume of a 10 mM solution of the reducing agent GSH in PBS was added to the EDTA solution (to yield a solution that was 50 mM EDTA, 5 mM GSH) to degrade the sacrificial polymer coating. Degradation of the underlying sacrificial film resulted in a free-floating film of hollow polymer capsules. A secondary substrate (e.g., a glass coverslip) was maneuvered under the free-floating film and the aqueous phase was then removed, first with a pipette and then by blotting any remaining solution with a Kimwipe. Samples were then dried overnight at ambient conditions resulting in a dried film of assembled hollow polymer capsules on the secondary substrate.

Results and Discussion

Fabrication and Characterization of Multilayer Assemblies of Mutually Reactive Particles

Assemblies of mutually reactive polymer capsules could, in principle, be fabricated by the

iterative exposure of substrates to suspensions of two different types of chemically reactive hollow polymer capsules. In practice, however, hollow microscale capsules do not sediment readily, and they also often bend or fold upon contact with solid surfaces and, thus, do not pack as efficiently as spheres upon deposition onto a surface. We therefore pursued an alternative approach involving the assembly of polymer-coated microparticles, followed by subsequent removal of their solid cores. This template-based approach has the relative advantage of rapid sedimentation and the potential to control particle packing. In addition, this approach provides opportunities to design coatings consisting of cargo-loaded capsules (e.g., by using cargo-loaded cores). Overall, this template-based approach provides opportunities to access films composed of hollow capsules with internal structures, geometries, and degrees of interconnectedness that would be otherwise difficult or impossible to achieve using a hollow-capsule assembly approach.

We fabricated amine- and azlactone-functionalized colloidal particle building blocks by depositing PEI/PVDMA films on $CaCO_3$ microparticle templates (average diameter ~3-5 μm; See Materials and Methods) using reactive layer-by-layer assembly.[32] $CaCO_3$ cores were selected as colloidal templates because they are readily fabricated, can be used to encapsulate cargo, and can be etched and removed under mild aqueous conditions to facilitate the formation of hollow polymeric capsules.[56,57] Coated particles terminated with outer layers that present either amine-reactive (azlactone), or amine-containing outermost layers were prepared by manipulating the number of cycles used during layer-by-layer assembly. For example, completion of four full PEI/PVDMA deposition cycles resulted in particles terminated with an outer layer of PVDMA (referred to from hereon as amine-reactive particles; shown schematically in Figure 1A). Likewise, particles coated with four and a half PEI/PVDMA deposition cycles contained an outer layer of amine-containing PEI referred to from hereon as amine-containing particles; shown schematically

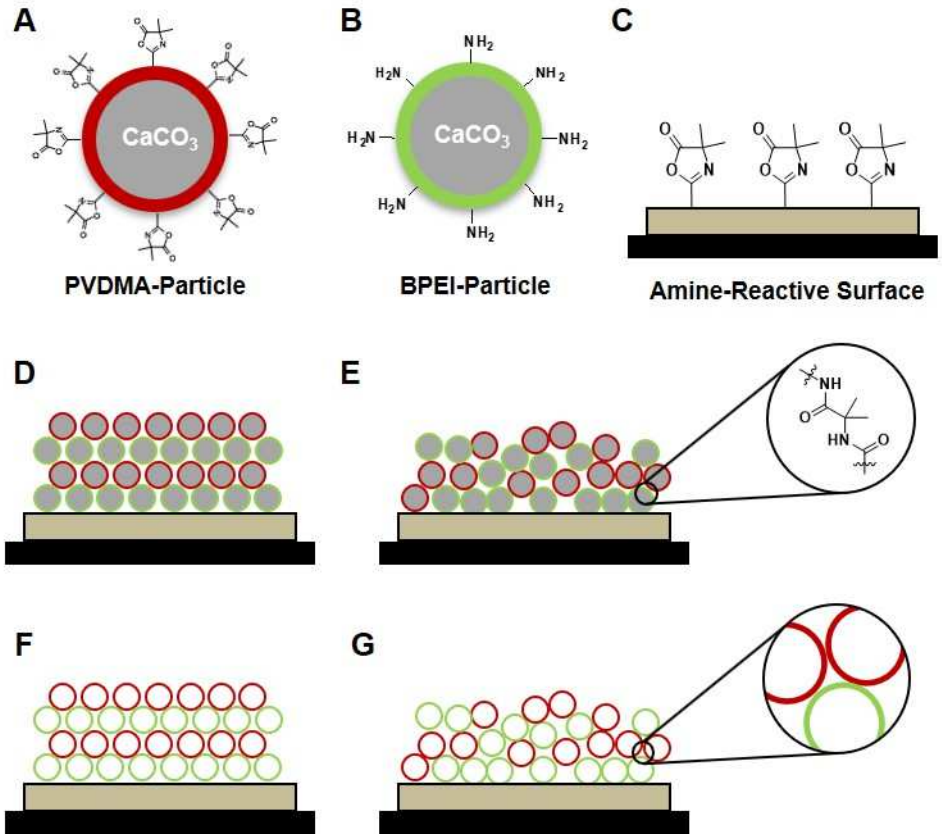


Figure 1: (A-C) Schematic illustrations showing (A) a PVDMA-terminated, PEI/PVDMA multilayer film-coated $CaCO_3$ microparticle (an amine-reactive particle), (B) a BPEI-terminated, PEI/PVDMA multilayer film-coated $CaCO_3$ microparticle (an amine-containing particle), and (C) a PEI/PVDMA base layer-coated (yellow) planar substrate (black) presenting amine-reactive azlactone functionality. (D-G) Schematic illustrations showing two possible arrangements (D,F, ordered; E,G, disordered) in assemblies of amine-containing and amine-reactive particles on amine-reactive surfaces before (D-E) and after (F-G) removal of the sacrificial $CaCO_3$ templates.

in Figure 1B. Planar glass or silicon substrates were then exposed iteratively to solutions of these mutually reactive particles. For these initial experiments, the glass or silicon substrates were coated with a thin PEI/PVDMA film presenting amine-reactive azlactone functionality (Figure 1C). We note that the speed and irreversibility of reactions between amine and azlactone functionalities could prevent particles from forming thermodynamically stable, closely-packed hexagonal assemblies (e.g., Figure 1D) typical of colloidal assemblies with reversible, non-covalent

interactions,[58,59] likely yielding assemblies with more disorganized and kinetically-trapped structures (e.g., Figure 1E; *vide infra*).

To facilitate characterization of coated particles and particle-containing films using fluorescence microscopy, we fabricated amine-containing and amine-reactive particles using fluorescently labeled PVDMA (amine-containing particles were fabricated using 6-aminofluorescein labeled PVDMA ($PVDMA_{FL}$), and amine-reactive particles were fabricated using tetramethylrhodamine cadaverine labeled PVDMA ($PVDMA_{TMR}$); see Materials and Methods and past studies[52]). In the fluorescence microscopy images discussed below, (i) green fluorescence corresponds to $PVDMA_{FL}$ in amine-containing particles and (ii) red fluorescence arises from $PVDMA_{TMR}$ in amine-reactive particles.

Panels A-F in Figure 2 show fluorescence microscopy images of a silicon substrate after iterative deposition of amine-containing and amine-reactive particles. Figure 2A,B shows an image after the deposition of amine-containing particles. Inspection of these images reveals a dense array of surface-immobilized amine-reactive particles, consistent with reactive immobilization on the amine-reactive surface. For convenience, substrates having been exposed to one deposition cycle are from hereon described as having one "layer" of particles, regardless of the specific morphology or degree of surface coverage. Further inspection of this image reveals some void spaces that were not covered with particles, as evidenced by the absence of green fluorescence.

This sample was then exposed to a solution of amine-reactive particles to produce a substrate containing two "layers" of particles (Figure 2C,D). These images reveal a large population of particles with red fluorescence (Figure 2D), and partial obstruction of green fluorescence arising from the underlying amine-containing particles (Figure 2C), consistent with the deposition of amine-reactive particles on top of the amine-containing particles. We then

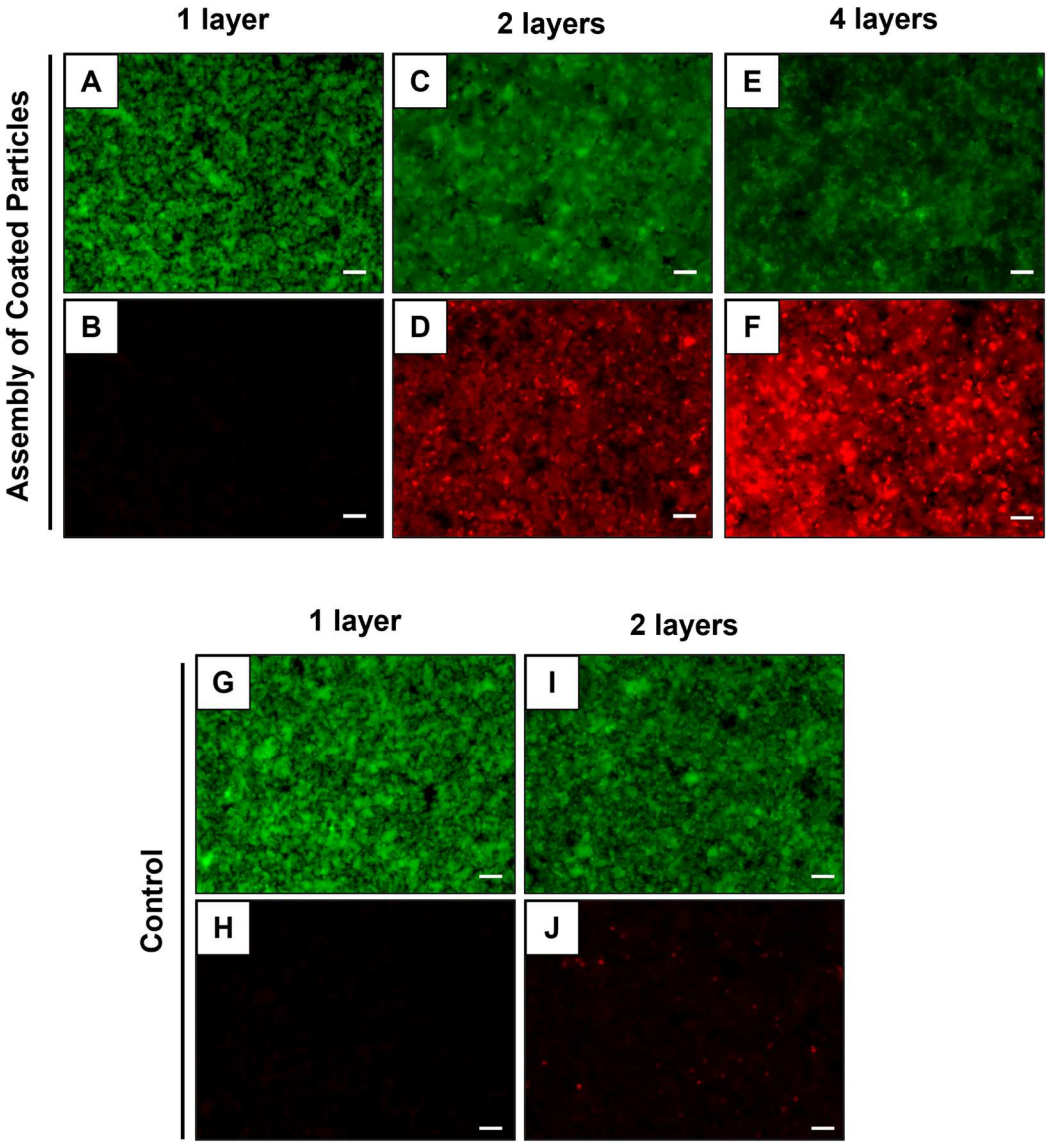


Figure 2: (A-F) Green (A,C,E) and red (B,D,F) fluorescence microscopy images of (A-B) a single layer, (C-D) a two-layer and (E-F) a four-layer assembly of amine-containing and amine-reactive particles on amine-reactive surfaces. (G-J) Green (G,I) and red (H,J) fluorescence microscopy images of a single layer (G,H) of PEI-particles after deposition of DMAPA-treated particles (I,J); see text for an additional discussion of this control experiment. Scale bars are 30 μm.

deposited a third layer of amine-containing particles and a fourth layer of amine-reactive particles, yielding an assembly with four nominal layers of coated particles. As shown in Figure 2E,F, these resulting four-layer assemblies appeared to exhibit nearly complete coverage of the surface, with

fewer void spaces, suggesting an increase in surface-immobilized particle density as the number of deposition cycles increased.

To provide further insight into the nature of inter-particle interactions driving assembly of these structures, we conducted additional experiments using amine-reactive particles that were first treated with dimethylaminopropylamine (DMAPA), a small-molecule primary amine-containing nucleophile, to consume remaining azlactone groups and decorate the surfaces of these particles with tertiary amine groups.[31] These DMAPA-treated particles were then deposited onto the one-layer particle coating shown in Figure 2G,H. Inspection of Figure 2I,J reveals the resulting surface to be almost completely devoid of red fluorescence associated with DMAPA-treated particles. When combined, these results are consistent with a mechanism of layer growth that involves reactions between amines and azlactones, and not simple, physical adsorption driven by other interactions.

We next characterized the morphologies and thicknesses of the assemblies above using SEM. Inspection of Figure 3A,C,E reveals the density of particles to increase as the number of layers increased, consistent with the results observed in Figure 2 using fluorescence microscopy. Inspection of cross-sectional images of these materials, shown in Figure 3B,D,F, reveals large differences in film thickness. We measured the average thicknesses of the 1, 2, and 4 layer particle coatings to be 7.3 ± 2 μm, 16.2 ± 3.5 μm, and 31.7 ± 2.9 μm respectively (Figure 3G), suggesting approximately linear growth in thicknesses as the number of layers of particles was varied. Each layer of particles deposited appeared to be thicker than the average diameter of a particle, an outcome that likely arises from particle polydispersity, the non-close-packed nature of reactive assembly, and the occasional deposition of larger aggregates of several particles as can be seen in Figure 3. From these images we conclude that the internal structures of these material are more

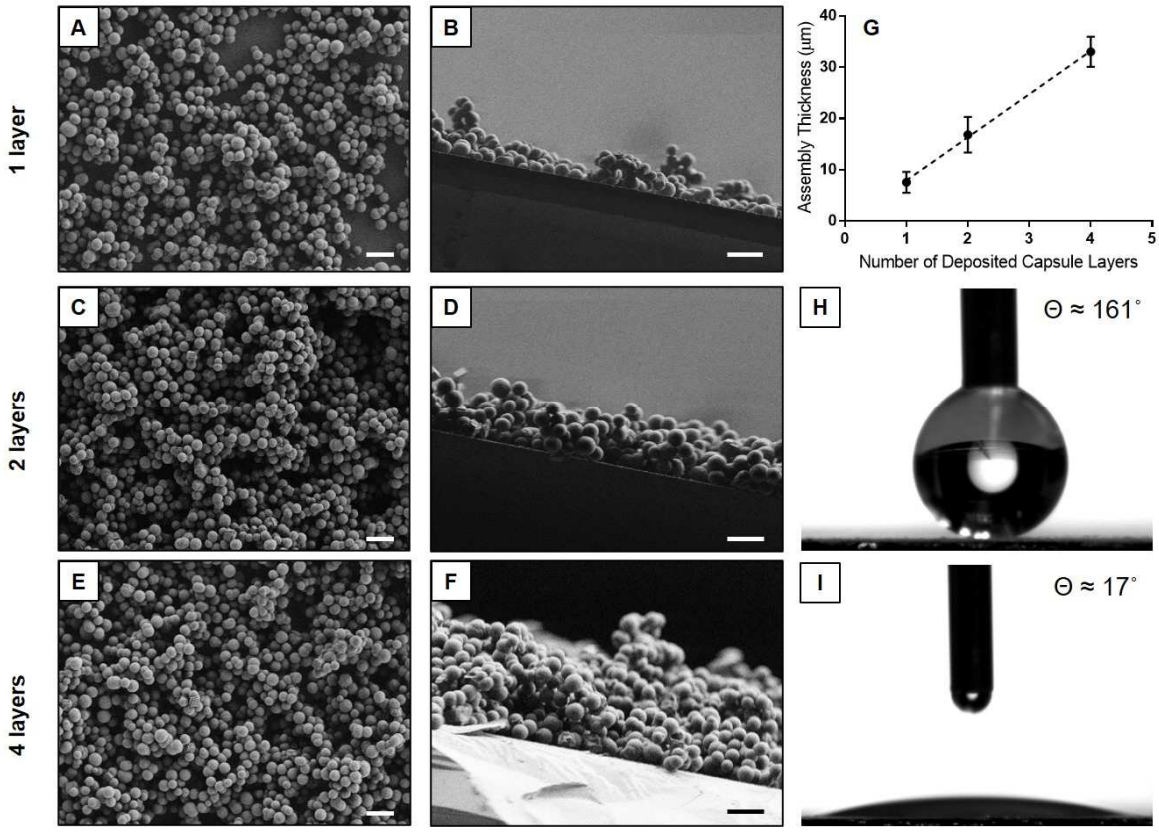


Figure 3: Top down (left column) and corresponding cross-sectional (middle column) SEM images for (A-B) one-layer, (C-D) two-layer, and (E-F) four-layer assemblies of amine-reactive and amine-containing particles on amine-reactive surfaces. (G) Growth profiles of amine-reactive and amine-containing capsule assemblies as measured by SEM. (H,I) Water contact angle analysis of four-layer assemblies of coated particles functionalized with either (H) decylamine or (I) DMAPA. Scale bars are 10 μm.

similar to the disordered arrangement of particles illustrated in Figure 1E than the ordered arrangement shown in Figure 1D.

These assemblies of coated particles could be further functionalized chemically by reacting the residual azlactone functionality in the particle coatings with small-molecule primary amines. Figure 3H,I shows water droplets placed on four-layer particle coatings after treatment with decylamine (a hydrophobic amine) and DMAPA (a hydrophilic amine). Inspection of these images reveals significant changes in water contact angles. Figure 3H reveals an advancing contact angle of 161.1 ± 4.7˚ for decylamine-treated films. This contact angle falls within the range generally

considered to be "superhydrophobic",[60-62] a result that likely arises from the microscale topography present on the surfaces of these decylamine treated films (the contact angle hysteresis of these films was high (57.2 ± 6.6˚), however, likely due to a lack of corresponding roughness at the nanoscale[61]). Figure 3I reveals a contact angle of 17.4 ± 5.8˚ for DMAPA-treated films, and droplets immediately wetted and soaked into these hydrophilic materials. These results are consistent with functionalization with hydrophobic and hydrophilic functional groups.

Fabrication and Characterization of Multilayer Assemblies of Hollow Capsules

Additional experiments demonstrated that the $CaCO_3$ cores in the particle assemblies above could be etched and removed to form assemblies or networks of hollow polymer capsules. We found treatment of these materials with EDTA for 30 minutes (200 mM; pH =8) at room temperature to be sufficient to remove all $CaCO_3$ cores. The removal of the solid particle cores permitted imaging and characterization of hollow capsule structures using epifluorescence and confocal microscopy. Panels A-B in Figure 4 show images of a four-layer particle assembly after EDTA treatment (images were acquired for assemblies hydrated in water; see Figure S1 for additional images of one- and two-layer assemblies). Inspection of these images reveals the both green and red fluorescence arising from the fluorescently labeled polymers used to fabricate the amine-reactive and amine-containing particle coatings, respectively (and as described in the experiments above). These images contrast to those shown in Figure 2E,F above, in which the presence of the particle cores obscured the observation of underlying layers of particles. No substantial detachment or disintegration of these assemblies was observed during these

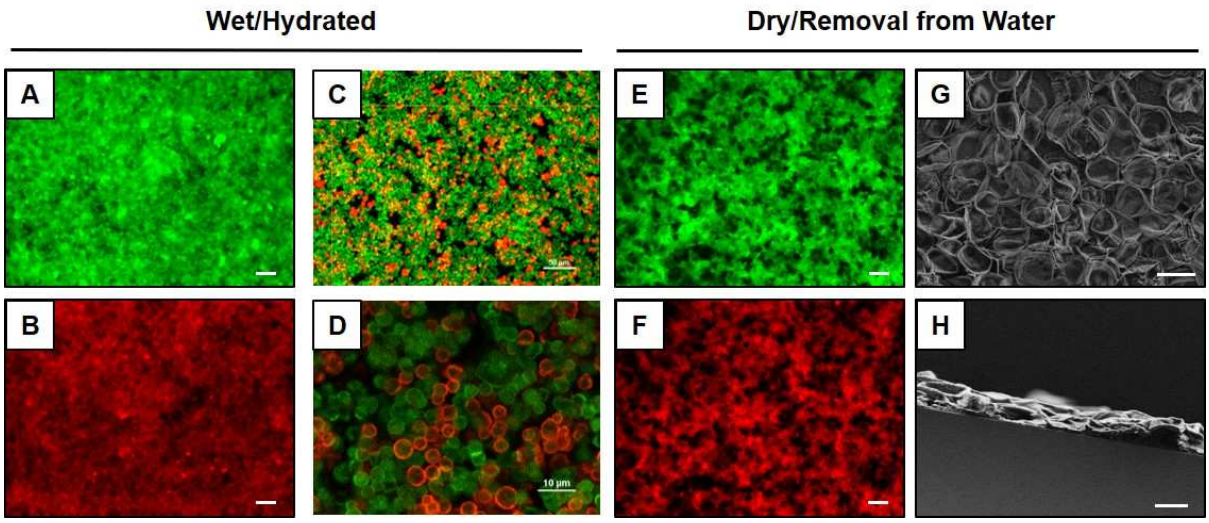


Figure 4: (A-B, E-F) Green (A,E) and red (B,F) fluorescence microscopy images of four-layer assemblies of amine-containing and amine-reactive particles after the removal of the $CaCO_3$ cores. Assemblies (A-B) incubated in water and (E-F) dried under vacuum. (C-D) Top-down confocal microscopy images of hydrated four-layer assemblies at different magnifications. (G-H) Top down (G) and cross-sectional (H) SEM images of the dried four-layer assembly shown in (A-B, E-F). Scale bars are 30 µm (A-B, E-F), 50 µm (C), 10 µm (D) and 4 µm (G-H).

experiments, suggesting the general preservation of the overall multilayer assembly after EDTA treatment.

The confocal images shown in Figure 4C,D obtained from a focal plane located near the middle of the z-axis of the coating, reveal circular cross-sections of both green and red fluorescent capsules. These capsules were hollow and generally intact; we did not observe substantial evidence of capsule tearing or rupture by confocal microscopy or interconnected channels or through-pores between adjacent capsules at micrometer length scales. The presence of both green and red capsules in the same focal plane (Figure 4C, D) provides further support for the view that the structures of these assemblies are disordered and more similar to that depicted in Figure 1G, as opposed to perfectly stratified layers of capsules in a close-packed arrangement (Figure 1F). Additional confocal images shown in Figure S2, acquired at different locations along the *z* axis of a four-layer capsule assembly, hint that some degree of stratification in the assemblies could

potentially be achieved, but the nature of the covalent assembly and dispersity of the model $CaCO_3$ microparticles used here likely leads to kinetically trapped structures.

The structures of these hollow capsule assemblies differ from those of open-cell structures fabricated in past studies by the deposition of bulk polymer or thin films on assemblies of sacrificial microparticle cores,[34-36] but are similar in some respects to recently reported 'protocellular' structures assembled from larger populations of microscale protein/polymer- or lipid-based vesicles.[48-50] The iterative approach to assembly used here allows for the design of compartmentalized capsule assemblies comprised of mixtures of different types of capsules. The capsule assemblies described here were fabricated using two kinds of reactive capsules; however, in principle, this approach could be used to design assemblies containing many different capsules with different individual properties (e.g., physicochemical properties, encapsulated cargo, stimuli responsiveness, permeability, etc.). For example, in the context of the azlactone chemistry used here, we have reported other amine-reactive, azlactone-containing capsules that degrade hydrolytically[53] or reductively[55] that could be used to introduce additional stimuli-responsive functionality.

The fluorescence microscopy images in Figure 4E-H show the multilayer assemblies of hollow capsules characterized above after they were removed from water and dried. We observed more open spaces on the surface compared to the hydrated four-layer capsules shown in Figure 4A-D, presumably due to capillary effects resulting from evaporation of water and reductions in capsule volume or size as a result of collapse upon drying. Further evidence of this is seen in SEM images of dried capsules shown in Figure 4G,H. These images reveal flattened hollow capsules with substantial folds, consistent with the morphology of dried multilayer capsules reported in past studies,[13,20,29] suggesting that these assemblies can be dried without substantial tearing or cracking

of the individual capsules that comprise them. Additional experiments discussed below demonstrated that these capsule assemblies can be dried, manipulated and rehydrated without substantial changes in overall structure.

The ability to dissolve and etch the cores of these particle assemblies creates opportunities to design hollow capsule assemblies that have the potential to encapsulate and release one or more other agents. We fabricated coated particles using $CaCO_3$ cores containing FITC-Dextran, a model water-soluble, fluorescently-labeled polymer. Figure 5A,B shows a microscopy image of hollow capsule assemblies fabricated by the assembly and subsequent etching of film-coated particles containing 2000 kDa FITC-Dextran. We observed high levels of green fluorescence localized within the capsules within an hour of etching the $CaCO_3$ cores (Figure 5A) and after seven days of immersion in PBS (Figure 5B), suggesting that the walls of the capsules in these coatings remained intact and impermeable to this macromolecular cargo for extended periods of time.

In contrast, experiments performed using particles encapsulating the small-molecule fluorophore calcein resulted in the rapid release of calcein upon etching of the $CaCO_3$ cores. Calcein is a small molecule (MW = 623 g/mol) and would be expected to pass readily through the walls of the capsules used here. In these experiments, calcein release generally appeared to be controlled by the concentration of EDTA added or the rate at which it infiltrated the assemblies, both of which would impact the rate of $CaCO_3$ dissolution. The strategies described above to tailor the interfacial wetting properties of these materials (Figure 3H-I) could thus be used to control rates of calcein release. Figure 5C shows the release of calcein from six-layer assemblies of coated particles functionalized either with DMAPA (open circles) or decylamine (closed circles) and incubated in ~30 mM EDTA solutions in PBS. These results reveal decylamine-functionalized assemblies to release calcein more slowly over an initial six-hour time period as compared to

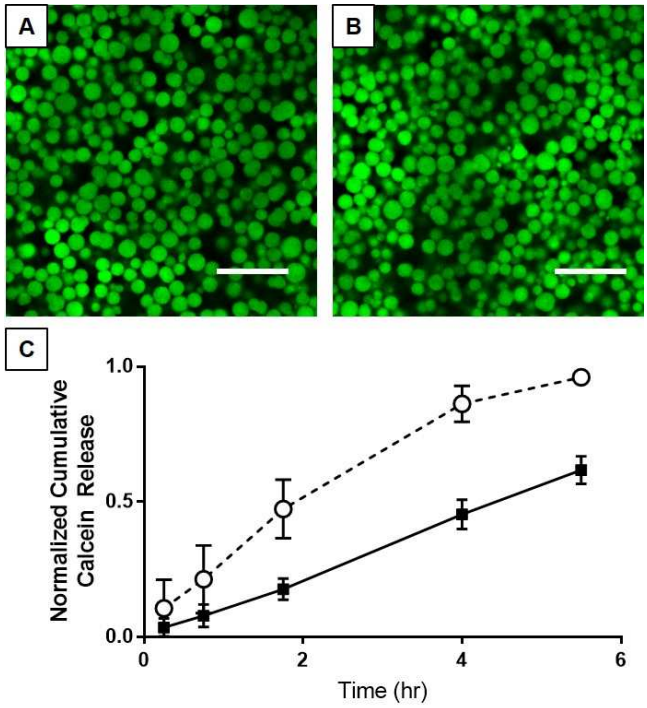


Figure 5: (A,B) Fluorescence confocal micrographs of four-layer assemblies of capsules loaded with 2000 kDa FITC-Dextran 1 hour (A) or 7 days (B) after core dissolution and incubation in PBS. (C) Plot showing the release of calcein from assemblies of coated particles incubated in 31 mM EDTA solutions in PBS with decylamine (filled) and DMAPA (open) surface functionality. The EDTA solutions were replaced at each of the timepoints shown. All data is normalized to the eventual cumulative release of calcein at the 24-hour timepoint, which is not shown here. Scale bars are 25 μm.

DMAPA-functionalized assemblies. These results likely reflect differential rates of penetration of the EDTA solutions into these superhydrophobic and hydrophilic films (and, thus, differences in the rates at which the $CaCO_3$ cores dissolve, as discussed above). These differences in release rates are small, in part owing to the low molecular weight nature of calcein used as model fluorescent cargo here. It is likely that the functional properties of these films (e.g., porosity or permeability) could be tailored to tune the release profiles of these capsules over a broader range. In addition, azlactone-functionalized multilayer capsules reported in past studies that degrade hydrolytically[53] or reductively[55] could be used to design films that host and release high molecular weight cargo

(e.g., enzymes, polymers, or particles) that are too large to diffuse through the capsule walls (e.g., Figure 5 A,B).

Fabrication of Freestanding Hollow Capsule Assemblies and Transfer to Secondary Substrates

During the course of these studies, we occasionally observed capsule assemblies stored in aqueous environments for prolonged periods to delaminate from underlying substrates and lift off as continuous sheets. Building from these observations, we conducted additional experiments using hollow multilayer assemblies of capsules fabricated intentionally on sacrificial coatings that can be actively and selectively degraded to promote delamination. As a model, we fabricated hollow multilayer assemblies on thin (~200 nm) polymer films that are reductively degradable (see schematic in Figure 6A).[55] Figure 6B shows a four-layer capsule assembly after treatment with the small-molecule reducing agent glutathione (GSH) and subsequent delamination (the film here is shown suspended in aqueous media). These free-floating films could be readily transferred onto secondary substrates such as glass slides or other surfaces.

Figure 6 C-D shows red and green fluorescence microscopy images of a capsule assembly transferred to a glass coverslip and then dried, and shows that the film generally remained intact after manipulation and subsequent transfer. Figure 6F,G shows confocal microscopy images of transferred capsule assemblies that were dried and rehydrated, and reveals red and green capsules in a single *xy* confocal slice, similar to those shown in Figure 4C,D and Figure S2 (images were acquired in aqueous solution; the non-spherical shapes of some of these capsules are the result of variability in the shapes of the $CaCO_3$ cores used to fabricate these films and are not a byproduct of the transfer process). Further inspection of the *xz* and *yz* confocal reconstructions on the sides of Panels F and G of Figure 6 show distributions of green and red capsules in these planes that

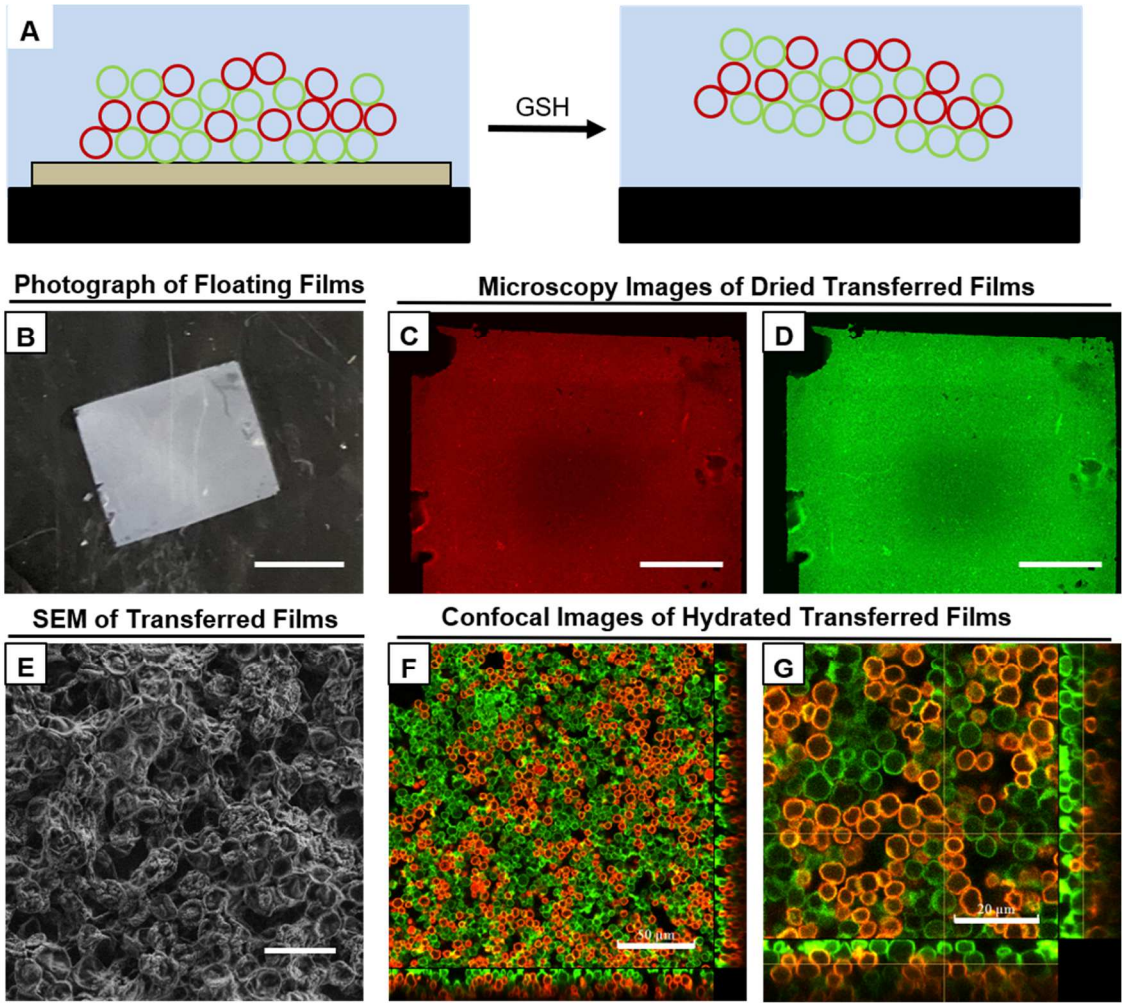


Figure 6: (A) Schematic illustration depicting the delamination of hollow-capsule assembly coatings from a substrate by the dissolution of a sacrificial redox-degradable film (yellow). (B) Digital photograph of a delaminated capsule assembly floating in buffer solution. (C-D) A reconstructed series of low magnification (4x) fluorescence microscopy images showing a dried film transferred onto a glass coverslip in the red (C) and green (D) channels. (E) SEM Image of a dehydrated capsule assembly after transfer to a glass cover slip. (F-G) Confocal microscopy images at various magnifications showing rehydrated capsule assemblies after transfer to a glass cover slip. Scale bars are (B) 5 mm, (C,D) 2.5 mm, (E) 10 µm, (F) 50 µm, and (G) 20 µm.

again hint at some degree of stratification that may arise from the iterative approach used to fabricate the coatings. Finally, Figure 6E shows a SEM image of a transferred capsule assembly after drying and removal of water. This image shows that these films can withstand lift-off,

manipulation, and transfer to other substrates without formation of substantial tears, pores, or other defects at micrometer length scales.

Summary and Conclusions

We have reported the fabrication and characterization of hollow, semi-permeable polymeric microcapsule networks on surfaces using an iterative LbL approach. Iterative exposure of substrates to suspensions of sacrificial microparticles coated with multilayers containing amine or azlactone functionality, followed by removal of the particle cores, led to coatings consisting of mixtures of hollow polymer capsules. These capsule assemblies had relatively disordered structures with some degree of potential stratification resulting from the iterative nature of the assembly process, as determined by confocal microscopy and SEM. These results are consistent with a process that leads to kinetically trapped structures rather than the close-packed structures typically exhibited by colloidal assemblies fabricated using weak/reversable interactions. These hollow capsule assemblies are physically stable in aqueous solutions and can be rehydrated and dried without apparent physical damage. Additionally, these semi-permeable capsules can be loaded with small-molecule and macromolecular cargo, suggesting potential applications in catalysis and controlled release. The residual azlactone groups in the colloidal building blocks used to fabricate these assemblies can also be used to tailor chemical properties that further influence the behaviors of these materials (e.g., wetting behaviors and rates of release of encapsulated cargo). Finally, we demonstrated that these assemblies can be delaminated from the substrates on which they are fabricated and subsequently transferred onto other secondary surfaces.

The studies reported here used two mutually reactive colloidal building blocks to design assemblies composed of mixtures of two types of hollow capsules. However, the iterative nature

of this process could be used to design assemblies of many different types of building blocks to design hollow-capsule assemblies containing many different types of capsules. This approach could also be used with a range of other mutually reactive functional groups that could provide additional control over the properties of the capsules or the structure and organization of the resulting coatings.[63,64] The ability to define the properties or contents, and potentially the juxtaposition, of many different individual and compartmentalized capsules in a conformal coating could prove useful in a range of different contexts, ranging from drug delivery and catalysis to the development of new soft material coatings with tunable interfacial and mechanical properties.

Acknowledgments. Financial support for this work was provided by the National Science Foundation through a grant provided to the UW-Madison Materials Research Science and Engineering Center (MRSEC; DMR-1720415). The authors acknowledge the use of instrumentation supported by the NSF through the UW MRSEC. X. G. was supported in part by a 3M Graduate Fellowship. C. G. G. was supported in part by an NSF Graduate Research Fellowship.

References

1. Zhang, H.; Tumarkin, E.; Peerani, R.; Nie, Z.; Sullan, R. M. A.; Walker, G. C.; Kumacheva, E. Microfluidic Production of Biopolymer Microcapsules with Controlled Morphology. *J. Am. Chem. Soc.* **2006,** *128*, 12205-12210.

2. Kim, J. W.; Utada, A. S.; Fernandez-Nieves, A.; Hu, Z. B.; Weitz, D. A. Fabrication of Monodisperse Gel Shells and Functional Microgels in Microfluidic Devices. *Angew. Chem., Int. Ed.* **2007,** *46*, 1819-1822.

3. Zhang, J.; Coulston, R. J.; Jones, S. T.; Geng, J.; Scherman, O. A.; Abell, C. One-Step Fabrication of Supramolecular Microcapsules from Microfluidic Droplets. *Science* **2012,** *335*, 690-694.

4. Li, W.; Zhang, L. Y.; Ge, X. H.; Xu, B. Y.; Zhang, W. X.; Qu, L. L.; Choi, C. H.; Xu, J. H.; Zhang, A.; Lee, H. M.; Weitz, D. A. Microfluidic Fabrication of Microparticles for Biomedical Applications. *Chem. Soc. Rev.* **2018,** *47*, 5646-5683.

5. Loxley, A.; Vincent, B. Preparation of Poly(Methylmethacrylate) Microcapsules with Liquid Cores. *J. Colloid Interface Sci.* **1998,** *208*, 49-62.

6. Tiarks, F.; Landfester, K.; Antonietti, M. Preparation of Polymeric Nanocapsules by Miniemulsion Polymerization. *Langmuir* **2001,** *17*, 908-918.

7. Atkin, R.; Davies, P.; Hardy, J.; Vincent, B. Preparation of Aqueous Core/Polymer Shell Microcapsules by Internal Phase Separation. *Macromolecules* **2004,** *37*, 7979-7985.

8. Dowding, P. J.; Atkin, R.; Vincent, B.; Bouillot, P. Oil Core-Polymer Shell Microcapsules Prepared by Internal Phase Separation from Emulsion Droplets. I. Characterization and Release Rates for Microcapsules with Polystyrene Shells. *Langmuir* **2004,** *20*, 11374-11379.

9. Zha, L. S.; Zhang, Y.; Yang, W. L.; Fu, S. K. Monodisperse Temperature-Sensitive Microcontainers. *Adv. Mater.* **2002,** *14*, 1090-1092.

10. Zoldesi, C. I.; Imhof, A. Synthesis of Monodisperse Colloidal Spheres, Capsules, and Microballoons by Emulsion Templating. *Adv. Mater.* **2005,** *17*, 924-928.

11. Fu, G. D.; Shang, Z. H.; Hong, L.; Kang, E. T.; Neoh, K. G. Preparation of Cross-Linked Polystyrene Hollow Nanospheres via Surface-Initiated Atom Transfer Radical Polymerizations. *Macromolecules* **2005,** *38*, 7867-7871.

12. Zoldesi, C. I.; van Walree, C. A.; Imhof, A. Deformable Hollow Hybrid Silica/Siloxane Colloids by Emulsion Templating. *Langmuir* **2006,** *22*, 4343-4352.

13. Cui, J. W.; van Koeverden, M. P.; Mullner, M.; Kempe, K.; Caruso, F. Emerging Methods for the Fabrication of Polymer Capsules. *Adv. Colloid Interface Sci.* **2014,** *207*, 14-31.

14. Peyratout, C. S.; Dahne, L. Tailor-Made Polyelectrolyte Microcapsules: From Multilayers to Smart Containers. *Angew. Chem., Int. Ed.* **2004,** *43*, 3762-3783.

15. Wang, Y.; Angelatos, A. S.; Caruso, F. Template Synthesis of Nanostructured Materials via Layer-by-Layer Assembly. *Chem. Mater.* **2008,** *20*, 848-858.

16. del Mercato, L. L.; Rivera-Gil, P.; Abbasi, A. Z.; Ochs, M.; Ganas, C.; Zins, I.; Sonnichsen, C.; Parak, W. J. LbL Multilayer Capsules: Recent Progress and Future Outlook for Their Use in Life Sciences. *Nanoscale* **2010,** *2*, 458-467.

17. Such, G. K.; Johnston, A. P. R.; Caruso, F. Engineered Hydrogen-Bonded Polymer Multilayers: From Assembly to Biomedical Applications. *Chem. Soc. Rev.* **2011,** *40*, 19-29.

18. Tong, W. J.; Song, X. X.; Gao, C. Y. Layer-by-Layer Assembly of Microcapsules and Their Biomedical Applications. *Chem. Soc. Rev.* **2012,** *41*, 6103-6124.

19. Zhao, S.; Caruso, F.; Dahne, L.; Decher, G.; De Geest, B. G.; Fan, J. C.; Feliu, N.; Gogotsi, Y.; Hammond, P. T.; Hersam, M. C.; Khademhosseini, A.; Kotov, N.; Leporatti, S.; Li, Y.; Lisdat, F.; Liz-Marzan, L. M.; Moya, S.; Mulvaney, P.; Rogach, A. L.; Roy, S.; Shchukin, D.

G.; Skirtach, A. G.; Stevens, M. M.; Sukhorukov, G. B.; Weiss, P. S.; Yue, Z.; Zhu, D. C.; Parak, W. J. The Future of Layer-by-Layer Assembly: A Tribute to ACS Nano Associate Editor Helmuth Mohwald. *ACS Nano* **2019,** *13*, 6151-6169.

20. Antipov, A. A.; Sukhorukov, G. B. Polyelectrolyte Multilayer Capsules as Vehicles with Tunable Permeability. *Adv. Colloid Interface Sci.* **2004,** *111*, 49-61.

21. Sukhishvili, S. A. Responsive Polymer Films and Capsules Via Layer-by-Layer Assembly. *Curr. Opin. Colloid Interface Sci.* **2005,** *10*, 37-44.

22. Johnston, A. P. R.; Cortez, C.; Angelatos, A. S.; Caruso, F. Layer-by-Layer Engineered Capsules and Their Applications. *Curr. Opin. Colloid Interface Sci.* **2006,** *11*, 203-209.

23. Fery, A.; Weinkamer, R. Mechanical Properties of Micro- and Nanocapsules: Single-Capsule Measurements. *Polymer* **2007,** *48*, 7221-7235.

24. Delcea, M.; Mohwald, H.; Skirtach, A. G. Stimuli-Responsive LbL Capsules and Nanoshells for Drug Delivery. *Adv. Drug Delivery Rev.* **2011,** *63*, 730-747.

25. Anselmo, A. C.; Mitragotri, S. Impact of Particle Elasticity on Particle-Based Drug Delivery Systems. *Adv. Drug Delivery Rev.* **2017,** *108*, 51-67.

26. Zyuzin, M. V.; Timin, A. S.; Sukhorukov, G. B. Multilayer Capsules Inside Biological Systems: State-of-the-Art and Open Challenges. *Langmuir* **2019,** *35*, 4747-4762.

27. Decher, G.; Schlenoff, J. B., *Multilayer Thin Films : Sequential Assembly of Nanocomposite Materials*. 2nd ed.; Wiley-VCH: Weinheim, 2012.

28. Caruso, F.; Trau, D.; Mohwald, H.; Renneberg, R. Enzyme Encapsulation in Layer-by-Layer Engineered Polymer Multilayer Capsules. *Langmuir* **2000,** *16*, 1485-1488.

29. De Koker, S.; Hoogenboom, R.; De Geest, B. G. Polymeric Multilayer Capsules for Drug Delivery. *Chem. Soc. Rev.* **2012,** *41*, 2867-2884.

30. Sakr, O. S.; Borchard, G. Encapsulation of Enzymes in Layer-by-Layer (LbL) Structures: Latest Advances and Applications. *Biomacromolecules* **2013,** *14*, 2117-2135.

31. Guo, X.; Manna, U.; Abbott, N. L.; Lynn, D. M. Covalent Immobilization of Caged Liquid Crystal Microdroplets on Surfaces. *ACS Appl. Mater. Interfaces* **2015,** *7*, 26892-26903.

32. Saurer, E. M.; Flessner, R. M.; Buck, M. E.; Lynn, D. M. Fabrication of Covalently Crosslinked and Amine-Reactive Microcapsules by Reactive Layer-by-Layer Assembly of Azlactone-Containing Polymer Multilayers on Sacrificial Microparticle Templates. *J. Mater. Chem.* **2011,** *21*, 1736-1745.

33. Manna, U.; Zayas-Gonzalez, Y. M.; Carlton, R. J.; Caruso, F.; Abbott, N. L.; Lynn, D. M. Liquid Crystal Chemical Sensors That Cells Can Wear. *Angew. Chem., Int. Ed.* **2013,** *52*, 14011-14015.

34. Sher, P.; Custodio, C. A.; Mano, J. F. Layer-by-Layer Technique for Producing Porous Nanostructured 3D Constructs Using Moldable Freeform Assembly of Spherical Templates. *Small* **2010,** *6*, 2644-2648.

35. Silva, J. M.; Georgi, N.; Costa, R.; Sher, P.; Reis, R. L.; Van Blitterswijk, C. A.; Karperien, M.; Mano, J. F. Nanostructured 3D Constructs Based on Chitosan and Chondroitin Sulphate Multilayers for Cartilage Tissue Engineering. *PLoS One* **2013,** *8*, e55451.

36. Paulraj, T.; Feoktistova, N.; Velk, N.; Uhlig, K.; Duschl, C.; Volodkin, D. Microporous Polymeric 3D Scaffolds Templated by the Layer-by-Layer Self-Assembly. *Macromol. Rapid. Commun.* **2014,** *35*, 1408-1413.

37. Volodkin, D.; Arntz, Y.; Schaaf, P.; Moehwald, H.; Voegel, J. C.; Ball, V. Composite Multilayered Biocompatible Polyelectrolyte Films with Intact Liposomes: Stability and Temperature Triggered Dye Release. *Soft Matter* **2008,** *4*, 122-130.

38. Stadler, B.; Chandrawati, R.; Goldie, K.; Caruso, F. Capsosomes: Subcompartmentalizing Polyelectrolyte Capsules Using Liposomes. *Langmuir* **2009,** *25*, 6725-6732.

39. Volodkin, D. V.; Schaaf, P.; Mohwald, H.; Voegel, J. C.; Ball, V. Effective Embedding of Liposomes into Polyelectrolyte Multilayered Films: The Relative Importance of Lipid-Polyelectrolyte and Interpolyelectrolyte Interactions. *Soft Matter* **2009,** *5*, 2009.

40. Hosta-Rigau, L.; Stadler, B.; Yan, Y.; Nice, E. C.; Heath, J. K.; Alberico, F.; Caruso, F. Capsosomes with Multilayered Subcompartments: Assembly and Loading with Hydrophobic Cargo. *Adv. Funct. Mater.* **2010,** *20*, 59-66.

41. Hosta-Rigau, L.; Shimoni, O.; Stadler, B.; Caruso, F. Advanced Subcompartmentalized Microreactors: Polymer Hydrogel Carriers Encapsulating Polymer Capsules and Liposomes. *Small* **2013,** *9*, 3573-3583.

42. Lynge, M. E.; Laursen, M. B.; Hosta-Rigau, L.; Jensen, B. E. B.; Ogaki, R.; Smith, A. A. A.; Zelikin, A. N.; Stadler, B. Liposomes as Drug Deposits in Multilayered Polymer Films. *ACS Appl. Mater. Interfaces* **2013,** *5*, 2967-2975.

43. Acciaro, R. A.; Aulin, C.; Wagberg, L.; Lindstrom, T.; Claesson, P. M.; Varga, I. Investigation of the Formation, Structure and Release Characteristics of Self-Assembled Composite Films of Cellulose Nanofibrils and Temperature Responsive Microgels. *Soft Matter* **2011,** *7*, 1369-1377.

44. Clarke, K. C.; Dunham, S. N.; Lyon, L. A. Core/Shell Microgels Decouple the pH and Temperature Responsivities of Microgel Films. *Chem. Mater.* **2015,** *27*, 1391-1396.

45. Zavgorodnya, O.; Carmona-Moran, C. A.; Kozlovskaya, V.; Liu, F.; Wick, T. M.; Kharlampieva, E. Temperature-Responsive Nanogel Multilayers of Poly(N-Vinylcaprolactam) for Topical Drug Delivery. *J. Colloid Interface Sci.* **2017,** *506*, 589-602.

46. York-Duran, M. J.; Godoy-Gallardo, M.; Labay, C.; Urquhart, A. J.; Andresen, T. L.; Hosta-Rigau, L. Recent Advances in Compartmentalized Synthetic Architectures as Drug Carriers, Cell Mimics and Artificial Organelles. *Colloids Surf. B* **2017,** *152*, 199-213.

47. Huang, X.; Voit, B. Progress on Multi-Compartment Polymeric Capsules. *Polym. Chem.* **2013,** *4*, 435-443.

48. Galanti, A.; Moreno-Tortolero, O.; Azad, R.; Cross, S.; Davis, S.; Gobbo, P. A Floating Mold Technique for the Programmed Assembly of Protocells into Protocellular Materials Capable of Non-Equilibrium Biochemical Sensing. *Adv. Mater.* **2021,** *33*, 2100340.

49. Gobbo, P.; Patil, A. J.; Li, M.; Harniman, R.; Briscoe, W. H.; Mann, S. Programmed Assembly of Synthetic Protocells into Thermoresponsive Prototissues. *Nat. Mater.* **2018,** *17*, 1145-1153.

50. Makhoul-Mansour, M. M.; Freeman, E. C. Droplet-Based Membranous Soft Materials. *Langmuir* **2021,** *37*, 3231-3247.

51. Alferiev, I. S.; Connolly, J. M.; Levy, R. J. A Novel Mercapto-Bisphosphonate as an Efficient Anticalcification Agent for Bioprosthetic Tissues. *J. Organomet. Chem.* **2005,** *690*, 2543-2547.

52. Buck, M. E.; Lynn, D. M. Functionalization of Fibers Using Azlactone-Containing Polymers: Layer-by-Layer Fabrication of Reactive Thin Films on the Surfaces of Hair and Cellulose-Based Materials. *ACS Appl. Mater. Interfaces* **2010,** *2*, 1421-1429.

53. Guo, X.; Carter, M. C. D.; Appadoo, V.; Lynn, D. M. Tunable and Selective Degradation of Amine-Reactive Multilayers in Acidic Media. *Biomacromolecules* **2019,** *20*, 3464-3474.

54. Buck, M. E.; Zhang, J.; Lynn, D. M. Layer-by-Layer Assembly of Reactive Ultrathin Films Mediated by Click-Type Reactions of Poly(2-Alkenyl Azlactone)s. *Adv. Mater.* **2007,** *19*, 3951-3955.

55. Zayas-Gonzalez, Y. M.; Ortiz, B. J.; Lynn, D. M. Layer-by-Layer Assembly of Amine-Reactive Multilayers Using an Azlactone-Functionalized Polymer and Small-Molecule Diamine Linkers. *Biomacromolecules* **2017,** *18*, 1499-1508.

56. Volodkin, D. V.; Petrov, A. I.; Prevot, M.; Sukhorukov, G. B. Matrix Polyelectrolyte Microcapsules: New System for Macromolecule Encapsulation. *Langmuir* **2004,** *20*, 3398-3406.

57. Sukhorukov, G. B.; Volodkin, D. V.; Gunther, A. M.; Petrov, A. I.; Shenoy, D. B.; Mohwald, H. Porous Calcium Carbonate Microparticles as Templates for Encapsulation of Bioactive Compounds. *J. Mater. Chem.* **2004,** *14*, 2073-2081.

58. Lee, Y. L.; Du, Z. C.; Lin, W. X.; Yang, Y. M. Monolayer Behavior of Silica Particles at Air/Water Interface: A Comparison between Chemical and Physical Modifications of Surface. *J. Colloid Interface Sci.* **2006,** *296*, 233-241.

59. Tsai, P. S.; Yang, Y. M.; Lee, Y. L. Fabrication of Hydrophobic Surfaces by Coupling of Langmuir-Blodgett Deposition and a Self-Assembled Monolayer. *Langmuir* **2006,** *22*, 5660-5665.

60. Li, X. M.; Reinhoudt, D.; Crego-Calama, M. What Do We Need for a Superhydrophobic Surface? A Review on the Recent Progress in the Preparation of Superhydrophobic Surfaces. *Chem. Soc. Rev.* **2007,** *36*, 1350-1368.

61. Bhushan, B.; Her, E. K. Fabrication of Superhydrophobic Surfaces with High and Low Adhesion Inspired from Rose Petal. *Langmuir* **2010,** *26*, 8207-17.

62. Jeevahan, J.; Chandrasekaran, M.; Joseph, G. B.; Durairaj, R. B.; Mageshwaran, G. Superhydrophobic Surfaces: A Review on Fundamentals, Applications, and Challenges. *J. Coat. Technol. Res.* **2018,** *15*, 231-250.

63. Broderick, A. H.; Lynn, D. M., Covalent Layer-by-Layer Assembly Using Reactive Polymers. In *Functional Polymers by Post-Polymerization Modification: Concepts, Guidelines, and Applications*, Theato, P.; Klok, H.-A., Eds. Wiley-VCH: Weinheim, 2013; pp 371-406.

64. An, Q.; Huang, T.; Shi, F. Covalent Layer-by-Layer Films: Chemistry, Design, and Multidisciplinary Applications. *Chem. Soc. Rev.* **2018,** *47*, 5061-5098.

Supporting Information for Chapter 9

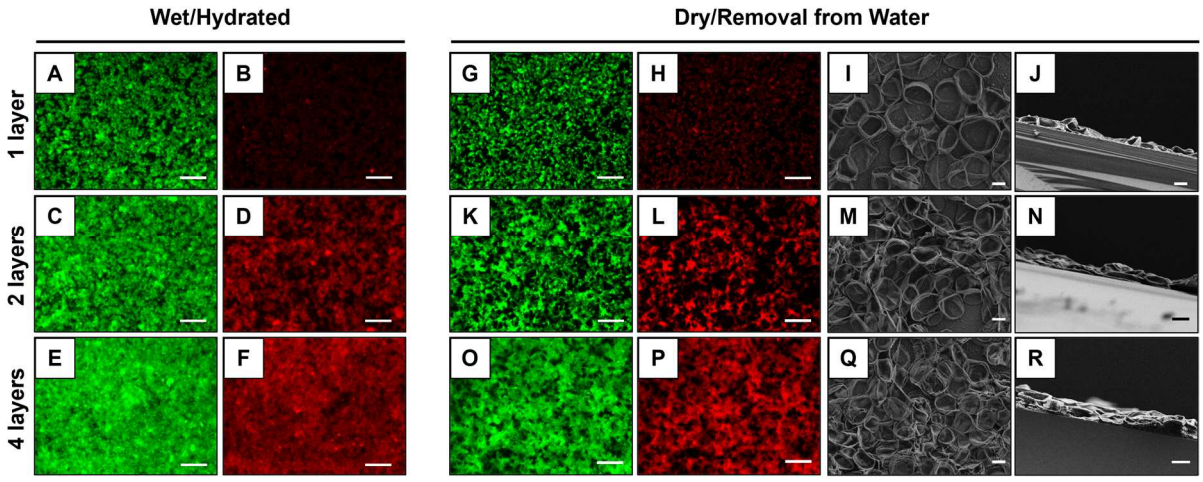


Figure S1: (A-F) Green channel (A,C,E) and red channel (B,D,F) fluorescence microscopy images of (A,B) one-layer, (C,D) two-layer, and (E,F) four-layer assemblies of amine-containing and amine-reactive capsules hydrated in water. (G-R) Green channel (G,K,O) and red channel (H,L,P) fluorescence microscopy images and top-down (I,M,Q) and cross-sectional (J,N,R) SEM images of (G-J) a one-layer, (K-N) two-layer, and (O-R) four-layer assemblies of polymer capsules dehydrated under vacuum. Scale bars are 60 μm (A-P) and 2 μm (I-R).

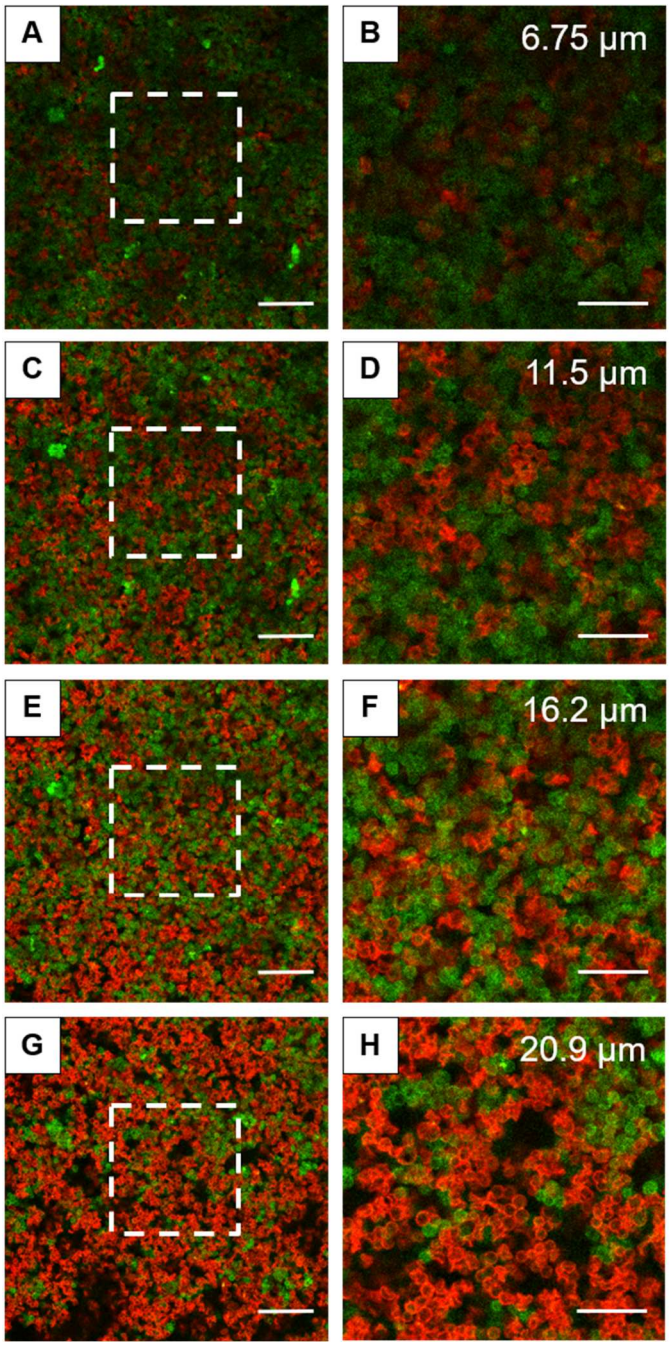


Figure S2: Confocal microscopy images of four-layer capsule assemblies acquired at different *z*-axis locations in the sample at low (A,C,E,G) and high (B,D,F,H) magnifications. The images were acquired at heights of (A,B) 6.75 µm, (C,D) 11.5 µm, (E,F) 16.2 µm, and (G,H) 20.9 µm relative to the lowest *z*-position acquired (approximately the location of the film/glass substrate interface). The dashed squares on the low magnification images indicate the approximate areas shown in the higher magnification images shown to the right. Scale bars represent 50 µm (A, C, E, G) and 25 µm (B, D, F, H).

Chapter 10

Summary and Recommendations for Future Work

Summary and Findings

The work reported in this thesis focused broadly on characterizing and exploiting the behaviors of amphiphilic bacterial quorum-sensing (QS) signals, and products in solution and at interfaces of other soft materials, including lipid bilayers. The work in Chapters 2-5 characterized the behaviors of N-acyl homoserine lactones (AHLs), a class of amphiphilic signaling molecules used by Gram-negative bacteria to coordinate group behaviors, in solution and in contact with lipid bilayers. Chapter 2 demonstrated that long-chained AHLs behave similarly to other amphiphilic compounds with the ability to self-assemble in aqueous solution forming spherical micelles and small unilamellar vesicles based on their molecular structure. Chapter 3 built upon the results of Chapter 2 to characterize interactions of the long-chained AHL 3-oxo-C12-AHL and its head-group hydrolysis product 3-oxo-C12-HS with lipid bilayers and demonstrated that these interactions can promote large-scale membrane reformation in the form of extended microtubules and hemispherical caps on the surface of the bilayers in ways that are controlled, at least in part, by the timescales over which AHLs translocate across the bilayer. Chapter 4 further investigated the interactions of structurally diverse, naturally occurring AHLs with lipid bilayers, and demonstrated that the presence of a single 3-oxo group in the tail of an AHL changes the type of remodeling observed on the surface of the bilayer, while the tail length of an AHL impacts the extent of those reformations. Finally, in Chapter 5 we explored the interactions of AHLs with multicomponent lipid bilayers containing cholesterol and glycerophospholipids with different head groups. Our results suggested that the type and extent of observed bilayer reformations depend heavily on bilayer composition. The results of Chapters 2-5 provide insight into the potential roles that long-chained AHLs may play in bacterial communities, including signal transport mechanisms, interkingdom signaling and control over host cell response. Additionally,

these results also provide guidance that could prove useful for the future development and design of synthetic self-assembled materials that selectively respond to bacterial amphiphiles in ways that are useful in the context of sensing and drug delivery and in other fundamental and applied contexts.

Chapters 6 and 7 of this thesis focused on approaches to controlling virulent behaviors in bacterial communities by exploiting and improving upon chemical tools that inhibit bacterial QS and developing methods to improve the ability of potent QS inhibitors to improve infection outcomes *in vivo*. Chapter 6 used the knowledge gained in the previous chapters about interactions of bacterial QS products with lipids to develop a lipid-based fluorescent sensor of bacterial virulence. This sensing platform was shown to selectively respond to bacterial communities that are actively engaged in bacterial communication and, by extension, to bacteria with QS systems that had been inhibited using chemical tools. These sensors were then used in a high-throughput screen that resulted in the discovery of two new potent compounds that inhibit *S. aureus* QS. In Chapter 7, potent peptide-based inhibitors of *S. aureus* QS were demonstrated to be effective at controlling bacterial virulence *in vivo* both through direct administration to a murine dermonecrosis abscess model and using strategies for the controlled release of this inhibitor from PLG microparticles. That work demonstrated the ability of a controlled release strategy to better control bacterial virulence as compared to a single-dose administration of a QS inhibitor and provides a blueprint for developing future formulations that control virulent bacterial behaviors in other pathogens.

Finally, Chapters 8 and 9 focused on using many of the microscopy techniques described in Chapters 2-7 to analyze both natural and synthetic soft materials systems. Chapter 8 investigated the relationship between lipid bilayer stability and membrane remodeling observed as a response

to the adsorption and aggregation of alpha-synuclein, a protein related to Parkinson's disease, on lipid vesicles. Chapter 9 described the design and characterization of a new soft-material coating platform consisting of interconnected networks of hollow and compartmentalized microcapsules with potential applications in catalysis and controlled release. The remainder of this chapter will describe potential future areas for continued research in these areas, including additional experimental techniques and potential applications of the work described here.

Recommendations for Future Work

The studies described in Chapters 2-6 provided insights into the behaviors of AHLs in solution and in contact with lipid bilayers. These insights included: (i) long-tailed, naturally occurring AHLs self-assemble in aqueous solution to form spherical micelles or extended bilayer vesicles, (ii) an array of naturally-occurring,[1] structurally diverse AHLs are able to interact with lipid membranes in ways that lead to large-scale membrane restructuring in the form of extended tubules or hemispherical caps, (iii) the type and extent of the restructuring observed is correlated to the timescale on which an AHL or other surfactant-like molecule is able to translocate across the bilayer, in a mechanism that is driven largely by asymmetrical bilayer stresses,[2, 3] and (iv) the concentration of AHLs found naturally in communities of bacteria are sufficient to promote large-scale membrane restructuring in lipid bilayers. In the following section, additional characterization techniques and potential research projects that either build upon or stem from the insights described above will be discussed. These projects primarily focus on the characterization of the interaction of AHLs with model bilayers that better approximate the structure and composition of mammalian cells and ways these interactions can be exploited for the development of soft materials.

Additional methods or techniques for characterizing the interaction of AHLs with membranes

The model membranes used in this thesis were symmetric bilayers composed of either one or two lipid components. The bilayers of living systems (e.g., mammalian cells) are far more complex than these model systems, containing a wide variety of lipid species and membrane-associated proteins that are asymmetrically distributed between the leaflets of the bilayer.[4, 5] One interesting avenue for further research would involve continuing to characterize interactions of AHLs with membranes of increasing complexity. In principle it should be possible to design experiments in which mammalian cells with fluorescently-labeled membranes could be placed in contact with exogenous AHLs or bacterial supernatants to observe the membrane restructuring that could occur. While these experiments could provide useful insight into *in vitro* interactions of AHLs and host cells, it may prove difficult to decouple many of the biological interactions of AHLs with mammalian cells that have been previously described[6, 7] from the physical interactions that could results from contact of AHLs with the lipids that compose cellular membranes. Therefore, there it would be useful to continue to develop and characterize model membrane systems that better approximate the complexity and membrane composition of mammalian or other host organism cells.

In previous reports, an emulsion-based method was used for the formation of asymmetrical giant unilamellar vesicles (GUVs).[8] These bilayers present an opportunity to understand the impacts of lipid asymmetry and associated bilayer stresses on modulating the interactions of AHLs (or more, generally, any surfactant-like species) with bilayers. GUV-based systems could also be useful for probing changes in membrane fluidity, rigidity, and curvature upon introduction to AHLs, further exploring the outcomes of these complex interactions.[9, 10] Additionally, there are an

increasing number of methods available to produce SLBs from mammalian membrane fragments (e.g., membrane vesicles or cellular blebs) as a more realistic model for host-cell membranes both in lipid and associated protein composition.[11-15] In past studies, these membrane fragments were combined with synthetic vesicles to promote adsorption and rupture on a substrate.[11-15] These SLBs were shown to maintain lipid compositions similar to that of the parent membrane and functional transmembrane proteins could subsequently be studied. SLBs produced from membrane fragments provide a unique opportunity to study the physical interactions of AHLs and mammalian cell membranes in ways that could be decoupled from other, more complex biological interactions noted above.[6, 16-18] Beyond the biological implications of these experiments, expanding the library of lipids available to be used in model lipid systems allows the characterization of the fundamental interactions between bacterial signaling molecules and lipid membranes to inform future materials design.

All the experiments described above expand the lipid compositions available to be used in fluorescence microscopy or QCM-D experiments, two techniques that were leveraged heavily in this thesis. Beyond fluorescense microscopy and QCM-D, there are several additional techniques that could prove useful for characterizing the interactions of AHLs and lipid bilayers. Each of these techniques and a brief description of how they could be used are provided below:

Cryo-TEM: In a set of preliminary experiments, we imaged solutions of large unilamellar vesicles (LUVs) in contact with 3-oxo-C12-AHL using negative-stained TEM and observed the formation of hemispherical buds and tubules on the vesicles. These experiments were difficult to reproduce in part due to the dehydration process involved with negative stain TEM destabilizing the vesicles. In future experiments, it should be possible to use cryo-TEM to

image these reformations as these samples remain hydrated, and likely undisturbed throughout the sample preparation and imaging process, to give insights into how membrane curvature plays roles in the membrane restructuring described here and provide mechanistic insight into calcein leakage from vesicles as observed in Chapters 2-5 of this thesis.[19, 20]

Isothermal titration calorimetry (ITC): Previous reports have described numerous experimental procedures in which ITC can be used to measure free energy changes associated with surfactants partitioning into or dissociating from a lipid bilayer.[21] These measurements would allow for the experimental determination of the free energy of an AHL associating to a lipid bilayer that could subsequently be compared to the predictions made by MD simulations in Chapters 2 this thesis and in the literature.[22] Additionally, ITC could provide additional information about the propensity of an AHL to translocate across the bilayer.

Localized surface plasmon resonance (LSPR): Reports have demonstrated the ability to simultaneously perform QCM-D and LSPR measurements.[23] LSPR is a complimentary technique to QCM-D that additionally allows for the determination the optical mass of adsorbed analytes,[24] the proximity of the bilayer to an underlying surface[24, 25] and additional information about the reformations observed in bilayers upon interaction with analytes.[26] This additional information could prove useful in future studies of the interactions of AHLs and the complex bilayers described above.

Potential applications stemming from the interactions of AHLs with bilayers

While the studies described in Chapters 2-6 of this thesis have many potential biological implications related to roles that AHLs may play beyond bacterial signaling, they could also be used to inform the development of new synthetic functional materials for sensing, drug delivery, or other applications. For example, the correlation between the type of bilayer reformation observed in SLBs upon contact with surfactants (e.g., formation tubules or hemispherical caps) and the ability of that surfactant to translocate across bilayers could, with further development, be used as a tool to characterize the relative timescales on which amphiphilic translocation occurs. In some exploratory experiments not discussed in depth here, there appears to be a strong correlation between previously reported timescales of surfactant translocation and the relative time it takes tubules to transform into hemispherical caps. Therefore, with additional experimental rigor, it could be feasible to determine relative timescales and, by extension, rate constants for the translocation of surfactants across lipid bilayers. Additionally, these optical microscopy measurements could be combined with machine-learning algorithms to more accurately determine the timescales on which tubule-to-capsule transitions occur and calculate timescales of translocation.

Beyond potential applications in sensing and monitoring, there are a number of other ways that the interactions of AHLs with bilayers could potentially be exploited for the development of functional materials. Results presented in this thesis and the literature suggest that AHLs are able to translocate across lipid bilayers.[27] As a result, it is possible to envision using lipid bilayers as semipermeable membranes for separating AHLs from, or detecting AHLs in, complex mixtures of natural and synthetic small-molecule amphiphiles and proteins such as those found in bacterial cultures or host fluids and tissues for selective detection or sequestration. Additionally, the

dynamic nature of the hydrolysable head groups of AHLs,[28] and associated changes in physicochemical properties, could be exploited through additional characterization and judicious choice of other natural or synthetic co-amphiphiles to develop materials that could be disrupted, change phase, or release cargo upon AHL head group hydrolysis, either over time or as a response to environmental stimuli such as pH or contact with enzymes that degrade the AHL head group.[28,29]

Expanding the vesicle lysis test to screen for inhibitors of a broad range of bacterial species

The work presented in Chapter 6 focused on developing a general lipid-based platform for sensing the inhibition of bacterial virulence that we then applied to two model bacterial species (*S. aureus* and *P. aeruginosa*). While we were able to use this materials platform to screen for novel inhibitors of *S. aureus* QS, the smaller differences in solution fluorescence observed between wild type *P. aeruginosa* cultures in the absence or presence of QS inhibitors made similar high-throughput screens more difficult. This is due, at least in part, to the complex architecture of *P. aeruginosa* QS pathways, which include multiple, interconnecting QS circuits, each with their own unique ligands and cognate receptors.[30] In a set of preliminary experiments, it was observed that the addition of LasR inhibitors to a *ΔrhlR* bacterial mutant increased the sensitivity of the vesicle lysis test (VLT) to these compounds when compared to the wild-type strain, demonstrating that the inhibition of multiple QS loops simultaneously better inhibits virulent behaviors in *P. aeruginosa*. This suggests that combinations of known QS inhibitors could be used to suppress multiple QS circuits, while retaining activity in others that could be subjected to high-throughput screening. This strategy could be used to perform high-throughput screens for compounds that inhibit the RhlR system in *P. aeruginosa*, a current challenge in the anti-virulence field.[31]

Additionally, the VLT could be expanded to screen for QS inhibitors of other bacterial species that produce amphiphilic products under the control of QS. As previously discussed in Chapter 7 of this thesis, this assay allows for detection of QS activity without the need to produce a genetically modified GFP/YFP reporter strain and can even be used with extracted clinical isolates, increasing the rate at which compound discovery can occur. Due to the relatively simple architecture of *agr* and *agr*-like QS systems, bacteria that use these systems to produce amphiphilic virulence factors would be a next logical step in additional studies.[1] For example, the gram-positive species *Staphylococcus epidermis* produces phenol soluble modulins under the control of the *agr* system and is therefore a likely candidates for high-throughput screens for novel QS inhibitors using the VLT assay.[32, 33] Additionally, four of the ESKAPE pathogens, six organisms that are highly virulent and antibiotic resistant (two of which are studied in Chapter 6), produce amphiphilic virulence factors under the control of QS and could be screened for new small-molecule inhibitors of bacterial QS as antibiotic resistance in these bacterial species continues to become more prevalent.[34-36]

Future work exploring the feasibility of anti-virulence approaches for murine wound healing

The work described in Chapter 7 of this thesis provides an approach to regulating or attenuating virulence in communities of bacteria and provides a framework for the development of approaches that could offer alternatives to common antibiotics. While this proof-of-concept study only demonstrated the inhibition of *S. aureus* virulence, the strategy of loading and releasing of QS inhibitors from polymeric materials can be expanded to other virulent bacterial species. For example, the Blackwell lab at UW-Madison has developed potent peptide-based inhibitors of QS in *S. epidermis* that have similar structures to the peptides used in Chapter 7, suggesting they could

be incorporated into polymeric materials for the attenuation of bacterial virulence *in vivo*.[37] The approach described in Chapter 7 also allows for the timescales on which QS inhibitors are released to be controlled through judicious choice of polymers with different degradation or dissolution rates.[38] Additionally, other fabrication procedures can be used to tailor the geometry of a controlled release platform to be compatible with other *in vivo* wound models or on the surface of implantable devices.[39, 40] Additionally, the versatility of many controlled release platforms allow for the co-encapsulation and simultaneous or staged release of two or more active agents. This presents the potential for synergistic control over bacterial infection through the release of anti-virulence agents and growth inhibitors either simultaneously or sequentially, or the ability to inhibit QS in multiple bacterial species through a single administration of polymer microparticles.

References

1. Miller, M. B.; Bassler, B. L., Quorum sensing in bacteria. *Annu. Rev. Microbiol.* **2001,** *55*, 165-199.

2. Staykova, M.; Arroyo, M.; Rahimi, M.; Stone, H. A., Confined Bilayers Passively Regulate Shape and Stress. *Phys. Rev. Lett.* **2013,** *110* (2), 028101.

3. Yoon, B. K.; Jackman, J. A.; Kim, M. C.; Cho, N. J., Spectrum of Membrane Morphological Responses to Antibacterial Fatty Acids and Related Surfactants. *Langmuir* **2015,** *31* (37), 10223-10232.

4. Rothman, J. E.; Lenard, J., Membrane Asymmetry. *Science* **1977,** *195* (4280), 743-753.

5. Spector, A. A.; Yorek, M. A., Membrane Lipid-Composition And Cellular Function. *J. Lipid Res.* **1985,** *26* (9), 1015-1035.

6. Telford, G.; Wheeler, D.; Williams, P.; Tomkins, P. T.; Appleby, P.; Sewell, H.; Stewart, G.; Bycroft, B. W.; Pritchard, D. I., The Pseudomonas aeruginosa quorum-sensing signal molecule N-(3-oxododecanoyl)-1-homoserine lactone has immunomodulatory activity. *Infect. Immun.* **1998,** *66* (1), 36-42.

7. Tao, S. Y.; Luo, Y. W.; He, B.; Liu, J.; Qian, X.; Ni, Y. D.; Zhao, R. Q., Paraoxonase 2 modulates a proapoptotic function in LS174T cells in response to quorum sensing molecule N-(3-oxododecanoyl)-L-homoserine lactone. *Sci. Rep.* **2016,** *6*, 28778.

8. Pautot, S.; Frisken, B. J.; Weitz, D. A., Engineering asymmetric vesicles. *Proc. Natl. Acad. Sci. U. S. A.* **2003,** *100* (19), 10718-10721.

9. Dimova, R., Giant Vesicles and Their Use in Assays for Assessing Membrane Phase State, Curvature, Mechanics, and Electrical Properties. *Annu. Rev. Biophys.* **2019,** *48*, 93-119.

10. Dimova, R.; Marques, C. M., The Giant Vesicle Book. 1 ed.; CRC Press: Boca Raton, 2019; pp 1-676.

11. Pace, H.; Nystrom, L. S.; Gunnarsson, A.; Eck, E.; Monson, C.; Geschwindner, S.; Snijder, A.; Hook, F., Preserved Transmembrane Protein Mobility in Polymer-Supported Lipid Bilayers Derived from Cell Membranes. *Anal. Chem.* **2015,** *87* (18), 9194-9203.

12. Richards, M. J.; Hsia, C. Y.; Singh, R. R.; Haider, H.; Kumpf, J.; Kawate, T.; Daniel, S., Membrane Protein Mobility and Orientation Preserved in Supported Bilayers Created Directly from Cell Plasma Membrane Blebs. *Langmuir* **2016,** *32* (12), 2963-2974.

13. Pace, H. P.; Hannestad, J. K.; Armonious, A.; Adamo, M.; Agnarsson, B.; Gunnarsson, A.; Micciulla, S.; Sjovall, P.; Gerelli, Y.; Hook, F., Structure and Composition of Native Membrane Derived Polymer-Supported Lipid Bilayers. *Anal. Chem.* **2018,** *90* (21), 13065-13072.

14. Pappa, A. M.; Liu, H. Y.; Traberg-Christensen, W.; Thiburce, Q.; Savva, A.; Pavia, A.; Salleo, A.; Daniel, S.; Owens, R. M., Optical and Electronic Ion Channel Monitoring from Native Human Membranes. *ACS Nano* **2020,** *14* (10), 12538-12545.

15. Su, H.; Liu, H. Y.; Pappa, A. M.; Hidalgo, T. C.; Cavassin, P.; Inal, S.; Owens, R. M.; Daniel, S., Facile Generation of Biomimetic-Supported Lipid Bilayers on Conducting Polymer Surfaces for Membrane Biosensing. *ACS Appl. Mater. Interfaces* **2019,** *11* (47), 43799-43810.

16. Davis, B. M.; Jensen, R.; Williams, P.; O'Shea, P., The Interaction of N-Acylhomoserine Lactone Quorum Sensing Signaling Molecules with Biological Membranes: Implications for Inter-Kingdom Signaling. *PLoS One* **2010,** *5* (10), e13522.

17. Tao, S. Y.; Luo, Y. W.; He, B.; Liu, J.; Qian, X.; Ni, Y. D.; Zhao, R. Q., Paraoxonase 2 modulates a proapoptotic function in LS174T cells in response to quorum sensing molecule N-(3-oxododecanoyl)-L-homoserine lactone. *Sci. Rep.* **2016,** *6*.

18. Song, D. K.; Meng, J. C.; Cheng, J.; Fan, Z.; Chen, P. Y.; Ruan, H. F.; Tu, Z. Y.; Kang, N.; Li, N.; Xu, Y.; Wang, X. B.; Shi, F.; Mu, L. B.; Li, T. F.; Ren, W. R.; Lin, X.; Zhu, J.; Fang, X. H.; Amrein, M. W.; Wu, W. H.; Yan, L. T.; Lu, J. H.; Xia, T.; Shi, Y., Pseudomonas aeruginosa quorum-sensing metabolite induces host immune cell death through cell surface lipid domain dissolution. *Nat. Microbiol.* **2019,** *4* (1), 97-111.

19. Heerklotz, H., Interactions of surfactants with lipid membranes. *Q. Rev. Biophys.* **2008,** *41* (3-4), 205-264.

20. Almgren, M., Mixed micelles and other structures in the solubilization of bilayer lipid membranes by surfactants. *Biochim. Biophys. Acta, Biomembr.* **2000,** *1508* (1-2), 146-163.

21. Heerklotz, H.; Seelig, J., Titration calorimetry of surfactant-membrane partitioning and membrane solubilization. *Biochim. Biophys. Acta, Biomembr.* **2000,** *1508* (1-2), 69-85.

22. Jin, T.; Patel, S. J.; Van Lehn, R. C., Molecular simulations of lipid membrane partitioning and translocation by bacterial quorum sensing modulators. *PLoS One* **2021,** *16* (2), e0246187.

23. Jonsson, M. P.; Jonsson, P.; Hook, F., Simultaneous Nanoplasmonic and Quartz Crystal Microbalance Sensing: Analysis of Biomolecular Conformational Changes and Quantification of the Bound Molecular Mass. *Anal. Chem.* **2008,** *80* (21), 7988-7995.

24. Ferhan, A. R.; Jackman, J. A.; Cho, N. J., Probing Spatial Proximity of Supported Lipid Bilayers to Silica Surfaces by Localized Surface Plasmon Resonance Sensing. *Anal. Chem.* **2017,** *89* (7), 4301-4308.

25. Ferhan, A. R.; Spackova, B.; Jackman, J. A.; Ma, G. J.; Sut, T. N.; Homola, J.; Cho, N. J., Nanoplasmonic Ruler for Measuring Separation Distance between Supported Lipid Bilayers and Oxide Surfaces. *Anal. Chem.* **2018,** *90* (21), 12503-12511.

26. Yoon, B. K.; Park, H.; Zhdanov, V. P.; Jackman, J. A.; Cho, N. J., Real-time nanoplasmonic sensing of three-dimensional morphological changes in a supported lipid bilayer and antimicrobial testing applications. *Biosens. Bioelectron.* **2021,** *174* (14), 112768.

27. Lentini, R.; Martin, N. Y.; Forlin, M.; Belmonte, L.; Fontana, J.; Cornella, M.; Martini, L.; Tamburini, S.; Bentley, W. E.; Jousson, O.; Mansy, S. S., Two-Way Chemical Communication between Artificial and Natural Cells. *ACS Cent. Sci.* **2017,** *3* (2), 117-123.

28. Yates, E. A.; Philipp, B.; Buckley, C.; Atkinson, S.; Chhabra, S. R.; Sockett, R. E.; Goldner, M.; Dessaux, Y.; Camara, M.; Smith, H.; Williams, P., N-acylhomoserine Lactones undergo lactonolysis in a pH-, temperature-, and acyl chain length-dependent manner during growth of Yersinia pseudotuberculosis and Pseudomonas aeruginosa. *Infect. Immun.* **2002,** *70* (10), 5635-5646.

29. Wang, L. H.; Weng, L. X.; Dong, Y. H.; Zhang, L. H., Specificity and enzyme kinetics of the quorum-quenching N-acyl homoserine lactone lactonase (AHL-lactonase). *J. Biol. Chem.* **2004,** *279* (14), 13645-13651.

30. de Kievit, T. R., Quorum sensing in Pseudomonas aeruginosa biofilms. *Environ. Microbiol.* **2009,** *11* (2), 279-288.

31. Boursier, M. E.; Combs, J. B.; Blackwell, H. E., N-Acyl L-Homocysteine Thiolactones Are Potent and Stable Synthetic Modulators of the RhlR Quorum Sensing Receptor in Pseudomonas aeruginosa. *ACS Chem. Biol.* **2019,** *14* (2), 186-191.

32. Vuong, C.; Durr, M.; Carmody, A. B.; Peschel, A.; Klebanoff, S. J.; Otto, M., Regulated expression of pathogen-associated molecular pattern molecules in Staphylococcus epidermidis: quorum-sensing determines pro-inflammatory capacity and production of phenol-soluble modulins. *Cell. Microbiol.* **2004,** *6* (8), 753-759.

33. Otto, M., Phenol-soluble modulins. *Int. J. Med. Microbiol.* **2014,** *304* (2), 164-169.

34. Boucher, H. W.; Talbot, G. H.; Bradley, J. S.; Edwards, J. E.; Gilbert, D.; Rice, L. B.; Scheld, M.; Spellberg, B.; Bartlett, J., Bad bugs, no drugs: no ESKAPE! An update from the Infectious Diseases Society of America. *Clin. Infect. Dis.* **2009,** *48* (1), 1-12.

35. Sarafzadeh, P.; Hezave, A. Z.; Ravanbakhsh, M.; Niazi, A.; Ayatollahi, S., Enterobacter cloacae as biosurfactant producing bacterium: differentiating its effects on interfacial tension and wettability alteration Mechanisms for oil recovery during MEOR process. *Colloids Surf., B* **2013,** *105*, 223-229.

36. Sharma, D.; Saharan, B. S.; Chauhan, N.; Procha, S.; Lal, S., Isolation and functional characterization of novel biosurfactant produced by Enterococcus faecium. *Springerplus* **2015,** *4* (1), 4.

37. Yang, T.; Tal-Gan, Y.; Paharik, A. E.; Horswill, A. R.; Blackwell, H. E., Structure-Function Analyses of a *Staphylococcus epidermidis* Autoinducing Peptide Reveals Motifs Critical for AgrC-type Receptor Modulation. *ACS Chem. Biol.* **2016,** *11* (7), 1982-1991.

38. Uhrich, K. E.; Cannizzaro, S. M.; Langer, R. S.; Shakesheff, K. M., Polymeric systems for controlled drug release. *Chem. Rev.* **1999,** *99* (11), 3181-3198.

39. Kamaly, N.; Yameen, B.; Wu, J.; Farokhzad, O. C., Degradable Controlled-Release Polymers and Polymeric Nanoparticles: Mechanisms of Controlling Drug Release. *Chem. Rev.* **2016,** *116* (4), 2602-2663.

40. Lu, Y.; Chen, S. C., Micro and nano-fabrication of biodegradable polymers for drug delivery. *Adv. Drug Delivery Rev.* **2004,** *56* (11), 1621-1633.